energies

Smart Energy Management for Microgrid and Photovoltaic Systems

Edited by
V Indra Gandhi

Printed Edition of the Special Issue Published in *Energies*

www.mdpi.com/journal/energies

MDPI

Smart Energy Management for Microgrid and Photovoltaic Systems

Smart Energy Management for Microgrid and Photovoltaic Systems

Editor

V Indra Gandhi

MDPI • Basel • Beijing • Wuhan • Barcelona • Belgrade • Manchester • Tokyo • Cluj • Tianjin

Editor
V Indra Gandhi
School of Electrical
Engineering
Vellore Institute of
Technology
Vellore
India

Editorial Office
MDPI
St. Alban-Anlage 66
4052 Basel, Switzerland

This is a reprint of articles from the Special Issue published online in the open access journal *Energies* (ISSN 1996-1073) (available at: www.mdpi.com/journal/energies/special_issues/Smart_Energy_Management_Microgrid_Photovoltaic_Systems).

For citation purposes, cite each article independently as indicated on the article page online and as indicated below:

LastName, A.A.; LastName, B.B.; LastName, C.C. Article Title. *Journal Name* **Year**, *Volume Number*, Page Range.

ISBN 978-3-0365-6719-8 (Hbk)
ISBN 978-3-0365-6718-1 (PDF)

© 2023 by the authors. Articles in this book are Open Access and distributed under the Creative Commons Attribution (CC BY) license, which allows users to download, copy and build upon published articles, as long as the author and publisher are properly credited, which ensures maximum dissemination and a wider impact of our publications.
The book as a whole is distributed by MDPI under the terms and conditions of the Creative Commons license CC BY-NC-ND.

Contents

Subramanian Vasantharaj, Vairavasundaram Indragandhi, Mohan Bharathidasan and Belqasem Aljafari
Power Quality Analysis of a Hybrid Microgrid-Based SVM Inverter-Fed Induction Motor Drive with Modulation Index Diversification
Reprinted from: *Energies* **2022**, *15*, 7916, doi:10.3390/en15217916 . . . . . **1**

Ingilala Jagadeesh and Vairavasundaram Indragandhi
Comparative Study of DC-DC Converters for Solar PV with Microgrid Applications
Reprinted from: *Energies* **2022**, *15*, 7569, doi:10.3390/en15207569 . . . . . **23**

Belqasem Aljafari, Subramanian Vasantharaj, Vairavasundaram Indragandhi and Rhanganath Vaibhav
Optimization of DC, AC, and Hybrid AC/DC Microgrid-Based IoT Systems: A Review
Reprinted from: *Energies* **2022**, *15*, 6813, doi:10.3390/en15186813 . . . . . **45**

Belqasem Aljafari, Ashok Kumar Loganathan, Indragandhi Vairavasundaram, Selvamathi Ramachadran and Amutha Prabha Nagarajan
Analysis of a Photovoltaic System Based on a Highly Efficient Single-Phase Transformerless Inverter
Reprinted from: *Energies* **2022**, *15*, 6145, doi:10.3390/en15176145 . . . . . **75**

Belqasem Aljafari, Senthil Kumar Ramu, Gunapriya Devarajan and Indragandhi Vairavasundaram
Integration of Photovoltaic-Based Transformerless High Step-Up Dual-Output–Dual-Input Converter with Low Power Losses for Energy Storage Applications
Reprinted from: *Energies* **2022**, *15*, 5559, doi:10.3390/en15155559 . . . . . **95**

Belqasem Aljafari, Kanagavel Rameshkumar, Vairavasundaram Indragandhi and Selvamathi Ramachandran
A Novel Single-Phase Shunt Active Power Filter with a Cost Function Based Model Predictive Current Control Technique
Reprinted from: *Energies* **2022**, *15*, 4531, doi:10.3390/en15134531 . . . . . **115**

Yu-Jie Hu, Lishan Yang, Fali Duan, Honglei Wang and Chengjiang Li
A Scientometric Analysis and Review of the Emissions Trading System
Reprinted from: *Energies* **2022**, *15*, 4423, doi:10.3390/en15124423 . . . . . **133**

V. Mounica and Y. P. Obulesu
Hybrid Power Management Strategy with Fuel Cell, Battery, and Supercapacitor for Fuel Economy in Hybrid Electric Vehicle Application
Reprinted from: *Energies* **2022**, *15*, 4185, doi:10.3390/en15124185 . . . . . **153**

Kiran Kumar Geddam and Elangovan Devaraj
Real Time Hardware-in-Loop Implementation of LLC Resonant Converter at Worst Operating Point Based on Time Domain Analysis
Reprinted from: *Energies* **2022**, *15*, 3634, doi:10.3390/en15103634 . . . . . **179**

Belqasem Aljafari, Jasmin Pamela Stephenraj, Indragandhi Vairavasundaram and Raja Singh Rassiah
Steady State Modeling and Performance Analysis of a Wind Turbine-Based Doubly Fed Induction Generator System with Rotor Control
Reprinted from: *Energies* **2022**, *15*, 3327, doi:10.3390/en15093327 . . . . . **199**

energies

Article

Power Quality Analysis of a Hybrid Microgrid-Based SVM Inverter-Fed Induction Motor Drive with Modulation Index Diversification

Subramanian Vasantharaj [1], Vairavasundaram Indragandhi [1,*], Mohan Bharathidasan [1] and Belqasem Aljafari [2]

[1] School of Electrical Engineering, Vellore Institute of Technology, Vellore 632 014, India
[2] Department of Electrical Engineering, Najran University, Najran 11001, Saudi Arabia
* Correspondence: indragandhi.v@vit.ac.in

Abstract: The effects of varying modulation indices on the current and voltage harmonics of an induction motor (IM) powered by a three-phase space vector pulse-width modulation (SVM) inverter are presented in this research. The effects were examined using simulation and an experimental setup. IMs can be governed by an SVM inverter drive or a phase-angle control drive for applications that require varying speeds. The analysis of THD content in this study used the modulation index (MI), whose modification affects the harmonic content, and voltage-oriented control (VOC) with SVM in three-phase pulse-width modulation (PWM) inverters with fixed switching frequencies. The control technique relies on two cascaded feedback loops, one controlling the grid current and the other regulating the dc-link voltage to maintain the required level of dc-bus voltage. The control strategy was developed to transform between stationary (α–β) and synchronously rotating (d–q) coordinate systems. To test the viability of the suggested control technique, a 1-hp/3-phase/415-V experimental prototype system built on the DSPACE DS1104 platform was created, and the outcomes were evaluated with sinusoidal pulse-width modulation (SPWM).

Keywords: induction motor drive; dc-link voltage balancing; space vector modulation; switching loss; total harmonic distortion

Citation: Vasantharaj, S.; Indragandhi, V.; Bharathidasan, M.; Aljafari, B. Power Quality Analysis of a Hybrid Microgrid-Based SVM Inverter-Fed Induction Motor Drive with Modulation Index Diversification. *Energies* **2022**, *15*, 7916. https://doi.org/10.3390/en15217916

Academic Editor: Adolfo Dannier

Received: 25 September 2022
Accepted: 21 October 2022
Published: 25 October 2022

Publisher's Note: MDPI stays neutral with regard to jurisdictional claims in published maps and institutional affiliations.

Copyright: © 2022 by the authors. Licensee MDPI, Basel, Switzerland. This article is an open access article distributed under the terms and conditions of the Creative Commons Attribution (CC BY) license (https://creativecommons.org/licenses/by/4.0/).

1. Introduction

Electric motors are used in many driving components worldwide, accounting for 40% to 50% of all electricity demand [1]. Seventy percent of the electricity needed to run industrial loads is provided by three-phase IMs [2]. Due to their appealing qualities, such as low cost, straightforward design, excellent reliability, and ease of maintenance, electric motor sales have climbed to 85% [3–5]. Although direct current (DC) motors are frequently seen in applications involving variable speed operations because of how simple it is to control torque and field flux with armature and field current, these motors possess the drawback of having a commutator and brushes that could cause corrosion and necessitate regular maintenance [6]. Due to their high output power, toughness, robustness, efficiency, affordability, capacity to tolerate hazardous or severe working situations, and ruggedness, IMs do not experience DC motor difficulties [7]. The abrupt variation in load, which uses a significant amount of electricity and raises the cost of energy, impacts the functioning of three-phase IMs [8]. To regulate speed and preserve high efficiency, a variable speed drive (VSD) may be employed [9]. Moreover, the controller and switching technique employed in VSD significantly impact the achievability of high efficiency and reliability for IMs [10,11]. Pulse-width modulation (PWM) techniques are often used to control the switches of voltage source inverters (VSIs), as well as the frequency and output voltage of IMs [12]. One of the better approaches for VSI is the SVM switching approach, which has reduced switching losses and the capacity to reduce the harmonic output signals generated by inverters [13].

Recent studies have proposed several control techniques for PWM rectifiers to enhance the input power factor and transform the input current into a sinusoidal waveform. Numerous PWM modulation techniques are in use, including sinusoidal PWM and the space vector method. Technically, the SVM methodology is the optimal modulation method overall. Compared to the conventional PWM approach, the harmonic distortion of current decreases with the SVM. The duty cycles of VSI switches have been determined via the SVM, using the space vector concept. The only things to have been digitally implemented are PWM modulators. The possibility of straightforward digital implementation and a large linear modulation range for line-to-line voltages are the distinguishing features of SVM. Despite the SVPWM technique's benefits over PWM, new techniques are continually being developed. The main objective [14] has been to find efficient methods to provide output voltages with low harmonic rates and less switch-level loss.

The voltage-oriented control (VOC) algorithm, which is well known among indirect power control algorithms that use current controllers and is equivalent to the field-oriented control (FOC) of the IM, is able to generate high dynamic and static performance by using internal current control loops and an outer voltage control loop. The basis of VOC is the orientation of the rotating synchronous reference frame with respect to the grid line voltage vector. The suggested VOC approach exhibits highly dynamic behavior, suitable output voltage, and a low input current THD [15,16].

The proper operation of the control system has generally been hampered by the hardware execution of the IM drive controller. Digital signal processors (DSPs) and field programmable gate arrays (FPGAs) are two integrated circuits that have been used extensively in control platforms [17,18]. Implementing a user-friendly control unit for online supervision and monitoring is now possible due to the presence of a graphical object-oriented package (Control Desk software) on a dSPACE system. The automation and automotive sectors both use the dSPACE system, which is extremely popular among controlling platforms. The development of PV standalone inverters uses the dSPACE system as a control platform as an additional application area. In this study, the SVM control method is demonstrated through a simulation to support actual inverter hardware. The Simpowersystems and dSPACE DS1104 blockset libraries were used in the simulation, performed in the Simulink/MATLAB environment.

The remaining sections of this article are organized as follows: A description of an IM drive is given in Section 2. Section 3 explains the VOC control for a three-phase VSI. A VSI using the SVM approach is introduced in Section 4. Section 5 contains the simulation and experimental discussion. Section 6 summarizes the research and presents the findings.

2. Overview of the Induction Motor Drive

The squirrel-cage three-phase IM is an asynchronous AC motor that operates on electromagnetic induction principles. The IM's primary purpose is to convert electrical energy into mechanical energy. A small air gap separates the stator and the rotor, the two components that make up the IM. The three-phase squirrel-cage IM [19–21] is the one most often used due to its insulated winding in both stator and rotor, which are formed of cast and solid bars with high conductivity, as shown in Figure 1.

For the rotor to rotate at synchronous speed (ω_{sm} in rad/s), where $\omega_{sm} = 2\pi f$ (rad/s), where f = synchronous frequency, three-phase voltages must first be applied to the stator winding. The stator currents produce a revolving magnetic field in the magnetic circuit, formed by the air gap between the stator and rotor cores. The number of poles (P) affects the mechanical synchronous speed (ω_{sm} in rad/s). This is how the synchronous speed is determined [22].

$$\omega_{sm} = \frac{2\omega_s}{P} \tag{1}$$

$$N_{sm} = \frac{120f}{P} \tag{2}$$

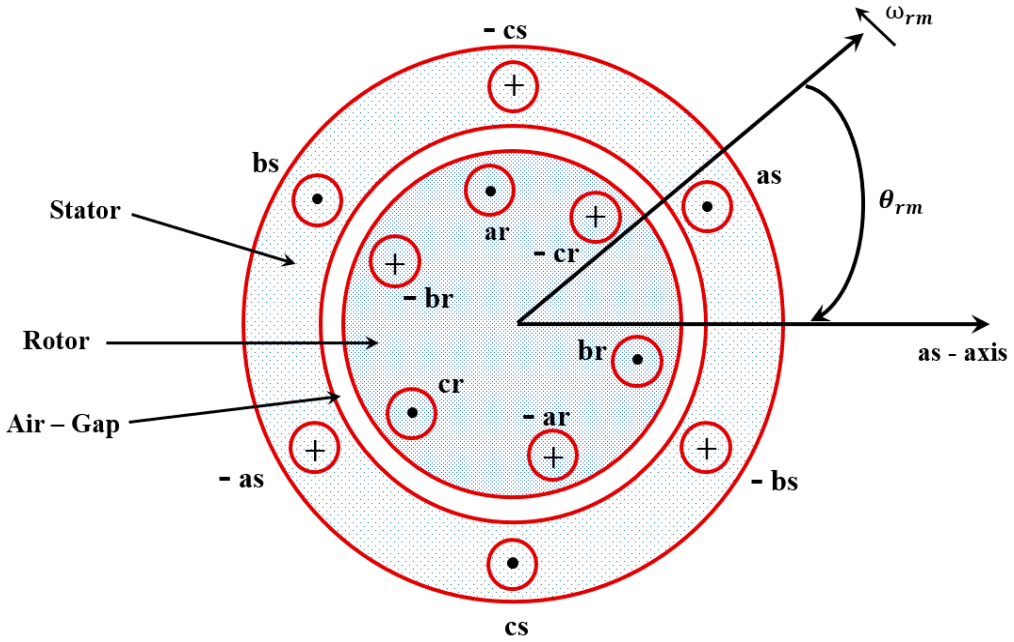

Figure 1. Three-phase IM cross-sectional model.

Modelling of the Induction Motor

To depict the physical systems, the computer models the mathematical model of the three-phase IM and its driving system [4]. The control parameters of the models are highlighted in this three-phase IM modelling. For the three-phase IM, the magnetic connection between the stator and rotor voltage equations can be expressed as follows [23].

$$V_{as} = i_{as}r_s + \frac{d\lambda_{as}}{dt};\ V_{bs} = i_{bs}r_s + \frac{d\lambda_{bs}}{dt};\ V_{cs} = i_{cs}r_s + \frac{d\lambda_{cs}}{dt} \tag{3}$$

$$V_{ar} = i_{ar}r_r + \frac{d\lambda_{ar}}{dt};\ V_{br} = i_{br}r_r + \frac{d\lambda_{br}}{dt};\ V_{cr} = i_{cr}r_r + \frac{d\lambda_{cr}}{dt} \tag{4}$$

where V_{as}, V_{bs}, V_{cs} = 3-φ stator voltages; V_{ar}, V_{br}, V_{cr} = 3-φ rotor voltages; i_{as}, i_{bs}, i_{cs} = 3-φ stator currents; i_{ar}, i_{br}, i_{cr} = 3-φ rotor currents; r_s = stator resistance; r_r = rotor resistance; λ_{as}, λ_{bs}, λ_{cs} = flux linkages of the stator; and λ_{ar}, λ_{br}, λ_{cr} = flux linkages of the rotor.

According to the winding currents and inductances, the flux linkages indicate the matrix formed between the rotor and stator windings, as depicted in the following matrix [24].

$$\begin{bmatrix} \lambda_s^{abc} \\ \lambda_r^{abc} \end{bmatrix} = \begin{bmatrix} L_{ss}^{abc} & L_{sr}^{abc} \\ L_{rs}^{abc} & L_{rr}^{abc} \end{bmatrix} \begin{bmatrix} i_s^{abc} \\ i_r^{abc} \end{bmatrix} \tag{5}$$

where $\lambda_s^{abc}=\begin{bmatrix}\lambda_{as} & \lambda_{bs} & \lambda_{cs}\end{bmatrix}^{\mathrm{T}}$, $i_s^{abc}=\begin{bmatrix}i_{as} & i_{bs} & i_{cs}\end{bmatrix}^{\mathrm{T}}$, $\lambda_r^{abc}=\begin{bmatrix}\lambda_{ar} & \lambda_{br} & \lambda_{cr}\end{bmatrix}^{\mathrm{T}}$, $i_r^{abc}=\begin{bmatrix}i_{ar} & i_{br} & i_{cr}\end{bmatrix}^{T}$, and superscript T = transpose of the array; L_{ss}^{abc} = stator-to-stator winding inductance; L_{rr}^{abc} = rotor-to-rotor winding inductance; and L_{sr}^{abc} = stator-to-rotor mutual inductance, which depends on the rotor angle θ_r.

To solve and simplify the computation of the three-phase IM performance, contemporary research analyzes the transient and steady-state performance of three Ims with a direct-quadrature-zero ($dq0$) stationary motor model [21,25,26]. As it can accurately represent the real-time motor model, a $dq0$ reference frame is chosen in this study to create the motor simulation model. The relationship between the rotor $dq0$ and the abc stator axes is shown in Figure 2. The mechanical rotor speed is denoted by ω_{rm}, and the reference frame speed is represented by ω. The transformation from abc to $dq0$ is analyzed using stationary and synchronously revolving frames. Similar to those typically used for supply networks, the stationary rotating frame has a speed frame that produces a value of $\omega = 0$. When the

synchronous reference frame revolves in the same direction as the rotor revolution, the speed frame becomes $\omega = \omega_s$. The matrix below contains their inverses and the transition from the *abc* to the *dq*0 reference frame [27].

$$\begin{bmatrix} x_d \\ x_q \\ x_0 \end{bmatrix} = \frac{2}{3}\begin{bmatrix} cos\ (\theta) & cos\ \left(\theta - \frac{2\pi}{3}\right) & cos\ \left(\theta + \frac{2\pi}{3}\right) \\ sin\ (\theta) & sin\ \left(\theta - \frac{2\pi}{3}\right) & sin\ \left(\theta + \frac{2\pi}{3}\right) \\ \frac{1}{2} & \frac{1}{2} & \frac{1}{2} \end{bmatrix}\begin{bmatrix} x_a \\ x_b \\ x_c \end{bmatrix} = \left[X_{dq0}(\theta)\right]\begin{bmatrix} x_a \\ x_b \\ x_c \end{bmatrix} \quad (6)$$

$$\begin{bmatrix} x_a \\ x_b \\ x_c \end{bmatrix} = \frac{2}{3}\begin{bmatrix} cos\ (\theta) & sin\ (\theta) & 1 \\ cos\ \left(\theta - \frac{2\pi}{3}\right) & sin\ \left(\theta - \frac{2\pi}{3}\right) & 1 \\ cos\ \left(\theta + \frac{2\pi}{3}\right) & sin\ \left(\theta + \frac{2\pi}{3}\right) & 1 \end{bmatrix}\begin{bmatrix} x_d \\ x_q \\ x_0 \end{bmatrix} = \left[X_{dq0}(\theta)\right]^{-1}\begin{bmatrix} x_a \\ x_b \\ x_c \end{bmatrix} \quad (7)$$

where variable x = the 3-φ IM's phase voltage, current, or flux linkage. The stator voltages are converted to the *dq*0 voltages into a matrix form that includes flux linkages, currents, and voltages of the *dq*0 reference frame to produce the *dq*0 voltages [28].

$$\begin{bmatrix} v_{ds} \\ v_{qs} \\ v_{0s} \end{bmatrix} = \frac{d\theta}{dt}\begin{bmatrix} 0 & 1 & 0 \\ -1 & 0 & 0 \\ 0 & 0 & 0 \end{bmatrix}\begin{bmatrix} \lambda_{ds} \\ \lambda_{qs} \\ \lambda_{0s} \end{bmatrix} + \frac{d}{dt}\begin{bmatrix} \lambda_{ds} \\ \lambda_{qs} \\ \lambda_{0s} \end{bmatrix} + r_s\begin{bmatrix} 1 & 0 & 0 \\ 0 & 1 & 0 \\ 0 & 0 & 1 \end{bmatrix}\begin{bmatrix} i_{ds} \\ i_{qs} \\ i_{0s} \end{bmatrix} \quad (8)$$

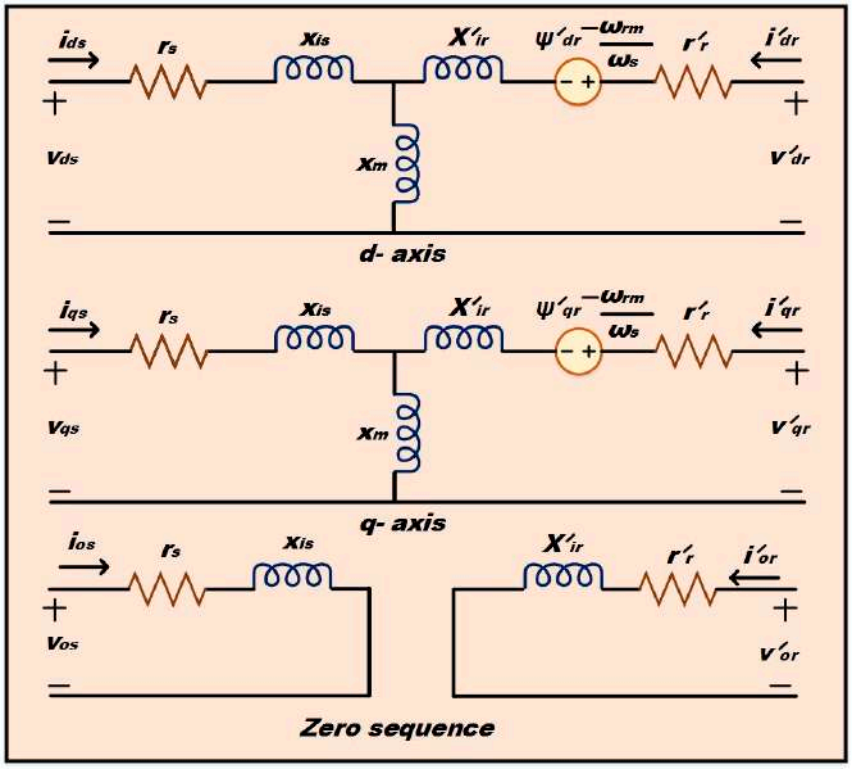

Figure 2. Equivalent circuits of the three-phase IM's *dq*0 stationary reference frames.

Similar to this, while transferring the voltages, currents, and flux linkages, the rotor voltages are converted to the *dq*0 frame into a matrix form that must be combined with the mechanical rotor angle $(\theta - \theta_{rm})$ to become $[X_{dq0}(\theta - \theta_{rm})]$ in order to achieve the subsequent equations shown below [29].

$$\begin{bmatrix} v_{dr} \\ v_{qr} \\ v_{0r} \end{bmatrix} = \frac{d(\theta - \theta_{rm})}{dt}\begin{bmatrix} 0 & 1 & 0 \\ -1 & 0 & 0 \\ 0 & 0 & 0 \end{bmatrix}\begin{bmatrix} \lambda_{dr} \\ \lambda_{qr} \\ \lambda_{0r} \end{bmatrix} + \frac{d}{dt}\begin{bmatrix} \lambda_{dr} \\ \lambda_{qr} \\ \lambda_{0r} \end{bmatrix} + r_s\begin{bmatrix} 1 & 0 & 0 \\ 0 & 1 & 0 \\ 0 & 0 & 1 \end{bmatrix}\begin{bmatrix} i_{dr} \\ i_{qr} \\ i_{0r} \end{bmatrix} \quad (9)$$

The stator *abc* flux linkage is transformed to produce the stator *dq*0 flux linkages, which are stated as follows.

$$\begin{bmatrix} \lambda_{ds} \\ \lambda_{qs} \\ \lambda_{0s} \end{bmatrix} = \begin{bmatrix} L_{ls} + \frac{3}{2}L_{ss} & 0 & 0 \\ 0 & L_{ls} + \frac{3}{2}L_{ss} & 0 \\ 0 & 0 & L_{ls} \end{bmatrix} \begin{bmatrix} i_{ds} \\ i_{qs} \\ i_{0s} \end{bmatrix} + \begin{bmatrix} \frac{3}{2}L_{sr} & 0 & 0 \\ 0 & \frac{3}{2}L_{sr} & 0 \\ 0 & 0 & 0 \end{bmatrix} \begin{bmatrix} i_{dr} \\ i_{qr} \\ i_{0r} \end{bmatrix} \tag{10}$$

The rotor *dq*0 flux linkages are produced in a similar manner to the rotor *abc* flux linkage.

$$\begin{bmatrix} \lambda_{dr} \\ \lambda_{qr} \\ \lambda_{0r} \end{bmatrix} = \begin{bmatrix} \frac{3}{2}L_{sr} & 0 & 0 \\ 0 & \frac{3}{2}L_{sr} & 0 \\ 0 & 0 & 0 \end{bmatrix} \begin{bmatrix} i_{ds} \\ i_{qs} \\ i_{0s} \end{bmatrix} + \begin{bmatrix} L_{lr} + \frac{3}{2}L_{rr} & 0 & 0 \\ 0 & L_{lr} + \frac{3}{2}L_{rr} & 0 \\ 0 & 0 & L_{lr} \end{bmatrix} \begin{bmatrix} i_{dr} \\ i_{qr} \\ i_{0r} \end{bmatrix} \tag{11}$$

The stator and rotor *dq*0 flux linkage relations can be stated as in Equation (12) [25], where λ'_{dr}, λ'_{qr} are the reference values on the stator side of the *dq* rotor flux linkages. This is based on Equations (10) and (11); the referred values on the stator side of the *dq* rotor currents are i'_{dr}, i'_{qr}.

$$\begin{bmatrix} \lambda_{ds} \\ \lambda_{qs} \\ \lambda_{0s} \\ \lambda'_{dr} \\ \lambda'_{qr} \\ \lambda'_{0r} \end{bmatrix} = \begin{bmatrix} L_{ls} + L_m & 0 & 0 & L_m & 0 & 0 \\ 0 & L_{ls} + L_m & 0 & 0 & L_m & 0 \\ 0 & 0 & L_{ls} & 0 & 0 & 0 \\ L_m & 0 & 0 & L'_{lr} + L_m & 0 & 0 \\ 0 & L_m & 0 & 0 & L'_{lr} + L_m & 0 \\ 0 & 0 & 0 & 0 & 0 & L'_{lr} \end{bmatrix} \begin{bmatrix} i_{ds} \\ i_{qs} \\ i_{0s} \\ i'_{dr} \\ i'_{qr} \\ i'_{0r} \end{bmatrix} \tag{12}$$

The governing equations [27] are produced by converting the final *dq*0 reference frame equations to the flux linkage, utilizing the formula $\psi = \omega_s \lambda$, and the inductance into reactance, using $x = \omega_s L$.

$$v_{ds} = \frac{1}{\omega_s}\frac{d\psi_{ds}}{dt} + \frac{\omega}{\omega_s}\psi_{qs} + r_s i_{ds} \tag{13}$$

$$v_{qs} = \frac{1}{\omega_s}\frac{d\psi_{qs}}{dt} + \frac{\omega}{\omega_s}\psi_{ds} + r_s i_{qs} \tag{14}$$

$$v_{0s} = \frac{1}{\omega_s}\frac{d\psi_{0s}}{dt} + r_s i_{0s} \tag{15}$$

$$v'_{dr} = \frac{1}{\omega_s}\frac{d\psi'_{dr}}{dt} + \left(\frac{\omega - \omega_{rm}}{\omega_s}\right)\psi'_{qr} + r'_r i'_{dr} \tag{16}$$

$$v'_{qr} = \frac{1}{\omega_s}\frac{d\psi'_{qr}}{dt} - \left(\frac{\omega - \omega_{rm}}{\omega_s}\right)\psi'_{dr} + r'_r i'_{qr} \tag{17}$$

$$v'_{0r} = \frac{1}{\omega_s}\frac{d\psi'_{0r}}{dt} + r'_r i'_{0r} \tag{18}$$

$$\begin{bmatrix} \psi_{ds} \\ \psi_{qs} \\ \psi_{0s} \\ \psi'_{dr} \\ \psi'_{qr} \\ \psi'_{0r} \end{bmatrix} = \begin{bmatrix} x_{ls} + x_m & 0 & 0 & x_m & 0 & 0 \\ 0 & x_{ls} + L_m & 0 & 0 & x_m & 0 \\ 0 & 0 & x_{ls} & 0 & 0 & 0 \\ x_m & 0 & 0 & x'_{lr} + x_m & 0 & 0 \\ 0 & x_m & 0 & 0 & x'_{lr} + x_m & 0 \\ 0 & 0 & 0 & 0 & 0 & x'_{lr} \end{bmatrix} \begin{bmatrix} i_{ds} \\ i_{qs} \\ i_{0s} \\ i'_{dr} \\ i'_{qr} \\ i'_{0r} \end{bmatrix}. \tag{19}$$

The electromagnetic torque can manifest itself in the following ways:

$$\begin{aligned} T_{em} &= \tfrac{3}{2}\tfrac{P}{2\omega_s}\left(\psi'_{dr} i'_{qr} - \psi'_{qr} i'_{dr}\right) \\ &= \tfrac{3}{2}\tfrac{P}{2\omega_s}\left(\psi_{qs} i_{ds} - \psi_{ds} i_{qs}\right) \\ &= \tfrac{3}{2}\tfrac{P}{2\omega_s} x_m \left(i'_{qr} i_{ds} - i'_{dr} i_{qs}\right) \end{aligned} \tag{20}$$

As depicted in Figure 2, the equivalent circuits of the $dq0$ stationary reference frames are generated by introducing Equation (19) into Equation (13) to Equation (18).

3. Voltage-Oriented Control

The VOC technique for AC-DC converters is derived from FOC for IMs. FOC provides a quick, dynamic reaction due to the utilization of current control loops. The theoretical elements of the VOC approach used for grid-connected rectifiers have received extensive coverage. The control system uses the PWM technique to ensure that the characteristics of the VOC control scheme are modified. It is possible to reduce the impact of interference (disturbances). By using the hysteresis pulse-width modulation approach, system solidity can be achieved. Power switching is stressed as a result of the fluctuating switching frequency, necessitating the use of an input filter at high-value parameters. To alleviate harmonic issues, the proposed method utilizes the VOC principle to regulate charging while maintaining low harmonic distortions to the grid. Figure 3 depicts VOC for AC-DC line-side converters. VOC operates most frequently in the two-phase zero and $dq0$ domains, where the Clarke and Park transformation matrices are employed.

$$\begin{bmatrix} V_{s\alpha} \\ V_{s\beta} \\ V_0 \end{bmatrix} = \sqrt{\frac{2}{3}} \begin{bmatrix} 1 & -\frac{1}{2} & -\frac{1}{2} \\ 0 & \frac{\sqrt{3}}{2} & -\frac{\sqrt{3}}{2} \\ \frac{1}{\sqrt{2}} & \frac{1}{\sqrt{2}} & \frac{1}{\sqrt{2}} \end{bmatrix} \begin{bmatrix} V_{sa} \\ V_{sb} \\ V_{sc} \end{bmatrix} \tag{21}$$

$$\begin{bmatrix} V_d \\ V_q \end{bmatrix} = \begin{bmatrix} sin(\theta) & cos(\theta) \\ -cos(\theta) & sin(\theta) \end{bmatrix} \begin{bmatrix} V_{s\alpha} \\ V_{s\beta} \end{bmatrix} \tag{22}$$

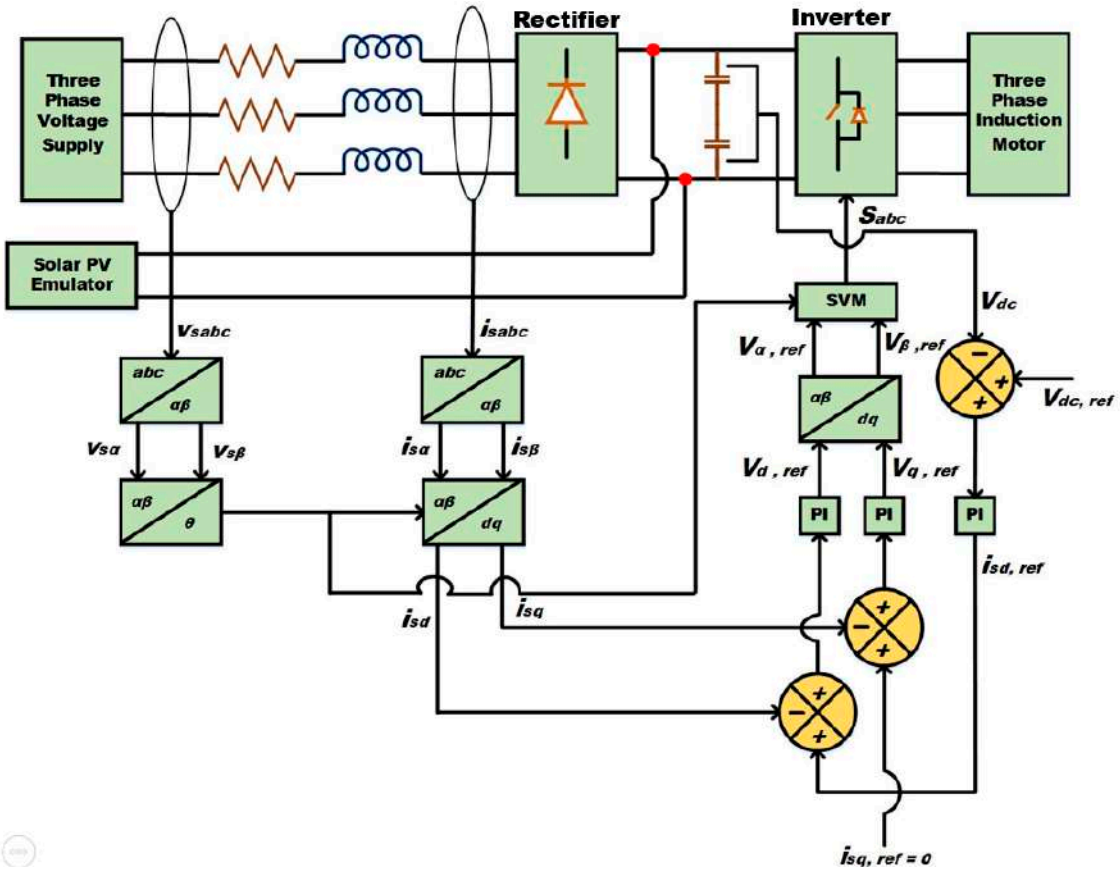

Figure 3. Overall control structure of VOC of a PWM inverter [30].

Note that V_{sa}, V_{sb}, and V_{sc} = 3-φ source voltages in the *abc* domain, while $V_{s\alpha}$, $V_{s\beta}$, and V_0 = source voltages in the $\alpha\beta 0$ domain. V_d, V_q, and V_0 are source voltages of the $dq0$ domain, and θ = the operating phase of the power system. As shown in Figure 2, an equivalent transformation procedure is used to transform the 3-φ source current i_{sabc}.

Based on the following techniques, steady-state errors are easily reduced by the proportional integral (PI) controllers by employing the transformation technique to convert AC-side control variables into DC signals:

$$v_{d,ref} = K_p\left(i_{sd,ref} - i_{sd}\right) + K_i \int \left(i_{sd,ref} - i_{sd}\right) dt \tag{23}$$

$$v_{q,ref} = K_p\left(i_{sq,ref} - i_{sq}\right) + K_i \int \left(i_{sq,ref} - i_{sq}\right) dt \tag{24}$$

where K_p and K_i = gains of the PI controller, i_{sd} and i_{sq} = source current in the $dq0$ domain, and $i_{sd,ref}$ and $i_{sq,ref}$ = reference signals for i_{sd} and i_{sq}, respectively. After obtaining the reference voltages $v_{d,ref}$ and $v_{q,ref}$, the gate switching pulses S_{abc}, which regulate the operation of the VOC inverter, are derived using the PWM switching approach and the inverse park transformation as given in Equation (25).

$$\begin{bmatrix} V_{\alpha,ref} \\ V_{\beta,ref} \end{bmatrix} = \begin{bmatrix} sin(\theta) & -cos(\theta) \\ cos(\theta) & sin(\theta) \end{bmatrix} \begin{bmatrix} v_{d,ref} \\ v_{q,ref} \end{bmatrix} \tag{25}$$

4. SVM Switching Techniques

The SVM approach, generally acknowledged as the optimum method for variable speed drive applications, creates PWM control signals in the 3-φ inverter. Compared to other PWM systems, this method provides an enhanced means of achieving a high output voltage, minimizing the harmonic output, and lowering switching losses. As a result, the SVM technique is confirmed as the best approach for reducing harmonic distortion [31–33].

$$\begin{bmatrix} V_{ab} \\ V_{bc} \\ V_{ca} \end{bmatrix} = V_{dc} \begin{bmatrix} 1 & -1 & 0 \\ 0 & 1 & -1 \\ -1 & 0 & 1 \end{bmatrix} \begin{bmatrix} s_1 \\ s_3 \\ s_5 \end{bmatrix} \tag{26}$$

$$\begin{bmatrix} V_{ab} \\ V_{bc} \\ V_{ca} \end{bmatrix} = \frac{V_{dc}}{3} \begin{bmatrix} 2 & -1 & -1 \\ -1 & 2 & -1 \\ -1 & -1 & 2 \end{bmatrix} \begin{bmatrix} s_1 \\ s_3 \\ s_5 \end{bmatrix} \tag{27}$$

Eight switch variables can be created using the inverter's six IGBTs. Six switch variables—V_1, V_2, . . . , V_6, and the last two—are zero vectors chosen for the three upper IGBT switches. The on and off patterns of the lower IGBT switches are the opposite of those of the higher switches. Figure 4 displays the eight switching vectors of the SVM [34].

The output waveform of the inverter is split into six hexagonal sectors, according to the SVM's working principle. The sector angle is 60° apart, and every sector is between two voltage space vectors (Figure 5) [35]. The SVM approach receives a 3-φ voltage (V_a, V_b, and V_c) with a 120° angle among the 2-φ and transforms it into 2-φ (V_α and V_β) with a 90° using Clark's transformation (Figure 6a).

To make the study of three-phase voltage more straightforward, 2-φ voltages (V_α and V_β) are used as part of a scientific transformation. The voltages are used to calculate the hexagon's voltage vector angle (α) and the reference voltage vector's magnitude (V_{ref}). V_{ref} is assumed as the magnitude of the V_α and V_β voltages, while α is the frequency of V_α and V_β. V_{ref} and α are situated among the two neighboring non-zero and zero vectors. The following formulas can be used to calculate them [29].

$$\begin{bmatrix} V_\alpha \\ V_\beta \end{bmatrix} = \frac{2}{3} \begin{bmatrix} 1 & \frac{-1}{2} & \frac{-1}{2} \\ 0 & \frac{\sqrt{3}}{2} & -\frac{\sqrt{3}}{2} \end{bmatrix} \begin{bmatrix} V_a \\ V_b \\ V_c \end{bmatrix} \tag{28}$$

$$\left|V_{ref}\right| = \sqrt{V_\alpha^2 + V_\beta^2} \tag{29}$$

$$\alpha = tan^{-1}\frac{V_\beta}{V_\alpha} \tag{30}$$

Sector 1 contains the vectors that can be used to synthesize V_{ref}, which is located here.

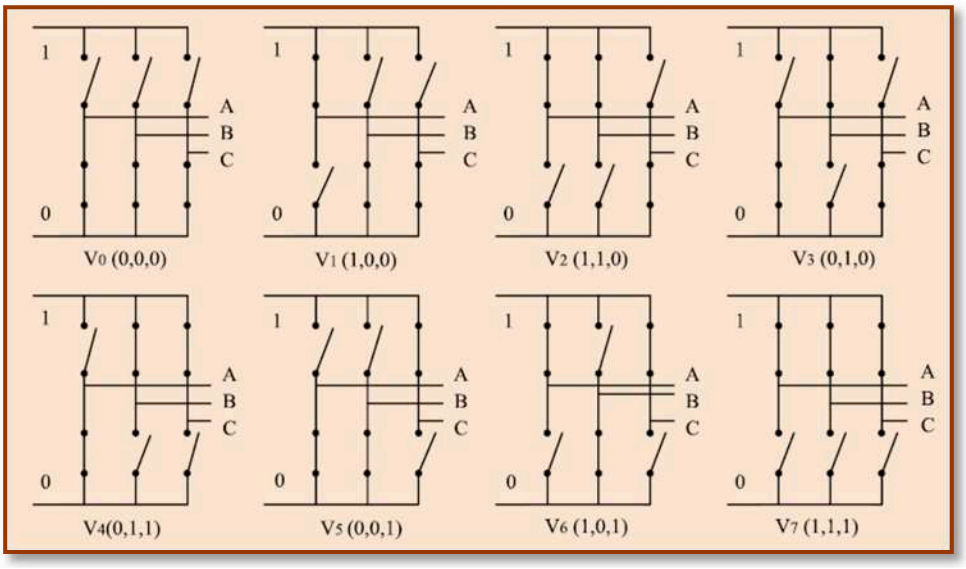

Figure 4. Eight switching states for the inverter voltage vectors (V_0 to V_7).

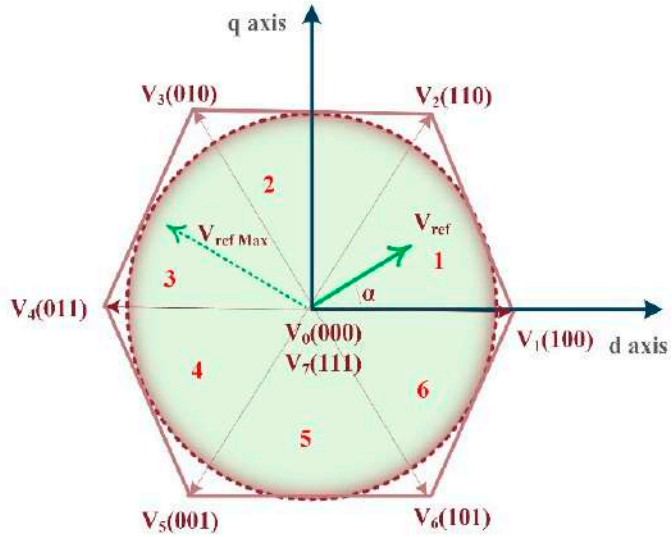

Figure 5. Space vector diagram.

The relevant space vectors and time intervals (T_1, T_2, and T_0) in sector 1 are depicted in Figure 6b. The duration of Vref is calculated by multiplying the reference voltage by the sampling time period, which is equivalent to the sum of the voltages times the time interval of the space vectors in the specified sector [36].

$$\int_0^{T_s} \overline{V}_{ref} dt = \int_0^{T_1} \overline{V}_1 dt + \int_{T_1}^{T_1+T_2} \overline{V}_2 dt + \int_{T_1+T_2}^{T_s} \overline{V}_0 dt T_s = T_1 + T_2 + T_0 \tag{31}$$

where Ts = switching time, which is calculated by $Ts = \frac{1}{f_s}$, and fs = switching frequency.

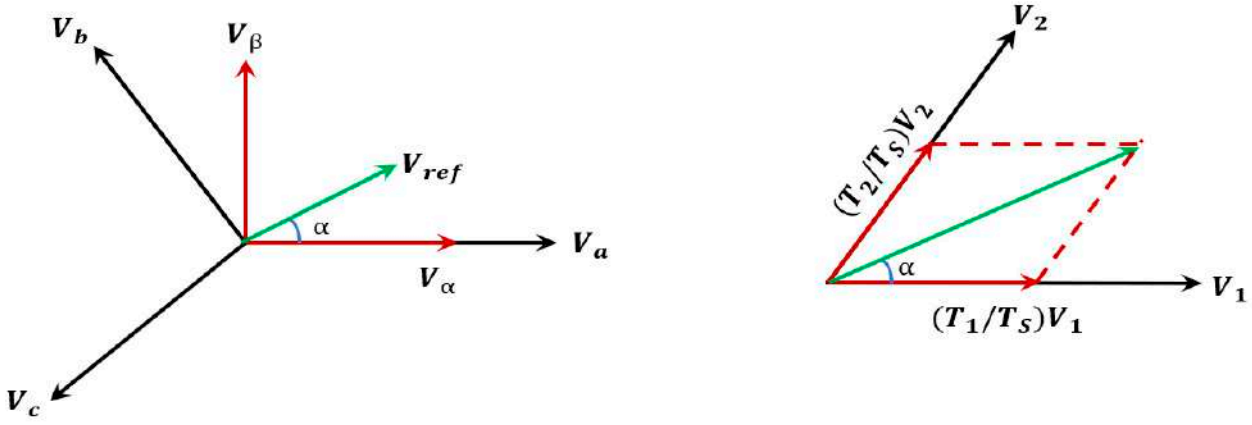

(**a**) (**b**)

Figure 6. (**a**) Space vector diagram. (**b**) Space of sector-1 between V_1 and V_2.

Equation (30) illustrates how $\overline{V_0}$ provides zero voltage to the output load. As a result, the equation is:

$$T_s\overline{V}_{ref} = T_1\overline{V}_1 + T_2\overline{V}_2 \tag{32}$$

When the values of $\overline{V_1}$ and $\overline{V_2}$ are substituted into the $\alpha\beta$ frame and the voltage vectors are evaluated, the results are as follows [37].

$$T_s\left|V_{ref}\right|\begin{bmatrix}cos(\alpha)\\ sin(\alpha)\end{bmatrix} = T_1\frac{2}{3}V_{dc}\begin{bmatrix}1\\0\end{bmatrix} + T_2\frac{2}{3}V_{dc}\begin{bmatrix}cos\frac{\pi}{3}\\ sin\frac{\pi}{3}\end{bmatrix} \tag{33}$$

$$T_1 = T_s\frac{3}{2}\frac{\left|V_{ref}\right|}{V_{dc}}\frac{sin\left(\frac{\pi}{3}-\alpha\right)}{sin\left(\frac{\pi}{3}\right)} \tag{34}$$

$$T_2 = T_s\frac{3}{2}\frac{\left|V_{ref}\right|}{V_{dc}}\frac{sin(\alpha)}{sin\left(\frac{\pi}{3}\right)} \tag{35}$$

The relation between the magnitude of the reference voltage and the *dc* voltage value represented by the following equation is known as the MI for the SVM [38].

$$MI = \frac{\left|V_{ref}\right|}{\frac{2}{\pi}V_{dc}} \tag{36}$$

Equation (35) can be substituted into Equations (33) and (34) to determine the time duration in the other sectors (n), and 60 degrees with α can be used for each sector to obtain the result [39,40].

$$T_1 = \frac{\sqrt{3}T_s\left|V_{ref}\right|}{V_{dc}}sin\left(\frac{n}{3}\pi - \alpha\right) \tag{37}$$

$$T_2 = \frac{\sqrt{3}T_s\left|V_{ref}\right|}{V_{dc}}sin\left(\alpha - \frac{n-1}{3}\pi\right) \tag{38}$$

$$T_0 = T_s - (T_1 + T_2) \tag{39}$$

Alternating the zero-vector sequence, the asymmetric sequence, the maximum current not switched sequence, and the right aligned sequence are the four different types of switching patterns. To reduce device switching frequency, all switching patterns must fulfill the following two requirements. Merely two switches in the same inverter leg are used to switch from one switching state to another. To minimize the switching frequency, one of the switches must be turned off if the other is activated. The least amount of

switching is necessary to move V_{ref} from one sector to the next to minimize switching losses. The optimum strategy, according to research, is the symmetric sequence method, since it minimizes switching losses. The generation of the SVM signal and the inverter output voltages and a comparison of the duty ratio waveform's three signals with the triangle waveform is shown in Figure 7. This comparison assumes that S is ON if $V_{DutyRatio} > V_{triangle}$; otherwise, S is OFF.

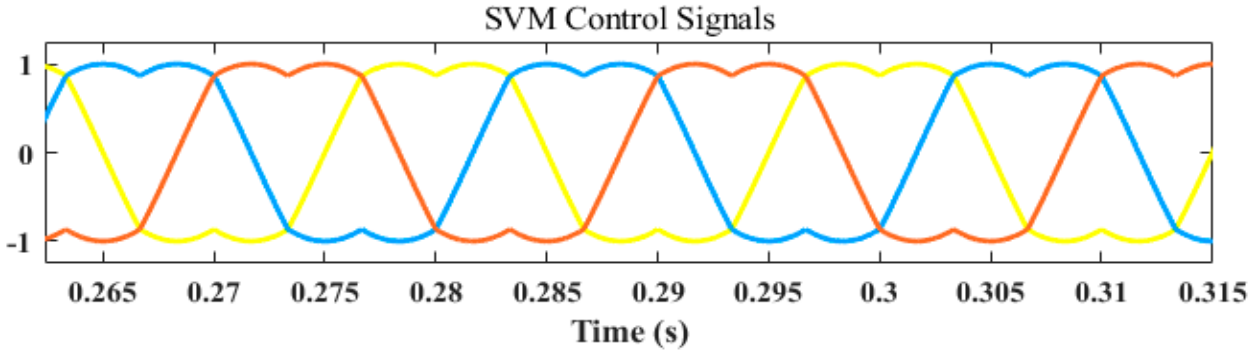

Figure 7. SVM waves for a three-phase inverter.

Every switch in a bipolar switching scheme operates in opposition to the facing switch, as seen in the example where the triangle waveform and the $V_{TaDutyRatio}$ are compared to produce the PWM signal for the IGBT1 and the opposing IGBT4 in leg 1, which is identical to leg 2 and leg 3.

5. Results and Discussion

5.1. Simulation Results

In the simulation studies, several experiments were carried out to confirm the effectiveness of the suggested VOC system. The DG capacities of the MG test system taken into consideration in this work are as follows. The SPV system has a 400 V output voltage rating with a 1 kW capacity. The load being considered is a three-phase, 1 hp squirrel cage IM connected at 415 V and 50 Hz.

The voltage control has been set up to satisfy each of the following requirements:

(1) Decentralized control is achieved normally;
(2) Under diverse system situations, the whole MG closed-loop model is stable;
(3) All of the associated DGs follow the reference signal that the SVM algorithm provides.

Each controller must successfully uphold the three requirements mentioned earlier and offer reliable control inside its application domain. The software platform MATLAB/Simulink has been used to implement the entire system. The SVM method is used to evaluate whether a PV system connected to a grid can improve power quality at the consumer terminals. Figure 7 depicts the creation of the SVM signal. The voltage waveforms and the current waveform share some phase and are both sinusoidal, as shown in Figure 8. Figure 9 illustrates how the speed of 1425 rpm was achieved while the load torque remained constant at 3.0 N-m, as shown in Figure 10. In accordance with carrier frequencies of 1 kHz and an MI of 0.9 (Figure 11), Figure 12 displays an FFT analysis of the current and voltage in the system under consideration. The THD_i and THD_v values were, respectively, 1.10% and 1.22%. Figure 13 depicts the voltage in the dc-link capacitor.

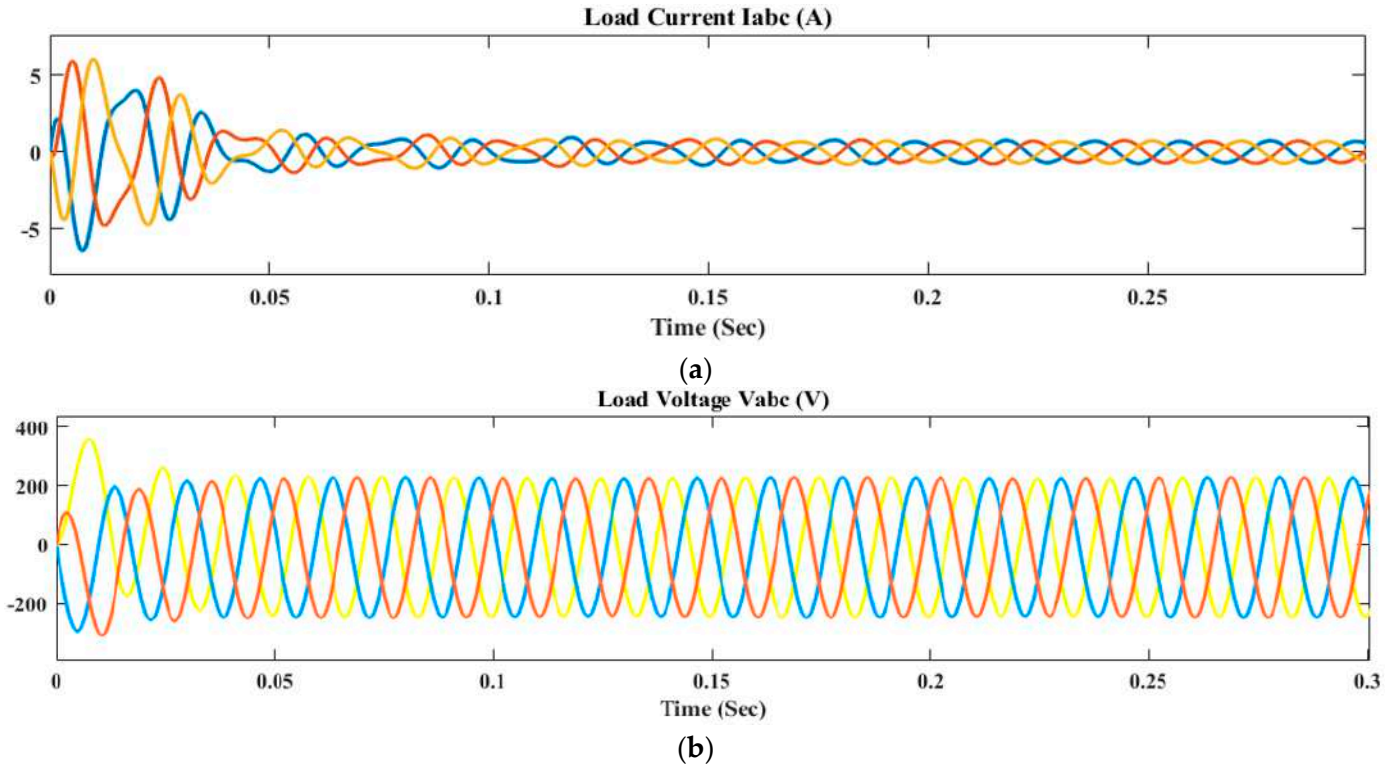

Figure 8. (**a**) Current and (**b**) Voltage waveform of the IM with the VOC-based SVM Controller.

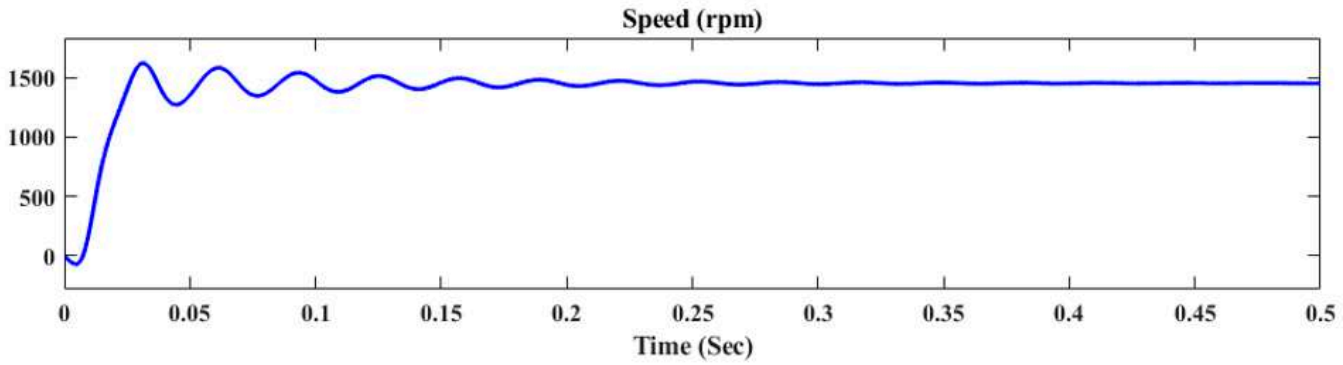

Figure 9. Speed of the Induction Motor when MI = 0.9.

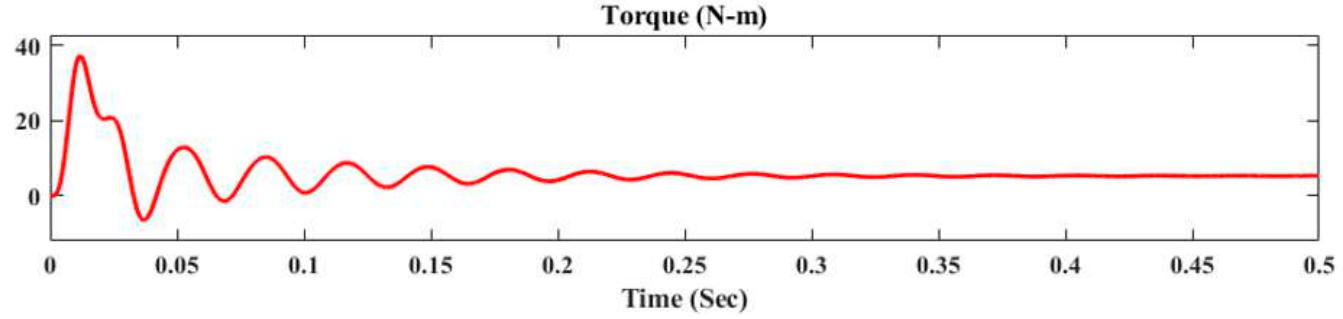

Figure 10. Torque of the Induction Motor.

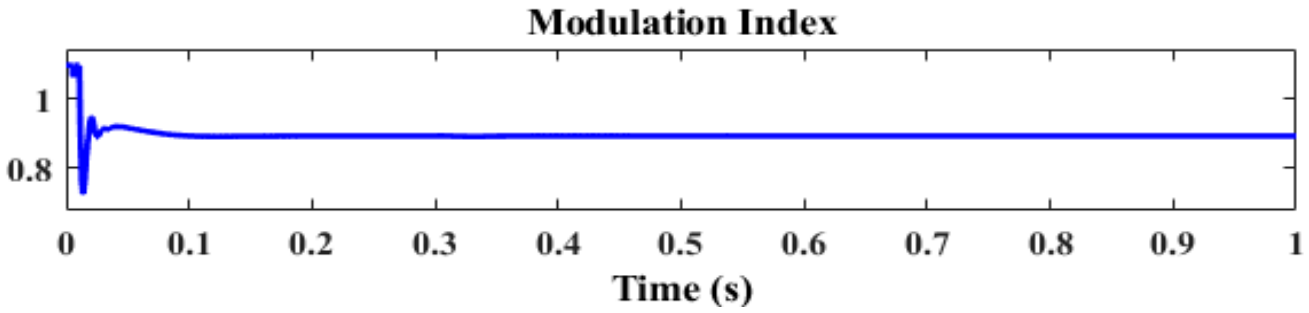

Figure 11. Modulation Index.

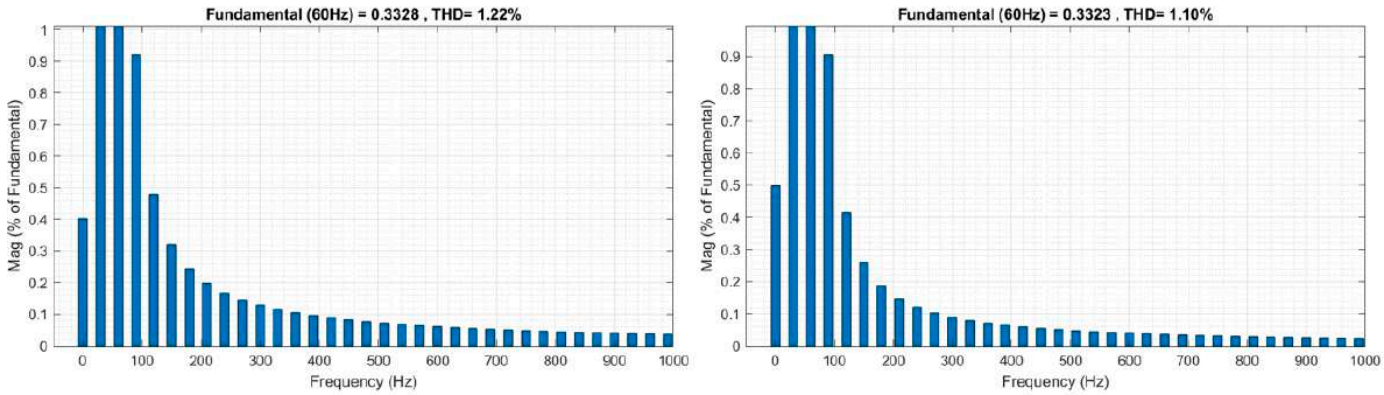

Figure 12. FFT analysis of the voltage and current of the Induction Motor.

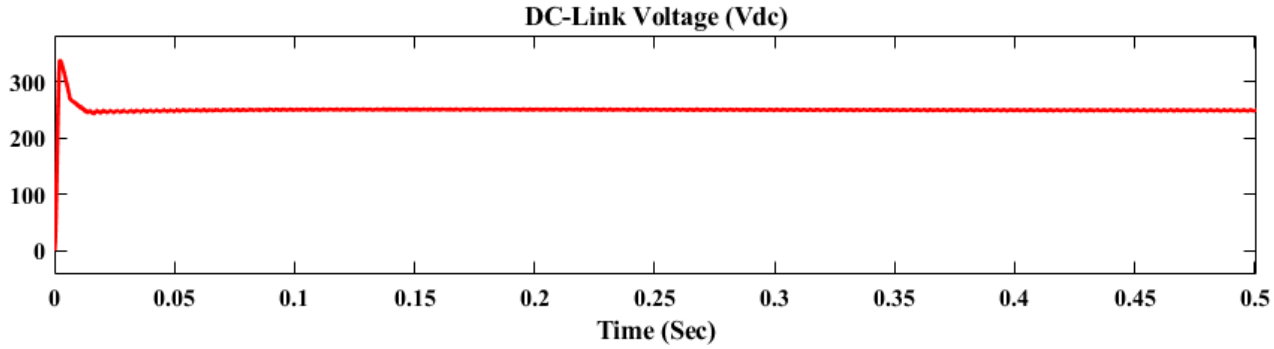

Figure 13. DC-Link voltage.

5.2. Experimental Verification of the Control Scheme

The efficiency of the suggested VOC-SVM control-based PI controller, shown in Figure 3, has been tested using a suitable configuration. Its primary components are a Fluke power quality analyzer, three-phase inverter, dSPACE kit, power analyzer, and PV simulator. A PVS1010 PV emulator with dc programming is used to determine the panel properties. A real-time dSPACE DS1104 controller interface controls the system by conditioning each field signal. A dSPACE platform, shown in Figure 14, is used to integrate the Simulink model with the external hardware. A D/A converter is used to interface the inverter gating signals with dSPACE. A dSPACE DS1104 board is used to run Simulink, which has been used to implement the simulated design modelling. The suggested control's main benefit is the ability to precisely adjust the THD and dc-link voltage. The testing was carried out using the MATLAB/Simulink interfaced dSPACE platform to realize the adequate performance of a VOC-SVM control-based grid-connected PV system.

For this reason, it was assumed that the grid phase voltage was 415 V with a frequency of 50 Hz and dc-link voltages of 250 V. The practical response to a dc-link voltage and SVM

switching pulse is illustrated in Figure 15. The test results clearly show that the SVM-based VOC controller optimizes the dc-link voltage.

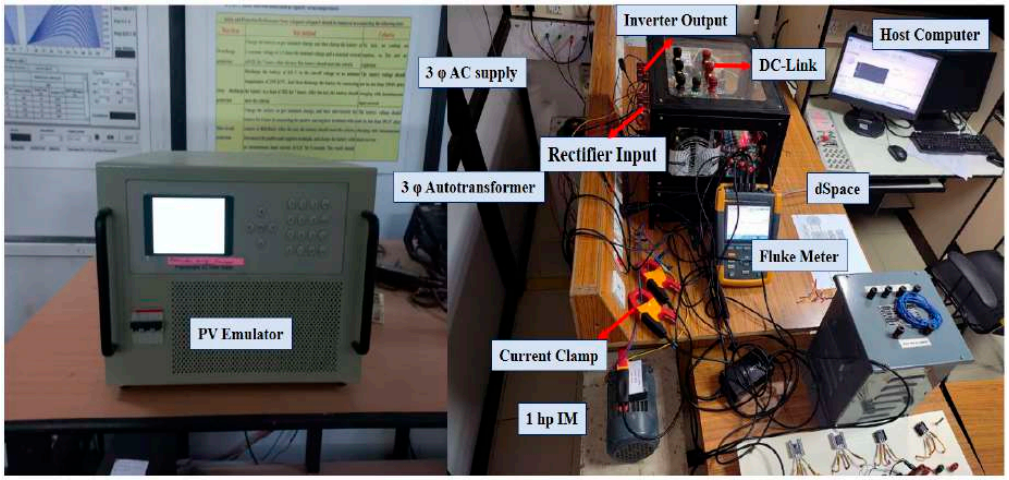

Figure 14. Experimental Setup of the three-phase inverter with VOC control using dSpace.

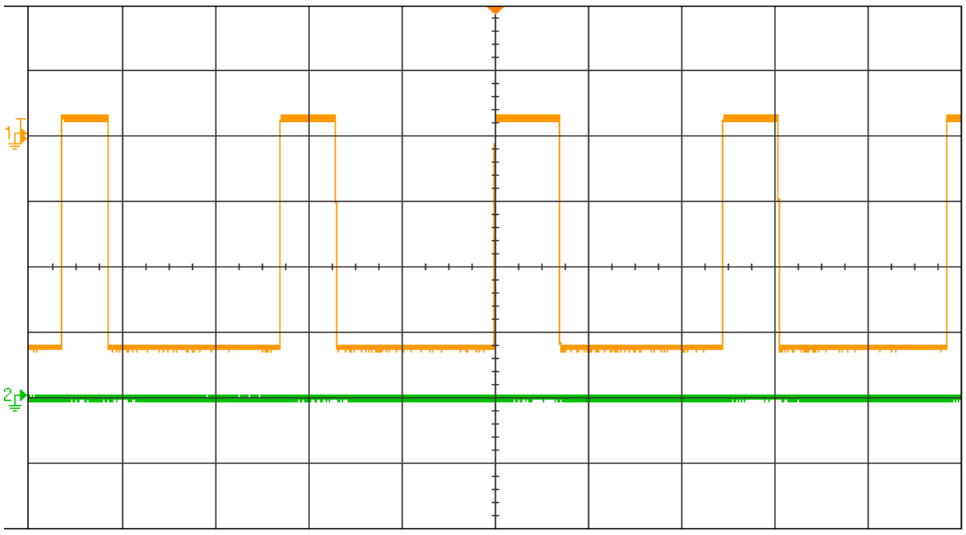

Figure 15. SVM Switching Pulse and DC-Link Voltage.

According to the IEEE 519 standard and Figure 14, an SVM based on ripple control was used to achieve reduced THD and described with the FFT spectrum of grid current under steady-state and dynamic operating circumstances. The waveforms were observed using a Fluke-43 spectrum analyzer with online numerical value illustration. The experimental voltage and current waveform of an inverter with a THD_i and THD_v for a modulation index of 0.3 are shown in Figure 16a–d.

Figure 17 depicts the voltage and current waveform with an FFT analysis with an MI of 0.6. Similarly, Figures 18 and 19 illustrate the voltage and current waveforms with FFT analysis for an MI of 0.9 using SPWM and SVM inverters.

Figures 16–19 illustrate output current waveforms with various modulation indices for comparison. It can be seen that when the MI is fixed at 0.9, the output current waveform is more sinusoidal. THD_i and THD_v results for various modulation indices are similarly displayed. The optimum output signal is created by increasing the MI with the SVM technique, as can be seen in Figure 20. It is also evident that increasing the MI results in a decrease in current and voltage harmonics. Figure 21 shows the change in speed with MI. The comparative analysis of the hybrid system with THDs with different modulation indices is shown in Table 1.

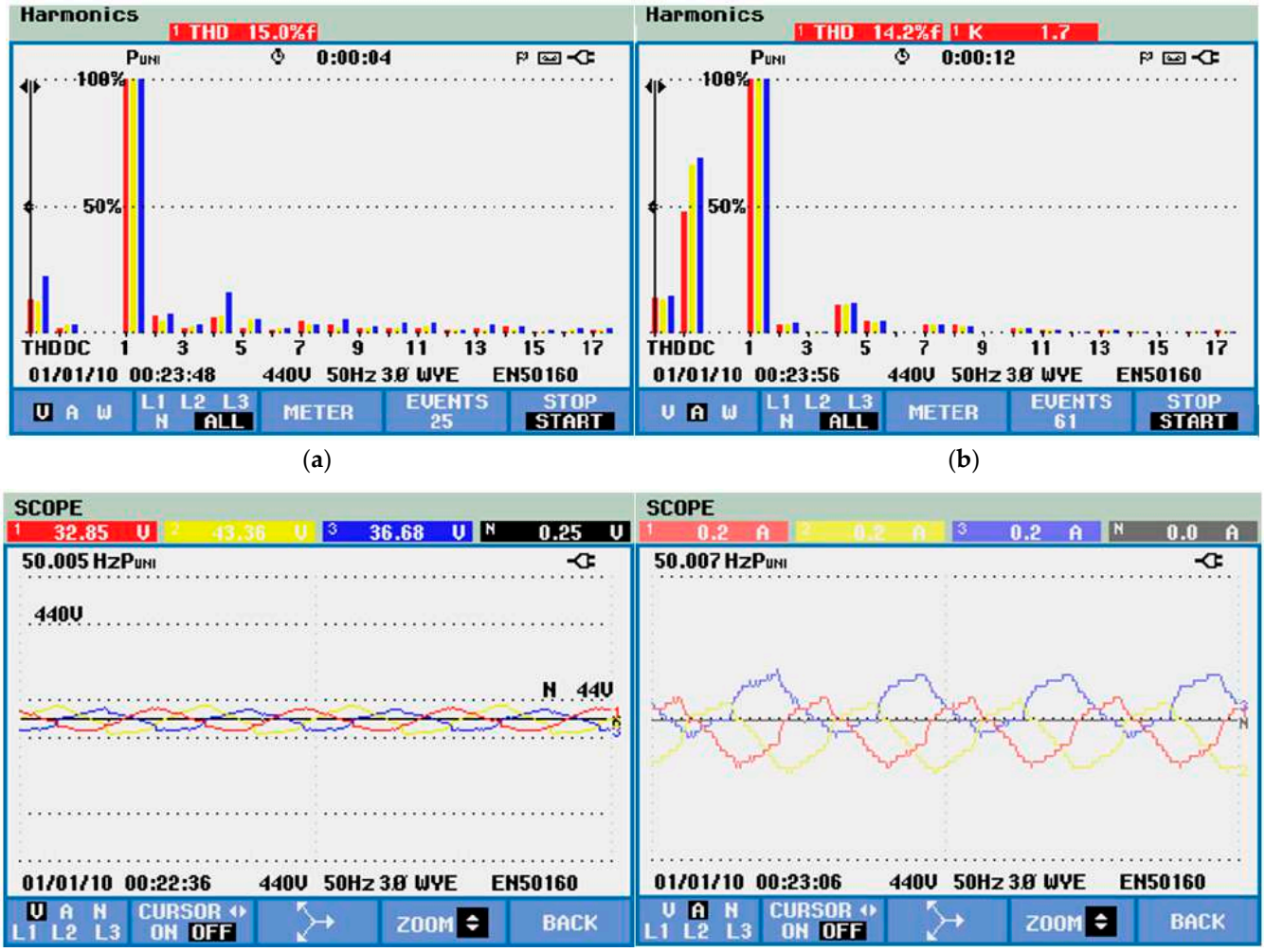

Figure 16. (**a**) Voltage THD (**b**) Current THD (**c**) Voltage (**d**) Current of a three-phase SVM inverter (**MI = 0.3**).

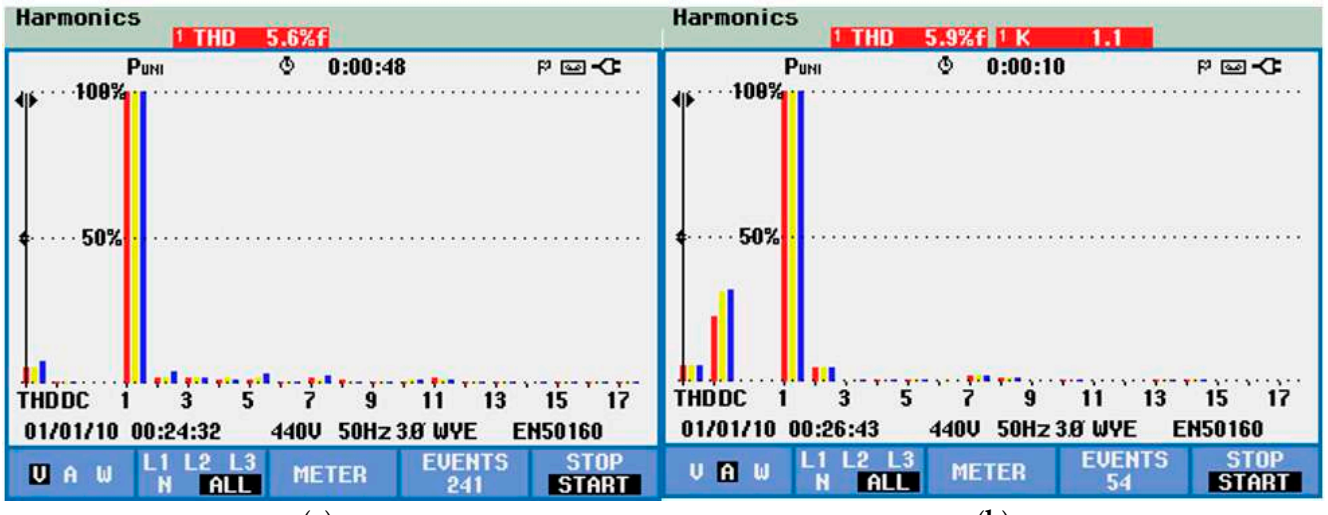

Figure 17. *Cont.*

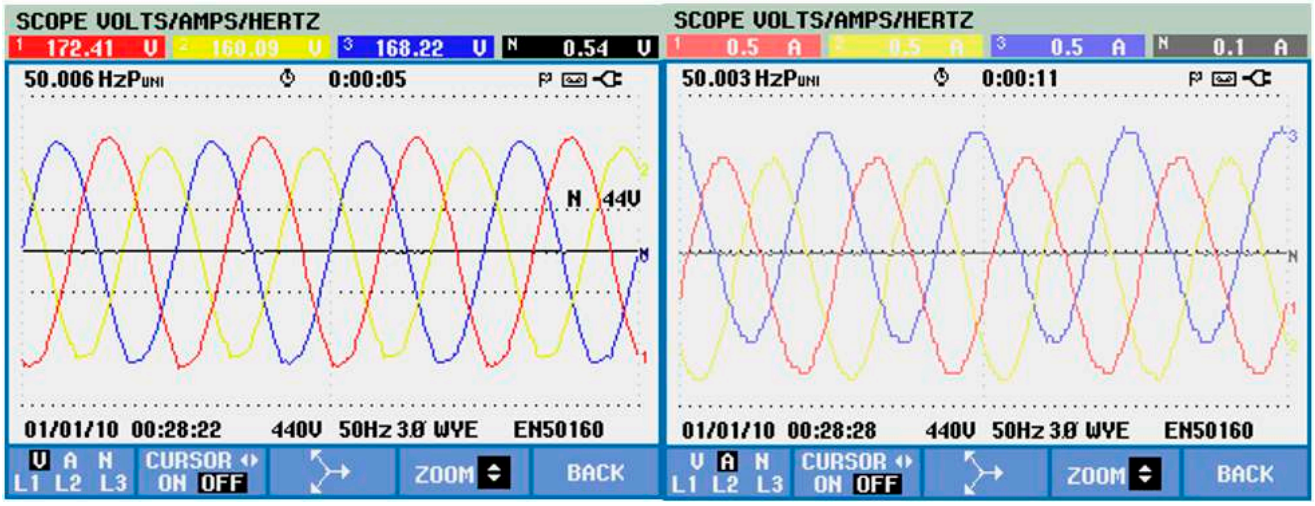

(**c**) (**d**)

Figure 17. (**a**) Voltage THD (**b**) Current THD (**c**) Voltage (**d**) Current of a three-phase SVM inverter (**MI = 0.6**).

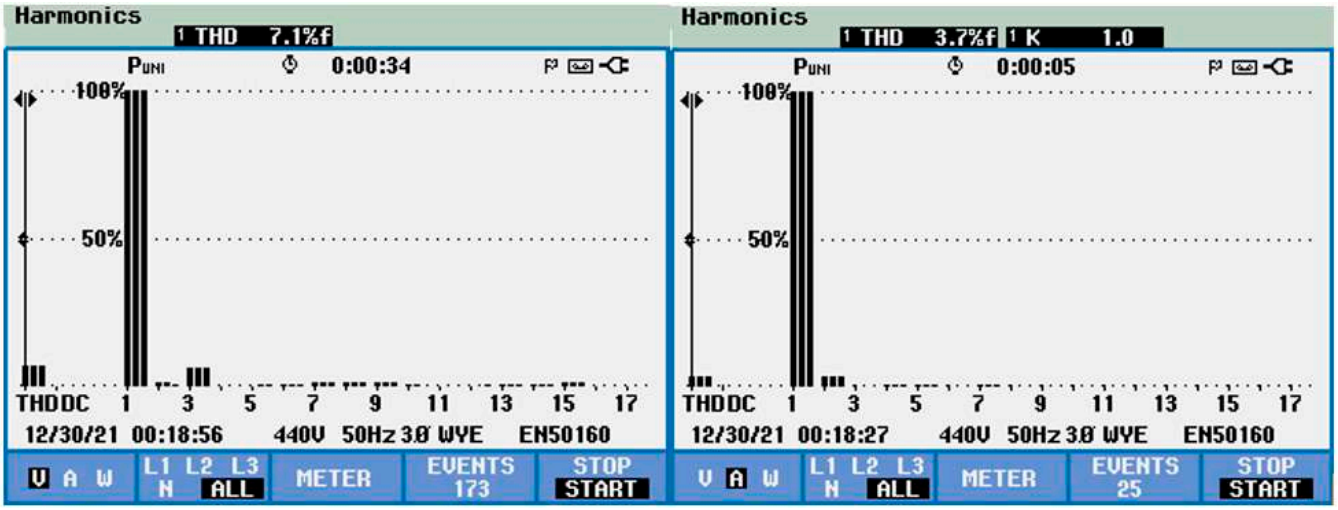

(**a**) (**b**)

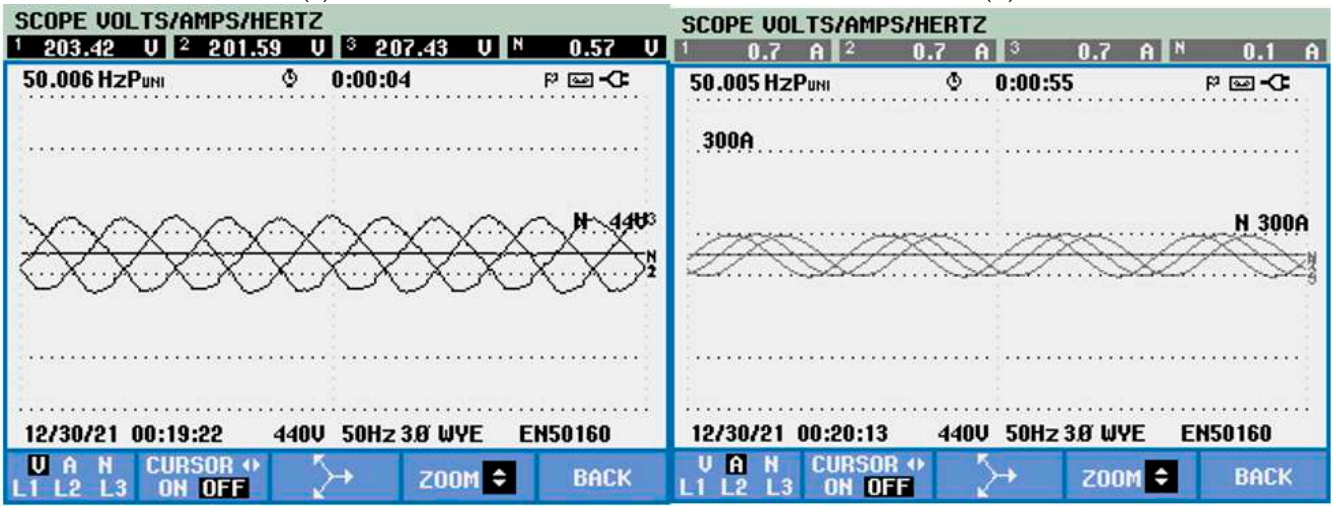

(**c**) (**d**)

Figure 18. (**a**) Voltage THD (**b**) Current THD (**c**) Voltage (**d**) Current of a three-phase SPWM inverter (**MI = 0.9**).

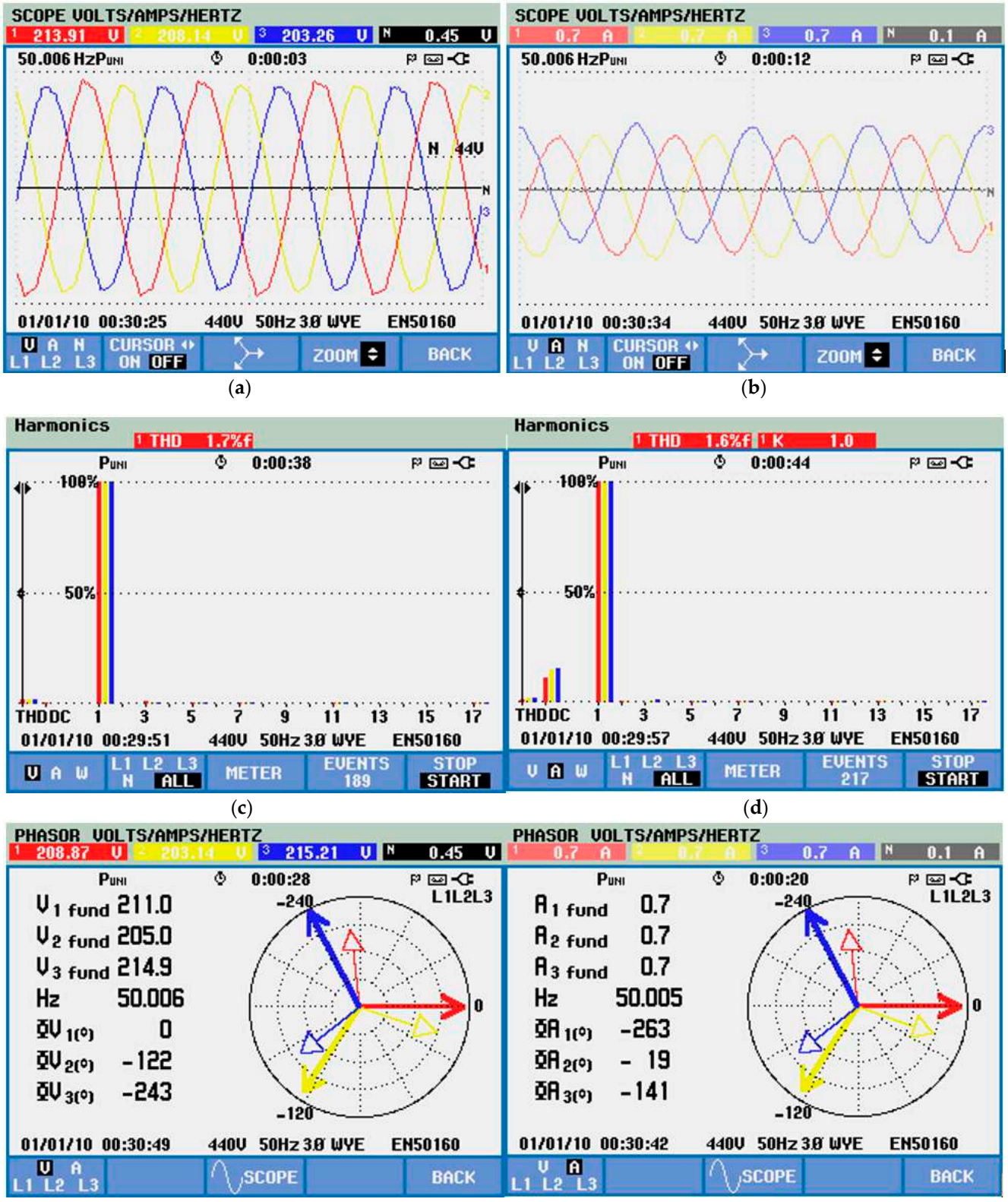

(**a**) (**b**)

(**c**) (**d**)

(**e**) (**f**)

Figure 19. (**a**) Voltage (**b**) Current (**c**) Voltage THD (**d**) Current THD (**e**) Voltage and (**f**) Current Phasor Diagrams of a three-phase SVM inverter (**MI = 0.9**).

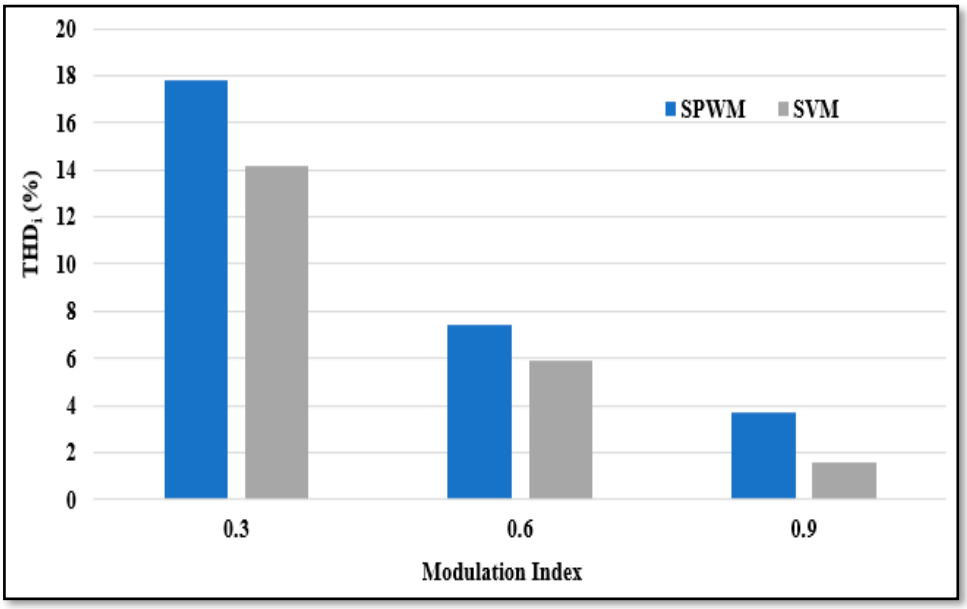

Figure 20. Comparison of Current THDs for the SPWM and SVM techniques.

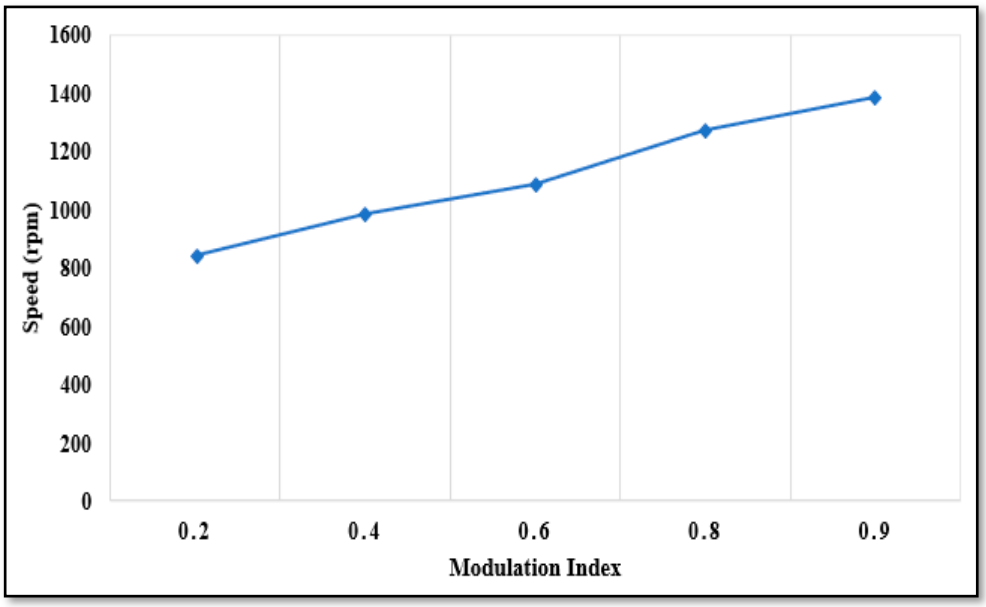

Figure 21. Change in speed vs. MI.

Table 1. Comparative analysis of THD with different modulation indices.

M.I	SPWM		SVM		Speed (rpm)
	THD$_i$ (%)	THD$_v$ (%)	THD$_i$ (%)	THD$_v$ (%)	
0.3	17.8	21.7	14.2	15.0	922
0.6	7.4	11.5	5.6	5.9	1138
0.9	3.7	7.1	1.6	1.7	1410

5.3. Power-Loss Analysis

Power loss is the most crucial factor when calculating an inverter's efficiency. The most power is lost at the power switches. Knowing the power loss and heat dissipation, in addition to the inverter efficiency, is critical for constructing the proper heat sink. Total power losses in semiconductor power switches are often classified as static or dynamic.

The static loss includes conversion loss (on-state power losses) and cut-off loss. Failure to switch on and turn off makes up for the dynamic loss. The switching loss (P_{sw}), conduction loss (P_{cond}), and blocking loss ($P_{blocking}$) are the three primary losses to calculate in power switches. The blocking losses caused by leakage currents must be noted, though they are usually overlooked. However, switching losses are insignificant. The huge reduction in switching losses in VSI devices is the consequence of the on-and-off switch procedure during one fundamental period [41]. The switching device used in the VSI is Si-MOSFET.

$$P_{Loss} = P_{Sw} + P_{Cond} + P_{blocking} \tag{40}$$

5.3.1. Conduction Losses

The conduction power losses (P_{cond}) of MOSFETs may be calculated using a MOSFET approximation of the drain-to-source resistance (R_{DSon}) [42].

$$V_{DS}(i_D) = R_{DSon}(i_D).i_D \tag{41}$$

where V_{DS}, i_D = root mean square of the drain-to-source voltage and the drain current. R_{DSon} can be determined by reference to the MOSFET datasheet because it depends on the gate-to-source voltage, the junction temperature (T_j), and the drain current (V_{GS}).

Equation (42) provides the instantaneous MOSFET conduction power.

$$P_{C,MOSFET}(t) = V_{DS}(t)i_D(t) = R_{DSon}i_D^2(t) \tag{42}$$

The following is an expression for the average conduction losses.

$$P_{C,MOSFET} = \frac{1}{T_{SW}} \int_{0+\varnothing}^{T_{on}} P_{C,MOSFET}(t)dt \tag{43}$$

T_{on} = on-state period and φ = the phase angle.

$$P_{C,MOSFET} = R_{DSon}i_{Drms}^2 \tag{44}$$

It is also possible to determine a body diode's ($P_{cond,diode}$) conduction loss using its resistance dynamics ($R_{on,diode}$) and diode threshold voltage (V_T), as demonstrated below:

$$P_{Cond,diode} = V_T I_{avg} + R_{on,diode} I_{rms}^2 \tag{45}$$

5.3.2. Switching Losses

Switching losses occur due to the slow transition from the on-state to the off-state and vice versa. Significant instantaneous power losses arise due to current flow and voltage via the switch becoming much more important than zero during the transition time [43].

During the turn-on interval, the energy dissipated.

$$E_{SW,MOSFET(on)} = \left(V_{dc} I_{dc} \frac{t_{c(on)}}{6}\right) - (V_{dc} - V_{on}) I_{dc} \frac{t_{c(on)}}{3} \tag{46}$$

where $t_{c(on)}$ = the turn-on crossover interval and $E_{Sw}(on)$ = energy dissipated during the turn-on interval.

When the MOSFET was turned off, the energy dissipated.

$$E_{SW,MOSFET(off)} = \left(V_{dc} I_{dc} \frac{t_{c(off)}}{6}\right) - V_{on} I_{dc} \frac{t_{c(on)}}{3} \tag{47}$$

The total energy during turn-on and -off is:

$$E_{SW,MOSFET} = E_{SW,MOSFET(on)} + E_{SW,MOSFET(off)} \tag{48}$$

The switching losses had linear relations to the switching frequency and the switching current. The general average losses from swapping can be expressed as follows.

$$P_{SW,MOSFET} = \frac{1}{T_{SW}} \int_{0+\varnothing}^{T_{on}} E_{SW,MOSFET} dt \tag{49}$$

Figure 22 shows the power-loss analysis of the MOSFET-fed three-phase inverter.

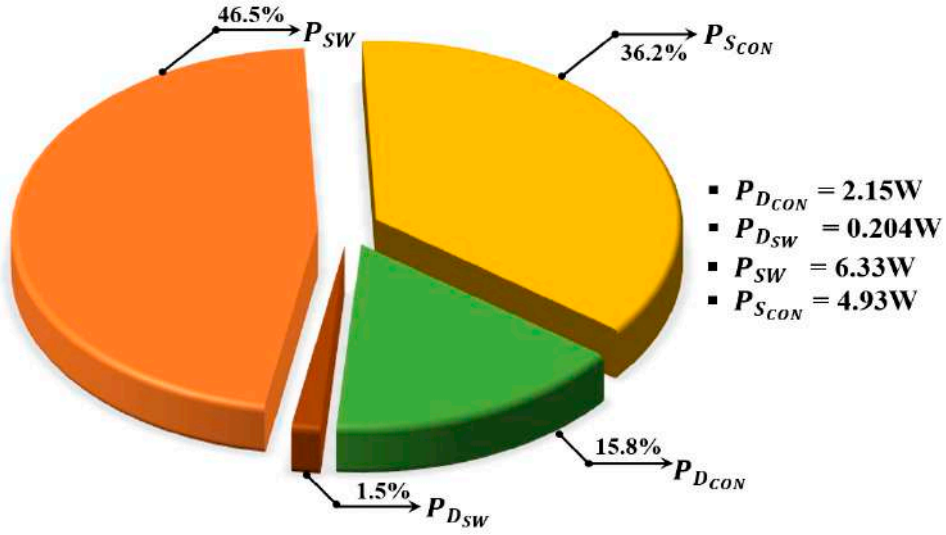

Figure 22. Power-Loss Analysis of Inverter.

6. Conclusions

In this study, SVM employing a PI controller was evaluated after considering the negative impacts of harmonics in a power system network. An SVM control technique was devised to reduce current harmonics and increase power quality. Pollution-free electricity generation via PV systems was prioritized along with improving power quality. This research paper focused on the harmonic analysis of a three-phase PWM inverter that supplies an IM using a variety of modulation indices. However, the work was limited, since losses were higher at high switching frequencies. The motor's speed can be controlled by creating suitable controls and switching methods. Since it can reduce switching losses and harmonic output signals, SVM is the ideal method for switching and regulating the inverter. In MATLAB, the three-phase PWM inverter that supplies the IM was modelled. An experimental setup was also created to validate the outcomes of the simulation. The results indicated that the IEEE Standard 519 limit of 5% for harmonic content in voltage and current was exceeded.

Additionally, it was found that THD declined as the MI rose. Future research could use various PWM techniques to reduce harmonics while maintaining constant MIs. Finally, the system was evaluated using a real-time scaled-down prototype based on dSPACE, and the simulation results were confirmed. Each scenario's harmonic analysis was adequately adjusted to the IEEE-519 Standard's limitations.

Author Contributions: Conceptualization. S.V., V.I., B.A. and M.B; Methodology. S.V., V.I. and M.B.; Software. S.V., Formal Analysis. S.V., V.I. and B.A.; Investigation. S.V.; Resources. S.V. and M.B.; Data Curation. S.V., V.I. and M.B.; Writing–original draft preparation. S.V. and V.I.; Writing—reviewing and editing. S.V., V.I. and B.A.; Visualization. V.I.; Supervision. B.A. and V.I. All authors provided critical feedback and collaborated in the paper. All authors have read and agreed to the published version of the manuscript.

Funding: This research received no external funding.

Institutional Review Board Statement: Not Applicable.

Informed Consent Statement: Not Applicable.

Data Availability Statement: Not Applicable.

Conflicts of Interest: The authors declare no conflict of Interest.

References

1. Lu, S.-M. A review of high-efficiency motors: Specification, policy, and technology. *Renew. Sustain. Energy Rev.* **2016**, *59*, 1–12. [CrossRef]
2. De Almeida, A.T.; Fong, J.; Falkner, H.; Bertoldi, P. Policy options to promote energy efficient electric motors and drives in the EU. *Renew. Sustain. Energy Rev.* **2017**, *74*, 1275–1286. [CrossRef]
3. Alsofyani, I.M.; Idris, N.R.N. A review on sensorless techniques for sustainable reliablity and efficient variable frequency drives of induction motors. *Renew. Sustain. Energy Rev.* **2013**, *24*, 111–121. [CrossRef]
4. Santos, T.H.d.; Goedtel, A.; da Silva, S.A.O.; Suetake, M. Scalar control of an induction motor using a neural sensorless technique. *Electr. Power Syst. Res.* **2014**, *108*, 322–330. [CrossRef]
5. Kashif, S.A.R.; Saqib, M.A.; Zia, S. Implementing the induction-motor drive with four-switch inverter: An application of neural networks. *Expert Syst. Appl.* **2011**, *38*, 11137–11148. [CrossRef]
6. Saidur, R.; Mekhilef, S.; Ali, M.B.; Safari, A.; Mohammed, H.A. Applications of variable speed drive (VSD) in electrical motors energy savings. *Renew. Sustain. Energy Rev.* **2012**, *16*, 543–550. [CrossRef]
7. Reza, C.M.F.S.; Islam, M.D.; Mekhilef, S. A review of reliable and energy efficient direct torque-controlled induction motor drives. *Renew. Sustain. Energy Rev.* **2014**, *37*, 919–932. [CrossRef]
8. Saidur, R. A review on electrical motors energy use and energy savings. *Renew. Sustain. Energy Rev.* **2010**, *14*, 877–898. [CrossRef]
9. Lipu, M.S.H.; Karim, T.F. Energy ef_ciency opportunities and savings potential for electric motor and its impact on GHG emissions reduction. *Int. J. Elect. Comput. Eng.* **2013**, *3*, 533–542.
10. Hannan, M.A.; Ali, J.A.; Mohamed, A.; Hussain, A. Optimization techniques to enhance the performance of induction motor drives: A review. *Renew. Sustain. Energy Rev.* **2017**, *81*, 1611–1626. [CrossRef]
11. Jannati, M. A review on variable speed control techniques for ef_cient control of single-phase induction motors: Evolution, classi_cation, comparison. *Renew. Sustain. Energy Rev.* **2017**, *75*, 1306–1319. [CrossRef]
12. Saad, N.; Arro, M. A PLC-based modi_ed-fuzzy controller for PWM-driven induction motor drive with constant V/Hz ratio control. *Robot. Comput.-Integr. Manuf.* **2012**, *28*, 95–112. [CrossRef]
13. Saribulut, L.; Teke, A.; Tümay, M. Vector-based reference location estimating for space vector modulation technique. *Electr. Power Syst. Res.* **2012**, *86*, 51–60. [CrossRef]
14. Vashishtha, S.; Rekha, K.R. A survey: Space vector PWM (SVPWM) in 3φ voltage source inverter (VSI). *Int. J. Electr. Comput. Eng. (IJECE)* **2018**, *8*, 11–18. [CrossRef]
15. Al-Ogaili, A.S.; Aris, I.B.; Verayiah, R.; Ramasamy, A.; Marsadek, M.; Rahmat, N.A.; Al-Masri, A.N. A three-level universal electric vehicle charger based on voltage-oriented control and pulse-width modulation. *Energies* **2019**, *12*, 2375. [CrossRef]
16. Young, H.A.; Perez, M.A.; Rodriguez, J.; Abu-Rub, H. Assessing finite-control-set model predictive control: A comparison with a linear current controller in two-level voltage source inverters. *IEEE Ind. Electron. Mag.* **2014**, *8*, 44–52. [CrossRef]
17. Liu, C.; Ma, R.; Bai, H.; Gechter, F.; Gao, F. A new approach for FPGA based real-time simulation of power electronic system with no simulation latency in subsystem partitioning. *Int. J. Electr. Power Energy Syst.* **2018**, *99*, 650–658. [CrossRef]
18. Gdaim, S.; Mtibaa, A.; Mimouni, M.F. Design and experimental implementation of DTC of an induction machine based on fuzzy logic control on FPGA. *IEEE Trans. Fuzzy Syst.* **2015**, *23*, 644–655. [CrossRef]
19. Hakami, S.S.; Mohd Alsofyani, I.; Lee, K.B. Low-speed performance improvement of direct torque control for induction motor drives fed by three-level NPC inverter. *Electronics* **2020**, *9*, 77. [CrossRef]
20. Wilamowski, B.M.; Irwin, J.D. *Power Electronics and Motor Drives*; CRC Press: Boca Raton, FL, USA, 2011.
21. Djoudi, A.; Bacha, S.; Iman-Eini, H.; Rekioua, T. Sliding mode control of DFIG powers in the case of unknown _ux and rotor currents with reduced switching frequency. *Int. J. Electr. Power Energy Syst.* **2018**, *96*, 347–356. [CrossRef]
22. Barnes, M. *Practical Variable Speed Drives and Power Electronics*; Newnes: Oxford, UK, 2003.
23. Singh, A.; Grant, B.; DeFour, R.; Sharma, C.; Bahadoorsingh, S. A review of induction motor fault modeling. *Electr. Power Syst. Res.* **2016**, *133*, 191–197. [CrossRef]
24. Chan, T.-F.; Shi, K. *Applied Intelligent Control of Induction Motor Drives*; Wiley: Hoboken, NJ, USA, 2011.
25. Krause, P.C.; Wasynczuk, O.; Sudhoff, S.D.; Pekarek, S. *Analysis of Electric Machinery and Drive Systems*; IEEE: Piscataway, NJ, USA, 2013.
26. Gandoman, F.H. Review of FACTS technologies and applications for power quality in smart grids with renewable energy systems. *Renew. Sustain. Energy Rev.* **2018**, *82*, 502–514. [CrossRef]
27. Abu-Rub, H.; Iqbal, A.; Guzinski, J. *High Performance Control of AC Drives with Matlab/Simulink Models*; Wiley: Hoboken, NJ, USA, 2012.
28. Talla, J.; Leu, V.Q.; Mídl, V.; Peroutka, Z. Adaptive speed control of induction motor drive with inaccurate model. *IEEE Trans. Ind. Electron.* **2018**, *65*, 8532–8542. [CrossRef]

29. Hannan, M.A. A quantum lightning search algorithm-based fuzzy speed controller for induction motor drive. *IEEE Access* **2018**, *6*, 1214–1223. [CrossRef]
30. Al-Ogaili, A.S.; Aris, I.; Othman, M.L.; Hoon, Y.; Isa, D.; Azis, N.; Abbas, H.F. A review of Different Control Methods in Power Electronics. *J. Eng. Appl. Sci.* **2018**, *13*, 2242–2253.
31. Liang, W.; Wang, J.; Luk, P.C.-K.; Fang, W.; Fei, W. Analytical modeling of current harmonic components in PMSM drive with voltage source inverter by SVPWM technique. *IEEE Trans. Energy Convers.* **2014**, *29*, 673–680. [CrossRef]
32. Zhang, X.; Zhang, W.; Chen, J.; Xu, D. Deadbeat control strategy of circulating currents in parallel connection system of three-phase PWM converter. *IEEE Trans. Energy Convers.* **2014**, *29*, 406–417.
33. Guzman, H.; Barrero, F.; Duran, M.J. IGBT-gating failure effect on a fault-tolerant predictive current-controlled five-phase induction motor drive. *IEEE Trans. Ind. Electron.* **2015**, *62*, 15–20. [CrossRef]
34. Velander, E.; Kruse, L.; Wiik, T.L.; Wiberg, A.; Colmenares, J.; Nee, H.-P. An IGBT turn-ON concept offering low losses under motor drive dv/dt constraints based on diode current adaption. *IEEE Trans. Power Electron.* **2018**, *33*, 1143–1153. [CrossRef]
35. Agarwal, P.; Langer, N.; Bhat, A.H. Neural-network-based space vector pulse-width modulation for capacitor voltage balancing of three-phase three-level improved power quality converter. *IET Power Electron.* **2014**, *7*, 973–983.
36. Amiri, M.; Milimonfared, J.; Khaburi, D.A. Predictive torque control implementation for induction motors based on discrete space vector modulation. *IEEE Trans. Ind. Electron.* **2018**, *65*, 6881–6889. [CrossRef]
37. Bose, B.K. Scalar decoupled control of induction motor. *IEEE Trans. Ind. Appl.* **1984**, *IA-20*, 216–225. [CrossRef]
38. Durgasukumar, G.; Pathak, M.K. Comparison of adaptive neuro-fuzzy-based space-vector modulation for two-level inverter. *Int. J. Electr. Power Energy Syst.* **2012**, *38*, 9–19. [CrossRef]
39. Boby, M.; Gopakumar, K.; Umanand, L.; Blaabjerg, F.; Bhattacharya, S. A low-order harmonic elimination scheme for induction motor drives using a multilevel octadecagonal space vector structure with a single DC source. *IEEE Trans. Power Electron.* **2018**, *33*, 2430–2437. [CrossRef]
40. Kirankumar, B.; Reddy, Y.V.S.; Vijayakumar, M. Multilevel inverter with space vector modulation: Intelligence direct torque control of induction motor. *IET Power Electron.* **2017**, *10*, 1129–1137. [CrossRef]
41. Sumithira, T.R.; Nirmal Kumar, A. Elimination of harmonics in multilevel inverters connected to solar photovoltaic systems using ANFIS: An experimental case study. *J. Appl. Res. Technol.* **2013**, *11*, 124–132. [CrossRef]
42. Ahmed, M.H.; Wang, M.; Hassan, M.A.S.; Ullah, I. Power loss model and efficiency analysis of three-phase inverter based on SiC MOSFETs for PV applications. *IEEE Access* **2019**, *7*, 75768–75781. [CrossRef]
43. Chaturvedi, P.K.; Jain, S.; Agrawal, P.; Nema, R.K.; Sao, K.K. Switching losses and harmonic investigations in multilevel inverters. *IETE J. Res.* **2014**, *54*, 297–307. [CrossRef]

energies

MDPI

Review

Comparative Study of DC-DC Converters for Solar PV with Microgrid Applications

Ingilala Jagadeesh and Vairavasundaram Indragandhi *

School of Electrical Engineering, Vellore Institute of Technology, Vellore 632014, India
* Correspondence: indragandhi.v@vit.ac.in

Abstract: This review emphasizes the role and performance of versatile DC-DC converters in AC/DC and Hybrid microgrid applications, especially when solar (photo voltaic) PV is the major source. Here, the various converter topologies are compared with regard to voltage gain, component count, voltage stress, and soft switching. This study suggests the suitability of the converter based on the source type. The merits of a coupled inductor and interleaved converters in micro gird applications are elucidated. The efficiency and operating frequencies of converts for different operating modes are presented to determine the suitable converters for inductive and resistive loads. The drawbacks of converters are discussed. Finally, the mode of operation of different converts with different grid power sources and its stability and reliability issues are highlighted. In addition, the significance of the converter's size and cost-effectiveness when choosing various PV source applications are discussed.

Keywords: coupled inductor converter; full bridge converter; half bridge converter; interleaved converter; micro grid; photo voltaic (PV); resonant converter; zero voltage switching (ZVS); zero current switching (ZCS)

Citation: Jagadeesh, I.; Indragandhi, V. Comparative Study of DC-DC Converters for Solar PV with Microgrid Applications. *Energies* **2022**, *15*, 7569. https://doi.org/10.3390/en15207569

Academic Editors: Alon Kuperman and Nicu Bizon

Received: 29 August 2022
Accepted: 10 October 2022
Published: 13 October 2022

Publisher's Note: MDPI stays neutral with regard to jurisdictional claims in published maps and institutional affiliations.

Copyright: © 2022 by the authors. Licensee MDPI, Basel, Switzerland. This article is an open access article distributed under the terms and conditions of the Creative Commons Attribution (CC BY) license (https://creativecommons.org/licenses/by/4.0/).

1. Introduction

The DC microgrid contains renewable energy sources and a hybrid energy storage unit. Hence, we are using Energy Management Methods to reduce power fluctuation on power quality [1]. We utilise many switching devices in renewable energy sources because high penetration occurs and switching losses or harmonics impact the utility grid's system reliability [2]. This paper presents an overview of microgrids' energy management strategies and grid integration technologies. To produce a clean energy future and minimize costs, renewable energy-based distributed generation is moving fast to meet the world's vital needs of utilizing clean energy sources [3]. By converting solar energy into electrical energy without environmental contamination photovoltaic system provides a direct method. PV systems convert solar power to electric power integrated with the grid if it meets the grid code [4]. The DC microgrid consists of a battery energy storage system, wind turbine, grid-connected converter system, and dc loads. Solar PV is one of the renewable energy technologies best suited for islands, hills, and forest areas such as,

- ➢ Minimal communication and transportation facilities.
- ➢ Illiterate and Poor technical knowledge places.

Here power electronics blocks are required for grid integration to maximize the benefits of solar energy [5].

Solar PV and load require a suitable DC-DC converter to increase the system's efficiency. Multiple converters are typically designed for high voltage gain of solar PV applications [6]. In addition, better dynamic response and less ripple are obtained by multiphase interleaved DC-DC converters, preserving their efficiency. This study presents a SEPIC, CUK combination converter-based interleaved converter for connecting distributed generation to bipolar DC micro grids and power architecture [7]. Finally, switched inductors

and switched capacitors are used to provide a high gain. All semiconductor devices have the same voltage stress. Therefore, it is possible to utilize devices with uniform ratings and minimal internal resistance [8]. Finally, a multi-port isolated DC-DC converter replaced the traditional Buck/Boost circuit to ensure electrical isolation of the energy storage system's micro sources [9]. The boost DC-DC converter topology has the following demerits: large capacitors are needed, there is a <4:1 voltage gain, parallel devices are required at high power levels, and there is a high ripple rate [10,11]. Due to their high conversion efficiency, minimal size, and low production costs, the described DC-DC converter topology a significant role in the power-generating industry, including microgrids. The DC-DC converters in are separated into isolated and non-isolated topologies [12,13]. The general classification of DC-DC converters are depicted in Figure 1.

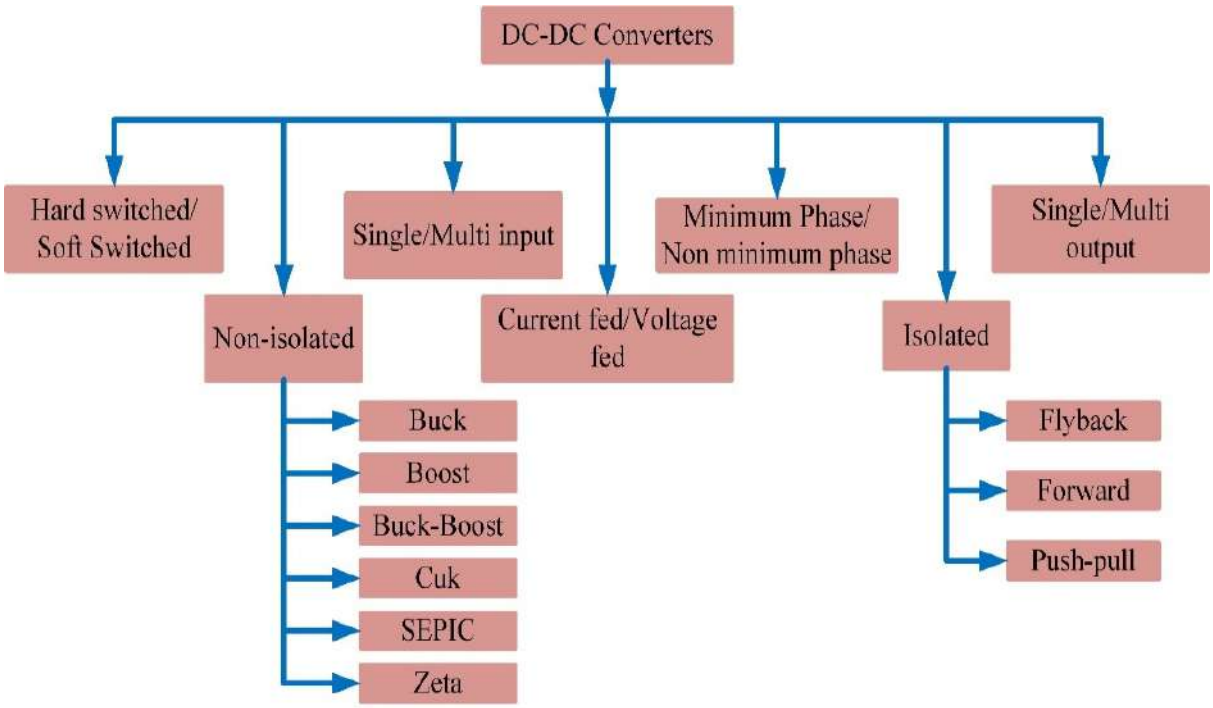

Figure 1. Types of DC-DC converters.

When the traditional boost converter is preferred in PV systems, it has to be operated at a duty cycle of 0.88, making it difficult in practical application due to the limitation of semiconductor devices. Moreover, the boost converters suffer the drawback of high switching voltage stress and reverse recovery issues [14]. The applications of smart grid system are summarized in Figure 2.

The grid functions today are the same as when there were minor improvements, and the energy cost was relatively low. There is currently no heavy electricity storage technology available. Therefore, if we use this power during off-peak hours, we will build an effective system. However, we may adjust load consumption to increase grid efficiency, which is how the Smart grid differs from a traditional grid.

These converters require a higher power transformer, as higher power converters cannot use a single switch topology. For example, Half-bridge, push-pull and Full-bridge converters comes under another DC-DC isolated converters which use a minimum of multi-switch. Figure 3 represents a simplified hybrid microgrid charging station for battery-powered electric vehicles.

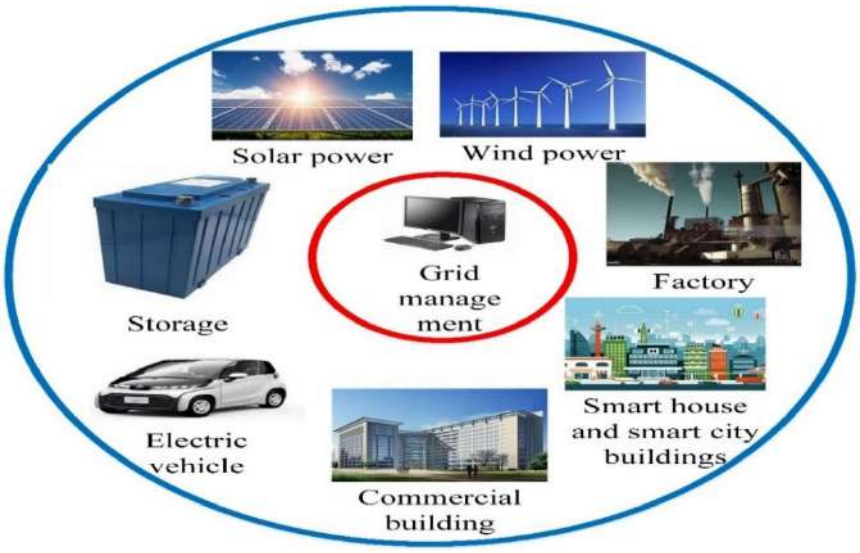

Figure 2. The architecture of smart grid management system applications.

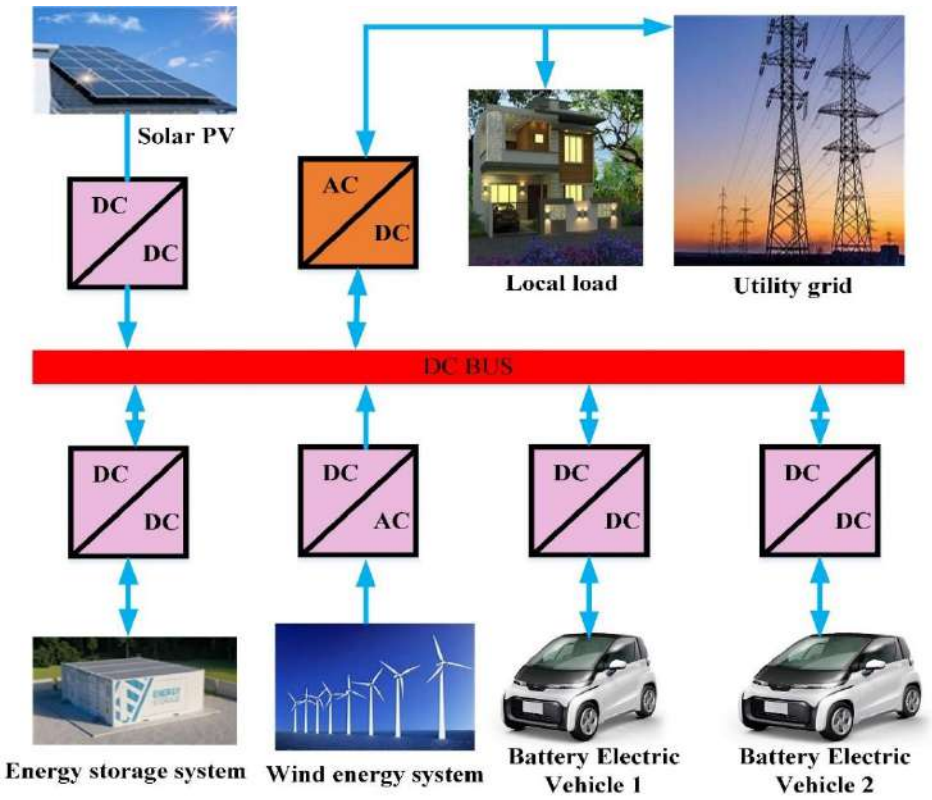

Figure 3. The battery-based electric vehicle's charging station with the hybrid microgrid model.

The PV technologies can be employed in various applications, including electric vehicles, domestic, and microgrid applications [15]. The different operating voltages of the DC-DC converters linked to the PV system are described. In addition, in grid-connected mode converters, suitable load types are identified along with their corresponding voltage gain and conversion efficiency. This review elucidates the operation of 14 types of DC-DC converters for grid-connected PV applications. This is followed by comparing the converters performance for different grid-connected PV systems operating modes along with discussed distributed energy sources. At last, each converters parametric analysis and

components sizing comparison are critically examined to further identify the drawbacks in each converter for a particular source application for a specific mode of operation.

2. Requirements for the Selection of DC-DC Converter Topology

The DC-DC converter topologies that are to be used in a PV-based power supply should meet the conditions given in the subsequent paragraphs. A typical layout of DC microgid is depicted in Figure 4. Without increasing the stack size, we can obtain the desired DC voltage value with the help of the DC-DC converter. For example, the DC output from the polymer electrolyte membrane (PEM) FC stack is mostly around several tens of volts. Therefore, the ripple current value observed across the PV due to the DC-DC converter switching should be low. Most importantly, a sharp rise or a fall in the current and high-frequency current ripple of a large magnitude should be avoided [16].

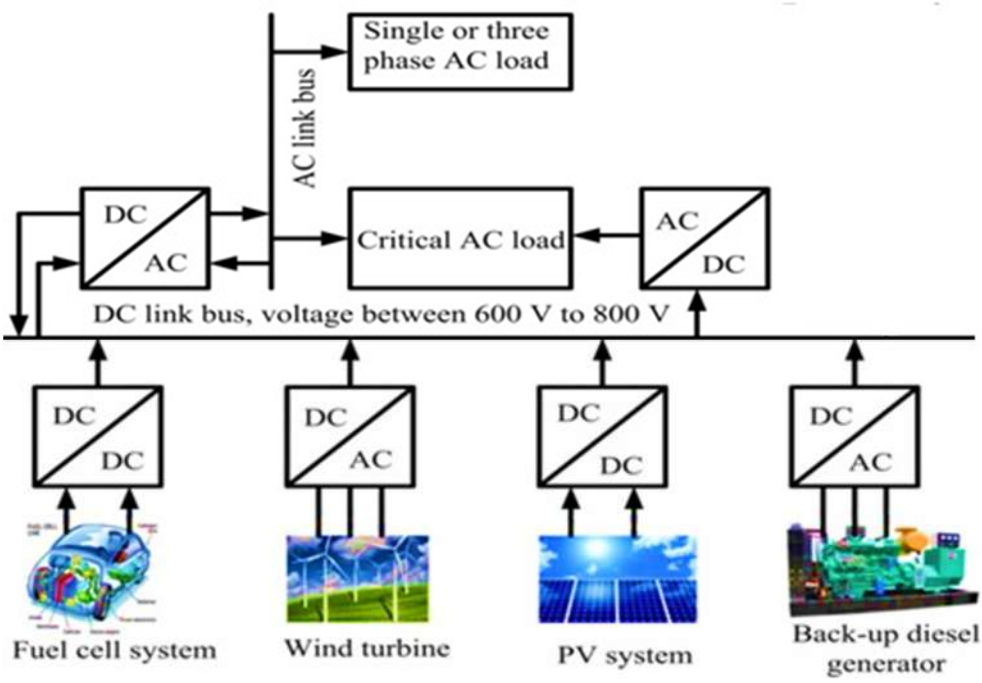

Figure 4. Layout of DC microgrid.

An overview of the present-day technology in isolated DC-DC converters for PV-based power generation is presented in Table 1. The study includes an analysis of literature to understand current achievements and viewpoints. While many papers on the subject have been published, many of them do not include details on the achieved efficiency or the complexity of the converter when operating a greater number of devices, and issues with power density maximization are mentioned. Within the limited information available, a comparison of published literature for high voltage gain DC-DC converters is attempted, and an overview of each solution is provided.

3. Survey of DC-DC Converter Topologies

3.1. Coupled Inductor Converter Topology

This section enumerates the published solutions of coupled inductor topology DC-DC converters possess high gain, as shown in Figures 5–8. Each published technique explains the topology used, the converter V_{in} and V_{out} range, and the power range of the experimental setup are given to validate the interfacing with FC for power generation. In [17] the authors proposed a DC-DC converter with soft switching exhibits continuous input current and a high voltage gain. Experimentally, a 200 W prototype having V_{in} = 24 V, and V_{out} = 360 V gives 96.4% efficiency at full load. The advantages of derived interleaved boost converter having Winding-Cross-Coupled Inductors (WCCIs) and passive-lossless

clamp circuits are increased voltage gain, reduced switching voltage stress, and reduced reverse recovery problem due to the leakage inductance when compared with conventional interleaved boost converters [18]. An interleaved boost converter rated 1 kW, 40 V to 380 V experimental findings show an efficiency of 90.7% at full load, which is 5% better than a typical interleaved boost converter. [19]. A three-winding coupled inductor produced a high voltage gain. The energy in the leakage inductor is released to the output directly, reducing the switch stress. The output diode's reverse recovery current is evaluated using a coupled inductor. A closed loop control method is used, which overcomes the power source voltage drift problem. The converter is used with a FC which gives a P_o = 300 W V_{out} = 400 V, V_{in} = 27 V–36.5 V and F_s = 100 kHz. It gives a maximum efficiency of 95.2% at 220 W. A 200 W boost converter having coupled inductors, and buck-boost active clamps for low V_{in} applications is proposed in [20]. The V_{in} range is 25–40 V, V_{out} is 200 V and output current of 1A with a switching frequency of 66 kHz. ZVS turns on the main and auxiliary switches, and the boost diode is turned on DC-DC ZCS. Thus, the switching losses are chopped. The converter efficiency is 92%, and the output power is 200 W. A high voltage gains 250 W non-isolated DC-DC converter having a three-stage switching cell and voltage multiplier is proposed and demonstrates the V_{in} range is 30–45 V, and V_{out} is 400 V. The three-stage switching cells reduce the converter's size and conduction losses while efficiency is 97% [20].

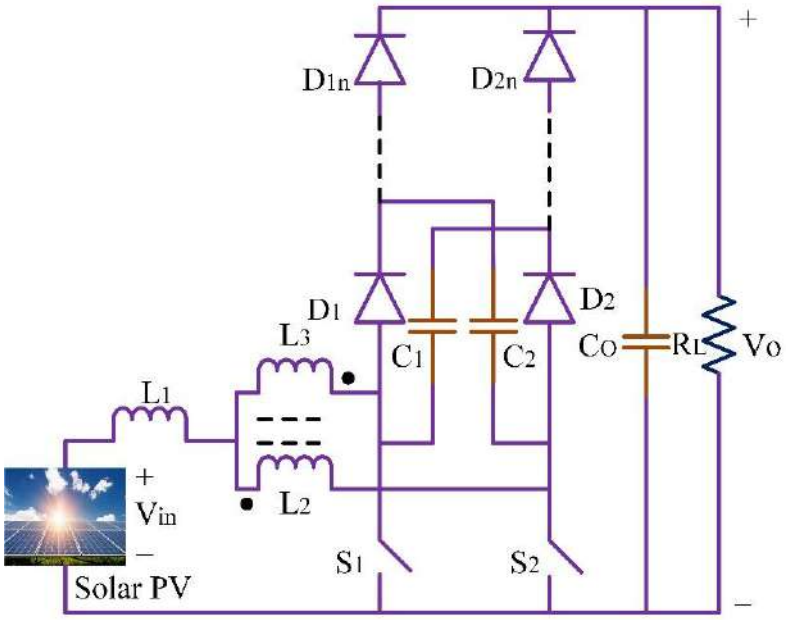

Figure 5. Coupled inductor 1.

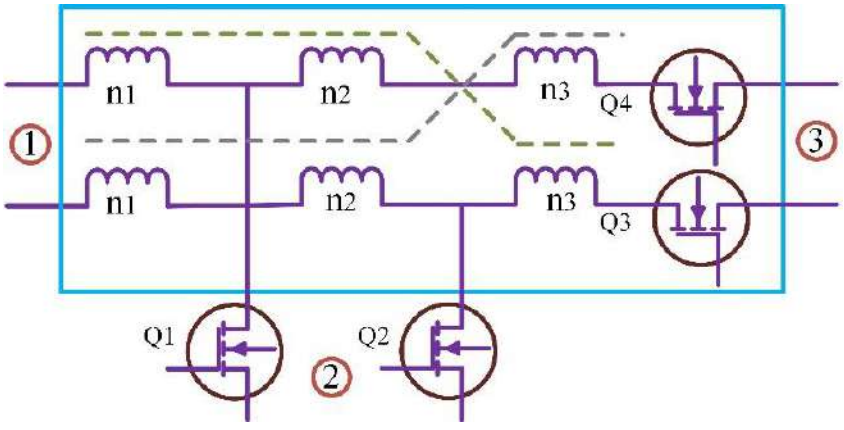

Figure 6. Coupled Inductor 2.

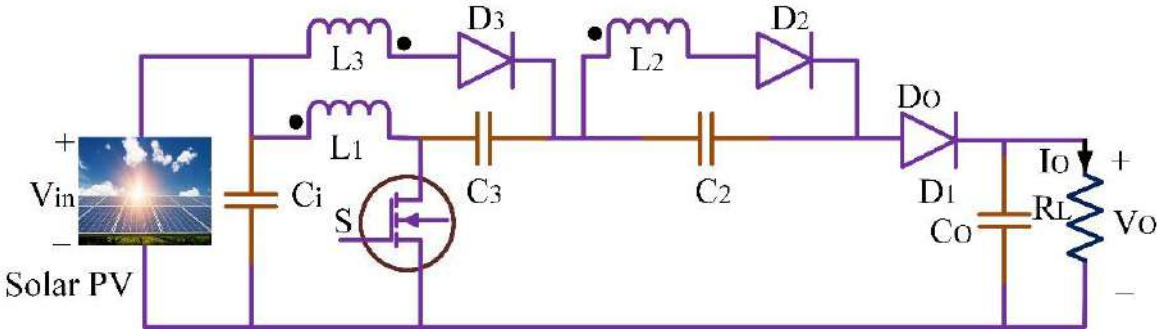

Figure 7. Coupled Inductor 3.

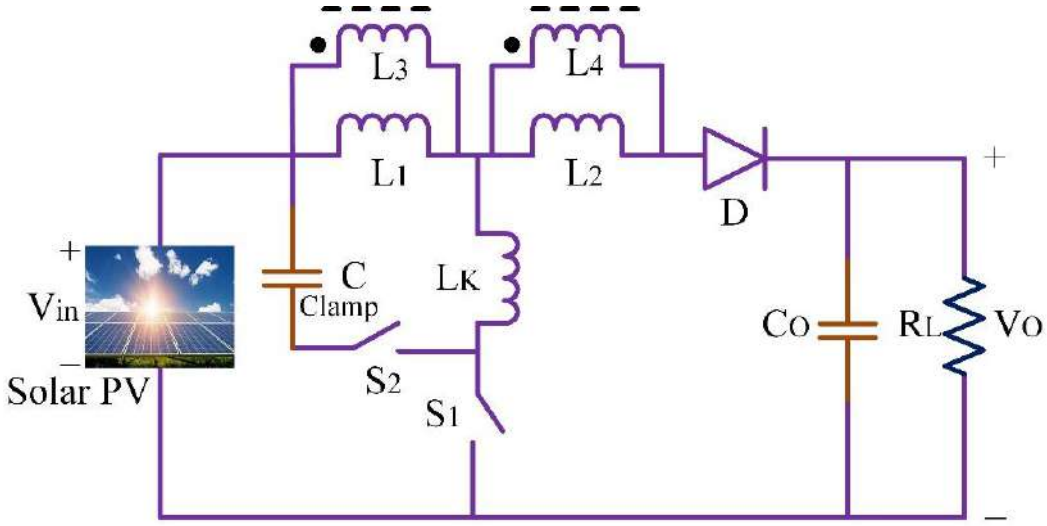

Figure 8. Coupled inductor 4.

A high step-up DC-DC converter is required to boost the voltage value generated through the 400 V DC bus voltage PV. Passive loss clamped technology is used to improve efficiency and limit voltage stress. Recycling of leakage energy is possible with the help of passive losses clamped technology. The basic boost converters' main disadvantages include problems with the electromagnetic interface, high voltage stress and hard switching on the semiconductor elements [21]. Coupled inductor DC-DC buck-boost converter is used for a step up and down by non-inverting voltage, this also offers high efficiency, control and regulation of input and output currents smoothly and immediately [22].

Table 1. Hybrid converters with observations.

Ref	Type of ASD	Converter Type	Supply Direction	Observations
[22]	Supercapacitor	Buck-boost	Buck-boost	The construction and design are simple, using the same modules for all the positions in the system.
[23]	Supercapacitor and Batteries	Buck-boost	Bidirectional buck-boost	The buck and boost modes of operation in the buck-boost converter connected with an FC, the operational dead-zone description, is not present in the system. It also consists of a design with complex control
[24]	Supercapacitor	Boost	Bidirectional buck-boost	The experimental result of the boost converter is not present in the system, and the converter also has some start-up problems.
[25]	Supercapacitor	Boost	Bidirectional buck-boost	The experimental load transient results of the boost converter are not present, and the converter has start-up problems.

Table 1. *Cont.*

Ref	Type of ASD	Converter Type	Supply Direction	Observations
[26]	Supercapacitor	Boost	Bidirectional buck-boost	The converter consists of a design with complex control, and the converter has start-up problems.
[27]	Supercapacitor	Boost	Bidirectional buck-boost	The boost converter consists of a design with complex control, and the converter has start-up problems.

The structure of the DC-DC boost converter consists of two hybrid, multiple voltage cells, and three winding coupled inductors. Using two multiple voltage cells, parallelly charged and discharged series, can provide very high voltage gain under the appropriate turns of ratio and duty cycle [28].

3.2. Interleaved Non-Isolated Topology

This section listed the published solutions of high gain interleaved non-isolated DC-DC converter topology. The voltage multiplier technique is used to the non-isolated DC-DC converters to possess a high step-up static gain, is presented in [29]. The V_{in} is 24 V, and the output V_{out} is 400 V. The output power is 400 W. The converter operated with a switching frequency of 40 kHz. The converter efficiency was 95%. Low electromagnetic interference production and commutation losses are attained. Without a power transformer, high static gain operation is possible. The V_{in} is 48 V and V_{out} is 380 V with an operating frequency of 100 kHz. The measured efficiency at 1 kW is 94.1%. The voltage doubler circuits increase the operating range of the converter by reducing the transformer's parasitic capacitor's effects. The interleaved Inductor-Inductor-Capacitor (LLC) converter for high gain is shown in Figure 9. This converter operates in two modes: independently and simultaneously. At the same frequency, both the interleaving converters are operated in the simultaneous mode. The single converter only operates in the independent mode.

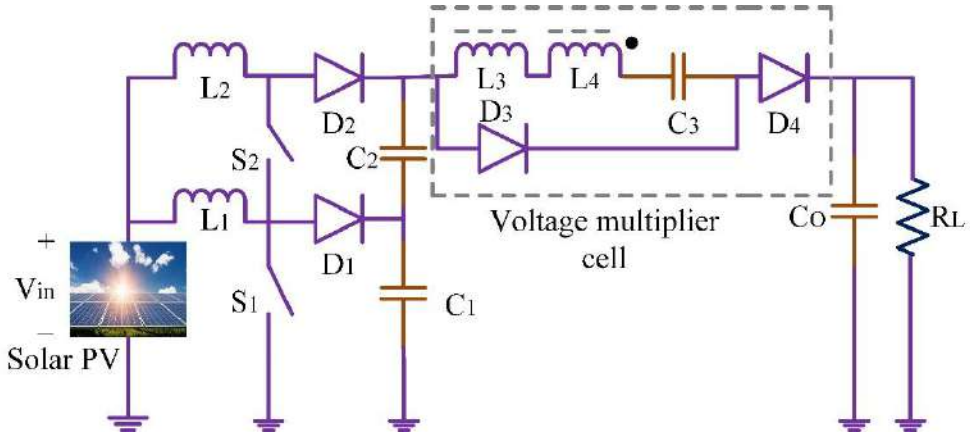

Figure 9. Interleaved non-isolated topology.

The wider V_{out} range is possible only with frequency control and combined mode changing [30]. The phase-shedding technique is used to improve the efficiency of the interleaved switched capacitor DC-DC converter. The high voltage gain is achieved in the converter with modular characteristics and an interleaved configuration [31]. Using the lower voltage rating, the MOSFETs in the converter reduce the conduction losses [32]. The typical schematic layout is shown in Figure 10.

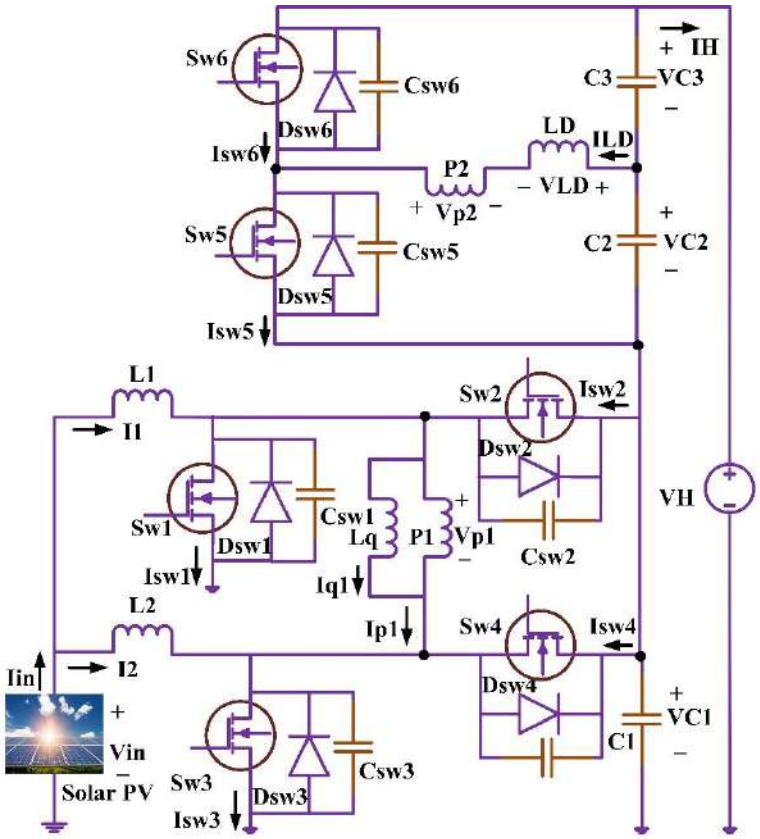

Figure 10. Non-isolated high voltage gain ratio interleaved coupled-inductor type DC-DC converter.

All diodes and switches operate on ZVS and ZCS techniques in the interleaved full soft-switching DC-DC converter. To reduce the power loss and to increase the efficiency of the DC-DC converters, the ZVS and ZCS are used. Finally, the auxiliary circuit is placed out of the main power path to avoid the switches' high current and voltage stress [33]. The schematic circuit diagram of interleaved high step-up converter is depicted in Figure 11. A highly efficient power system always insists a reliable DC-DC converter. An interleaved boost converter is required to convert the high-current low-voltage to low-current high-voltage.

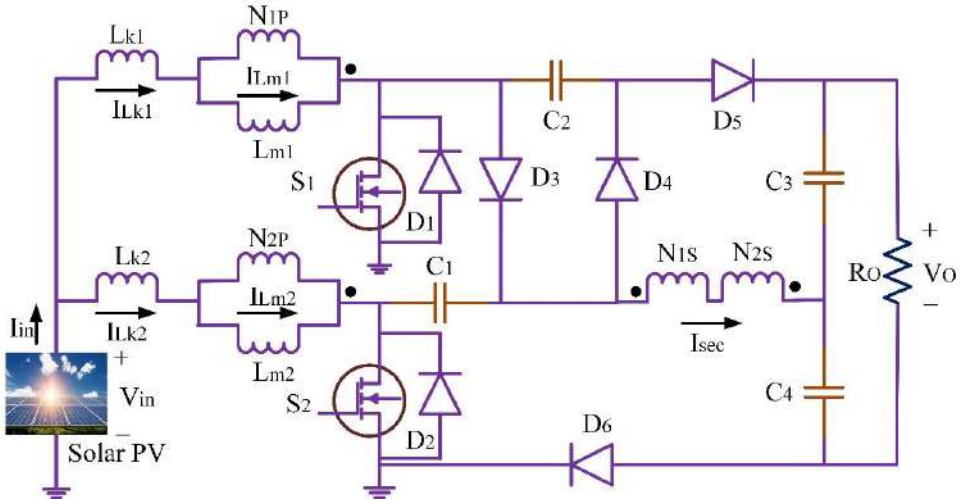

Figure 11. High step-up interleaved converter.

Classical boost converter deemed to be less advance then interleaved boost converter which offers high efficiency, low input ripple current, fast transient response, high reliability and less electromagnetic emission. Interleaved boost converters are suitable for the design of a highly efficient FC power system. To improve the system efficiency three-phase directly coupled interleaved boost converter using CoolMOS transistor and silicon carbide diode is used. Analysis based on the performances of interleaved converters are summarized in Table 2.

Table 2. Performance analysis of the interleaved converters.

Parameter	[34]	[35]	[36]	[37]
Input ripple current	Low	Low	Low	Moderate
Number of diodes	4	8	4	6
The voltage stress on the switches (n = 1)	$\left(\frac{V_0}{6}\right)$	$\left(\frac{V_0}{4}\right)$	$\left(\frac{V_0}{4}\right)$	$\left(\frac{V_0}{3}\right)$
Number of windings	4	6	4	6
Voltage gain	$\left(\frac{2\ (n+2)}{1-D}\right)$	$\left(\frac{3n+1}{1-D}\right)$	$\left(\frac{2(n+1)}{1-D}\right)$	$n_2+\left(\frac{(2n_3D+2-D)}{1-D}\right)$

3.3. Isolated Push-Pull Boost Converter

This section lists the published solutions of isolated push-pull boost converter topology for high-gain DC-DC converters [38]. The proposed converter is a push-pull type hard switched isolated boost converter. The proposed converter is implemented along with a voltage clamp circuit on the isolation transformer's primary and secondary sides. After the front end, the push-pull converter H-bridge DC-AC converter follows. The range of converter input V_{in} is taken as 25–45 V and V_{out} as 350–400 V. For the 900 W power level, the maximum calculated efficiency is 91%. Utilizing the resonant converter gives an advantage of a 1.5 kW front-end converter for FC applications, which is presented in [39]. On the secondary side of isolation transformer, a voltage doubler concept was introduced to tune the current resonance to minimize the diode losses (recovery). Switching active clamp circuits' blocking voltage is used on both sides to clamp the peak. The proposed converter follows with an H-bridge DC-AC converter. Overall, a calculated system efficiency of 92.5% is achieved with an V_{in} range of 30 V and an V_{out} of 350 V for 700 W power level.

3.4. Fly Back Converter Topology

This section lists the published solutions of Fly-back converter topology for high-gain DC-DC converters as shown in Figures 12 and 13. A 300 W isolated high step-up ratio DC-DC converter that uses a voltage multiplier on the secondary side and active clamp on the transformer main side is proposed in [40]. The V_{in} range is 25–35 V, and V_{out} is 400 V. The circulating current through the active clamp is reduced due to the resonant phases between transformer leakage inductances and diode parasitic capacitances, which also lowers the conduction losses.

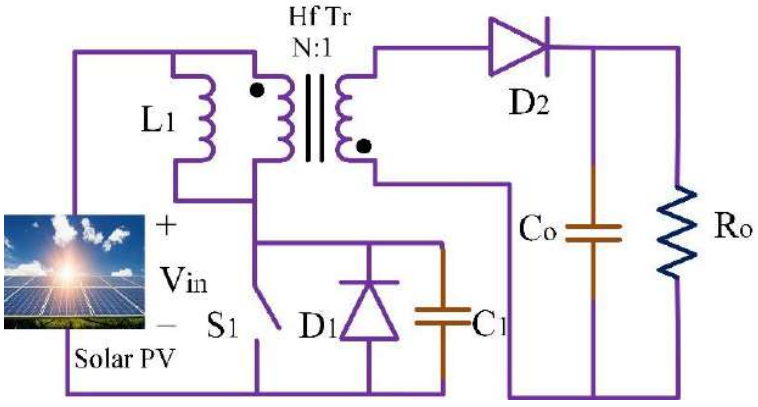

Figure 12. Boost fly-back converter topology.

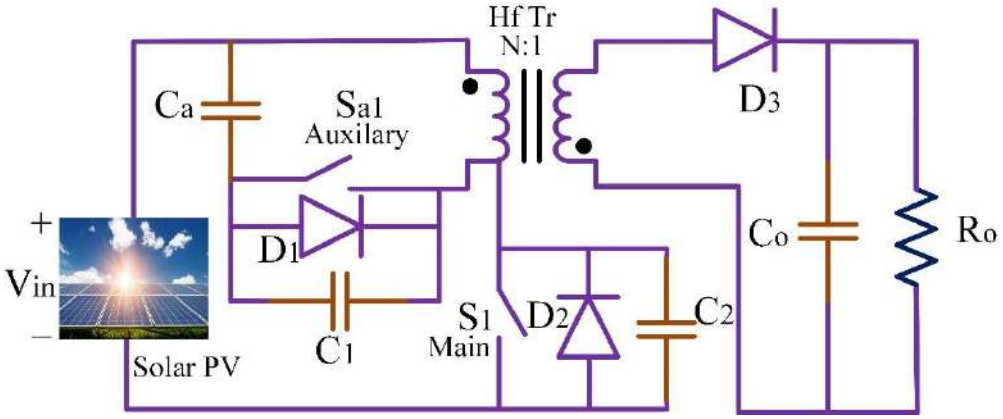

Figure 13. Active clamp boost fly-back converter.

The converter's efficiency of 92% to 94% for the entire V_{in} range and 300 W output power. A 300 W high step-up ratio converter for low-voltage and high-current energy sources is proposed [41]. The clamping diode integrated with boost-flyback (IBF) topology that naturally clamps parasitic oscillations. Resonance caused by the parasitic components helps to increase the voltage gain. The V_{in} range is 25–35 V, and V_{out} is 400 V. Various parameter has been evaluated and summarized in Table 3 for various converters. A simple design of asymmetrical forward cells of stacked multiple output topology is depicted in Figure 14.

Table 3. Parameter analysis of various DC-DC converters.

Parameter	[42]	[21]	[43]	[44]
MOSFET voltage stress	$\frac{V_0}{1+2N-ND}$	$\frac{V_0}{2(1+N)}$	$\frac{V_0}{1+N}$	$\frac{V_0}{2}$
MOSFET Soft switching	ZVS	ZVS	Hard switching	ZVS
No. of MOSFETs	2	2	1	2
The voltage stress on output diode	$\frac{NV_0}{1+2N-ND}$	$\frac{V_0}{2}$	$\frac{NV_0}{1+N}$	$\frac{V_0}{2}$
Soft switching of diodes	ZCS	Hard switching	Hard switching	ZCS
Diodes	3	4	3	2
Number of magnetic components	1	1	1	2
Voltage gain	$\frac{1+2N-ND}{1-D}$	$\frac{2(1+N)}{1-D}$	$\frac{1+N}{1-D}$	$\frac{2}{1-D}$

The converter efficiency is about 94% for a 100 kHz frequency of operation, and the output power is 300 W. The conventional isolated converter with N-outputs requires 2 N primary switches. The above circuit requires $N + 1$ primary switches to independently regulate the secondary side N output voltages [45].

3.5. Half Bridge Converter Topology

The concept of two inductor boost converters was introduced by [46]. The boost converter topology is the boost version of the abovementioned current double topology, also called the HY-Bridge rectifier. Many papers have already been published on the high-power low-V_{in} application of the two inductor boosts [46–51], representing some important works on this topic. Two inductor isolated boost converters are often referred to as half-bridge converters, as shown in Figure 15. A 1 kW isolated current fed half-bridge LLC resonant DC-DC converter of 24–28 V input and 400 V output was presented in [52]. An un-regulated LLC converter is implemented, which acts as isolated voltage amplifier having constant voltage gain. Experimental efficiency of 90.2 % was achieved with 24 volts input under full load conditions. The LLC converter has inherent bi-directional power flow capability. A 1.2 kW isolated current fed active clamped half-bridge circuit with a V_{in} range of 28–43 V and an output of 380 Volts is presented in [53]. The proposed converter in this paper is compared with the existing converter topologies. The converter also tested for high power rating, and overall efficiency of 94% was achieved with better

component utilization. Here a 200 W active clamped L-L current fed half-bridge isolated DC-DC converter with a 22 V input and 350 V output. [54]. The topology shown in this study achieves a wide-ranged ZVS of primary side switches from full load to light load conditions. Moreover, the auxiliary active clamp circuit absorbs the turn-off voltage spikes and also assists in achieving soft switching of primary devices [55]. Represents a 1 kW modified isolated two-inductor boost by active clamping and reset. The two transformers integrated by the individual rectifiers are connected in parallel on the input and output sides. Triangular switch currents can be observed due to active clamping. The V_{in} range is 26–50 V. The obtained V_{out} is 400 V. At 600 W output power, the maximum efficiency value is 95.6%. For the measured efficiency, the V_{in} condition is not published. [56] have used a 1 kW two-inductor boost converter with an active clamping. The V_{in} is 48 V. The observed V_{out} is 350 V. At a power rating of 500 W, an approximate peak efficiency of 87% is observed. The efficiency value drops to 77% at 1 kW output. A full-bridge boost converter reports 6–10% less efficiency on a comparative basis. As a part of the two-stage DC-DC converter for FC applications, a 1 kW two-inductor boost stage is designed in [57] as depicted in Figure 16.

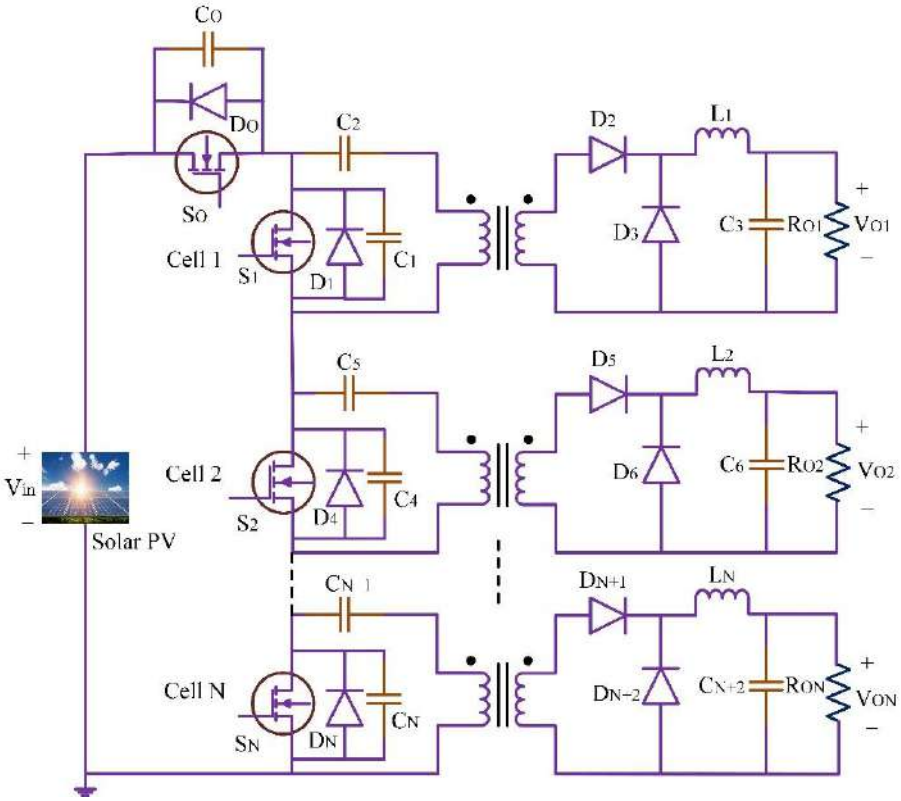

Figure 14. Asymmetrical forward cells of stacked multiple output topology.

Ref. [50] represent a 1.5 kW bi-directional two-inductor boost for a bi-directional interface between a 28 V and a 270 V aircraft power bus. On the low voltage side, active clamping and the rest is used to clamp the switching overvoltage. The range is 22–32 V. At V_{in} = 32 V and 750 W output, a peak efficiency value of 96% is achieved in the boost mode. Efficiency drops below 89% at 22 V_{in} and 1.5 kW output. A typical layout of DC-DC dual active bridge converter is shown in Figure 17.

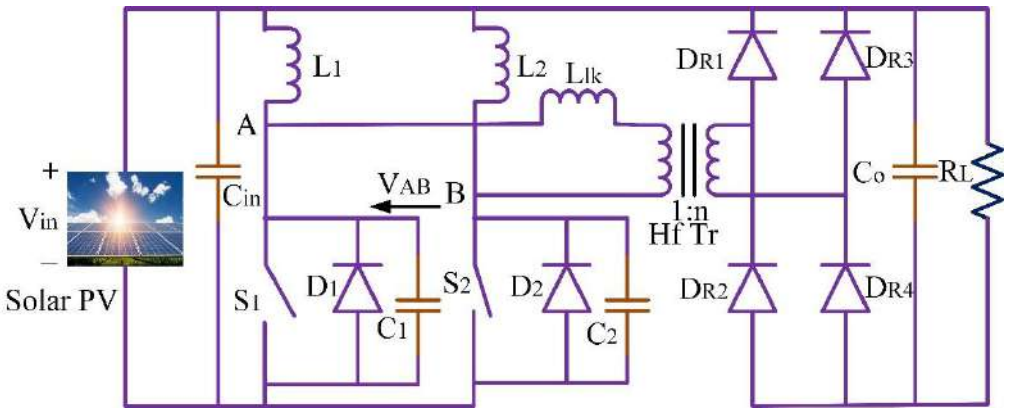

Figure 15. Two inductors isolated boost converter or Half Bridge converter.

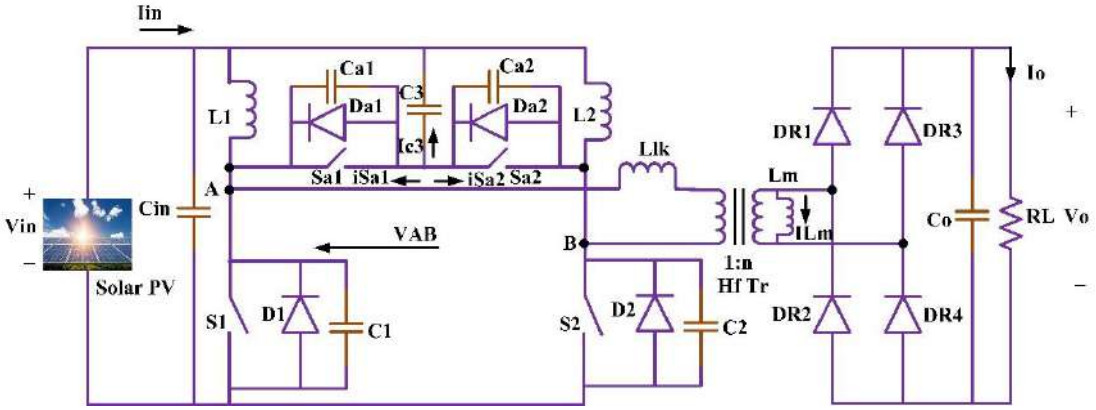

Figure 16. Two inductors isolated boost converter with active clamp.

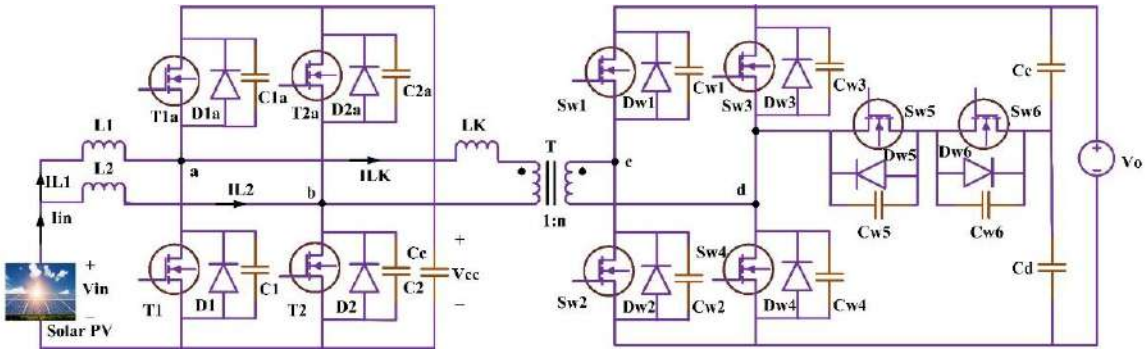

Figure 17. DC-DC converter with Dual active bridge.

A current fed hybrid dual active bridge DC-DC converter reduces the input high-frequency ripple current. While Power MOSFETs are switched with the ZVS technique. Low-voltage FC power conditioning systems employ two active bridge converters. Four power MOSFETs (T_1, T_{1a}, T_2, and T_{2a}) and two inductors L $_1$ and L$_2$ make up the input side. S_{w1}, S_{w2}, S_{w3}, and S_{w4} are the four MOSFETs that make up the output side. The auxiliary half-bridge consists of S_{w5} and S_{w6}. The power MOSFETs and (C_d and C_u) capacitors make up the auxiliary half-bridge. The transformer T is used to link the input and output sides. Here, the ratio of the transformer turns to the leakage inductance L $_k$ is 1: n [58]

3.6. Full Bridge Converter Topology

This section listed the published solutions of full-bridge converter topology for high gain DC-DC converters, as shown in Figure 18. A 500 W current fed full bridge isolated ZVS

active clamp full-bridge converter with 22 V input and 350 V output for FC applications is presented in [59]. This converter uses active clamp switch to clamp the voltage spikes across the full bridge switches in the turn-off mode. Moreover, this active clamp switch helps to achieve soft switching of primary side devices. For example, a 100 W full-bridge isolated ZVS DC-DC converter with an input range of 48 V and an output range of 380 V is presented in [60]. The proposed converter uses an integrated magnetic concept to utilize the transformer better. Though the converter is unsuitable for high power grid applications, soft switching is claimed for 100 kHz switching operation. A 1.2 kW current-fed full-bridge topology with an input of 30 V and an output of 600 V was observed. The presented converter topology uses the current fed full bridge topology for FC applications. Based on the theoretical limitations of transferrable power, the optimized converter is designed for the given specifications.

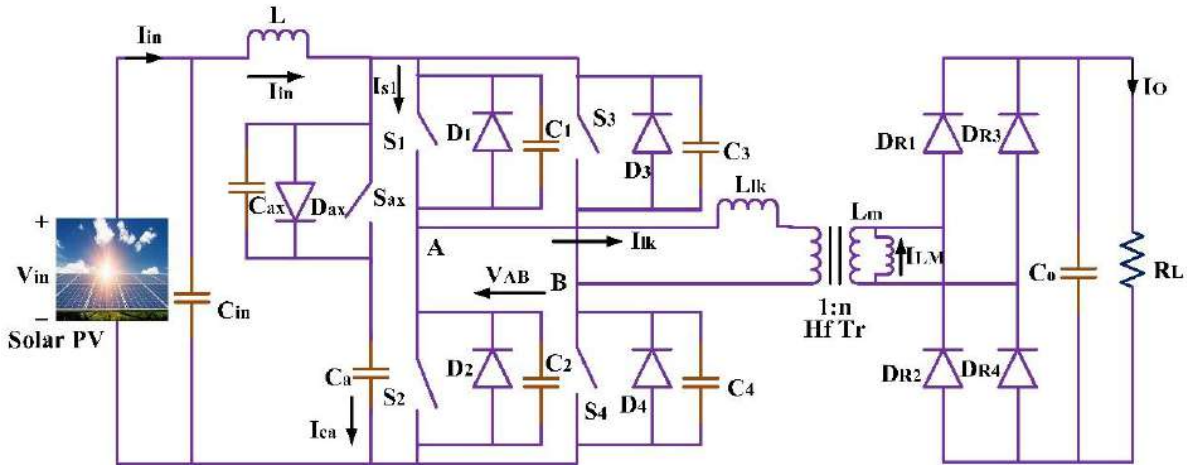

Figure 18. Active clamp full-bridge current fed converter.

A 5 kW isolated full bridge topology is proposed to apply FC vehicles [60]. The voltage clamping concept was introduced using a passive circuit to clamp the primary side switch blocking voltage. The proposed converter was analysed with a 24 V input and an output of 300 V. The calculated efficiency at peak power was 94%. Limited design data are provided to validate the converter. A soft switched 1 kW full-bridge isolated converter is demonstrated in [61]. During the switching, an overlap period of slow resonant commutation is achieved with the proposed converter. For the primary side switches, ZCS turn-off and ZCS turn-on is achieved. With the V_{in} = 22–27 V, V_{out} = 1 kV, a peak efficiency of 88% was achieved with 22 V input. An isolated full bridge converter for a 1.4 kW power level is proposed with a resonant LC circuit [62]. The resonant circuit is formed by connecting resonant capacitors parallel to the primary side switches and the LC tank circuit, forming a complete resonant circuit. With a V_{in} of 100 V and an output of 374 V with a narrow band frequency regulation, the maximum efficiency achieved is 90%.

3.7. Resonant Converters

Below, Figure 19 shows the Series Resonant Converter topology (SRC). This paper [63] uses a parallel tank circuit formed by an (L-C)||L combination to achieve soft switching of high-frequency switches. The important feature of these converters including (1) Achieving an improved efficiency even at varying load and line conditions. (2) A wide range of soft switching ZVS can be achieved. (3) The Peak current capability of the switch varies with the input current variation and not with the load current changes.

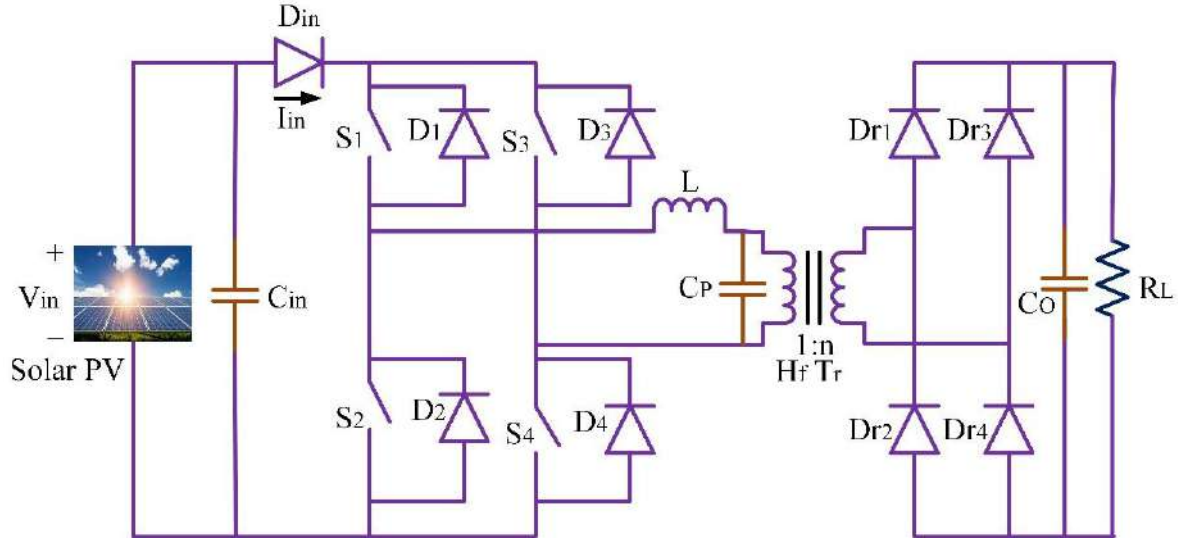

Figure 19. Series resonant converter having inductive output filter.

Here Figure 20 shows is a full bridge phase shifted converter having an inductive output filter configuration. The Soft switched converter configuration for high-power applications vividly uses it. The proposed converter configuration uses a constant frequency capable of realizing ZVS of the main switches on the primary side with a minimal circulating circuit configuration. The ZVS is realized with a filter inductance, a leakage inductance of the transformer, a parasitic capacitance of the switches, and a snubber capacitance. The phase-shifted technique achieves control over the Vout with constant frequency. The important characteristics of the proposed converter include:

1. The duty cycle loss at the secondary side is a major limitation of this configuration.
2. A huge stress on the secondary side is rectifying diodes.
3. The parasitic ringing problem on the secondary side transformer.
4. For a wide range of ZVS, a large inductor is needed, but the transformer needs to decrease the Np/Ns ratio, which will increase the primary side current. Therefore, the conduction losses of the devices occur. A compromise between the Np/Ns ratio and inductor should be carried out to minimize the conduction losses of the active switches.

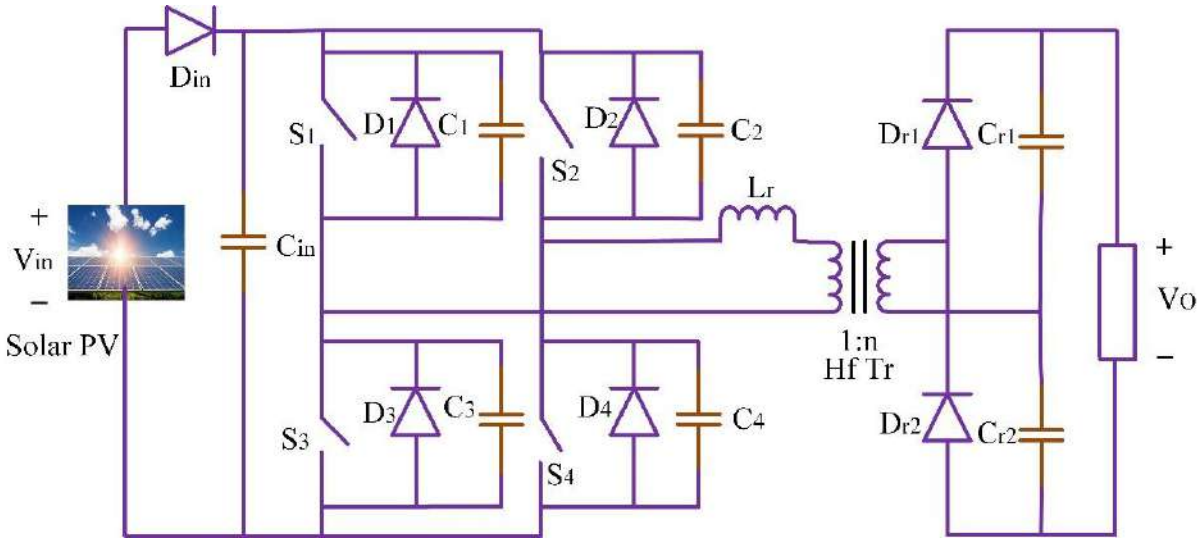

Figure 20. Phase shifted full bridge converter.

3.8. Interleaved Isolated Topology (ITLD Isolated Boost Converter)

A 200 W interleaved current fed ZVS active clamp full-bridge, and a V_{out} of 200 V is presented in [64]. The input current stress will be reduced due to interleaving and V_{out} extracted up to 700 V for three-phase grid-connected applications. A 1 kW interleaved current fed half-bridge topology with a V_{in} of 22–41 V and an output of 350 V is presented in [65]. The overall efficiency at full load achieved 92.8% with maximum converter utilization. The switching frequency is very low for the designed converter. Two current-fed full-bridge isolated converters are connected parallel to make an interleaved topology [66] and depicted in Figure 21. The voltage doubler circuit is connected in series to form a parallel input and a serial output configuration on the secondary side. The voltage clamping is carried out for the primary side switches using an active clamp circuit. With the V_{in} = 33 V, V_{out} = 400 V and the efficiency is 90.5% at 1.2 kW power levels.

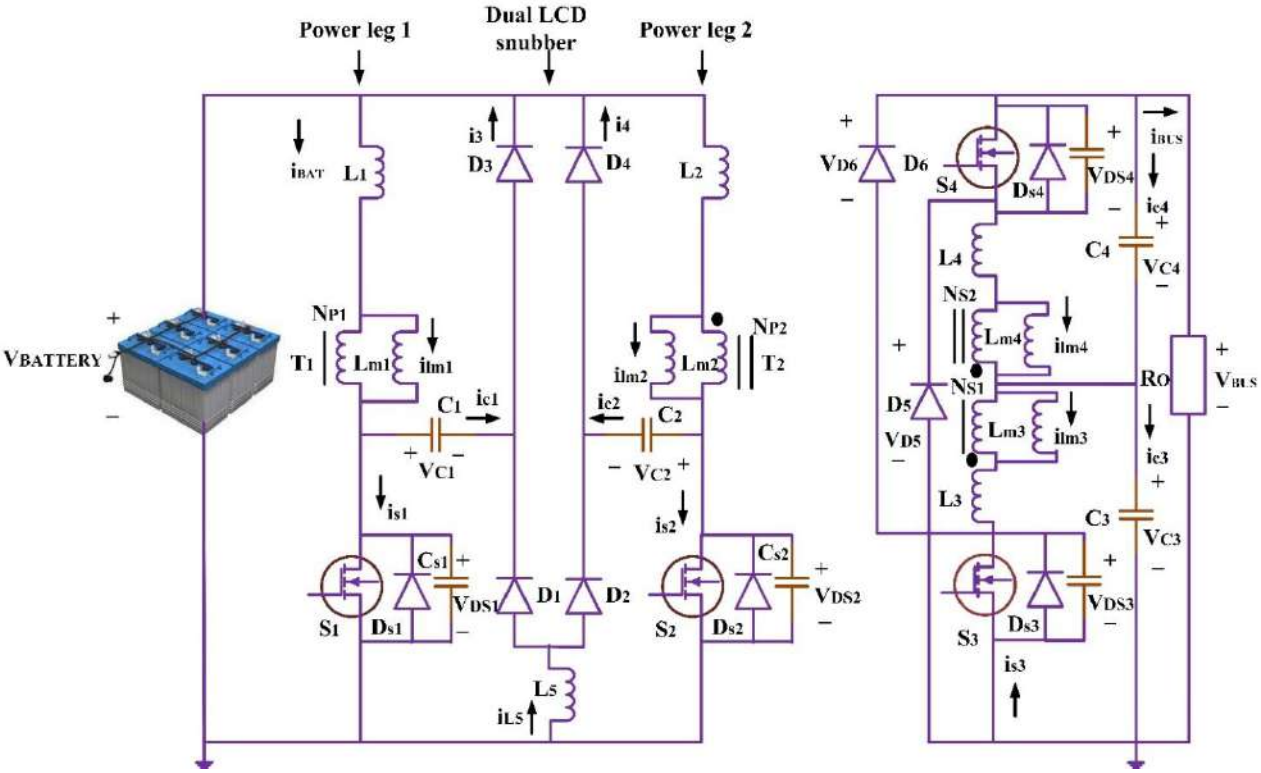

Figure 21. Interleaved isolated bidirectional DC-DC converter circuit.

The bidirectional isolated DC-DC converter technique reduces the input ripple current. The converter increases the conversion ratio and also the efficiency. Generally, a passive resistor capacitor-diode (RCD) snubber is required to store the energy in leakage inductance and clamp down the voltage spikes. Due to the use of the dual-inductor-capacitor-diode (LCD) snubber instead of the RCD snubber, the recycling of the leakage inductance, which is presented in the energy storing devices, is possible. Hence, the efficiency of the system increases [67].

Figure 22 shows the full bridge converter topology for high-gain DC-DC converters.

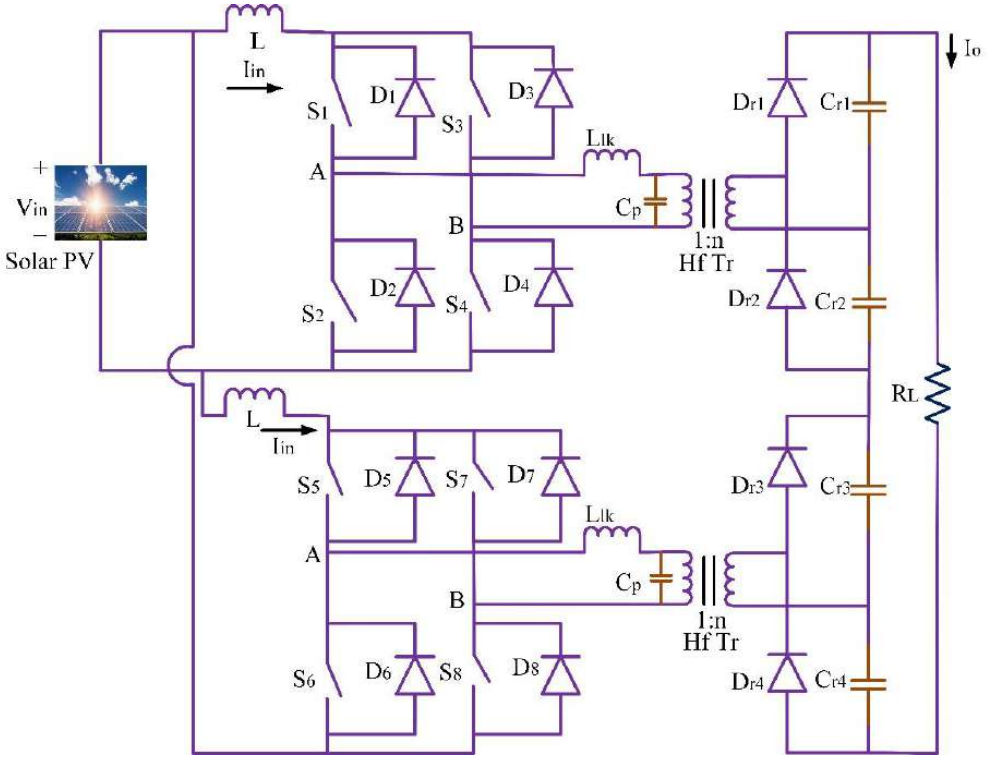

Figure 22. Interleaved Isolated Full Bridge Converter Topology.

4. Summary of the Analysis

The comparison includes an analysis of high-gain converters meant for PV applications. The published performance details are provided in Table 4. It should be noted that the critical test conditions, such as V_{in} and V_{out} levels and the measurement tolerances, are usually not provided, making it difficult to compare the efficiency achieved wherever provided. The optimum comparison was achieved by considering 1. Worst-case efficiency, 2. The number of active devices, 3. Switching frequency, and 4. Size of the converter data. Beyond the performance data, the papers reveal an analysis of different types of converters. The boost converters do not deliver high step-up ratios efficiently in continuous conduction mode due to the switch's high current and voltage stress and the diode reverse recovery loss. The non-isolated converter topologies are the suboptimal solution because it is directly connected to output high voltage side and the high boost ratios make it difficult to develop in non-isolated single-stage converter. The greater the differences in the voltage between the output of the FC (low voltage) and the DC link (high voltage), the greater there is need for electrical isolation between the two circuits [17,18,68]. Push-pull converters are typically unsuitable for FC power generation, especially at high power, due to the difficulty in overcoming transformer saturation [38,39]. The modified fly-back converters [69,70] suffer from voltage stress across the rectifier diode. The single winding carries a current, operates in a discontinuous mode (to avoid core saturation), and has high off-state voltage and poor core utilization. Current-fed full bridge converter operates at 10 kHz [66] (as it is a hard-switched converter), resulting in a larger converter due to the greater size of magnets and filters. The voltage clamping requirements [59] show that these circuits are necessary to reduce the switch stress. An active clamp (or reset) circuit requires greater switches and results in greater conduction losses due to the formation of the triangular current waveforms.

The comparison of measured efficiency in converter [18] and conventional boost converter is given in Figure 23. The conversion of 40 V to 380 V DC-DC gives the maximum efficiency of 92.6%.

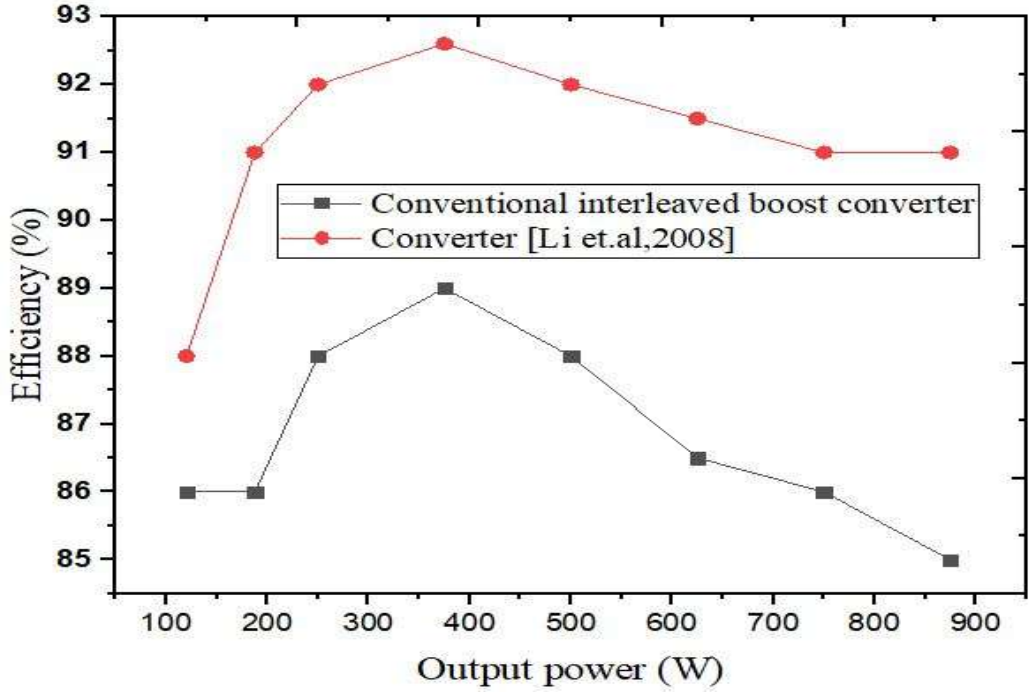

Figure 23. Measured efficiency Vs power [18].

Table 4. High voltage gain DC-DC converter topology comparison.

Topology	Power Rating in W	Input Voltage (V_{in})	Output Voltage(V)	No. of Active Devices	Switching Frequency (kHz)	Trans-Former Turns Ratio	Switching	References
Flyback	300	25–35	400	2	100	5.375	Soft	[70]
	300	25–35	400	1	100	4.5	Hard	[69]
Coupled Inductor	200	24	360 V	2	100	5	ZVS	[17]
	1000	40	380 V	2	50	40/22	ZCS	[71]
	300	27–36.5	400 V	1	100	N2 = 6.33, N3 = 5	-	[72]
	200	25–40	200	2	66	20	Soft	[20]
	250	30–45	400	2	20	1	Hard	[73]
Non-Isolated Interleaved	400	24	400	2	40	-	Soft	[29]
	1000	40	380	2	50	1.818	Soft	[74]
	1000	48	380	2	100	1	Soft	[18]
Push Pull	1000	25–45	350–400	-	-	-	-	[38]
	1500	30	350	-	-	-	-	[39]
Half bridge	1000	24–28	400	3	300	1:11	Hard	[54]
	1200	28–43	380	4	50	1:3.5	Soft	[75]
	200	22–41	350	4	100	1:4	Soft	[76]
	1000	26–50	400	4	50	4:14	ZVS	[77]
	1000	24	200	4	100		Hard	[47]
	1500	22–32	270	6	100	10/21	ZVS	[78]

Table 4. *Cont.*

Topology	Power Rating in W	Input Voltage (V_{in})	Output Voltage(V)	No. of Active Devices	Switching Frequency (kHz)	Trans-Former Turns Ratio	Switching	References
Full bridge	500	22–41	350	5	100 kHz	1:8	Soft	[59]
	1200	30	600	4	60 kHz	1:10	Hard	[79]
	1000	22–27	1000	4	100 KHz	1:30	Soft	[80]
	1400	100	374	4	250	-	ZVS	[81]
Interleaved isolated	200	22–41	200	10	100 kHz	-	Soft	[63]
	1200	33	400	8	10 kHz	1:2	Hard	[82]
	200	11	200	8	100 kHz	1:4	Soft	[83]

5. Conclusions

This paper evaluates the 14 DC-DC boost converters' efficiency, number of components, and stability. The significance of choosing a converter based on load and source requirements is evaluated. The importance of voltage gains and voltage stress factors when connecting solar PV to the grid is discussed. In addition to the non-isolated step up, interleaved and coupled inductors' reliability with respect to solar PV system applications are outlined. The stress on the switches is reduced by coupled inductor with the ZVS operation system to reduce grid instability and synchronization drawbacks. Each converter importance is fully discussed in this review. Microgrids with solar PV will significantly increase the flexibility of the power system, but to make it reliable, it is necessary to choose the proper converters based on corresponding ratings. Selecting a suitable Converter linking PV source and Dc link bus enhances system performance. In addition, the bidirectional interleaved switched capacitor DC-DC converter implemented in grid connection helps reduction of capacitor voltage stress is discussed in this review. This further extends to by interleaved converter use in diminishing the current ripples at low voltage. Even though the converters pose the following merits, many constraints still need to be resolved, such as exceeding duty values to 50% and linear increases of switch voltage stress with increasing duty cycle.

Author Contributions: Implementation, Investigation, I.J.; Analysis, Supervision, Proofreading, V.I. All authors have read and agreed to the published version of the manuscript.

Funding: This research received no external funding.

Data Availability Statement: Not applicable.

Conflicts of Interest: The authors declare no conflict of interest.

References

1. Sri Revathi, B.; Prabhakar, M. Solar PV Fed DC Microgrid: Applications, Converter Selection, Design and Testing. *IEEE Access* **2022**, *10*, 87227–87240. [CrossRef]
2. Ahmad, J.; Zaid, M.; Sarwar, A.; Lin, C.H.; Asim, M.; Yadav, R.K.; Tariq, M.; Satpathi, K.; Alamri, B. A New High-Gain Dc-Dc Converter with Continuous Input Current for DC Microgrid Applications. *Energies* **2021**, *14*, 2629. [CrossRef]
3. Ramesh, P.; Gouda, P.K.; Lakshmikhandan, K.; Ramanathan, G.; Bharatiraja, C. A Three Port Bidirectional DC-DC Converter for PV—Battery—DC Microgrid Application Using Fuzzy Logic Control. *Mater. Today Proc.* **2022**, in press. [CrossRef]
4. Zengin, S. A Hybrid Current Modulated DAB DC-DC Converter for Connecting PV Modules to DC Grid Considering Partial Shading. *Comput. Electr. Eng.* **2022**, *101*, 108109. [CrossRef]
5. Mothilal Bhagavathy, S.; Pillai, G. PV Microgrid Design for Rural Electrification. *Designs* **2018**, *2*, 33. [CrossRef]
6. Santosh Kumar Reddy, P.L.; Obulesu, Y.P. A Non-Cascading DC-DC Quadratic Boost Converter with High Voltage Gain for PV Applications. *Int. J. Electron.* **2022**, 1–22. [CrossRef]
7. Aranda, E.D.; Litran, S.P.; Prieto, M.B.F. Combination of Interleaved Single-Input Multiple-Output DC-DC Converters. *CSEE J. Power Energy Syst.* **2022**, *8*, 132–142. [CrossRef]

8. Khan, S.; Zaid, M.; Mahmood, A.; Nooruddin, A.S.; Ahmad, J.; Alghaythi, M.L.; Alamri, B.; Tariq, M.; Sarwar, A.; Lin, C.H. A New Transformerless Ultra High Gain DC-DC Converter for DC Microgrid Application. *IEEE Access* **2021**, *9*, 124560–124582. [CrossRef]
9. Liang, Y. Parallel Coordination Control of Multi-Port DC-DC Converter for Stand-Alone Photovoltaic-Energy Storage Systems. *CPSS Trans. Power Electron. Appl.* **2020**, *5*, 235–241. [CrossRef]
10. Saravanakumar, T.; Saravana kumar, R. Design, Validation, and Economic Behavior of a Three-Phase Interleaved Step-Up DC–DC Converter for Electric Vehicle Application. *Front. Energy Res.* **2022**, *10*, 13081. [CrossRef]
11. Saravanakumar, T.; Kumar, R.S. Fuzzy Based Interleaved Step-up Converter for Electric Vehicle. *Intell. Autom. Soft Comput.* **2023**, *35*, 1103–1118. [CrossRef]
12. Arunkumari, T.; Indragandhi, V. An Overview of High Voltage Conversion Ratio DC-DC Converter Configurations Used in DC Micro-Grid Architectures. *Renew. Sustain. Energy Rev.* **2017**, *77*, 670–687. [CrossRef]
13. Jagadeesh, I.; Indragandhi, V. A Novel PV Based High Voltage Gain Soft Switching DC—DC Boost Converter. *Int. J. Eng. Technol.* **2018**, *7*, 1034–1039. [CrossRef]
14. Pan, C.T.; Lai, C.M. A High-Efficiency High Step-up Converter with Low Switch Voltage Stress for Fuel-Cell System Applications. *IEEE Trans. Ind. Electron.* **2010**, *57*, 1998–2006. [CrossRef]
15. Kim, H.; Yoon, C.; Choi, S. An Improved Current-Fed ZVS Isolated Boost Converter for Fuel Cell Applications. *IEEE Trans. Power Electron.* **2010**, *25*, 2357–2364. [CrossRef]
16. Rajashekara, K. *Propulsion System Strategies for Fuel Cell Vehicles*; SAE International: Warrendale PA, USA, 2000.
17. Do, H.L. A Soft-Switching DC-DC Converter with High Voltage Gain. *IEEE Trans. Power Electron.* **2010**, *25*, 1193–1200. [CrossRef]
18. Li, W.; He, X. A Family of Interleaved DC-DC Converters Deduced from a Basic Cell with Winding-Cross-Coupled Inductors (WCCIs) for High Step-Upor Step-down Conversions. *IEEE Trans. Power Electron.* **2008**, *23*, 1791–1801. [CrossRef]
19. Wai, R.; Member, S.; Lin, C.; Duan, R.; Chang, Y. High-Efficiency DC-DC Converter With High Voltage Gain and Reduced Switch Stress. *IEEE Trans. Ind. Electron.* **2007**, *54*, 354–364. [CrossRef]
20. Wu, T.; Member, S.; Lai, Y.; Hung, J.; Chen, Y.; Member, S. Boost Converter With Coupled Inductors and Buck—Boost Type of Active Clamp. *IEEE Trans. Ind. Electron.* **2008**, *55*, 154–162. [CrossRef]
21. Molavi, N.; Adib, E.; Farzanehfard, H. Soft-Switched Non-Isolated High Step-up DC-DC Converter with Reduced Voltage Stress. *IET Power Electron.* **2016**, *9*, 1711–1718. [CrossRef]
22. Ramírez-Murillo, H.; Restrepo, C.; Konjedic, T.; Calvente, J.; Romero, A.; Baier, C.R.; Giral, R. An Efficiency Comparison of Fuel-Cell Hybrid Systems Based on the Versatile Buck-Boost Converter. *IEEE Trans. Power Electron.* **2018**, *33*, 1237–1246. [CrossRef]
23. Hilairet, M.; Béthoux, O.; Ghanes, M.; Tanasa, V.; Barbot, J.P.; Normand-Cyrot, M.D. Experimental Validation of a Sampled-Data Passivity-Based Controller for Coordination of Converters in a Fuel Cell System. *IEEE Trans. Ind. Electron.* **2015**, *62*, 5187–5194. [CrossRef]
24. Thounthong, P.; Raël, S.; Davat, B. Control Strategy of Fuel Cell and Supercapacitors Association for a Distributed Generation System. *IEEE Trans. Ind. Electron.* **2007**, *54*, 3225–3233. [CrossRef]
25. Hu, X.; Wang, J.; Li, L.; Li, Y. A Three-Winding Coupled-Inductor DC—DC Converter Topology With High Voltage Gain And. *IEEE Trans. Power Electron.* **2018**, *33*, 1453–1462. [CrossRef]
26. El Fadil, H.; Giri, F.; Member, S.; Guerrero, J.M.; Member, S. Modeling and Nonlinear Control of a Fuel Cell/Supercapacitor Hybrid Energy Storage System for Electric Vehicles. *IEEE Trans. Veh. Technol.* **2014**, *63*, 3011–3018. [CrossRef]
27. Vural, B.; Dusmez, S.; Uzunoglu, M.; Ugur, E.; Akin, B. Fuel Consumption Comparison of Different Battery/Ultracapacitor Hybridization Topologies for Fuel-Cell Vehicles on a Test Bench. *IEEE J. Emerg. Sel. Top. Power Electron.* **2014**, *2*, 552–561. [CrossRef]
28. Tani, A.; Camara, M.B.; Dakyo, B. Energy Management Based on Frequency Approach for Hybrid Electric Vehicle Applications: Fuel-Cell/Lithium-Battery and Ultracapacitors. *IEEE Trans. Veh. Technol.* **2012**, *61*, 3375–3386. [CrossRef]
29. Prudente, M.; Pfitscher, L.L.; Emmendoerfer, G.; Romaneli, E.F.; Gules, R. Voltage Multiplier Cells Applied to Non-Isolated DC-DC Converters. *IEEE Trans. Power Electron.* **2008**, *23*, 871–887. [CrossRef]
30. Shahzad, M.I.; Iqbal, S.; Taib, S. Interleaved LLC Converter with Cascaded Voltage Doubler Rectifiers for Deeply Depleted PEV Battery Charging. *IEEE Trans. Transp. Electrif.* **2017**, *4*, 89–98. [CrossRef]
31. Zhang, Y.; Gao, Y.; Li, J.; Sumner, M. Interleaved Switched-Capacitor Bidirectional DC-DC Converter with Wide Voltage-Gain Range for Energy Storage Systems. *IEEE Trans. Power Electron.* **2018**, *33*, 3852–3869. [CrossRef]
32. Amiri, M.; Farzanehfard, H.; Adib, E. A Nonisolated Ultrahigh Step Down DC–DC Converter with Low Voltage Stress. *IEEE Trans. Ind. Electron.* **2018**, *65*, 1273–1280. [CrossRef]
33. Bahrami, H.; Farhangi, S.; Iman-eini, H. A New Interleaved Coupled-Inductor Nonisolated Soft-Switching Bidirectional DC—DC Converter With High Voltage Gain Ratio. *IEEE Trans. Ind. Electron.* **2018**, *65*, 5529–5538. [CrossRef]
34. Fekri, M.; Molavi, N.; Adib, E.; Farzanehfard, H. High Voltage Gain Interleaved DC-DC Converter with Minimum Current Ripple. *IET Power Electron.* **2017**, *10*, 1924–1931. [CrossRef]
35. Nouri, T.; Hosseini, S.H.; Babaei, E.; Ebrahimi, J. Interleaved High Step-up DC-DC Converter Based on Three-Winding High-Frequency Coupled Inductor and Voltage Multiplier Cell. *IET Power Electron.* **2015**, *8*, 175–189. [CrossRef]
36. Tseng, K.; Huang, C.; Shih, W. A High Step-Up Converter With a Voltage Multiplier Module for a Photovoltaic System. *IEEE Trans. Power Electron.* **2013**, *28*, 3047–3057. [CrossRef]

37. Tseng, K.C.; Chen, J.Z.; Lin, J.T.; Huang, C.C.; Yen, T.H. High Step-up Interleaved Forward-Flyback Boost Converter with Three-Winding Coupled Inductors. *IEEE Trans. Power Electron.* **2015**, *30*, 4696–4703. [CrossRef]
38. Andersen, G.K.; Klumpner, C.; Kjær, S.B.; Blaabjerg, F. A New Power Converter for Fuel Cells with High System Efficiency. *Int. J. Electron.* **2003**, *90*, 737–750. [CrossRef]
39. Kwon, J.; Kim, E.; Kwon, B.; Nam, K. High-Efficiency Fuel Cell Power Conditioning System With Input Current Ripple Reduction. *IEEE Trans. Ind. Electron.* **2009**, *56*, 826–834. [CrossRef]
40. Spiazzi, G.; Mattavelli, P.; Gazoli, J.R.; Magalhaes, R.; Frattini, G. Improved Integrated Boost-Flyback High Step-up Converter. In Proceedings of the IEEE International Conference on Industrial Technology, Via del Mar, Chile, 14–17 March 2010; pp. 1169–1174.
41. Spiazzi, G.; Mattavelli, P.; Costabeber, A.; Member, S. High Step-Up Ratio Flyback Converter With Active Clamp and Voltage Multiplier. *IEEE Trans. Power Electron.* **2011**, *26*, 3205–3214. [CrossRef]
42. Shitole, A.B.; Sathyan, S.; Suryawanshi, H.M.; Talapur, G.G.; Chaturvedi, P. Soft Switched High Voltage Gain Boost Integrated Flyback Converter Interfaced Single-Phase Grid Tied Inverter for SPV Integration. *IEEE Trans. Ind. Appl.* **2017**, *54*, 482–493. [CrossRef]
43. Das, M.; Member, S.; Agarwal, V. Design and Analysis of a High Efficiency DC—DC Converter with Soft Switching Capability for Renewable Energy Applications Requiring High Voltage Gain. *IEEE Trans. Ind. Electron.* **2016**, *63*, 2936–2944. [CrossRef]
44. Park, Y.; Jung, B.; Choi, S. Nonisolated ZVZCS Resonant PWM Dc-Dc Converter for High Step-up and High-Power Applications. *IEEE Trans. Power Electron.* **2012**, *27*, 3568–3575. [CrossRef]
45. Chen, G.; Deng, Y.; Wang, K.; Hu, Y.; Jiang, L.; Wen, H.; He, X. Topology Derivation and Analysis of Integrated Multiple Output Isolated DC-DC Converters with Stacked Configuration for Low-Cost Applications. *IEEE Trans. Circuits Syst. I Regul. Pap.* **2017**, *64*, 2207–2218. [CrossRef]
46. Wolfs, P.J. A Current-Sourced DC-DC Converter Derived via the Duality Principle from the Half-Bridge Converter. *IEEE Trans. Ind. Electron.* **1993**, *40*, 139–144. [CrossRef]
47. Wen, J.; Jin, T.; Smedley, K. A New Interleaved Isolated Boost Converter for High Power Applications. In Proceedings of the Conference Proceedings—IEEE Applied Power Electronics Conference and Exposition—APEC, Dallas, TX, USA, 19–23 March 2006; Volume 2006, pp. 79–84.
48. Attanasio, R.; Cacciato, M.; Gennaro, F.; Consoli, A. An Innovative Boost Converter for Fuel Cells Stationary Generation Systems. In Proceedings of the 30th Annual Conference of IEEE Industrial Electronics Society, Busan, Korea, 2–6 November 2004; pp. 2831–2836.
49. Harfman Todorovic, M.; Palma, L.; Enjeti, P.N. Design of a Wide Input Range DC-DC Converter with a Robust Power Control Scheme Suitable for Fuel Cell Power Conversion. *IEEE Trans. Ind. Electron.* **2008**, *55*, 1247–1255. [CrossRef]
50. Xiao, H.; Xie, S. A ZVS Bidirectional DC-DC Converter With Phase-Shift Plus PWM Control Scheme. *IEEE Trans. Power Electron.* **2008**, *23*, 813–823. [CrossRef]
51. Liu, C.; Johnson, A.; Lai, J.S. A Novel Three-Phase High-Power Soft-Switched DC-DC Converter for Low-Voltage Fuel Cell Applications. *IEEE Trans. Ind. Appl.* **2005**, *41*, 1691–1697. [CrossRef]
52. Lee, J.; Jeong, Y.; Han, B. An Isolated DC/DC Converter Using High-Frequency Unregulated LLC Resonant Converter for Fuel Cell Applications. *IEEE Trans. Ind. Electron.* **2011**, *58*, 2926–2934. [CrossRef]
53. Jang, S.J.; Won, C.Y.; Lee, B.K.; Hur, J. Fuel Cell Generation System with a New Active Clamping Current-Fed Half-Bridge Converter. *IEEE Trans. Energy Convers.* **2007**, *22*, 332–340. [CrossRef]
54. Rathore, A.K.; Bhat, A.K.S.; Oruganti, R. Analysis, Design and Experimental Results of Wide Range ZVS Active-Clamped L-L Type Current-Fed DC-DC Converter for Fuel Cells to Utility Interface. *IEEE Trans. Ind. Electron.* **2012**, *59*, 473–485. [CrossRef]
55. Danyali, S.; Moradkhani, A.; Aazami, R.; Mejbel, M.T. New Dual-Source High-Gain ZVS DC-DC Converter for Integrating Renewable Power Source and Battery Storage. *Electr. Power Syst. Res.* **2022**, *213*, 108740. [CrossRef]
56. Hadelu, L.M.; Noorpoor, A.; Boyaghchi, F.A.; Mirjalili, S. A New Molten Carbonate Fuel Cell Hybrid Power Generation System Using Two-Stage Sodium Thermo-Electrochemical Converter/Two-Stage Thermoelectric Generator: Performance Analysis and Multi-Objective Grasshopper Optimization. *J. Power Sources* **2022**, *547*, 232006. [CrossRef]
57. Abdollahi Arjanaki, A.; Dehestani Kolagar, A.; Alizadeh Pahlavani, M.R. A Two-Level Power Management Strategy in a DC-Coupled Hybrid Microgrid Powered by Fuel Cell and Energy Storage Systems with Model Predictive Controlled Interface Converter. *J. Energy Storage* **2022**, *52*, 104861. [CrossRef]
58. Sha, D.; Xu, Y.; Zhang, J.; Yan, Y. Current-Fed Hybrid Dual Active Bridge DC-DC Converter for a Fuel Cell Power Conditioning System With Reduced Input Current Ripple. *IEEE Trans. Ind. Electron.* **2017**, *64*, 6628–6638. [CrossRef]
59. Prasanna, U.R.; Rathore, A.K. Analysis and Design of Zero-Voltage-Switching Current-Fed Isolated Full-Bridge Dc/Dc Converter. In Proceedings of the 2011 IEEE Ninth International Conference on Power Electronics and Drive Systems, Singapore, 5–8 December 2011; pp. 5–8.
60. Jiang, X.; Wen, X.; Xu, H. Study on Isolated Boost Full Bridge Converter in FCEV. In Proceedings of the 7th International Power Engineering Conference, IPEC2005, Singapore, 29 November–2 December 2005; Volume 2005.
61. Chen, R.Y.; Liang, T.J.; Chen, J.F.; Lin, R.L.; Tseng, K.C. Study and Implementation of a Current-Fed Full-Bridge Boost DC-DC Converter with Zero-Current Switching for High-Voltage Applications. *IEEE Trans. Ind. Appl.* **2008**, *44*, 1218–1226. [CrossRef]
62. Jalbrzykowski, S.; Citko, T. Current-Fed Resonant Full-Bridge Boost DC/AC/DC Converter. *IEEE Trans. Ind. Electron.* **2008**, *55*, 1198–1205. [CrossRef]

63. Rathore, A.K. Interleaved Soft-Switched Active-Clamped L-L Type Current-Fed Half-Bridge DC-DC Converter for Fuel Cell Applications. *Int. J. Hydrogen Energy* **2009**, *34*, 9802–9815. [CrossRef]
64. Dharmesh, P.D.; Rathore, A.K. Interleaved Zero-Voltage-Switching Active-Clamped Current-Fed Full-Bridge Isolated Dc/Dc Converter for Fuel Cell Applications : A Case Study Analysis. In Proceedings of the 2012 IEEE Third International Conference on Sustainable Energy Technologies (ICSET), Kathmandu, Nepal, 24–27 September 2012; pp. 23–29.
65. Reshma Gopi, R.; Sreejith, S. Converter Topologies in Photovoltaic Applications—A Review. *Renew. Sustain. Energy Rev.* **2018**, *94*, 1–14. [CrossRef]
66. Kong, X.; Lim, T.C.; Khambadkone, A.M. Analysis and Control of Isolated Current-Fed Full Bridge Converter in Fuel Cell System. In Proceedings of the IECON Proceedings (Industrial Electronics Conference), Busan, Korea, 2–6 November 2004; Volume 3, pp. 2825–2830.
67. Shen, C.L.; Liou, H.; Liang, T.C.; Gong, H.Z. An Isolated Bidirectional Interleaved Converter with Minimum Active Switches and High Conversion Ratio. *IEEE Trans. Ind. Electron.* **2018**, *65*, 2313–2321. [CrossRef]
68. Aiswarya, P.; Varghese, B.M.; Joy, N.; George, A. Switched Inductor Based Bidirectional DC-DC Converter for High Voltage Gain. *Mater. Today Proc.* **2022**, *58*, 569–576. [CrossRef]
69. Goudarzian, A.; Khosravi, A.; Ali Raeisi, H. Modeling, Design and Control of a Modified Flyback Converter with Ability of Right-Half-Plane Zero Alleviation in Continuous Conduction Mode. *Eng. Sci. Technol. Int. J.* **2022**, *26*, 101007. [CrossRef]
70. Mirzaei, A.; Rezvanyvardom, M. High Voltage Gain Soft Switching Full Bridge Interleaved Flyback DC-DC Converter for PV Applications. *Sol. Energy* **2020**, *196*, 217–227. [CrossRef]
71. Mumtaz, F.; Zaihar Yahaya, N.; Tanzim Meraj, S.; Singh, B.; Kannan, R.; Ibrahim, O. Review on Non-Isolated DC-DC Converters and Their Control Techniques for Renewable Energy Applications. *Ain Shams Eng. J.* **2021**, *12*, 3747–3763. [CrossRef]
72. Shibu, S.; Babu, E.; Neema, S.; Joy, N. High Gain DC-DC Converter with Low Voltage Stress. *Mater. Today Proc.* **2022**, *58*, 600–606. [CrossRef]
73. Araújo, S.V.; Bascopé, R.P.T.; Bascopé, G.V.T.; Menezes, L. Step-Up Converter with High Voltage Gain Employing Three-State Switching Cell and Voltage Multiplier. In Proceedings of the 2008 IEEE Power Electronics Specialists Conference, Rhodes, Greece, 15–19 June 2008; pp. 2271–2277.
74. Jang, Y.; Jovanović, M.M. Interleaved Boost Converter with Intrinsic Voltage-Doubler Characteristic for Universal-Line PFC Front End. *IEEE Trans. Power Electron.* **2007**, *22*, 1394–1401. [CrossRef]
75. Aglawe, K.R.; Dhande, M.; Matey, M.; Shelare, S. State of the Art and Materials Based Characteristics in Power Converters for Electric Vehicles. *Mater. Today Proc.* **2022**, *58*, 726–735. [CrossRef]
76. Tanzim Meraj, S.; Zaihar Yahaya, N.; Hasan, K.; Hossain Lipu, M.S.; Madurai Elavarasan, R.; Hussain, A.; Hannan, M.A.; Muttaqi, K.M. A Filter Less Improved Control Scheme for Active/Reactive Energy Management in Fuel Cell Integrated Grid System with Harmonic Reduction Ability. *Appl. Energy* **2022**, *312*, 118784. [CrossRef]
77. Ingilala Jagadeesh, V.I. A Review on Isolated DC–DC Converters Used in Renewable Power Generation Applications. In *Artificial Intelligent Techniques for Electric and Hybrid Electric Vehicles*; Wiley: Hoboken, NJ, USA, 2020; pp. 233–240. [CrossRef]
78. Karthikeyan, V.; Gupta, R. Light-Load Efficiency Improvement by Extending ZVS Range in DAB-Bidirectional DC-DC Converter for Energy Storage Applications. *Energy* **2017**, *130*, 15–21. [CrossRef]
79. Averberg, A.; Mertens, A. Characteristics of the Single Active Bridge Converter with Voltage Doubler. In Proceedings of the 2008 13th International Power Electronics and Motion Control Conference, Poznan, Poland, 1–3 September 2008; pp. 213–220.
80. Paul, A.K. Choice of Control Function in Magnetically-Coupled Full Bridge DC-DC Power Controller for Arc Welding: A Practical Approach. *Power Electron. Devices Components* **2022**, *2*, 100005. [CrossRef]
81. Salem, M.; Jusoh, A.; Dahidah, M.; Ishak, D.; Richelli, A.; Alhamroni, I.; Kamarol, M. Improved Topology of Three-Phase Series Resonant DC-DC Boost Converter with Variable Frequency Control. *Alexandria Eng. J.* **2022**, *61*, 1701–1713. [CrossRef]
82. Zhou, H.; Khambadkone, A.M.; Member, S.; Kong, X. Fast Dynamic Response in a Fuel Cell Based Converter Using Augmented Energy Storage. In Proceedings of the 2007 IEEE Power Electronics Specialists Conference, Orlando, FL, USA, 17–21 June 2007; pp. 1255–1260.
83. Rezvanyvardom, M.; Mirzaei, A.; Shabani, M.; Mekhilef, S.; Rawa, M.; Wahyudie, A.; Ahmed, M. Interleaved Step-up Soft-Switching DC–DC Boost Converter without Auxiliary Switches. *Energy Rep.* **2022**, *8*, 6499–6511. [CrossRef]

energies

MDPI

Review

Optimization of DC, AC, and Hybrid AC/DC Microgrid-Based IoT Systems: A Review

Belqasem Aljafari [1], Subramanian Vasantharaj [2], Vairavasundaram Indragandhi [2,*] and Rhanganath Vaibhav [3]

[1] Department of Electrical Engineering, Najran University, Najran 11001, Saudi Arabia
[2] School of Electrical Engineering, Vellore Institute of Technology, Vellore City 632014, India
[3] School of Mechanical Engineering, Vellore Institute of Technology, Vellore City 632014, India
* Correspondence: indragandhi.v@vit.ac.in

Abstract: Smart microgrids, as the foundations of the future smart grid, combine distinct Internet of Things (IoT) designs and technologies for applications that are designed to create, regulate, monitor, and protect the microgrid (MG), particularly as the IoT develops and evolves on a daily basis. A smart MG is a small grid that may operate individually or in tandem with the electric grid, and it is ideal for institutional, commercial, and industrial consumers, as well as urban and rural societies. A MG can operate in two methods (stand-alone and grid-connected), with the ability to transition between modes due to local grid faults, planned maintenance, expansions, deficits and failures in the host system, and other factors. Energy storage is the process of storing and converting energy that can be used for a variety of purposes, including voltage and frequency management, power backup, and cost optimization. IoT is designed to deliver solutions for optimal energy management, security protocols, control methods, and applications in the MG, with numerous distributed energy resources (DER) and interconnected loads. The use of IoT architecture for MG operations and controls is discussed in this research. With the use of power grid equipment and IoT-enabled technology, MGs are enabling local networks to give additional services on top of the essential supply of electricity to local networks that operate simultaneously or independently from the regional grid. Additionally, this review shows how hybrid AC/DC MGs are advantageous compared to AC and DC MGs. The state-of-the-art optimization techniques and trends in hybrid MG research are included in this work.

Keywords: smart microgrid; optimization; hybrid renewable energy source; internet of things; cost of electricity; information and communication technology

Citation: Aljafari, B.; Vasantharaj, S.; Indragandhi, V.; Vaibhav, R. Optimization of DC, AC, and Hybrid AC/DC Microgrid-Based IoT Systems: A Review. *Energies* **2022**, *15*, 6813. https://doi.org/10.3390/en15186813

Academic Editor: Emilio Lorenzani

Received: 20 July 2022
Accepted: 14 September 2022
Published: 18 September 2022

Publisher's Note: MDPI stays neutral with regard to jurisdictional claims in published maps and institutional affiliations.

Copyright: © 2022 by the authors. Licensee MDPI, Basel, Switzerland. This article is an open access article distributed under the terms and conditions of the Creative Commons Attribution (CC BY) license (https://creativecommons.org/licenses/by/4.0/).

1. Introduction

A MG is a group of electrical loads and small-scale generation resources that can meet all or part of the demand. MGs can be built individually (islanding mode) or in groups (connected to an upstream grid). If a MG is linked to the grid system, surplus intrinsic resource generation can be sold to the upstream grid to boost the MG profit. To increase efficacy, the majority of MG-producing units can be employed in a combined heat and power scheme [1]. The overview of MG generating and storage possibilities is presented in Table 1 [2].

Table 1. Summary of MG generation and its storage possibilities.

Table	Sources	Pros	Cons
Generation	Diesel and spark ignition reciprocating internal combustion engines [3]	• Dispatchable • Quick startup • Load-following • Can be used for CHP	• Nitrogen oxide and particulate emissions • Greenhouse gas emissions • Noise generation
	Micro-turbines [4]	• Dispatchable • Numerous fuel options • Fewer emissions • Mechanical easiness • CHP-capable	• Greenhouse gas emissions
	Fuel cells [5–7]	• Dispatchable • Zero on-site pollution • CHP-capable • Compared to micro-turbines; increased efficiency is obtainable	• Relatively expensive • Limited lifetime
	Renewable generation (solar PV, WT, and mini-hydro)	• Zero fuel cost • Zero emissions	• Without storage, it is not possible to transfer • Unpredictable and uncontrollable
Storage	Batteries [8]	• Long history of research and development	• Fewer charge–discharge cycles • Waste disposal
	Regenerative fuel cells [9]	• Decouple power and energy storage • Able to support a continuous operation at the maximum load and complete the discharge without risk of damage	• Relatively early stage of deployment
	Hydrogen from hydrolysis [10]	• Clean	• Relatively low end-to-end efficiency • Challenge to store hydrogen
	Kinetic energy storage [10]	• Fast response • High charge–discharge cycles • High efficiency	• Limited discharge time • High standing losses

Numerous hybrid approaches have been developed to examine the combined operation of the MG's micro-sources and storage facilities [11]. The MG administrator is in charge of the internal control of the MG's elements. The operators of the main grid, the market operator, or the regional transmission organization have no monitoring or control over the MG's micro-sources in this circumstance. A portion of the energy may be limited due to the MG's internal restrictions and inherent uncertainty.

The Internet of Energy (IoE) refers to the combination of IoT and MG technologies. The IoE takes advantage of the MG's bidirectional energy flow and information to gather data on power consumption and forecast future activities to improve energy efficiency and reduce net costs [12]. The MG relies on a number of IoT technologies. From the physical to the application layers, such technologies comprise the entire network protocols.

In 2017, the number of internet devices reached 8.4 billion, and by 2020, it is expected to reach 30 billion. The IoT is a system of these units that will communicate and share data. The IoT is at the zenith of its growth stage in the environment of MGs, with smart analytics promising a bright future. Energy-based analytic data sent from users to utilities have the ability to improve MG efficacy and minimize congestion, leading to increased power distribution reliability in a (future) 100% renewable energy paradigm.

The future MG will be made possible by the transition of a device-electric grid into a smart, self-healing bidirectional intelligent system [13]. Energy suppliers seem to be

more interested in delivering efficient power, minimizing CO_2 emissions, helping to bring in green energy, and lowering prices while maximizing utility profits with these modern technologies. This IoT-enabled MG enterprise contributes to the global smart city mission. Table 2 shows the primary capabilities of a MG.

Table 2. Primary capabilities of a MG.

Functionality	Microgrid Description
Self-healing	A MG has the ability to assess, respond, and discover serious flaws very quickly. Smart metering systems are used to identify faulty circumstances and blackout scenarios.
Consumers motivation	Consumers can choose their suitable tariffs and more efficiently manage their energy usage. The case for enhanced energy consumer interaction and cost planning has been made.
Resist attack	The main challenges that a MG can readily combat are cyber-attacks and physical attacks. For MGs, several data conservation strategies have been implemented.
Improved power quality	Constant voltage is the most common consumer demand across all domestic, commercial, and industrial sectors. The MG has the ability to keep a constant voltage, therefore improving power quality.

The MG design [14] necessitates constant device monitoring, examination, and total management of the overall grid, in which large numbers of monitoring equipment of various sorts are placed at several power plants, transmission and distribution regions, and at the customer's side [15]. The IoT is described as collections of physical objects that are linked together via the internet [14,16].

Despite the commitment and availability of IoT technology, a MG will be impossible to accomplish in the future. Interconnectivity via communication devices, such as mobile phones, allow for quick decision-making through social cooperation and lowering application TCO. There are numerous advantages to cloud computing from a financial standpoint, where the TCO of a product is calculated from its acquisition, taking into account both service and running expenditures. The utility receives detailed information from smart meters and sensors, allowing it to prepare a compressed service order and the closest work to be delivered. Once the power goes out in the modern era of IoT and the MG junction, a message from the power line sensor is delivered quickly to the utility providers, who can then monitor the transformer operation. The IoT allows for more seamless activity and interactions between the two parties, resulting in a more effective wireless system. The primary contributions of this paper are to illustrate the benefits of hybrid AC/DC MGs over AC and DC MGs, to discuss the role of the IoT in the design and development of smart MGs, including benefits, challenges, and risks, and to expose a number of technologies, architectural designs, and applications that use the IoT with the goal of preserving and regulating innovative smart microgrids in accordance with contemporary optimization features and regulations. Figure 1 depicts the framework of this study.

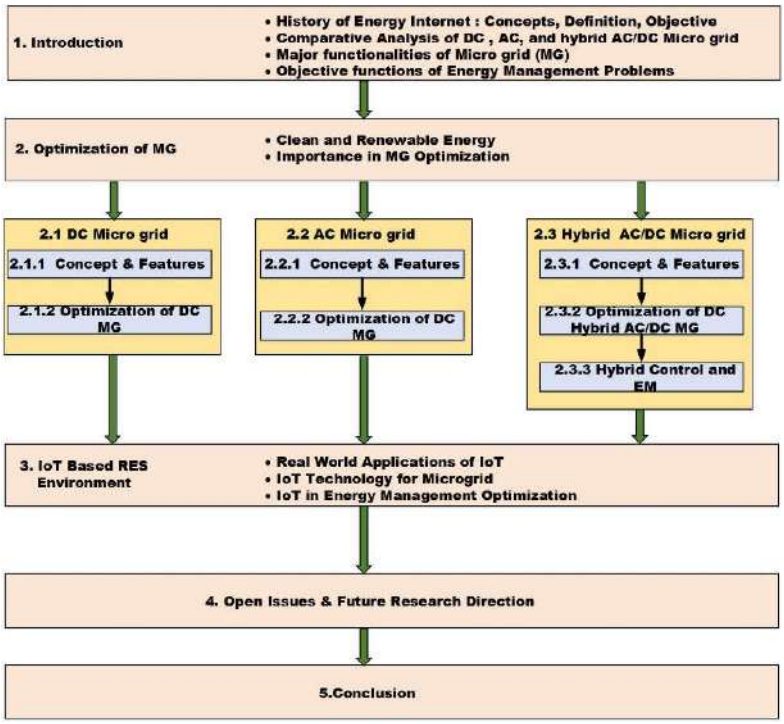

Figure 1. Framework of the paper.

2. Optimization of MG

Clean and renewable energy is advancing in order to achieve energy sustainability and harmonious growth in the economy and society. MGs are important tools for implementing clean and renewable energy. MG operation optimization has grown in importance as a study area. This study examines the recent improvements in MG operation optimization.

2.1. DC Microgrid

A DC MG has a DC bus that provides power to the DC loads coupled to it. Cell phones, internet routers, DVD players, battery-powered vacuum cleaners, wireless phones, and laptops are examples of low-power electronic devices. In a DC MG configuration, resources with DC output are simply coupled to the DC bus [17]. There are few converter elements necessary since these are more DC-generating RESs than AC-generating RESs. It increases the total efficacy of the DC MG.

2.1.1. Concept and Features

In this environment, the use of DC-operated technology in regular life has increased dramatically [18]. DC loads are generally linked to AC inputs because of an absence of independent DC supply networks at the consumer's end. Multiple conversions are required because the AC power is adjusted by converters for various DC load demands. Conversion losses and harmonics created by converters are steadily increasing, contaminating the power grid. The average power loss from these conversion procedures is 10–30% [19]. Regarding the principle of a MG—it was developed in response to an increased usage of DC systems and to handle low-powered DG resources. It complements the development of MG operations and improves the BESS [20]. Figure 2 shows the circuit of DC MG.

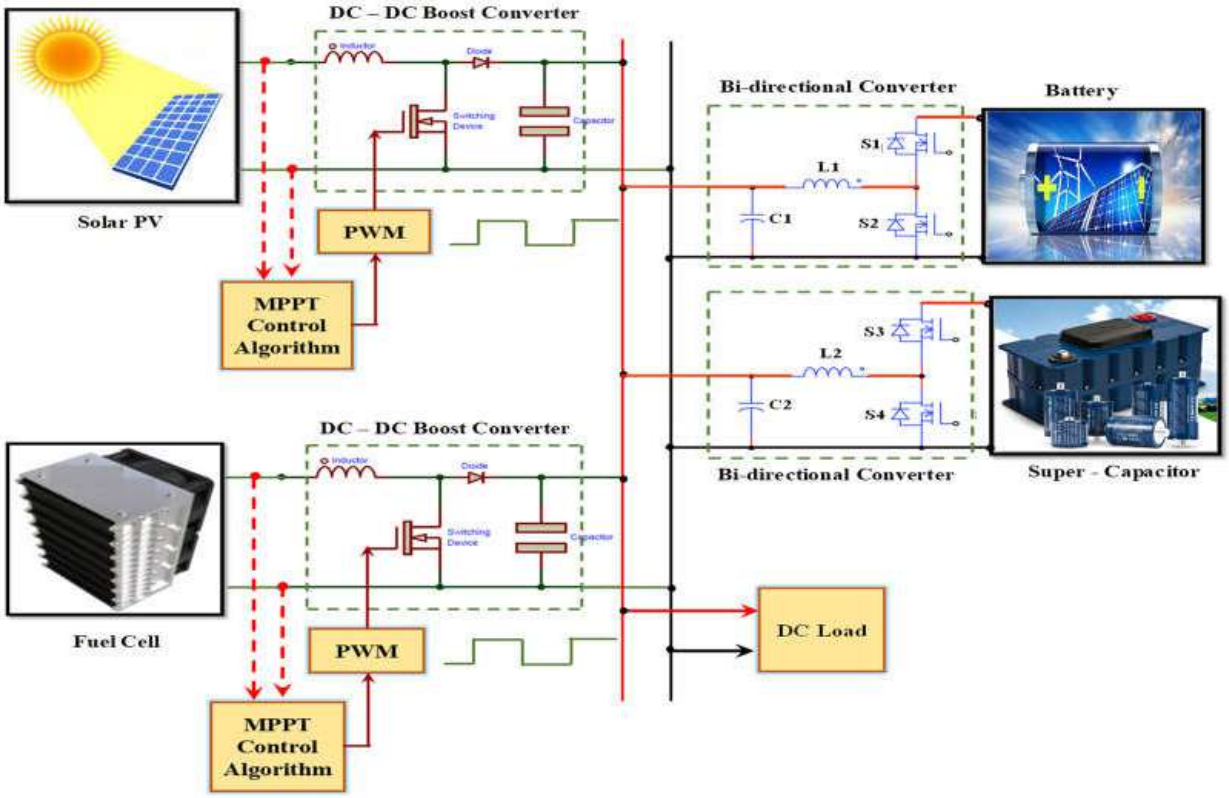

Figure 2. Circuit of DC MG.

If a BESS is attached to standard AC ports, massive conversion losses occur because of multiple conversion processes. As a result, BESS reliability has diminished. However, in a MG, the BESS is (most of the time) run within the DC bus. As a result, the losses experienced in the charge operations are considerably reduced, and the BESS behavior in a MG configuration is significantly enhanced. Electricity is presently unavailable to approximately 1.1 billion people [21], the majority of whom live in rural parts of Sub-Saharan Africa and Southeast Asia, as well as, to a smaller extent, the Middle East, Central Asia, and Latin America [22].

2.1.2. Optimization in DC MG

Thousands of SHSs [23] have been built in distant areas as a result of rural electrification schemes, typically in areas with no electricity grid, no regular wired telecommunication networks, and (mostly) poor availability by ordinary transport. SAPV systems are SHSs. Typically, crystalline-silicon PV modules are used in these setups. The most typical battery type used in a battery backup unit is lead-acid, and many tiny SHSs use charge controllers with PWM to optimize the charge current to the battery [24]. The lack of appropriate SHS monitoring and, hence, the inability to recognize O&M issues, can result in a severe reduction in the lifespans of PV systems, or even their removal from use [25]. The contributions of different optimization methods for DC MG are discussed in the various research works mentioned in Table 3.

Table 3. Optimization methods for DC MG.

Reference	Year	Optimization Algorithm/Method	Contribution	Drawbacks
[26]	2015	Decentralized voltage droop control	It is possible to achieve balanced and reliable load distribution, and it causes a steady-state voltage drift.	Lacks speed and robustness.
[27]	2020	Novel grasshopper	It includes energy conversion efficiency and oscillation minimization in terms of tracking time.	Contains more iterations and a slower rate of convergence.
[28]	2014	Game-theoretic cold-start	Reduces losses and reaches the steady-state operating point that is needed.	-
[29]	2016	Unified distributed dynamic optimizer	Voltage regulation and cost optimization by coordinating source voltages and optimally sharing power among sources.	-
[30]	2017	Optimal power flow strategy	Ohmic line loss, converter loss, and transmission loss are minimized.	An excess of reactive power can occur when the load is reduced.
[31]	2019	GA	Improves current sharing between the DGs, total loss minimization, and system voltage regulation.	Convergence speed is slower than other algorithms.
[32]	2020	Robust stability analysis	Stability analysis of a specific equilibrium under known constant power loads.	-
[33]	2020	Model predictive control	Provides economic, reliable, and rapid real-time control by solving the planned model in a time-sharing approach.	Cannot tune offline.
[34]	2020	Second-order Cone Optimization	It improves DC MG functioning while lowering operating costs.	-
[35]	2015	Newton Raphson method	Provides electrical power to areas that are off the grid. Optimizes the voltage level for efficiency, safety, and regulation.	Difficulty in calculating the derivative of a function.
[36]	2020	Adaptive differential evolution	Reduces DC MGs' operational costs and surpasses traditional GAs in terms of cost savings.	-
[37]	2019	Fuzzy control	The optimization time is significantly decreased, and the running cost is minimized.	Limited capability of current sharing.
[38]	2016	Frequency droop control	Even in the presence of unknown load demand and modeling errors, voltage regulation is achieved.	Poor transient characteristics.
[39]	2019	3G with IoT	The data logger could be put at a minimal cost to solve the challenge of monitoring PV systems in remote areas.	Speed is less compared to 4G.

Grid-connected PV plants typically require large expenditures, and the related data collecting systems allow for monitoring key variables and the execution of required maintenance operations without considerably increasing the overall cost of installation. Nevertheless, it is extremely complex to monitor the functioning of SHSs, owing to the reality that the necessary commercial data loggers are costlier in comparison to the overall system cost. As a result, more precise and independent external sources of data collecting systems must be developed at a smaller cost. Analytical control has progressively been implemented in small PV systems in recent years. Monitoring has been highlighted as one of the variables that lead to the viability of rural electrification programs since these efforts improve the lifetime of the system and reduce PV system failure, enhancing the user's confidence in the system. Table 4 lists the parameters in real-time PV systems that should be monitored.

Table 4. PV System parameters to be monitored in real-time.

General Parameters	Specific Parameters
Meteorology	Total irradiance Ambient temperature
PV array	Output voltage Output current Output power PV module temperature

2.2. AC Microgrid

An AC bus system connects the numerous energy-producing sources and loads in an AC MG network. AC MGs are often made up of dispersed generating units, such as renewables and traditional power production sources, such as engine-based generators. Such distributed generators are linked to an energy storage media, such as BESS, via an AC bus system. DC output is generated by renewable generators, such as solar PV and wind turbines. Through power electronic-based converters, this output can be transformed to AC.

2.2.1. Concept and Features

Wind energy has emerged as an essential alternate energy resource for power generation, owing to the diminishing reserves of global real-world resources and the progressive development of low-carbon and environmental protection principles. Wind energy is useful to the world's natural resources and ecology [40]. It is also conducive to sustainable economic development as a non-polluting and clean energy source [41]. According to studies, wind power generated roughly 12% of global electricity production in 2020 [42]. Wind energy is also expected to account for 22% of the worldwide power supply in 2030 [43]. Wind speed fluctuations and intermittency can have negative impacts on the stability and reliability of power grid operations, resulting in high costs and low efficiency. To increase the accuracy and reliability of WSP, it is critical to build strong prediction techniques. Physical techniques [44], traditional statistical strategies [45], spatial correlation strategies [46], and AI strategies [47] are the four basic kinds [48] of WSP methods that have been established in the last several decades [49]. Figure 3 depicts the AC MG circuit.

2.2.2. Optimization in AC MG

The following are the shortcomings of the forecasting strategies:

1. Physical methods are unable to successfully handle small time horizons; as a result, they are unable to produce efficient and precise solutions in short-term WSPs [50]. Furthermore, environment data must be updated on a regular basis, lengthening the time it takes to execute, and increasing the cost of resources.
2. With non-linear trends and unpredictable variations, conventional statistical methodologies fail to estimate wind speed TS. This is due to TS's prior assumption that all forms are linear. Furthermore, these techniques rely heavily on data for WSP under real-world conditions; as a result, if the original TS changes dramatically because of societal or ecological causes, forecasting errors will increase [51].
3. For this condition, substantial volumes of sophisticated monitoring of data are needed, and the predicting results will be inefficient due to data measurement limits and temporal delays.
4. Despite the usage of alternative methods, AI technologies were thoroughly investigated and are now being utilized to handle complex relationships and make accurate assumptions. These techniques can be used to capture the actual series in non-linear patterns.

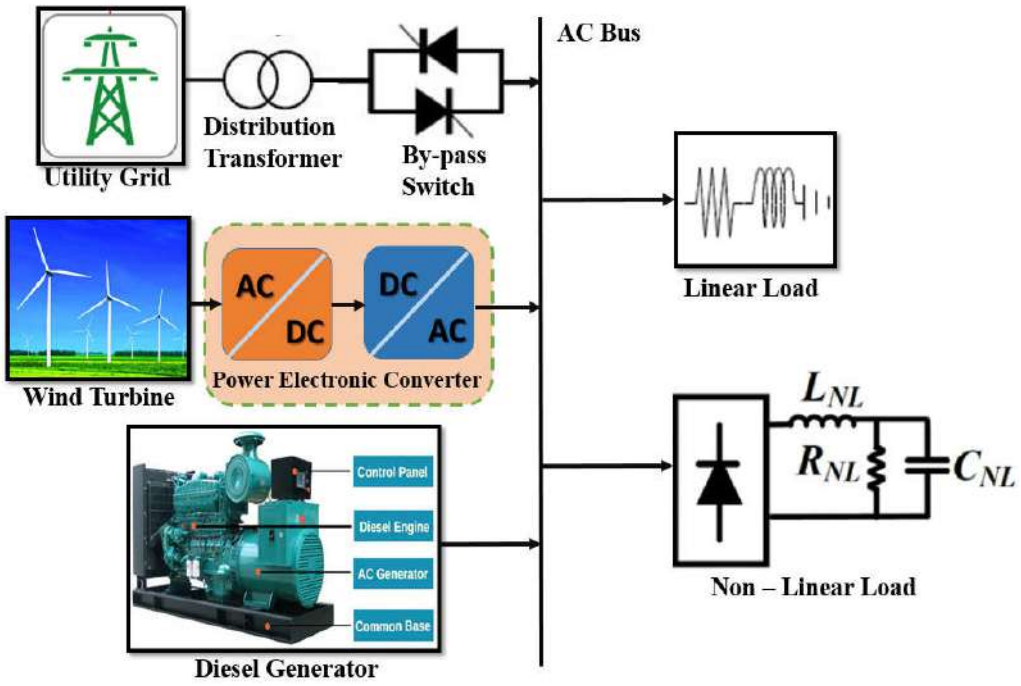

Figure 3. Circuit of AC MG.

The contributions of different optimization methods for AC MG are discussed in the various research works mentioned in Table 5; the parameters to be monitored in a real-time wind energy system are given in Table 6.

Table 5. Optimization methods in AC MG.

Reference	Year	Optimization Algorithm/Method	Contribution	Drawbacks
[52]	2020	Techno-economical	Single-axis and dual-axis solar trackers are used to test and optimize the performance of a stand-alone solar PV power system.	Does not consider a grid-connected PV system.
[53]	2018	GA	The TCE and LPSP of the load are both minimized simultaneously in order to solve the optimization challenge.	Cannot assure constant optimization response time.
[54]	2016	Frequency droop control	Keeps the MG system running at the necessary degree of dependability while lowering the net operating cost.	Communication systems are used to eliminate or reduce errors in reactive power sharing.
[55]	2020	Swarm intelligence	Enhances dynamic stability, improves dynamic response, and optimizes power quality.	Cannot work out the problems of the non-coordinate systems.
[56]	2020	Computational intelligence	Extremely effective at eliminating problems with power quality and transient responses.	More sensitive to fault resistance.
[57]	2017	Recursive algorithm	Recovers voltage and frequency synchronization, resulting in a more powerful control scheme even in noisy environments.	Complex algorithm.
[58]	2018	Pontryagin's minimum principle	Optimizes parallel connected inverter systems in an islanded MG.	It specifies only the need to hold over a particular trajectory.

Table 5. *Cont.*

Reference	Year	Optimization Algorithm/Method	Contribution	Drawbacks
[59]	2014	Stochastic energy management technique	RES has a great impact on the optimal operation and programming of interconnected MGs. Reduces the cost functions of AC MGs	Network constraints can affect the optimal scheduling of units.
[60]	2016	Sliding mode direct voltage control	Improves the system's disturbance rejection and power distribution accuracy.	Complex and low speed.
[61]	2016	Neuro-fuzzy controller	Frequency control without any storage.	The structure is not totally interpretable.
[62]	2017	Day-ahead MG EM optimization	The O&M costs of lithium batteries and fuel cells, the interruptible compensation of interruptible loads, and the price of energy, are all part of the target function.	-
[63]	2018	Iterative consistency algorithm	Increases the AC MG control's durability and flexibility, and only requires little communication between surrounding agents to achieve a global optimum.	Sensitive to communication failure.

Table 6. Factors to be monitored in real-time wind energy (a survey of cyber-physical advances).

General Parameters	Specific Parameters
Environmental	Wind Humidity Lighting Icing
Mechanical	Positions Speed Angle Stress Strain
Electrical	Voltage Current Power factor Frequency Faults
Temperature	Bearings Oil Windings Electronic components
Fluid	Pressure, level, flow

2.3. Challenges, Need for a Hybrid AC/DC MG, and Its Implementation

The main hurdles for successfully implementing hybrid AC/DC generation systems are described in detail in this section. In addition, the current scenario's solutions to the difficulties are offered. The second portion of the section discusses the need for AC/DC MG integration as well as its advantages. Figure 4 shows the hybrid renewable energy generation by source, measured in terawatt-hour (TWh).

Figure 4. Hybrid renewable energy generation. (**Source:** Statistical review of world energy).

2.3.1. Concept and Features

One of the most intriguing strategies in the evolution of the MG principle in the present distribution network is the hybrid AC/DC MG. Figure 5 depicts a typical hybrid MG structure, with the AC and DC networks. Several devices can be observed in the diagram: PV, fuel cell, a diesel generator, DG and ESS units, VSD, AC and DC loads, etc. Interlinking converters have been used to connect AC and DC sub-grids. This arrangement confines greater interfacing, which in turn minimizes the cost and improves overall efficiency. This architecture is the most appealing option for a future MG framework.

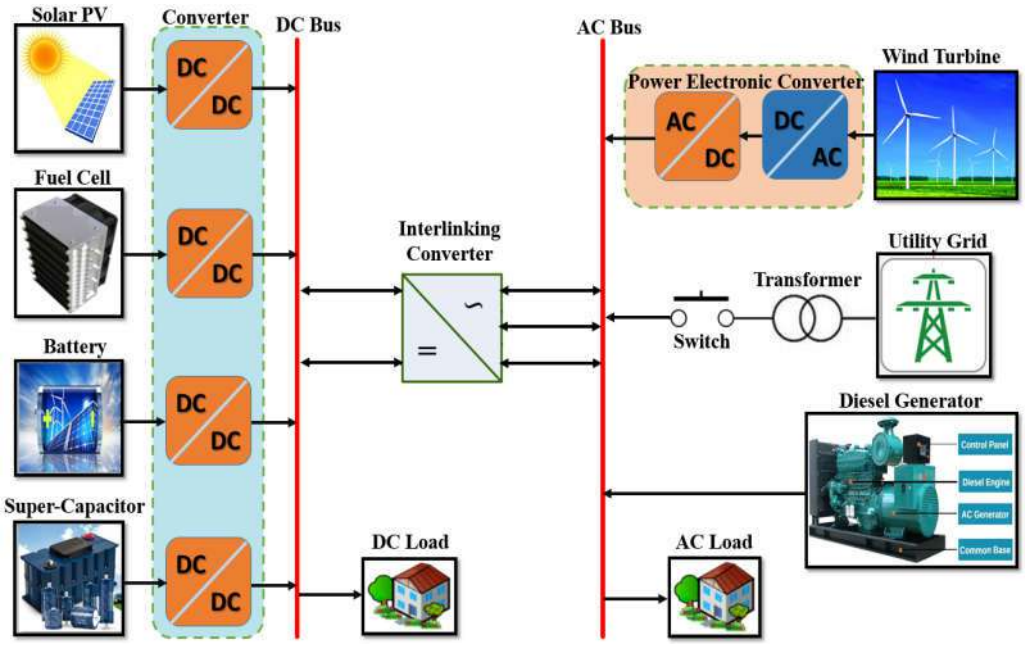

Figure 5. Hybrid AC/DC MG with interlinking converter.

The following are the most significant advantages of these MGs:

Integration: Devices that are powered by AC or DC are directly interconnected with the fewest interfacing devices possible, eliminating conversion stages and, thereby, energy losses.

Synchronization: Because the generation and storage devices are directly coupled to the AC or DC network, there is no need for them to be synchronized. As a result, the device's control method is simplified.

Voltage transformation: Use of such transformers on the AC side can be used to modify voltage levels in a straightforward manner. On the DC side, DC–DC converters are used to conduct the conversion.

Economic feasibility: By adding a power converter to the existing distribution grid and a communication network for linked devices, a hybrid MG can be created. With the use of a power converter, the net prices are higher than that of AC MGs. Although, if the number of connected devices grows, the expenditure will be repaid more quickly because the overall number of interfacing converters will decrease.

2.3.2. Optimization of Hybrid AC/DC MG

Integration of renewable energy resources, such as solar panels, batteries, and other energy storage devices with low voltage systems, will be a viable method for reducing multiple energy conversion losses in the proposed system.

The utilization of RESs has rapidly increased to address the critical concerns of increasing energy demand and global warming [64,65] as a result of increasing energy consumption, which is expected to reach 53% by 2035 [66]. For instance, HMGS [67] delivers energy delivery to rural places where essential T&D amenities are not accessible or costlier to install. When three features are met, DERs can be considered a MG: electrical boundaries are set, an EMS is included, and the power generation capacity must surpass the peak critical load [68,69]. In [70], a novel load flow algorithm for AC/DC distribution systems that makes use of matrix algebra and graph theory is presented. To find load flow solutions, four designed matrices (the loads beyond the branch matrix, the path impedance matrix, the path drop matrix, and the slack bus to other buses drop matrix), as well as basic matrix operations, are used. Similarly, in [71], AC/DC hybrid distribution systems provide a single load flow (LF) model (DSs). The suggested approach can be used in hybrid distribution systems (DSs) that have AC/DC buses and AC/DC lines configured in a wide variety of ways. Additionally, a new DS bus category is presented for LF analysis. There are a number of important factors to consider when making a decision. First, the COE that relates to the cost of operation to fulfill the load demand. Second the stability needs to be at the highest level so that the power supply breakdowns are prevented. The LPSP, which will be discussed in the following sessions, is one of the metrics that can be used to describe HMGS reliability.

(i) Designing objectives with ESS.

The imbalance between peak demand and generation can be smoothed out by energy storage. As a result, matching electricity generating sources for the setup of an HRES is simply a designer's optimization challenge with several limitations to meet. The design techniques must strike a balance between reliability and cost [72]. Supply security issues were also taken into account in the design of the MG design in a recent study [73], which defined a probability adequacy index. Leou [74] analyzed installation costs, O&M costs, and income, considering energy price arbitrage for minimizing transmission access costs and postponing facility construction. Sundararagavan [75] conducted a cost analysis of eleven types of energy storage technology for essential applications linked with a wind farm combined with an electric grid.

Chedid et al. [76] developed the core of a computer-assisted evaluation tool that can assist designers in determining the best design of a hybrid wind–solar–diesel generator–battery power system for independent- or grid-connected applications. Batteries, at relatively low costs and with widespread availability, are the most widely used components in hybrid systems. Tewari et al. [77] looked at a nNaS battery system for transferring power generation from off-peak to on-peak, as well as ramp rate limitation to smooth out wind output. Using model predictive control theory, Khalid [78] devised a new semi-distributed approach that efficiently lowers the BESS capacity required, lowering the total system cost. Brekken et al. [79] employed flow batteries in conjunction with an ANN method to handle the uncertainty in wind output and reduce energy prices even further. The uncertainties

in an HRES integrating PV–wind–diesel and a hydrogen-based ESS were investigated by Giannakoudis et al. [80].

The first was a typical strategy relying on the battery's state of charge, and the second was an enhanced ANN algorithm that was evaluated based on energy storage costs. According to the findings, the hybrid battery–hydrogen system storage costs 48% less than a hydrogen-alone system and just 9% less than a traditional battery-only system. Katsigiannis, on the other hand, used NSGA-II optimization and discovered that the hydrogen-based system had higher LCE and emissions than the lead–acid-based system [81]. Choi [82] aimed to reduce battery charging current variations and energy losses in super-capacitors by optimizing a battery/super-capacitor hybrid ESS. Thounthong et al. [83] developed a novel approach for combining a super-capacitor with a hybrid PV–fuel cell power plant as an additional source and short-term storage units.

(ii) Sizing objectives.

The optimal sizing of producing units is critical for efficiently and economically utilizing RESs. With an appropriate and complete utilization of the HRES components, the sizing optimization approaches can help to ensure the cheapest investment. Economic and environmental objectives are the most typical goals considered while sizing an HRES. Nehrir et al. [84] examined several methods for system setup, unit sizing, control, and energy management of hybrid systems under investigation. Details about HRES initiatives being implemented around the world were also compiled. Bernal-Agustin et al. [85] and Zhou [86] have also provided their analyses on HRES design, simulation, and control employing PV, wind, and diesel with battery storage. Luna-Rubio provided a review of sizing approaches, including several metrics that were adjusted for maximum performance at the lowest cost [87]. Elma and Selamogullari [88] investigated a stand-alone hybrid system that met the electrical requirements of a residential house.

Numerous research has taken into account economic system parameters, such as LPSP, LCOE, and fuel costs while sizing. With LPSP as the main restriction, Hongxing built and studied a hybrid solar–wind–battery system optimal model for lowering system costs [89,90]. Ekren [91] investigated the difficulty in scaling a PV/Wind/BESS system for use in a GSM station in Turkey. RSM was used to address the sizing problem, and a minimum energy cost of USD 37,033.9 was attained. A siting strategy was devised by comparing this COE to transmission line expenses using the break-even analysis [92].

Using a controlled elitist GA, Reference [93] proposed a triple multi-objective optimization technique to assist developers in taking into account both environmental and economic issues. LCC, EE, and LPSP indicators were merged in the optimal solution. Di-Silvestre et al. [94] established a multi-objective optimum operation using a distinct layered technique. In Reference [95], decision support tools based on the fuzzy technique for order preference by similarity to ideal situation (TOPSIS) and level diagrams were used to build HRES. Arnette [96] devised a multi-objective linear programming approach for HRES planning that allows the decision maker to balance generation costs and emissions under a variety of operating situations. As a result, the wind and solar potential capabilities were assessed separately, taking into account the sizing objectives. Zhang et al. [97] introduced a unique technique for optimizing power dispatch simulations in a PV–battery–diesel system by reducing LCE, which also took into account maintenance costs, capital depreciation costs, pollution damage costs, and fuel costs. Tan et al. [98] introduced a new optimization model for DG siting and size that took into account technical factors including grid VA need, voltage profile, real power losses, and so on.

2.3.3. HRES Control and Energy Management

In order to attain the needed quality power at predefined costs, optimization approaches play a critical part in the functioning of an HRES. Any portion of the HRES can benefit from optimization. The main functional areas for optimization are generation controls such as power dispatch control, energy management decision-making controls,

operation controls for power quality and cost control, and MPPT control systems. The following are some examples of the state-of-the-art in control and management.

(i) Power quality and cost control.

Power conditioning devices such as STATCOM and quality management procedures in distribution systems increase power quality [99–101]. It is critical to install them in the best possible location and execute them properly in order to save money and improve efficiency [102]. Serban [103] devised a system for optimization and testing of the frequency control mechanism in MGs, using BESS. By incorporating an ESS in small, isolated power systems, Sigrist [104] calculated the economic advantage of primary frequency control reserve and peak-shaving generation, resulting in a total cost savings of 23.2 Mio €/year and an internal rate of return of 7.25 percent. In Agios Efstratios, Greece, Vrettos et al. [105] investigated the infiltration of WT-ESS into an emerging diesel unit. Applying GA to optimize the LCOE, it was discovered that a 10–15% reduction in LCOE could be obtained with a 75% RES saturation level. In 2013, Zhao [106] addressed the lifetime properties of lead–acid batteries while doing multi-objective optimization to minimize power generation costs and increase the usable life of lead-acid batteries for a similar HRES MG. It has been demonstrated that a higher RES penetration level might result in a 30% drop in total expenditures. The control objectives defined by Younsi et al. [107] are to fulfill the power sought by the AC grid, control the transfer of energy among the hybrid system and the AC grid, optimize the use of wind energy, and minimize fuel costs of diesel generators. Arabali et al. [108] applied GA to a hybrid system that served a single HVAC load, analyzing the cost and efficiency of operation during different scenarios. With the introduction of commercial power system simulators that include powerful analytical and visualization tools, studying power flow controls in a MG has become considerably simpler [109,110].

(ii) Power dispatch control.

In power system applications, such as economic dispatch, unit commitment, and generation scheduling, optimization approaches are becoming increasingly popular. Conti et al. [111] developed an optimization approach for DG and ESS dispatch in a medium-voltage islanded MG with the goal of lowering emissions and operational costs. Zhang et al. [112] proposed a unique power scheduling technique for reducing utility costs of dispatchable loads, worst transaction costs due to renewable source uncertainty, and generation and storage costs. When combined with an HRES, CHP significantly increases efficacy and pays for itself. A CHP-based DG MG with ESS and three different forms of thermal power generation units and DRPs was studied in Reference [113]. Maa et al. [114] conducted a viability analysis on a residential MG system with a hybrid PV–WT and CHP generator. For power dispatching challenges, most new methods use commercial simulators, such as Power World [109]. It simplifies inquiries and the evaluation of complex market policies. MILP was a commercially available solver-based method that avoided the use of complex heuristics or decomposition methodologies [115].

(iii) Energy management control

The efficiency of HRES subsystems can be improved by appropriate resource management [116,117]. Zhao et al. [118] adjusted the reactive power output of a wind farm and the network infrastructure at the same time to reduce system actual power losses and bus voltage deviations, resulting in enhanced power control and voltage profile. Trifkovic et al. [119] used decentralized adaptive model prediction control and decision-making techniques to describe a power management strategy for a wind–PV–electrolyzer–fuel cell integrated standalone system. It was discovered that operating the electrolyzer at a lower power level increased the efficiency of the renewable energy produced, resulting in more hydrogen production. Table 7 shows the optimization methods used in a hybrid AC/DC MG.

CAES results in a 43% higher operating profitability and 6.7% less net load serving costs, even when capital expenses are not taken into account. For enlightening energy management techniques, a mixture of optimization techniques and AI methods has also been tried. Multi-objective smart power management tries to reduce a MG's operating costs and emissions while taking into consideration pre-operational variables such as future renewable energy supply and load demand. For optimal operation of an HRES system, controlling variables coming from renewable generation and load demand projections are also examined. Hong's PEM was used by Mohammadi et al. [120] to optimize a MG by modeling the uncertainty in load demands, market prices, and renewable energy generation. In Reference [121], rather than using Hong's estimate, an optimal stochastic approach was used, which included the usage of probability density functions for each unknown parameter and roulette wheel mechanism scenarios. The stochastic approach captured roughly three times the number of uncertainties as the deterministic approach.

Table 7. Optimization methods in Hybrid AC/DC MG.

Reference	Year	Optimization Algorithm/Method	Contribution
[122]	2013	Discrete harmony search	Optimizes the size of wind–PV hybrid energy systems.
[123]	2019	GA	Optimize a hybrid solar-wind energy system with storage for a remote island.
[124]	2011	Iterative optimization technique	For power reliability and system costs.
[125]	2012	PSO	Achieve the lowest MG cost possible during an interlinked operation by optimizing the local DG generation, and power exchanges with the main distribution grid.
[126]	2013	GA	The proposed BMS reduces operating expenses while accounting for various battery operating points and aging factors.
[127]	2014	Techno-economic approach	Optimizes the size of the main distribution system.
[128]	2018	Interval optimization approach	More variation profits are lost, but a smaller amount of average profit is lost, making the retailer more resilient to pricing volatility in the pool market.
[129]	2018	Annealing-chaotic search	A hybrid reverse osmosis desalination plant fueled by solar and wind energy was designed using an optimization approach.
[130]	2019	Wind-driven optimization	Excellent rate of success and high efficiency in monitoring time.
[131]	2019	Grasshopper optimization	According to the DPSP and COE, develops the best system configuration for supplying energy demand efficiently.
[132]	2020	Multi-objective PSO	Reduces the LCOE and increases the transmission channel utilization rate.
[133]	2020	Chance Constraint optimal power flow method	Proposes a two-stage voltage control system for a combined central and local voltage control mechanism.
[134]	2017	Multi-objective PSO	Every region determines the best system configuration and component size.
[135]	2018	Nelder–Mead—cuckoo search	By controlling the power output of RES, the power losses in hybrid AC/DC MG systems can be reduced.
[136]	2013	Multi-objective	Minimizes lifecycle costs and CO_2 emissions from the system.
[137]	2021	GA	Minimizes conventional distribution network losses in residential areas. Uses a time-of-use tariff system, and lowers the COE.
[138]	2016	GA	Minimizes DS installation and operation costs.
[139]	2018	Newton—Raphson algorithm	Models converter losses because it will lead to different load flow values.

Table 7. *Cont.*

Reference	Year	Optimization Algorithm/Method	Contribution
[140]	2020	Graph-theoretic-based approach	Tested on several AC/DC test networks that include different operating modes of power converters and various models of DGs, which prove the feasibility and legitimacy of the technique.

2.3.4. Future Prospects of Hybrid AC/DC Microgrid

The flexible control capabilities of AC/DC hybrid DER systems are further utilized as one of the development directions of the power distribution system for the energy internet. In future studies, researchers might find great interest in investigating cooperative planning with gas, heat, and cooling systems within the context of multi-energy complementarity [141]. The important principles for the futuristic approach in an AC/DC microgrid environment for a smart and intelligent system with uninterrupted, secure, and safe power flow are listed below [142].

- Communications infrastructure that is functional and affordable.
- Enhancing energy efficiency via a cutting-edge communication system that uses clever relaying techniques and coordinated multipoint algorithms.
- Using linked communication methods, such as optical wireless.
- Self-healing should be sufficient in a hybrid environment.
- Advanced algorithms for compelling current to zero before it is interrupted by CBs.
- Robust AC/DC interface should be designed.
- Limitation of SCC should be taken care of.
- Smooth conversion between microgrid mode of operations.

3. IoT-Based Hybrid AC/DC RES Environment

Communication networks are critical components of HRES because they allow data to flow between data sources (sensors and meters), control centers, and controllers. The data flow from various elements establishes the system architecture in addition to facilitating the control operation and remote monitoring [143]. Sensing, communication, processing, and actuation will all benefit from IoT technology, which will facilitate a variety of MG applications. This research concentrates on the amount of communication between the HRES local controller and the MG control center, in which the condition of various RESs and loads can be gathered and reported to a central controller, which decides the required system action.

3.1. Real World Applications of IoT

From agriculture to health care, IoT services and intelligence can alter the lives of ordinary people. As this innovation [144] advances at a breakneck pace, it will logically anticipate population requirements and benefit society as a whole. The real-world implementations of IoT are depicted in Figure 6, which range from the retail industry to health services. In terms of IoT, the most popular phrase is "smart home." It has emerged as a progressive component in the residential sector, and smart homes are expected to be as common as smartphones in the future. Smart home devices [145] will gain branded household products as energy, and automation progresses, reducing consumers' time and, ultimately, money. This is a critical aspect for certain smart items to communicate digitally in order to provide users with a cost-effective experience. IoT devices are always being improved to make them more compact and energy efficient.

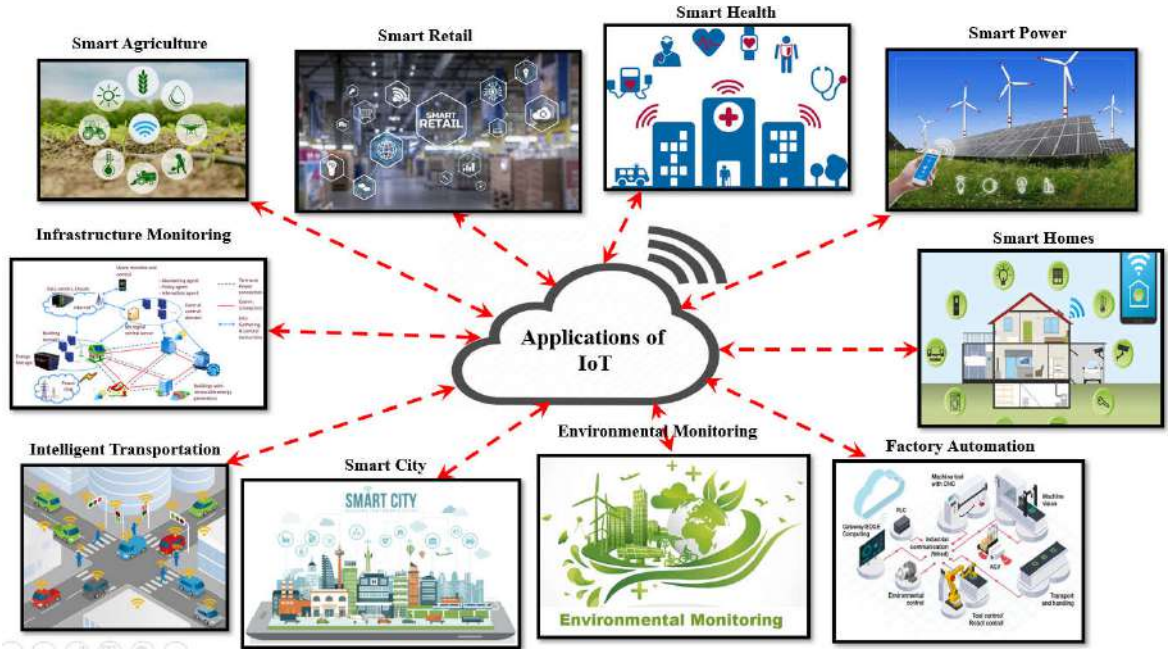

Figure 6. IoT in the real world.

As per a Forbes survey [146], leading brand businesses are expected to sell over 411 million wearables on the digital market by 2020. In article [147], the future necessity for addressing those uncertainties is explored using an IoT-based architecture. With the advancement of IoT technology, the theory of smart cities is gaining popularity. The requirement to analyze necessary protocols for urban IoT platforms [148,149] with optimized speed routing algorithms in smart streets for specific situations must be prepared for in the future.

In the automotive digital industry, IoT provides the way for vehicles that are more stable and robust in terms of performance. Connected automobiles with IoT capabilities use pre-stored inputs based on several sensors to regulate the vehicle's functioning more independently. IoT-enabled automotive revolution brought together larger branded firms from both the IT and automotive industries. The industrial sector is the next most important market for economic growth. With the growth of analytics, big data [150], progressive software resources, and enhanced sensors, Industrial IoT has the potential to empower whole sectors. Figure 7 shows that the majority of the market is focused on smart cities and industrial IoT.

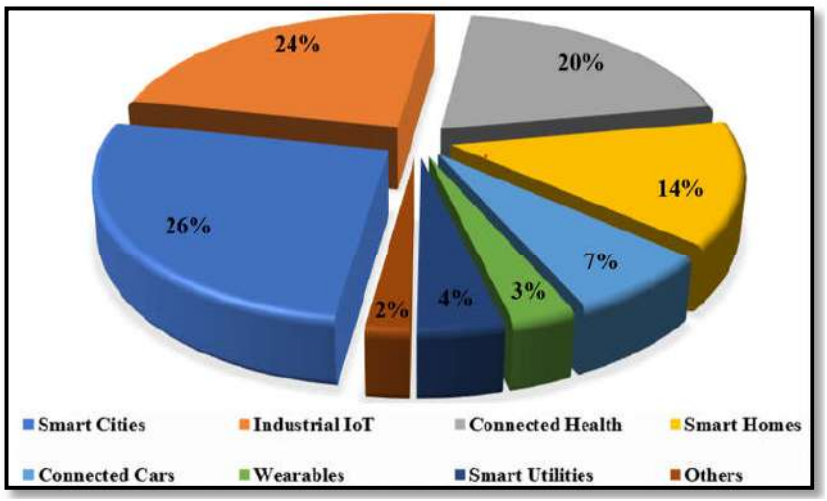

Figure 7. General market structure of IoT technologies [151].

By actively communicating with industrial data, the IoT helps create a more trustworthy solution. As a result, industries may more efficiently address inefficiencies and identify issues earlier, resulting in higher profits and productivity. In the near future, industrial IoT will focus on sensor cloud-based integrity communication [152]. New agricultural innovation is desperately required to meet the increasing demand for food supply. Only by combining innovative agronomics techniques with end-to-end IoT technologies can this be possible. Crop monitoring is performed effectively, and the persistence of a range of crops may be done in a very fair manner, resulting in more efficient water management.

Another important sector where IoT solutions are becoming more prevalent is healthcare, which aims to provide high-quality and timely services to patients. Patients and doctors can engage with each other on a routine basis because of the IoT. The global market can be expanded as a result of the use of various IoT-based smart devices that have high consumer satisfaction. With this technology, the requirements for luxury, security, safety, and cost-effectiveness can be met. Table 8 depicts the fundamental characteristics of IoT, as well as its benefits and drawbacks.

Table 8. Benefits and drawbacks of IoT.

Features	Pros of IoT	Cons of IoT	Possible Concerns towards the Remedy
Automation	The key benefit is that it can keep the entire M2M communication process transparent.	-	-
Efficacy	The system's performance is enhanced, and the presence of a M2M interface allows workers to focus on other tasks.	-	-
Security and Privacy	-	The data stored are immediately available because many equipment and services are dynamically connected to one another. The data are susceptible to hackers and unauthorized concerns.	Concentrating on more data verification tools can help solve this problem.
Communication	By talking with devices [3 N] on a daily basis, IoT develops a platform that enhances the quality and time factors.	-	-
Compatibility	-	Currently, few worldwide compatibility standards; it is difficult for suppliers and consumers to interface with services.	Similar protocols for multiple sectors, such as commercial, industrial, and residential, might be used to generate new standards.
Savings of Cost	IoT solutions aid in the development of more expensive systems for day-to-day activities in a variety of sectors, as well as efficient systems.	-	-
Difficulty	-	Because a huge network is interconnected, even minor software and hardware component failures can cause system harm.	Rapid failures at node junctions can be detected by a central control center, and necessary corrective action can be taken.

Table 8. *Cont.*

Features	Pros of IoT	Cons of IoT	Possible Concerns towards the Remedy
Instant data access	Immediate access to data in a timely manner aids in the efficient management of the process. This, in turn, makes people's lives easier and more comfortable.	-	-
Fewer jobs and technologically dependent life	-	As the number of M2M interfaces grows and automation control is implemented, the need for personnel decreases, and technology reduces human interaction.	Different control centers might be set up with the help of new competent staff.

3.2. IoT Technologies for MG

In today's world, several IoT-based solutions are accessible to meet the demands of MG applications. Despite the fact that numerous communication technologies are suitable, there are currently few standards for the effective implementation of MG. IoT technologies are mostly employed in MG for long-range bi-directional data exchange among the utility and the user via IoT-based equipment, such as smart meters. In most cases, IoT-based MG systems require advanced wireless technologies rather than wired-based technologies to alleviate the difficulty of long-distance data transfer. Certain wired methods [153], are necessary for the event of signal attenuation-related interference because these technologies will not depend on batteries to operate.

Wireless methods can be used to transfer data between smart meters and IoT-enabled devices, as shown in Table 9. Various wireless communication technologies based on IoT are detailed in this table, along with their coverage ranges, which can be utilized for MG systems. IoT can facilitate the flow of data between utility data centers and different smart meters. Different wireless techniques are required to obtain these systems together, which presents a difficult microcosm for IoT-based MG systems. Long-range connectivity is demonstrated by cellular-based networks such as LoRa [154] and Sigfox [155], which are used to build the backbone network for future grids with cloud-based service domains. MG systems will primarily focus on exhibiting long-range connectivity [156,157] and establishing a network structure with cloud-based application areas.

Table 9. Wireless technology based on the IoTs with an MG coverage range.

Technology	Usage of the Protocol Needed	Pros	Cons	MG Application
IoT-based wireless Technology	Zigbee	• It has 16 channels with 2.4 GHz and 5 MHz of bandwidth. • Less complexity. • Cost of deployment is less. • Power utilization is low.	• It has a very short range. • Processes fewer data capabilities. • Data rate transfer is less.	• Home automation • Coverage range—to 100 m.
	Long range WAN (LoRaWAN)	• Long-range connectivity • Bidirectional communication with less interface. • Provides virtual channels for the improvement of IoT gateways.	• No drawbacks in terms of data transfer.	• Monitors the transmission line networks with an online facility. • Coverage range—to 15 km.
	Z-wave	• Latency found to be low. • Less interference with other wireless devices.	• Start range. • Less suitable for NAN.	• Smart home automation. • Coverage range—30 m.

Table 9. *Cont.*

Technology	Usage of the Protocol Needed	Pros	Cons	MG Application
	IPv6 over low-power wireless personal area networks (6LoWPAN)	• Robust technology. • Less power needed. • Connectivity easier with large wireless platforms.	• Short range. • Less data rate transfer.	• Smart meter. • Coverage range—to 100 m
	Thread	• Low power. • More secure. • Connectivity easier.	• Less data rate transfer.	• Smart meter
	sigFox	• Low levels of data transfer speed. • Less power needed. • More connectivity.	• No drawbacks in terms of data transfer.	• Smart home automation. • Coverage range—10 to 30 km.

The majority of MG systems center on NAN and WAN [155], which need maximum range and minimum power technologies. For such technologies, LoRaWAN [158] emerges as a potential player. Aside from these wireless technologies, it is important to remember that determining the optimum technology for MG is impossible because most of these wireless technologies are possible candidates for MG-based applications. Several wired technologies, such as DSL [159] and power line communications [160–164], are widely employed in rural settings, and are paving the way for smarter technology. Table 10 depicts IoT device which is connected worldwide.

Table 10. IoT devices connected worldwide.

Connected Devices	Year
0.2 million	1999
80 million	2010
9.0 billion	2013
1.0 trillion	2025

3.3. IoT in Energy Management Optimization

MGs are becoming more popular as a result of renewable energy projects around the world. They have a lot of benefits, but they also have a lot of drawbacks, especially when it comes to working with traditional MG's. SEMS are developed to assist grid operators in managing energy production and consumption as efficiently as possible in order to save money, minimize CO_2 emissions, and ensure that electrical networks remain stable at all times. In the last few years, the IoT industry has developed quickly, with the advent of very effective open source IoT platforms that are especially well adapted to the development of SEMS. The most significant benefit of the open source IoT strategy is its vendor independence and ability to adapt to changing market conditions [165]. This gives grid operators more control over their assets, allows them to stay current with market demands, and allows them to improve or expand their EMSs to meet their needs. Figure 8 shows the IoT-based optimal EMS for MG.

3.3.1. IoT and Wind Energy Optimization

In terms of efficiency and size, wind technologies are quickly evolving. The primary stumbling block to the growth of wind energy is the intrinsic intermittency of these resources. As a result, if wind units have a high infiltration in fulfilling demand, extreme inequalities could jeopardize the system's security. Furthermore, IoT technology combined with ICT infrastructures enables wind farm owners to plan precise predictive maintenance plans, avoiding costly downtime. On-time maintenance, for example, can lower the LCOE index for wind assets [166], which represents the net present value of the unit–cost of power throughout the turbine's lifespan.

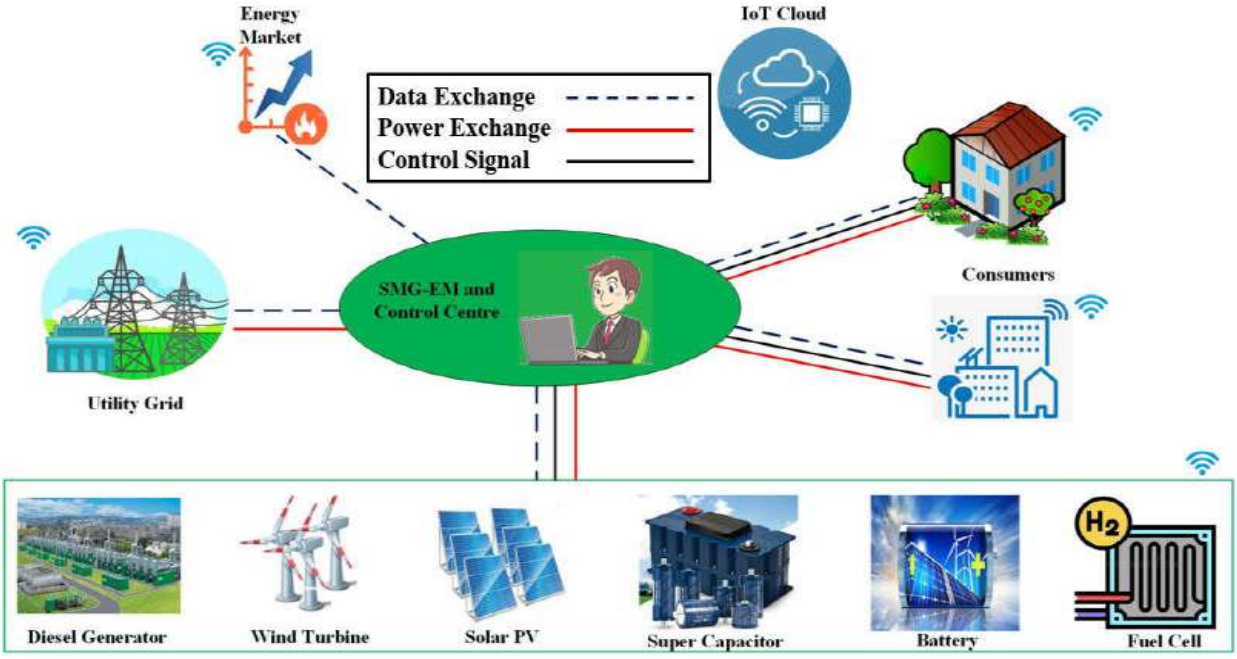

Figure 8. IoT-based optimal energy management and control for a MG.

The need for IoT in the wind energy industry stems from the fact that data related to WTs and wind farms must be obtained and evaluated quickly. Offshore wind farm data transmission delays and limited bandwidth for relaying information to remote areas were two major concerns that can be addressed right now. As a result, decision-making processes can be sped up or automated if important information can be gathered and processed in real time. The use of IoT technologies in the wind industry emphasizes the necessity for better comprehensive strategies for designing and operating wind farms and also installing and maintaining turbines that are cost-effective, secure, and safe. There are a lot of sensors and actuators in the WT controller layer. Each fundamental component's health and function can be reported by the sensors. Using a series of actuators, the control system regulates and configures the components.

The controller accepts sensor information and utilizes power amplifiers to convey electric, hydraulic, and mechanical signals and instructions. Cyber-physical devices must be combined to link the physical layer of wind turbines to the cyber layer via a network architecture. The network, condition-monitoring system, and SCADA make up the cyber layer. The design of a communication network, particularly for offshore wind farms, is largely dependent on local conditions. To connect to a LAN, each turbine must be fitted with an RTU. Such devices share data with a central data center that uses a cloud-based WAN.

All WTs in a wind farm are furnished with IoT-based-distributed intelligence systems and embedded systems that benefit from WSN, as well as M2M communication under cloud-based systems that transmit information to servers using internet-enabled and open communication protocols, and can be controlled and regulated using mobile HMIs or unified computer-aided interfaces. The IoT-based controlling system is said to be more expensive than current SCADA platforms, but due to the higher sampling rate and data frequency, it is said to be more effective at diagnosing. The IEC61400-25 standard, which improves the standardization of the data exchange gateway, diagnostics, autonomy, and extensibility was designed in order to execute unified monitoring and information exchange.

3.3.2. IoT and Solar Energy Optimization

Solar energy offers the greatest potential for renewable energy power generation. As a result, this source is expected to be a significant provider of future clean power systems. Solar panels, switches, wiring, mounting systems, and inverters make up a PV

system. A battery storage unit can be added to these items. Modern techniques, such as the MPPT controlling scheme, global positioning system (GPS) solar tracker, anemometer, solar irradiance sensors, and similar task-specific accessories, are available in modern PV systems for more efficient solar power extraction. Unlike traditional PV systems, CPVs have curved mirrors and optical lenses that assist irradiance onto a small but highly effective multi-junction solar cell. Because solar energy must be stored whenever it is available and the stored energy must be delivered once it is required, the installation of a storage unit is required. IoT can aid in the real-time sharing of data collected from PV sensors, as well as remote controllability of solar unit operation for failure and fault diagnosis, as well as prediction and preventative maintenance. Furthermore, grid-scale synchronization of unpredictable ESS and solar production necessitates real-time communication, which IoT infrastructure may provide. Uncertainties are largely linked to the appraisal of solar resources and the functioning of PV systems.

Monitoring the operation of the arrays is critical because it affects the PV unit's profitability as well as its dependability. In terms of income and O&M performance, identifying and responding to losses caused by a variety of factors is crucial. The performance of arrays can be measured via contracts between the PV system manufacturer, the PV owner, and the utility that guarantee the purchase of the energy produced. The intensity of solar radiation varies with time and is heavily influenced by the weather. As a result, there is no way to generate at a consistent rate. Several system components, such as the battery SOC and the voltage levels of the power converter, are affected indirectly by this issue. It is difficult for people to monitor every PV panel to prevent losses and outages, whether it is a rooftop PV system or a solar park in the desert. Additionally, frequent site visits and monitoring of operating data are necessary, which takes time when the PV facility is situated in a remote area. Human failures take a long time to address, and they are not always obvious. As a result, continuous monitoring of a real-time system that monitors parameters of the PV system and stores relevant information in a cloud-based network is necessary to be installed alongside the PV panels. The information can be utilized to gain a better understanding of the performances of PV systems and the causes of their failure. As a result, the deployment of IoT technology enables diagnosis and on-time maintenance.

3.3.3. IoT and Energy Storage Facilities

By redressing imbalances, ESS assists in boosting the dispatch capabilities of uncertain RESs. Incorporating IoT and processing a massive amount of data, on the other hand, adds a lot of complexity to the equation, but it improves autonomy. One must always strike a healthy balance between intricacy and performance (usefulness). Bulk energy time-shifting, small-scale frequency management, large-scale frequency stability, and power dependability are some of the applications of energy storage devices. Diverse energy storage systems have been developed so far for various uses. Energy storage units are critical for increasing the flexibility of power networks while also ensuring their reliability. The insecurity and intermittent nature of RESs is the key impediment to increased adoption. The use of energy storage facilities can help to decrease the danger of these uncertainties. As a result, real-time integration between these units is essential to avoid undesirable restrictions due to excess generation or detriments as a result of inadequacies. IoT infrastructure can help to make this a reality by allowing wind farms or solar parks to work together with grid-scale energy storage facilities, increasing the profitability of both types of facilities.

3.3.4. Drawbacks of IoT in Microgrid

Specific technological difficulties would need to be overcome in order to support the rapid technical development of IoT technologies as well as innovative potential application areas [167]. One of the main issues is associated with the development of different tools for the monitoring of network operations [168], then issues with security tools and their management [169], issues with software bugs, demanding maintenance of IoT networks, and finally, security issues related to IoT networks [170]. The key issue with the effective

adoption of IoT technologies is related to the speed and coverage of wireless networks (Wi-Fi), where expectations are high due to both noticeable gains in Wi-Fi network coverage and increases in Wi-Fi speed over the period of 2017–2022. Globally, rises in Wi-Fi speed of more than a factor of two, or from around 24 Mbps to more than 54 Mbps, are anticipated. The Asian region is predicted to experience the greatest improvement in Wi-Fi speed [171].

4. Open Issues and Future Research Directions

IoT-based MG systems operate in a variety of situations, such as transmission line monitoring; thus, it is critical to consider aspects, such as dependability, accessibility, and compatibility with various communication technologies [172–174]. In the future, self-healing measures should be explored in conjunction with IoT technologies. If, for example, a large number of IoT devices break down, a remedial method based on self-healing capacity must be chosen, and the validity of IoT-based systems must be governed by the manufacturer. Energy acquisition, security challenges, and creating standards are also key considerations for IoT-based MG systems. Real-time power line monitoring necessitates a variety of sensors and nodes for delivering data, which is often powered by batteries. For IoT-based MG systems, most end devices are powered by batteries. As a result, obtaining power for such IoT-enabled equipment is a major outstanding question to implement such systems in the coming years. As a solution, novel energy harvesting tools in conjunction with IoT equipment must be created.

For implementing the IoT in their applications, different power supply solutions are required. Because not every power supply is suited for it, the task of designing the power supply items must also be economical, efficient, and capable of balancing heavy and light loads. Smart meters, for example, transmit a large quantity of data between the consumers and the utility. Future smart meter data flow will necessitate more sophisticated communication networks such as 5G and 6G to provide adequate wireless connectivity. Knowing the consequences prior to deployment is a critical component of this system, creating an open problem for IoT-based MG. Communication and information networking are crucial for the efficient implementation of IoT-based MG systems. As IoT MG systems evolve on various wireless networks for transferring information ranging from device scheduling to real-time EMS and power delivery, desirable and dependable network performance becomes increasingly crucial.

Expanding to modern wireless communication from 2G to 6G networks is essential for current MG structures, which will pave the way for future interdisciplinary research between electronics and electrical engineers. For such devices, different data fusion solutions are required, as they must combine data from several sources. As a result of the low processing capabilities of several IoT devices in IoT-based MG systems, storage capacity becomes a resource constraint. As a result, all of the gateways are insufficient to handle the data. Data fusion solutions for IoT-based MG systems will be a unique and innovative sector in the future for identifying the essential data from devices. Due to the different research interests on IoT [175] and MG standards, the focus on developing complete principles of IoT-based MG technologies in the future has been eliminated. The need to shift actual concentration criteria for this technology in a complementary manner is a critical open issue in the modern energy market. Data integrity [176] is becoming more important in these systems because it ensures that data collected from devices, such as smart meters, are not tampered with by unauthorized individuals.

5. Conclusions

The paper provides a brief summary of the various elements that make up a HMGS, including optimization and control topologies, as well as the problems that have to be addressed. The implementation of a decentralized power system and the smart grid paradigm was developed by the HMGS. It has many advantages over standard power networks due to its increased reliability, removal of numerous conversions, and auxiliary service. Similarly, the convergence of IoT is predicted to significantly enhance energy

efficiency, functionality, and cost-effectiveness, paving the way for total automation to an IoT-based MG state. Several regulatory-based organizations and government organizations across the world have increased their focus on MGs in the electricity market in industrial, commercial, and residential buildings as a result of the creation of IoT-based regulatory standards and frameworks. Continuous regulation, including authorization based on carbon emission objectives, is required in all regions of the world, according to this remark. As a result, energy stakeholders should investigate next-generation IoT technologies in order to deal with the complexity of EMSs. As the globe proceeds toward the smart MG revolution, as addressed in this review article, there are many prospects for boosting the economy as MGs based on IoT systems face certain hurdles. Furthermore, the rapid growth of appropriate IoT designs with MGs, as well as standards, are required and will be useful in the technological arena. The operation of a HMGS depends greatly on power management strategies and control techniques, necessitating a thorough analysis of various MGs under various conditions. Additionally, it offers suggestions for future (focused) lines of inquiry in this sector.

Author Contributions: Conceptualization, S.V., V.I., B.A. and R.V.; Methodology, S.V., V.I. and B.A.; Software, S.V.; Formal Analysis, S.V., V.I. and B.A.; Investigation, S.V.; Resources, S.V. and B.A.; Data Curation, S.V., V.I. and R.V.; Writing–original draft preparation, S.V. and V.I.; Writing—reviewing and editing, S.V., V.I. and R.V.; Visualization, V.I.; Supervision, B.A. and V.I. All authors provided critical feedback and collaborated in the paper. All authors have read and agreed to the published version of the manuscript.

Funding: This research received no external funding.

Data Availability Statement: Not applicable.

Conflicts of Interest: The authors declare no conflict of Interest.

Nomenclature

AI	artificial intelligence	ANN	artificial neural network
ARCH	auto regressive conditional heteroskedasticity	ARIMA	auto regressive integrated moving average
BESS	battery energy storage system	BPNN	back-propagation neural network
CAES	compressed air energy storage	CHP	combined heat and power
COE	cost of energy	CPV	concentrator photovoltaic
DER	distributed energy resources	DG	distributed generation
DPSP	deficiency of power supply probability	DRP	demand response program
DSL	digital subscriber lines	EE	embodied energy
EMS	energy management system	ESS	energy storage system
GA	genetic algorithm	GRNN	general regression neural network
GSM	global system for mobile communication	HMGS	hybrid microgrid system
HMI	human–machine interfaces	HRES	hybrid renewable energy source
ICT	information and communication technology	IoE	Internet of Energy
IoT	Internet of Things	LAN	local area network
LCC	life cycle cost	LCOE	levelized cost of electricity
LPSP	loss of power supply probability	M2M	machine-to-machine
MG	Microgrid	MILP	mixed-integer linear programming
MPPT	maximum power point tracking	NAN	neighboring area network
O&M	operating and maintenance	PEM	point estimate method
PSO	particle swarm optimization	PV	photovoltaic
PWM	pulse width modulation	RES	renewable energy source
RSM	response surface methodology	RTU	remote terminal unit
SAPV	stand-alone PV	SCADA	supervisory control and data acquisition
SEMS	smart energy management systems	SHS	solar home system
SOC	state of charge	T & D	transmission and distribution
TCE	total cost of electricity	TCO	total cost of ownership
TS	tropical storm	VSD	variable speed drive
WAN	wide area network	WSN	wireless sensor network
WSP	wind speed prediction	WT	wind turbine

References

1. Julien, M.; Mazhelis, O.; Su, X.; Tarkoma, S. A gap analysis of internet-of-things platforms. *Comput. Commun.* **2016**, *89*, 5–16.
2. Hirsch, A.; Parag, Y.; Guerrero, J. Microgrids: A review of Technologies, Key drivers and outstanding issues. *Renew. Sustain. Energy Rev.* **2018**, *90*, 402–411. [CrossRef]
3. Akorede, M.F.; Hizam, H.; Pouresmaeil, E. Distributed energy resources and benefits to the environment. *Renew. Sustain. Energy Rev.* **2010**, *14*, 724–734. [CrossRef]
4. Bayindir, R.; Hossain, E.; Kabalci, E.; Perez, R. A comprehensive study on microgrid technology. *Int. J. Renew. Energy Res.* **2014**, *4*, 1094–1107.
5. Kirubakaran, A.; Jain, S.; Nema, R.K. A review on fuel cell technologies and power electronic interface. *Renew. Sustain. Energy Rev.* **2009**, *13*, 2430–2440. [CrossRef]
6. Mekhilef, S.; Saidur, R.; Safari, A. Comparative study of different fuel cell technologies. *Renew. Sustain. Energy Rev.* **2012**, *16*, 981–989. [CrossRef]
7. Neef, H.J. International overview of hydrogen and fuel cell research. *Energy* **2009**, *34*, 327–333. [CrossRef]
8. Abu-Sharkh, S.; Arnold, R.J.; Kohler, J.; Li, R.; Markvart, T.; Ross, J.N.; Steemers, K.; Wilson, P.; Yao, R. Can microgrids make a major contribution to UK energy supply? *Renew. Sustain. Energy Rev.* **2006**, *10*, 78–127. [CrossRef]
9. Díaz-González, F.; Sumper, A.; Gomis-Bellmunt, O.; Villafáfila-Robles, R. A review of energy storage technologies for wind power applications. *Renew. Sustain. Energy Rev.* **2012**, *16*, 2154–2171. [CrossRef]
10. Suvire, G.O.; Mercado, P.E.; Ontiveros, L.J. Comparative analysis of energy storage technologies to compensate wind power short-term fluctuations. In Proceedings of the 2010 IEEE/PES Transmission and Distribution Conference and Exposition: Latin America (T&D-LA), Sao Paulo, Brazil, 8–10 November 2010; pp. 522–528.
11. Tang, J.; Zhou, Z.; Niu, J. An energy efficient hierarchical clustering index tree for facilitating time-correlated region queries in the Internet of Things. *J. Netw. Comput. Appl.* **2014**, *40*, 1–11. [CrossRef]
12. Sun, Y.; Song, H.; Jara, A.J.; Bie, R. Internet of things and big data analytics for smart and connected communities. *IEEE Access* **2016**, *4*, 766–773. [CrossRef]
13. Bhatt, J.; Shah, V.; Jani, O. An instrumentation engineer's review on smart grid: Critical applications and parameters. *Renew. Sustain. Energy Rev.* **2014**, *40*, 1217–1239. [CrossRef]
14. Andrea, M. Internet of Things Drives Growth for Smart Grid Innovation. Available online: https://developer.att.com/blog/internet-of-things-drives-growth-for-smart-gridinnovation (accessed on 24 March 2021).
15. Ashton, K. That 'internet of things' thing. *RFiD J.* **2009**, *22*, 97–114.
16. Elkhodr, M.; Shahrestani, S.; Cheung, H. The Internet of Things: Vision & challenges. In Proceedings of the IEEE 2013 Tencon-Spring, Sydney, Australia, 17–19 April 2013; pp. 218–222.
17. Gerber, D.L.; Liou, R.; Brown, R. Energy-saving opportunities of direct-DC loads in buildings. *Appl. Energy* **2019**, *248*, 274–287. [CrossRef]
18. Rodriguez-Otero, M.A.; O'Neill-Carrillo, E. Efficient home appliances for a future DC residence. In Proceedings of the 2008 IEEE Energy 2030 Conference, Atlanta, GA, USA, 17–18 November 2008; pp. 1–6.
19. Porter, S.F.; Denkenberger, D.; Mercier, S.; May-Ostendorp, P. Reviving the war of currents: Opportunities to save energy with DC distribution in commercial buildings. *Proc. ACEEE Summer Study Energy Effic. Build.* **2014**, *85*, 85–97. Available online: https://www.researchgate.net/publication/281210054 (accessed on 24 March 2021).
20. Mahmoud, M.S. *Microgrid Advanced Control Methods and Renewable Energy System Integration*; Elsevier: Amsterdam, The Netherlands, 2016; Volume 1.
21. IEA. *Energy Access Outlook 2017 Report*; IEA: Paris, France, 2017; Available online: https://www.iea.org/reports/energy-access-outlook-2017 (accessed on 24 March 2021).
22. International Energy Agency. Available online: http://www.iea.org/ (accessed on 19 September 2018).
23. Kempener, R.; Lavagne, O.; Saygin, D.; Skeer, J.; Vinci, S.; Gielen, D. *Off-Grid Renewable Energy Systems: Status and Methodological Issues*; Tech. Rep.; The International Renewable Energy Agency (IRENA): Abu Dhabi, United Arab Emirates, 2015.
24. Williams, N.J.; van Dyk, E.E.; Vorster, F.J. Monitoring solar home systems with pulse width modulation charge control. *J. Sol. Energy Eng.* **2011**, *133*, 021006–1–021006–7. [CrossRef]
25. Fuentes, M.; Vivar, M.; Hosein, H.; Aguilera, J.; Muñoz-Cerón, E. Lessons learned from the field analysis of PV installations in the Saharawi refugee camps after 10 years of operation. *Renew. Sustain. Energy Rev.* **2018**, *93*, 100–109. [CrossRef]
26. Zhao, J.; Dörfler, F. Distributed control and optimization in DC microgrids. *Automatica* **2015**, *61*, 18–26. [CrossRef]
27. Mansoor, M.; Mizra, A.F.; Ling, Q.; Javed, M.Y. Novel Grass Hopper optimization based MPPT of PV Systems for complex partial shading conditions. *Sol. Energy* **2020**, *198*, 499–518. [CrossRef]
28. Ekneligoda, N.C.; Weaver, W.W. Game-theoretic cold-start transient optimization in DC microgrids. *IEEE Trans. Ind. Electron.* **2014**, *61*, 6681–6690. [CrossRef]
29. Moayedi, S.; Davoudi, A. Unifying distributed dynamic optimization and control of islanded DC microgrids. *IEEE Trans. Power Electron.* **2016**, *32*, 2329–2346. [CrossRef]
30. Ma, J.; Yuan, L.; Zhao, Z.; He, F. Transmission loss optimization-based optimal power flow strategy by hierarchical control for DC microgrids. *IEEE Trans. Power Electron.* **2016**, *32*, 1952–1963. [CrossRef]

31. Dissanayake, A.M.; Ekneligoda, N.C. Multiobjective optimization of droop-controlled distributed generators in DC microgrids. *IEEE Trans. Ind. Inform.* **2019**, *16*, 2423–2435. [CrossRef]
32. Liu, J.; Zhang, W.; Rizzoni, G. Robust stability analysis of DC microgrids with constant power loads. *IEEE Trans. Power Syst.* **2017**, *33*, 851–860. [CrossRef]
33. Su, W.; Yu, S.S.; Li, H.; Iu, H.H.C.; Fernando, T. An MPC-based dual-solver optimization method for DC microgrids with simultaneous consideration of operation cost and power loss. *IEEE Trans. Power Syst.* **2020**, *36*, 936–947. [CrossRef]
34. Gil-González, W.; Montoya, O.D.; Grisales-Noreña, L.F.; Cruz-Peragón, F.; Alcalá, G. Economic dispatch of renewable generators and BESS in DC microgrids using second-order cone optimization. *Energies* **2020**, *13*, 1703. [CrossRef]
35. Farooq, R.; Mateen, L.; Ahmad, M.; Akbar, S.Q.; Khan, H.A.; Zaffar, N.A. Smart DC microgrids: Modeling and power flow analysis of a DC Microgrid for off-grid and weak-grid connected communities. In Proceedings of the 2014 IEEE PES Asia-Pacific Power and Energy Engineering Conference (APPEEC), Hong Kong, China, 7–10 December 2014; pp. 1–6.
36. Qian, X.; Yang, Y.; Li, C.; Tan, S.C. Operating cost reduction of DC microgrids under real-time pricing using adaptive differential evolution algorithm. *IEEE Access* **2020**, *8*, 169247–169258. [CrossRef]
37. Knöchelmann, E.; Männel, A.; Goetjes, B.; Tappe, S.; Ortmaier, T. Decentralized Cost-Optimized Fuzzy Control of DC Microgrids. In Proceedings of the 2019 IEEE Third International Conference on DC Microgrids (ICDCM), Matsue, Japan, 20–23 May 2019; pp. 1–7.
38. Cucuzzella, M.; Lazzari, R.; Trip, S.; Rosti, S.; Sandroni, C.; Ferrara, A. Sliding mode voltage control of boost converters in DC microgrids. *Control Eng. Pract.* **2018**, *73*, 161–170. [CrossRef]
39. Lopez-Vargas, A.; Fuentes, M.; Vivar, M. IoT application for real-time monitoring of solar home systems based on ArduinoTM with 3G connectivity. *IEEE Sens. J.* **2019**, *19*, 679–691. [CrossRef]
40. Liu, H.; Chen, C. Data processing strategies in wind energy forecasting models and applications: A comprehensive review. *Appl. Energy* **2019**, *249*, 392–408. [CrossRef]
41. Zuluaga, C.D.; Alvarez, M.A.; Giraldo, E. Short-term wind speed prediction based on robust Kalman filtering: An experimental comparison. *Appl. Energy* **2015**, *156*, 321–330. [CrossRef]
42. Fan, S.; Liao, J.R.; Yokoyama, R.; Chen, L.; Lee, W.J. Forecasting the wind generation using a two-stage network based on meteorological information. *IEEE Trans. Energy Convers.* **2009**, *24*, 474–482. [CrossRef]
43. Meng, A.; Ge, J.; Yin, H.; Chen, S. Wind speed forecasting based on wavelet packet decomposition and artificial neural networks trained by crisscross optimization algorithm. *Energy Convers. Manag.* **2016**, *114*, 75–88. [CrossRef]
44. Zhang, J.; Draxl, C.; Hopson, T.; Monache, L.D.; Vanvyve, E.; Hodge, B.M. Comparison of numerical weather prediction based deterministic and probabilistic wind resource assessment methods. *Appl. Energy* **2015**, *156*, 528–541. [CrossRef]
45. Jiang, P.; Liu, Z. Variable weights combined model based on multi-objective optimization for short-term wind speed forecasting. *Appl. Soft Comput.* **2019**, *82*, 105587. [CrossRef]
46. Lucheroni, C.; Boland, J.; Ragno, C. Scenario generation and probabilistic forecasting analysis of spatio-temporal wind speed series with multivariate autoregressive volatility models. *Appl. Energy* **2019**, *239*, 1226–1241. [CrossRef]
47. Yang, W.; Wang, J.; Lu, H.; Niu, T.; Du, P. Hybrid wind energy forecasting and analysis system based on divide and conquer scheme: A case study in China. *J. Clean. Prod.* **2019**, *222*, 942–959. [CrossRef]
48. Wang, J.; Li, H.; Lu, H. Application of a novel early warning system based on fuzzy time series in urban air quality forecasting in China. *Appl. Soft Comput.* **2018**, *71*, 783–799. [CrossRef]
49. Tian, C.; Hao, Y. Point and interval forecasting for carbon price based on an improved analysis-forecast system. *Appl. Math. Model.* **2020**, *79*, 126–144. [CrossRef]
50. Cassola, F.; Burlando, M. Wind speed and wind energy forecast through Kalman filtering of Numerical Weather Prediction model output. *Appl. Energy* **2012**, *99*, 154–166. [CrossRef]
51. Wang, J.; Niu, T.; Lu, H.; Yang, W.; Du, P. A Novel Framework of Reservoir Computing for Deterministic and Probabilistic Wind Power Forecasting. *IEEE Trans. Sustain. Energy* **2020**, *11*, 337–349. [CrossRef]
52. Salameh, T.; Ghenai, C.; Merabet, A.; Alkasrawi, M. Techno-economical optimization of an integrated stand-alone hybrid solar PV tracking and diesel generator power system in Khorfakkan, United Arab Emirates. *Energy* **2020**, *190*, 116475. [CrossRef]
53. Abdelkader, A.; Rabeh, A.; Ali, D.M.; Mohamed, J. Multi-objective genetic algorithm based sizing optimization of a stand-alone wind/PV power supply with enhanced battery/supercapacitor hybrid energy storage. *Energy* **2018**, *163*, 351–363. [CrossRef]
54. Cingoz, F.; Elrayyah, A.; Sozer, Y. Optimized Resource Management for PV-Fuel-cell-based microgrids using load characterizations. *IEEE Trans. Ind. Appl.* **2016**, *52*, 1723–1735. [CrossRef]
55. Jumani, T.A.; Mustafa, M.W.; Alghamdi, A.S.; Rasid, M.M.; Alamgir, A.; Awan, A.B. Swarm intelligence-based optimization techniques for dynamic response and power quality enhancement of AC microgrids: A comprehensive review. *IEEE Access* **2020**, *8*, 75986–76001. [CrossRef]
56. Jumani, T.A.; Mustafa, M.W.; Hamadneh, N.N.; Atawneh, S.H.; Rasid, M.M.; Mirjat, N.H.; Bhayo, M.A.; Khan, I. Computational intelligence-based optimization methods for power quality and dynamic response enhancement of ac microgrids. *Energies* **2020**, *13*, 4063. [CrossRef]
57. Abhinav, S.; Schizas, I.D.; Ferrese, F.; Davoudi, A. Optimization-based AC microgrid synchronization. *IEEE Trans. Ind. Inform.* **2017**, *13*, 2339–2349. [CrossRef]

58. Dissanayake, A.M.; Ekneligoda, N.C. Transient optimization of parallel connected inverters in islanded ac microgrids. *IEEE Trans. Smart Grid* **2018**, *10*, 4951–4961. [CrossRef]
59. Dabbaghjamanesh, M.; Mehraeen, S.; Kavousi-Fard, A.; Ferdowsi, F. A new efficient stochastic energy management technique for interconnected AC microgrids. In Proceedings of the 2018 IEEE Power & Energy Society General Meeting (PESGM), Portland, OR, USA, 5–10 August 2018; pp. 1–5.
60. Zhang, Q.; Liu, Y.; Zhao, Y.; Wang, N. A multi-mode operation control strategy for flexible microgrid based on sliding-mode direct voltage and hierarchical controls. *ISA Trans.* **2016**, *61*, 188–198. [CrossRef]
61. Sekhar, P.C.; Mishra, S. Storage free smart energy management for frequency control in diesel-PV-fuel cell-based hybrid AC microgrid. *IEEE Trans. Neural Netw. Learn. Syst.* **2016**, *27*, 1657–1671. [CrossRef]
62. Kang, Y.; Yu, H.; Wang, J.; Qin, W. Day-ahead microgrid energy management optimization scheduling scheme. In Proceedings of the 2017 IEEE Conference on Energy Internet and Energy System Integration (EI2), Beijing, China, 26–28 November 2017; pp. 1–6.
63. Gao, Y.; Ai, Q. Distributed cooperative optimal control architecture for AC microgrid with renewable generation and storage. *Int. J. Electr. Power Energy Syst.* **2018**, *96*, 324–334. [CrossRef]
64. Bauer, N.; Mouratiadou, I.; Luderer, G.; Baumstark, L.; Brecha, R.J.; Edenhofer, O.; Kriegler, E. Global fossil energy markets and climate change mitigation e an analysis with REMIND. *Clim. Chang.* **2013**, *136*, 69–82. [CrossRef]
65. Zhang, S.; Bauer, N.; Luderer, G.; Kriegler, E. Role of technologies in energy-related CO2 mitigation in China within a climate-protection world: A scenarios analysis using REMIND. *Appl. Energy* **2014**, *115*, 445–455. [CrossRef]
66. Dusonchet, L.; Telaretti, E. Comparative economic analysis of support policies for solar PV in the most representative EU countries. *Renew. Sustain. Energy Rev.* **2015**, *42*, 986–998. [CrossRef]
67. Ismail, M.; Moghavvemi, M.; Mahlia, T.; Muttaqi, K.; Moghavvemi, S. Effective utilization of excess energy in standalone hybrid renewable energy systems for improving comfort ability and reducing cost of energy: A review and analysis. *Renew. Sustain. Energy Rev.* **2015**, *42*, 726–734. [CrossRef]
68. Davari, M.; Mohamed, Y.A.-R.I. Robust multi-objective control of VSC-based DC voltage power port in hybrid AC/DC multi-terminal micro-grids. *IEEE Trans. Smart Grid* **2013**, *4*, 1597–1612. [CrossRef]
69. Parhizi, S.; Lotfi, H.; Khodaei, A.; Bahramirad, S. State of the art in research on microgrids: A review. *IEEE Access* **2015**, *3*, 890–925. [CrossRef]
70. Murari, K.; Padhy, N.P. A network-topology-based approach for the load-flow solution of AC–DC distribution system with distributed generations. *IEEE Trans. Ind. Inform.* **2018**, *15*, 1508–1520. [CrossRef]
71. Ahmed, H.M.; Eltantawy, A.B.; Salama, M.M.A. A generalized approach to the load flow analysis of AC–DC hybrid distribution systems. *IEEE Trans. Power Syst.* **2017**, *33*, 2117–2127. [CrossRef]
72. Maheri, A. Multi-objective design optimization of standalone hybrid wind–PV diesel systems under uncertainties. *Renew. Energy* **2014**, *66*, 650–661. [CrossRef]
73. Arefifar, S.A.; Yasser, A.R.M.; El-Fouly, T.H. Optimum microgrid design for enhancing reliability and supply-security. *IEEE Trans. Smart Grid* **2013**, *4*, 1567–1575. [CrossRef]
74. Leou, R. An economic analysis model for the energy storage systems applied to a distribution substation. *Int. J. Electr. Power Energy Syst.* **2012**, *34*, 132–137. [CrossRef]
75. Sundararagavan, S.; Baker, E. Evaluating energy storage technologies for wind power integration. *Sol. Energy* **2012**, *86*, 2707–2717. [CrossRef]
76. Chedid, R.; Rahman, S. Unit sizing and control of hybrid wind-solar power systems. *IEEE Trans. Energy Convers.* **1997**, *12*, 79–85. [CrossRef]
77. Tewari, S.; Mohan, N. Value of NaS energy storage toward integrating wind: Results from the wind to battery project. *IEEE Trans. Power Syst.* **2012**, *28*, 532–541. [CrossRef]
78. Khalid, M.; Savkin, A.V. Minimization and control of battery energy storage for wind power smoothing: Aggregated distributed and semi-distributed storage. *Renew. Energy* **2014**, *64*, 105–112. [CrossRef]
79. Brekken, T.K.A.; Yokochi, A.; von Jouanne, A.; Yen, Z.Z.; Hapke, H.M.; Halamay, D.A. Optimal energy storage sizing and control for wind power applications. *IEEE Trans. Sustain. Energy* **2010**, *2*, 69–77. [CrossRef]
80. Giannakoudis, G.; Papadopoulos, A.I.; Seferlis, P.; Voutetakis, S. Optimum design and operation under uncertainty of power systems using renewable energy sources and hydrogen storage. *Int. J. Hydrogen Energy* **2009**, *35*, 872–891. [CrossRef]
81. Katsigiannis, Y.A.; Georgilakis, P.S.; Karapidakis, E.S. Multi-objective genetic algorithm solution to the optimum economic and environmental performance problem of small autonomous hybrid power systems with renewables. *IET Renew. Power Gener.* **2010**, *4*, 404–419. [CrossRef]
82. Choi, M.E.; Kim, S.W.; Seo, S.W. Energy management optimization in a battery/super-capacitor hybrid energy storage system. *IEEE Trans. Smart Grid* **2012**, *3*, 463–472. [CrossRef]
83. Thounthong, P.; Luksanasakul, A.; Koseeyaporn, P.; Davat, B. Intelligent model based control of a standalone photovoltaic/fuel cell power plant with super-capacitor energy storage. *IEEE Trans. Sustain. Energy* **2012**, *4*, 240–249. [CrossRef]
84. Nehrir, M.H.; Wang, C.; Strunz, K.; Aki, H.; Ramakumar, R.; Bing, J.; Miao, Z.; Salameh, Z. A review of hybrid renewable/alternative energy systems for electric power generation: Configurations, control, and applications. *IEEE Trans. Sustain. Energy* **2011**, *2*, 392–403. [CrossRef]

85. Bernal-Agustín, J.L.; Dufo-López, R. Simulation and optimization of standalone hybrid renewable energy systems. *Renew. Sustain. Energy Rev.* **2009**, *13*, 2111–2218. [CrossRef]
86. Zhou, W.; Lou, C.; Li, Z.; Lu, L.; Yang, H. Current status of research on optimum sizing of stand-alone hybrid solar–wind power generation systems. *Appl. Energy* **2010**, *87*, 380–389. [CrossRef]
87. Luna-Rubio, R.; Trejo-Perea, M.; Vargas-Vazquez, D.; Rıos-Moreno, G.J. Optimal sizing of renewable hybrids energy systems: A review of methodologies. *Sol. Energy* **2012**, *86*, 1077–1088. [CrossRef]
88. Elma, O.; Selamogullari, U.S. A comparative sizing analysis of a renewable energy supplied stand-alone house considering both demand side and source side dynamics. *Appl. Energy* **2012**, *96*, 400–408. [CrossRef]
89. Yang, H.; Zhou, W.; Lou, C. Optimal design and techno-economic analysis of a hybrid solar–wind power generation system. *Appl. Energy* **2009**, *86*, 163–169. [CrossRef]
90. Yang, H.; Lu, L.; Zhou, W. A novel optimization sizing model for hybrid solar-wind power generation system. *Sol. Energy* **2007**, *81*, 76–84. [CrossRef]
91. Ekren, O.; Ekren, B.Y. Size optimization of a PV/wind hybrid energy conversion system with battery storage using response surface methodology. *Appl. Energy* **2008**, *85*, 1086–1101. [CrossRef]
92. Ekren, O.; Ekren, B.Y.; Ozerdem, B. Break-even analysis and size optimization of a PV/wind hybrid energy conversion system with battery storage—A case study. *Appl. Energy* **2008**, *86*, 1043–1054. [CrossRef]
93. Abbes, D.; Martinez, A.; Champenois, G. Life cycle cost, embodied energy and loss of power supply probability for the optimal design of hybrid power systems. *Math. Comput. Simul.* **2014**, *98*, 46–62. [CrossRef]
94. Di-Silvestre, M.L.; Graditi, G.; Sanseverino, E.R. A generalized framework for optimal sizing of distributed energy resources in micro-grids using an indicator-based swarm approach. *IEEE Trans. Ind. Inform.* **2013**, *10*, 152–162. [CrossRef]
95. Perera, A.T.D.; Attalage, R.A.; Perera, K.K.C.K.; Dassanayake, V.P.C. A hybrid tool to combine multi-objective optimization and multi-criterion decision making in designing standalone hybrid energy systems. *Appl. Energy* **2013**, *107*, 412–425. [CrossRef]
96. Arnette, A.; Zobel, C.W. An optimization model for regional renewable energy development. *Renew. Sustain. Energy Rev.* **2012**, *16*, 4606–4615. [CrossRef]
97. Zhang, X.; Tan, S.C.; Li, G.; Li, J.; Feng, Z. Components sizing of hybrid energy systems via the optimization of power dispatch simulations. *Energy* **2013**, *52*, 165–172. [CrossRef]
98. Tan, W.S.; Hassan, M.Y.; Rahman, H.A.; Abdullah, M.P.; Hussin, F. Multi-distributed generation planning using hybrid particle swarm optimization- gravitational search algorithm including voltage rise issue. *IET Gener. Transm. Distrib.* **2013**, *7*, 929–942. [CrossRef]
99. Al-Saedi, W.; Lachowicz, S.W.; Habibi, D.; Bass, O. Power quality enhancement in autonomous microgrid operation using particle swarm optimization. *Electr. Power Energy Syst.* **2012**, *42*, 139–149. [CrossRef]
100. Al-Saedi, W.; Lachowicz, S.W.; Habibi, D.; Bass, O. Power flow control in grid connected microgrid operation using particle swarm optimization under variable load conditions. *Electr. Power Energy Syst.* **2013**, *49*, 76–85. [CrossRef]
101. Suvire, G.O.; Mercado, P.E. DSTATCOM with flywheel energy storage system for wind energy applications: Control design and simulation. *Electr. Power Syst. Res.* **2009**, *80*, 345–353. [CrossRef]
102. Farhoodnea, M.; Mohamed, A.; Shareef, H.; Zayandehroodi, H. Optimum placement of active power conditioners by a dynamic discrete firefly algorithm to mitigate the negative power quality effects of renewable energy-based generators. *Int. J. Electr. Power Energy Syst.* **2014**, *61*, 305–317. [CrossRef]
103. Serban, I.; Teodorescu, R.; Marinescu, C. Analysis and optimization of the battery energy storage systems for frequency control in autonomous microgrids. In Proceedings of the 3rd IEEE International Symposium on Power Electronics for Distributed Generation Systems, Aalborg, Denmark, 25–28 June 2012; pp. 374–379.
104. Sigrist, L.; Lobato, E.; Rouco, L. Energy storage systems providing primary reserve and peak shaving in small isolated power systems: An economic assessment. *Int. J. Electr. Power Energy Syst.* **2013**, *53*, 675–683. [CrossRef]
105. Vrettos, E.I.; Papathanassiou, S.A. Operating policy and optimal sizing of a high penetration RES–BESS system for small isolated grids. *IEEE Trans. Energy Convers.* **2011**, *26*, 744–756. [CrossRef]
106. Zhao, B.; Zhang, X.; Chen, J.; Wang, C. Operation optimization of standalone microgrids considering lifetime characteristics of battery energy storage system. *IEEE Trans. Sustain. Energy* **2013**, *4*, 934–943. [CrossRef]
107. Younsi, S.; Jraidi, M.; Hamrouni, N.; Cherif, A. Modelling and control of hybrid renewable energy system connected to AC grid. *Int. J. Comput. Sci. Eng.* **2011**, *3*, 3854–3865.
108. Arabali, A.; Ghofrani, M.; Amoli, M.E.; Fadali, M.S.; Baghzouz, Y. Genetic-algorithm based optimization approach for energy management. *IEEE Trans. Power Deliv.* **2013**, *28*, 162–170. [CrossRef]
109. Zhang, D.; Li, S.; Zeng, P.; Zang, C. Optimal microgrid control and power-flow study with different bidding policies by using power world simulator. *IEEE Trans. Sustain. Energy* **2014**, *5*, 282–292. [CrossRef]
110. Vahidinasab, V. Optimal distributed energy resources planning in a competitive electricity market: Multi-objective optimization and probabilistic design. *Renew. Energy* **2014**, *66*, 354–363. [CrossRef]
111. Conti, S.; Nicolosi, R.; Rizzo, S.A.; Zeineldin, H. Optimal dispatching of distributed generators and storage systems for MV islanded microgrids. *IEEE Trans. Power Deliv.* **2010**, *27*, 1243–1251. [CrossRef]
112. Zhang, Y.; Gatsis, N.; Giannakis, G.B. Robust energy management for microgrids with high-penetration renewables. *IEEE Trans. Sustain. Energy* **2013**, *4*, 944–953. [CrossRef]

113. Aghaei, J.; Alizadeh, M.I. Multi-objective self-scheduling of CHP based microgrids considering demand response programs and ESSS. *Energy* **2013**, *55*, 1044–1054. [CrossRef]
114. Maa, X.; Wang, Y.; Qin, J. Generic model of a community-based microgrid integrating wind turbines, photovoltaics and CHP generations. *Appl. Energy* **2013**, *112*, 1475–1482. [CrossRef]
115. Parisio, A.; Rikos, E.; Glielmo, L. A model predictive control approach to microgrid operation optimization. *IEEE Trans. Control Syst. Technol.* **2014**, *22*, 1813–1827. [CrossRef]
116. Carapellucci, R.; Giordano, L. Modeling and optimization of an energy generation island based on renewable technologies and hydrogen storage systems. *Int. J. Hydrogen Energy* **2012**, *37*, 2081–2093. [CrossRef]
117. Pourmousavi, S.A.; Nehrir, M.H.; Colson, C.M.; Wang, C. Real-time energy management of a stand-alone hybrid wind-microturbine energy system using particle swarm optimization. *IEEE Trans. Sustain. Energy* **2010**, *1*, 193–201. [CrossRef]
118. Zhao, J.; Li, X.; Hao, J.; Lua, J. Reactive power control of a wind farm made up with doubly fed induction generators in distribution system. *Electr. Power Syst. Res.* **2010**, *80*, 698–706. [CrossRef]
119. Trifkovic, M.; Sheikhzadeh, M.; Nigim, K.; Daoutidis, P. Modeling and control of a renewable hybrid energy system with hydrogen storage. *IEEE Trans. Control Syst. Technol.* **2013**, *22*, 169–179. [CrossRef]
120. Mohammadi, S.; Mozafari, B.; Solimani, S.; Niknam, T. An adaptive modified firefly optimization algorithm based on hong's point estimate method to optimal operation management in a microgrid with consideration of uncertainties. *Energy* **2013**, *51*, 339–348. [CrossRef]
121. Mohammadi, S.; Soleymani, S.; Mozafari, B. Scenario-based stochastic operation management of microgrid including wind, photovoltaic, micro-turbine, fuel cell and energy storage devices. *Int. J. Electr. Power Energy Syst.* **2014**, *54*, 525–535. [CrossRef]
122. Askarzadeh, A. Developing a discrete harmony search algorithm for size optimization of wind-photovoltaic hybrid energy system. *Sol. Energy* **2013**, *98*, 190–195. [CrossRef]
123. Javed, M.S.; Song, A.; Ma, T. Techno-economic assessment of a stand-alone hybrid solar-wind-battery system for a remote island using genetic algorithm. *Energy* **2019**, *176*, 704–717. [CrossRef]
124. Kaabeche, A.; Belhamel, M.; Ibtiouen, R. Techno-economic valuation and optimization of integrated photovoltaic/wind energy conversion system. *Sol. Energy* **2011**, *85*, 2407–2420. [CrossRef]
125. Mohammadi, M.; Hosseinian, S.H.; Gharehpetian, G.B. optimization of hybrid solar energy sources/wind turbine systems integrated to utility grids as microgrid (MG) under pool/bilateral/hybrid electricity market using PSO. *Sol. Energy* **2012**, *86*, 112–125. [CrossRef]
126. Merei, G.; Berger, C.; Sauer, D.U. Optimization of an off-grid hybrid PV-Wind-Diesel system with different battery technologies using genetic algorithm. *Sol. Energy* **2013**, *97*, 460–473. [CrossRef]
127. Kaabeche, A.; Ibtiouen, R. Techno-economic optimization of hybrid photovoltaic/wind/diesel/battery generation in a stand-alone power system. *Sol. Energy* **2014**, *103*, 171–182. [CrossRef]
128. Nojavan, S.; Zare, K. Interval optimization based performance of photovoltaic/wind/FC/electrolyzer/electric vehicles in energy price determination for customarily electricity retailer. *Sol. Energy* **2018**, *171*, 580–592. [CrossRef]
129. Zhang, G.; Wu, B.; Maleki, A.; Zhang, W. Simulated annealing-chaotic search algorithm based optimization of reverse osmosis hybrid desalination system driven by wind and solar energies. *Sol. Energy* **2018**, *173*, 964–975. [CrossRef]
130. Abdalla, O.; Rezk, H.; Ahmed, E. wind driven optimization algorithm based global MPPT for PV system under non-uniform solar irradiance. *Sol. Energy* **2019**, *180*, 429–444. [CrossRef]
131. Bukar, A.L.; Tan, C.W.; Lau, K.Y. Optimal sizing of an autonomous photovoltaic/wind/battery/diesel generator microgrid using grasshopper optimization algorithm. *Sol. Energy* **2019**, *188*, 685–696. [CrossRef]
132. Guo, S.; He, Y.; Pei, H.; Wu, S. The multi-objective capacity optimization of wind-photovoltaic-thermal energy storage hybrid power system with electric heater. *Sol. Energy* **2020**, *195*, 138–149. [CrossRef]
133. Sun, X.; Zhang, W.; Chen, J. Optimize globally, control locally: Coordinated optimal local voltage control in hybrid AC/DC microgrid. *Int. J. Electr. Power Energy Syst.* **2020**, *118*, 105734. [CrossRef]
134. Azaza, M.; Wallin, F. Multi objective particle swarm optimization of hybrid micro-grid system: A case study in Sweden. *Energy* **2017**, *123*, 108–118. [CrossRef]
135. Senthil Kumar, J.; Charles Raja, S.; Jeslin Drusila Nesamalar, J.; Venkatesh, P. Optimizing renewable based generations in AC/DC microgrid system using hybrid Nelder-Mead—Cuckoo Search algorithm. *Energy* **2018**, *158*, 204–215. [CrossRef]
136. Agarwal, N.; Kumar, A.; Varun. Optimization of grid independent hybrid PV-diesel-battery system for power generation in remote villages of Uttar Pradesh, India. *Energy Sustain. Dev.* **2013**, *17*, 210–219. [CrossRef]
137. Azeem, O.; Ali, M.; Abbas, G.; Uzair, M.; Qahmash, A.; Algarni, A.; Hussain, M.R. A comprehensive review on integration challenges, optimization techniques and control strategies of hybrid AC/DC microgrid. *Appl. Sci.* **2021**, *11*, 6242. [CrossRef]
138. Ahmed, H.M.; Eltantawy, A.B.; Salama, M.M. A planning approach for the network configuration of AC-DC hybrid distribution systems. *IEEE Trans. Smart Grid* **2016**, *9*, 2203–2213. [CrossRef]
139. Khan, M.O.; Zaman Jamali, S.; Noh, C.H.; Gwon, G.H.; Kim, C.H. A load flow analysis for AC/DC hybrid distribution network incorporated with distributed energy resources for different grid scenarios. *Energies* **2018**, *11*, 367. [CrossRef]
140. Murari, K.; Padhy, N.P. Graph-theoretic-based approach for solving load flow problem of AC–DC radial distribution network with distributed generations. *IET Gener. Transm. Distrib.* **2020**, *14*, 5327–5346. [CrossRef]

141. Liu, X.; Liu, Y.; Liu, J.; Xiang, Y.; Yuan, X. Optimal planning of AC-DC hybrid transmission and distributed energy resource system: Review and prospects. *CSEE J. Power Energy Syst.* **2019**, *5*, 409–422. [CrossRef]
142. Sarangi, S.; Sahu, B.K.; Rout, P.K. Distributed generation hybrid AC/DC microgrid protection: A critical review on issues, strategies, and future directions. *Int. J. Energy Res.* **2020**, *44*, 3347–3364. [CrossRef]
143. Shahraeini, M.; Javidi, H.; Ghazizadeh, M.S. Comparison between Communication Infrastructures of Centralized and Decentralized Wide Area Measurement Systems. *IEEE Trans. Smart Grid* **2010**, *2*, 206–211. [CrossRef]
144. Smith, I.G. (Ed.) *The Internet of Things 2012: New Horizons*; CASAGRAS2: Halifax, UK, 2012.
145. Curry, E.; Hasan, S.; Kouroupetroglou, C.; Fabritius, W.; ul Hassan, U.; Derguech, W. Internet of things enhanced user experience for smart water and energy management. *IEEE Internet Comput.* **2018**, *22*, 18–28. [CrossRef]
146. Available online: https://www.forbes.com/sites/paullamkin/2016/02/17/wearable-tech-market-to-be-worth-34-billion-by-2020/?sh=78b3dea03cb5 (accessed on 26 March 2021).
147. Ciavarella, S.; Joo, J.Y.; Silvestri, S. Managing contingencies in smart grids via the internet of things. *IEEE Trans. Smart Grid* **2016**, *7*, 2134–2141. [CrossRef]
148. Ahmed, S.H.; Rani, S. A hybrid approach, Smart Street use case and future aspects for Internet of Things in smart cities. *Future Gener. Comput. Syst.* **2018**, *79*, 941–951. [CrossRef]
149. Silva, B.N.; Khan, M.; Han, K. Towards sustainable smart cities: A review of trends, architectures, components, and open challenges in smart cities. *Sustain. Cities Soc.* **2018**, *38*, 697–713. [CrossRef]
150. Moharm, K. State of the art in big data applications in microgrid: A review. *Adv. Eng. Inform.* **2019**, *42*, 100945. [CrossRef]
151. Nizetic, S.; Djilali, N.; Papadopoulos, A.; Rodrigues, J.J. Smart technologies for promotion of energy efficiency, utilization of sustainable resources and waste management. *J. Clean. Prod.* **2019**, *231*, 565–591. [CrossRef]
152. Zhu, C.; Rodrigues, J.J.; Leung, V.C.; Shu, L.; Yang, L.T. Trust-based communication for the industrial internet of things. *IEEE Commun. Mag.* **2018**, *56*, 16–22. [CrossRef]
153. Shaukat, N.; Ali, S.M.; Mehmood, C.A.; Khan, B.; Jawad, M.; Farid, U.; Majid, M. A survey on consumer's empowerment, communication technologies, and renewable generation penetration within smart grid. *Renew. Sustain. Energy Rev.* **2018**, *81*, 1453–1475. [CrossRef]
154. Georgiou, O.; Raza, U. Low power wide area Network Analysis: Can LoRa scale? *IEEE Wirel. Commun. Lett.* **2017**, *6*, 162–165. [CrossRef]
155. Arghandeh, R.; von Meier, A.; Mehrmanesh, L.; Mili, L. On the definition of cyber physical resilience in power systems. *Renew. Sustain. Energy Rev.* **2016**, *58*, 1060–1069. [CrossRef]
156. Roy, S.S.; Puthal, D.; Sharma, S.; Mohanty, S.P.; Zomaya, A.Y. Building a sustainable internet of things: Energy-efficient routing using low-power sensors will meet the need. *IEEE Consum. Electron. Mag.* **2018**, *7*, 42–49. [CrossRef]
157. Li, Y.; Cheng, X.; Cao, Y.; Wang, D.; Yang, L. Smart choice for the smart grid: Narrowband internet of things (NB-IoT). *IEEE Internet Things J.* **2017**, *5*, 1505–1515. [CrossRef]
158. Song, Y.; Lin, J.; Tang, M.; Dong, S. An internet of energy things based on wireless LPWAN. *Engineering* **2017**, *3*, 460–466. [CrossRef]
159. Mahmood, A.; Javaid, N.; Razzaq, S. A review of wireless communications for smart grid. *Renew. Sustain. Energy Rev.* **2015**, *41*, 248–260. [CrossRef]
160. Lin, J.; Yu, W.; Zhang, N.; Yang, X.; Zhang, H.; Zhao, W. A survey on internet of things: Architecture, enabling technologies, security and privacy, and applications. *IEEE Internet Things J.* **2017**, *4*, 1125–1142. [CrossRef]
161. Siryani, J.; Tanju, B.; Eveleigh, T.J. A machine learning decision-support system improves the internet of things smart meter operations. *IEEE Internet Things J.* **2017**, *4*, 1056–1066. [CrossRef]
162. Tonyali, S.; Akkaya, K.; Saputro, N.; Uluagac, A.S.; Nojoumian, M. Privacy-preserving protocols for secure and reliable data aggregation in IoT-enabled smart metering systems. *Future Gener. Comput. Syst.* **2018**, *78*, 547–557. [CrossRef]
163. Ponce-Jara, M.A.; Ruiz, E.; Gil, R.; Sancristóbal, E.; Pérez-Molina, C.; Castro, M. Smart grid: Assessment of the past and present in developed and developing countries. *Energy Strategy Rev.* **2017**, *18*, 38–52. [CrossRef]
164. Minoli, D.; Sohraby, K.; Occhiogrosso, B. IoT considerations, requirements, and architectures for smart buildings—Energy optimization and next-generation building management systems. *IEEE Internet Things J.* **2017**, *4*, 269–283. [CrossRef]
165. Albăstroiu, I.; Enache, C.; Cepoi, A.; Istrate, A.; Andrei, T.L. Adopting IoT-based solutions for smart homes. The perspective of the Romanian users. *Amfiteatru Econ.* **2021**, *23*, 325–341. [CrossRef]
166. Kakkavas, G.; Gkatzioura, D.; Karyotis, V.; Papavassiliou, S. A review of advanced algebraic approaches enabling network tomography for future network infrastructures. *Future Internet* **2020**, *12*, 20. [CrossRef]
167. Conti, M.; Kaliyar, P.; Rabbani, M.M.; Ranise, S. Attestation-enabled secure and scalable routing protocol for IoT networks. *Ad Hoc Netw.* **2020**, *98*, 102054. [CrossRef]
168. Almusaylim, Z.A.; Alhumam, A.; Jhanjhi, N.Z. Proposing a secure RPL based internet of things routing protocol: A review. *Ad Hoc Netw.* **2020**, *101*, 102096. [CrossRef]
169. Gagliordi, N. *IoT to Drive Growth in Connected Devices Through 2022: Cisco*; ZDNet: San Francisco, CA, USA, 2018.
170. Georgiou, K.; Xavier-de-Souza, S.; Eder, K. The IoT energy challenge: A software perspective. *IEEE Embed. Syst. Lett.* **2017**, *10*, 53–56. [CrossRef]

171. Lotfi, H.; Khodaei, A. Levelized cost of energy calculations for microgrid. In Proceedings of the 2016 IEEE Power and Energy Society General Meeting (PESGM), Boston, MA, USA, 17–21 July 2016; pp. 1–5.
172. Saleem, Y.; Crespi, N.; Rehmani, M.H.; Copeland, R. Internet of things-aided smart grid: Technologies, architectures, applications, prototypes, and future research directions. *IEEE Access* **2019**, *7*, 62962–63003. [CrossRef]
173. Lopez, J.; Rios, R.; Bao, F.; Wang, G. Evolving privacy: From sensors to the internet of things. *Future Gener. Comput. Syst.* **2017**, *75*, 46–57. [CrossRef]
174. Ou, Q.; Zhen, Y.; Li, X.; Zhang, Y.; Zeng, L. Application of internet of things in smart grid power transmission. In Proceedings of the 3rd FTRA International Conference on Mobile, Ubiquitous, and Intelligent Computing (MUSIC), Vancouver, BC, Canada, 26–28 June 2012; pp. 96–100.
175. Swetina, J.; Lu, G.; Jacobs, P.; Ennesser, F.; Song, J. Toward a standardized common M2M service layer platform: Introduction to oneM2M. *IEEE Wirel. Commun.* **2014**, *21*, 20–26. [CrossRef]
176. Miazi, M.N.S.; Erasmus, Z.; Razzaque, M.A.; Zennaro, M.; Bagula, A. Enabling the Internet of Things in developing countries: Opportunities and challenges. In Proceedings of the 5th International Conference on Informatics, Electronics and Vision (ICIEV), Dhaka, Bangladesh, 13–14 May 2016; pp. 564–569.

energies

MDPI

Article

Analysis of a Photovoltaic System Based on a Highly Efficient Single-Phase Transformerless Inverter

Belqasem Aljafari [1], Ashok Kumar Loganathan [2], Indragandhi Vairavasundaram [3,*], Selvamathi Ramachadran [4] and Amutha Prabha Nagarajan [3]

[1] Department of Electrical Engineering, Najran University, Najran 11001, Saudi Arabia
[2] Department of Electrical and Electronics Engineering, PSG College of Technology, Coimbatore 641004, India
[3] School of Electrical Engineering, Vellore Institute of Technology, Vellore 632014, India
[4] Department of Electrical and Electronics Engineering, AMC Engineering College, Bangalore 560083, India
* Correspondence: indragandhi.v@vit.ac.in

Abstract: The essential requirement for a cleaner environment, along with rising consumption, puts a strain on the distribution system and power plants, reducing electricity availability, quality, and security. Grid-connected photovoltaic systems are one of the solutions for overcoming this. The examination and verification of transformerless topologies and control techniques was a significant goal of this study. The transformerless concept is advantageous for its high efficiency; the transformerless converter has added advantages of reduced price, complexity, weight, and size. This study presents a novel high-efficiency transformerless architecture that does not create common-mode currents and does not inject DC current into the grid. A single-phase transformerless inverter circuit with two step-down converters was constructed in this study. Low-frequency switches determine the polarity of the grid connection. In order to control the gate pulses of switching devices, which each regulate a half-wave of the output current, a PIC 16F877 was employed. Because there were fewer semiconductors and they were simpler to operate, it was possible to achieve a high degree of efficiency and reliability. A prototype model with input 12 V, 2 A was fabricated, test results were obtained with reduced common-mode current and DC current, and high efficiency was obtained with reduced switching losses. Further investigation for the improvement of efficiency with the elimination of ground current and leakage current has been analysed through simulation.

Keywords: transformerless inverter; photovoltaic; high-efficiency inverter; grid-connected system; single-phase inverter

Citation: Aljafari, B.; Loganathan, A.K.; Vairavasundaram, I.; Ramachadran, S.; Nagarajan, A.P. Analysis of a Photovoltaic System Based on a Highly Efficient Single-Phase Transformerless Inverter. *Energies* **2022**, *15*, 6145. https://doi.org/10.3390/en15176145

Academic Editor: Marco Pasetti

Received: 3 July 2022
Accepted: 20 August 2022
Published: 24 August 2022

Publisher's Note: MDPI stays neutral with regard to jurisdictional claims in published maps and institutional affiliations.

Copyright: © 2022 by the authors. Licensee MDPI, Basel, Switzerland. This article is an open access article distributed under the terms and conditions of the Creative Commons Attribution (CC BY) license (https://creativecommons.org/licenses/by/4.0/).

1. Introduction

For safety reasons, galvanic isolation is employed in most photovoltaic (PV) systems. When the isolation transformer is removed, the inverter may be more efficient, lighter in weight and size, and more affordable. When the transformer is removed, the overall efficiency of the PV system can be boosted by 1–2%. When compared to PV systems with galvanic separation, the most significant gains of transformerless PV systems are less weight, small size, and improved efficiency.

Transformer-less inverters have recently been presented as a way to shrink the size and cost of photovoltaic power systems. The earth-leakage current problem then arises, posing a significant challenge in the system. Both the general public and the power industry acknowledge the importance of renewable energy sources. According to some scholars, environmental concerns have taken precedence above the necessity to conserve scarce natural resources for future generations. The following are some of the advantages of reformation: increased rivalry in the energy-producing business; and individual consumers' opportunity to pick the greatest cost-effective dealer to distribute electricity to them.

According to consumer polls, both urban and rural electricity customers are prepared to pay a higher power cost to promote the growth of renewable energy sources. This

strong public backing has offered an incentive for developing a technically proved low-cost alternative to fossil-fuel-based power. Photovoltaic generation is one of these options, albeit it is currently not a cost-effective technique of generating electrical energy except in a few, generally remote, applications.

Many electrical experts are investigating grid-connected PV systems as a viable substitute energy source. When installed at the point of use, grid-connected PV systems can save money by reducing: (i) transmission power losses; (ii) required transmission line capacity; (iii) the necessity for traditional power generation; (iv) emissions of CO_2 and the cost of gasoline.

The quantity of electricity generated by a solar system linked to a customer does not necessarily match that consumer's energy consumption. As a result, utilizing all the energy generated by such a system requires the use of a huge energy storage capacity in combination with PV generating. Any excess energy from the PV system may be sent directly into the grid network, which would be more budget friendly. The benefit of the PV system that is generating power connected to the utility grid, versus a stand-alone PV generation, is that backup power and massive capacity are shared.

Utility backup capability is required in the grid-shared PV system being examined. Without battery storage, the PV energy is directly converted to utility energy in the Utility Tie Technology method. The benefits of not using batteries to store surplus energy from PV panels in household applications are: (i) lower PV system capital and maintenance costs; (ii) elimination of all battery-related health and safety issues from customers' homes.

The designed inverter can also be used in classic applications, including voltage regulation systems, uninterruptible power supply systems, and motor controllers, even though it is intended for grid-connected PV systems. The primary drawbacks of consuming solar power are its high initial price compared to other energy sources and its low conversion efficiency, which is less than 20% in commercially available PV systems. When the price of the solar panels and inverter system decreases along with their improved efficiency, then utility-connected PV generation becomes a viable alternative power source.

Institutions in India are conducting research into producing more efficient PV panels, which was not included in this paper's mandate. However, the inverter is quite important in the utilization of solar energy. The major goal of this paper was to increase the inverter efficiency. Greater efficiency was expected to be obtained through enhanced inverter output power quality and lower costs.

In India, inverters are used in household systems. A home system's distribution capacity is often less than 5 kW. The infrastructure, on the other hand, uses transformers to connect the inverter output to the grid system. As a result, there is no undesired DC offset current injected into the grid network. However, one of the strategies employed in the proposed circuit is not to use 50 Hz power transformers in the inverter to decrease price, size, and power loss. Whether or not transformers are required depends on how the quantity of the injected DC offset current into the grid system is controlled. The injection of DC current into PV inverters that are directly linked to the grid is limited to 5 mA, or 0.5 percent of the rated output current; whichever is larger.

As a second method of boosting PV inverter efficiency, the use of unipolar switching inverters for utility-connected systems, was proposed. Unipolar switching has the benefit of resulting in fewer power losses. It was also necessary to improve approaches to current controller design to maximize inverter efficiency. This targeted increased efficiency, on the other hand, could only be achieved if the IEEE Standards and the local electrical supply authority's requirements were attained by the output from the inverter system, without raising the cost of the inverter system, and the conventional supply system's safety and reliability were not jeopardized.

This research is difficult due to the vast number of control loops that must be examined to obtain better efficiencies without losing inverter power quality, as well as the limits set by the IEEE Std. 1547, 2003. Table 1 summarizes the tactics, potential difficulties, and potential

solutions to be researched to obtain better inverter efficiency, reduced costs, and enhanced power quality.

Table 1. Summary of Tactics to Maximize Inverter Efficiencies.

Solution No	Tactics for Maximizing Efficiency	Consequences for Power Quality	Types of Keys to Be Examined
1	Transformerless Operation	Offset DC current intrusion into the grid system at unacceptably high levels is a source of worry.	Progress of low-cost methods for removing DC offset current
		Electromagnetic compatibility issues are more likely to occur.	Current and voltage controller design options that decrease EMC concerns
2	Unipolar Switching	Current distortion at zero crossing, as well as high amounts of low and switching frequency harmonics fed into the grid system, could cause issues.	Current harmonics are eliminated using (a) Low frequency harmonics are reduced utilising current steering AC filter designs. (b) designs for feedback loops

The primary goal of this essay was to increase the efficiency of a PV inverter system while maintaining the quality of the power generated and lowering the cost.

The study describes a system that is controlled by a microcontroller that consists of stand-alone PV system with an energy storage system and a complete bridge inverter. It is made up of two sets of Boost-type chopper circuits, a modest number of switching elements and a complete bridge voltage source inverter resulting in a small overall system volume. As a result, the systems' costs are kept to a minimum. Pulse Width Modulation (PWM) signals reduce the number of pulses on the output waveform, increasing conversion efficiency. The suggested inverter's output power is less than 288 W. It is not necessary for the system to connect to a utility grid line using an inductor or a transformer. The theory underpinning the system is that there is no earth-leakage current. Simulated and experimental findings are presented in this research using prototype devices with a power of 37 W.

2. Literature Review

Multilevel converters for single-phase grid-connected solar systems were invented by M. Calais et al. [1]. They investigated the applicability of several multilevel topologies for single-phase grid-connected solar systems. The system power rating, component count, stress, and solar array earth capacitance influence of several transformerless photovoltaic systems with multilayer converters were all investigated.

Inverters for single-phase grid-linked solar systems were created by M. Calais, J. M. A. Myrzik, and V. G. Agelidis [2]. The information included not only commercially available topologies but also efficiency, pricing trends, market share, switching devices and switching frequencies. Finally, the article analysed the difficulties associated with defining acceptable worldwide industry standards for PV inverter technology.

For single-phase grid-connected solar systems, J. M. A. Myrzik et al. investigated string and module integrated inverters [3]. They discussed PV inverters, their efficiency, pricing trends, and market share, as well as innovative inverter topologies and PV system concepts that have recently emerged.

Single-phase grid-connected inverters for solar modules were studied by S. B. Kjaer et al. [4]. They focused on PV inverter technology used to link PV modules to a single-phase grid. Several inverter topologies were explained, compared, and evaluated in terms of their requirements, longevity, price, and component ratings. The optimal topologies for single- or multi-module applications were highlighted in their last section.

A transformerless inverter for residential solar energy systems was created by Amitava Das and Debasish Lahiri [5]. They created a Z-source inverter that eliminated the need

for a transformer. The system's operating concept, control approach, and attributes were discussed and the article compared the new and conventional system configurations. To showcase the new features, analysis, and simulation results were provided.

The earliest PV inverters were based on technology that had been used in electrical drives since the early 1980s as line commutated inverters with several kW of power rating. High efficiency, cheap cost, and robustness were the key advantages; however, with values ranging from 0.6 to 0.7, the power factor constituted a major disadvantage.

These days, inverters with a power range greater than 1.5 kW are force-commutated inverters. Traditional transformerless architecture having switching frequencies larger than 16 kHz of H-Bridge is used to eliminate sound disturbance. Due to the significant switching losses, the line commutated topology has lower efficiency. However, it is indeed a reliable, low-cost, and famous technology.

If the PV voltage level falls below the necessary minimum, a boost converter is added between the PV array and the inverter. In the European scenario, this increases the PV input voltage to a DC-link value of roughly 700 V for three-phase grid connection and 400 V for single-phase. In Figure 1a, a single-phase topology is shown.

The H-bridge forced commutated inverter, see Figure 1b, consists of a boost rectifier that elevates the PV array voltage from 100 V to more than 680 V. When there is a need for positive output voltage the upper switches are used, and bottom switches are used for getting the negative output voltage.

The Highly Efficient and Reliable Inverter Concept (HERIC) makes use of an enhanced version of the H-Bridge, as illustrated in Figure 1c, by connecting two diodes with two more switches in series for the freewheeling period and to boost the inverter's efficiency, two additional switches (T5 and T6) are used, thus depending on the current's signal, the freewheeling current finds a way via T5 or T6 and the appropriate diode rather than returning to the DC-link capacitor.

Figure 1d shows the H5 inverter for a grid-connected PV system. It has a normal H-Bridge architecture with a fifth switch added to the DC side. Maximum conversion efficiencies utilizing this circuit design have been reported to reach up to 98 percent, depending on the input voltage.

In all the above topologies of transformerless PV systems, inverters have been proposed, however their primary flaw is that they require a complicated control structure and several transformation stages, which lowers total conversion efficiency and increases inverter complexity and element computation. In the previous several decades, the PV inverter business has advanced significantly. Many transformerless topologies have been developed throughout the years, but only a handful have been approved as appropriate topologies for grid-connected PV systems by the industry. As a result, inverters are among the most promising topologies in terms of efficiency, price, safety, structure, and complexity on the feasible market.

For solar power generation, Y. Chen et al. [6] presented a single-stage inverter with maximum power point tracking at a reasonable price in conjunction with one-cycle control (OCC). The output current-adjusting capability of OCC is used in this control method. The inverter's output current may be modified based on the voltage of the photovoltaic (PV) array to get the most power out of it. All of this is accomplished with a single power stage and a straightforward control circuit. This strategy is far more efficient and cost-effective than the previously offered ways while still delivering good results.

The investigation, design, and implementation of a maximum power point tracking (MPPT) system for standalone solar power generation were the topics covered by Roger Gules et al. [7]. They constructed a solar streetlamp with a locally developed smart charge controller by L. Nirupa Rathnayake and T. Chandana Peiris [8]. This intelligent charger controller was built with the utmost commonly available less price PIC microcontroller, offering the system design flexibility. The newly designed charge controller gave the maximum amount of electricity from the solar panel; besides it protected the battery from overcharging. Another important aspect was that automatically the streetlamp turned on

and off. The smart charge controller was cost-effective, and it could certainly be adapted to various energy sources, including wind turbines.

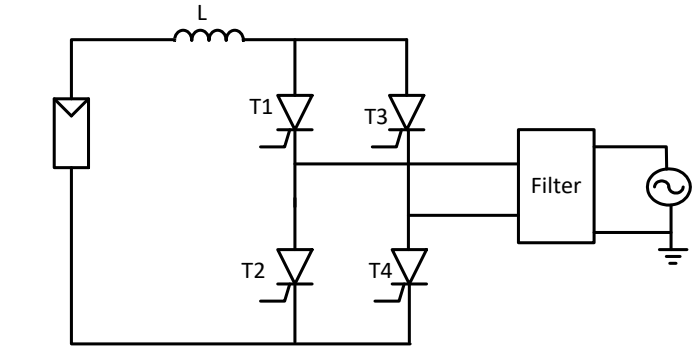

(**a**)

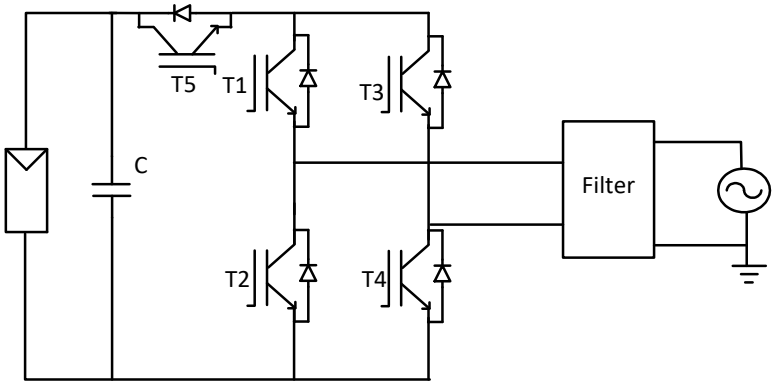

(**b**)

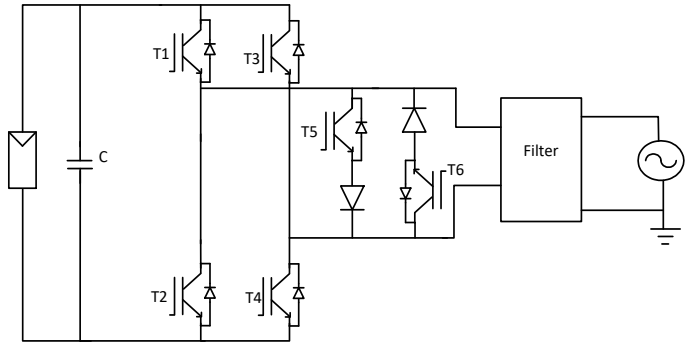

(**c**)

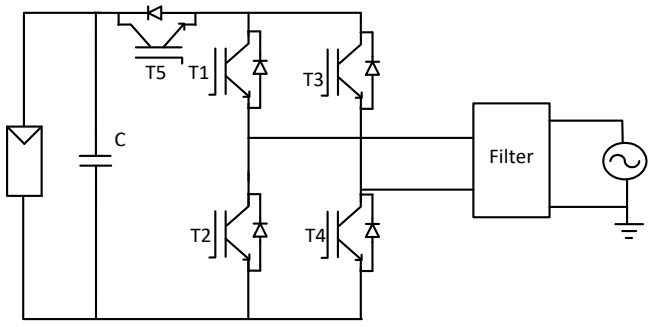

(**d**)

Figure 1. (**a**) Line commutated inverter; (**b**) H-bridge forced commutated inverter; (**c**) Highly Efficient and Reliable Inverter; (**d**) H5 topology inverter.

R. Akkaya and A. A. Kulaksiz [9] devised and constructed a stand-alone solar power system to power domestic AC-powered equipment, including fluorescent lamps and fans. By maintaining the solar module perpendicular to the sun's rays, the sun-tracker increased the system's efficacy. The charging technique was implemented using a buck-boost DC-DC converter with closed-loop current regulation. The PWM approach employed eliminated chosen harmonics with the fewest number of switches, resulting in an increase in system efficiency by minimizing switching losses and making inverter output filtering easier. The PWM inverter systems and charge controllers were built using PIC16F873 microcontrollers. To validate the system's efficiency, simulation, and experimental data were provided.

A new form of utility-interactive inverter for solar systems was created by Y. Nishida et al. [10]. This inverter lacked a transformer to save space, but it did have a unique power processing system. In addition, the DC-DC converter limited the input current, trapping the utility's ripple-power fed hack in the inductor. Since then, with this new method, a huge capacitor does not need to be connected to the inverter's input.

A single-phase multilevel-based solar inverter without a transformer was reported by Roberto Gonzalez et al. [11]. This notion not only reduced the conversion step's cost, size, and weight, but it also enhanced the system's overall efficiency. The novel high-efficiency topology described in this study prevented common-mode currents and assures that no topological DC is introduced into the grid for transformerless systems.

A cascaded inverter for transformerless single-phase grid-connected solar systems was created by Martina Calaisa et al. [12].

The IEEE Std. 1547, published in 2003, is the IEEE Standard for Interconnecting Distributed Resources with Electric Power Systems [13]. The technical requirements for, and testing of, the interconnection itself are the emphasis of this standard. It specifies performance, operating, testing, safety concerns, and maintenance standards for the interconnection. Design, production, installation evaluation, as well as general requirements, commissioning, and abnormal condition response, periodic tests power quality, islanding, and test standards and requirements, are all included. The aforementioned requirements are often required for the interconnection of distributed resources (DR), like power inverters and converters, induction machines, and synchronous machines, and they are appropriate for the great majority of installation scenarios. The DR is a 60 Hz source. Thus, this standard was created with that in mind.

S. M. Babu, et al. [14] presented a new three phase transformerless stepup inverter with pulsating DC-link for PV/EV applications with reduced components and capacitor size.

Informed by to a thorough literature search, the goal of this work was to reduce concerns linked to implementation delays, which are all crucial to the research work's success and will need to be investigated.

Reference [10] compared three alternative standards (IEEE 1547, EN 61000-3-2 and IEC 61727), with an emphasis on the formerly mentioned difficulties. Table 2 summarizes the criteria set out by each standard for DC current inserted (an essential problem in the case of grid-connected inverters).

Table 2. DC current injection maximum per various standards.

	IEEE 1547	**IEEE 929-2000**	**VDE 0126-1-1**	**EN 61000-3-2**	**IEC 61727**
DC current injection	<0.5% of rated output current	<0.5% of rated output current	<1 A	<0.22 A corresponds to a 50 W half-wave rectifier	<1% of rated output

Moreover, when a DC current injection surpasses 1 A, the VDE 0126-1-1 standard mandates that disconnection must occur within 0.2 s. A time requirement for disconnection is not mentioned in any of the other standards. There is just one standard that particularly

addresses failure and leakage current levels in transformerless PV systems: the German VDE 0126-1-1 standard. There are three separate currents that must be measured according to the standard.

- Ground Fault Current, which occurs when the insulation on the ground wire fails and current flows through it.
- Fault current, which is equivalent to the sum of the major currents' instantaneous values and is zero in normal conditions.
- Leakage Ground currents are caused by potential changes in capacitive coupled parasitic components.

3. Transformerless Utility Connected PV Systems

The research success was dependent on overcoming the technological obstacles associated with connecting the inverter system to the mains supply without using 50 Hz power transformers. Table 3 compares 30 single-phase inverters with outputs up to 12 kW for grid-connected PV systems, including seven that were transformerless. The price disparity between the two types of inverters is particularly apparent when the weight and price data are adjusted to the inverters' rated power; the transformerless kind was nearly 25 percent less expensive.

Table 3. Comparison of Inverters.

A Total of 30 Inverters for Single Phase Grid Connected PV Systems (1–2 kW) Were Examined, 23 with Transformers and 7 without			
Type of Inverter	**Price Rs/W**	**Weight kg/kW**	**Max. Efficiency %**
With Transformer	81.90	16.1	93.1
Transformerless	61.74	12.3	95.9

Calais examined string inverters, central inverters, module-oriented or module integrated inverters, and inverter topologies in single-phase utility-linked PV systems. Because it offered the most freedom in developing and testing each stage independently, the module integrated inverter was recommended as the most acceptable configuration for the household PV application being examined in this study (Figure 2).

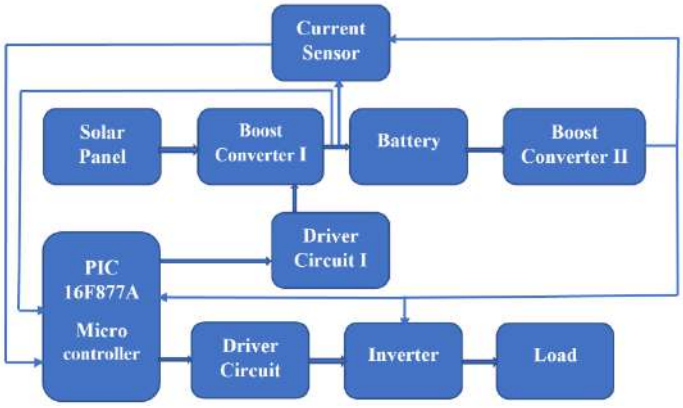

Figure 2. Utility connected PV System Configurations.

A Maximum Power Point Tracking (MPPT) capacity is usually included in a photovoltaic energy conversion system to ensure optimal efficiency. As previously stated, the voltage controller is responsible for maintaining Vc constant in the proposed inverter system. It does so by ensuring that all the electricity generated by the PV panels is fed into the grid. The magnitude of the output current is controlled by the voltage controller, which regulates the power flow. The current controller's task is to generate a sinusoidal output with adjustable amplitude and frequency.

This sort of half-bridge would require double the DC voltage from the boost converter without the usage of a step-up transformer as compared to the full-bridge version. As a result, this approach was deemed inappropriate, and the single-phase full-bridge inverter was adopted.

Using the PWM method, the electronic switches in the single-phase bridge's current loop can be operated in either bipolar or unipolar mode. In bipolar mode, the diagonally opposed switches are switched in pairs for the two legs of the inverter bridge. The two legs of the bridge are not switched simultaneously in the unipolar mode but are controlled individually. The output voltage swing in unipolar mode is half of that in the bipolar mode for the same input DC voltage. When comparing several elements, as given in Table 4, the achieved simplicity becomes clear not only in terms of function but also in terms of structure.

Table 4. Comparison of Existing Transformerless Inverters with Proposed model.

Existing Topology	H5	HERIC	Proposed
Low-frequency switches	2	2	2
High-frequency switches	3	4	2
The total number of switches	5	6	4
Number of inductors	1	1	1
Semiconductor in the current path	3	2	2

Furthermore, all the high-frequency switches in the form of the proposed circuit do not require high-side drivers, which, as previously said, decreases the cost and increases the efficiency greatly.

4. AC Filter Design

The use of sinusoidal PWM and proper voltage control loop design reduces low-frequency harmonics below the values allowed by the standard. These harmonics can be minimized to fulfil EMC requirements by using a Radio Frequency Interference (RFI) filter and excellent circuit layout and design during implementation.

Harmonics can even be seen around the switching frequency of the inverter. These frequencies are in the kHz range. Inverters with electronic switches are increasingly being used in distributed renewable energy generation to switch currents at high frequencies. This can cause waveform distortion and the possibility of harmonic resonance, which can cause shunt capacitors to fail. To minimize such concerns, numerous national and international standards limit the permitted degree of current distortion. The maximum Total Harmonic Current Distortion (THCD) is limited to fewer than 5% per the IEEE standard. As these requirements become stricter and the technology for switching huge currents at high frequencies improves, the necessity to filter switching frequency current harmonics becomes increasingly important.

The ripple current must be attenuated without reducing the inverter system's efficiency, which is a crucial prerequisite of a switching frequency filter made specifically for this document. As a result, current filter designs must be assessed to find appropriate AC filter configurations for this research.

Passive and active power filters have both been utilized to reduce current harmonics and control reactive power. Active power filters provide the advantage of greater output control and a faster reaction time, as well as being smaller in size. The cut-off frequency of the active filter determines the order of harmonics that can be controlled. This approach has the following drawbacks:

- It necessitates a high number of active components.
- It may necessitate sophisticated algorithms to operate several switches.
- In rare cases, they can act as negative resistances, enhancing the supply system's harmonic content.
- A higher price.

Apart from power losses, the filter in the household PV inverter system under consideration must be simple in design and affordable in cost. Because of its complexity and expense, active filtering was ruled out as a viable solution. Instead, passive filtering would be employed for this work.

A filter is any circuit that removes some components of a signal or power source while allowing the other parts to function normally. The filter in a power supply must eliminate or greatly minimize ac fluctuations while still providing the necessary dc to the load circuits.

To smooth the pulsations and give the load circuit a much "cleaner" dc power source, when the load current is high, the RC filter reduces the ripple voltage but introduces excessive resistive losses. We may replace the resistor with an inductor to minimize the ripple even further without adding a lot of dc resistance.

$$Lc = 1/(2 \times \pi \times fc)2 \cdot Cc \quad (1)$$

The DC currents in transformerless commercial inverters are around three times larger than those seen in their counterparts with transformers due to grid requirements for Total Harmonic Distortion (THD), output-current control, DC component limits and islanding-detection techniques. To avoid exceeding these limits, extra attention is paid to the control and measurement of transformerless systems to minimize losses.

5. Proposed Single-Phase Inverter System

The single-stage sans transformer contributes to a highly efficient single-phase inverter design at minimal cost in this study. Prior single-stage systems had the restriction of possessing the PV array voltage over a certain threshold to supply the grid directly. To overcome these concerns, a novel architecture was established, with the basic notion of retaining a single-stage circuit when the input voltage is sufficient and simply using the step-up operation while the voltage drops beneath a particular level. The gains of this hybrid technique compared to the usual two stage system include lower losses due to the step-up stage being active for a short period of time and improved efficiency due to the stage being built for a low power level. The disadvantages are the enormous quantity of semiconductors used and the complicated process.

A single-stage single-phase circuit with excellent efficiency is suggested. Integrating two parallel step-down converters in series with their outputs linked to the opposite polarities of the load is the primary goal. A single switch regulates the output voltage at a high frequency for one half-wave, while a second switch commutated at a low frequency connects the load properly. The direct manipulation of the current makes this circuit a voltage-source-inverter method. The positive and negative half-waves are produced, respectively, by the two step-down and step-up converters T1-L1-D1-T3 and T2-L2-D2-T4. The PV array is represented by V_{in} as the input source, while the utility grid is represented by V_{out} as the output source. When paired with the impedance of the low-voltage grid, just a minute quantity of filtering action, indicated by the inductors L1 and L2, is required to meet common grid needs (Figure 3).

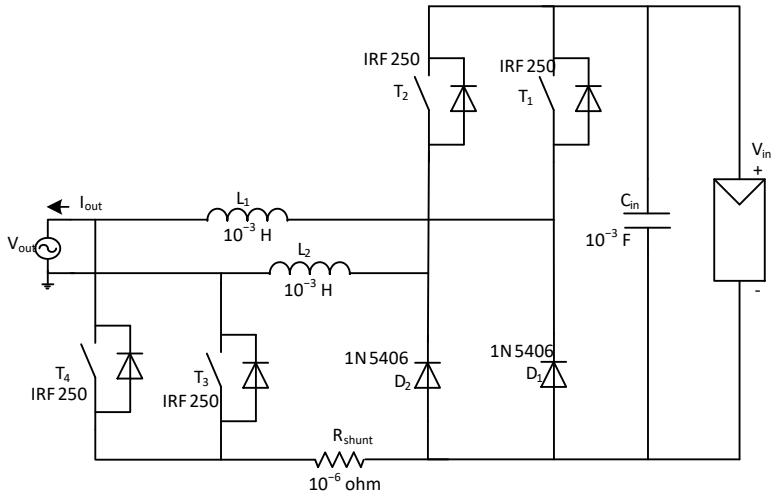

Figure 3. Proposed inverter circuit.

The employment of various inductors increases the presence of dc components in the output current, which increases the possibility of asymmetry between each stopped wave. Despite having a significant influence on the overall cost but not on efficiency, using separate inductors increases the likelihood of asymmetry between each halt-wave, leading to the existence of dc components in the output current. As a result, the construction of such inductors may be done with great accuracy. The recommended circuit offers a high level of dependability because the risk of a leg short circuit only arises at zero crossing rather than at each commutation of the high-frequency switches. It is also less costly as the output-current measurement may be completed using a straightforward resistive shunt and does not require galvanic separation. Because there are no high-frequency oscillations as the PV array's negative output is connected directly to the neutral and phase output during the positive and negative half-waves, leakage currents are avoided. Reactive processing is also not possible as the dc-link capacitance and current freewheeling are independent. The suggested circuit's high-frequency switches (T1 and T2) necessitate galvanic-isolated driver circuits; hence a different architecture is recommended. Low-frequency switches lead to cost savings and enhanced dependability in this case. Although the diodes D3 and D4 have little impact in normal operation, they were added to clamp the voltage between the switches T3 and T4 during input voltage level transients (Table 5). The most notable change is that during the negative half-wave, the PV array's positive terminal is linked to the phase output.

Table 5. Full-Bridge Single-Phase VSI Switch States.

State	State #	V0	Components	Conducting
T_1 and T_3 are on and T_2 and T_4 are off	1	V_i	T_1 and T_3 D_{1+} and D_{2-}	if $i_a > 0$ if $i_a < 0$
T_2 and T_4 are on and T_1 and T_3 are off	2	$-V_i$	D_{1-} and D_{2+} T_2 and T_4	if $i_a > 0$ if $i_a < 0$
T_1 and T_4 are on and T_2 and T_3 are off	3	0	T_1 and D_{2+} D_{1+} and T_4	if $i_a > 0$ if $i_a < 0$
T_2 and T_3 are on and T_1 and T_4 are off	4	0	D_{1-} and T_3 T_2 and D_{2-}	if $i_a > 0$ if $i_a < 0$
T1, T_2, T_3 and T_4 are all off	5	$-V_i$ V_i	D_{1-} and D_{2+} D_{1+} and D_{2-}	if $i_a > 0$ if $i_a < 0$

This design works similarly to a Voltage Source Inverter (VSI); the main difference is that inductors are used in the output to provide waveform filtering. An extra capacitor is

frequently placed in the same direction as the load to subordinate the inductor size. An LC filter could be used to filter the entire solution. A limiting resistor can be used to alleviate the problem of capacitor charging current and then switching it with a relay, or at the zero-crossing instant, synchronizing the grid connection.

6. Results and Discussion

The simulation result is a filtered output, which shows that the inverter's output voltage is 78% of the input rate due to the filter parameters presented in the model (Figure 4) and current waveform presented in Figure 5. Table 6 lists the simulation parameters.

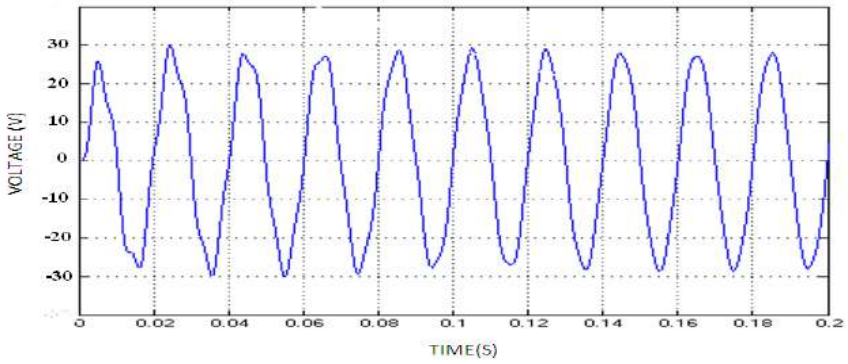

Figure 4. Output Voltage Waveform of the Inverter.

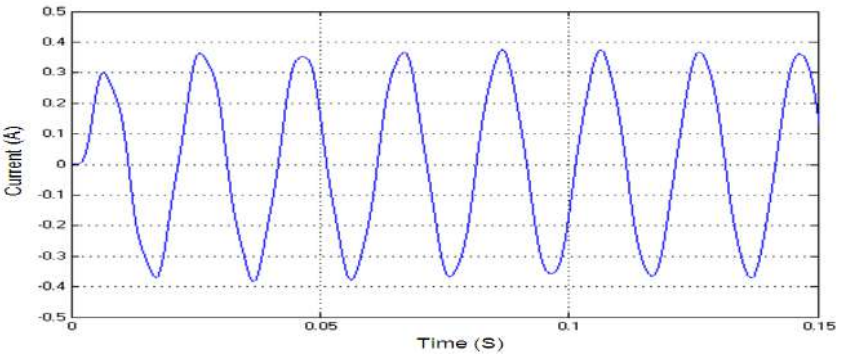

Figure 5. Output Current Waveform of the Inverter.

Table 6. Simulation Parameters and Input Values.

Simulation Parameters	Values
Output filter Inductance	6 mH
Output filter Capacitance	100 μF
Output frequency	50 Hz
DC voltage	12 V

The output voltage and current waveform harmonic spectrum with a filter circuit is shown in Figures 6 and 7, which were obtained from FFT analysis in MATLAB software. From the simulation results, the THD (Total Harmonic Distortion) in voltage and the current waveform is less than 0.7%. When compared to the preceding section's THD of voltage and current waveforms, it is an advantage that the output waveforms have lower THD than that of the inverter without the filter circuit, which reduces the problems due to the harmonics.

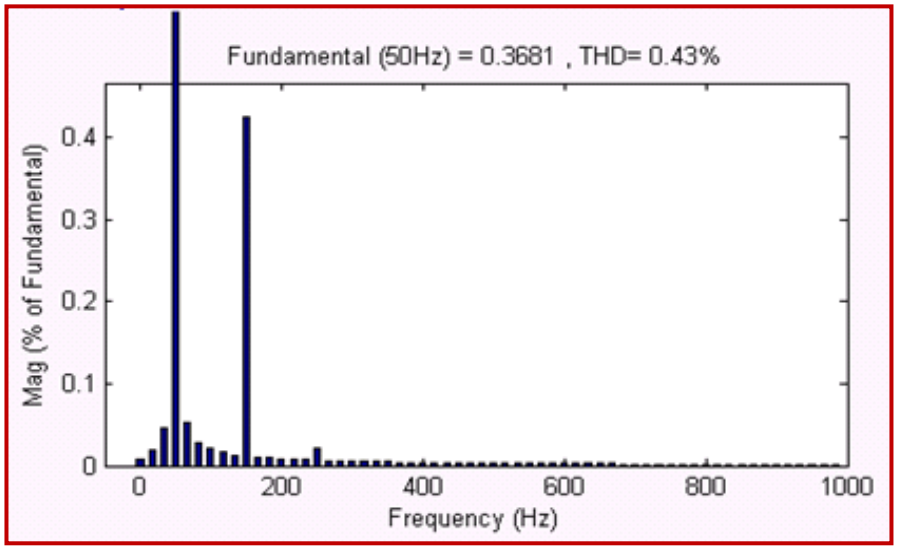

Figure 6. Harmonic Spectrum of Output Current with Filter Circuit.

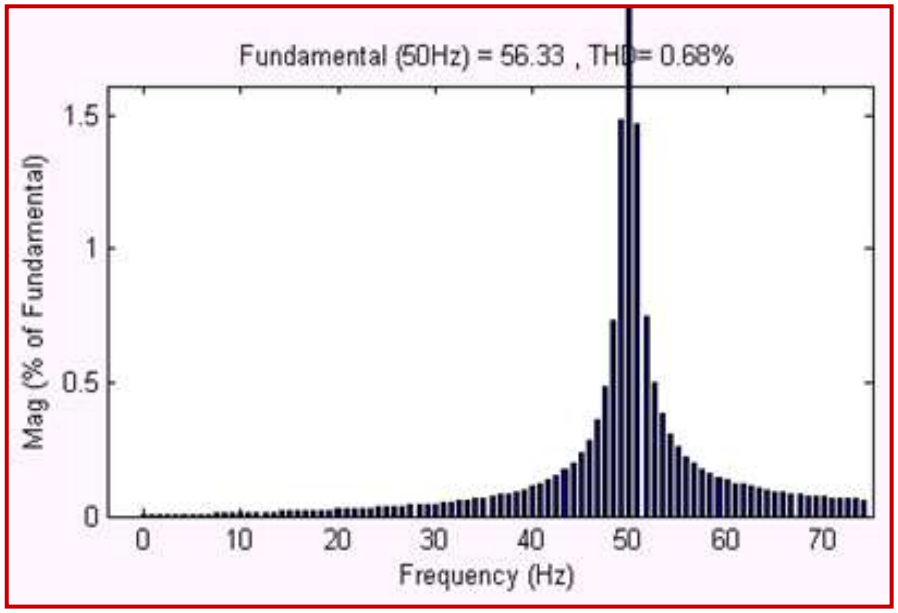

Figure 7. Harmonic Spectrum of Output Voltage with Filter Circuit.

Moreover, the simulation results were verified for the high-power rating. The simulated inverter voltage across the output terminals, the current flowing through the output terminals and the measured current THD are presented in Figures 8–10, respectively. The AC output voltage is obtained for the given DC input of 360 V. The current THD was very low at only 0.22%.

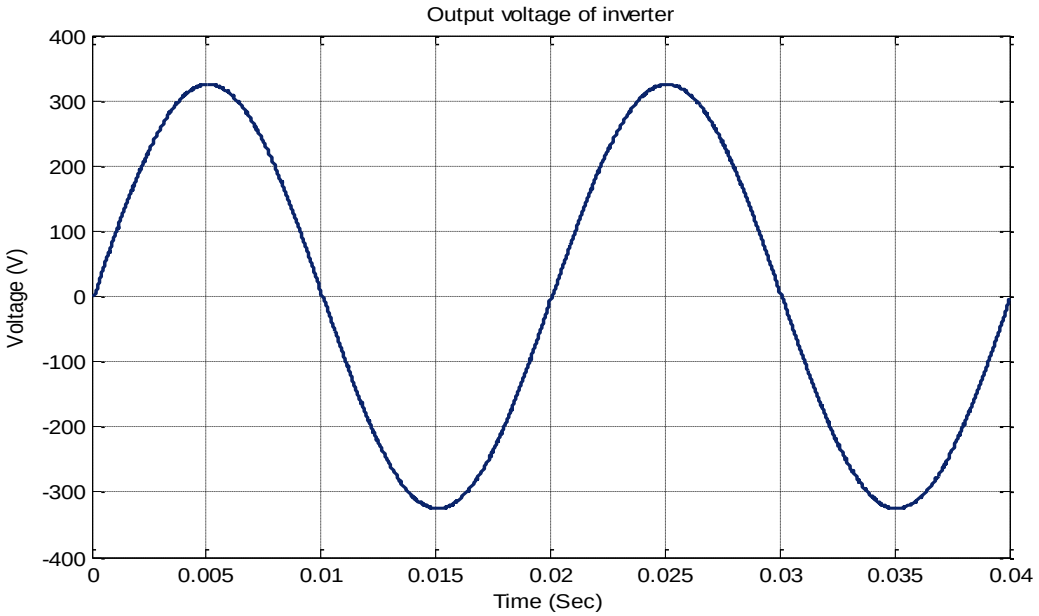

Figure 8. Output Voltage of Proposed Inverter.

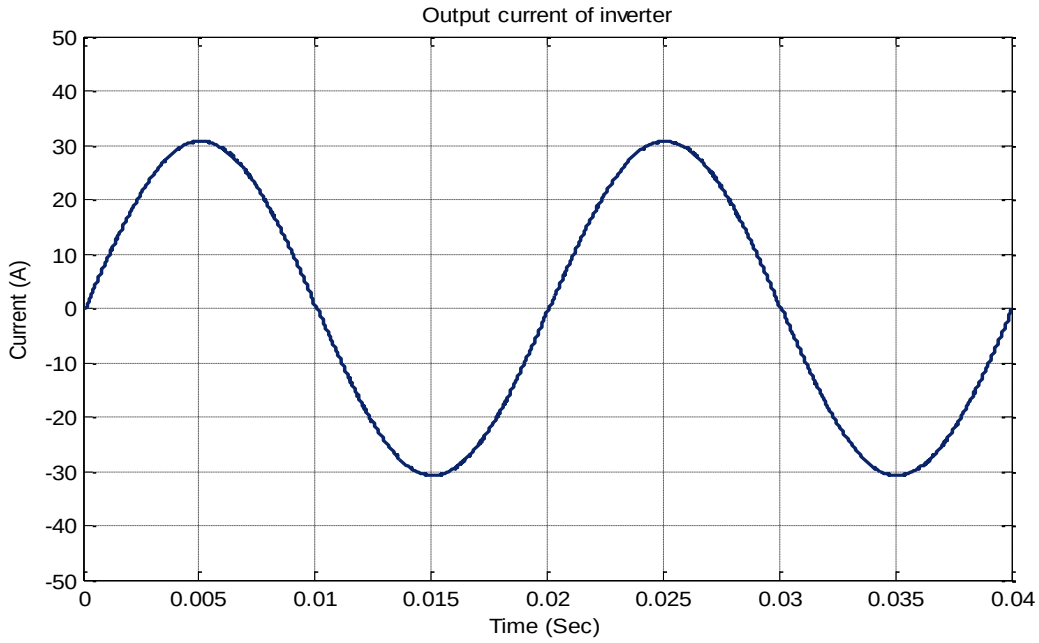

Figure 9. Output Current of Proposed Inverter.

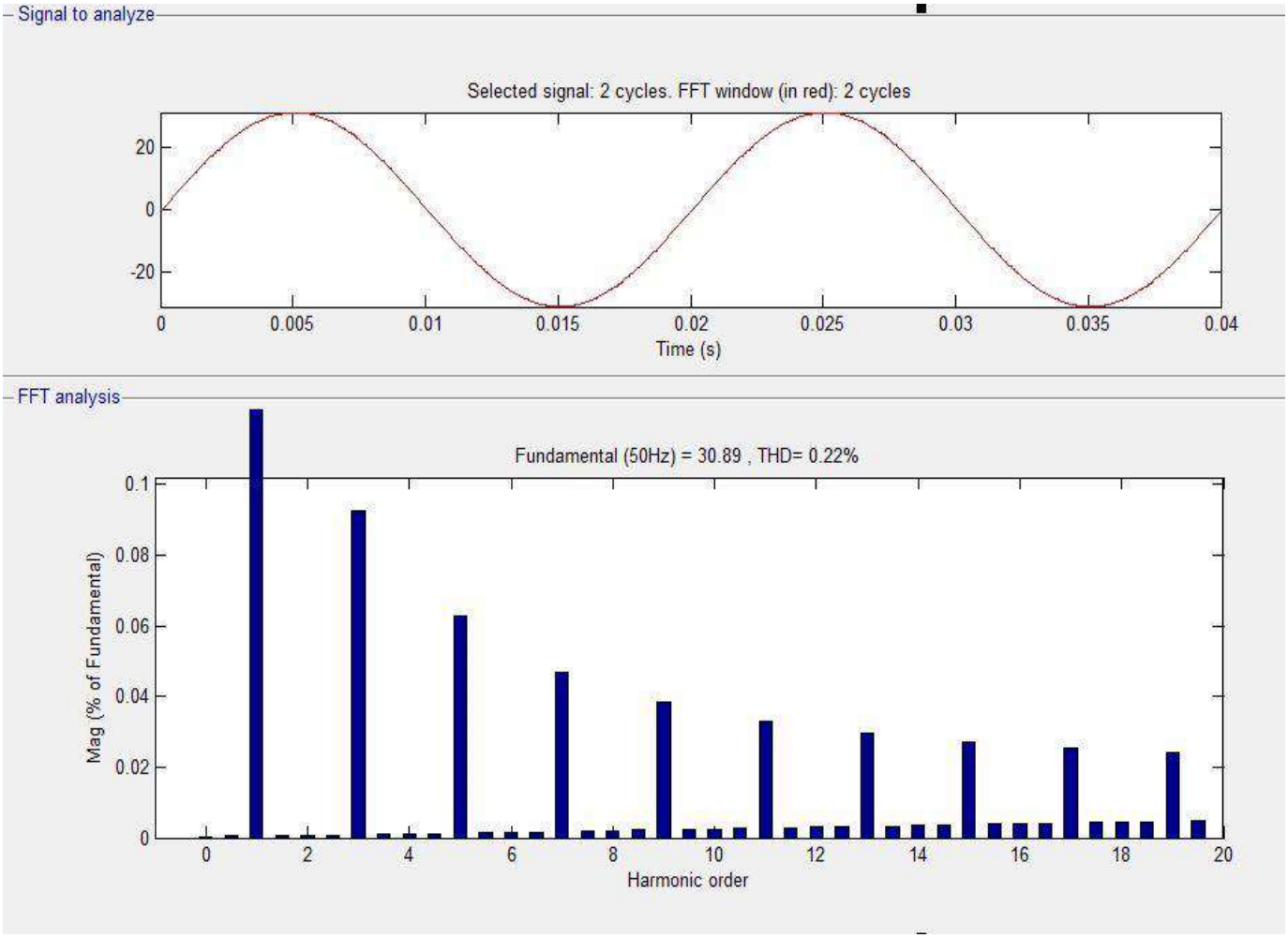

Figure 10. Output Current THD.

7. Experimental Result

An experimental setup was created to verify the simulation results. Tables 7 and 8 depict the experimental setup recorded results for 2 continuous days during summer.

Table 7. Recorded Experimental Values (Day 1).

Day 1	Short Circuit Current (A)	Open Circuit Voltage (V)	Solar Radiation (W/m^2)	Output from Inverter (V)
10.00 am	1.64	17.2	670	28.12
11.00 am	1.59	19.3	761	30.76
12.00 pm	1.71	18.8	782	32.27
01.00 am	1.80	19.0	931	34.20
02.00 pm	1.76	18.6	921	32.80
03.00 pm	1.64	17.4	872	28.56
04.00 pm	1.55	16.6	714	25.78
04.30 pm	1.60	15.6	508	25.07

Table 8. Recorded Experimental Values (Day 2).

Day 2	Short Circuit Current (A)	Open Circuit Voltage (V)	Solar Radiation (W/m^2)	Output from Inverter (V)
10.00 am	1.60	19.2	665	30.72
11.00 am	1.89	17.3	716	32.70
12.00 pm	2.04	16.8	809	34.27
01.00 am	1.90	17.0	801	32.30
02.00 pm	1.77	17.2	720	30.44
03.00 pm	1.58	17.4	590	27.49
04.00 pm	1.16	17.6	418	32.42
04.30 pm	0.84	17.6	312	23.78

The system design leads us to the hardware design of the control unit. The hardware design is the most important part of the work because it is the one that is to be tested in real mode. The hardware design starts by selecting the components for the individual modules and integrating them into a single system. The hardware should be designed such that it meets the requirements of the proposed control strategy (Figure 11). Before beginning the actual hardware design, a generic system design was essential to ensure the control requirements were met. It should be noted that sometimes it may not be possible to implement all the features of the proposed strategy. At such times, some compromises may be made such that the performances are achieved. In this work, it was attempted to implement all the essential features of the proposed control strategy.

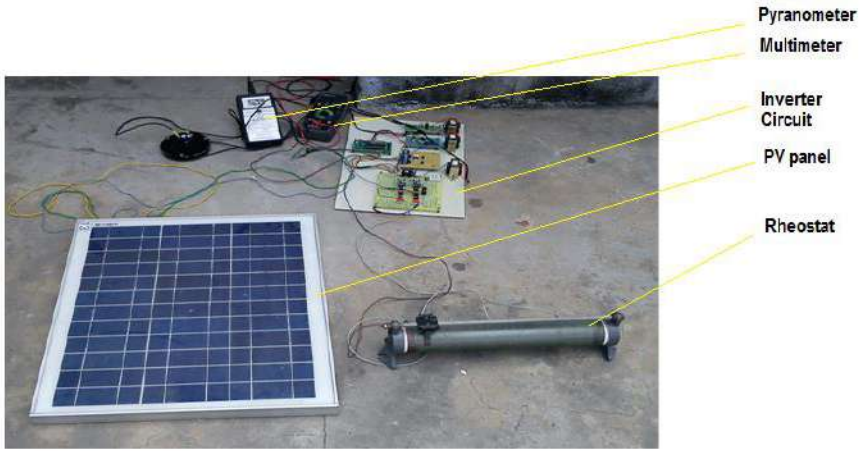

Figure 11. Experimental setup of proposed Inverter.

In designing the control unit, as said above, difficulty may arise because some of the components may not be available, components may be expensive, and sometimes it may be difficult to implement things in practice. In this work, the control unit was designed considering some of the practical difficulties. However, it was decided at least to implement the basic features of the system through the control unit to be designed.

The proposed control strategy in this paper was to maximize the system efficiency and minimize the cost. However, the design of the actual control unit could not be designed to achieve full-fledged performance. In this work, the defined strategies were simplified and implemented in the hardware unit. The control unit's major goal was to implement all the voltage control modes of operation for the boost converter first. The control of current or the impedance matching between the source and the load were not done in this work, as it was a complex design process.

As shown by the above data (Figures 12 and 13), the output waveform from the experimental findings had a frequency of 50 Hz, which is identical to that of the grid. The output voltage of a single-phase inverter is 27 V, according to both simulation and

experimental investigations, which were found to agree. The leakage current was also reduced, and overall harmonic aberrations in the output waveforms were less than 1%. Figure 14 presents the output of voltage and leakage current.

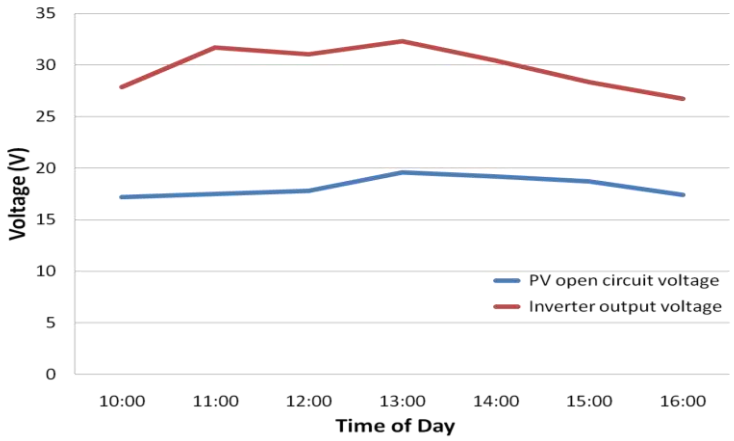

Figure 12. PV panel DC and inverter AC voltage output curves.

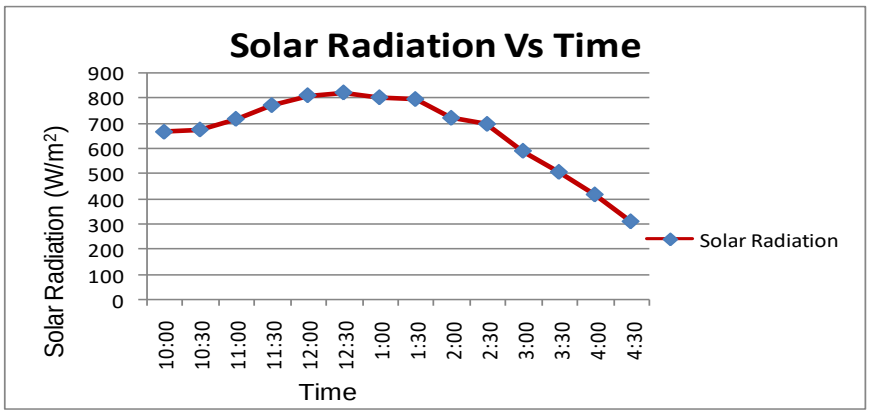

Figure 13. Solar Radiation Vs. Time Curve.

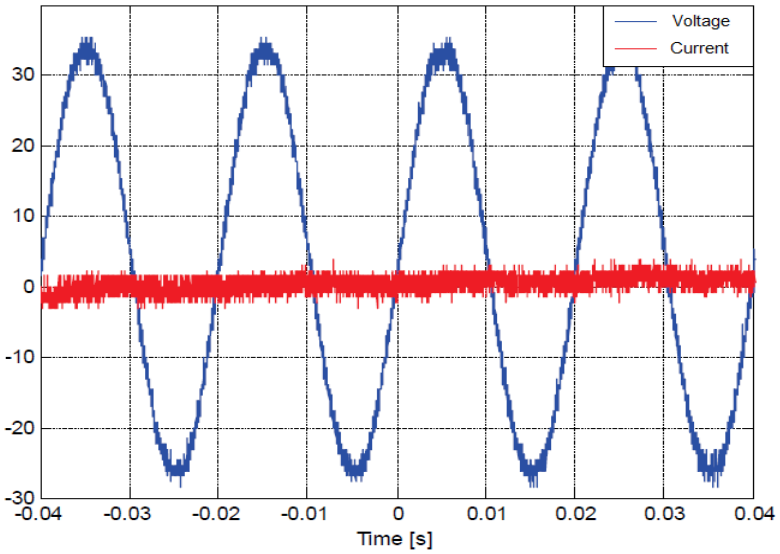

Figure 14. Output of Voltage and Leakage Current.

In this work, the inverter has four switches and two diodes. Considering the requirements, a driver circuit Printed Circuit Board (PCB) for six switches was designed. To drive to high side switches, two IR2112 drivers were used in the design, and for isolation purposes, MCT2E opt isolators were used for the switches. Figure 15 shows the PCB, which consists of six MCT2E opt isolators on the top of the board and two IR2112 drivers with bootstrap circuit on the bottom right of the board. A PC74HC08P AND gate was used to get unipolar PWM signals from the PIC-16F877A, and was placed on the bottom left of the PCB.

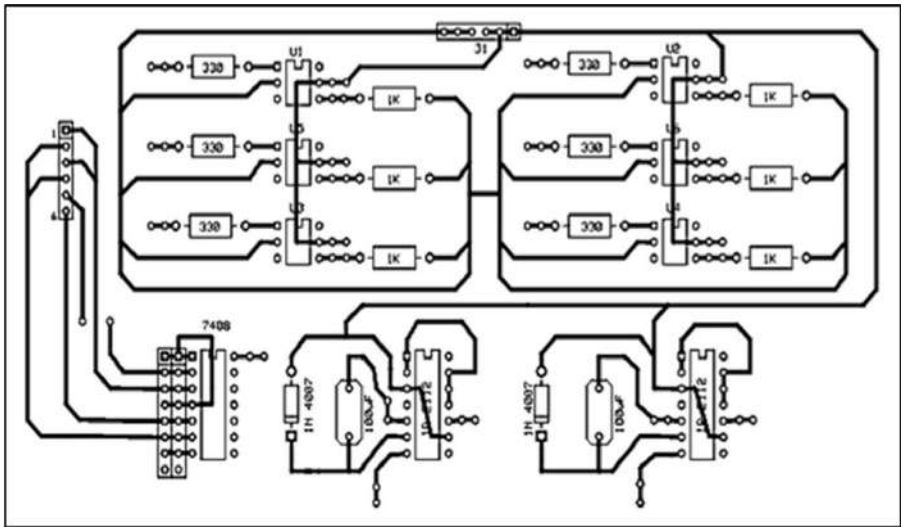

Figure 15. PCB Layout of Driver Circuit.

Figure 16 shows the single layer driver circuit PCB layout; it was designed in Express PCB software, which is very simple to use, even for complicated circuits. By default, this software can generate two-layer PCB layouts. But for this circuit it was sufficient to design a single layer PCB layout, which can be implemented in a short time.

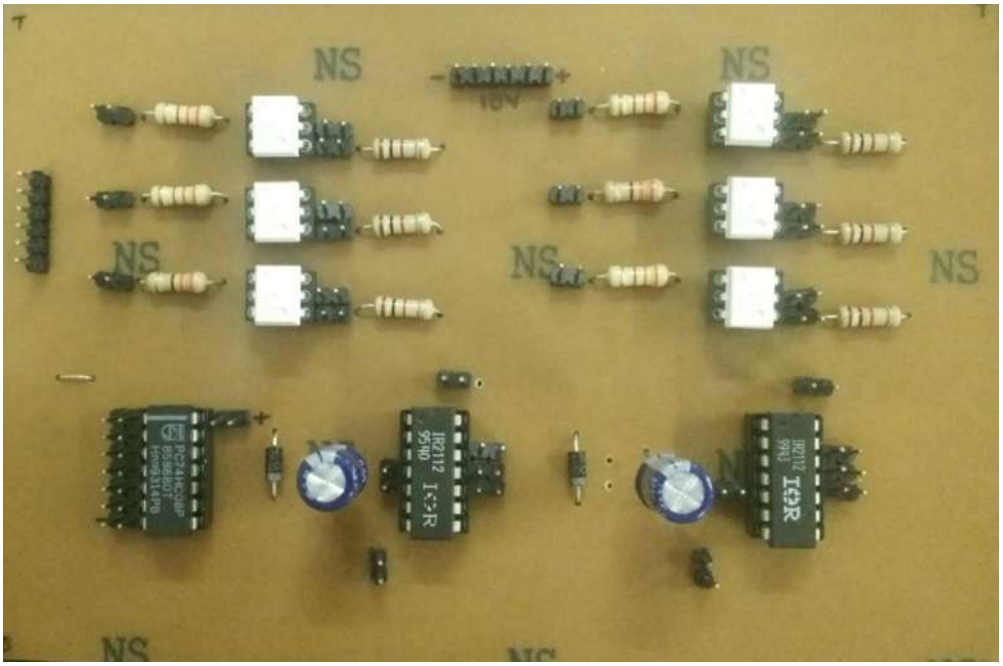

Figure 16. PCB Implementation of Driver Circuit.

The transformerless inverter was connected to a load of 100 W in steps of 10 W, as observed in Figure 17. It is seen that there was no flickering observed in lamp loads. Because of the Cool-MOS used in the transformerless inverter, it was observed that the MOSFET's does not heat up, until 100 W loads. The common mode voltage of the transformerless inverter was constant, which will reduce the leakage currents in the solar PV system.

Figure 17. Resistive (Lamp) Load Connected to the Transformerless Inverter.

The corresponding output power and efficiency of the transformerless inverter was calculated and is plotted in Figure 18. The efficiency of the proposed inverter is better than the existing inverter topology [15]. The efficiency of the inverter increases with an increase in the load value (Figure 18). This inverter can be used up to 500 W, and efficiency can be improved further.

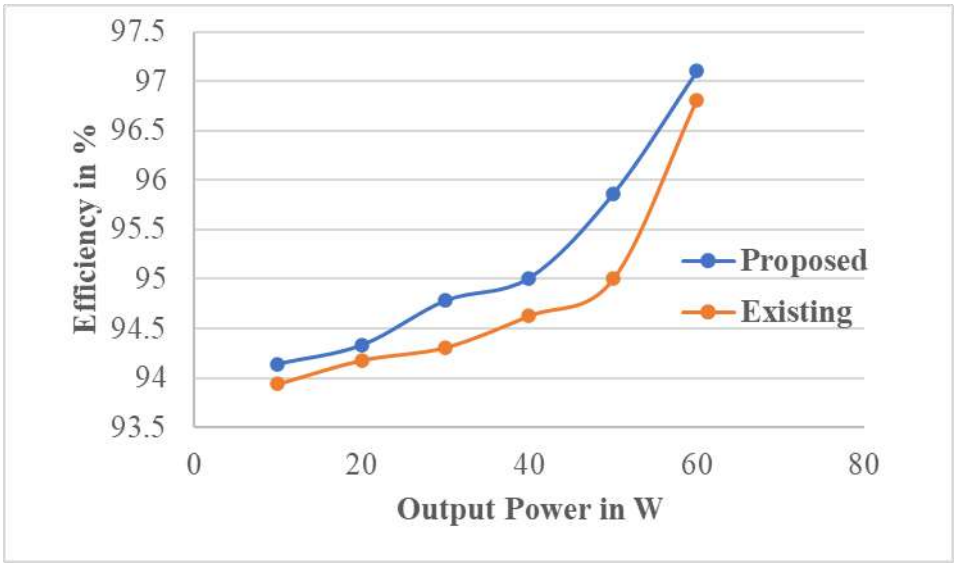

Figure 18. Efficiency Comparison of Transformerless Inverter.

8. Conclusions

Technical concerns for the systematic design of a transformerless inverter for free-standing PV systems were addressed in this study. The research work's major goal was to offer a design approach that would result in high inverter conversion efficiency, higher output power quality, and lower capital costs.

The system's performance was evaluated in simulations using Simulink in stand-alone mode, demonstrating that the suggested scheme might be a good option for a home solar power generating system. The experimental findings were in agreement

with the computational outcomes. With overall voltage and current THD of less than 0.68 percent and 0.43 percent, respectively, the controller board can deliver an inverter output frequency of nearly 50 Hz. Leakage current is eliminated through low-frequency switching, and ground current is eliminated through proper PV panel grounding. The inverter switches are controlled by Sinusoidal Pulse Width Modulation (SPWM). The inverter control circuit hardware is simplified due to the development of a control circuit employing a PIC microcontroller. The frequency modulation ratio and duty cycle of a microcontroller unit may be readily altered by programming without requiring any further hardware adjustments. However, it should be noted that this work did not consider in great detail the hardware control unit and so the hardware design could be improved further.

There are various study challenges for future work, as the simulations in the provided work contained perfect components, and the efficiency of the topology was not measured. However, by accounting for switching and conduction losses for switching parts, and losses for passive components, the efficiency may be calculated in simulations. In transformerless PV inverters, DC-current injection is a hot topic. As a result, potential routes for further reducing low frequency harmonic current production by unipolar switching inverters must be investigated.

Author Contributions: Conceptualization, I.V.; Formal analysis, S.R.; Funding acquisition, B.A.; Investigation, A.K.L.; Methodology, A.K.L.; Project administration, I.V.; Resources, B.A.; Validation, S.R.; Writing—original draft, A.P.N.; Writing—review & editing, A.P.N. All authors have read and agreed to the published version of the manuscript.

Funding: The authors are thankful to the Deanship of Scientific Research at Najran University for funding this work under the Research Groups Funding program grant code (NU/RG/SERC/11/6).

Conflicts of Interest: The authors declare no conflict of interest.

References

1. Chowdhury, A.S.K.; Razzak, M.A. Single phase grid-connected photovoltaic inverter for residential application with maximum power point tracking. In Proceedings of the 2013 International Conference on Informatics, Electronics and Vision (ICIEV), Dhaka, Bangladesh, 17–18 May 2013; pp. 1–6.
2. Jana, J.; Saha, H.; Bhattacharya, K.D. A review of inverter topologies for single-phase grid-connected photovoltaic systems. *Renew. Sustain. Energy Rev.* **2017**, *72*, 1256–1270. [CrossRef]
3. Wen, X.Y.; Lin, P.J.; Chen, Z.C.; Wu, L.J.; Cheng, S.Y. A grid-connected single-phase photovoltaic micro inverter. *IOP Conf. Ser. Earth Environ. Sci.* **2017**, *93*, 012079. [CrossRef]
4. Khan, M.N.H.; Forouzesh, M.; Siwakoti, Y.P.; Li, L.; Kerekes, T.; Blaabjerg, F. Transformerless Inverter Topologies for Single-Phase Photovoltaic Systems: A Comparative Review. *IEEE J. Emerg. Sel. Top. Power Electron.* **2020**, *8*, 805–835. [CrossRef]
5. Tsai, M.T.; Chu, C.L.; Mi, C.M.; Lin, J.Y.; Hsueh, Y.C. Designing a Single-Stage Inverter for Photovoltaic System Application. *Math. Probl. Eng.* **2013**, *2013*, 912487. [CrossRef]
6. Chen, Y.; Smedley, K.M. A cost-effective single-stage inverter with maximum power point tracking. *IEEE Trans. Power Electron.* **2004**, *19*, 1289–1294. [CrossRef]
7. Gules, R.; Pacheco, J.D.P.; Hey, H.L.; Imhoff, J. A Maximum Power Point Tracking System with Parallel Connection for PV Stand-Alone Applications. *IEEE Trans. Ind. Electron.* **2008**, *55*, 2674–2683. [CrossRef]
8. Thimbiripolage, P.; Nirupa, R. Development of a Microcontroller Based Solar Smart Charge Controller for Solar Street Lamps. In Proceedings of the World Renewable Energy Congress 2009—Asia the 3rd International Conference on Sustainable Energy and Environment (SEE 2009), Bangkok, Thailand, 18–23 May 2009.
9. Akkaya, R.; Kulaksiz, A.A. A microcontroller-based stand-alone photovoltaic power system for residential appliances. *Appl. Energy* **2004**, *78*, 419–431. [CrossRef]
10. Nishida, Y.; Nakamura, S.; Aikawa, N.; Sumiyoshi, S.; Yamashita, H.; Omori, H. A novel type of utility-interactive inverter for photovoltaic system. In Proceedings of the IECON'03. 29th Annual Conference of the IEEE Industrial Electronics Society (IEEE Cat. No. 03CH37468), Roanoke, VA, USA; 2003; Volume 3, pp. 2338–2343.
11. Gonzalez, R.; Gubia, E.; Lopez, J.; Marroyo, L. Transformerless Single-Phase Multilevel-Based Photovoltaic Inverter. *IEEE Trans. Ind. Electron.* **2008**, *55*, 2694–2702. [CrossRef]
12. Calais, M.; Agelidis, V.G.; Dymond, M.S. A cascaded inverter for transformerless single-phase grid-connected photovoltaic systems. *Renew. Energy* **2001**, *22*, 255–262. [CrossRef]
13. *IEEE Standards 1547*; IEEE Standard for Interconnecting Distributed Resources with Electric Power Systems. IEEE: Piscataway, NJ, USA, 2003.

14. Babu, S.M.; Narasimharaju, B.L.; Rathore, A.K. A New Pulsating DC-link Three-Phase Transformerless Inverter for Renewable Applications. In Proceedings of the 2020 IEEE International Conference on Power Electronics, Drives and Energy Systems (PEDES), Jaipur, India, 16 December 2020; pp. 1–4.
15. Ashok Kumar, L.; Indragandhi, V.; Sujith Kumar, N. Design and implementation of single-phase inverter without transformer for PV applications. *IET Renew. Power Gener.* **2018**, *12*, 547–554.

energies

MDPI

Article

Integration of Photovoltaic-Based Transformerless High Step-Up Dual-Output–Dual-Input Converter with Low Power Losses for Energy Storage Applications

Belqasem Aljafari [1], Senthil Kumar Ramu [2,*], Gunapriya Devarajan [3] and Indragandhi Vairavasundaram [4]

[1] Department of Electrical Engineering, College of Engineering, Najran University, Najran 11001, Saudi Arabia; bhaljafari@nu.edu.sa
[2] Department of Electrical and Electronics Engineering, Sri Krishna College of Technology (Autonomous), Coimbatore 641042, Tamil Nadu, India
[3] Department of Electrical and Electronics Engineering, Sri Eshwar College of Engineering, Coimbatore 641202, Tamil Nadu, India; gunapriyadevarajan@gmail.com
[4] School of Electrical Engineering, Vellore Institute of Technology, Vellore 632014, Tamil Nadu, India; indragandhi.v@vit.ac.in
* Correspondence: senthilme90@gmail.com

Abstract: The synchronous integration of numerous input and output loads is possible with multi-input (MI) and multi-output (MO) DC–DC converters. In this paper, the non-isolated DC–DC converter described, which has a high step-up capability and multiple ports for outputs and inputs for energy storage system (ESS) applications. The voltage level of the converter is changeable. The capacity to provide the large voltage increases with a low duty cycle portion, the ease with which each duty cycle can be controlled, and minimal power losses are all advantages of the proposed design. The proposed system offers advantages for applications requiring energy storage. In the continuous conduction mode (CCM), the operation principles, steady-state evaluation, and extracting of the voltage and current coefficients are performed. The supply sources can be inserted or withdrawn without causing a cross-regulation issue in the proposed converter. Ultimately, the functionality of the proposed structure is examined using simulation and the laboratory prototype that has been implemented. The proposed converter achieved 94.3% efficiency at maximum power. In addition, the proposed converter attained minimum losses with a difference of 28.5 W when compared to a conventional converter.

Keywords: multi-input multi-output; step-up converter; energy storage; DC–DC converter

Citation: Aljafari, B.; Ramu, S.K.; Devarajan, G.; Vairavasundaram, I. Integration of Photovoltaic-Based Transformerless High Step-Up Dual-Output–Dual-Input Converter with Low Power Losses for Energy Storage Applications. *Energies* **2022**, *15*, 5559. https://doi.org/10.3390/en15155559

Academic Editor: Nicu Bizon

Received: 8 July 2022
Accepted: 28 July 2022
Published: 31 July 2022

Publisher's Note: MDPI stays neutral with regard to jurisdictional claims in published maps and institutional affiliations.

Copyright: © 2022 by the authors. Licensee MDPI, Basel, Switzerland. This article is an open access article distributed under the terms and conditions of the Creative Commons Attribution (CC BY) license (https://creativecommons.org/licenses/by/4.0/).

1. Introduction

Due to the rapid development of power electronic technology, the ESS dependent on batteries or ultracapacitors has been widely employed in various scenarios, such as photovoltaic and wind energy systems, smart grids, electric vehicles, urban rail transportation systems, etc. [1]. The renewable energy (RE) sources are frequently combined with other clean energy sources. The energy source is varied by using numerous inputs in order to boost dependability, and the use of RE sources have DC voltage outputs, and each source has its unique voltage and current features. MI converters are used to decrease the quantity of converters needed to transform the voltage [2,3]. However, MO converters are required to give the necessary power to loads operating at various voltages. A multi-input–multi-output converter (MIMO) is created by a cascading connection of single-input–multi-output (SIMO) and multi-input–single-output (MISO) converters [4]. The MIMO converter provides benefits over multiple individual converters, such as fewer circuit components and conversion phases that will lead toward a more compact design and a cheaper price. In some circumstances, it could be necessary to integrate various renewable sources with varying power levels, such as photovoltaic (PV) panels, fuel cells,

batteries, and ultracapacitors, in order to provide a single load [5]. Therefore, it is important to combine the various energy sources as efficiently as feasible. A MIMO can resolve this problem by combining the advantages of each source into a single converter to provide a controlled DC output and energy storage, or it can provide the AC load after passing through a DC–AC inverter, as shown in Figure 1.

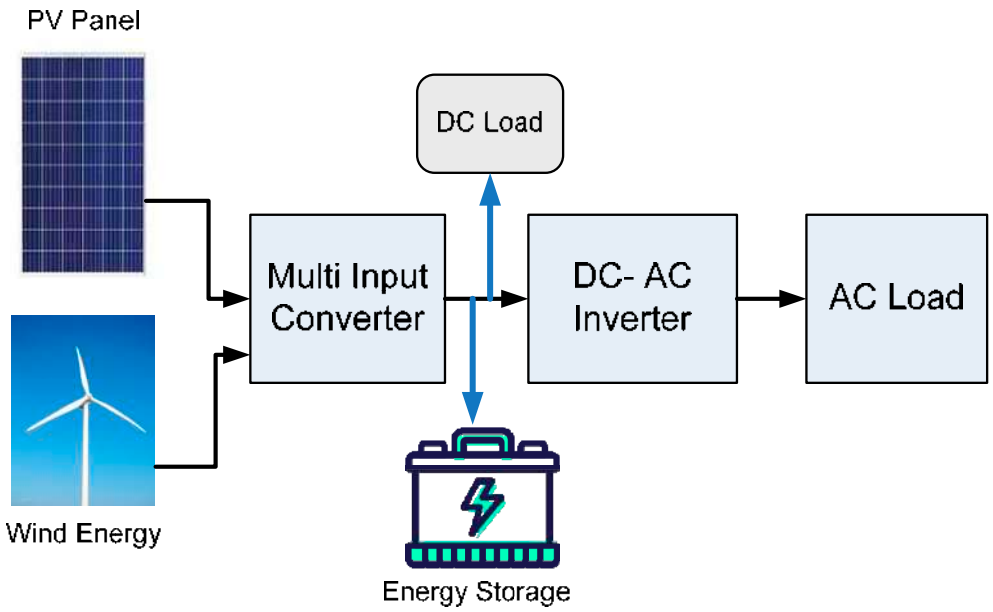

Figure 1. Block diagram of MIMO converter in energy storage.

MIMO converter offers various merits, when compared to single-input–single-output (SISO), SIMO, and MISO converters. A MIMO converter enables customers to employ them in numerous sorts of loads by enabling input from several sources. These converters often assist in combining several sources that produce DC power directly. Due to environmental concerns and the need for stability, research emphasis has recently shifted to micro grids that combine various energy storage devices and renewable energy sources. MIMO converters are essential in such situations for integrating and merging these energy sources to serve the loads when compared to SISO and SIMO converters. The MISO converter is the most often suggested method by researchers to mix various energy sources at various voltage levels [6]. These converters have the drawback of having just one source able to power the load simultaneously. By splitting the current from sources, the MIMO guarantees a seamless transition of power across loads and finally divides the power appropriately when relating to the MISO converter.

MIMOs can be classified as isolated or non-isolated. The isolated-type MIMO uses a transformer with numerous secondary circuits to interact with numerous loads. In this instance, just one of the outputs is highly restricted; the other outputs are connected to additional subordinate windings. In non-isolated MIMOs, there is no electrolytic separation between various ports [7]. Additionally, they are further divided into single and numerous inductors depending on the quantity of the inductive loads. MIMO converters provide the benefits of a lower device count, better power density, and fewer power transmission phases as compared to the traditional DC–DC system design with separate converters. The input cells are typically linked in parallel at the input stage of numerous single inductor MIMO converters, but the output cells may be linked in series or in parallel [8,9]. Due to the common inductor, there is a cross-regulation issue with the output cells that are linked in parallel. Implementing the appropriate control to decrease the reciprocal coupling among output cells coupled in parallel is inherently difficult [10].

The charge sharing method for creating numerous outputs is described in [11]. The authors suggested that even in the CCM, the outputs are load-dependent. A MIMO

converter's setup and its transactional and analytical challenges are addressed in [12]. The functionality of this converter family depends on a time-multiplexing technique [13]. There were a lot of cross-regulation issues, since the outputs of this specific type of MPC are all linked to the same switch node. The dynamic responsiveness of the converters discussed before is typically insufficient in terms of efficiency. A DC–DC converter with resonant MI and MO has been developed [14]. To ensure zero-voltage switching (ZVS) including all power switches during both turn-on and turn-off, the control system must adhere to a certain PWM technique. To address the cross-regulation issue, a model predictive control-based digital control system has been presented [15].

In [16], a unique construction for MIMO DC–DC boost converters is put forth, one that features a high switching frequency without a transformer, a constant current, a high voltage gain without a large duty cycle, and a high voltage gain. A unique non-isolated SEPIC-based multi-input structure is discussed in [17] to address the issues with intermittency of discontinuous power supply. The authors of [18] introduce a new double-input architecture built from a boost and Y-source DC–DC converter [19]. A deadbeat-based solution that incorporates input current and output voltage regulation has been suggested to enhance the performance of regulation [20]. These techniques demand some quite challenging computations. A limitless number of input devices cannot be integrated in a large portion of the previous research work because the time-multiplexing regulation cannot be ignored [21]. Furthermore, the shared inductor and the cross-regulation issue cannot be solved when the outputs are connected with one another. In some circumstances, this limitation exponentially increases the related control complexity. There are various uses, including solar power supply, energy storage, and Internet-of-Things (IoT) devices, despite the non-common ground caused by the series assembly type [22,23]. The design technique is rigorously followed to obtain the controller's optimal performance. In this research, a dsPIC30F4013 controller was used to execute the proposed converter.

A switched capacitor-based MIMO converter with a high voltage gain and an easy control scheme is given in [24]. But the number of components is very high. A boost converter using MIs and MOs has been proposed in [25], and it is appropriate for combining various energy sources in EVs. The inability to use two sources together is a drawback of this arrangement. In [26], a non-isolated MIMO converter with a high gain and no linked inductor was constructed. With this converter, the voltage increase ratio is greater. However, compared to the proposed converter, it has less voltage gain. The MI step-up converter is reported in [27] for integrating several energy sources. However, the voltage gain of this converter is less than the proposed converter. Hence in this paper, non-isolated structure, high voltage gain, minimum number of components are considered to design the proposed converter.

This paper focuses on analyzing and proposing a new MIMO boost converter with high efficiency and constant input and output currents. There is no requirement for time-multiplexing, and the accompanying control technique is fairly simple. In addition, adjustable additions and deletions of inputs and outputs are possible without altering the control strategy. The proposed converter enables the two inputs to feed the load simultaneously with a continuous input current. As a function, this arrangement is very generic for expansion, has uncomplicated control, is highly flexible, and has no cross-regulation issue.

The structure of this paper is as follows: The operation of the proposed converter is provided in Section 2. The steps in the proposed converter's design are described in Section 3. The simulation and experimental results of the proposed converter are discussed in Section 4. A comparison of the results obtained to previously released works is shown in Section 5. The paper's conclusion is the focus of Section 6.

2. Operation of the Proposed Converter

In its most basic form, an MI converter is a circuit layout that incorporates several input voltage sources with various voltage levels and delivers an output DC load. If a

DC–DC converter is synthesized using a pulsing voltage source, or a pulsating current source relies on the characteristics of circuits and systems [28], these modules must be linked in parallel to provide the load in the event of pulsing current sources, such as boost converters. This paper studies and analyses the converter's MI and MO configurations, which are depicted in Figure 2.

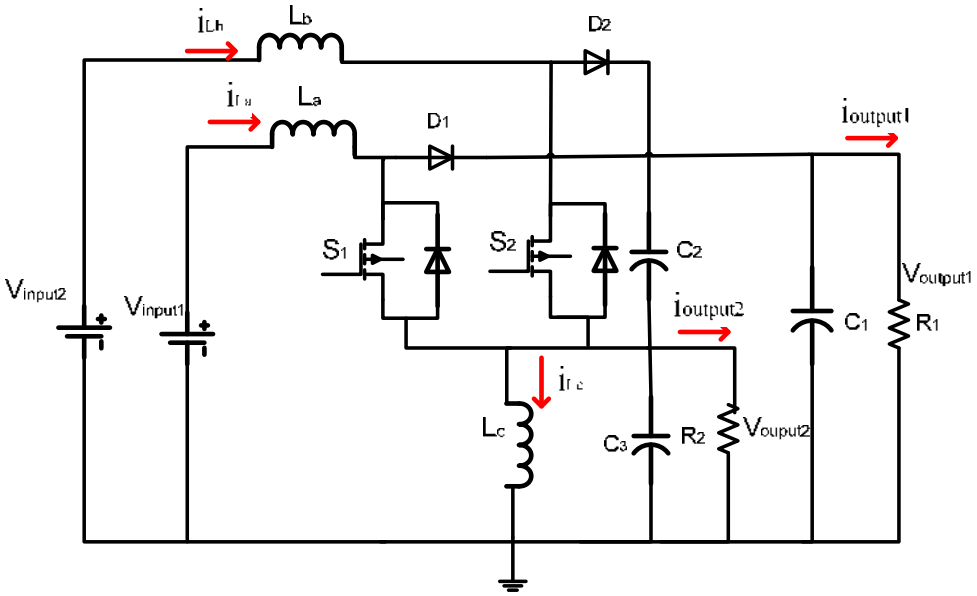

Figure 2. Circuit diagram of proposed converter.

Each of the pulsing current sources is made up of inductors (L_a and L_b), diodes (D_1 and D_2) and power switches (S_1 and S_2). They are each linked to various voltage sources at various voltage levels, notably V_{input1}–V_{input2}. Additionally, regardless of the switching strategy, the capacitors C_1 and C_3 and the inductor L_c are to guarantee the output current's continuance. The proposed converter's working principal is explained below, with discussions of theoretical voltage and current studies of each CCM and discontinuous conduction mode (DCM).

2.1. Mode 1 Operation

The schematic diagram of Mode 1 is represented in Figure 3. In Mode 1, switch S_1 conducts, while switch S_2 remains non-conducting at the beginning of this time period. The corresponding time period is represented as T_{on}. Since the inductor L_a's current rises proportionately as a result of being closely linked to the first voltage input (V_{input1}), the amount of energy that can be stored in L_a also grows. Diode D_1 is reverse-biased. As a result, the output load's currents are provided by the inductors L_b and Lc via the capacitors C_1 and C_3. To do this, there is a steady reduction in the stored energy of C_1, C_3, L_b, and L_c.

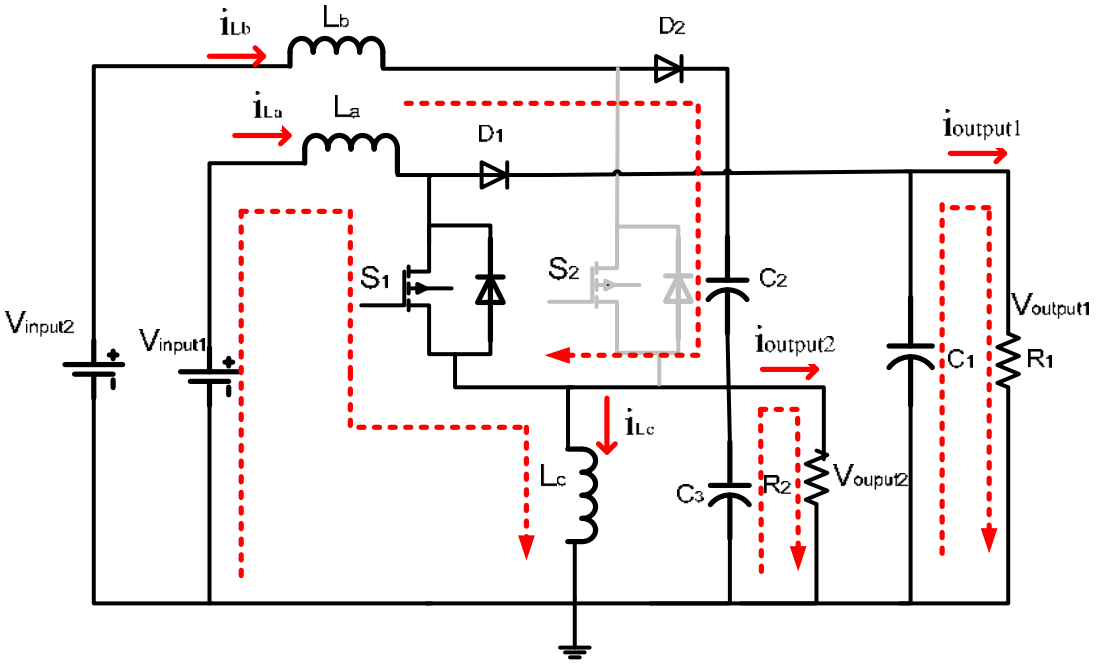

Figure 3. Mode 1 operation (— Current flow direction).

2.2. Mode 2 Operation

The schematic diagram of Mode 2 is represented in Figure 4. In this state, switch S_1 is turned off, while switch S_2 is active. The period of time is now represented as Toff. In this mode, the circuit is supplied by input source V_{input2}, which are both present. Reverse bias is present in diode D_1. As a result, the capacitors C_1 and C_3 and the inductors L_b and Lc, are linked. L_a's current is thereafter sharply decreased from its peak level to bottom value as a result of the energy stored in L_a being recycled to inductor L_c and capacitor C_3. As a consequence, from its lowest value to its highest value, the current passing through L_b and L_c is sharply increased. The capacitors C_1 and C_3's voltages are increasing. The key waveforms under the CCM condition are displayed in Figure 5.

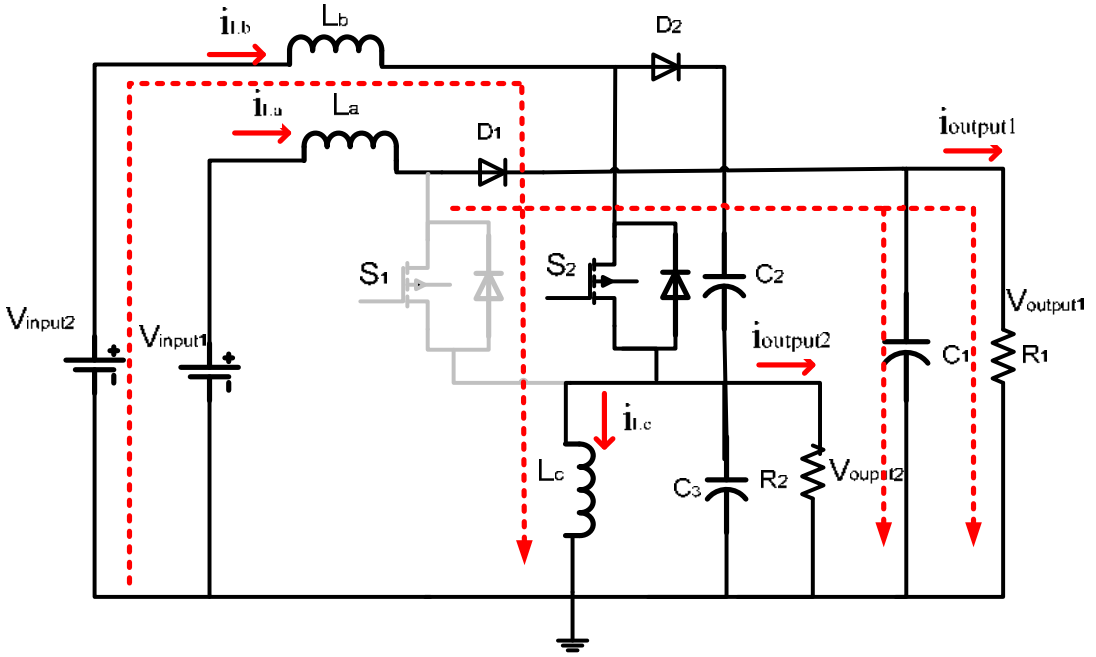

Figure 4. Mode 2 operation (— Current flow direction).

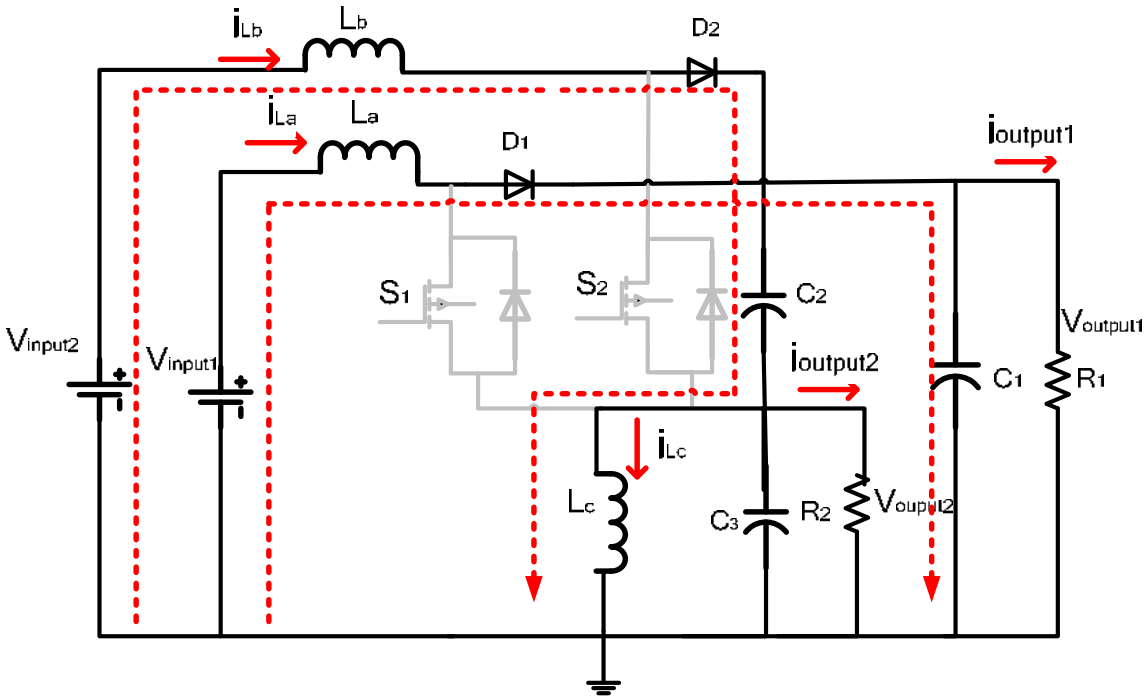

Figure 5. Mode 3 operation (—- Current flow direction).

2.3. Mode 3 Operation

The schematic diagram of Mode 3 is represented in Figure 5. In this state, both switches S_1 and S_2 are turned off. The stored energy in L_b is released through D_2 for charging C_2, and the energy stored in L_a is supplied to R_1 at the same time. Currents going through L_a and L_b are gradually decreased. The key waveforms are displayed in Figure 6.

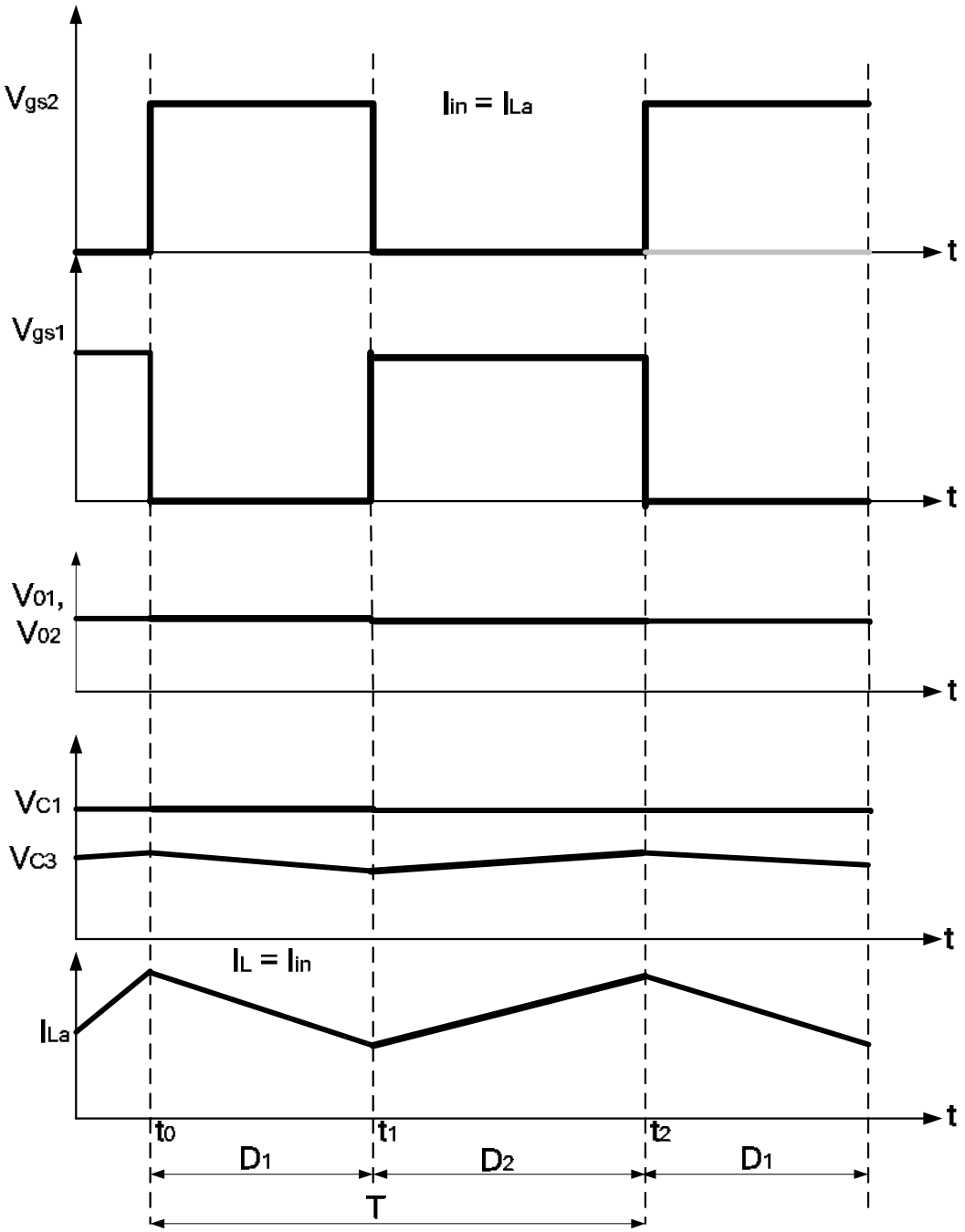

Figure 6. The proposed converter's theoretical operational waveform.

3. The Proposed MIMO Converter's Design Process

The basic control strategy on the input side involves controlling the input sources while employing the matched input cells as controllable sources. The steady-state flow analyses are only computed in the CCM since the converter operation is chosen in CCM. Under the CCM scenario, the optimum voltage gain of the proposed converter is first determined, followed by the average current of the power components. The equipment's current stress predictions are determined in the last phase.

It is possible to regulate the output cells separately. Direct duty cycle control is achieved using the switches S_1 and S_2 of the output voltage source mode (VSM) cell if a controllable output current is needed [29]. Voltage-programmed regulation can be used when a controlled output voltage is necessary. We show the MI and MO types of

the proposed converter here with an experiment, where one output provides a constant current via direct duty cycle control, while the second output delivers constant voltage via voltage-programmed regulation. Here, the MI and MO types of the proposed converter are presented, where the first output offers a fixed current, and the second output delivers a fixed voltage.

3.1. Voltage Gain

The output voltages of the converters are,

$$V_{Ouput1} = V_{c1} = \frac{V_{input1}}{1 - D_1} = \frac{5}{1 - 0.79} = 23.80 \text{ V} \tag{1}$$

$$V_{Ouput2} = V_{c3} = \frac{V_{input2}}{1 - D_2} = \frac{12}{1 - 0.67} = 36.36 \text{ V} \tag{2}$$

This configuration's conversion ratio can be written as [30],

$$G_1 = \frac{V_{output1}}{V_{input1}} = \frac{1}{1 - D_1} \tag{3}$$

$$G_2 = \frac{V_{output2}}{V_{input2}} = \frac{1}{1 - D_2} \tag{4}$$

The load current can be represented as,

$$I_0 = \frac{V_{output}}{R} = (1 - D_1)I_{La} + (1 - D_2)I_{Lb} \tag{5}$$

The inductor current I_{Lc} can be written as,

$$I_{Lc} = D_1 I_{La} + D_2 I_{Lb} \tag{6}$$

3.2. Power Consumed by Each Source

The closed-loop regulation of the output current of all sources, the inductor current I_{La}, is kept constant. A closed-loop control is also used to adjust the output voltage of the second output. The output and input currents of the VSM cell are directly related to one another. As a result, fixed duty cycle regulation can be used to produce a constant current at the first output. Here, we employ a basic duty cycle regulation to retain the steady output current. Considering that the duty cycle D_1 of switch S_1 and the duty cycle D_2 of switch S_2 are equal, the power produced from the input sources through the associated input cell during ideal circumstances can be stated as,

$$P_{input1} = V_{input1} D_1 I_{La} \tag{7}$$

$$P_{input2} = V_{input2} D_2 I_{Lb} \tag{8}$$

where I_{La} and I_{Lb} are the steady-state inductor current, and P_{input1} and P_{input1} are the power supplied from the input sources V_{input1} and V_{input2}, respectively. The connection shown below can therefore be obtained:

$$\frac{P_{input1}}{P_{input2}} = \frac{V_{input1}}{V_{input2}} \tag{9}$$

According to the calculations provided, every input source's power consumption is related to its associated voltage when the fixed current regulation is used. It is a result of the switches on the respective input cells having the same duty cycle.

It is important to remember that when there are more than two input cells, some of them are regulated to supply a fixed current, while other inputs are directly controlled by

duty cycle regulation. The functionality of this setup will not be impacted if any of these input cells are removed. Power supplied over the first current of input would instantly rise whenever the power supplied through the second cell diminishes. The direct connection between the input and output currents remains constant at the same moment. In this technique, the input voltage providing the second input cell, i.e., V_{input2}, is subjected to a designing restraint to guarantee appropriate operation. Particularly, V_{input2} needs to be lower than the power needed mostly by the output loads.

The necessary power through the loads Po can be represented as follows:

$$P_o = (1 - D_1)^2 I_{La}^2 R_1 + (1 - D_2)^2 I_{Lb}^2 R_2 \tag{10}$$

where R_1 and R_2 are the respective loads of the two output cells.

3.3. Inductor Selection

The inductor current selection is significant since it is the primary variable in the entire control strategy. The input and output power must comply with the relationship $P_{in,\max} > P_o$ in order for the proposed converter to function properly. The selection of inductor and change in inductor current can be represented as,

$$\Delta i_{La} = \frac{1}{L_a} V_{input1} D_1 T \tag{11}$$

$$L_a = \frac{V_{input1} D_1 T}{\Delta I_{La}} = \frac{V_{input1} D_1}{f \Delta I_{La}} = \frac{5 \times 0.79}{25,000 \times 7} = 0.225\ \mu\text{H} \tag{12}$$

$$\Delta i_{Lb} = \frac{1}{L_b} V_{input2} D_2 T \tag{13}$$

$$L_b = \frac{V_{input2} D_2 T}{\Delta I_{Lb}} = \frac{V_{input2} D_2}{f \Delta I_{Lb}} = \frac{12 \times 0.67}{25,000 \times 7} = 0.8\ \mu\text{H} \tag{14}$$

The choice of the inductor is crucial to guaranteeing a constant source current for the output cells. The proposed arrangement operates in its worst possible condition when there is just a single source of power going to the output cells, and the switches for the two output cells are continuously off. The source with the fixed input cell is the source that consistently supplies power for the proposed control mechanism.

3.4. Capacitor Selection

The output voltage of the VSM unit should be constant in order to preserve the steady-state connection between the input and the current. The choice of the appropriate capacitor is determined by this criterion. The voltage drop of C_1 can be written as,

$$\Delta V_{c1} = \frac{I_{La}}{f \times C_1} \tag{15}$$

To guarantee a constant output voltage, the values of C_1 and C_3 must meet the inequality shown below:

$$C_1 = \frac{I_{01}}{f \times \Delta V_c} = \frac{2.4}{25,000 \times 15} = 6.4\ \mu\text{F} \tag{16}$$

$$C_3 = \frac{I_{03}}{f \times \Delta V_c} = \frac{1.5}{25,000 \times 15} = 4\ \mu\text{F} \tag{17}$$

3.5. Stability Analysis

To achieve system stability, the closed-loop poles of the characteristic polynomial should be within the unit circle [30]. Because it transfers the left half of the S-plane to the inside of the unit circle in the Z-plane it preserves compensator stability. The projected error variables must meet at zero from any non-zero beginning value, since the controller

is primarily designed to check the robustness of the control rule. This validates that the system under consideration is stable with the appropriate pole positions. The transfer function of the proposed converter for C_3 = 4 µF is found as follows,

$$H(s) = \frac{6 \times 10^6 s^2 + 3 \times 10^7 s + 11 \times 10^{12}}{4s^4 + 5200s^3 + 7500s^2 - 4 \times 10^5 s + 750 \times 10^{11}} \quad (18)$$

The converter remains steady even when the value of the capacitor C_1 is increased. The system poles, on the other hand, migrate to the right side of the axis, and their imaginary values are falling. As a result, by lowering the imaginary quantities of the poles, the frequency of the converter's dampening variations will be lowered.

4. Results and Discussion

To assess its performance, the proposed converter was simulated under various circumstances. The proposed system was developed and modeled using MATLAB/Simulink software. The values of the parameters are shown in Table 1. Figure 7 shows the input voltage waveforms of the proposed converter. The matching input voltages 5 V and 12 V are kept at a constant state.

Table 1. Design parameters.

Parameters	Symbol	Value
Input Voltages	V_{input1} V_{input2}	5 V 12 V
Output Voltages	$V_{output1}$ $V_{Output2}$	24 V 36 V
Capacitors	C_1 C_2 C_3	6.4 µF 4 µF 4 µF
Inductors	L_a L_b L_c	0.225 µH 0.8 µH 0.8 µH
Load Resistance	R_1 R_2	10 Ω 15 Ω
Duty Cycle	D_1 D_2	0.79 0.67
Switching Frequency	*Fs*	25,000 Hz

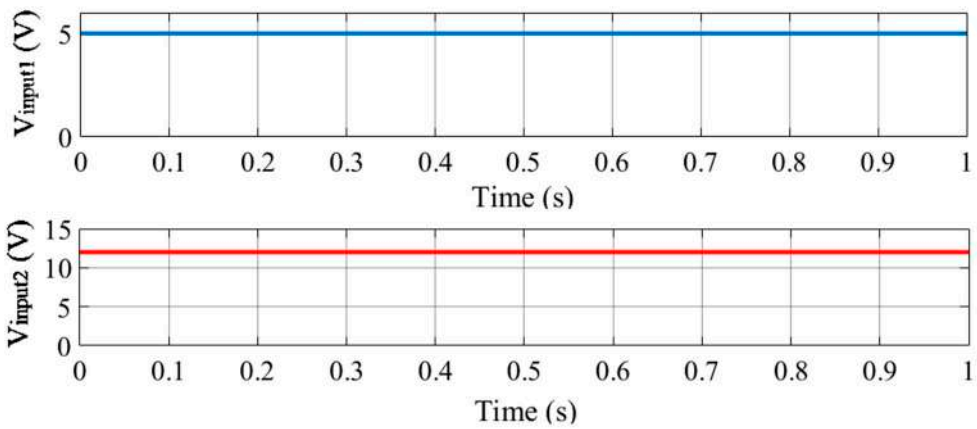

Figure 7. Simulation response of input voltage waveform.

Figure 8 shows the equivalent switching pulse waveforms. The corresponding input voltages 5 V and 12 V are maintained as a steady-state. The corresponding switching pulse waveforms are illustrated in Figure 8. By switching the inductor at a frequency of 25 kHz, the inductor waveform is produced. Figure 9 shows the input inductance currents (I_{La} and I_{Lb}) and the output capacitance ($V_{output2}$). The current in the circuit tries to increase, while the coil stores energy when the switch is turned on, and the input voltages are given to the inductor circuit. The output capacitor provides the load current during this time. The proposed converter has a characteristic that minimizes switching fatigue and capacitive turn-on loss since there is no voltage spike across the switch because the energy stored in the leakage current is released through the diodes in the switch turn-off time. Figure 10 shows the simulation response of the output voltages. The output voltages can produce up to 24 V and 36 V. As a result, it was determined that combining a MIMO converter with a PV system produces 3 to 4 times the amount of input voltages.

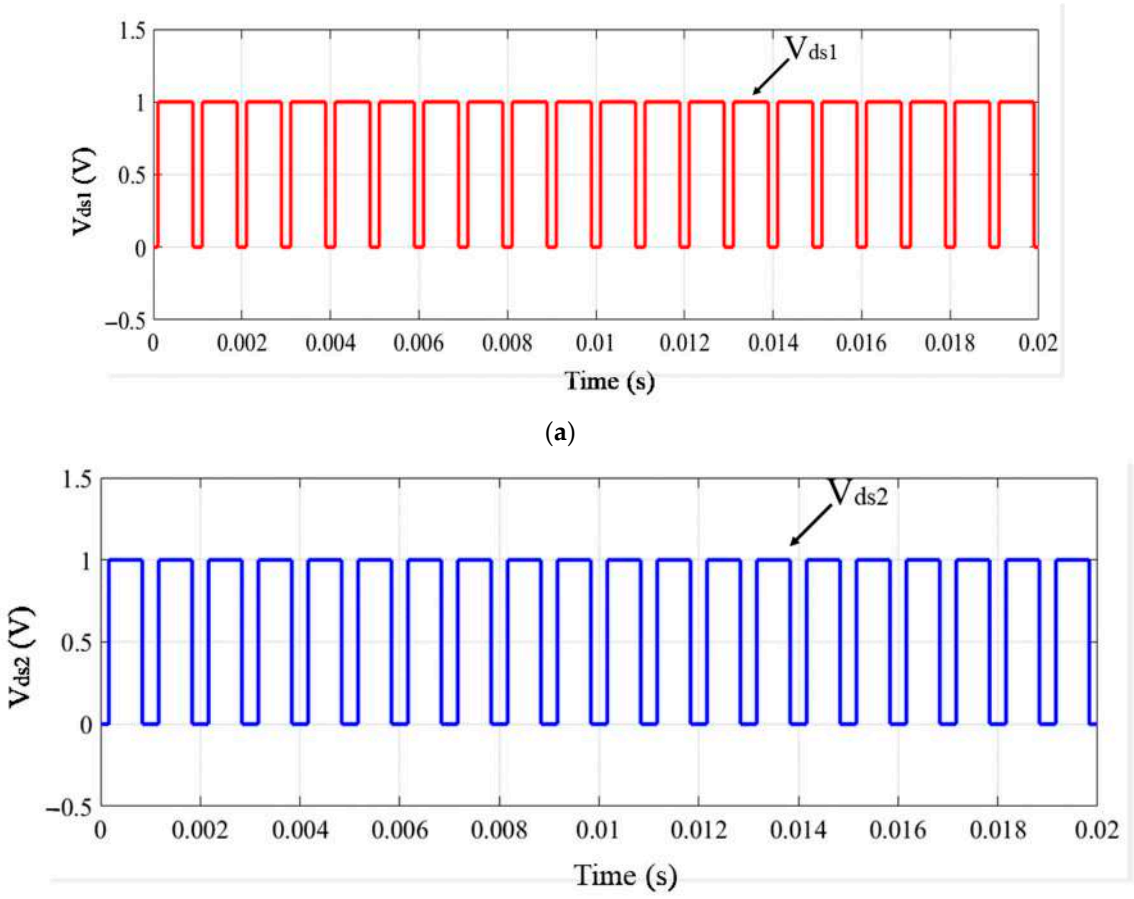

Figure 8. Simulation response of gate pulses (**a**) V_{ds1} and (**b**) V_{ds2}.

Experimental Results

To show off the effectiveness of the proposed converter, a lab prototype was designed and is represented in Figure 11. The switching gate pulses are produced using a dsPIC 30F4013 micro controller. The proposed converter was tested under a constant load, step change in load, and variable load change conditions.

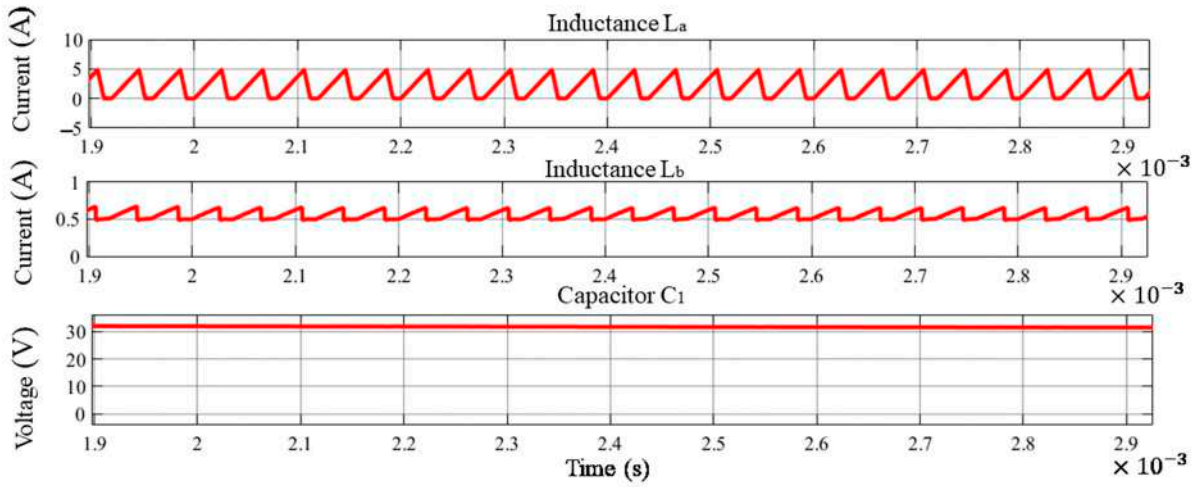

Figure 9. Simulation response of input inductor currents and capacitance voltage.

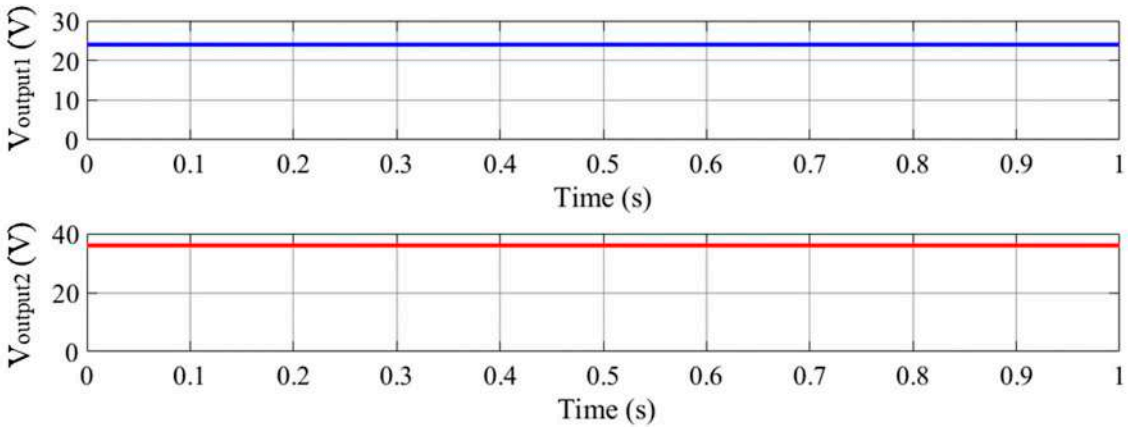

Figure 10. Simulation response of output voltages.

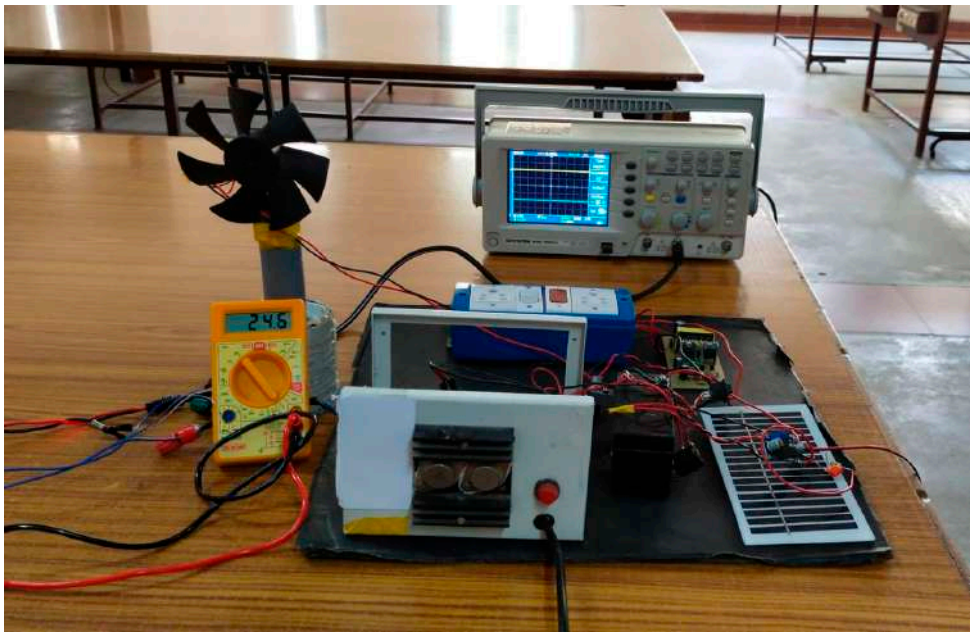

Figure 11. Experimental setup.

When the fixed current control is the supplied input, the appropriate waveform is seen in Figure 12. To assess the converter's ability to balance the voltage, this input voltage (5 V) was recorded during steady-state execution (1 Div. = 5 V). The experimental waveform of input voltage 2 is represented as Figure 13 under a fixed current control state. It demonstrates that the proposed MIMO converter can maintain a steady DC voltage level under CCM while operating with both stable and unstable loads.

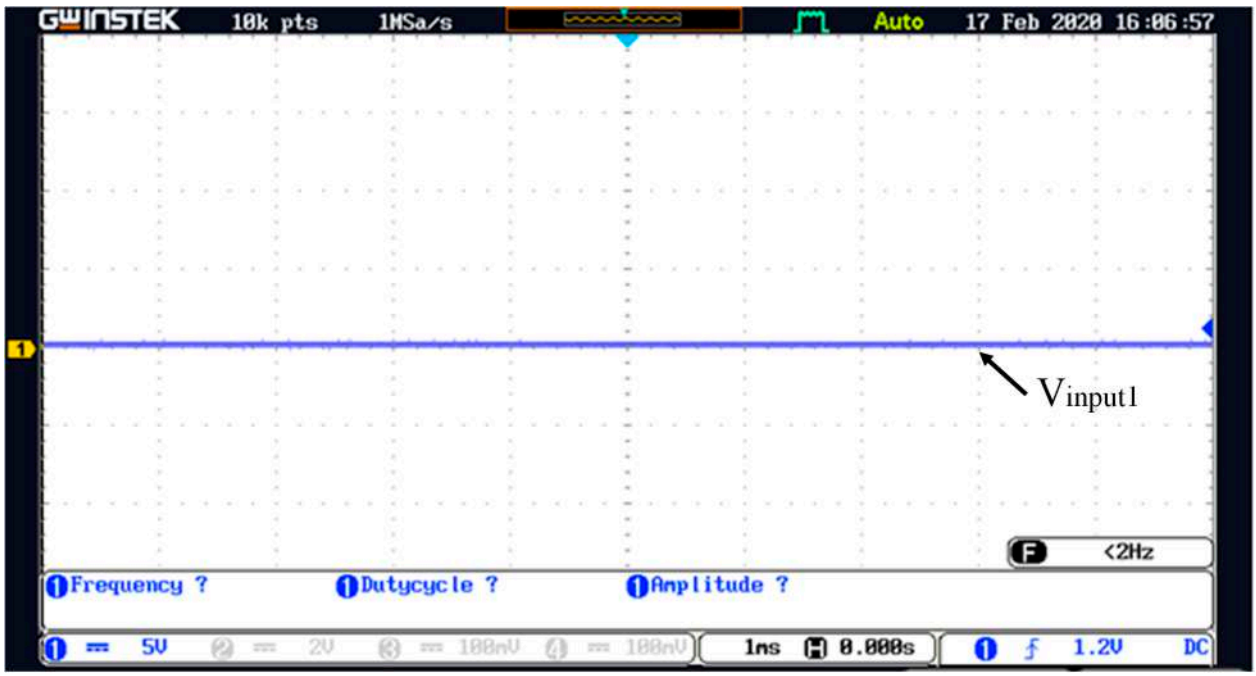

Figure 12. Input voltage 1 waveform.

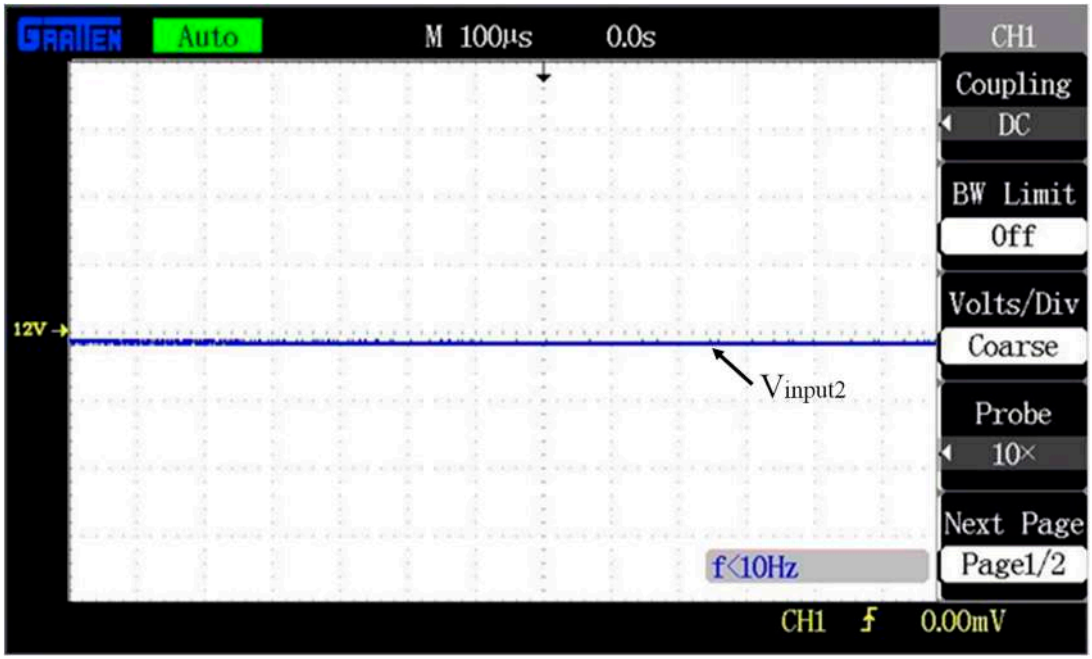

Figure 13. Input voltage 2 waveform.

Figure 14 shows the output voltage 1, the inductance voltage V_{La}, and the drain-to-source voltage of switch 1. The driving signal for the two input units is identical in this scenario since it is produced through closed-loop regulation. The inductive voltage (V_{Lb})

waveform is shown in Figure 15 (1 Div. = 2 V). It displays how the converter can function in two modes when the frequency is pulse-width-modulated. It is important to observe that at the conclusion of each switching cycle, the current flowing through the inductor $L_{a,b}$ becomes continuous. As a result, the proposed converter's operation in the CCM is confirmed. Figure 16 exhibits the output voltage 1 and the drain-to-source voltages of switch 2. Figure 17 depicts the output voltage 2 experiment waveform (1 Div. = 10 V). The proposed converter could deliver many outputs at once, according to the experimental findings. It is clear that duty cycles and switching periods of the two input cells varied. It demonstrates that the input voltage is triple the output voltage.

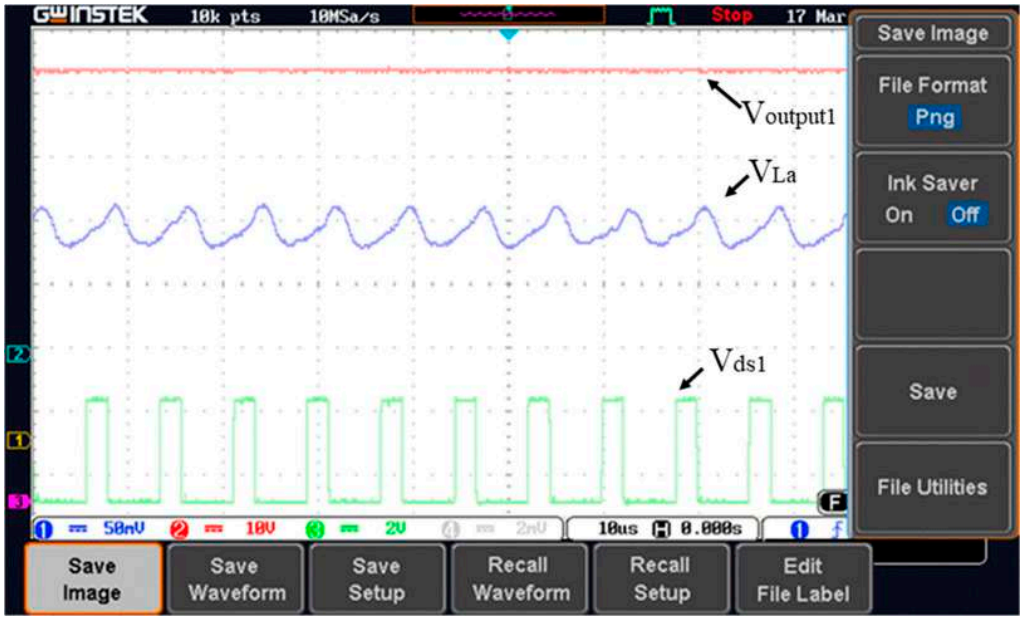

Figure 14. Switching voltage 1, inductor voltage V_{La}, and output voltage 1 waveform.

Figure 15. Inductance voltage V_{Lb} waveform.

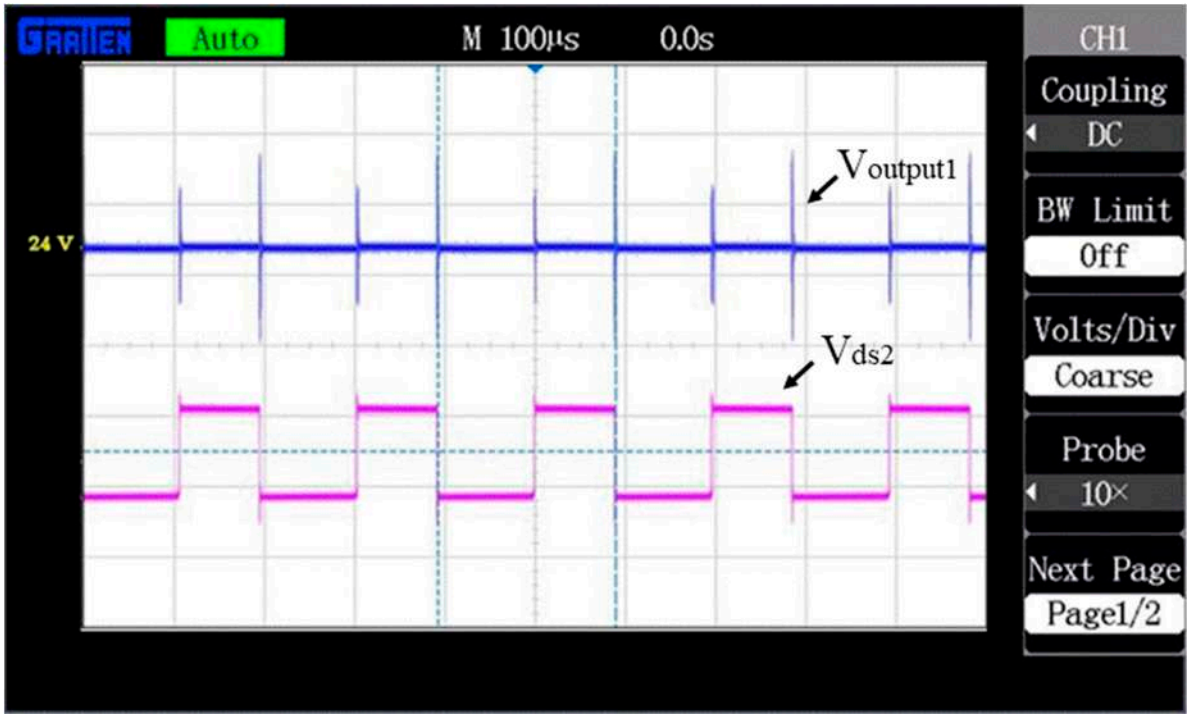

Figure 16. Switching voltage 2 waveform.

Figure 17. Output voltage 2 waveform.

Figure 18 illustrates the relevant functioning waveforms of variable loads under the CCM. The output status is also unchanged as before. We confirm that the two output streams are separate of one another without needing any additional control obtained from the experiments. Therefore, regardless of the quantity of outputs, the control strategy can be the same straightforward constant current regulation. A step voltage command response is shown to demonstrate the proposed multi-objective control. An acceptable overshoot and a disturbance were seen as presented. The proposed converter is integrated into the PV system during fluctuating load under the CCM as shown in Figure 19 (1 Div. = 10 V). This

result implies that the proposed converter can operate with ease in conditions of fluctuating irradiance and load.

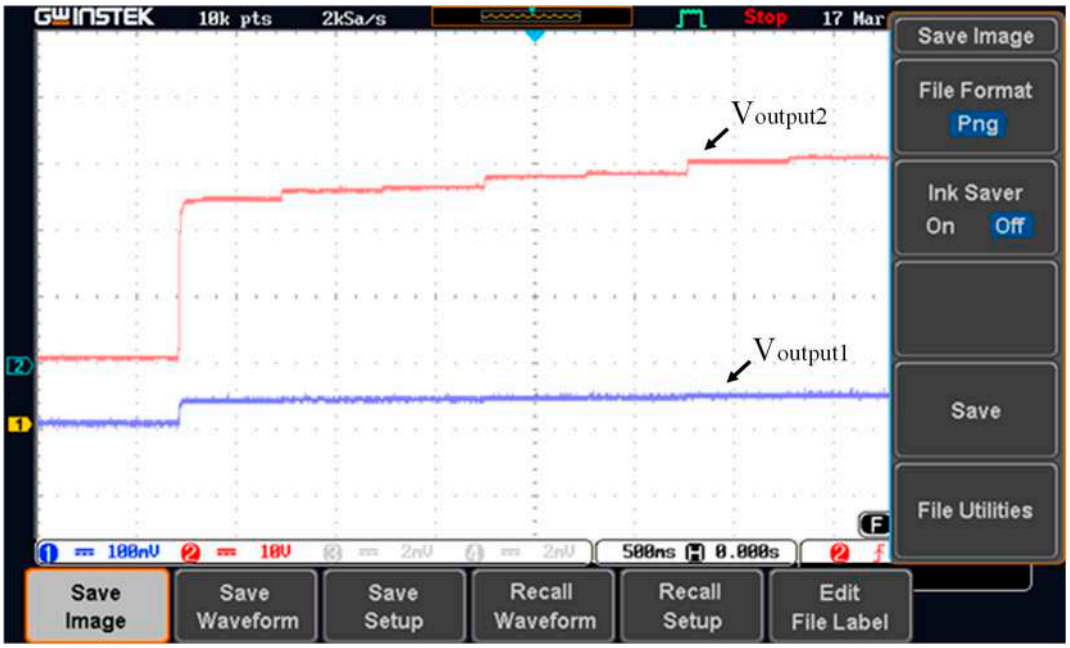

Figure 18. Variable voltages waveform when step change in load.

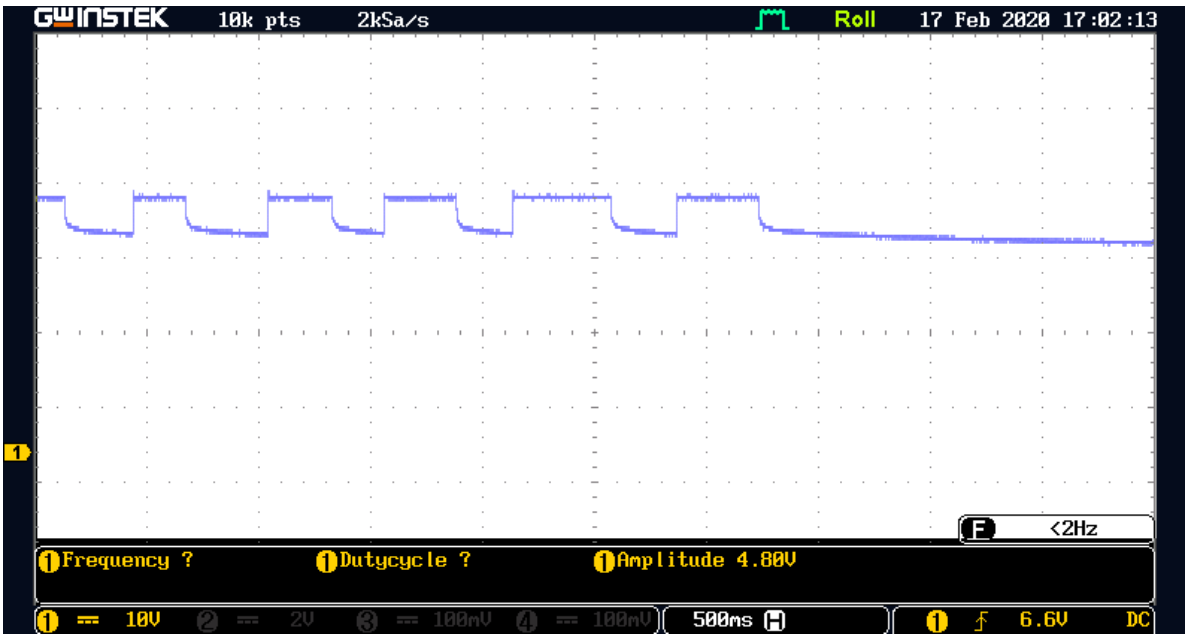

Figure 19. The output voltage ($V_{output2}$) under variable changes in the load conditions.

5. Discussion

A detailed comparative analysis of a proposed converter with existing published converters is provided in Table 2 to further highlight the essential characteristics of the pro-posed converter. These converters are primarily contrasted in terms of converter type, quantity of switches, inputs, outputs, efficiency, and capacity for expansion and inferences. The proposed converter has a fewer number of switches as compared to the previous converters. Since, cross-regulation is not an issue, the appropriate control is simple and very effective. Furthermore, the stability study finds a high power density,

which results in a high extended capacity. Figure 20 compares the proposed converter's power losses to that of a typical converter, with an anticipated total loss difference of 28.5 W. With conduction losses (S_1 and S_2), inductor core losses, induction winding losses, diode conduction losses, and capacitor losses, the proposed converter has lower losses than the conventional converter. Reduced conduction losses for switches and diodes as a consequence account for most of the efficiency gap between the two converters. The experimental results of the proposed converter's maximum efficiency under various load conditions are shown in Figure 21. At maximum loading power, the converter efficiency is predicted to be 94.3%.

Table 2. Comparison with existing works.

Ref.	Converter Type	Number of Switches					IV	OV	PD	EC	Stability	Efficiency	Observations
		D	C	S	L	Outputs							
[1]	MIMO high step-up transformerless converter	4	3	4	1	2	30 V, 20 V	21 V, 8 V	Medium	Medium	NR	93.98	Hybrid energy sources integration and MO
[8]	Step-up boost converter with CLD cell	1	5	2	2	2	34 V, 48 V	80 V, 40 V	Medium	Medium	NR	93.4	high voltage gain without maximum value of duty cycle
[12]	Switching boosting action-based MIMO converter	3	5	4	1	2	25 V, 20 V	22 V, 11 V	High	Low	NR	92.1	Improve the power density in various load applications
[16]	Single-inductor MIMO converter	4	3	4	2	1	24 V, 20 V	12 V, 8 V	Medium	Low	NR	89.7	Integration of various loads with minimum number of components
[28]	Single-inductor–multi-input–multi-output DC–DC converter	4	3	4	1	3	18 V, 22 V	12 V, 8 V	Low	Medium	NR	91.5	Integration of multiple loads with fixed current control
Proposed Work	High step-up MIMO Converter with low power losses	2	3	2	3	2	5 V, 12 V	24 V, 36 V	High	High	Reported	94.3	Tarnsformerless MIMO converter with fewer number of switches

D—Diode, C—Capacitors, S—Switch, L—Inductors, IV—Input Voltage, OV—Output voltage, PD—Power Density, EC—Extension capability, and NR—Not Reported.

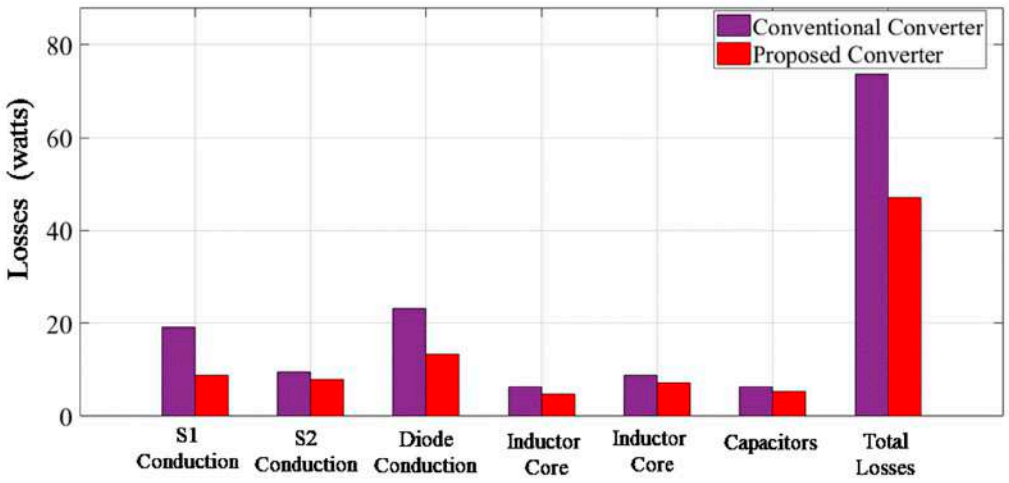

Figure 20. Power loss comparison of proposed converter with traditional converter.

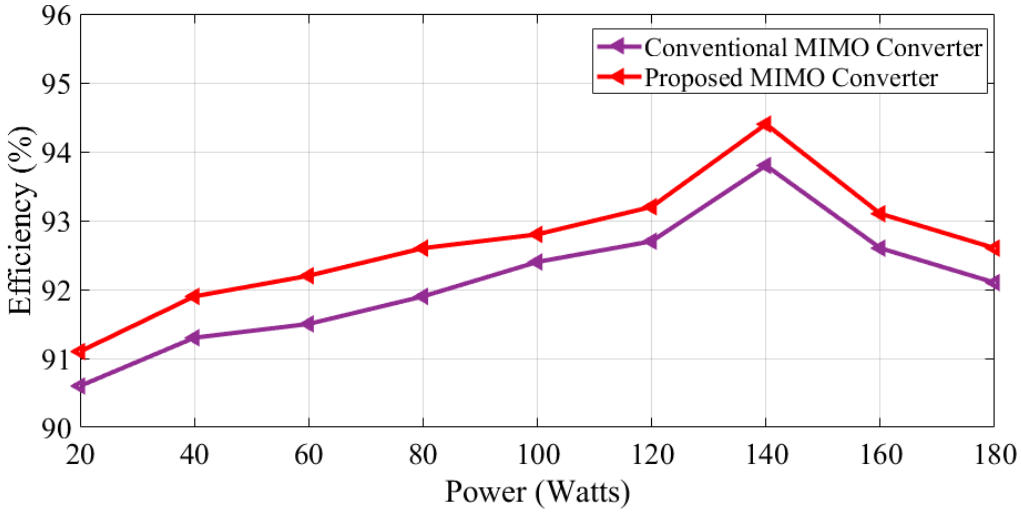

Figure 21. Power versus efficiency graph.

6. Conclusions

This work developed a transformerless and non-isolated rapid step-up MIMO DC–DC power converter with low power losses. The proposed converter is suitable for energy storage applications since it simply has two switches. Because the proposed converter runs in just two operational modes throughout each duty cycle, the converter's control technique is simple. The performance concepts, theoretical voltage or current assessments, and steady-state analysis have been described. Furthermore, the proposed converter has two voltage gains for the first and second outputs. To ensure that the proposed converter works properly, it was compared to several different topologies. According to the comparative results, the proposed converter has a greater output voltage, fewer components, and minimal power dissipation. To that objective, a simulation and laboratory prototype was built for testing purposes, and experimental findings have been presented.

Author Contributions: Conceptualization, S.K.R.; methodology, S.K.R.; investigation, I.V.; writing—original draft preparation, S.K.R. and I.V.; writing—review and editing, G.D.; resources, B.A.; visualization and administration, S.K.R. and I.V.; funding acquisition, B.A. All authors have read and agreed to the published version of the manuscript.

Funding: This work was funded by the Research Groups Funding program grant code (NU/RG/SERC/11/6).

Institutional Review Board Statement: Not applicable.

Informed Consent Statement: Not applicable.

Data Availability Statement: Not applicable.

Acknowledgments: The authors are thankful to the Deanship of Scientific Research at Najran University for funding this work under the Research Groups funding program grant code (NU/RG/SERC/11/6).

Conflicts of Interest: There are no conflict of interest declared by the authors.

References

1. Saadatizadeh, Z.; Heris, P.C.; Mantooth, H.A. Modular expandable multiinput multioutput (MIMO) high step-up transformerless DC–DC converter. *IEEE Access* **2022**, *10*, 53124–53142. [CrossRef]
2. Shayeghi, H.; Pourjafar, S.; Hashemzadeh, S.M.; Sedaghati, F. Presenting of the magnetic coupling-based transformer-less high step-up DC-DC converter for Renewable Energy Applications. *Int. Trans. Electr. Energy Syst.* **2022**, *2022*, 3141119. [CrossRef]
3. Madhana, R.; Mani, G. Power enhancement methods of renewable energy resources using multiport DC-DC converter: A technical review. *Sustain. Comput. Inform. Syst.* **2022**, *35*, 100689. [CrossRef]
4. Bahrami, H.; Allahyari, H.; Adib, E. An improved wide ZVS soft-switching range PWM bidirectional forward converter for low power applications with simple control circuit. *IET Power Electron.* **2022**, 1–12. [CrossRef]

5. Appikonda, M.; Dhanalakshmi, K. Small-signal model and control approach for a dual input boost converter with VMC. *Int. J. Electron.* **2021**, *109*, 1035–1058. [CrossRef]
6. Ahmad, F.; Haider, A.A.; Naveed, H.; Mustafa, A.; Ahmad, I. Multiple input multiple output DC to DC converter. In Proceedings of the 2018 5th International Multi-Topic ICT Conference (IMTIC), Jamshoro, Pakistan, 25–27 April 2018.
7. Li, X.L.; Tse, C.K.; Lu, D.D.-C. Synthesis of reconfigurable and scalable single-inductor multiport converters with no cross regulation. *IEEE Trans. Power Electron.* **2022**, *37*, 10889–10902. [CrossRef]
8. Malik, M.Z.; Chen, H.; Nazir, M.S.; Khan, I.A.; Abdalla, A.N.; Ali, A.; Chen, W. A new efficient step-up boost converter with CLD cell for electric vehicle and New Energy Systems. *Energies* **2020**, *13*, 1791. [CrossRef]
9. Shoaei, A.; Abbaszadeh, K.; Allahyari, H. A single-inductor multi-input multi-level high step-up DC-DC converter based on switched-diode-capacitor cells for PV applications. *IEEE J. Emerg. Sel. Top. Ind. Electron.* **2022**. [CrossRef]
10. Dhimish, M.; Schofield, N. Single-Switch Boost-Buck DC-DC converter for industrial fuel cell and photovoltaics applications. *Int. J. Hydrogen Energy* **2022**, *47*, 1241–1255. [CrossRef]
11. Azmoon-Asmarood, S.; Maalandish, M.; Shoghli, I.; Nazemi-Oskuee, S.H.; Hosseini, S.H. A non-isolated high step-up MIMO DC–DC converter for renewable energy applications. *IET Power Electron.* **2022**, *15*, 962–963. [CrossRef]
12. Mishra, S.K.; Nayak, K.K.; Rana, M.S.; Dharmarajan, V. Switched-boost action based Multiport Converter. *IEEE Trans. Ind. Appl.* **2019**, *55*, 964–975. [CrossRef]
13. Saadatizadeh, Z.; Heris, P.C.; Babaei, E.; Sabahi, M. A new nonisolated single-input three-output high voltage gain converter with low voltage stresses on switches and diodes. *IEEE Trans. Ind. Electron.* **2019**, *66*, 4308–4318. [CrossRef]
14. Keyhani, H.; Toliyat, H.A. A ZVS single-inductor multi-input multi-output DC-DC converter with the step up/down capability. In Proceedings of the 2013 IEEE Energy Conversion Congress and Exposition, Denver, CO, USA, 15–19 September 2013. [CrossRef]
15. Gupta, J.; Singh, B. Bridgeless isolated positive output Luo converter based high power factor single stage charging solution for Light Electric Vehicles. *IEEE Trans. Ind. Appl.* **2022**, *58*, 732–741. [CrossRef]
16. Wang, B.; Xian, L.; Kanamarlapudi, V.R.; Tseng, K.J.; Ukil, A.; Gooi, H.B. A digital method of power-sharing and cross-regulation suppression for single-inductor multiple-input multiple-output DC–DC converter. *IEEE Trans. Ind. Electron.* **2017**, *64*, 2836–2847. [CrossRef]
17. Gorji, S.A.; Sahebi, H.G.; Movahed, M.; Ektesabi, M. Multi-input Boost DC-DC converter with continuous input-output current for Renewable Energy Systems. In Proceedings of the 2019 IEEE 4th International Future Energy Electronics Conference (IFEEC), Singapore, 25–28 November 2019.
18. Ramu, S.K.; Paramasivam, S.; Muthusamy, S.; Panchal, H.; Sadasivuni, K.K.; Noorollahi, Y. A novel design of switched boost action based multiport converter using dsPIC controller for Renewable Energy Applications. *Energy Sources Part A Recovery Util. Environ. Eff.* **2021**, *44*, 75–90. [CrossRef]
19. Williams, B.W. DC-to-DC converters with continuous input and output power. *IEEE Trans. Power Electron.* **2019**, *28*, 2307–2316. [CrossRef]
20. Wang, B.; Zhang, X.; Ye, J.; Gooi, H.B. Deadbeat control for a single-inductor multiple-input multiple-output DC–DC converter. *IEEE Trans. Power Electron.* **2019**, *34*, 1914–1924. [CrossRef]
21. Li, Y.; Han, Y. A module-integrated distributed Battery Energy Storage and Management System. *IEEE Trans. Power Electron.* **2016**, *31*, 8260–8270. [CrossRef]
22. Li, X.L.; Dong, Z.; Tse, C.K. Complete family of two-stage single-input multioutput configurations of interconnected power converters. *IEEE Trans. Power Electron.* **2010**, *35*, 3713–3728. [CrossRef]
23. Saadatizadeh, Z.; Chavoshipour Heris, P.; Babaei, E.; Blaabjerg, F.; Cecati, C. Sido coupled inductor-based high voltage conversion ratio DC–DC converter with three operations. *IET Power Electron.* **2021**, *14*, 1735–1752. [CrossRef]
24. Hou, S.; Chen, J.; Sun, T.; Bi, X. Multi-input step-up converters based on the switched-diode-capacitor voltage accumulator. *IEEE Trans. Power Electron.* **2016**, *31*, 381–393. [CrossRef]
25. Nahavandi, A.; Hagh, M.T.; Sharifian, M.B.; Danyali, S. A nonisolated multiinput multioutput DC–DC boost converter for Electric Vehicle Applications. *IEEE Trans. Power Electron.* **2015**, *30*, 1818–1835. [CrossRef]
26. Varesi, K.; Hossein Hosseini, S.; Sabahi, M.; Babaei, E.; Saeidabadi, S.; Vosoughi, N. Design and analysis of a developed multiport high step-up DC–DC converter with reduced device count and normalized peak inverse voltage on the switches/diodes. *IEEE Trans. Power Electron.* **2019**, *34*, 5464–5475. [CrossRef]
27. Deihimi, A.; Seyed Mahmoodieh, M.E.; Iravani, R. A new multi-input step-up DC–DC converter for Hybrid Energy Systems. *Electr. Power Syst. Res.* **2017**, *149*, 111–124. [CrossRef]
28. Li, X.L.; Dong, Z.; Tse, C.K.; Lu, D.D.-C. Single-inductor multi-input multi-output DC–DC converter with high flexibility and simple control. *IEEE Trans. Power Electron.* **2020**, *35*, 13104–13114. [CrossRef]
29. Pourjafar, S.; Sedaghati, F.; Shayeghi, H.; Maalandish, M. High step-up DC–DC converter with coupled inductor suitable for renewable applications. *IET Power Electron.* **2019**, *12*, 92–101. [CrossRef]
30. Samanes, J.; Urtasun, A.; Barrios, E.L.; Lumbreras, D.; Lopez, J.; Gubia, E.; Sanchis, P. Control Design and Stability Analysis of power converters: The MIMO generalized Bode Criterion. *IEEE J. Emerg. Sel. Top. Power Electron.* **2020**, *8*, 1880–1893. [CrossRef]

energies

MDPI

Article

A Novel Single-Phase Shunt Active Power Filter with a Cost Function Based Model Predictive Current Control Technique

Belqasem Aljafari [1], Kanagavel Rameshkumar [2], Vairavasundaram Indragandhi [3,*] and Selvamathi Ramachandran [4]

[1] Department of Electrical Engineering, College of Engineering, Najran University, Najran 11001, Saudi Arabia; bhaljafari@nu.edu.sa
[2] Department of Electrical and Electronics Engineering, Dr. Mahalingam College of Engineering and Technology, Coimbatore 642003, Tamil Nadu, India; rameshvel.k@gmail.com
[3] School of Electrical Engineering, Vellore Institute of Technology, Vellore 600040, Tamil Nadu, India
[4] Department of Electrical and Electronics Engineering, AMC Engineering College, Bangalore 582103, Karnataka, India; selvamathir@gmail.com
* Correspondence: indragandhi.v@vit.ac.in

Abstract: For a single-phase Shunt Active Power Filter (SAPF) with a two-step prediction, this research presents a modified current control based on a Model Predictive Current Control (MPCC) technique. An H-bridge inverter, a DC link capacitor, and a filter inductor comprise the single-phase SAPF topology. The SAPF reference current is computed using the DC-link capacitor voltage regulation-based PI control technique. The weighting factor-based model predictive current controller is used to track the current commands. The essential dynamic index for evaluating waveform quality is the Total Harmonic Distortion (THD) of a source current and switching frequency of power switches. The conventional methods the THD and switching frequency are not considered as an objective function, so that a weighting factor-based MPCC technique is used to obtain a good compromise between the THD of the source current and switching frequency of power switches. Through MATLAB simulation and experimentation with the Cyclone-IV EP4CE30F484 FPGA board, the usefulness of the proposed control technique is proven. As compared with hysteresis, predictive PWM, and conventional MPCC control methods, the cost function-based MPCC algorithm provides a lower switching frequency (13.4 kHz) with an optimal source current THD value.

Keywords: cost function; model predictive current control; single-phase shunt active power filter; THD

Citation: Aljafari, B.; Rameshkumar, K.; Indragandhi, V.; Ramachandran, S. A Novel Single-Phase Shunt Active Power Filter with a Cost Function Based Model Predictive Current Control Technique. *Energies* **2022**, *15*, 4531. https://doi.org/10.3390/en15134531

Academic Editors: Tek Tjing Lie and Enrique Romero-Cadaval

Received: 16 May 2022
Accepted: 20 June 2022
Published: 21 June 2022

Publisher's Note: MDPI stays neutral with regard to jurisdictional claims in published maps and institutional affiliations.

Copyright: © 2022 by the authors. Licensee MDPI, Basel, Switzerland. This article is an open access article distributed under the terms and conditions of the Creative Commons Attribution (CC BY) license (https://creativecommons.org/licenses/by/4.0/).

1. Introduction

Exclusively, for commercial and household applications, a single-phase active power filter has emerged as a very promising converter technology for enhancing power quality. The deterioration of power quality has become the most significant issue in modern society. The presence of harmonics in the commercial and domestic applications causes equipment heating, malfunctioning of electrical and electronics equipment, and transformer heating. Compared with traditional passive filters, the active power filter has promising features in power semiconductor device losses, power quality, structural simplicity, power regulation ability, and expanding flexibility. According to filter connection, the active power filter is classified into shunt, series, series shunt, and hybrid. Due to their small size, low cost, ability to adjust both current harmonics and reactive power, and improved efficiency, SAPF are mostly employed in medium- and low-power installations. The voltage source inverter and passive energy storage devices, such as filter inductance and DC-link capacitor, make up the basic construction of the shunt active power filter.

The primary control goal of SAPF is to adjust for harmonics and reactive power produced by the Nonlinear Load (NLL). During the harmonic compensation procedure, current control is one part and reference harmonic current extraction is the other part.

Several approaches have been presented to determine the compensation current, such as DC-link capacitor voltage control, PQ theory, and DQ theory [1–6]. The author in [6] used a DC-link capacitor voltage management approach that did not require sophisticated calculations and was simple to apply. Various current control strategies, such as hysteresis control [7,8], double-band hysteresis current control [9], and the predictive PWM control technique [10], were advocated, and their quality was appraised in many research publications that can be found in the literature. Over the last decade, many researchers have focused on power converters using model predictive control due to its simplicity, rapid transient response, easy inclusion of constraints, and nonlinearities [11,12]. To reduce the algorithm complexity and shaping, traditional MPC approaches rely on one sample forward prediction. Long prediction horizons were proposed by the authors in [13] in order to enhance power converter performance control. The two-sample-ahead predictive control approach for an NPC inverter with an output LC filter was suggested, experimentally tested, and proven in [14].

The main issue in using the MPC approach is determining the way in which the weighting factors affect future system operations in order to produce the lowest feasible error in the controlled variables [11]. The approach of selecting appropriate weighting factors is another non-trivial multi-objective optimization issue [15]. Thus, MPCC is one of the most interesting techniques for SAPF application to achieve a good dynamic performance [16–19]. The authors in [16] used an MPCC method to a single-phase shunt active power filter for harmonics and reactive power compensation. In [17], the author proposed an MPC based on three-phase SAPFs to avoid using the weighting factor to compensate the unbalanced current and current harmonic components produced by single-phase nonlinear loads. The DC-link voltage during load fluctuations was measured using a multi-objective predictive control approach applied to a single-phase three-level neutral-point-clamped (NPC)-based active power filter (APF) for harmonic compensation and self-support in [18]. In [19], the author suggested a modified U-cell five-level inverter (MPUC5) for a single-phase Active Power Filter (APF) using a Model Predictive Control (MPC) technique. Authors in [20] proposed a PV-based dual-stage, multi-functional grid-connected inverter. This approach offers better efficiency and more stability under load changing conditions.

The majority of work reported in the literature focuses on the dynamic performance of SAPF and THD of the source current. The lowering of power converter switching frequency is still a study area in the realm of FCS-MPC-based SAPFs [20].

This manuscript presents a novel current control technique based on the cost function-based MPCC of a single-phase SAPF. The novelty of this manuscript is the use of a weighting factor in the cost function, which reduces the switching frequency and enhances the reactive power in the utility and removes harmonic currents in the PCC. The outcomes were compared with various traditional current control methods, and it was found that it effectively tracked references with reduced switching frequency. Complete simulations were conducted using the MATLAB/Simulink environment, and real-time analysis was performed using a single-phase SAPF prototype with the Cyclone-IV EP4CE30F484 FPGA control board to confirm the efficacy of the suggested method control approach. The main aims and contributions of this manuscript are as follows.

Designs and analyzes a weighting factor-based MPCC technique to improve power quality.

To minimize the switching frequency of power switches and THD of the source current.

To assess the results using MATLAB/Simulink and verify them in real time using Cyclone-IV EP4CE30F484 FPGA technology.

The rest of this paper is organized as follows: Section 2.1 describes and models the single-phase SAPF; Section 2.2 elaborates on the weighting factor-based MPCC approach and Section 2.3 elaborates DC-link PI control scheme; Section 3 contains simulation outcomes; Section 4 provides hardware results where MPCC-based single-phase SAPF is also described; And, finally, the conclusions are presented in Section 5.

2. A Modeling and Control Algorithm

2.1. Single-Phase SAPF Description and Modeling

The single-phase MPCC-based SAPF was designed to compensate for reactive power and current harmonics. Figure 1 illustrates how the single-phase SAPF comprises a single-phase VSI with four power switches and a DC side capacitor. While connected in parallel to the grid, the DC side capacitor supplies a DC voltage to the VSI and acts as an energy buffer. The SAPF is directly linked to the low-voltage grid via filter inductance (Lf) at the point of common coupling (PCC). This supplies a compensating current, which eliminates harmonics. The compensatory current is achieved via the use of DC-link capacitor voltage control method.

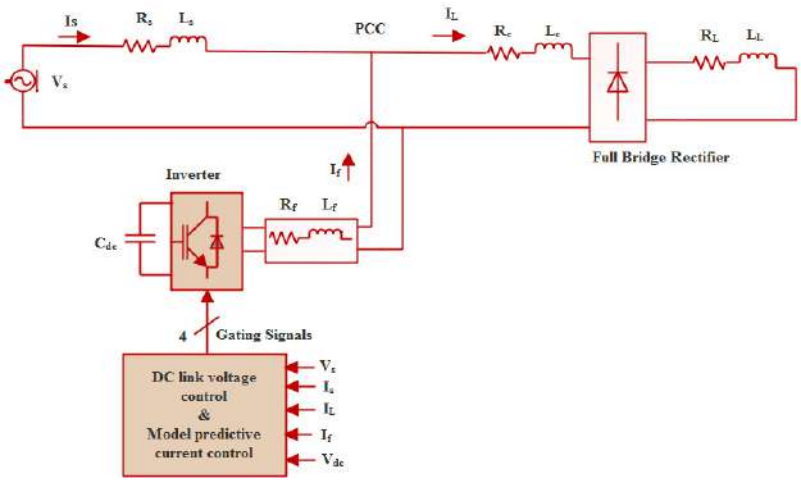

Figure 1. Configuration of the single-phase shunt active power filter.

In both simulation and real-time analysis, a single-phase uncontrolled bridge rectifier with RL load was considered as the NLL.

Typical supply voltage and current may be expressed as

$$v_s(t) = V_m \sin \omega t \tag{1}$$

$$i_s(t) = i_L(t) - i_f(t) \tag{2}$$

where V_m —magnitude of supply voltage

A nonsinusoidal current is drawn when a nonlinear load is linked to a single-phase supply. This can be stated in the following way:

$$i_L(t) = \sum_{n=1}^{\infty} I_n \sin(n\omega t + \theta_n)$$

$$i_L(t) = I_1 \sin(n\omega t + \theta_1) \sum_{n=2}^{\infty} I_n \sin(n\omega t + \theta_n) \tag{3}$$

where I_1 & I_n—peak value of load current with fundamental and nth harmonic components, and θ_1& θ_n—phase angle of load current.

The current SAPF compensation is then stated as

$$i_f(t) = i_L(t) - i_s(t) \tag{4}$$

The total instantaneous supply current, including losses after compensation, are then be stated as

$$i_s^*(t) = I_{sp} \sin \omega t \tag{5}$$

where I_{sp}—peak value of supply current. The supply current's peak value and phase angle must be established. The amplitude of the supply current is then computed using a standard proportional integral (PI) controller to evaluate the DC-link voltage error.

2.2. Model Predictive Current Control Algorithm

The block diagram of the proposed cost function-based MPCC algorithm in a single phase SAPF is shown in Figure 2. The two perditions are mainly used to improve the control performances [12]. With two-step prediction, the number of calculations and computational burdens are reduced, which is suitable for higher-power applications. It also improves load current control for various references and load circumstances [13].

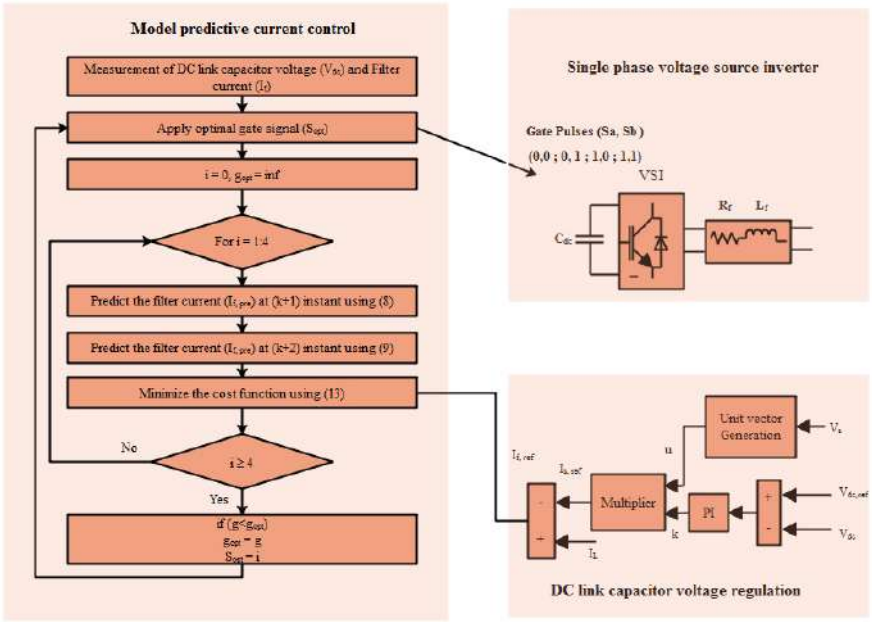

Figure 2. Model predictive current control algorithm and DC-link capacitor voltage regulation-based reference current extraction of single-phase SAPF.

The vector equation models of the SAPF filter current dynamics are expressed as

$$V_o = V_i - R_{eq} i_o - L_{eq} \frac{di_o}{dt} \tag{6}$$

Single-phase SAPF system equivalent resistance and inductance R_{eq}, L_{eq}, which may alternatively be written as

$$R_{eq} = R_f$$

and

$$L_{eq} = L_s + L_f$$

To estimate the filter current at the instant of k + 1 with a sample period T_s, the first-order approximation of the derivative is used.

$$\frac{di_o}{dt} = \frac{i_f(k+1) - i_f(k)}{T_S} \tag{7}$$

Then, 4 possible predicted filter current values of the single-phase VSI related to the inverter output voltage V_i can be attained from (6) and (7) as

$$i_{f,\,pre}(k+1) = \frac{T_s}{L_{eq}}(V_i(k) - V_s(k)) + \left(1 - \frac{R_{eq} T_s}{L_{eq}}\right) i_f(k) \tag{8}$$

where T_s is the sampling time, $i_{f,\,pre}$ and i_f, are the predicted filter currents at the next and present states, respectively. For one-step prediction (N = 1), the four switching states are used to predict the SAPF filter current, as presented in Figure 3a.

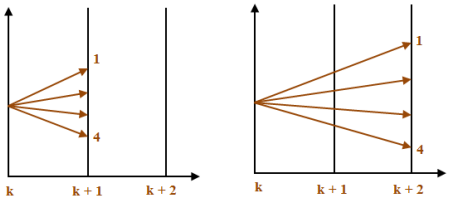

(**a**) (**b**)

Figure 3. (**a**) Control variable of one-step prediction horizon, (**b**) control variable of two-step prediction horizon.

The four switching states are predicted at the sampling time (k + 2) for a two-step prediction horizon (N = 2) in Figure 3b.

To put it another way, the filter current may be extended to a two-step prediction horizon time as follows:

$$i_{f,\,pre}(k+2) = \frac{T_s}{L_{eq}}(V_i(k+1) - V_s(k+1)) + \left(1 - \frac{R_{eq}T_s}{L_{eq}}\right) i_f(k+1) \tag{9}$$

As a result, at the sampling instant (k), the control approach identifies a switching state that lowers the cost function in the sampling instant (k + 2). Table 1 shows the valid single-phase SAPF switching states.

Table 1. Switching states of single-phase SAPF.

S_a	S_b	V_i
1	0	V_{dc}
0	1	$-V_{dc}$
1	1	0
0	0	0

The suggested approaches' primary control goals are to improve reference current tracking and minimize switching frequency. The cost function might be stated as [5]:

$$g_1 = \left(i_{f,ref}(k+2) - i_{f,\,pre}(k+2)\right)^2 \tag{10}$$

$$g_2 = \lambda_{sw} \times n_c \tag{11}$$

where λ_{sw} is weighting factor for switching frequency reduction of the VSI; when $\lambda_{sw} > 0$, switching frequency minimization can be achieved. n_c is the number of commutations of the power semiconductors in VSI.

n_c can be expressed as follows:

$$n_c = \sum_{x=a,b} |S_x(k) - S_x, opt(k)| \tag{12}$$

where $S_x(k)$ is the predicted switching state and $S_x, opt(k)$ is the optimal switching state in the previous sample.

Usually, λ_{sw} is obtained using repetitive simulations to achieve optimal results for the control objective. λ_{sw} is evaluated using the switching frequency f_{sw} and source current Total Harmonic Distortion (THD).

The final cost function combining (10) and (11) is given as

$$g = g_1 + g_2 \tag{13}$$

The first-term focuses on the current tracking and the second-term focuses on the reduction in switching frequency.

The switching frequency (F_{sw}) is determined by counting the number of switching changes (n_{sw}) during a particular time interval $\left(T_f\right)$.

$$F_{sw} = \frac{n_{sw}}{T_f}$$

So the overall cost function aims to reduce the switching frequency and THD as much as possible. The detailed cost function based MPCC is demonstrated in Modified MPCC Algorithm (Algorithm 1).

The DC-link voltage should be kept constant in SAPF applications, and the source current reference is determined using the DC-link capacitor voltage regulation technique to compensate for the harmonic and reactive power provided by the non-linear load.

Algorithm 1. Cost Function-Based Model Predictive Current Control Algorithm

Input : $\left(i_f\right)$, (V_{dc})
Output : S_a, S_b
Step 1: At the instant (k + 1) based on (8), predict the filter current $i_{f,\,pre}$
Step 2: At the instant (k + 2) based on (9), predict the filter current $i_{f,\,pre}$
Step 3: Calculate n_c for all switching states based on (12)
Step 4: Evaluate the cost function (g) based on (13)
Step 5: Choose the ideal switching state and apply to the SAPF. Return to Step 1

2.3. DC-Link Capacitor Voltage Control PI Control Scheme

The voltage of the DC-link capacitor is regulated using a traditional PI controller. To retain the DC-link capacitor voltage constant, compensate the total losses of the converter; to obtain the amplitude of source current reference, the PI control is used. The source current amplitude from the PI controller output is expressed as

The PI controller obtains the value of k, which can be stated as follows:

$$k = k_p\left(V_{dc,ref} - V_{dc}\right) + k_i \int V_{dc,ref} - V_{dc})dt \tag{14}$$

where k_p and k_i are the gain values of the PI controller, $V_{dc,ref}$ is the DC-link voltage reference, and V_{dc} is the measured DC-link voltage.

The PLL is used to generate the sine waveform. The output of the PI controller is multiplied by the sine waveform to generate the source current reference.

$$i_{s.ref} = k \times u = k \times \sin \omega t \tag{15}$$

The NLL current is then combined with the supply current reference to produce the filter reference current. Finally, the MPCC receives the filter reference current and actual filter current signals to generate SAPF gating signals. This PI controller employs optimal gain values (k_p,k_i).

3. Simulation Results

To validate the suggested control strategy, simulations were run in the MATLAB/Simulink program with the parameters listed in Table 2. A two-step prediction horizon with a sampling time of T_s = 10 μs and cost function are indicated in Equation (4), where the switching frequency reduction term is considered. The execution times required for the one step and two-step prediction algorithms are 5 μs and 8 μs, respectively. With the developments in the microprocessor technology, it is easy to handle this higher computational requirement and also the easy inclusion of constraints and nonlinearities.

Table 2. Major components of single-phase SAPF.

S. No	Description	Components	Value
1	Supply voltage	V_s	100 V (rms)
2	DC-link capacitor voltage	V_{dc}	200 V
3	Supply frequency	F	50 Hz
4	Switching Frequency	F_{sw}	15 kHz
5	DC-link capacitance	Cdc	800 µF
6	Filter resistance and inductance	R_f and L_f	0.01 Ω and 5 mH
7	Source resistance and inductance	R_s and L_s	0.1 Ω and 1 mH
8	AC side resistance and inductance	R_c and L_c	
9	DC side resistance, inductance, and capacitance	RL_{Cdc}	28 Ω, 160 mH, and 100 µF
10	Voltage sensor	LEM-V	LV 25-p
11	Processor	Cyclone-IV EP4CE30F484 FPGA	-
12	Power-quality analyzer	Fluke 435	-
13	Mixed-signal oscilloscope	Agilent DSO-X 3014A	-

3.1. Performance Analysis with Resistive and Inductive (RL) Load Condition

The simulation results of the proposed control approach with resistive and inductive loads are shown in Figure 4. When the proposed algorithm-based SAPF was switched on at 0.1 s, with a power factor of one, the source current became sinusoidal.

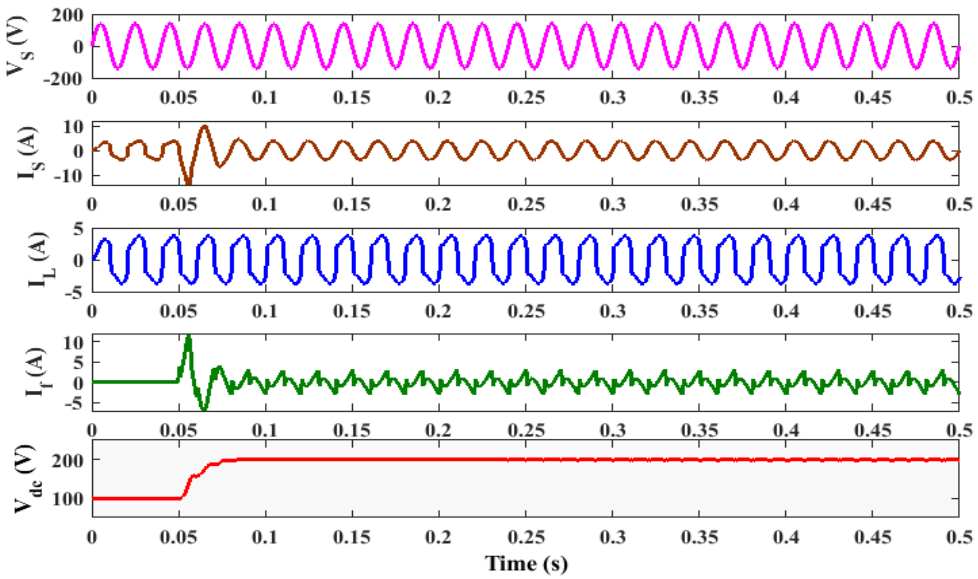

(**a**)

Figure 4. *Cont.*

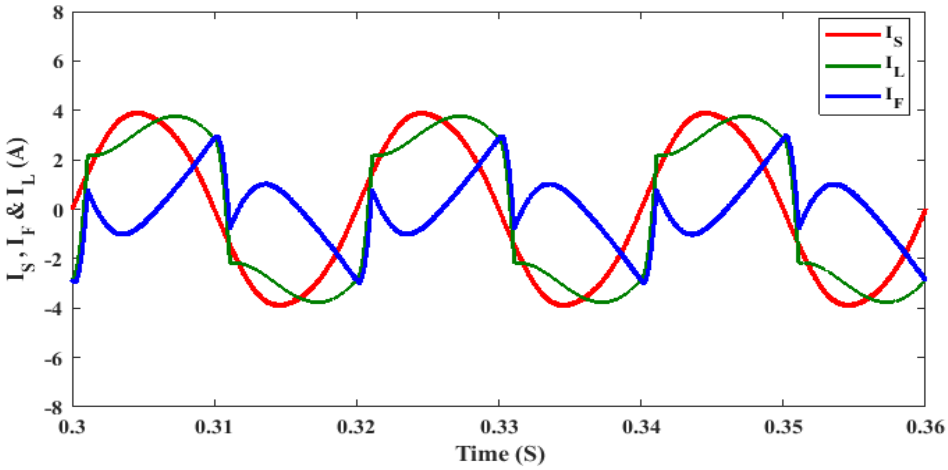

(**b**)

Figure 4. (**a**) Single-phase SAPF switch on response (**b**) source, load, and filter currents.

Weighting factor λ_{sw} in the control algorithm must be adjusted heuristically through simulations. By varying λ_{sw} from 0 to 0.35, the switching frequency was reduced from 15.071 to 7.284 kHz and the THD increased from 3.53 to 6.203%, as presented in Figure 5. The effect of λ_{sw} on the source current for different weight factors is presented in Figure 6. The THD level of the source current before filtering was 28.47%, and the matching harmonic spectrum is given in Figure 6A.

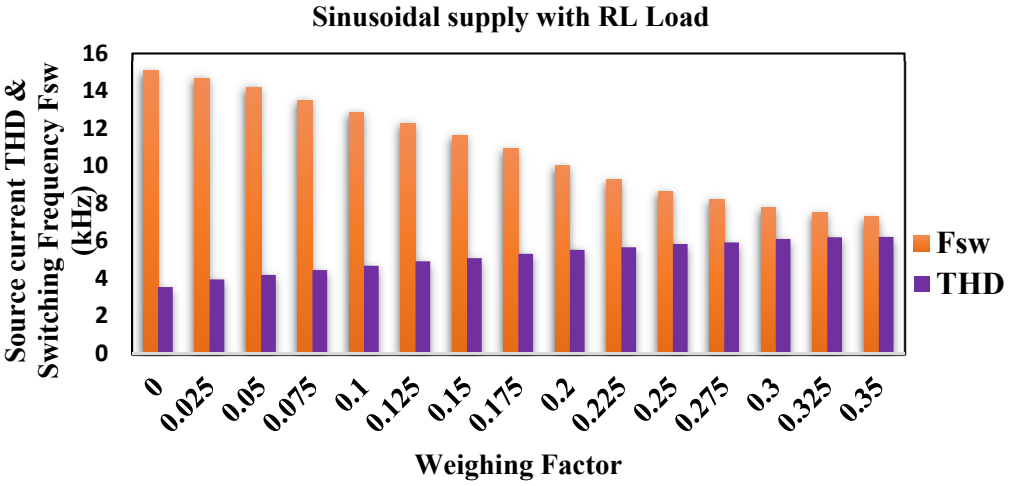

Figure 5. Variation effect of weighting factor λ on the supply current THD and switching frequency.

An acceptable value of λ_{sw} for the validation testing would be 0.1 since, with weight factor λ_{sw} = 0.1, the source current THD was determined to be 4.66% and the switching frequency was reduced from 15.071 to 12.866 kHz as shown in Figure 6B.

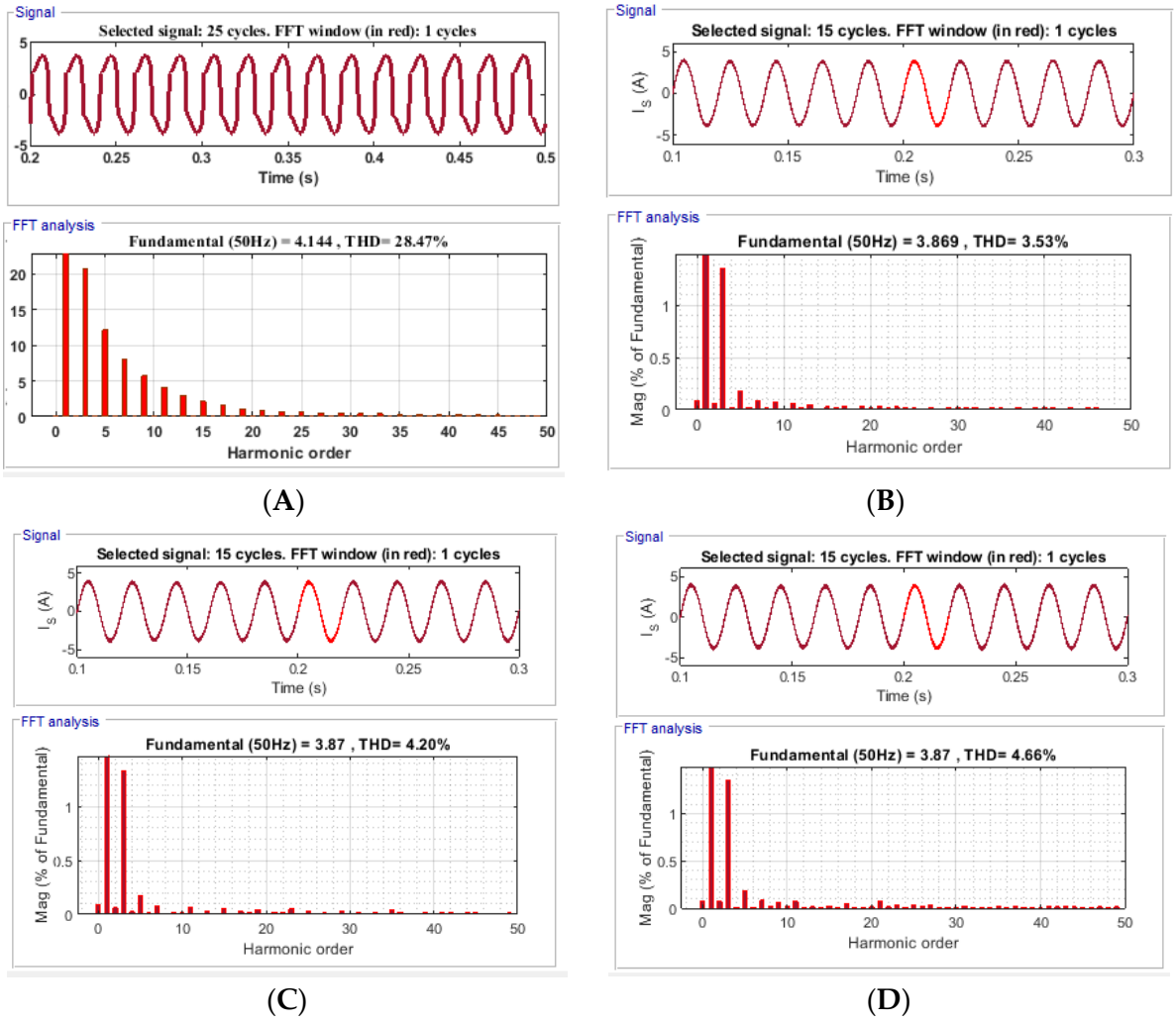

Figure 6. Simulation results of source current and harmonic spectrum: (**A**) source current (before compensation), (**B**) source current waveform ($\lambda = 0$), (**C**) source current waveform ($\lambda = 0.05$), (**D**) source current waveform ($\lambda = 0.1$).

3.2. Performance Analysis with Resistive and Capacitive (RC) Load

In this analysis, the SAPF system was analyzed with the RC load condition. The supply current THD before compensation was 35.36%. When SAPF was connected to the PCC at 0.05 s, the source current THD reduced from 35.36 to 3.97%.

The comparative analysis of the proposed controller with a conventional MPCC is shown in Table 3. From the results, it can be observed that the proposed MPCC offers a better performance in terms of reduced source current THD and switching frequency.

Table 3. Summary of the simulation test results for weighting factor-based MPCC of single-phase SAPF, including THD and switching frequency with RC load.

RC Load	Before Compensation	After Compensation	
		MPCC	Proposed MPCC (λ = 0.1)
Source Current THD (%)	35.36	3.58	3.97
F_{SW} (kHz)	-	14.307	12.620

4. Experimental Results

Figure 7 shows the complete assembly of a single-phase SAPF. VSI was developed using four IGBT switches with protection and control circuits from Mitsubishi Intelligent Power Modules (IPMs). A diode bridge rectifier with a series resistor and an inductor was also included. Load variation was achieved by connecting and disconnecting parallel loads. A current transformer (CT) detected the supply, load, and filter currents, whereas an LEM voltage transducer (LV25-P) detected the DC-link capacitor voltage and source voltage. The signal sensing and conditioning circuit are shown in Figure 8. A signal conditioning circuit feds the detected signals to the FPGA board's A/D converters. The single-phase SAPF was controlled in the digital platform based on Cyclone-IV EP4CE30F484 FPGA of the altera controller (Intel, Santa Clara, CA, USA), which is shown in Figure 9.

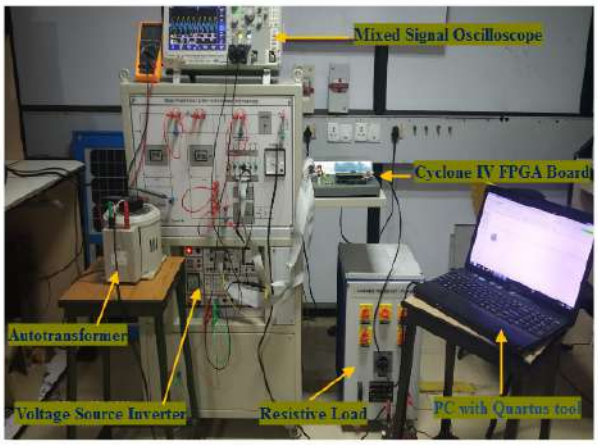

Figure 7. Complete assembly of single-phase SAPF.

Figure 8. Signal sensing and conditioning circuit.

The design is done using Quartus II 15.0 software. The digital platform consisted of an FPGA and EPCS16 PROM devices, USB blaster, 4-channel 12-bit SPI bipolar ADC, 4-channel 12-bit SPI bipolar DAC, LCD, and on-board isolated RS232. Flash memory EPCS16 was used to configure the FPGA by connecting personal computers through a USB blaster. The VHDL code for the control of SAPF was verified, analyzed, and synthesized in the Quartus II 15.0 software platform. The JAM file was downloaded to the PROM device, which was used to configure the controller and experimental setup. The voltage and current signals were sampled using the ADC controller. Then, the controller read the signal from the ADC and generated the firing pulses to the SAPF.

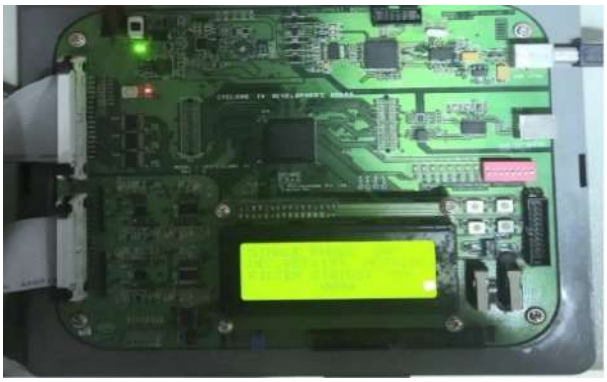

Figure 9. Cyclone-IV EP4CE30F484 FPGA controller.

The SAPF system settings were unchanged from the simulated test. The DC-link capacitor voltage was set at 200 V, while the root mean square and also the grid frequency remained at 100 V and 50 Hz, respectively. The sampling time for the proposed control scheme was 10 µs, which was suitable for high-speed FPGA processing. The suggested control technique's steady-state and switch-on responses were evaluated to ensure its practicality. The waveforms are shown in Figure 10a,b is the source voltage and the source current. Where the source current is not compensated. The supply current THD was found to be 24.9% before SAPF is connected to the PCC. It clearly showed the high harmonics of the supplying current waveform. During compensation, the supply current became harmonic-free, and the supply THD reduced from 24.9 to 3.7%. All of these waveforms were obtained using an Agilent DSO-X 3014A digital oscilloscope. Figure 10c–f illustrates the switch-on response and steady-state performance of SAPF. The harmonic current in the NLL was compensated by the operation of SAPF, so that the source current was sine in nature. The measure source current, SAPF current, and DC-link voltage are presented in Figure 10d–f, where the harmonics generated by the NLL are almost eliminated by the SAPF. The measured source voltage, filter current, and source current during switch-off conditions are exposed in Figure 10g. Figure 10h shows the PLL output. The test results show the ability to track the reference current very well and achieved source current in sinusoidal waveform with a power factor value of one. In the test, the switching frequency was nearly 15 kHz when not including the weighting factor in the cost function.

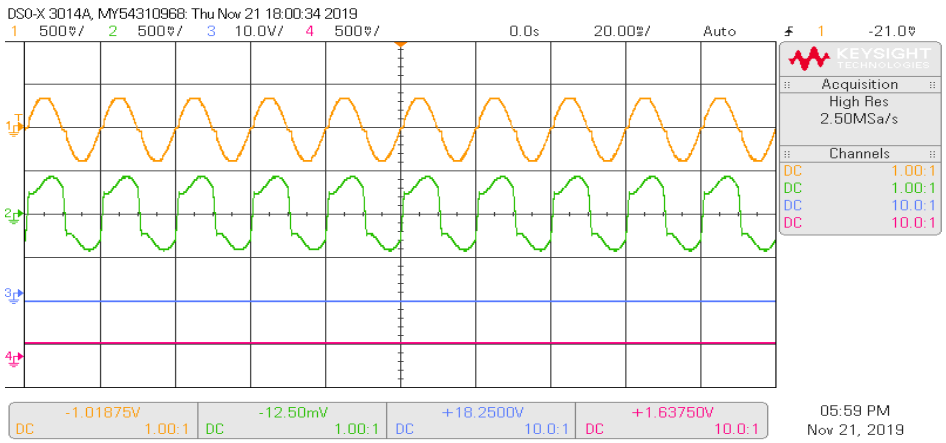

(a)

Figure 10. *Cont.*

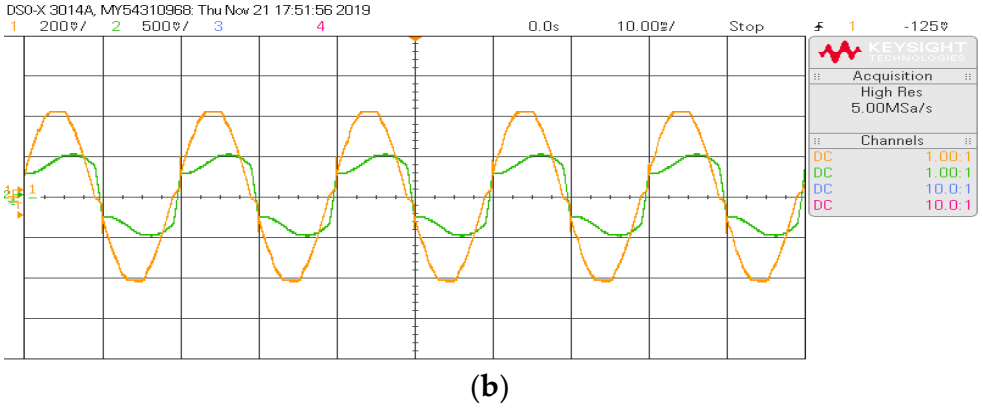

(**b**)

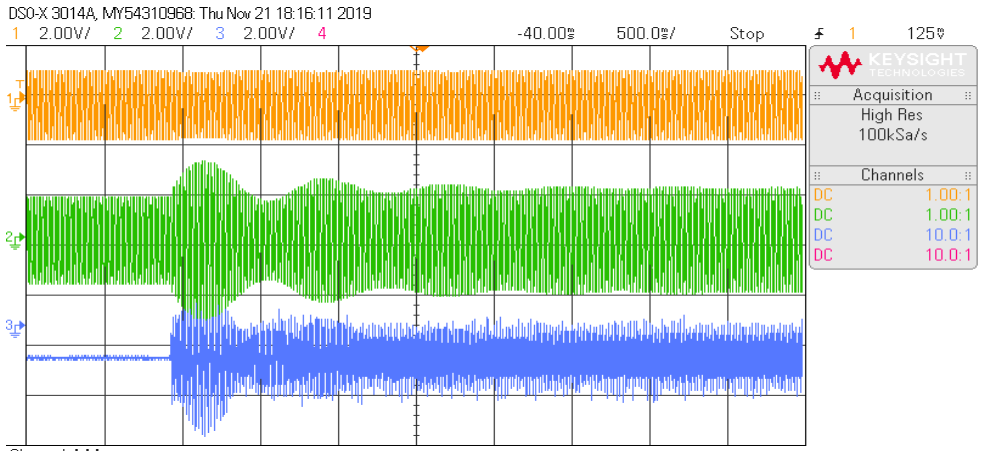

(**c**)

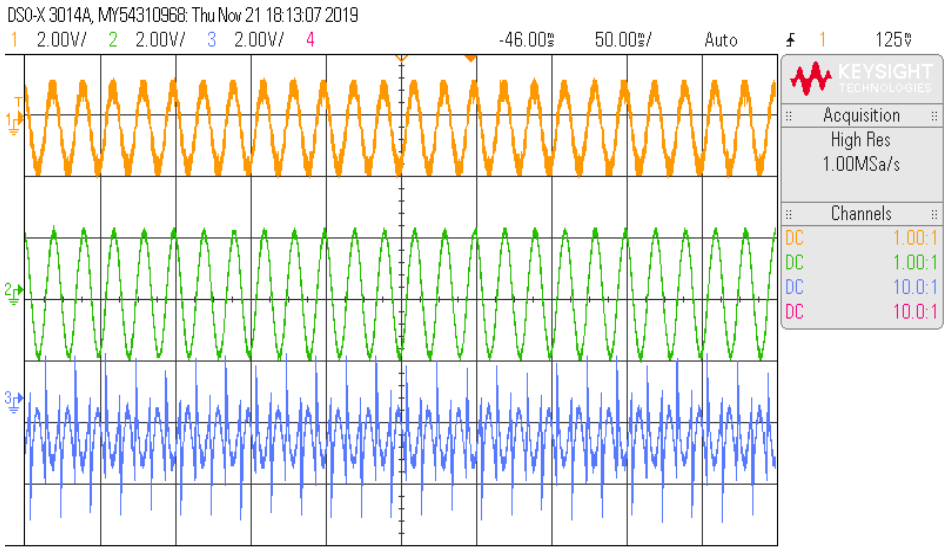

(**d**)

Figure 10. *Cont*.

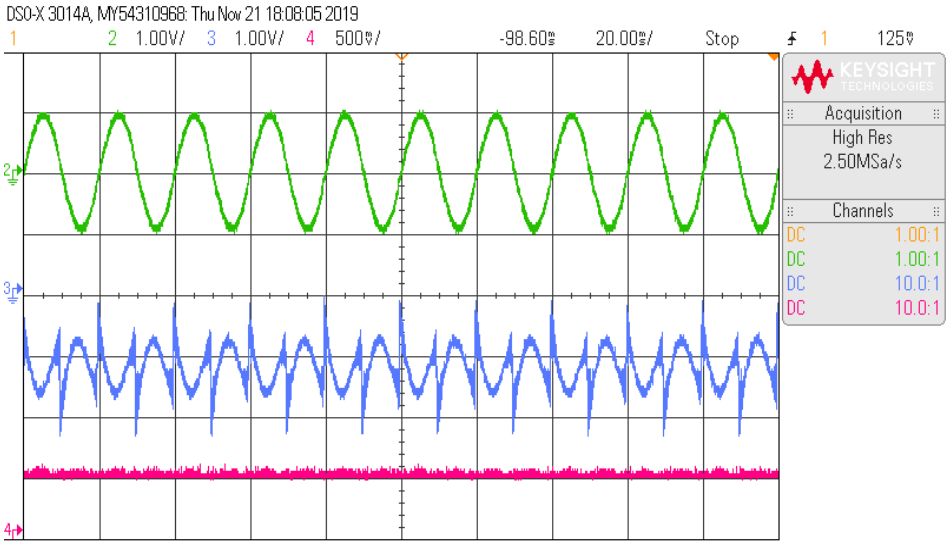

(**e**)

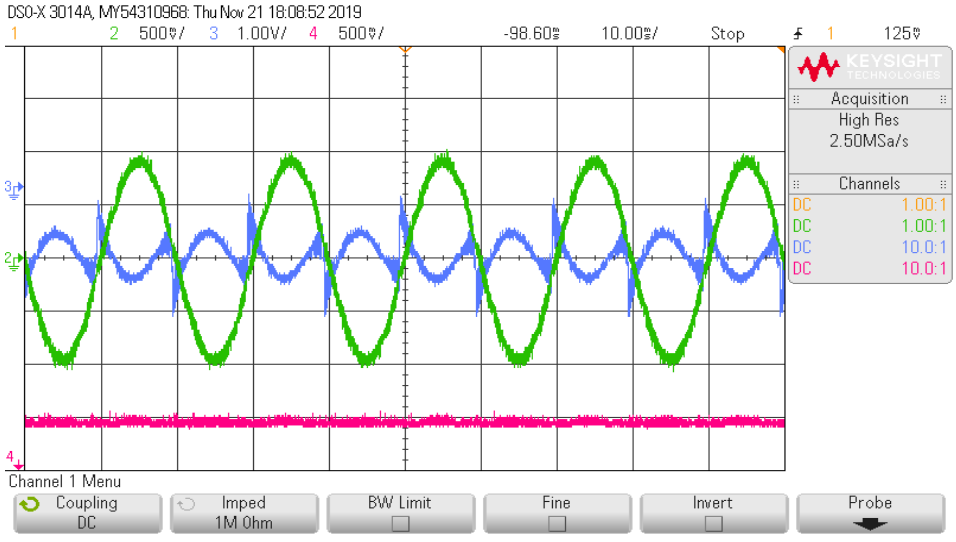

(**f**)

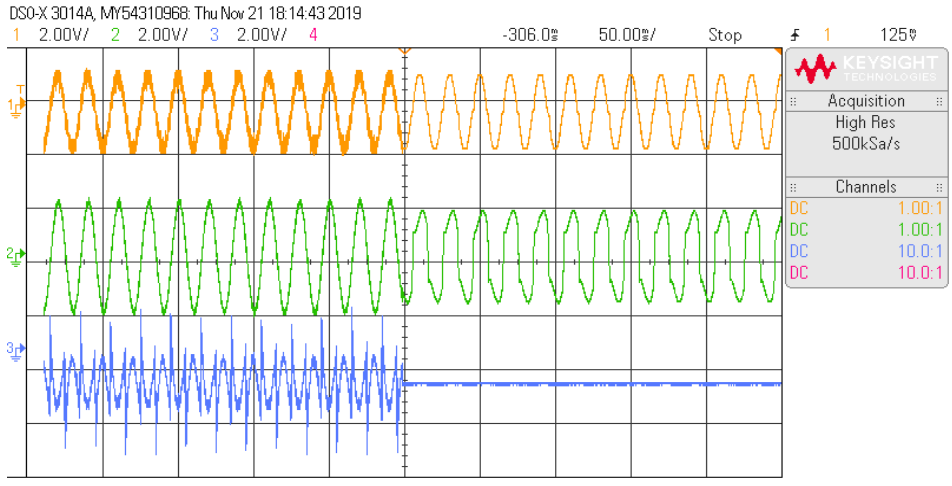

(**g**)

Figure 10. *Cont*.

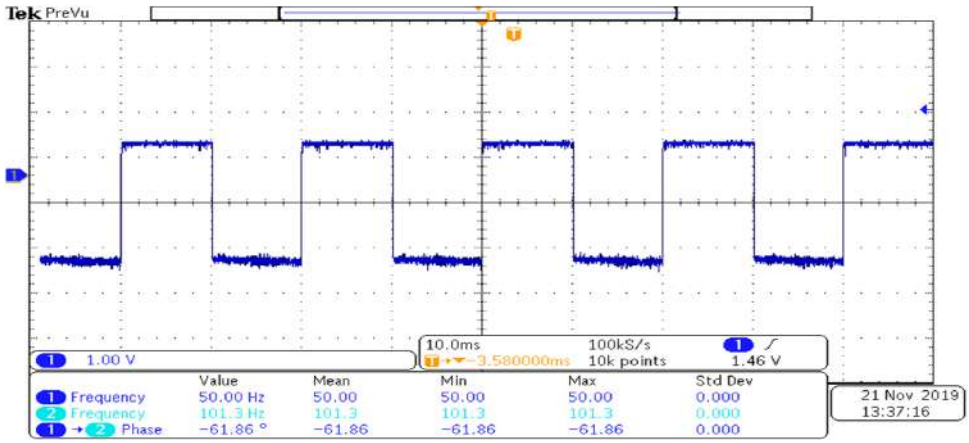

(**h**)

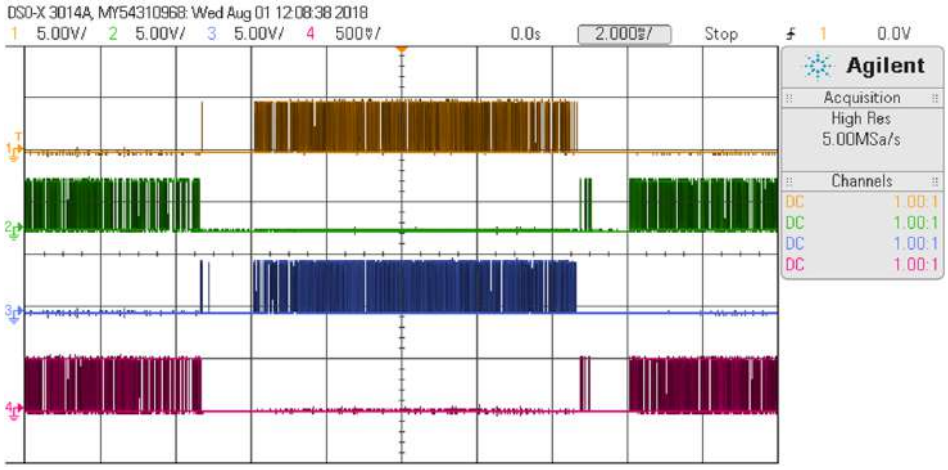

(**i**)

Figure 10. Experimental results of proposed SAPF (**a**) source voltage and current, load current, filter current (before compensation). (**b**) Source current and voltage. (**c**) Source voltage, source current, and filter current (switch-on condition). (**d**) Filter current, source voltage, and current. (**e**) Source current, filter current, and DC-link voltage. (**f**) Source current, filter current, and DC-link voltage. (**g**) Source voltage and current, filter current (switch-off condition). (**h**) PLL output. (**i**) Gating signals.

As shown in Figure 11a–d, the weighting factor is changed from 0 to 0.1, according to the change in the source current THD from 3.7 to 4.8%, and the switching frequency of VSI for the proposed control method decreases from 15.2 to 13.4 kHz in comparison to the conventional MPCC. Table 3 provides a comparison of the THD of the source current and switching frequency for the four dissimilar weighting factor values. Additionally, the comparison between various current controllers in the simulation and hardware based on source current THD is summarized in Table 4. As compared with hysteresis, predictive PWM, and conventional MPCC control methods, the cost function-based MPCC algorithm provides a lower switching frequency with an optimal source current THD value.

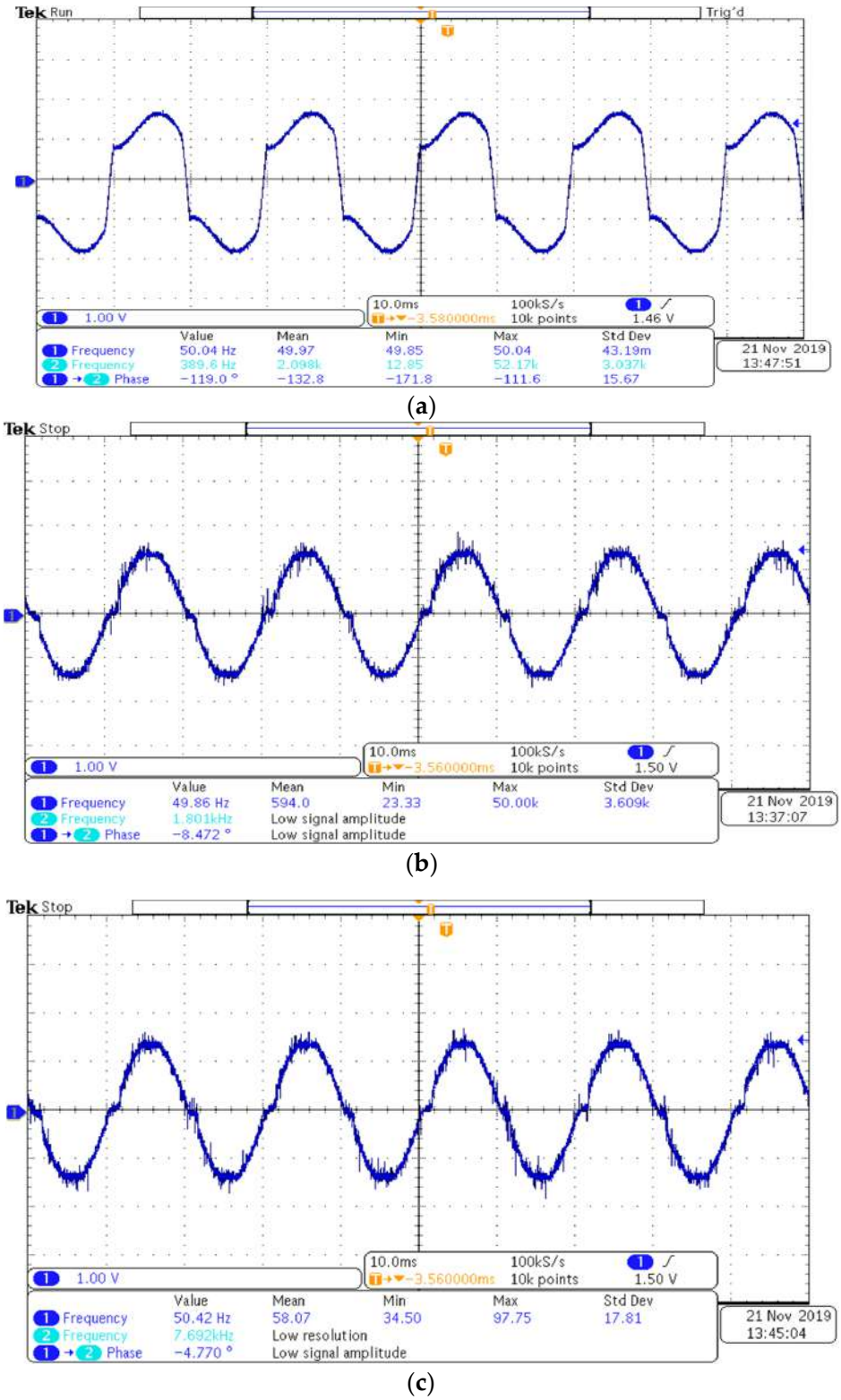

Figure 11. *Cont*.

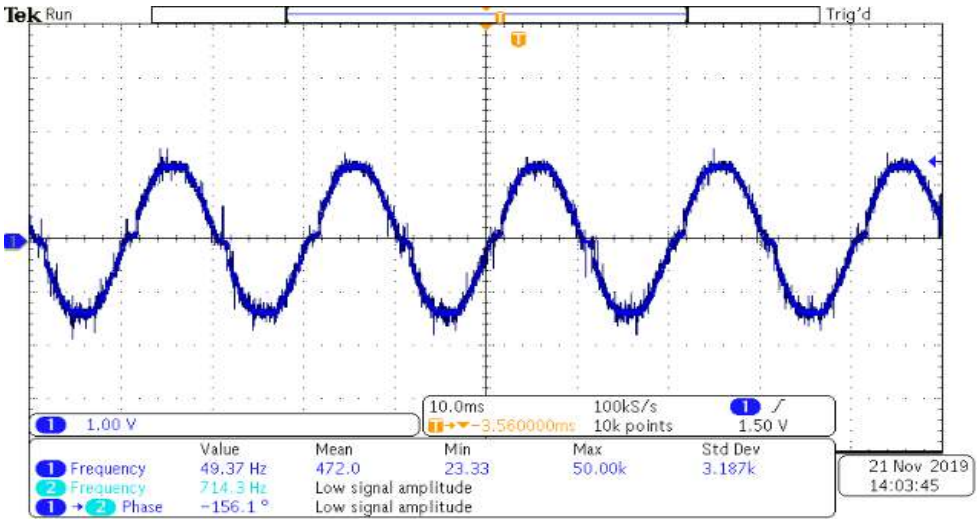

(**d**)

Figure 11. Experimental outcomes: (**a**) source current (before compensation), (**b**) source current $\lambda = 0$, (**c**) source current $\lambda = 0.05$, (**d**) source current $\lambda = 0.1$.

Table 4. Summary of the simulation and practical test results for weighting factor-based MPCC of single-phase SAPF, including THD and switching frequency.

Source Current THD (%) (RL Load)	Before Compensation	After Compensation				
		Hysteresis Controller	Predictive PWM Controller	(Weighting Factor-based MPCC)		
				0	0.05	0.1
Simulation Results	28.47	3.82	4.5	3.53	4.20	4.66
Hardware Results	24.9	3.76	4.21	3.7	4.6	4.8
Switching Frequency (Fsw) in kHz	**Before Compensation**	**Hysteresis Controller**	**Predictive PWM Controller**	**After Compensation (Weighting Factor-based MPCC)**		
				0	**0.05**	**0.1**
Simulation Results	0	15.27	15	15.071	14.208	12.866
Hardware Results	0	15.13	15	15.200	14.600	13.400

As presented above the following conclusions have been ended from the experimental study.

- The NLL's current harmonics and reactive power were efficiently adjusted.
- The supply current took on a sine wave and aligned with the supply voltage.
- Under all working conditions, the DC-link capacitor voltage returned to its reference value. The suggested control approach also reduced supply current THD to far below 5% within the IEEE 519-2014 standard.
- When compared to traditional current control approaches, the MPCC algorithm based on a cost function provided a great trade-off between VSI switching frequency and harmonic performance. The results show that this technology is suited for both commercial and industrial applications.
- The proposed SAPF system was realized with the Cyclone-IV EP4CE30F484 FPGA controller. From the hardware outcomes, it can be seen that, during the load changing condition, the source current is sinusoidal in nature and in phase with the source voltage.

5. Conclusions

In this manuscript, a cost function-based MPCC was presented for reducing the switching frequency. The outcomes illustrate that the proposed system archives an excellent

trade-off among the VSI switching frequency and harmonics performance. A comparison study indicates that the proposed technique achieves a reduced switching frequency of 13.4 kHz, and also decreases the THD of the supply current well below 5% within the IEEE 519-2014 limit. In addition, the simulation and experiment results show the effectiveness of the proposed method. The suggested approach is easy to calculate, and the simulation and experimental results show that it performs well in terms of dynamic features, operational efficiency, and output power quality. This approach is applicable to all types of converters for which power quality is a primary concern.

Author Contributions: Conceptualization, V.I.; Formal analysis, S.R.; Funding acquisition, B.A.; Investigation, K.R.; Methodology, K.R.; Project administration, V.I.; Resources, B.A.; Writing—review & editing, S.R. All authors have read and agreed to the published version of the manuscript.

Funding: This work was funded by under the Research Groups Funding program grant code (NU/RG/SERC/11/6).

Acknowledgments: The authors are thankful to the Deanship of Scientific Research at Najran University for funding this work under the Research Groups Funding program grant code (NU/RG/SERC/11/6).

Conflicts of Interest: The authors declare no conflict of interest.

References

1. Mahela, O.P.; Shaik, A.G. Topological aspects of power quality improvement techniques: A comprehensive overview. *Renew. Sustain. Energy Rev.* **2016**, *1*, 1129–1142. [CrossRef]
2. Singh, B.; Chandra, A.; Al-Haddad, K. *Power Quality: Problems and Mitigation Techniques*; John Wiley & Sons: Hoboken, NJ, USA, 2014.
3. Kumar, P.; Mahajan, A. Soft computing techniques for the control of an active power filter. *IEEE Trans Power Deliv.* **2009**, *24*, 452–461. [CrossRef]
4. Singh, B.; Al-Haddad, K.; Chandra, A. A universal active power filter for single-phase reactive power and harmonic compensation. In Proceedings of the Power Quality, Hyderabad, India, 18 June 1998; IEEE: Manhattan, NY, USA, 1998; pp. 81–87.
5. Khadkikar, V.; Chandra, A.; Singh, B.N. Generalised single-phase pq theory for active power filtering: Simulation and DSP-based experimental investigation. *IET Power Electron.* **2009**, *2*, 67–78. [CrossRef]
6. Kim, J.S.; Kim, Y.S. A new control method for a single-phase hybrid active power filter based on a rotating reference frame. *J. Power Electron.* **2009**, *9*, 718–725.
7. Gupta, R. Generalized frequency domain formulation of the switching frequency for hysteresis current controlled VSI used for load compensation. *IEEE Trans Power Electron.* **2012**, *27*, 2526–2535. [CrossRef]
8. Mahanty, R. Indirect current controlled shunt active power filter for power quality improvement. *Electr. Power Energy Syst.* **2014**, *62*, 441–449. [CrossRef]
9. Komurcugil, H. Double-band hysteresis current-controlled single-phase shunt active filter for switching frequency mitigation. *Int. J. Electr. Power Energy Syst.* **2015**, *69*, 131–140. [CrossRef]
10. Hamad, M.S.; Fahmy, A.M.; Abdel-Geliel, M. Power quality improvement of a single-phase grid-connected PV system with fuzzy MPPT controller. In Proceedings of the Industrial Electronics Society, IECON 2013—39th Annual Conference of the IEEE, Vienna, Austria, 10–13 November 2013; Volume 213, pp. 1839–1844.
11. Rodriguez, J.; Kazmierkowski, M.P.; Espinoza, J.R. State of the art of finite control set model predictive control in power electronics. *IEEE Trans. Ind. Inf.* **2013**, *9*, 1003–1016. [CrossRef]
12. Kouro, S.; Cortés, P.; Vargas, R.; Ammann, U.; Rodríguez, J. Model predictive control—A simple and powerful method to control power converters. *IEEE Trans. Ind. Electron.* **2008**, *56*, 1826–1838. [CrossRef]
13. Yaramas, V.; Rivera, M.; Narimani, M.; Wu, B.; Rodriguez, J. High performance operation for a four-leg NPC inverter with two-sample-ahead predictive control strategy. *Electr. Power Syst. Res.* **2015**, *123*, 31–39. [CrossRef]
14. Yaramasu, V.; Wu, B.; Rivera, M.; Rodriguez, J. A new power conversion system for megawatt PMSG wind turbines using four-level converters and a simple control scheme based on two-step model predictive strategy—Part I: Modeling and theoretical analysis. *IEEE J. Emerg. Sel. Top. Power Electron.* **2013**, *2*, 3–13. [CrossRef]
15. Vyncke, T.; Thielemans, S.; Melkebeek, J. Finite-set model-based predictive control for flying-capacitor converters: Cost function design and efficient fpga implementation. *IEEE Trans. Ind. Inform.* **2013**, *9*, 1113–1121. [CrossRef]
16. Kanagavel, R.; Vairavasundaram, I.; Padmanaban, S. Design and prototyping of single-phase shunt active power filter for harmonics elimination using model predictive current control. *Int. Trans. Electr. Energy Syst.* **2020**, *30*, 2. [CrossRef]
17. Acuna, P.; Moran, L.; Rivera, M.; Dixon, J.; Rodriguez, J. Improved active power filter performance for renewable power generation systems. *IEEE Trans. Power Electron.* **2014**, *29*, 687–694. [CrossRef]

18. Acuna, P.; Morán, L.; Rivera, M.; Aguilera, R.; Burgos, R.; Agelidis, V.G. A single-objective predictive control method for a multivariable single-phase three-level NPC converter-based active power filter. *IEEE Trans. Ind. Electron.* **2015**, *62*, 4598–4607. [CrossRef]
19. Sahli, A.; Krim, F.; Laib, A.; Talbi, B. Model predictive control for single phase active power filter using modified packed U-cell (MPUC5) converter. *Electr. Power Syst. Res.* **2020**, *180*, 106139. [CrossRef]
20. Boukezata, B.; Gaubert, J.P.; Chaoui, A.; Hachemi, M. Predictive current control in multifunctional grid connected inverter interfaced by PV system. *Sol. Energy* **2016**, *139*, 130–141. [CrossRef]

energies

MDPI

Review

A Scientometric Analysis and Review of the Emissions Trading System

Yu-Jie Hu [1,2,*], Lishan Yang [1], Fali Duan [2], Honglei Wang [1,3] and Chengjiang Li [1,4]

1 School of Management, Guizhou University, Guiyang 550025, China; yanglishanyls@163.com (L.Y.); hlwang@gzu.edu.cn (H.W.); chengjiang.li@utas.edu.au (C.L.)
2 State Key Laboratory of Public Big Data, Guizhou University, Guiyang 550025, China; faliduan@163.com
3 Key Laboratory of "Internet+" Collaborative Intelligent Manufacturing in Guizhou Provence, Guiyang 550025, China
4 School of Engineering, University of Tasmania, Hobart, TAS 7005, Australia
* Correspondence: yjhu@gzu.edu.cn

Abstract: As a vital market mechanism to mitigate global warming, the emissions trading system (ETS) has critical research and practice value. According to articles from Web of Science's core collection, quantitative statistics are used to analyze the ETS, including statistics on the number of articles, distributions of time and geography, journals and subjects, productive authors and institutions, academic collation, article citations, and hot topics. Moreover, this paper presents a qualitative analysis of research on the ETS, exploring hot issues, including its origin, allowance allocation, the impact of allowance allocation, and the ETS in the power sector. The results show that it is necessary to launch ETS to mitigate climate change effectively and reduce emissions at a low cost. Allowance allocation as its critical component has also caused heated discussion among scholars. In allowance allocation, exploring a desire to assign the future allowable carbon emissions reasonably and efficiently is vital, yet scholars widely do not accept this. Moreover, free allocation can only be applied to the transitional stage, and auctioning will be inevitable. In addition, scholars have studied the impact of different allowance allocation schemes from macro and micro perspectives and take the power sector, namely the largest emitter, as an example, by linear programming, equilibrium modeling, and multi-agent modeling. However, the quota allocation scheme needs improvement due to firms' accuracy of emission data. Finally, governments are encouraged to launch the ETS to reduce emissions and combat climate change. The ETS should be improved gradually, including aspects such as cap setting, covering sectors, and the allocation method. Additionally, some key emission sectors and regions can be taken as the research and practice objects in the initial stage of the ETS.

Keywords: emissions trading system; allowance allocation; quantitative statistics; qualitative analysis

Citation: Hu, Y.-J.; Yang, L.; Duan, F.; Wang, H.; Li, C. A Scientometric Analysis and Review of the Emissions Trading System. *Energies* **2022**, *15*, 4423. https://doi.org/10.3390/en15124423

Academic Editor: V. Indra Gandhi

Received: 19 May 2022
Accepted: 14 June 2022
Published: 17 June 2022

Publisher's Note: MDPI stays neutral with regard to jurisdictional claims in published maps and institutional affiliations.

Copyright: © 2022 by the authors. Licensee MDPI, Basel, Switzerland. This article is an open access article distributed under the terms and conditions of the Creative Commons Attribution (CC BY) license (https://creativecommons.org/licenses/by/4.0/).

1. Introduction

Global greenhouse gas (GHG) emissions continued to rise until 2019; the aggregate reductions suggested by the current nationally determined contributions (NDCs) until the year 2030 would still make it impossible to limit warming to 1.5 °C with no or limited overshoot [1]. Therefore, it is necessary to take more ambitious mitigation actions to limit warming to 1.5 °C while achieving sustainable development and poverty eradication. The Kyoto Protocol proposes the three flexible mechanisms of "joint implementation (JI)", the "Clean Development Mechanism (CDM)", and the "emissions trading system (ETS)" to help developed countries and countries with economies in transition achieve their emission reduction targets. Moreover, as an essential market mechanism to mitigate global warming, deal with climate change, and promote green development, the ETS has become the focus of international attention in the past 20 years and has profoundly impacted the global economy and industrial structure in the 21st century. In 2021, the number of emissions regulated by the emissions trading system increased to three times that of 2005, by nearly

17%, and the GDP of the jurisdictions that established the ETS accounted for 55% of that figure [2].

The carbon emissions trading system can be traced back to Ronald Coase [3], who argued that under certain conditions, the externalities or inefficiencies of the economy could be corrected through negotiation by parties, thus achieving the maximization of social benefits. Based on this idea, J.H. Dales put forward the idea of an emissions trading system. In the early 1970s, Montgomery rigorously proved that the emissions trading system is characterized by controlling pollution at an efficient cost, i.e., it requires the minimum price to achieve pollution control objectives. Accordingly, various types of emissions trading systems, including carbon emissions, are beginning to be widely launched worldwide. Therefore, it is necessary to research the emissions trading system, systematically analyze its research progress, work on, and solve scientific and technological problems that need to be solved, and promote the healthy development of the carbon trading system, which facilitates the realization of national emission reduction targets.

Regarding the systematic and quantitative literature analysis, the bibliometric method has been widely used to assess the performance of various disciplines [4,5]. Focusing on the topic of economic, energy, and climate policy, Kiriyama et al. used the bibliometric method to illustrate an overview of trends in nuclear energy technology and related fields [6]. Wei et al. utilized the bibliometric method to summarize the important research topics and methodologies in the field of climate policy modeling based on the SCIE and SSCI datasets [7]. Yu et al. applied the bibliometric method to analyze the scientific publications on low-carbon energy technology investment [8]. Zhang et al. used the bibliometric method to characterize the carbon tax literature from 1989 to 2014 [9]. In terms of research on the ETS, Wang and Tang used the bibliometric method to analyze comparative studies on different market mechanisms applied to carbon reduction between 1970 and 2016 [10]. Ji et al. used the bibliometric method to analyze the characteristics of the most relevant studies of carbon prices in emissions trading schemes [11]. Tang et al. presented a comprehensive literature review on full-scale types of quantitative models in the research on emissions trading systems [12]. Unlike previous research, this study, using a bibliometric method and combining in-depth qualitative analysis, offers a comprehensive and systematic literature review on the ETS, including its origin, core mechanism, and research hotspots. This study points out the practical problems and research gaps in the ETS.

All in all, this research on the ETS has great practical guiding significance and value. This study focuses on the in-depth quantitative statistics and qualitative analysis of research on the ETS in general and finds the research hotspots in the ETS. This study draws on ETS research, including its origin, core mechanism, research hotspot, and impact. This paper attempts to provide an effective guarantee for improving ETS mechanism construction, promoting emission reduction, and mitigating climate change through a comprehensive scientific review.

2. Materials and Methodology

The data are from Web of Science's core collection, including the Science Citation Index Expanded (SCIE, 1990–present) and the Social Sciences Citation Index (SSCI, 1981–present). A total of 2726 articles containing topics (titles, keywords, and abstracts) about the "emission trading system" were obtained on 6 April 2022. The number of articles published in different years and regions and the research hot spots comprise the quantitative statistics. A total of 832 articles were gained whose topics were "emission trading system" and "allowance allocation". As for the articles, on the one hand, quantitative statistics were used to analyze them in terms of factors such as the number of pieces, distributions of time and geography, the journal and subject, productive authors and institutions, academic collation, article citations, and hot topics. On the other hand, in this paper, we performed a qualitative analysis of research on the ETS, exploring hot topics, allowance allocation, the impact of allowance allocation, and the ETS in the power sector.

2.1. Quantitative Statistic

Based on the articles obtained, this study applied indicators such as the h index, impact factor, citation frequency, co-operation degree, and other indicators to evaluate the scientific output of the ETS comprehensively.

The h index is a mixed quantitative indicator that can be used to assess the amount of academic output and the academic output levels of researchers. The h index was proposed by Hirsch (2005). He indicated that when a scholar's h-many papers are cited at least h times, and the remaining (N-h)-many papers are not cited more than h times, then the scholar's h index is h. The impact factor (IF) refers to the data from the Journal Citation Reports (JCR) produced by Thomson Reuters. It was devised by Eugene Garfield, the Institute for Scientific Information founder. It means that the total number of citations for papers published in the first two years of a journal in the year of the report (JCR year) is divided by the total number of papers published by the journal in the two years. This is an internationally accepted evaluation indicator for journals. Citation frequency is the number of times an article is cited in the statistics year. It is an important indicator that reflects the influence of the paper, which is directly obtained by the WoS data platform. The total citation frequency is the sum of citations for a given number of papers, and the average citation frequency is the average number of citations for each article. The co-operation degree indicator measures international partnerships in a research area, indicating the amount of co-authoring or co-citing. This study explored the co-operation between productive authors and institutions.

In addition, this study used the Bibexcel software to analyze the keywords in all the literature in the field and to find research hotspots and future development trends using word frequency analysis on the keywords.

2.2. Qualitative Analysis

In this paper, we also performed a qualitative analysis of the research hotspots from quantitative statistics. We adopted the method of classifying topics and comparing methodology. We conducted an in-depth literature review on the dimensions of research problems, techniques, and specific empirical evidence.

In terms of the ETS, this paper explored why the ETS should be launched and focused on the critical issue of the ETS, i.e., allowance allocation. Moreover, this paper discussed the research on the methods and principles of the ETS and tried to find which scheme is the best for allowance allocation. In addition, scholars also care about the impacts of the ETS or its allowance allocation. They have conducted qualitative and quantitative analyses from macro and micro perspectives to study the implications of different allowance allocation schemes. They consistently choose the power industry for empirical research. Therefore, this paper compared the methodology used by these studies and tried to find a more appropriate method.

3. Quantitative Statistics Results

3.1. Research Hotspots on ETS Research: Allowance Allocation

Based on the 2726 articles obtained whose topics were related to the "emission trading system", this paper analyzed their frequency of keywords and clustered them. This clustering indicated that most articles focus on the EU ETS, China's ETS, climate change, climate policy, transaction costs, tradable permits, allocation, national allocation plans, burden sharing, grandfathering, auctioning, and so on (as shown in Figure 1). Therefore, in this paper, quantitative statistics on the issue of allowance allocation is conducted.

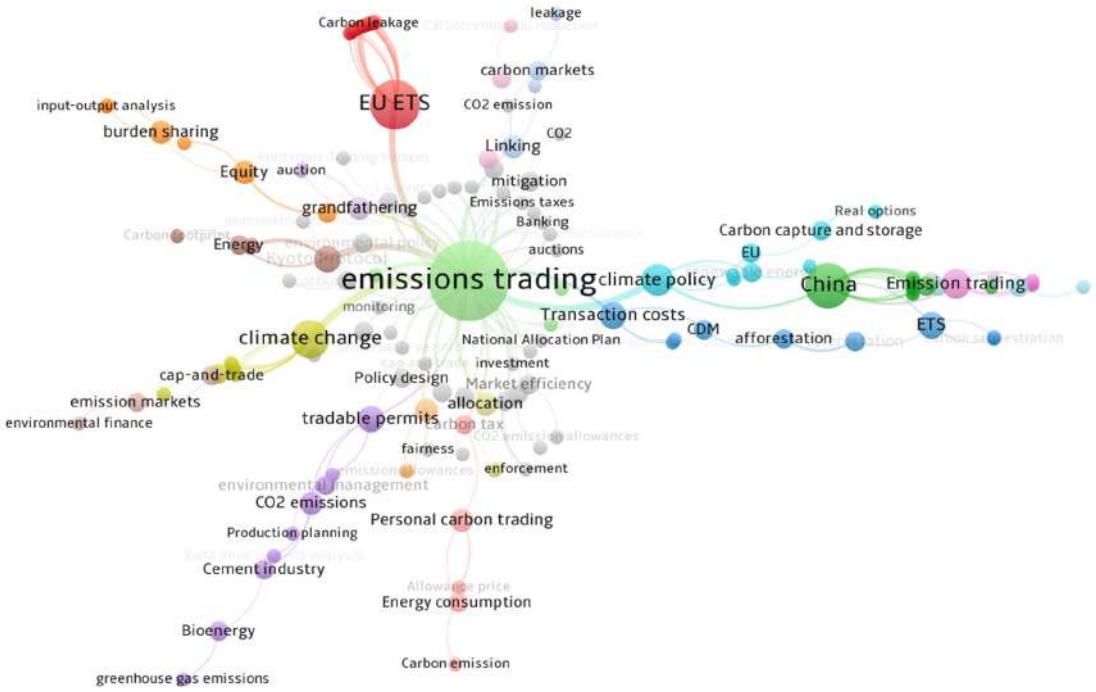

Figure 1. The frequency of keywords: research hotspots.

3.2. Productive Subjects of Research on Allowance Allocation

A total of 832 articles on the topics of the "emission trading system" and "allowance allocation" were selected. According to the ten productive subjects listed (as shown in Table 1), research on allowance allocation is interdisciplinary, referring to the environment, economics, energy fuel, engineering, chemistry, management, and so on. Most subjects are environmental studies, environmental sciences, economics, and studies related to energy fuel. Environmental studies are the most popular, with 318 publications on allowance allocation, accounting for 38.22% of the total studies, and environmental sciences and economics, accounting for 34.38% and 34.26% of the full records, respectively.

Table 1. Productive subjects.

Subjects	Publications	Percentage
Environmental Studies	318	38.22%
Environmental Sciences	286	34.38%
Economics	285	34.26%
Energy Fuels	205	24.64%
Green Sustainable Science Technology	126	15.14%
Environmental Engineering	77	9.26%
Public Administration	76	9.14%
Chemical Engineering	37	4.45%
Operations Research/Management Science	22	2.64%
Business	21	2.52%

3.3. The Amount and Distribution of Publications on Allowance Allocation

It can be seen from Figure 2 that the number of publications on allowance allocation increased from 1 (1995) to 110 (2021). The number of publications showed an overall upward trend.

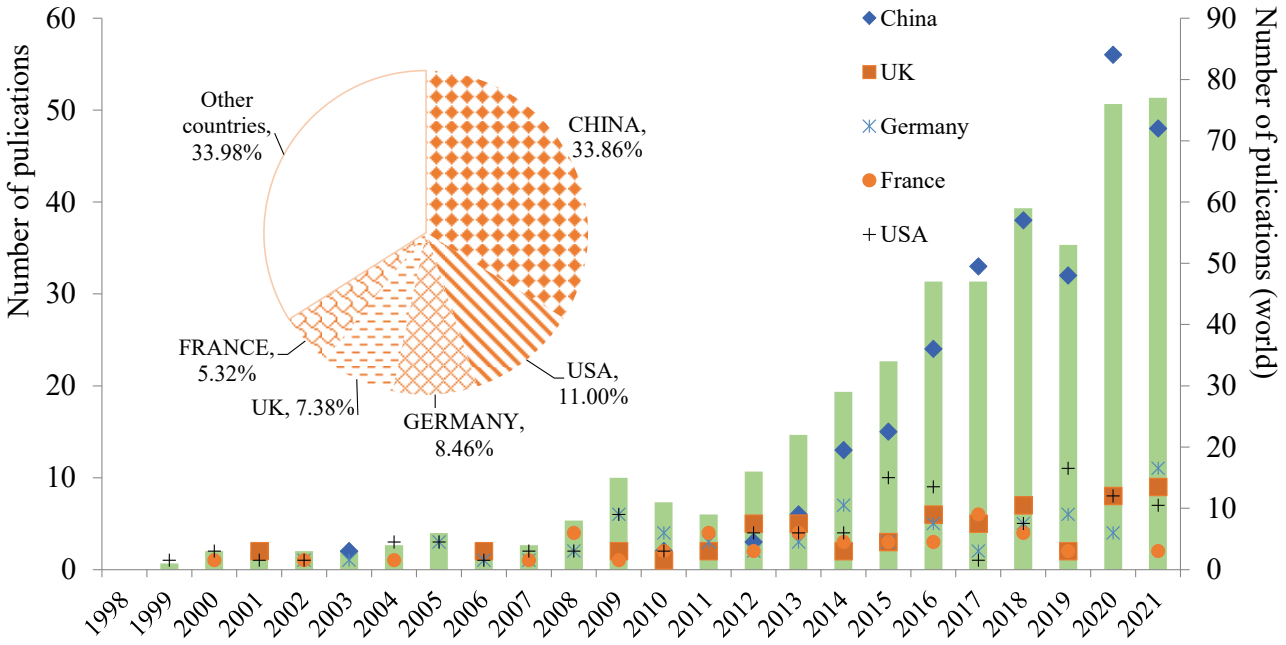

Figure 2. Timeline and percentages of publications in producing countries.

Journal distribution and the impact thereof has been a popular field research area. The world's top articles in this field are mainly concentrated in China, North America, Europe, and Australia. With further analysis, the top five productive countries in this area are listed as China, the United States of America, Germany, the United Kingdom, and France. The proportion of articles written by researchers from these countries has reached 66.02%. Since 2013, when China began to launch the ETS pilots, the number of publications from China has shown a rapidly increasing trend, and the number of publications from China has surpassed those from the United States, the United Kingdom, and Germany. It is seen that with the strong determination of China to launch the ETS, academic circles have had heated discussions on this topic, and they are trying to work out an effective and theoretically instructive allowance allocation scheme that is more suitable for China's national conditions, which is a very realistic and theoretical research direction.

Table 2 shows that 832 publications on ETS's allowance allocation (accounting for 45% of the total articles on this topic) are included in the top ten journals in the research fields of climate change, energy and the environment, and the economy. Their impact factor is about 2.8 to 12.5, indicating that these studies have decisive academic importance in these fields. Among the articles, 70 articles that were cited 2680 times were published in Energy Policy, whose impact factor in 2021 was 5.354 and whose h index was 30, followed by The Journal of Cleaner Production and Energy Economics, with impact factors of 7.646 and 7.042 in 2021, and which contained 66 articles cited 1554 times and 51 articles cited 1927 times, respectively. These are the three most famous journals. Moreover, Renewable and Sustainable Energy Reviews and Applied Energy are the most influential journals, with 13 articles cited 464 times and 33 articles cited 1334 times, respectively.

Table 2. Journal distribution.

Journal	2021 Impact Factor	Average Citations	h Index
Energy Policy	5.354	38.29	30
Journal of Cleaner Production	7.646	23.55	24
Energy Economics	7.042	37.78	23
Applied Energy	9.007	40.42	22
Climate Policy	5.085	21.63	22
Ecological Economics	4.718	45.36	9
Sustainability	2.806	7.71	9
Energy	6.255	32.08	9
Renewable and Sustainable Energy Reviews	12.549	35.69	8
Journal of Environmental Economics and Management	4.624	14.69	8

3.4. Productive Authors and Institutions and the Co-Operation between Them

3.4.1. Productive Authors and the Co-Operation between Them

These articles were written by 1839 authors. As shown in Table 3, the top 15 most productive authors studying allowance allocation are from different countries, mainly from the USA, China, and Germany. China, as the only developing country among them, has active scholars in the field of ETS and allowance allocation and has put mitigating actions into practice. The top 15 most productive authors have published 11 articles that were cited 338 times on average. Bohringer C, Wei YM, and Chevallier J published 16, 19, and 19 articles that were cited 478, 615, and 541 times, respectively, and which have more oversized h indexes, i.e., 13, 11, and 10, respectively. Wei YM is 2021's most cited Chinese researcher in the energy economy and climate change field, and they are from the Beijing Institute of Technology. Although Ellerman AD, Neuhoff K, and Quirion P published less, they are cited more, resulting in a more significant number of average citations per article, i.e., 67.30, 59.88, and 45.63 with h indexes of 8, 7, and 7, respectively.

Table 3. The top 15 most productive authors.

Authors	Average Citations per Article	h Index	Country
Bohringer C	29.88	13	Germany
Wei YM	32.37	11	China
Chevallier J	28.47	10	France
Loschel A	25.50	9	Germany
Den Elzen MGJ	30.67	9	Netherlands
Burtraw D	29.50	9	USA
Ellerman AD	67.30	8	USA
Stranlund JK	16.67	8	USA
Zhang ZX	17.88	7	China
Jotzo F	29.13	7	Australia
Fan Y	14.54	7	China
Quirion P	45.63	7	France
Neuhoff K	59.88	7	Germany
Cason TN	33.71	7	USA
Wettestad J	13.71	6	Norway

This paper analyzed the co-operation between productive authors with seven or more publications on this topic. As shown in Figure 3, there are many relationships between them, and Wei YM, Loschel A. Fan Y, and Neuhoff K are the most active. Firstly, Wei YM and Chevallier J discussed the ETS and carbon prices together. Wei YM and Den Elzen MGJ explored the economic and energy implications for China and India in an international climate regime. In addition, there is some co-operation between Wei YM and Tang BJ, and Peterson S and Zhang YJ. Chevallier J and Quirion P also discussed carbon prices. Secondly, Loschel A and Bohringer C assessed emission regulations in Europe. They explored how US withdrawal has consequences on environmental effectiveness, compliance costs, and

excess costs of market power under the Kyoto Protocol. Loschel A and Jotzo F published the study Emissions trading in China: Emerging experiences and international lessons. Loschel A and Zhang ZX discussed the economic and environmental implications of the US repudiation of the Kyoto Protocol and the subsequent deals in Bonn and Marrakech. Thirdly, Fan Y, Zhu L, and Wang X explored how China can achieve the emission reduction target and China's ETS. Finally, Neuhoff K and Grubb M discussed the EU ETS allocation plans and their implications. In addition, Fan J, Wang SY, and Li J from the University of Science and Technology of China explored the importance of a personal carbon trading scheme. Moreover, Liu Y, Ozturk I., and Lin BQ have been committed to the extent of mitigation mechanisms.

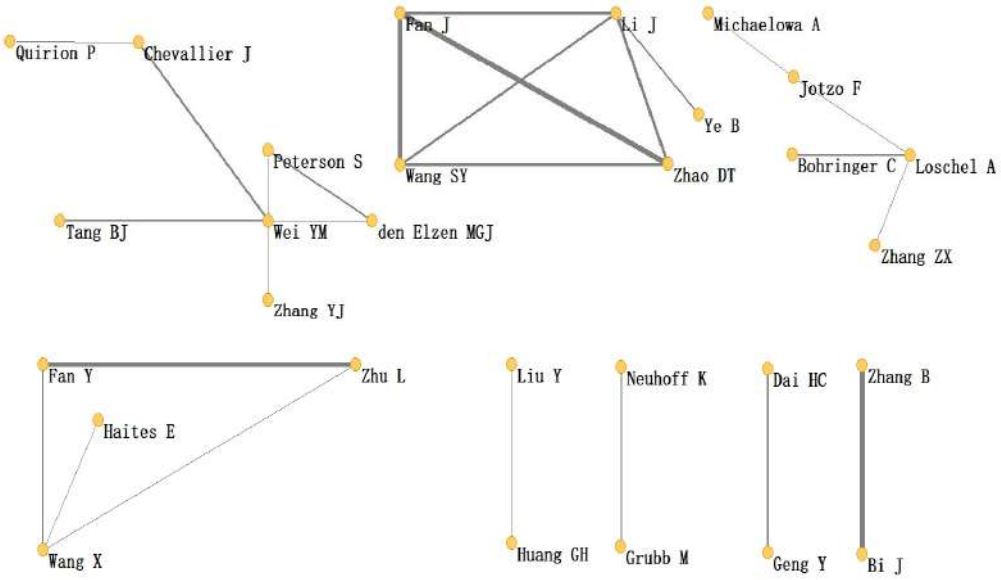

Figure 3. Co-operation among productive authors.

As a whole, there is much co-operation between productive authors, which is conducive to us scientifically solving the problem of allowance allocation in China's construction of its own ETS. In terms of bibliographic coupling by authors (as shown in Figure 4), it can be seen that there are many connections between the scholars' research on allowance allocation. Chevallier J, Peterson S, and Fan Y have cited many of the same references. Chevallier J, Wei YM, Wang K, and Zhang YJ have cited many of the same references. Additionally, Wei YM, Ye B, and Wu R have cited many of the same references. This indicates that there is a solid academic relevance in the research on China's ETS, and scholars continue to exchange ideas and realize the process of development in the study of issues concerning the ETS.

3.4.2. Productive Institutions and Co-Operation between them

The authors are from 1192 different research institutions around the world. The top 15 most productive institutions are shown in Table 4. Among them, MIT, Cambridge University, Harvard University, and Resources for the Future are world-class and famous and have rich research resources and experience to ensure the smooth realization of scientific research (according to QS World University Rankings, Times Higher Education, and RePEc/IDEAS Ranking). The institutions are in different countries, most of which are in the USA and Germany, some of which are in developed countries trying to transform, and China, a developing country trying to avoid significant emissions. Therefore, this research is vital for them. The top 15 most productive institutions have published 19 articles that were cited 435 times on average. Among them, the Beijing Institute of Technology, MIT, and Cambridge University published 33, 25, and 18 articles that were cited 786, 905, and 887 times, with relatively extensive h indexes of 15, 13, and 12, respectively. In addition,

although Harvard University and Massachusetts University published less, they are cited more, resulting in a more significant number of average citations per article, i.e., 40 and 31, respectively, with h indexes of 9.

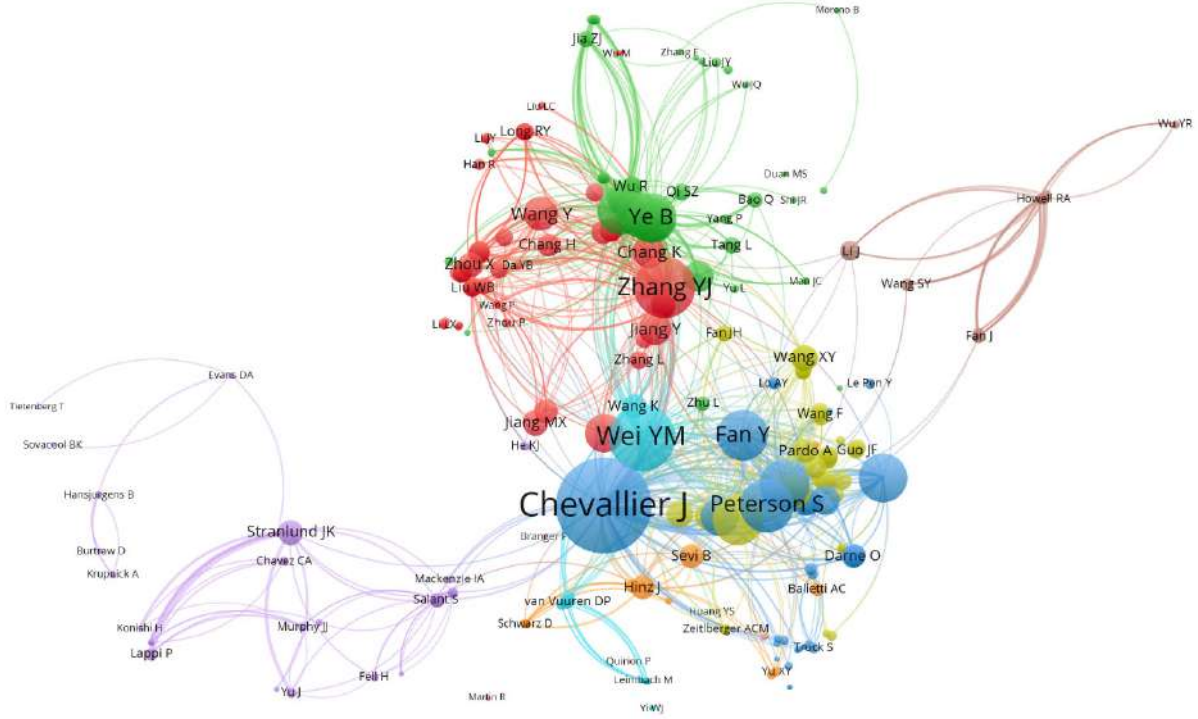

Figure 4. Bibliographic coupling by authors.

This paper also analyzed the co-operation between institutions. It can be seen that there are many connections between productive institutions (as shown in Figure 5). The Beijing Institute of Technology has a certain level of co-operation with Hunan University and Nanjing University. Tsinghua University co-operates with Nanjing University, National Singapore, MIT, and Duke University. The Chinese Academy of Sciences co-operates with Wuhan University, Shanghai Jiao Tong University, and Beihang University. In addition, there are many connections between University College Dublin, Cambridge University, Harvard University, MIT, and ZEW. In general, university alliances or co-operation has dramatically promoted the resolution of scientific problems regarding the ETS.

Table 4. The top 15 productive institutions.

Institutions	All Articles	All Citations	h Index	Country
Beijing Inst. Technol.	33	786	15	China
MIT	25	905	13	USA
Univ. Cambridge	18	887	12	UK
Chinese Acad. Sci.	39	635	12	China
Potsdam Inst. Climate Impact Res.	14	291	10	Germany
Univ. Maryland	14	349	10	USA
Ctr. European Econ. Res. ZEW	19	387	10	Germany
Tsinghua Univ.	31	260	10	China
Univ. Paris 09	12	211	9	France
Harvard Univ.	9	357	9	USA
ETH	13	277	9	Switzerland
Univ. Massachusetts	12	373	9	USA
Univ. Groningen	15	190	9	Netherlands
Resources Future Inc.	13	256	9	USA
Univ. Coll. Dublin	14	366	9	Ireland

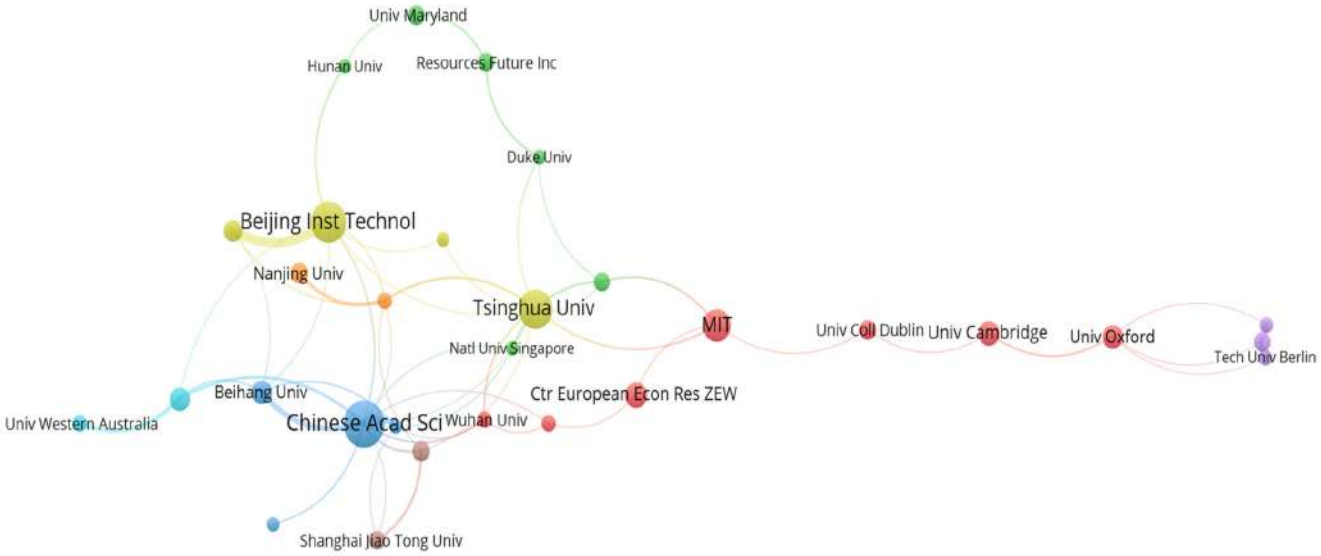

Figure 5. Co-operation of institutions.

4. Research Hotspots

This paper analyzed word frequency via the induction of all the keywords, titles, and abstracts in the retrieved 1991–2021 research literature on the ETS, and the research hotspots are drawn as follows: emissions trading, carbon, allocation, energy, power, China, European, market, policy, cost, and model (as shown in Figures 6 and 7). Therefore, it is necessary to research climate change mitigation using an effective climate policy, i.e., the emission trading scheme, which has been well developed in the European Union and has just been launched in China, and allowance allocation. Additionally, multi-objective optimization, data envelopment analysis, game theory, and input–output analysis are the most used methods.

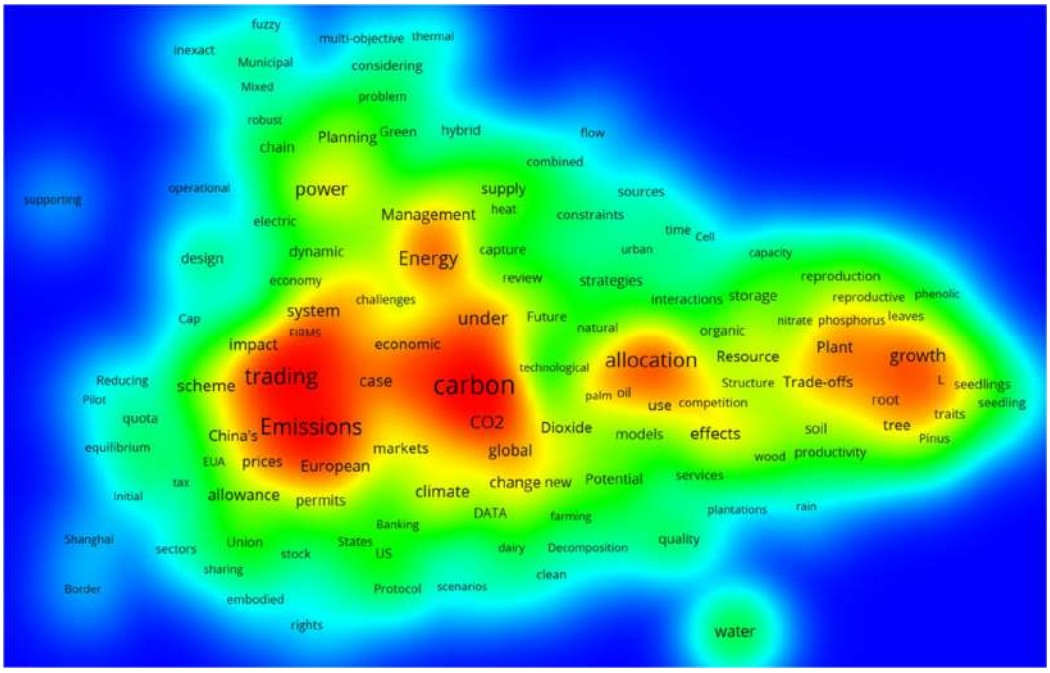

Figure 6. Thermal map of title word density.

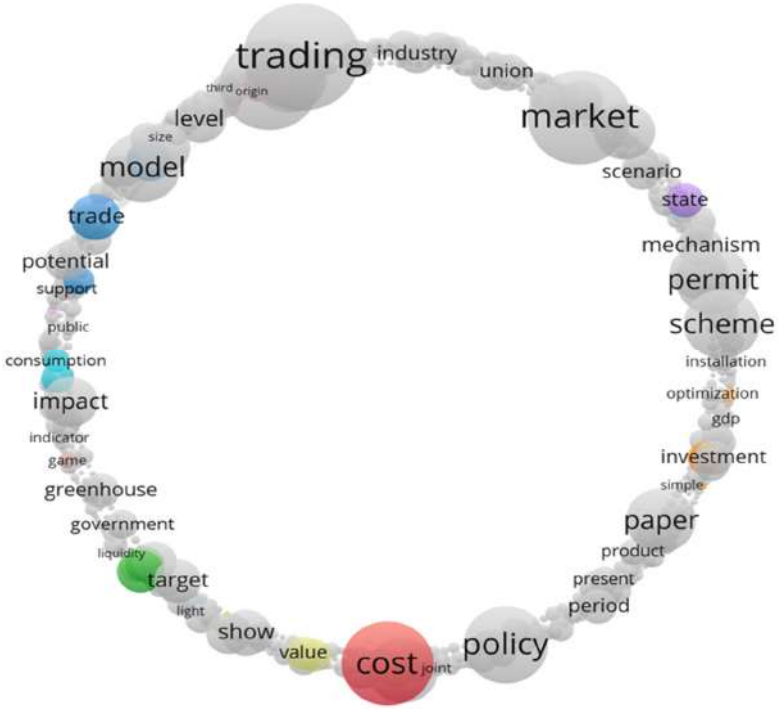

Figure 7. Words that appear more than ten times in the abstracts.

As for the power sector, it frequently appears 1007 times ("power" and "electricity"), and scholars focus on the impacts of the ETS and allocation allowance plans on the power sector: evidence from the power sector, including effects on the electricity market (electricity demand, enterprises, and price), investment decisions, electrical technology (generation, supply system, and transmission), electricity planning, and so on.

Therefore, this paper focused on three research hotspots in the field. They are: Why should ETS be launched? What is a better allowance allocation plan? What are the implications of the ETS and its allowance allocation, and what evidence exists from the power sector?

4.1. Carbon Emissions Trading System Has Cost Effects and Comparative Advantages

Scholars have recently had heated discussions on achieving national emission reductions. They compared the quantitative mechanism or the command-and-control regulation of emission reductions, namely the ETS, as a typical representative, with price incentives, namely carbon tax, as a typical representative. Additionally, they found that the ETS can achieve more significant environmental benefits at a lower cost and has comparative advantages. Hepburnexamined the relative advantages of price, quantity, and hybrid instruments according to the efficiency, trade-off, implementation, international considerations, and political economy [13]. Weitzman used the relative slope decision-making criterion (RSDC) to compare the social welfare of quantity and price regulation under uncertainty, significantly contributing to the emission reduction mechanisms' comparison [14,15].

Given the research on costs and benefits, researchers praise taxation policies for their abatement benefits. Pearce showed that the carbon tax not only improves the environmental quality but also offsets the income from carbon tax against other corporate taxes, increases employment and investment, and makes the economy more efficient [16]. Lin and Jia indicated that the tax mechanism is easier to understand and implement than the total amount control [17]. Gao pointed out that although the ETS's emission reduction effect is better than the carbon tax policy in the short term, the emission reduction potential for a carbon tax is more significant in the long run, and the emission reduction cost is also lower than the ETS [18]. Jia and Lin pointed out that in the long run, the emission reduction capacity of the carbon tax is slightly greater than that of the carbon trading mechanism [19].

Harstad et al. indicated the price agreement dominates the quantity agreement because when firms are free to modify the investment levels of another government defect, the punishment for defection is more substantial [20].

However, the advantages of quantity policies are increasingly prominent. Tang, Wang, and Wei found that quantity regulation results in learning how to eliminate cost uncertainty endogenously [21]. On the one hand, it can achieve more significant environmental benefits at a lower cost. Zhao et al. indicated a carbon emissions policy harms the economy. Compared to a carbon tax, a carbon trading scheme has a relatively slight impact on the economy [22]. Blackman et al. indicated that market-based policies are believed to be more effective in achieving the minimum cost of compliance and alleviating information asymmetry [23]. Wei showed it is difficult to control pollution using "command-control" regulations at the lowest price since technological innovation has insufficient incentives to eliminate and reduce pollution. Instead, Wei argued that market-oriented governance is more flexible [24]. Soto proposed using market mechanisms to solve environmental problems. The emissions trading system under total control shows that the cost of achieving emission reduction between different pollution sources is additional [25].

On the other hand, the carbon emissions trading system also has comparative advantages compared with other market instruments. In theory, if the goal is to maximize welfare, then taxation is superior to emissions trading [26,27], but Newell and Pizer pointed out that the cost of reducing carbon emissions offsets the gains from carbon taxes, which leads to a loss [28]. Karp and Zhang also pointed out that the carbon emissions trading system can cope better with these problems [29]. Murray et al. further pointed out that if the storage, banking, or borrowing of emission rights is allowed, the welfare effect of the cap-and-trade system will be better than the carbon tax [30]. Dong et al. indicated that the ETS significantly contributed greatly to reducing emissions [31]. Gao et al. pointed out that the ETS is a unique market mechanism to curb excessive GHG emissions, and its effectiveness has been a broad concern for governments and scholars [18]. Dong et al. indicated the carbon emissions trading policy significantly affects the co-benefits of the total carbon emissions reduction and air quality improvement [32].Zhang et al. stated that carbon emissions trading inhibits green technology innovation in the current stage but dramatically reduces carbon emissions [33] (as shown in Figure 8).

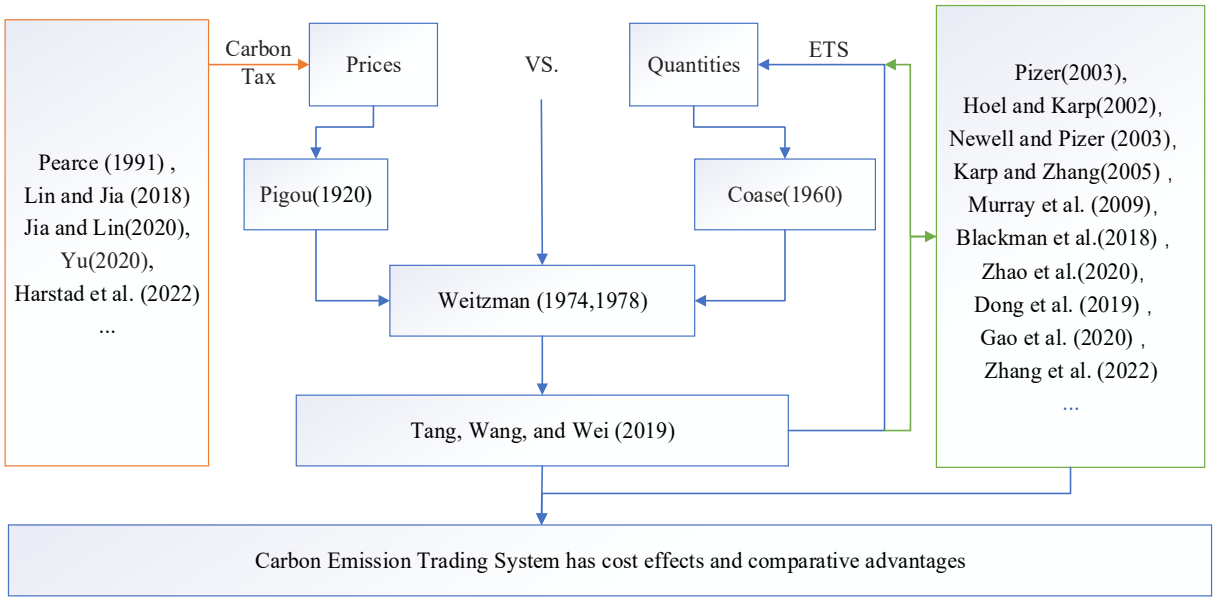

Figure 8. Prices vs. quantities; ETS has cost effects and comparative advantages [13–33].

As a result, the carbon emissions trading system has cost effects and comparative advantages in the short term based on previous research. Additionally, the research value

of the carbon emissions trading system is increasing. Therefore, the ETS should be launched and improved gradually to reduce emissions and mitigate climate change, which cannot be separated from academic contributions.

4.2. Methods of Allowance Allocation in the ETS

The issue of allowance allocation as the critical component in ETS construction has also caused heated discussion among scholars. From the perspective of fairness [34–36] or efficiency [37,38], top-down or bottom-up [39–41], scholars try to create reasonable and accepted allowance allocation schemes. With a desire to assign the future allowable carbon emissions, researchers and supranational institutions reasonably and efficiently have put forward over 20 allocation proposals. Yet, none have been widely accepted by climate conferences [42]. Therefore, it is necessary to explore a better allowance allocation scheme.

There are two ways to allocate quotas: for free or by public auction (as shown in Figure 9). Coaseproposed that whether or not the transaction cost is zero, as long as the emissions rights are clearly defined, the market will realize resource allocation effectively and internalize the external cost [3]. Free allocation, with zero transaction costs, is generally considered to apply to the initial stage of the carbon emissions trading system due to its low execution resistance and easy implementation. Stavins believed that with the support of political power and energy sectors, it is predicted that EU countries will still maintain a free allocation plan based on grandfathering in the short term [43]. However, Woerdman feared that there may be a lack of enough financial capacity to support the operation of grandfathering [44]. Matthes and Neuhoff pointed out that the long-term continuous use of the free allocation method will pull down the efficiency of the emissions trading system [45]. Christian et al. recommended that emission allowance should be applied to benchmarking based on historical output data, but the proportion of free allocation should also gradually decrease [46].

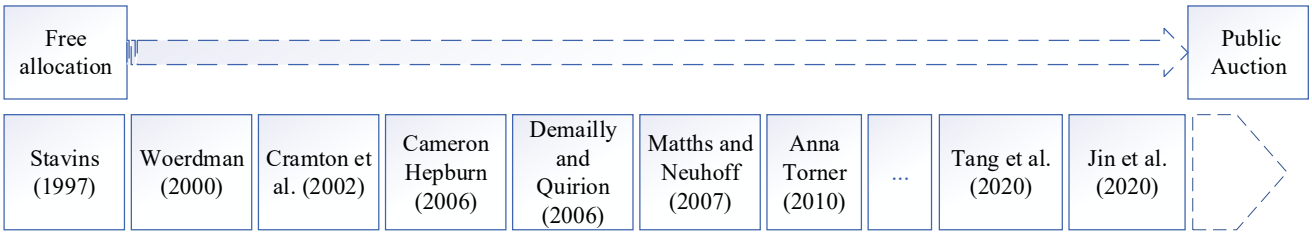

Figure 9. Scholars of study free allocation and public auction [43–56].

Although many enterprises favor free allocation due to the unpaid use of the environment and the unfairness toward newcomers, some scholars have proposed using pricing and auction methods to conduct carbon emissions trading more effectively. The most important and challenging problem in carbon pricing is determining the initial price. Many scholars proposed different techniques and ideas, such as the multi-variate analysis of environmental values [47], governance costs and the pollution pricing model [48], the shadow price pricing model [49–51], and so on. At present, more scholars believe that the auction method, a paid initial allocation method, is a better way to reflect the principles of fairness and justice and is suitable for carbon emissions trading. Demailly and Quirion pointed out that free allocation would make the dividends generated by the system tilt towards the regulated enterprises, and the overall improvement of society would be slight. This auction rule would be more effective [52]. In addition, Cramton et al. and Cameron Hepburn further pointed out that the auction method helps improve the efficiency of the carbon emissions trading system and maximizes government revenue [53,54]. The transition from free allocation to auction does not affect the products of regulated companies. Tang et al. simulated the marginal abatement cost curves of different sectors in China's ETS and calculated the optimal carbon price of sector coverage scenarios based on the criteria

involving eight industries [55]. Jin et al. simulated a national ETS of ten carbon-intensive sectors with the mass-based, output-based allocation (OBA) of emission allowances [56].

The issue of allowance allocation is a critical part of the ETS. It is necessary to explore a better allowance allocation scheme. However, there are still some problems to be solved in allowance allocation schemes, such as cap setting, covering sectors, and the allocation method. It has been determined that bottom-up quota allocation schemes can achieve national emission reduction targets from the up-bottom. Additionally, due to the accuracy of carbon emission data from key emitting enterprises, how to ensure that caps are neither loose nor tight should be determined. The timing and order should be explored and determined for sectors stepping into the ETS to avoid a loss of national welfare or the failure of emissions reduction. Research on the initial allocation of carbon emission allowance mainly focuses on the methods, and the pilot cities launching the ETS mostly rely on free allocation. Free allocation is based on historical emissions, but this method could only be applied to the transitional stage. With ETS's development, the use of the principles of benchmarking and auctioning will be inevitable.

4.3. Research on the Impact of Allowance Allocation and Evidence from the Power Sector

Scholars have conducted qualitative and quantitative analyses from macro and micro perspectives to study the impact of different allowance allocation schemes. However, international scholars always focus on the EU ETS, RGGI, and other ETSs, exploring the cost, supply, and demand planning models and the micro depth analysis of the different allowance allocation schemes. They found that an increase in carbon costs led to varying fluctuations in the market price, which affects demand and changes in the returns of different types of firms.

From a macro perspective and based on the equilibrium model, Chinese scholars worked out different economic and environmental impacts of different allowance allocation plans. They mainly focused on the qualitative comparison between the allocation methods. Xu examined various allocation methods of the total allowable pollutant discharge in China according to the principles of fairness and benefit and pointed out the advantages and disadvantages of each technique [57]. Ding and Feng explored the policy considerations of different allocation methods, analyzed the fundamental factors at the Chinese and international levels, and then put forward suggestions regarding the allocation methods that should be established in China [58]. Qi and Wangconducted a comparative analysis of the mode and methods of initial allocation and obtained China's progressive mixed way of free allocation [59]. Li and Wang conducted a comparative study of the allocation methods in the six pilot provinces and cities which launched ETSs and found that the allocation methods of the pilot ETSs have specific common characteristics, but each one also has its own features [60]. At present, there is no unified allocation method.

Some scholars have researched the power industry and the impact of allowance allocation in the power industry. As a significant emission sector, most scholars have taken the power industry as an example because of the standardization of its emissions accounting and the fact that it is the first to be covered by the ETS. Based on different allocation schemes, they studied the macroeconomic, environmental, and micro enterprises costs and other effects.

Macroscopically, as shown in Table 5, Bohringer and Lange used the general equilibrium model to quantitatively analyze the economic impact of different allocation methods based on ten integrated sectors [61]. Li and Jia set ten free allowance ratio scenarios, using a dynamic equilibrium model to simulate the ETS. They explored the free ratio and carbon price relationship, measuring the economic and environmental impact [62]. Using eight different allocation schemes, Li et al. used the dynamic equilibrium model to measure its economic impact [63]. Based on the general equilibrium model, Zhanganalyzed the effect of different allocation schemes on the power industry and tried to propose a better allocation scheme for the power industry [64]. Lin and Jia set up six allocation scenarios,

and the equilibrium model was used to analyze the energy, economic, and environmental impacts [17].

Table 5. Macroscopical research on the impact of allowance allocation in the power industry [17,60–64].

Title	Authors, Year	Regions	Model
Economic Implications of Alternative Allocation Schemes for Emission Allowances	Bohringer C, Lange A. 2005	EU and USA	CGE
The impact of emission trading scheme and the ratio of free quota: A dynamic recursive CGE model in China	Li W, Jia ZJ. 2016	China	CGE
The impact on electric power industry under the implementation of national carbon trading market in China: A dynamic CGE analysis	Wei Li, Yan-Wu Zhang, Can Lu. 2018	China	A dynamic CGE
Impact of carbon allowance allocation on power industry in China's carbon trading market: Computable General Equilibrium based analysis	Lirong Zhang, Yakun Li, Zhijie Jia. 2018	China	CGE
Impact of quota decline scheme of emission trading in China: A dynamic recursive CGE model	Boqiang Lin, Zhijie Jia. 2018	China	A dynamic recursive CGE model

At the micro level, scholars have adopted linear programming, equilibrium models, market simulation/multi-agents, etc., to explore the cost–benefit issues of power firms (as shown in Table 6). Burtraw et al. used the Haiku model to explore the power industry's cost and allocation effects of grandfathering, benchmarks, and auction allocation methods [65]. Neuhoff et al. used a comprehensive planning model (linear programming) to quantitatively analyze the ratio of firms' costs transferred to electricity prices and the final realized income under different allocation schemes [66–68]. Sijm, Chen and Lise used the enterprise competition and market power model (equilibrium model) in power transmission and energy simulation [69–72]. Additionally, they explored the transmission ratio of firms' costs to determine electricity prices under different allocation schemes.

Sterner and Muller used a simple multi-cycle model to study the impact of various free allocation schemes on incentives, emissions reductions, and outputs [73]. Zhou et al. modeled the Australian national electricity market in the ETS, based on historical emissions and historical power generation allocation methods, to analyze the potential profit impact and the possible compensation impact on the affected power generation companies [74]. Cong et al. used multi-agent modeling to measure the effect of different proportions of allowance auction schemes on electricity prices and power generation structures [75,76]. Westner and Madlener first showed that implementing the modified allocation mechanism significantly reduced the net present value of the power generation technology, then analyzed the decision-making problem [77]. Pierre and Boris explored the impact of fluctuations in carbon abatement costs on electricity prices using different theoretical and empirical models [78]. Ahn used a hybrid complementarity model to examine the effects of various initial allocation schemes on the Korean electricity market [79]. Liu et al. calculated the estimates of optimal power generation structures and technical structures at different auction rates and the cost of a reduction in China's power generation industry [80]. Goulde et al. assessed China's TPS's cost-effectiveness and distributional impacts on reducing CO_2 emissions from the power sector [81].

Table 6. Microscopical research on the impact of allowance allocation in the power industry [64–72].

Title	Authors, Year	Regions	Model
The Effect of Allowance Allocation on the Cost of Carbon Emission Trading	Dallas Burtraw, Karen Palmer, RanjitBharvirkar, and Anthony Paul. 2001	USA	Haiku model with an Industrial Sector Model (INSECT)
Allocation of carbon emission certificates in the power sector: how generators profit from grandfathered rights	Martinez KK; Neuhoff K. 2005	EU	Integrated Planning Model® (IPM)
Impact of the allowance allocation on prices and efficiency	Karsten Neuhoff, Michael Grubb and Kim Keats. 2005	EU	Analytic models and IPM
CO_2 cost pass-through and windfall profits in the power sector	Sijm J; Neuhoff K; Chen Y. 2006	Germany and Netherlands	COMPETES and IPM
Allocation, incentives and distortions: the impact of EU ETS emissions allowance allocations to the electricity sector	Neuhoff K; Martinez KK; Sato M. 2006	EU	IPM
Implications of CO_2 emissions trading for short-run electricity market outcomes in northwest Europe	Chen YH; Sijm J; Hobbs BF; Lise W. 2008	Nortwesern Europe	COMPETES
The Impact of the EU ETS on Prices, Profits and Emissions in the Power Sector: Simulation Results with the COMPETES EU20 Model	Lise W; Sijm J; Hobbs BF. 2010	EU	Carbon cost pass-through, COMPETES
CO_2 price dynamics: The implications of EU emissions trading for the price of electricity	J.P.M. Sijm, S.J.A. Bakker, Y. Chen H.W. Harmsen, W. Lise. 2005.	Nortwesern Europe	COMPETES model
Output and abatement effects of allocation readjustment in permit trade	Sterner T; Muller A. 2008	EU	A multiple-period model
Partial Carbon Permits Allocation of Potential Emission Trading Scheme in Australian Electricity Market	Zhou X; James G; Liebman A; Dong ZY; Ziser C. 2010	Australian	Australian National Electricity Market modeling
The impact of modified EU ETS allocation principles on the economics of CHP-based district heating systems	Westner G; Madlener R. 2012	EU	A spread-based real options model and discounted cash-flow model
An overview of CO_2 cost pass-through to electricity prices in Europe	Pierre-AndréJouvet, BorisSolier. 2013	EU	The marginal abatement cost function
Assessment of initial emission allowance allocation methods in the Korean electricity market	Jaekyun Ahn. 2014	Korea	A mixed complementarity problem (MCP) model
How will auctioning impact on the carbon emission abatement cost of electric power generation sector in China?	Liu LW; Sun XR; Chen CX; Zhao ED. 2016	China	The modified Trans-log production function, dynamic simulation model and multi-objective linear programming
China's unconventional nationwide CO_2 emissions trading system: Cost-effectiveness and distributional impacts	Lawrence H. Goulder, Xianling Long, Jieyi Lu, Richard D. Morgenstern. 2022	China	Analytically and numerically solved models

Based on the above research, most scholars use linear programming, equilibrium modeling, and multi-agent modeling to explore firms' cost and socio-economic and environmental impacts under different allocation schemes, which has excellent academic research value. However, due to the accuracy and availability of firms' emission data, the

effectiveness and scientificalness of the quota allocation scheme for the power industry need to be demonstrated, leading to firms getting too many or too few quotas, thus affecting emission reduction and development of critical emitters.

Therefore, it has practical significance and realistic value to research the ETS, which has cost effects and comparative advantages in reducing emissions and mitigating climate change. The issue of allowance allocation as the critical component in the ETS has also caused heated discussion among scholars. In allowance allocation, exploring a desire to assign the future allowable carbon emissions reasonably and efficiently is critical, yet scholars widely do not accept this. Moreover, free allocation is applied to the transitional stage, and auctioning will be inevitable. In addition, scholars from macro and micro perspectives used linear programming, equilibrium modeling, and multi-agent modeling to explore the impact of different allowance allocation schemes and took the power industry as an example.

5. Conclusions and Discussion

Unlike previous research, this study presented a comprehensive and systematic literature review on the ETS, including its origin, core mechanism, research hotspots, and future research focus, using a bibliometric method and combining in-depth qualitative analysis. This study explored the practical problems and research gaps in constructing the ETS. In conclusion, it is necessary to research the ETS to mitigate climate change and reduce emissions at a low cost. As the carbon market is paid much attention, the issue of allowance allocation as the critical component in ETS construction has also caused heated discussion among scholars. In allowance allocation, exploring a desire to assign the future allowable carbon emissions reasonably and efficiently is critical, yet scholars widely do not accept this. Moreover, free allocation is based on historical emissions, but this method can only be applied to the transitional stage. With the development of the ETS, the use of the principles of benchmarking and auctioning will be inevitable. In addition, scholars have carried out qualitative and quantitative analyses from macro and micro perspectives to study the impact of different allowance allocation schemes and took the power industry, the largest emitter sector, as an example. Most scholars use linear programming, equilibrium modeling, and multi-agent modeling to explore firms' cost and socio-economic and environmental impacts under different allocation schemes. However, due to the accuracy of industry data, the quota allocation scheme needs to be improved.

Launching the ETS to mitigate climate change effectively and reduce emissions at a low cost is necessary. However, different emission reduction commitments of each country lead to different levels of progress in carbon market construction. Countries launching the ETS are gradually improving their core mechanisms, such as allowance allocation, cap setting, covering sectors, and the allocation method. However, due to the accuracy of obtaining historical quota data, the effect of the quota allocation scheme needs to be improved, including how to set neither loose nor tight caps and construct a quota allocation scheme with effective emission reduction and cost. Regarding sectors stepping into the ETS, it is vital to determine the ordering and timing. Moreover, in terms of the allocation method, auctioning will be inevitable in the future, but the dynamic timing of the shift from free to auction quotas is worth exploring. All these problems need to be further studied. Countries not launching the ETS lack the responsibility and confidence to actively mitigate climate change, which has caused widespread adverse impacts and related losses and damages to nature and people beyond natural climate variability (IPCC,2022). They should reduce emissions through energy restructuring, clean energy, and technology development and upgrading instead of the ETS, but they will face high emission reduction costs if they do. Carbon markets can be an excellent way to balance emissions and development.

6. Policy Implications

Governments are encouraged to launch the ETS to reduce emissions and combat climate change. This paper showed that the emissions trading system has cost effects and

comparative advantages of reducing emissions and mitigating climate change. Additionally, it is also an object of excellent academic and research value, which is indicated by the amount and distribution of the publications, journal distribution, productive authors, and institutions. Therefore, it is critical to research the ETS and its research, including the initial allowance allocation, its impact, and the empirical analysis focusing on the largest emitter, the power sector. According to research on the ETS, governments can obtain scientific advice on how to launch the ETS and gradually improve its core mechanics. For countries establishing the ETS, governments should enhance their core mechanisms, such as allowance allocation. For countries not launching the ETS, carbon markets can be an excellent way to balance emissions and development in the future, which do not pay for energy restructuring, clean energy, and technology development and upgrading. In addition, external factors and development influence ETS launches, such as sudden international political events. This year, the tension between Russia and Ukraine triggered pessimism about the carbon market. It led to the large-scale selling of carbon quotas, seriously affecting the ETS's sustainable development. Moreover, some international negotiations could help boost the ETS, such as COP21, COP26, and so on. Therefore, in constructing the ETS, the government should treat and respond to the influence of external factors reasonably and effectively.

The ETS should be improved gradually, including the improvement of issues such as cap setting, covering sectors, and the allocation method. To better reduce emissions and mitigate climate change, the ETS should be progressively enhanced to play its role in reducing emissions at low costs. In the process of carbon trading in various countries, quota allocation has always been complex. Therefore, allocating allowance effectively and somewhat reasonably is crucial, which involves determining how to set a reasonable cap, when and who is stepping into the ETS, and how to select a scientific and rational allocation method. Regarding cap setting, top-down and bottom-up approaches should be well docked. Namely, bottom-up quota allocation schemes can achieve national emission reduction targets. Additionally, the carbon emission data of key emitting enterprises should be obtained accurately, ensuring that caps are neither loose nor tight. Regarding sectors stepping into the ETS, the timing and order should be explored and determined to avoid a loss of national welfare or the failure of emissions reduction. In terms of the allocation method, auctioning will be inevitable in the future, but the pace of the shift from free to auction quotas is worth exploring. Auctioning at the right time is more acceptable for participants in the ETS.

Some key emission sectors and regions can be taken as the research and practice objects in the initial stage of the ETS. The ETS will initially only cover the more significant emitters. This paper found that most scholars focus on research on allowance allocation in the power industry, trying to microscopically analyze the impact of different allocation schemes, such as free and auctioning schemes, the cost and cost transfer, firms' income, and electricity prices in the market. However, due to the accuracy and availability of firms' emission data, the effectiveness and scientificalness of the quota allocation scheme for key emitters such as the power industry need to be demonstrated, leading to firms getting too many or too few quotas, thus affecting emission reduction and the development of critical emitters. Regarding the regions, some regions with good growth and resource endowment can be used as pilot areas to accumulate experience for national ETS construction. However, the determination of how to solve the problem of docking between the pilot and ETS is also very important. In general, the research and practice of critical sectors and pilot regions aim to improve the country's effective emission reduction mechanism and fully play its role in addressing climate change.

Author Contributions: Conceptualization, methodology, writing—original draft preparation, funding acquisition, Y.-J.H.; investigation, methodology, L.Y.; data curation, software, F.D.; formal analysis, validation, resources, H.W. and C.L. All authors have read and agreed to the published version of the manuscript.

Funding: This research was funded by [National Natural Science Foundation of China] grant number [72104062], [Humanities and Social Science Research Youth Fund project of the Ministry of Education] grant number [21YJC630041], and [Key Laboratory of "Internet+" Collaborative Intelligent Manufacturing in Guizhou Provence] grant number [20165103].

Institutional Review Board Statement: Not applicable.

Informed Consent Statement: Not applicable.

Data Availability Statement: Not applicable.

Conflicts of Interest: The authors declare no conflict of interest.

References

1. IPCC. *Climate Change 2022: Mitigation of Climate Change*; Skea, J., Shukla, P.R., Slade, R., al Khourdajie, A., van Diemen, R., McCollum, D., Pathak, M., Some, S., Vyas, P., Fradera, R., et al., Eds.; IPCC: Geneva, Switzerland, 2022.
2. ICAP. *Emissions Trading Worldwide: Status Report 2022*; ICAP: Berlin, Germany, 2022.
3. Coase, R.H. The Problem of Social Cost. *J. Law Econ.* **1960**, *3*, 1–44. [CrossRef]
4. Cañas-Guerrero, I.; Mazarrón, F.R.; Calleja-Perucho, C.; Pou-Merina, A. Bibliometric analysis in the international context of the "Construction & Building Technology" category from the Web of Science database. *Constr. Build. Mater.* **2014**, *53*, 13–25.
5. Du, H.; Li, B.; Brown, M.A.; Mao, G.; Rameezdeen, R.; Chen, H. Expanding and shifting trends in carbon market research: A quantitative bibliometric study. *J. Clean. Prod.* **2015**, *103*, 104–111. [CrossRef]
6. Kiriyama, E.; Kajikawa, Y.; Fujita, K.; Iwata, S. A lead for transvaluation of global nuclear energy research and funded projects in Japan. *Appl. Energy* **2013**, *109*, 145–153. [CrossRef]
7. Wei, Y.-M.; Mi, Z.-F.; Huang, Z. Climate policy modeling: An online SCI-E and SSCI based literature review. *Omega* **2015**, *57*, 70–84. [CrossRef]
8. Yu, H.; Wei, Y.-M.; Tang, B.-J.; Mi, Z.; Pan, S.-Y. Assessment on the research trend of low-carbon energy technology investment: A bibliometric analysis. *Appl. Energy* **2016**, *184*, 960–970. [CrossRef]
9. Zhang, K.; Wang, Q.; Liang, Q.-M.; Chen, H. A bibliometric analysis of research on carbon tax from 1989 to 2014. *Renew. Sustain. Energy Rev.* **2016**, *58*, 297–310. [CrossRef]
10. Wang, X.-Y.; Tang, B.-J. Review of comparative studies on market mechanisms for carbon emission reduction: A bibliometric analysis. *Nat. Hazards* **2018**, *94*, 1141–1162. [CrossRef]
11. Ji, C.J.; Li, X.Y.; Hu, Y.J.; Wang, X.Y.; Glade, T.; Murty, T.S. Research on carbon price in emissions trading scheme: A bibliometric analysis. *Nat. Hazards* **2019**, *99*, 1381–1396. [CrossRef]
12. Tang, L.; Wang, H.; Li, L.; Yang, K.; Mi, Z. Quantitative models in emission trading system research: A literature review. *Renew. Sustain. Energy Rev.* **2020**, *132*, 110052. [CrossRef]
13. Hepburn, C. Regulation by Prices, Quantities, or Both: A Review of Instrument Choice. *Oxf. Rev. Econ. Policy* **2006**, *22*, 226–247. [CrossRef]
14. Weitzman, M. *Prices vs. Quantities*; Massachusetts Institute of Technology (MIT), Department of Economics: Cambridge, MA, USA, 1973.
15. Weitzman, M.L. Optimal Rewards for Economic Regulation. *Am. Econ. Rev.* **2001**, *68*, 683–691.
16. Pierce, D. The role of carbon taxes in adjusting to global warming. *Econ. J.* **1991**, *101*, 938–948. [CrossRef]
17. Lin, B.; Jia, Z. Impact of quota decline scheme of emission trading in China: A dynamic recursive CGE model. *Energy* **2018**, *149*, 190–203. [CrossRef]
18. Gao, Y.; Li, M.; Xue, J.; Liu, Y. Evaluation of effectiveness of China's carbon emissions trading scheme in carbon mitigation. *Energy Econ.* **2020**, *90*, 104872. [CrossRef]
19. Jia, Z.; Lin, B. Rethinking the choice of carbon tax and carbon trading in China. *Technol. Forecast. Soc. Chang.* **2020**, *159*, 120187. [CrossRef]
20. Harstad, B.; Lancia, F.; Russo, A. Prices vs. quantities for self-enforcing agreements. *J. Environ. Econ. Manag.* **2022**, *111*, 102595. [CrossRef]
21. Tang, B.-J.; Wang, X.-Y.; Wei, Y.-M. Quantities versus prices for best social welfare in carbon reduction: A literature review. *Appl. Energy* **2019**, *233–234*, 554–564. [CrossRef]
22. Zhao, L.; Yang, C.; Su, B.; Zeng, S. Research on a single policy or policy mix in carbon emissions reduction. *J. Clean. Prod.* **2020**, *267*, 122030. [CrossRef]
23. Allen, B.; Li, Z.; Liu, A.A. Efficacy of Command-and-Control and Market-Based Environmental Regulation in Developing Countries. *Annu. Rev. Resour. Econ.* **2018**, *10*, 381–404. [CrossRef]
24. Wei, C. China's urban CO_2 marginal abatement costs and its influencing factors. *World Econ.* **2014**, *431*, 115–137.
25. Soto, H.D. *The Mystery of Capital: Why Capitalism Triumphs in the West and Fails Everywhere Else*; Basic Books: New York, NY, USA, 2000.
26. Hoel, M.; Karp, L. Taxes versus quotas for a stock pollutant. *Resour. Energy Econ.* **2002**, *24*, 367–384. [CrossRef]
27. Hoel, M.; Karp, L. Taxes vs. Quotas for a Stock Pollutant with Multiplicative Uncertainty. *Resour. Energy Econ.* **2001**, *82*, 91–114.

28. Newell, R.G.; Pizer, W.A. Regulating stock externalities under uncertainty. *J. Environ. Econ. Manag.* **2003**, *45*, 416–432. [CrossRef]
29. Larry Karp, J.Z. Regulation of Stock Externalities with Correlated Abatement Costs. *Environ. Resour. Econ.* **2005**, *32*, 273–300. [CrossRef]
30. Murray, B.C.; Newell, R.G.; Pizer, W.A. Balancing Cost and Emissions Certainty: An Allowance Reserve for Cap-and-Trade. *Rev. Environ. Econ. Policy* **2009**, *3*, 84–103. [CrossRef]
31. Dong, F.; Dai, Y.; Zhang, S.; Zhang, X.; Long, R. Can a carbon emission trading scheme generate the Porter effect? Evidence from pilot areas in China. *Sci. Total Environ.* **2019**, *653*, 565–577. [CrossRef]
32. Dong, Z.; Xia, C.; Fang, K.; Zhang, W. Effect of the carbon emissions trading policy on the co-benefits of carbon emissions reduction and air pollution control. *Energy Policy* **2022**, *165*, 112998. [CrossRef]
33. Zhang, W.; Li, G.; Guo, F. Does carbon emissions trading promote green technology innovation in China? *Appl. Energy* **2022**, *315*, 119012. [CrossRef]
34. Ringius, L.; Torvanger, A.; Holtsmark, B. Can multi-criteria rules fairly distribute climate burdens?: OECD results from three burden sharing rules. *Energy Policy* **1998**, *26*, 777–793. [CrossRef]
35. William, N. *A Question of Balance: Weighing the Options on Global Warming Policies*; Yale University Press: London, UK, 2008; Volume 9, pp. 146–147.
36. Rose, A.; Stevens, B.; Edmonds, J.; Wise, M. International Equity and Differentiation in Global Warming Policy. *Environ. Resour. Econ.* **1998**, *12*, 25–51. [CrossRef]
37. Miao, Z.; Geng, Y.; Sheng, J. Efficient allocation of CO_2 emissions in China: A zero sum gains data envelopment model. *J. Clean. Prod.* **2016**, *112*, 4144–4150. [CrossRef]
38. Wang, K.; Zhang, X.; Wei, Y.-M.; Yu, S. Regional allocation of CO_2 emissions allowance over provinces in China by 2020. *Energy Policy* **2013**, *54*, 214–229. [CrossRef]
39. Ellerman, A.D.; Buchner, B.K. The European Union Emissions Trading Scheme: Origins, Allocation, and Early Results. *Rev. Environ. Econ. Policy* **2007**, *1*, 66–87. [CrossRef]
40. Betz, R.; Eichhammer, W.; Schleich, J. Designing National Allocation Plans for Eu-Emissions Trading—A First Analysis of the Outcomes. *Energy Environ.* **2004**, *15*, 375–425. [CrossRef]
41. Betz, R.; Rogge, K.; Schleich, J. EU emissions trading: An early analysis of national allocation plans for 2008–2012. *Clim. Policy* **2006**, *6*, 361–394. [CrossRef]
42. Wei, Y.-M.; Zou, L.-L.; Wang, K.; Yi, W.-J.; Wang, L. Review of proposals for an Agreement on Future Climate Policy: Perspectives from the responsibilities for GHG reduction. *Energy Strategy Rev.* **2013**, *2*, 161–168. [CrossRef]
43. Stavins, R.N. Policy Instruments for Climate Change: How Can National Governments Address a Global Problem? *Univ. Chic. Leg. Forum* **1997**, *1997*, 10.
44. Woerdman, E. Implementing the Kyoto protocol: Why JI and CDM show more promise than international emissions trading. *Energy Policy* **2000**, *28*, 29–38. [CrossRef]
45. Matthes, F.C.; Neuhoff, K. *Auctioning in the European Union Emissions Trading Scheme*; Öko-Institut: Berlin, Germany; University of Cambridge: Cambridge, UK, 2007.
46. Egenhofer, C.; Georgiev, A.; Torner, A.; van den Bergh, H. *Benchmarking in the EU: Lessons from the EU Emissions Trading System for the Global Climate Change Agenda*; CEPS Task Force Report, 11 June 2010; Centre for European Policy Studies: Brussels, Belgium, 2022.
47. Li, S.; Wang, J. The impact of the transaction under the different distribution of initial emission rights on the market structure. *J. Wuhan Univ. Technol. (Transp. Sci. Eng. Ed.)* **2004**, *28*, 40–43.
48. Bangtao, H.T.W. Emissions trading pricing model based on governance cost and pollutant income. *Shanghai Manag. Sci.* **2004**, *6*, 34–36.
49. Min, H. Analysis of Shadow Price Model for Emission Permit Pricing. *Price Mon.* **2007**, *2*, 19–22.
50. Yunhua, L. On the pricing mechanism and influencing factors of the emissions trading market. *Contemp. Econ. Manag.* **2009**, *31*, 1–4.
51. Yan, L.; Wu, T. Initial allocation and transaction model of emission rights based on shadow price. *J. Chongqing Univ. Technol. (Soc. Sci. Ed.)* **2010**, *24*, 53–56.
52. Demailly, D.; Quirion, P. CO_2 abatement, competitiveness and leakage in the European cement industry under the EU ETS: Grandfathering versus output-based allocation. *Clim. Policy* **2006**, *6*, 93–113. [CrossRef]
53. Hepburn, C.; Grubb, M.; Neuhoff, K.; Matthes, F.; Tse, M. Auctioning of EU ETS phase II allowances: How and why? *Clim. Policy* **2006**, *6*, 137–160. [CrossRef]
54. Cramton, P.; Kerr, S. Tradeable carbon permit auctions: How and why to auction not grandfather. *Energy Policy* **2002**, *30*, 333–345. [CrossRef]
55. Tang, B.-J.; Ji, C.-J.; Hu, Y.-J.; Tan, J.-X.; Wang, X.-Y. Optimal carbon allowance price in China's carbon emission trading system: Perspective from the multi-sectoral marginal abatement cost. *J. Clean. Prod.* **2020**, *253*, 119945. [CrossRef]
56. Jin, Y.; Liu, X.; Chen, X.; Dai, H. Allowance allocation matters in China's carbon emissions trading system. *Energy Econ.* **2020**, *92*, 105012. [CrossRef]
57. Baifu, X. Allowable Total Distributing Method and Equity-Benefit Principle. *Pollut. Prev. Technol.* **1994**, *1*, 14–16.
58. Ding Ding, F.J. On the choice of China's carbon trading quota allocation method. *Int. Bus. (J. Univ. Int. Bus. Econ.)* **2013**, *1*, 83–92.

59. Qi, S.; Wang, B. Initial quota allocation for carbon trading: A comparative analysis of patterns and methods. *J. Wuhan Univ. (Philos. Soc. Sci. Ed.)* **2013**, *5*, 19–28.
60. Li, F.; Wang, W. Comparative Research on Quota Allocation Methods in China's Pilot Carbon Market. *Res. Econ. Manag.* **2015**, *36*, 9–15.
61. Böhringer, C.; Lange, A. Economic Implications of Alternative Allocation Schemes for Emission Allowances: A Theoretical and Applied Analysis. *ZEW Discuss. Pap.* **2003**, *107*, 563–581.
62. Li, W.; Jia, Z. The impact of emission trading scheme and the ratio of free quota: A dynamic recursive CGE model in China. *Appl. Energy* **2016**, *174*, 1–14. [CrossRef]
63. Li, W.; Zhang, Y.-W.; Lu, C. The impact on electric power industry under the implementation of national carbon trading market in China: A dynamic CGE analysis. *J. Clean. Prod.* **2018**, *200*, 511–523. [CrossRef]
64. Zhang, L.; Li, Y.; Jia, Z. Impact of carbon allowance allocation on power industry in China's carbon trading market: Computable general equilibrium based analysis. *Appl. Energy* **2018**, *229*, 814–827. [CrossRef]
65. Burtraw, D.; Palmer, K.; Bharvirkar, R.; Paul, A. The Effect on Asset Values of the Allocation of Carbon Dioxide Emission Allowances. *Electr. J.* **2002**, *15*, 51–62. [CrossRef]
66. Neuhoff, K.; Åhman, M.; Betz, R.; Cludius, J.; Ferrario, F.; Holmgren, K.; Pal, G.; Grubb, M.; Matthes, F.; Rogge, K.; et al. Implications of announced phase II national allocation plans for the EU ETS. *Clim. Policy* **2006**, *6*, 411–422. [CrossRef]
67. Neuhoff, K.; Grubb, M.; Keats, K. Impact of the allowance allocation on prices and efficiency. *Camb. Work. Pap. Econ.* **2005**, 19–603. [CrossRef]
68. Neuhoff, K.; Martinez, K.K.; Sato, M. Allocation, incentives and distortions: The impact of EU ETS emissions allowance allocations to the electricity sector. *Clim. Policy* **2006**, *6*, 73–91. [CrossRef]
69. Chen, Y.; Sijm, J.; Hobbs, B.F.; Lise, W. Implications of CO_2 emissions trading for short-run electricity market outcomes in northwest Europe. *J. Regul. Econ.* **2008**, *34*, 251–281. [CrossRef]
70. Lise, W.; Sijm, J.; Hobbs, B.F. The Impact of the EU ETS on Prices, Profits and Emissions in the Power Sector: Simulation Results with the COMPETES EU20 Model. *Environ. Resour. Econ.* **2010**, *47*, 23–44. [CrossRef]
71. Sijm, J.; Neuhoff, K.; Chen, Y. CO_2 cost pass-through and windfall profits in the power sector. *Clim. Policy* **2006**, *6*, 49–72. [CrossRef]
72. Sijm, J.P.M.; Bakker, S.J.A.; Chen, Y.; Harmsen, H.W.; Lise, W. CO_2 price dynamics: The implications of EU emissions trading for electricity prices & operations. In Proceedings of the 2006 IEEE Power Engineering Society General Meeting, Montreal, QC, Canada, 18–22 June 2006; p. 4.
73. Sterner, T.; Muller, A. Output and abatement effects of allocation readjustment in permit trade. *Clim. Chang.* **2008**, *86*, 33–49. [CrossRef]
74. Zhou, X.; James, G.; Liebman, A.; Dong, Z.Y.; Ziser, C. Partial Carbon Permits Allocation of Potential Emission Trading Scheme in Australian Electricity Market. *IEEE Trans. Power Syst.* **2010**, *25*, 543–553. [CrossRef]
75. Cong, R.-G.; Wei, Y.-M. Potential impact of (CET) carbon emissions trading on China's power sector: A perspective from different allowance allocation options. *Energy* **2010**, *35*, 3921–3931. [CrossRef]
76. Cong, R.-G.; Wei, Y.-M. Experimental comparison of impact of auction format on carbon allowance market. *Renew. Sustain. Energy Rev.* **2012**, *16*, 4148–4156. [CrossRef]
77. Westner, G.; Madlener, R. The impact of modified EU ETS allocation principles on the economics of CHP-based district heating systems. *J. Clean. Prod.* **2012**, *20*, 47–60. [CrossRef]
78. Jouvet, P.-A.; Solier, B. An overview of CO_2 cost pass-through to electricity prices in Europe. *Energy Policy* **2013**, *61*, 1370–1376. [CrossRef]
79. Ahn, J. Assessment of initial emission allowance allocation methods in the Korean electricity market. *Energy Econ.* **2014**, *43*, 244–255. [CrossRef]
80. Liu, L.; Sun, X.; Chen, C.; Zhao, E. How will auctioning impact on the carbon emission abatement cost of electric power generation sector in China? *Appl. Energy* **2016**, *168*, 594–609. [CrossRef]
81. Goulder, L.H.; Long, X.; Lu, J.; Morgenstern, R.D. China's unconventional nationwide CO_2 emissions trading system: Cost-effectiveness and distributional impacts. *J. Environ. Econ. Manag.* **2022**, *111*, 102561. [CrossRef]

energies

MDPI

Article

Hybrid Power Management Strategy with Fuel Cell, Battery, and Supercapacitor for Fuel Economy in Hybrid Electric Vehicle Application

V. Mounica and Y. P. Obulesu *

School of Electrical Engineering (SELECT), Vellore Institute of Technology, Vellore 632014, Tamil Nadu, India; v.mounica2018@vitstudent.ac.in

* Correspondence: yp.obulesu@vit.ac.in

Abstract: The power management strategy (PMS) is intimately linked to the fuel economy in the hybrid electric vehicle (HEV). In this paper, a hybrid power management scheme is proposed; it consists of an adaptive neuro-fuzzy inference method (ANFIS) and the equivalent consumption minimization technique (ECMS). Artificial intelligence (AI) is a key development for managing power among various energy sources. The hybrid power supply is an eco-acceptable system that includes a proton exchange membrane fuel cell (PEMFC) as a primary source and a battery bank and ultracapacitor as electric storage systems. The Haar wavelet transform method is used to calculate the stress (σ) on each energy source. The proposed model is developed in MATLAB/Simulink software. The simulation results show that the proposed scheme meets the power demand of a typical driving cycle, i.e., Highway Fuel Economy Test Cycle (HWFET) and Worldwide Harmonized Light Vehicles Test Procedures (WLTP—Class 3), for testing the vehicle performance, and assessment has been carried out for various PMS based on the consumption of hydrogen, overall efficiency, state of charge of ultracapacitors and batteries, stress on hybrid sources and stability of the DC bus. By combining ANFIS and ECMS, the consumption of hydrogen is minimized by 8.7% compared to the proportional integral (PI), state machine control (SMC), frequency decoupling fuzzy logic control (FDFLC), equivalent consumption minimization strategy (ECMS) and external energy minimization strategy (EEMS).

Keywords: ANFIS; ECMS; hybrid electric vehicle; Haar wavelet transform; hydrogen consumption; power management scheme; system efficiency

Citation: Mounica, V.; Obulesu, Y.P. Hybrid Power Management Strategy with Fuel Cell, Battery, and Supercapacitor for Fuel Economy in Hybrid Electric Vehicle Application. *Energies* **2022**, *15*, 4185. https://doi.org/10.3390/en15124185

Academic Editors: Nicu Bizon and Tek Tjing Lie

Received: 14 March 2022
Accepted: 9 May 2022
Published: 7 June 2022

Publisher's Note: MDPI stays neutral with regard to jurisdictional claims in published maps and institutional affiliations.

Copyright: © 2022 by the authors. Licensee MDPI, Basel, Switzerland. This article is an open access article distributed under the terms and conditions of the Creative Commons Attribution (CC BY) license (https://creativecommons.org/licenses/by/4.0/).

1. Introduction

Freshwater, electricity and the atmosphere are interconnected factors that have emerged as the most significant and prominent topics in engineering. In particular, global warming and resource shortages are key challenges that have been addressed. As a result, manufacturing practices and engineering communities are rapidly transforming the approach to energy-efficient applications; environmental and economic considerations are driving the transportation sector's development [1]. Transportation is mostly reliant on fossil fuels and produces greenhouse gases. Here, several attempts have been made to enhance the requirement of fuel cells (FCs) in transportation applications as a sustainable electric power source that emits no greenhouse gas [2,3]. The usage of fuel cells in electric vehicles, trains, aircraft, etc., helps to protect the environment, thereby providing a clean fuel source for transportation [4]. Fuel cells are new energy conversion solutions that have many advantages over traditional devices, including high energy efficiency, small size, environmental safety, long lifespan and so on. The proton exchange membrane fuel cell (PEMFC) seems to be the most suitable form for use in automotive applications because it has a high density in producing electricity, leading to lower heat generation and resulting in a lower temperature, which is important in transportation applications. The key drawback of fuel cells in

transportation applications is the low dynamic response. Since the fuel cell lags against load variations, this means that they are unable to react appropriately to sudden changes in load.

As a result, the fuel cell should be associated with the battery storage and ultracapacitor (UC) [5,6], while the battery storage seems to have a high-power density, with some limitations, such as lower energy capacity, a long charging period, a high price and a short lifespan. The usage of a hybrid FC/B/UC network is the best strategy to overcome the described issues. This type of combination allows the hybrid sources to exploit their unique characteristics. The battery bank acts as an energy buffer, whereas the ultracapacitor supplies transient peak power units. A power management scheme (PMS) is essential to achieve certain hybridization and achieve the main goal of distributing load requirements through power sources. By limiting the fuel cell performance to wider operating levels, the PMS successfully maintains the consumption of hydrogen and enhances the energy efficiency. To regulate the system load among these integrated input sources, a set of conventional PMS was implemented [7].

They are PI control, state machine control (SMC), the equivalent consumption minimization scheme (ECMS), fuzzy logic control (FLC) and the external energy minimization scheme (EEMS), and several other modern optimization-based techniques have also been developed. In Ref. [8], Wang et al. developed a power management technique for state machine control (SMC) that contains the battery bank, fuel cell and ultracapacitors as a multi-input network. In Ref. [9], power management with the proportional integral (PI) technique was implemented by the authors to regulate the energy across photovoltaics (PV), fuel cells (FCs), batteries and supercapacitors (SCs). Multiple operational modes were operated for a hybrid device consisting of B/SC/FC in [10] using a rule-based energy management technique. In Ref. [11], Jiang et al. proposed a dynamic programming (DP) method for reducing hydrogen consumption in a hybrid power system with a fuel cell, battery and supercapacitor to provide energy to the power train. The authors Li et al. [12] implemented a novel power management technique with rule-based fuzzy logic control with various multi-input sources, i.e., at first, the input sources consist of FC/B, and, later, the input sources consist of B/SC/FC for powering an electric vehicle.

In Ref. [13], the authors present an adaptive neuro-fuzzy inference system (ANFIS) to adequately manage the power between the FC and battery often used to provide power to electric vehicles (EV). The authors Chen et al., in [14], proposed a power management technique divided into two sections, a wavelet-based and a radial-based solution, to refine the power output in an electric vehicle using neural networks. The authors designed a novel energy management mechanism focusing on wavelet transform approaches for controlling power among FC/B/SC to EVs. A Gray Wolf Optimizer (GWO) was designed by authors Djerioui et al. considering FC/B/UC as a hybrid power system for electric vehicle applications [15]. In a parallel HEV, an FLC-based technique was designed to optimize the SoC, enhance fuel efficiency, minimize NO_x emissions and ensure greater drivability. For power split across accessible sources, an FLC-based intelligent energy management agent (IEMA) has been developed. The author of Ref. [16] created an FLC to optimize system operation using the energy demands and the speed of the vehicle, as well as the SoC, as input variables.

A rule-based method was utilized in a parallel HEV to increase fuel economy in Ref. [17]. In Ref. [18], FLC was used in a parallel HEV to establish a predictive EMS in terms of speed as well as reinforcement learning. In consideration of SoC and torque limitations, an FLC-enabled EMS for series HEVs has been designed. A dual FLC technique for a parallel HEV is reported in Ref. [19], in which membership functions (MFs) are optimized to use a genetic algorithm (GA) to improve performance when compared to the dynamic programming (DP) approach. For controlling the power across FC/B/SC, the authors implemented an equivalent consumption minimization scheme (ECMS) employing a sequential quadratic programming approach. ECMS is a greedy (immediate) optimization method. The ECMS cost factor takes into account fuel consumption as well as the cost of us-

ing battery energy. The equivalency factor is the weighting for these penalties. Pontryagin's Minimum Principle (PMP) can be used to generate ECMS. As a result, if the battery state of charge does not exceed the limitations, ECMS provides the best fuel efficiency. However, identifying the best equivalency factor necessitates a priori knowledge of the full driving cycle. This type of information is not widely available. Adaptive ECMS (A-ECMS) is a suggested method for estimating the appropriate ECMS equivalence factor for industrial cases [20]. An A-ECMS is also utilized to keep the battery's level of charge within the limits. The equivalency factor is determined in A-ECMS by using an instant estimation algorithm or even a prediction-based estimation approach. In Ref. [21], Marzougui et al. designed a new power management technique incorporating three different aspects—a rule-based algorithm, fuzzy-based control and flatness control—for FC/B to supply electric vehicles (EV). Authors Fathy et al. suggested a novel energy management technique focusing on the slap swarm methodology (SSA) for maintaining energy in FC/BSC by assessing the consumption of hydrogen as the main objective function. In Ref. [22], Li et al. adopted three methods to study the performance of energy management by combining the sources of FC/SC for sourcing an excavator: firstly, the dynamic programming method is applied; second, a model predictive control is designed, and third, Pontryagin's Minimum Principle (PMP) with reduced consumption of hydrogen is applied. Multiple metaheuristic architectures for controlling the capacity of fuel cell hybrid power systems for supplying aircraft were proposed by authors Zhao et al.

To reduce the cost of the overall system, the authors Yu et al. [23] introduced a novel hybrid FC/B/SC-fed EV architecture. In Ref. [24], to deliver power to a hybrid energy network, the authors developed a rule-based distribution method; in addition, to measure the strength of the batteries and ultracapacitors, a Bayes Monto Carlo methodology was also implemented. Authors Thounthong et al. implemented an adaptive energy management system for FC/B/SC for electric vehicle applications. In Ref. [25], authors Han et al. designed a two-level power management technique for solar (PV), fuel cell and battery power that is integrated into a DC microgrid. In [26], the author examines various approaches to energy management strategies used in maintaining electric power in electric vehicles that are powered by fuel cells. The authors Bendjedia et al. investigated three power management approaches to create a hybrid energy storage system (HESS) that represents fuel cells plus an additional source for powering small vehicles.

Various energy management solutions for EVs driven by FC are reported in [27]. Bizon et al. suggested a new optimization approach based on a two-dimensional mechanism that characterizes the fuel economy of hybrid vehicles [28]. The authors Li et al., in [29], combined the fuzzy logic and wavelet transformation approaches to optimize the energy management of hybrid tramways. The research's primary feature is the development of an optimal EMS for minimizing the hydrogen demand and loss of FC functionality. None of the individual algorithms completely address all optimization challenges. This is in line with the No Free Lunch Scientific Theory, discussed in [30], which signifies that novel optimization algorithms are indeed required in the field of research in the power management of EVs. Measuring hydrogen consumption with a hybrid energy storage system to the DC voltage bus is a key issue that might be addressed. It also consolidates all DC/DC converters into a single unit. This research work describes a novel hybrid energy management system that integrates an external energy minimization strategy (ECMS) with an adaptive neuro-fuzzy inference system (ANFIS) and functions as an adaptive control system. Regarding cost and lifespan cycle maintenance, this control system is simulated with MATLAB/Simulink software to reduce hydrogen utilization in the FC, as well as to maintain the battery levels (SoC percent) as high as possible. A hybrid power management scheme is proposed for better fuel economy in a hybrid electric vehicle using FC/B/UC and PMS configurations, as illustrated in Figure 1. The paper is structured as follows. Section 2 presents the system optimization problem. Section 3 presents the modeling and description of the hybrid power storage system. Section 4 explores various power management strategies (PMS). Section 5 shows the proposed hybrid power management

strategy (ECMS + ANFIS). Section 6 elaborates on the results and comparisons of power management schemes. Section 7 presents the main conclusions that were obtained from the realization of the present work.

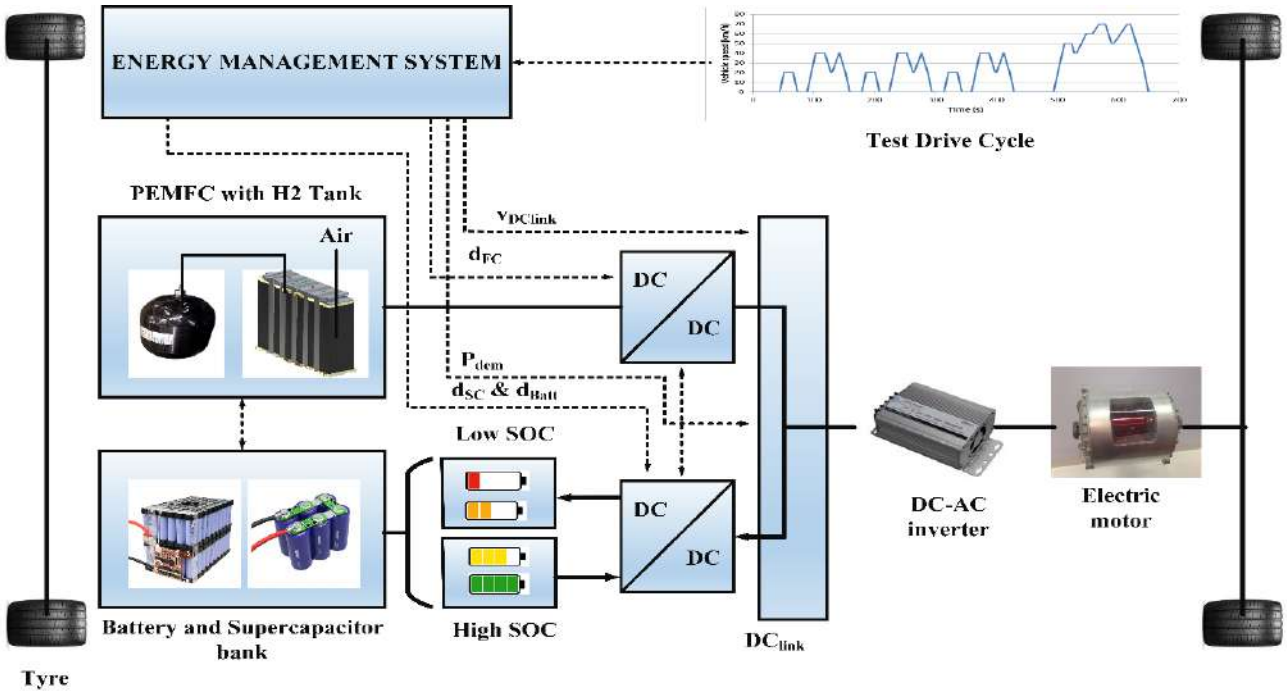

Figure 1. Configuration of energy management in a hybrid electric vehicle.

2. System Optimization Problem

To fulfill maximum power needs, hybrid systems rely on at least one to two sources of energy. This system is combined with one or more renewable resources. Hybrid systems are often designed to have an optimization technique working in conjunction with an adequate power management system to reduce fuel usage and ensure system dependability and functioning with an appropriate power management system (PMS), which assesses which source provides the demand with its required power, as well as how much energy this source might deliver [31]. To achieve this objective, hybrid system components such as fuel cells, batteries as well as supercapacitors are combined for an optimal minimization and control method to obtain the power level set by the PMS depending on the requirement of load [32]. The PEMFC electrical energy, as well as the power storage systems—the Li-ion battery bank and UC bank—will be changed to relative hydrogen usage. The corresponding hydrogen usage for a particular load named "C" is determined by a combination of the utilization of hydrogen in a fuel cell (C_{FC}) and the usage of hydrogen in a battery (C_{batt}) as well as a supercapacitor (C_{sc}). The following equation represents a mathematical model for optimizing fuel usage:

$$P_{FC} = \min(C_{FC} + k_1 \cdot C_{batt} + k_2 \cdot C_{sc}) \quad (1)$$

Here, P_{FC} represents the output power for a fuel cell, whereas k_1 and k_2 denote the converter penalty coefficient for the consumption of hydrogen. Meanwhile, the battery converter controls the DC power, and the ultracapacitor power can be ignored in the optimization procedure [33–36]. Here, the UCs are drained or recharged using the same power from a battery bank, distributing the total load between the fuel cell and also the batteries across each phase. Then, the optimization problem is expressed as follows:

$$x = [P_{FC} + k_1 \cdot P_{batt}] \quad (2)$$

Finding the optimal solution (x) minimizes (F):

$$F = [P_{FC} + k_1 \cdot P_{batt}]\Delta T. \quad (3)$$

Here, x represents the optimal solution, k_1 denotes the penalty coefficient and ΔT denotes the sampling time. The penalty coefficient is given as

$$k_1 = 1 - 2\mu \frac{(SoC - 0.5(SoC_{max} - SoC_{min}))}{SoC_{max} - SoC_{min}} \quad (4)$$

The estimated hydrogen usage of the battery (C_{batt}) can be computed using the power of the battery (P_{batt}) and the state of charge of the battery. Now, under the conditions of equality,

$$P_{load} = P_{FC} + P_{batt} \quad (5)$$

with the constraints of boundaries

$$P_{fc_min} \leq P_{FC} \leq P_{fc_max} \quad (6)$$

$$P_{batt_min} \leq P_{batt} \leq P_{batt_max} \quad (7)$$

$$0 \leq k_1 \leq 100 \quad (8)$$

This might be the overall target value, and it is a fundamental issue for every hybrid power system with hydrogen fuel and energy storage devices, but this multi-objective optimization model has been addressed clearly in this paper.

3. Modeling and Description of Hybrid Power Storage System

A hybrid energy storage system (HESS) is a combination of PEMFC, Li-ion batteries and a supercapacitor. These three sources are often considered as an FCHEV to ensure reliable power sufficiency of the load. The configuration of the hybrid system analysis can be seen in Figure 1. The fuel cell and rechargeable battery, as well as capacitors, are the three sources of power in this setup. A DC/DC boost converter has been used with the fuel cell to enhance its voltage level towards the desired level and sustain this at the outputs. There are batteries, where a DC/DC bidirectional power device converts variable power to a fixed voltage. Supercapacitors, similarly to some other capacitors, have been integrated into bidirectional converters, which enable power to be exchanged in both directions.

3.1. Proton Exchange Membrane Fuel Cell (PEMFC)

A fuel cell is a power conversion device that converts chemical energy in hydrogen fuel to electrical power without using heat or mechanical power. As per the chemical process defined in Equation (9) [14], the basic working principle of a fuel cell is described by a chemical process in which oxygen and hydrogen are linked together to form power, heat and water.

$$2H_2 + O_2 \rightarrow H_2O + \text{electricity} + \text{heat} \quad (9)$$

There are several types of fuel cell technology, which are categorized depending upon their electrolytes. Another type of fuel cell that is widely used in vehicular applications is the proton exchange membrane fuel cell (PEMFC) [15]. There are several new fuel cell prototypes, each with a combination of benefits and drawbacks based on the topic under study. Any model must be concise and accurate. Furthermore, this paper presents a simple electrochemical concept that might be used to determine the behavior of such a fuel cell both in dynamic and static conditions [16]. The hydrogen fuel design used in this study is based on the interaction between both the fuel cell voltage level and hydrogen, water, plus oxygen absolute pressures. The specifications of the fuel cell stack are illustrated in Table 1. The fuel cell voltage is regulated via oxygen and hydrogen relative pressures, the

chemical process temperature of membrane hydration and also the output current. The mathematical model is given in [17].

$$V_{FC} = E_{Nernst} - V_{act} - V_{ohmic} - V_{con} \quad (10)$$

where E_{Nernst} represents the mean value of thermodynamic potential in every single cell unit and it is calculated by Equation (11) [10].

$$E_{Nernst} = 1.229 - 0.85 \times 10^{-3}(T - 298.15) + 4.3085 \times 10^{-5} T\left[\ln\left(P_{H_2}\right) + 0.5 \times \ln\left(P_{O_2}\right)\right] \quad (11)$$

Table 1. Specifications of a fuel cell.

Fuel Cell Model Input Parameters	Specifications
Voltage	52.5 V
Number of fuel cells	65
Nominal efficiency of the fuel stack	50%
Operating temperature	45 °C
Nominal supply pressure	1.16 fuel (bar),1 air (bar)
Nominal composition (%) [H_2, O_2, H_2O (Air)]	99% H_2, 95% O_2, 21% H_2O (air)
Response time of fuel cell voltage	1 s
Peak utilization of O_2	60%
Voltage undershoot	2 V

Here,
V_{act} = Activation voltage drop;
V_{ohmic} = Ohmic voltage drop;
V_{con} = Concentration voltage drop.
Hence, for N number of cells connected in series, the stack voltage V_{stack} is described as

$$V_{stack} = N \cdot V_{FC} \quad (12)$$

The fuel cell's polarization curves indicate the voltage of the battery as a factor in the output current under several temperatures plus hydrogen pressure levels. The overall polarization patterns for FCs increase as the optimal temperature and hydrogen pressure reduce. As much as this is provided by oxygen and fuel to sustain a chemical reaction mechanism, a fuel cell can produce a constant amount of power. Proton exchange membrane fuel cells are widely used in automotive applications due to their high-power density and low and moderate operating temperatures [18]. Furthermore, its effectiveness when reacting under peak load is restricted because of certain chemical processes that occur in FCs [19]. As an outcome, such sources are integrated into the batteries as well as the supercapacitor-based hybrid storage systems.

3.2. Supercapacitors

Supercapacitors are one of the recent advancements for power storage devices, especially in integrated devices. A capacitance (C_{sc}) is linked to an equivalent series resistance R_{sc} under this setup. The parameters of UC are shown in Table 2. The below formula is used to determine the supercapacitor voltage (V_{sc}) as a result of the SC current (I_{sc}):

$$V_{sc} = V_1 - R_{sc} \times I_{sc} = \frac{Q_{sc}}{s_{sc}} - R_{sc} \times I_{sc} \quad (13)$$

where Q_{SC} denotes the quantity of electricity present in the cell, and the power of the supercapacitor is calculated by using Equation (14),

$$P_{SC} = \frac{Q_{SC}}{C_{SC}} \times I_{SC} - R_{SC} \times I_{SC}^2 \quad (14)$$

Table 2. Specifications of supercapacitors.

Supercapacitor Model Input Parameters	Specifications
Surge voltage	307 V
Capacitor number in series	6
Capacitor count in parallel	1
Rated voltage	291.6 V
DC series resistance equivalent	0.15 ohms
Rated capacitance	15.6 F
Molecular radius	0.4×10^{-9} m
Operating temperature	25 °C

Utilizing supercapacitors as a storage system in such an electric vehicle implies the construction of such a stacking of cells, where N_S cells are interconnected in series and N_p cells are parallelly connected. Equations (15) and (16) determine the capacity and resistance of the supercapacitor stack.

$$C_{SC} = C_{elem} . \frac{N_P}{N_S} \quad (15)$$

$$R_{SC} = R_{elem} . \frac{N_S}{N_P} \quad (16)$$

Equations (17) and (18) determine both the current and voltage of a stack as a measure of such component's current and voltage [20].

$$V_{SC} = N_S \cdot V_{elem} \quad (17)$$

$$I_{SC} = N_P \cdot I_{elem} \quad (18)$$

3.3. Battery

The battery is designed with a modest controlled power supply in series with such a fixed resistance [21]. Li-ion battery specifications are given in Table 3. Equation (1) defines the battery voltage V_{bat} (18).

$$V_{batt} = E - R_{bat} \cdot I_{bat} \quad (19)$$

Table 3. Specifications of Li-ion battery.

Input Parameters for the Battery Model	Specifications
Minimal voltage	48 V
Esteemed capacity	40 Ah
Determined capacity	40 Ah
Fully charged voltage	56.88 V
Minimal discharge current	17.4 A
Internal resistance	0.012 ohms
Nominal voltage capacity	36.25 Ah
Exponential region	52.3 Volts, 1.96 Ah
Response time of battery voltage	30 s

The controlled source voltage is calculated by using Equation (19).

$$E = E_0 - K\frac{Q}{Q_0 - \int i \cdot dt} + A \cdot \exp\left(-B \int i \cdot dt\right) \quad (20)$$

where E represents no-load voltage (V), E_0 denotes a constant voltage of the battery (V), K denotes the polarization voltage (V), Q indicates the capacity of the battery (Ah), whereas A denotes the amplitude of the exponential zone (V) and B denotes the inverse time constant of the exponential zone $(Ah)^{-1}$.

4. Power Management Strategies (PMS)

By using a reliable PMS, one can control the power response of HESS with load demand. In this paper, a hybrid power management design is obtained, as shown in Figure 2, and the requirements are listed in Table 4. Significantly, the PMS relies on obtaining the reference power of fuel cells.

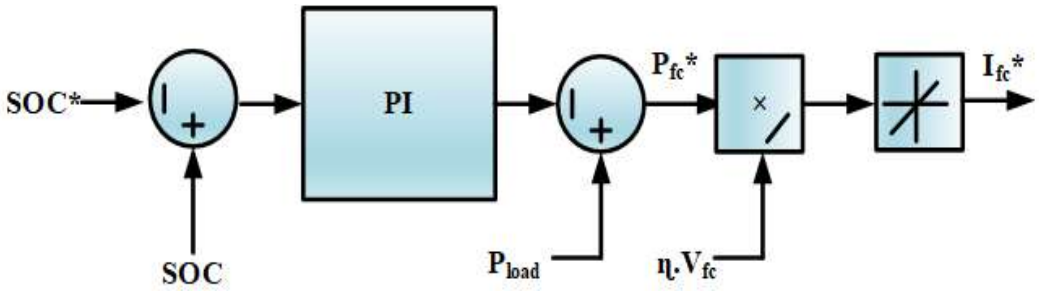

Figure 2. Classical PI control method.

Table 4. Power management design requirements.

Requirements of Power Management Strategies	
Fuel cell power [P_{fcmin}–P_{fcmax}]	1–10 KW
Battery power [$P_{battmin}$–$P_{battmax}$]	−1.2–4 KW
State of charge of battery [SoC min–SoC max]	60–90%
DC bus voltage [V_{dcmin}–V_{dcmax}]	250–280 V
Maximum slope of fuel cell current	40 A/S

A reliable power management scheme (PMS) should essentially ensure the following:

- Lower consumption of hydrogen (H_2) (gm) of PEMFC;
- DC bus voltage regulation should be desired value;
- Tracking the battery and SC set-point values;
- Corroborate the global constancy of the system structure;
- The system should operate at a high level of efficiency;
- The long life cycle of a hybrid energy storage system (HESS).

These are attained by using a reliable PMS. The proper PMS controls the power response of HESS with load demand. In this work, the power management design requirements are as listed in Table 4. Significantly, the PMS relies on obtaining the reference power of fuel cells. Various types of PMS are considered in detail. Managing the power of HESS, which comprises the PEMFC, Li-ion batteries and SC, is reported as follows.

4.1. Classical Proportional Integral (PI) Control Method

The amount of the HESS's energy is identical to the load energy. This PI strategy controls the SoC of the battery by using a PI regulator, as illustrated in Figure 2.

Fuel cell reference power is attained by regulating the battery power by using a PI controller. As a result, the rated output of the PI controller is estimated by the predetermined rate (proportional) and predefined rate (integral) of its input. If the battery's SoC is higher than the actual rate, then the FC's power is reduced, and the battery supplies the load with maximum power. If the battery's state of charge (SoC) is less than the set-point, the fuel cell provides power to the load. The major role of the PI controller is that when the battery's SoC exceeds the average SoC (SoC*), the controller permits the battery to power

the demand, and the gains of PI are to be tuned online to obtain a better response [22]. A block diagram of the PI scheme is illustrated in Figure 2. The transfer function of the PI controller is given in Equation (21) [22],

$$P_{batt} = \left(K_P + \frac{K_i}{S}\right) \cdot (SoC^* - SoC) \quad (21)$$

Here, the output current of the FC (I_{FC}) is determined in terms of fuel cell output power (P_{FC}), which remains obtained from the controller and output voltage of the FC (V_{FC}).

4.2. State Machine Control Approach

Figure 3 shows the control technique for the state machine scheme. This scheme is executed in eight states. In this strategy, the power of the FC can be determined through the load power (P_{load}) and SOC of the battery bank. The reference power of the fuel cell is the output of the SMC strategy.

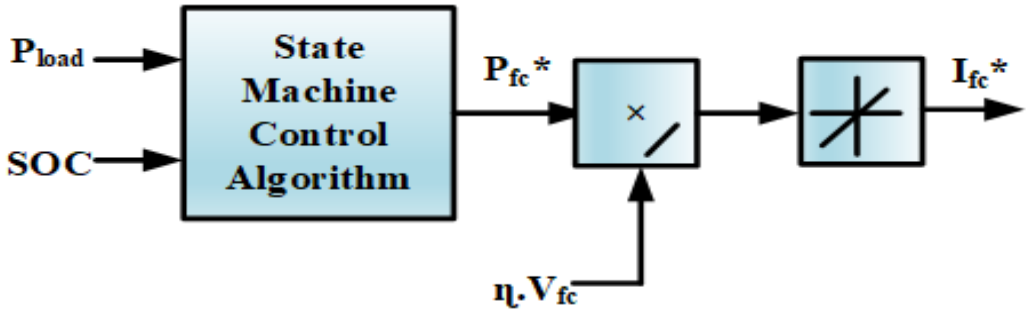

Figure 3. State machine control technique.

By dividing the output of SMC by the voltage of the FC and efficiency of the boost converter, the FC reference current is attained [23]. While switching the states from one to another, hysteresis control is required for the SMC strategy, which may affect the PMS' response to changes in load demand, and the pattern is shown in Figure 4.

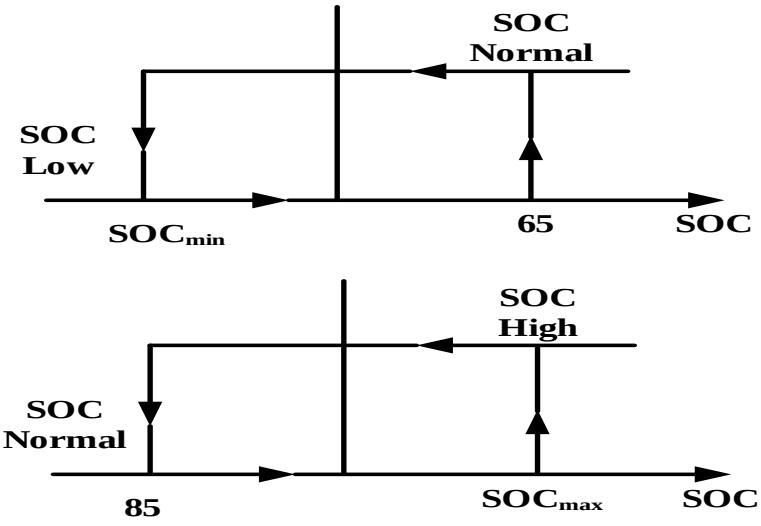

Figure 4. State machine control hysteresis.

4.3. Frequency Decoupling Fuzzy Logic Control Scheme (FDFLCS)

This method permits the structure of the fuel cell to accommodate a load request with a lower frequency while the battery and supercapacitors supply the load demand with a higher frequency. The control technique is shown in Figure 5. The vital advantage of this

scheme is that the Li-ion battery's mean energy is closer to zero, ensuring a narrow range of SoC [24]. A filter is used for frequency decoupling, and a fuzzy logic controller is required to maintain the battery's state of charge within a certain range.

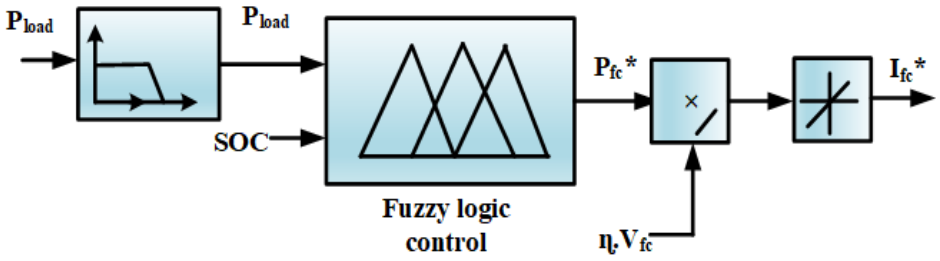

Figure 5. Frequency decoupling and fuzzy logic control technique.

4.4. External Energy Maximization Strategy (EEMS)

In FCHEV, for upgrading the performance of HESS, it is important to interchange the energy optimally within the FC, SC and also the battery. This is achieved by reducing the fuel cells' hydrogen consumption (H_2) by maintaining the limits of the state of charge of the SC and battery. In this EEMS technique, the hydrogen consumption (H_2) is minimized by raising the battery and SC demand. The EEMS technique requires the battery and SC cost function; it does not require the determined battery energy calculation. In Figure 6, it is shown that the EEMS algorithm's inputs are the voltage of the DC bus and battery SoC or supercapacitor, while the outputs are the charge/discharge voltage (ΔV) for the supercapacitor and battery reference power. Thus, a comparison of the battery and load power for the FC's reference power via the FC current (I^*_{FC}) is derived. The SC charge/discharge voltage is obtained by estimating the actual DC bus voltage through the sum of $(V_{dc.ref})$, a, the reference voltage of the DC bus and the SC's voltage. In the process of this EEMS optimization problem, the SC charge/discharge voltage (ΔV) and power of the battery (P_{batt}) have to be assessed. The minimized objective function is the power supplied via both secondary sources during a certain period of intermission, which is described in Equation (22) [25].

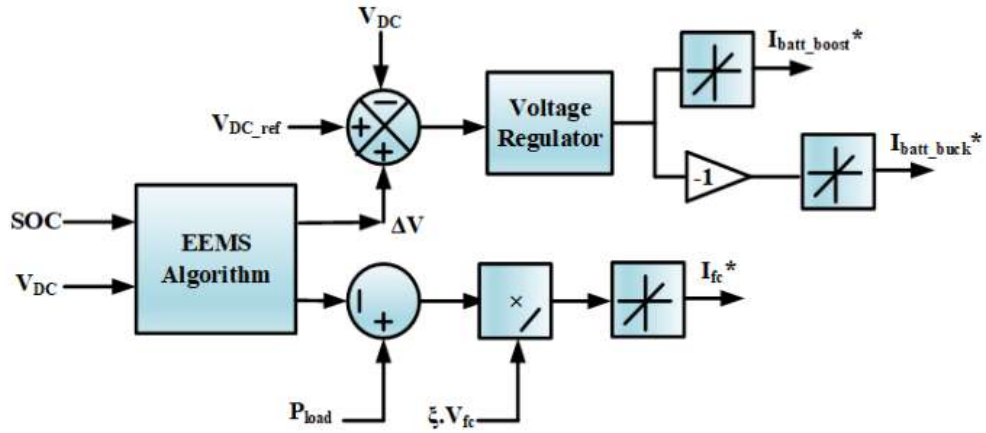

Figure 6. External energy maximization scheme.

Minimize

$$J = -\left(P_{batt}.\,\Delta T + \frac{1}{2}.C_r.\Delta V^2\right) \tag{22}$$

Based on the battery's power output, the EEMS optimization procedure is carried out and the key parameter is represented by inequality constraints, and the constraints are subject to

$$P_{batt}.\Delta T \;\leq\; \left(SoC - SoC^{min}\right).V_{batt}.Q \tag{23}$$

whereas the power of the battery and voltage of the DC bus parametric inequality constraints are formulated as follows:

$$P_{batt}^{min} \leq P_{batt} \leq P_{batt}^{max} \tag{24}$$

$$V_{DC}^{min} \leq V_{DC} \leq V_{DC}^{max} \tag{25}$$

Here, $P_{batt}.\Delta T$ denotes the delivered battery power over a sampling time (ΔV). C_r represents the rated capacitance of SC. V_{DC}^{min} and V_{DC}^{max} denote the bus voltage minimum and maximum limits. V_{batt} represents the optimum voltage of the battery, and the rated capacity of the battery is denoted by the letter Q.

5. Proposed Hybrid Power Management Strategy (ECMS + ANFIS)

5.1. Equivalent Consumption Minimization Strategy (ECMS)

To reduce hydrogen usage and extend the life of a fuel cell, Adaptive-ECMS is introduced for the duration of a cell's life. The primary concept of ECMS is to convert electricity usage through energy storage devices to corresponding hydrogen consumption with a combination of equivalent and actual hydrogen consumption from fuel cells being kept as low as possible, which is shown in Figure 7. Similarly, various limits have been placed to ensure that the energy sources continue to function effectively. The optimization function is as follows [26,27]:

$$\begin{aligned} &\min f_w(t) = m_{FC}(t) + m_{BA}(t) + m_{SC}(t) \\ &\begin{cases} I_{FC}^{min} \leq I_{FC} \leq I_{FC}^{max} \\ I_{SC}^{min} \leq I_{SC} \leq I_{SC}^{max} \\ -dI_{FC} \leq \frac{I_{FC}(t) - I_{FC}(t-1)}{T} \leq dI_{FC} \end{cases} \end{aligned} \tag{26}$$

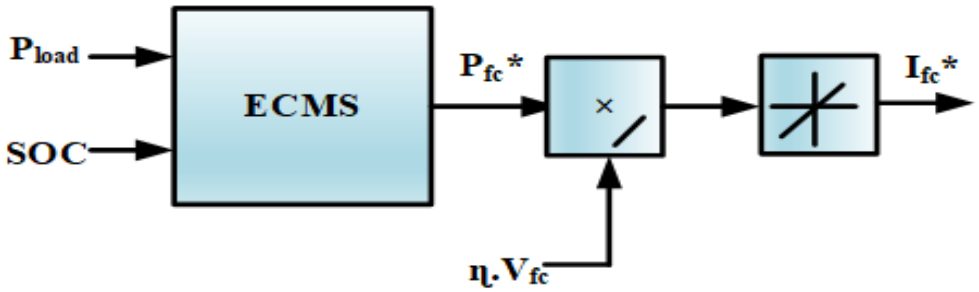

Figure 7. Equivalent consumption minimization method.

I_{FC}* represents fuel cell reference current. Here, $f_w(t)$ denotes utilization hydrogen consumption at sample time (t), $m_{FC}(t)$ represents the usage of hydrogen in fuel cells, whereas $m_{BA}(t)$ indicates that the hydrogen demand is comparable to the battery and $m_{SC}(t)$ indicates that the hydrogen demand is identical to the ultracapacitor, while I_{FC} and I_{SC} indicate the current flowing through the fuel cell as well as the UC correspondingly. Several other respective penalty parameters are incorporated into the optimization problem of Equation (9), which are given in Equation (10), to enable the fuel cell to obtain its optimum efficiency location within the efficient power boundary. Meanwhile, the charge sustenance of the energy storage systems is maintained, which means supporting the state of charge of the UC and battery to be approximately equal to their initial conditions.

$$\begin{aligned} f_w(t) &= K_{FC}m_{FC}(t) + K_{BA}m_{BA}(t) + K_{SC}m_{SC}(t) \\ &= K_{FC}m_{FC}(t) + K_{BA}\lambda_{BA}P_{BA}(t) + K_{SC}\lambda_{SC}P_{SC}(t) \end{aligned} \tag{27}$$

Here, K_{BA} and K_{SC} are penalty factors that cover a range of SoC for energy storage sources such as UC and batteries and the difference between the maximum and minimum SoC. Meanwhile, K_{FC} represents the cost factor for hydrogen fuel efficiency and λ_{BA} and λ_{SC}

indicate comparable factors. $P_{BA}(t)$ as well as $P_{SC}(t)$ denote the power of the battery bank and UC bank. The penalty factor for fuel cell efficiency is expressed as in Equation (28) [27]:

$$K_{FC} = \begin{cases} \left(1 - 2 * \frac{\eta - \eta_{opt}}{\eta_{max} - \eta_{min}}\right)^2 & \eta \geq 0.4 \\ \left(1 - 2 * \frac{\eta - \eta_{opt}}{\eta_{max} - \eta_{min}}\right)^4 & \eta < 0.4 \end{cases} \quad (28)$$

where n indicates instant efficiency; n_{opt} represents adequate efficiency, which is 0.4283 approximately; n_{max} denotes the maximal efficiency of 0.4283, and the base efficiency is denoted by n_{min}. Whenever the performance of a fuel cell system declines under 0.4, a significant penalty rate (K_{FC}) is estimated to discontinue or maintain the fuel cell to supply energy based on the driving conditions of HEV depending on the batteries and SC state of charge levels. K_{FC} are 2 and 4 for two circumstances that are governed by the drive cycle generation capacity. K_{FC} regulates the pursuit of optimal efficiency and the limitations of the high-performance region (efficiency beyond 0.4). The K_{BA} cost rate for the SoC of the battery is given in Equation (29) [28,29]:

$$K_{BA} = \begin{cases} \left(1 - \frac{2*(u - B_{int})}{B_{max} - B_{min}}\right)^4 & B_{min} \leq u \leq B_{max} \\ \left(1 - \frac{2*(u - B_{int})}{B_{max} - B_{min}}\right)^{20} & u < B_{min}, u > B_{max} \end{cases} \quad (29)$$

Here, u denotes the battery's current state of charge. B_{mt} denotes the battery SoC. Meanwhile, B_{max} and B_{min} represent the lowest and highest SoC of the battery. K_{BA} resets the lithium battery SoC to its original state. Once the battery capacity SoC crosses B_{min} and B_{max}, a higher K_{BA} amount is established as a penalty factor to prevent the battery from proceeding to charge and drain. The parameter of UC (K_{SC}) comprises SoC constraints and the maximum power index (S_{eff} and S_{peak}). S_{eff} functions similarly to K_{BA} to keep the SoC level of UC within a specified tolerance. Let the UC provide a maximum output, which is employed by S_{peak}. To minimize on/off loops of the fuel cell and charging/discharging phases caused by massive changes in amplitude in both the SoC of the battery and SC in a short amount of time, the SoC of the UC and battery pack are identical, which is estimated by S_{eff}. The differential calculations for K_{SC}, S_{eff} and S_{peak} are given as follows [30]:

$$K_{SC} = S_{eff} * S_{peak} \quad (30)$$

$$S_{eff} = \begin{cases} \left(1 - 2\frac{ax + b - S_{opt}}{S_{max} - S_{min}}\right)^4 & S_{min} \leq x \leq S_{max} \\ \left(1 - 2\frac{ax + b - S_{opt}}{S_{max} - S_{min}}\right)^{20} & x < S_{min}, x > S_{max} \end{cases} \quad (31)$$

$$S_{peak} = \begin{cases} 1 & 0 \leq I_{load} \leq 30 \\ -0.01 * I_{load} + 1 & I_{load} < 0, I_{load} > 30 \end{cases} \quad (32)$$

Here, x represents the instant SoC of the ultracapacitor capacity, whereas S_{opt} indicates the absolute SoC, S_{max} and S_{min} denote the upper and lower limit of SoC, and also the DC bus desired demand is denoted by I_{load}. The supportive transform terms between UC and battery SoC are represented by a and b, respectively, and their respective levels are specified by the battery's allowable SoC.

5.2. Adaptive Network-Based Fuzzy Interface System (ANFIS)

Power management methods have emerged for an automated learning experience to assist industrial uses such as fuzzy approaches, which are more common in system control. The ANFIS is a vital approach, which integrates both the artificial neural network (ANN)-based learning ability and also a rule-based fuzzy logic control technique based on inference capacity to build a full set over all different types of neural networks in the feed-forward type using a supervisory learning functionality [31,32]. The ANFIS strategy

accomplishes a hybrid training process based on appropriate information and parameters of input/output and connections.

Figure 8 illustrates that the ANFIS architecture comprises a single hidden layer. Layer 1 indicates the input node, layer 2 comprises the fuzzification nodes, layer 3 comprises the result nodes (hidden), layer 4 comprises the defuzzification nodes and layer 5 represents the output node [33]. Furthermore, a node can be updated, and it will be classified as dynamic and static. Dynamic nodes include layers 2 and 4, whereas the stable nodes are layer 1 and layer 3. The ANFIS control technique uses the SoC of a Li-ion battery with three membership functions (MFs) and also utilizes the vehicle energy load, which is represented by P_{load}, as inputs to anticipate the fuel cell's output power [34,35]. The ANFIS outcome is the estimated proportional gain from the PEMFC level. The ANFIS measures and adjusts the norms rapidly while using proportional variables.

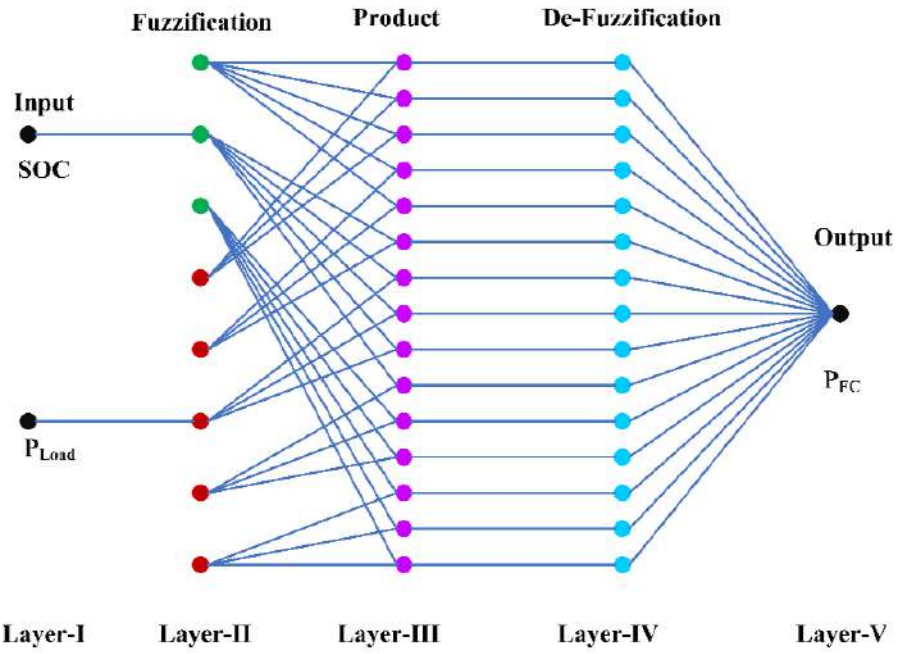

Figure 8. Structure of ANFIS.

Figure 9 illustrates the result region of the ANN approach: the label of the *Z*-axis is SoC, the *X*-axis is the load power (P_{load}) and the *Y*-axis is the fuel cell power (P_{FC}). The purpose of adopting ANFIS, particularly for non-linear systems and networks that necessitate rapid selection in real time, is that the operation will be performed because of a learning result that has already been pre-obtained through an existing attempt. The genetic PMS can be adopted throughout the framework in airplanes, boats or automobiles, depending on the specific application. The PMS with a fuel cell and energy storage network (battery, UC) can also be used in planes, ships as well as electric vehicles, although the major objective of operating the PMS is a primary objective. The electric vehicles' main criteria are durability and mitigating fuel consumption and enhancing the battery and UC usage. The EMS contains two parameters, which are illustrated in Figure 9. The first set of data are the SoC of the battery, which determines the battery capacity and wealth status. The optimal state is approximately 65 to 85% [36]. Another intention is to maintain the battery charging process (SoC within conventional ranges to prolong its duration). The power output of the vehicle might be the next EMS signal. To ensure operation stability, the maximum fuel cell capacity is constrained to 1–10 KW. The closed-loop management system of the ANN approach is derived from past expert data. The ANFIS training process determines the effectiveness of the output signal. ANFIS is conditioned to have the appropriate membership functions (MFs) throughout this environment by training samples across the state of charge, peak

load and fuel cell energy, enabling the ANN model to estimate a linear relationship with endpoints (input and output).

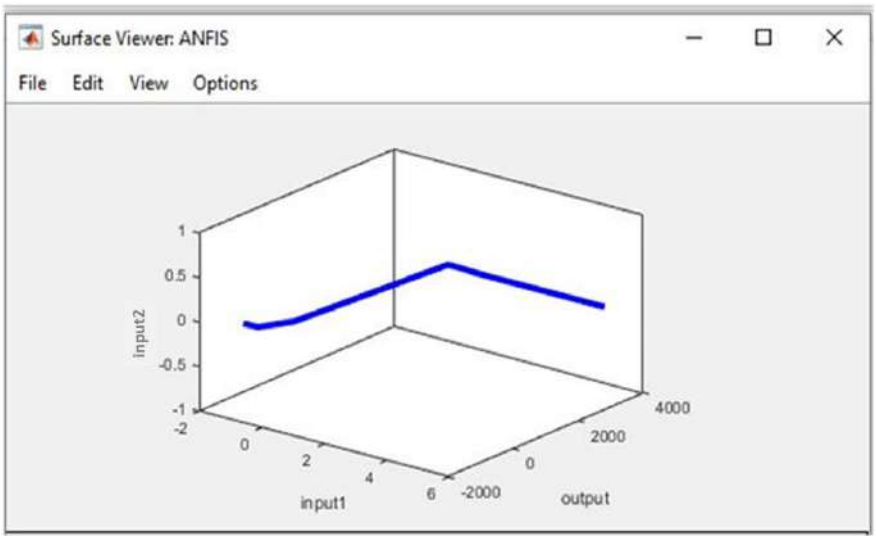

Figure 9. The MATLAB simulation output surface of the ANFIS.

The input/output samples' specialized information is applied to enhance the control system's performance with a minimal number of errors. To limit training problems, (1000) epochs are performed till the error rate is below 0.0001 for the training samples; this signifies the ANN-based output signal and is close to perfect. Figure 10 shows the flowchart of ANFIS training and testing.

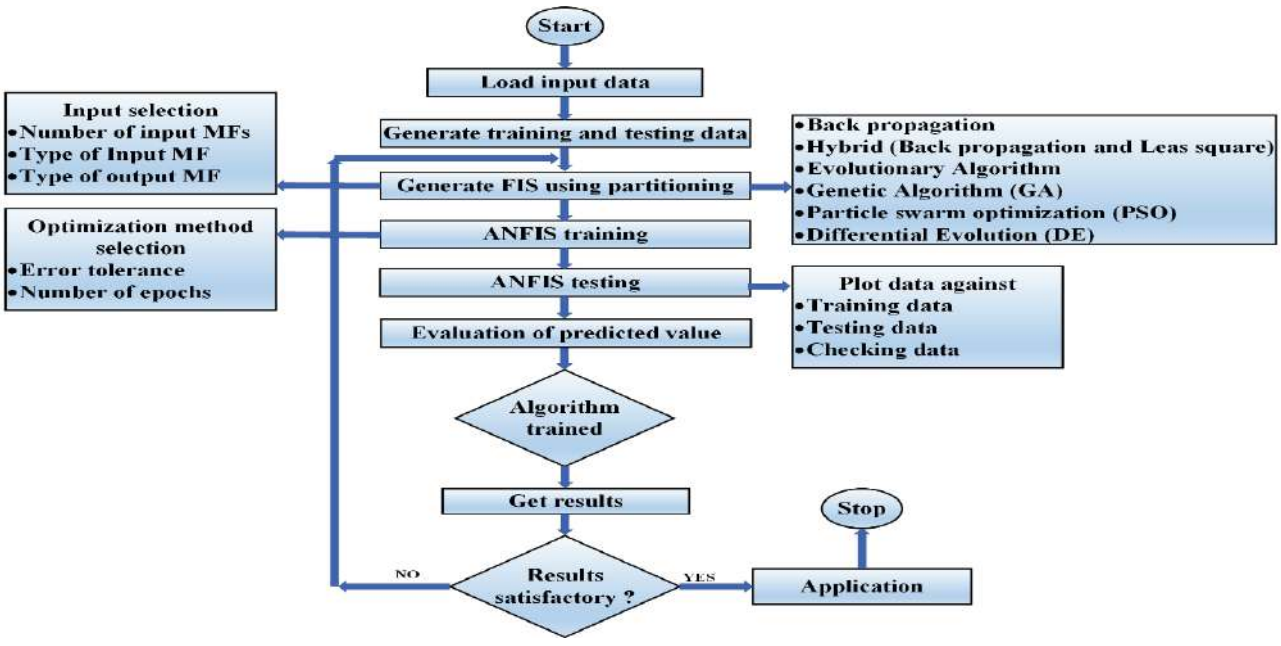

Figure 10. The procedure flowchart of ANFIS.

5.3. Proposed Algorithm

The proposed algorithm is a hybridized algorithm (ECMS+ANFIS), and the flowchart is illustrated in Figure 11. It states a multi-objective PMS for the better reduction of hydrogen consumption as well as efficiency and with reduced stresses on hybrid sources when compared to PI, SMC, ECMS and EEMS.

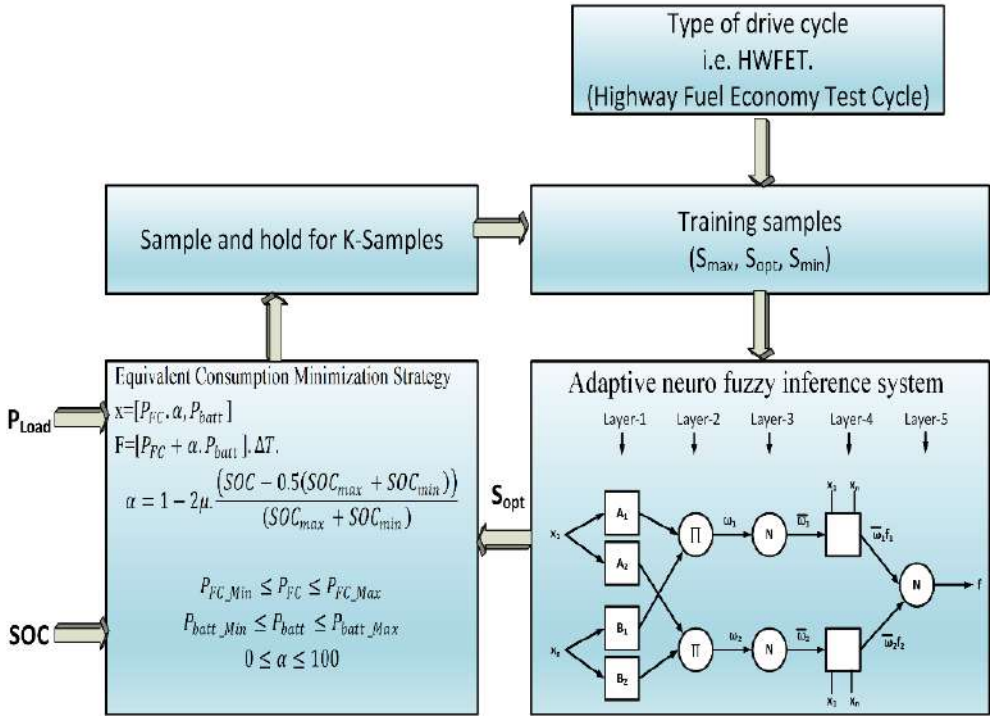

Figure 11. Flowchart of hybrid power management scheme (HPMS).

5.3.1. Collection of Equivalent Factor Samples

The corresponding factors, as is widely known, are directly linked to the driving cycle information and system condition, and they play an important role in saving fuel. A continuous optimization technique may be used to derive the ideal equivalent component Sopt from the acquired control trajectory. The Smin and Smax bounds of the analogous factor are established. In the allowable range [Smin, Smax], S decreases and increases with optimal value of equivalent samples. with When the vehicle's power demand is low, the cost of consuming electricity is smaller. The corresponding factor increases as the vehicle's power requirement increases, indicating that the engine can produce more power. Whenever the battery's state of charge (SoC) is lower, the greater corresponding factor is used. It indicates that the discharge tendency is inhibited, resulting in a reduction in the motor's power output, preventing the batteries from over-discharging.

5.3.2. Optimal Control Trajectory Acquisition

A simultaneous hybrid electrical bus's energy optimization is a non-linear optimization challenge with various restrictions. As explained previously, the optimization issue can be solved using a variety of techniques. The DP technique is used to resolve hard issues by utilizing recursion calculation, which does not depend on differential equations, to find the best power distribution in the hybrid engine. The entire optimization issue may be broken down into various simple subproblems in this work, such as constrained segments across time. Once all possible case changes with various control variables have been computed in each segment, the solution of each pathway and the associated cost will be noted. Following the completion of the above computation, the ideal solution may be found by minimizing an objective function. Due to precise gird points for both the state and the controlling vector, the globally optimum outcome is provided.

6. Results and Comparisons

6.1. Hydrogen Consumption, Overall Efficiency and Stress Analysis

Different power managing methods for hybrid storage structures were implemented. Each power management scheme was implemented with the same initial conditions: state of

charge of battery = 70%, temperature of battery = 30 °C, voltage of supercapacitor = 270 V, temperature of supercapacitor = 25 °C, voltage of fuel cell = 52 V, temperature of fuel cell = 40 °C. The model of FC/B/SC comprised 12.5 KW, 30–60 V PEMFC, a 48 V,40 Ah Li-ion battery and 15.6 F, 291.6 V-6 series-connected supercapacitors. The battery storage was controlled by two DC/DC converters. The converter operated for discharging the battery in a 4 KW boost mode and for charging the battery in a 1.2 KW buck mode. The comparison of the various power management strategies based on hydrogen consumption, overall efficiency and stress on the fuel cell, battery and supercapacitor is tabulated in Table 5. The consumption of hydrogen in (Ipm and grams), is illustrated in Figure 12 (HWFET—Drive Cycle) and Figure 13 (WLTP—Class 3 Drive Cycle) and Figures 14–17, and the overall efficiency of all power management schemes was calculated. For the fuel cell, battery and supercapacitor energy, the stress assessment was performed using the Haar wavelet approach at 270 V DC. A wavelet toolbox is available in MATLAB. The power degradation in low-frequency and high-frequency apparatuses was evaluated via Haar wavelet decomposition. The component with a high frequency has a zero-mean value, and the standard deviation (σ) of this module provides a better insight into how a separate storage system is managed. The amount of hydrogen consumption used (in grams) is given as

$$\mathrm{Cons_{H2}} = \frac{\mathrm{N}}{\mathrm{F}} \int_0^{1800} \mathrm{i_{fc}} \cdot \mathrm{dt} \tag{33}$$

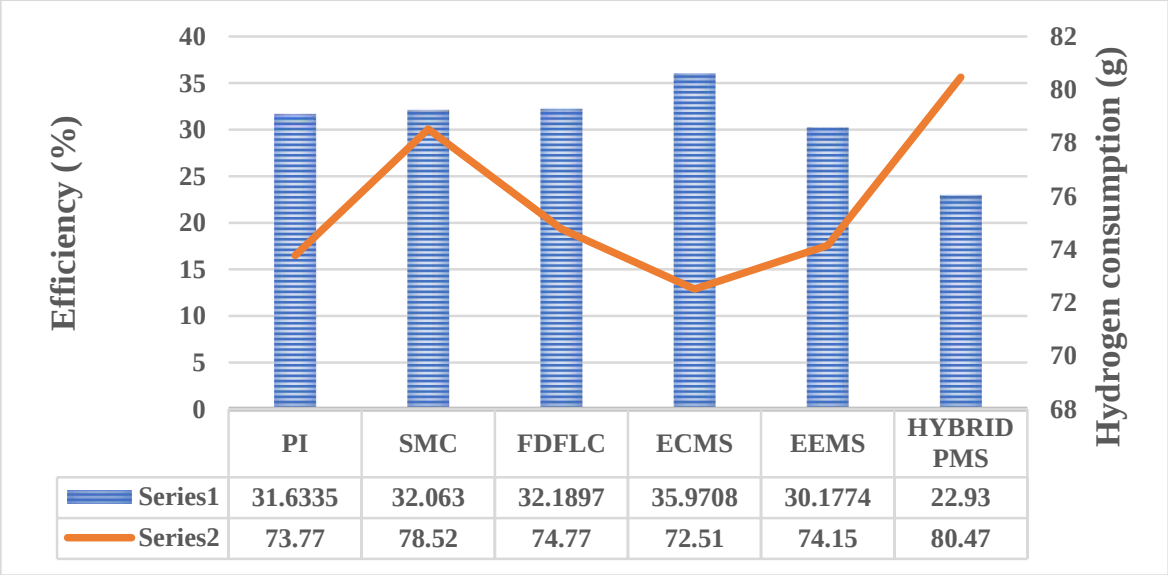

Figure 12. System efficiency and hydrogen consumption for each scheme (HWFET—Drive Cycle).

Here, F = Faraday fundamental (A.s/mol).
Global efficiency is expressed as

$$\text{Efficiency } (n\%) = \frac{\mathrm{P_{load}}}{\mathrm{P_{FC}^{in}} + \mathrm{P_{batt}^{in}} + \mathrm{P_{cap}^{in}}}. \tag{34}$$

Here; $\mathrm{P_{FC}^{in}}, \mathrm{P_{batt}^{in}}, \mathrm{P_{cap}^{in}}$ = Power of FC/B/UC.

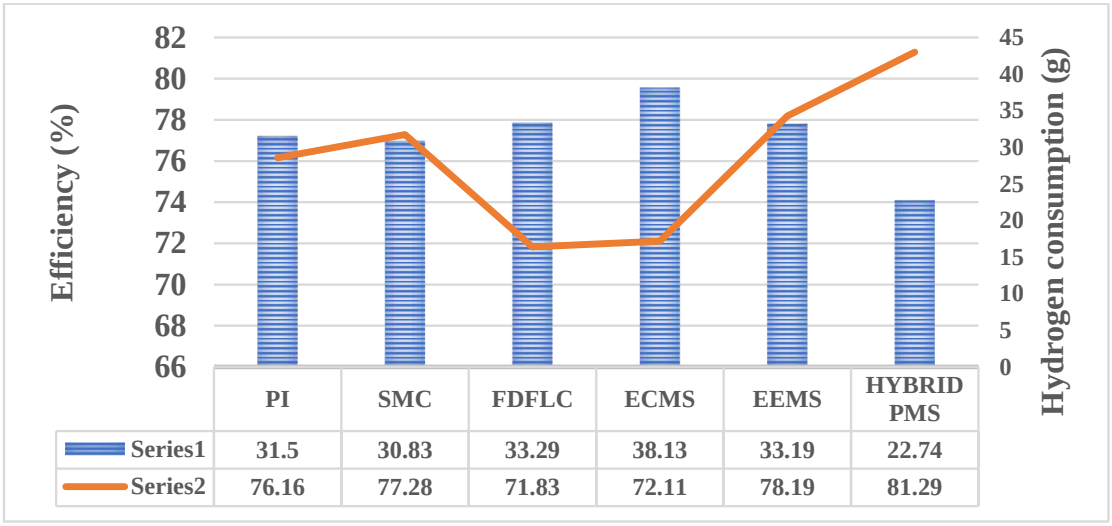

Figure 13. System efficiency and hydrogen consumption for each scheme (WLTP—Class 3 Drive Cycle).

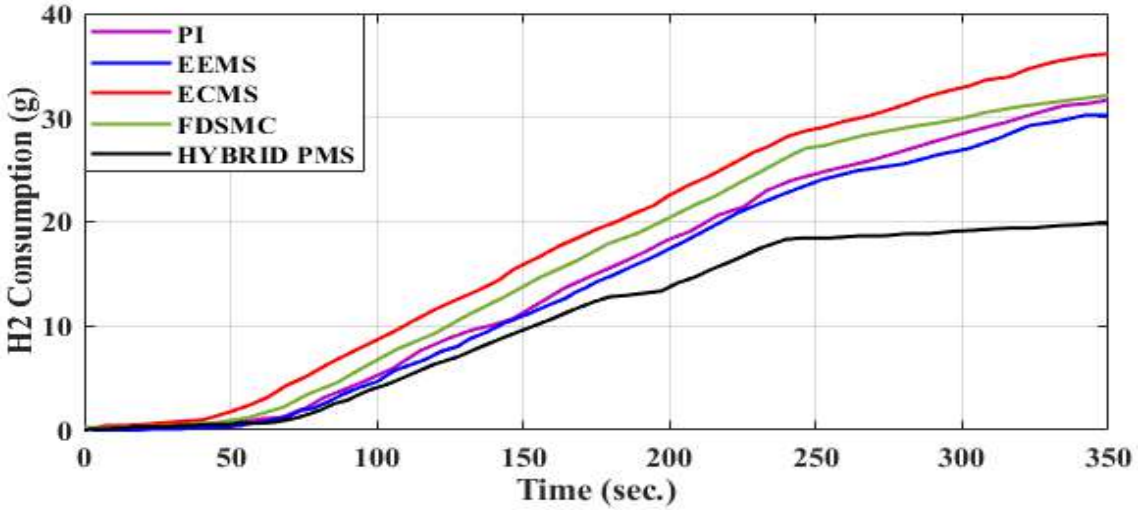

Figure 14. Hydrogen consumption in grams for studied approaches (HWFET—Drive Cycle).

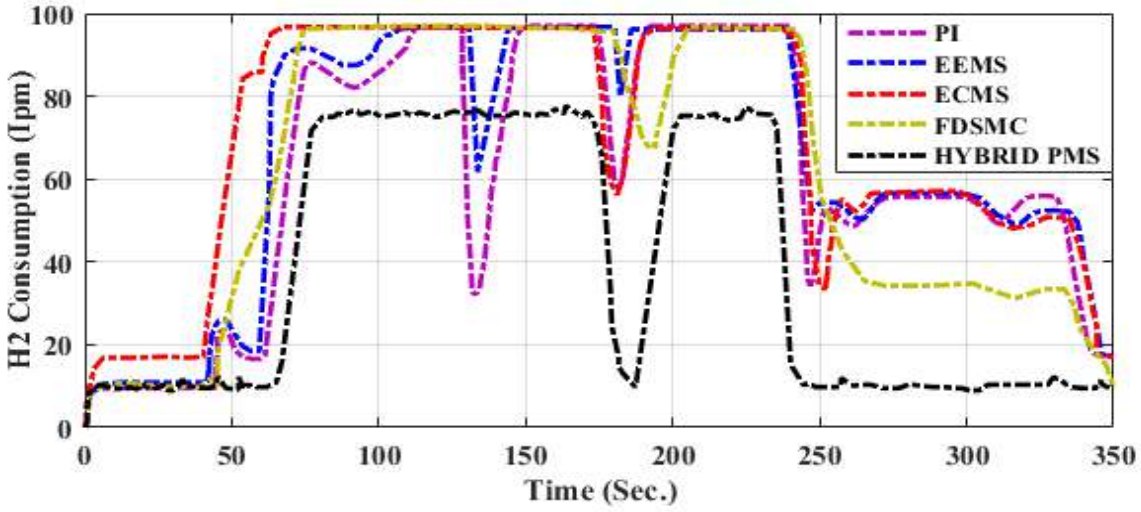

Figure 15. Hydrogen consumption in Ipm for studied approaches (HWFET—Drive Cycle).

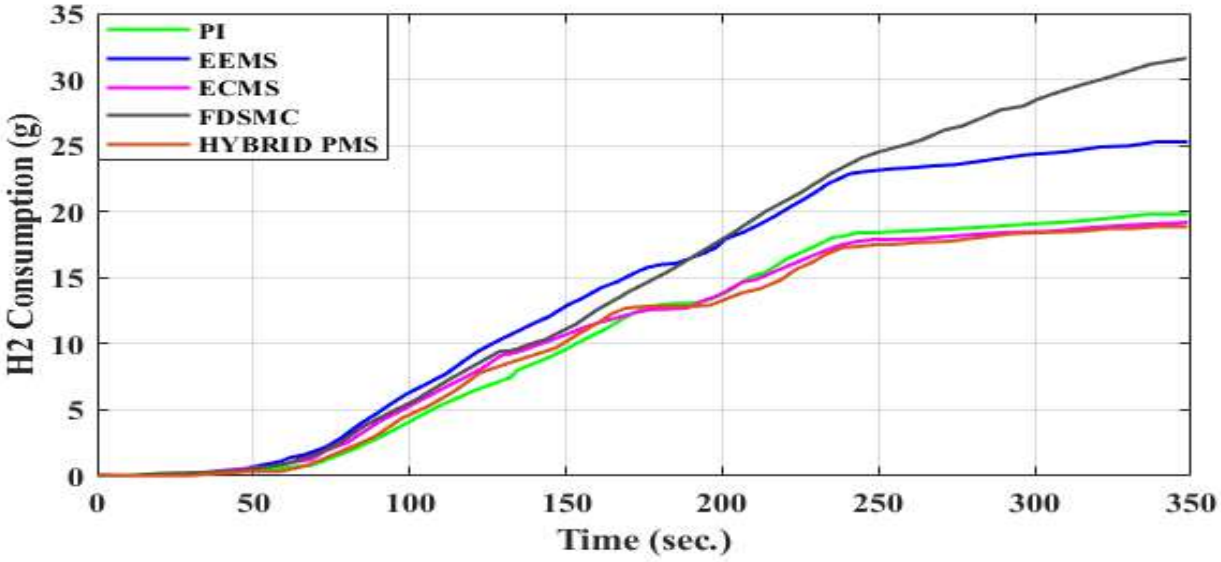

Figure 16. Hydrogen consumption in grams for studied approaches (WLTP—Class 3 Drive Cycle).

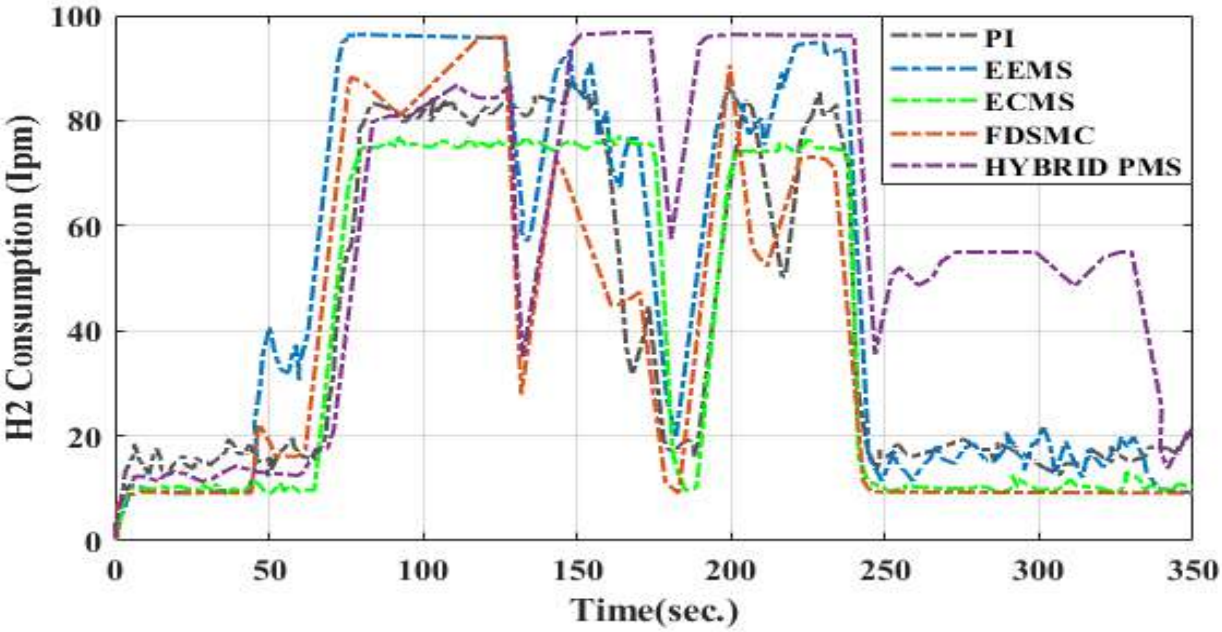

Figure 17. Hydrogen consumption in lpm for studied approaches (WLTP—Class 3 Drive Cycle).

6.2. SoC of Battery and Supercapacitor Voltage

In the classic PI strategy, to attain the reference SoC, there is a faster discharging of the battery in which the load is controlled by the primary source—the fuel cell—and recharging the battery. In the case of state machine control, if the SoC of the Li-ion battery bank reaches its minimum limit, then the fuel cell charges the supercapacitors over their reference voltage (270 V), forcing the DC bus to regulate the charge of the batteries. Meanwhile, in the case of the frequency decoupling fuzzy logic strategy, constant power is supplied by the fuel cells, which allows the battery to recharge compared to other strategies. An equivalent consumption minimization scheme and external energy minimization scheme perform better because higher battery power is used. The variation in the fuel cell voltage and current is shown in Figures 18 and 19.

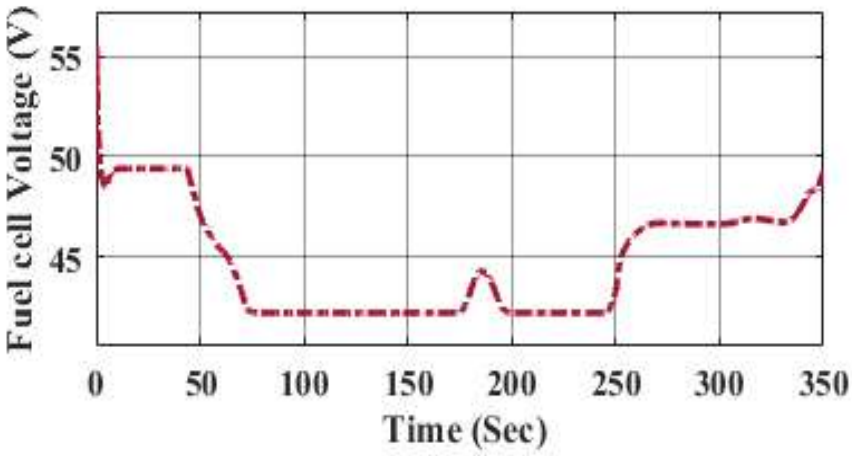

Figure 18. Variation in fuel cell input voltage.

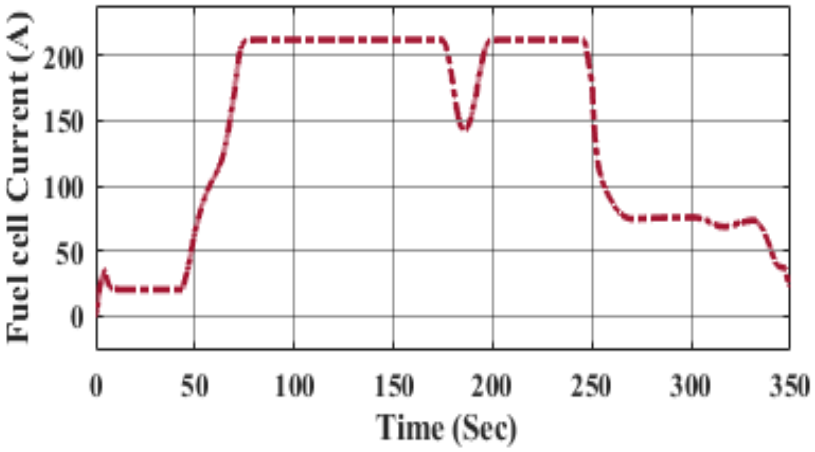

Figure 19. Variation in fuel cell input current.

The battery and UC's time response plots are shown in Figures 20–24. The Li-ion battery and UC's states of charge are approximately the same, indicating that the system would be in a fully charged condition when the primary input is disconnected from the operation. The battery and UC currents are increased at this point. This means that the UC and batteries are being used to match the increasing load requirement, and their interface voltages are being decreased as a result. At the same time, the battery and UC circumstances are then modified as the load changes.

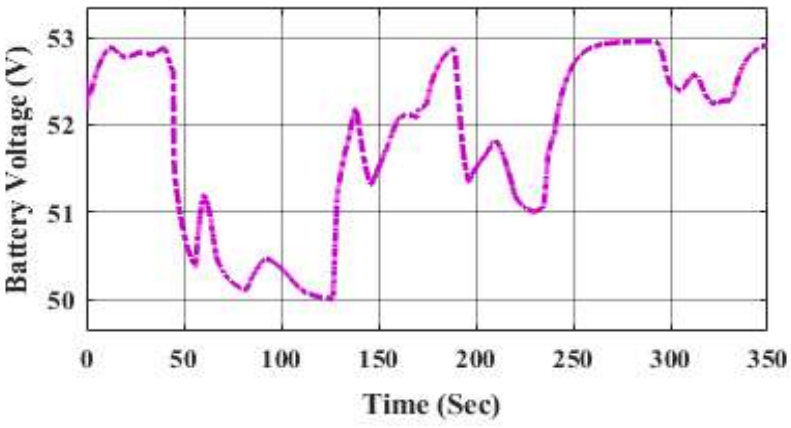

Figure 20. Battery voltage–time response.

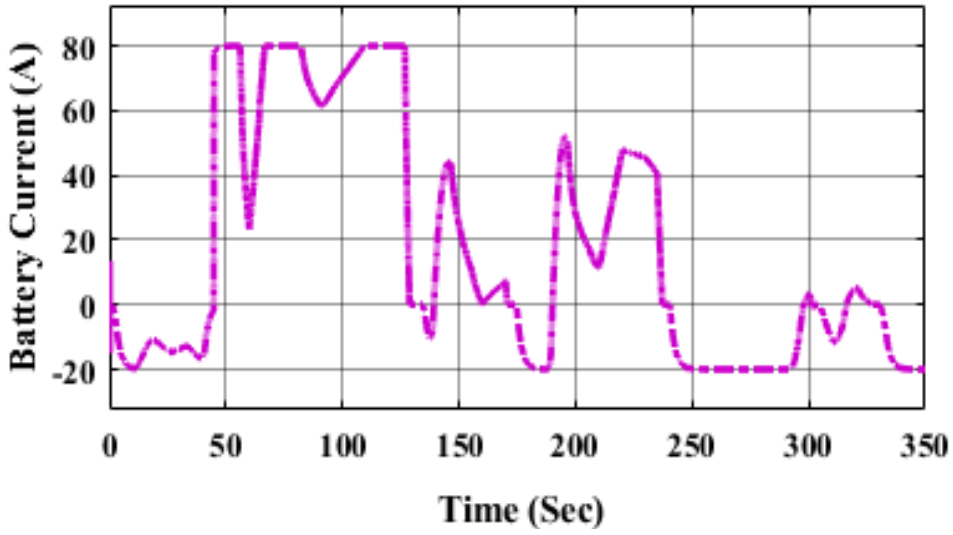

Figure 21. Time response of battery current.

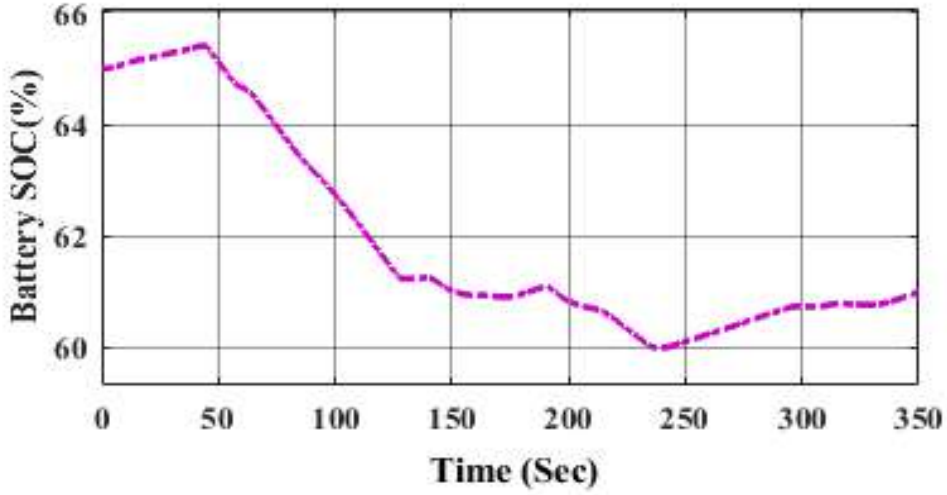

Figure 22. Time response of battery state of charge (SoC).

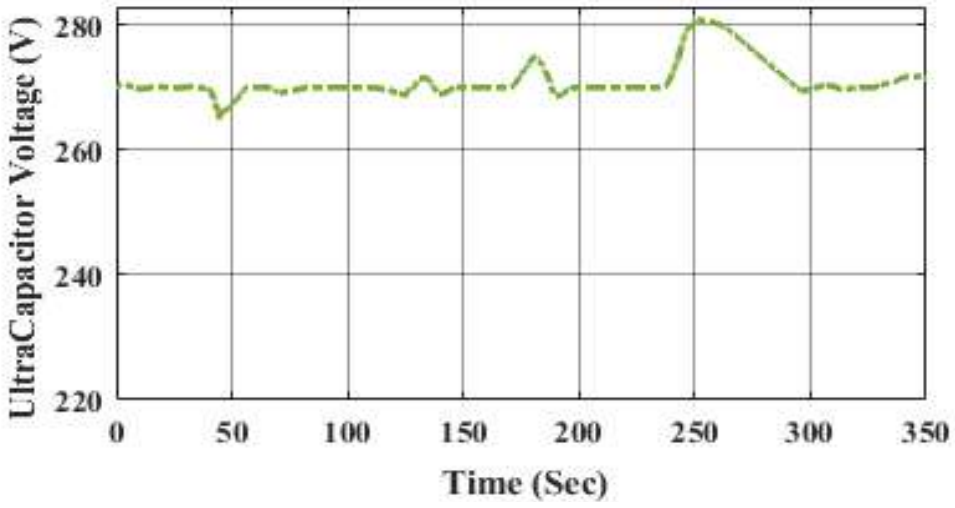

Figure 23. Time response of ultracapacitor voltage.

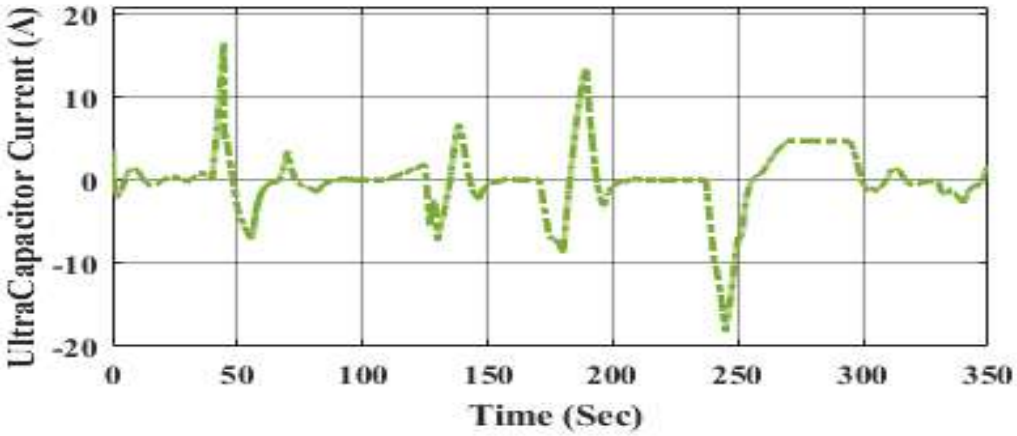

Figure 24. Responses of ultracapacitor current.

This means that the power supplied by both the battery bank and UC bank for supplying the required load is superior when compared to the power supplied by the FC, resulting in the lowest hydrogen consumption.

6.3. Distribution of Power to Load by Using Drive Cycle Data

The overall hybrid storage system is tested with the following drive cycles: HWFET and WLTC—Class 3.

- Highway Fuel Economy Driving Schedule (HWFET—Drive Cycle)

Figure 25 illustrates the Highway Fuel Economy Test (HWFET or HFET) cycle, which is a vehicular dynamometer operating program designed by the United States Environmental Protection Agency (EPA) for determining the fuel economy of light-duty cars [40 CFR 600, Section B]. The HWFET is employed to calculate the vehicle fuel economy rating, whereas the FTP-75 is employed to obtain the urban fuel economy rating.

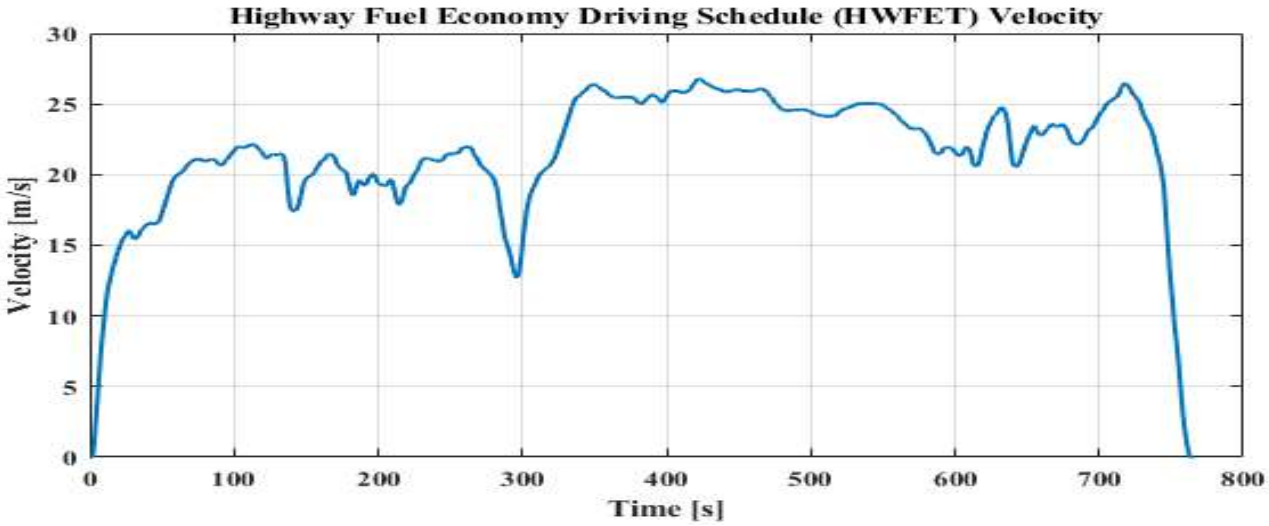

Figure 25. Drive cycle data—HWFET.

- Worldwide Harmonized Light Vehicles Test procedures (WLTP–Class 3 Drive Cycle)

Shown in Figure 26, the Worldwide Harmonized Light Vehicle Test Cycles (WLTC) are automotive testing machine measurements used to evaluate energy consumption and emissions from light-duty cars. Class 3 represents automobiles operated in Europe as well as Japan, as it has the highest power-to-mass ratio. Class 3 vehicles are divided into two

subclasses based on their higher speed: Class 3a with a maximum speed of 120 km/h and Class 3b with a maximum speed of 120 km/h.

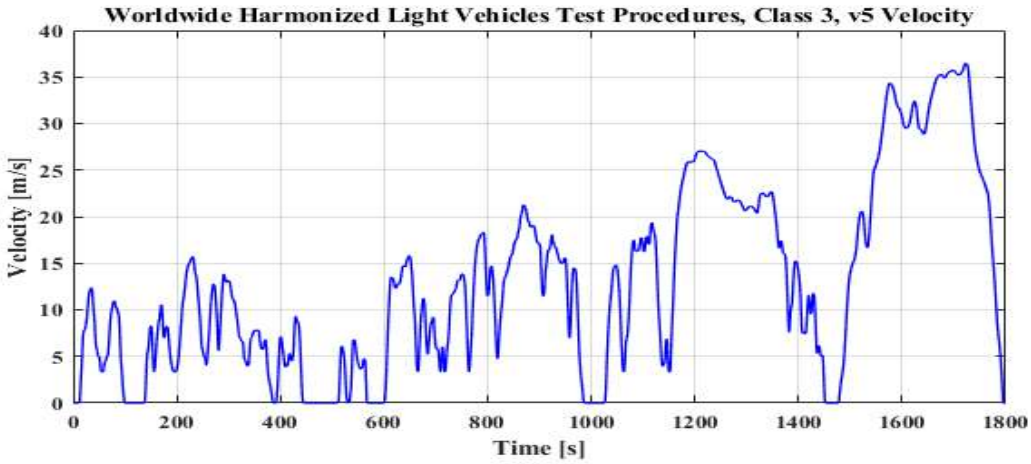

Figure 26. Drive cycle data—WLTC (Class 3).

A hybrid energy source (FC/B/UC) supplies the power to load, which is shown in Figure 27. During a period of time, a span of 350 s, regarding the performance of the system at t = 0, the system starts with no load demand, so load power is zero. Here, the battery is charged by the fuel cell. At the time of 40 s, there is a distribution of the power supply to the battery and supercapacitor, and also the power of the fuel cell increases gradually. Later, at 45 s, the level of supercapacitor voltage reduces to the 270 V reference value. At time t = 60 s, the power of the fuel cell rises predominantly, whereas the supercapacitor provides extra transient demand beyond the maximum power of the primary source. Thus, the secondary sources are charged by extra fuel cell power. At 330 s, there is a lower load demand; hence, the power of the primary source also reduces gradually while recharging the battery container; a comparison of each PMS is given in Table 5.

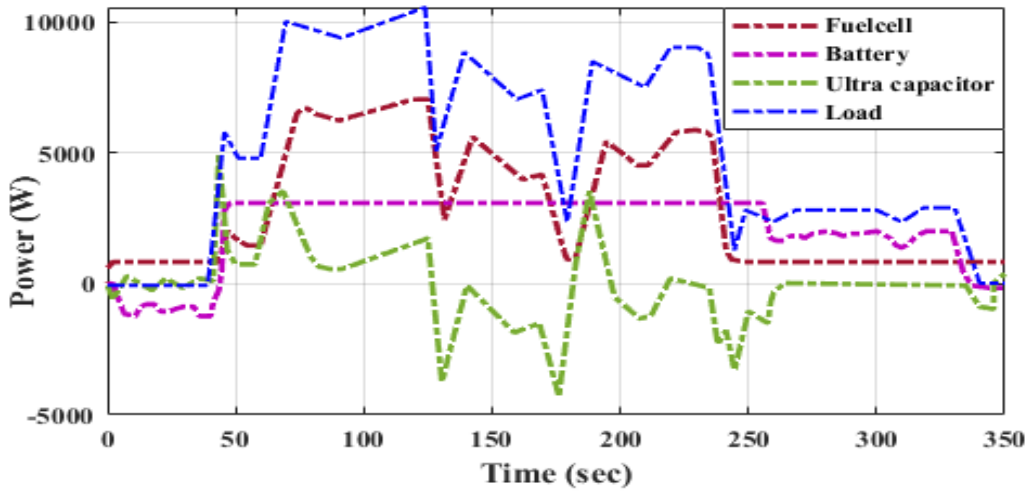

Figure 27. Power of hybrid sources (fuel cell, Li-ion battery and ultracapacitor) delivering the load request versus time.

Table 5. Overall performance of each PMS scheme.

Drive Cycle	Criteria for PMS	PI	SMC	FDFC	ECMS	EEMS	ANFIS-Based ECMS
HWFET (Highway Fuel Economy Test Cycle)	State of charge of the battery (%)	70–51	70–54	70.54	70–54	70–59	70–58
	Consumption of H_2 (g)	31.63	32.06	32.97	35.97	30.17	22.93
	Overall efficiency (%)	73.77	78.52	74.77	72.51	74.15	80.47
	Stress on battery (σ)	22	21.91	24.6	24.6	22.4	23.7
	Stress on fuel cell (σ)	20.42	22.59	22.04	23.42	18.6	15.8
	Stress on ultracapacitor (σ)	35.92	34.7	37.84	37.84	35.9	36.76
WLTC (Worldwide Harmonized Light Vehicle Test Cycles)	State of charge of the battery (%)	70–52	70–54	70.53	70–53	70–59	70–59
	Consumption of H_2 (g)	31.5	30.83	33.29	38.13	33.19	22.74
	Overall efficiency (%)	76.16	77.28	71.83	72.11	78.19	81.29
	Stress on battery (σ)	28	24.81	27.9	29.4	24.46	24.38
	Stress on fuel cell (σ)	24.23	23.19	21.84	27.17	19.23	19.82
	Stress on ultracapacitor (σ)	36.12	32.45	31.93	34.92	37.1	31.15

7. Conclusions

An ANFIS-based ECMS-integrated control strategy for power management in hybrid electric vehicles is proposed in this paper to conserve maximum fuel, with the main power source as a PEMFC and secondary sources as a battery bank (BB) and ultracapacitors (UC). The ECMS is a cost function-based optimization approach where the SoC of the battery is regulated by the penalty coefficients of battery power. The power of UC is overlooked in this optimization approach. The voltage profile of the DC bus is regulated by converters of the battery bank such that, once the UCs are drained, they are restored with the same power from the battery bank. The load demand is balanced via a battery and FC over a load cycle. The ANFIS-based controller efficiently monitors the fluctuating energy demand but also continues to maintain a DC bus voltage profile with a limited error signal as well as a rapid trackability level compared to that of a conventional control system. Since continuous monitoring enhances the battery's lifespan, the performance of HEVs will be superior and more reliable. The performance analysis was conducted in terms of the consumption of hydrogen, SoC, global efficiency and stress on individual sources. The state machine control technique (SMC) attains an efficiency of 78.52%, and the stress (σ) on the supercapacitor and battery is 34.7 and 22.59. In the case of the frequency decoupling and fuzzy logic technique, the stress σ is 22.04 and the battery SoC is 70–57%, but there is moderate fuel consumption of 32.1897 (g) of H2 with an overall efficiency of 74.77%. Regarding the equivalent consumption minimization strategy (ECMS), there is higher stress (23.42) on fuel cells with an efficiency of 72.51%. Meanwhile, in the external energy maximization control technique (EEMS), there is the lowest fuel consumption of 30.1774 (g) of H2 and higher usage of the Li-ion battery, whose SOC is 70–59%, while the stress on the fuel cell is low. In the hybrid PMS, fuel consumption is 22.93 (g), with reduced stress (σ) on the fuel cell, which is 15.8.

For all the control strategies, the value of the DC link is maintained at around (270 V_{DC}). Energy management in hybrid vehicles must adopt a multi-scheme EMS since each approach is chosen as per key variables. For instance, depending on the actual lifespan of the input sources, EMS can indeed be employed to optimize the source lifespan or reduce the stress on FC/B/UC. Further, ANFIS with ECMS has been validated across different drive cycles, i.e., HWFET and WLTC—Class 3.

Author Contributions: Conceptualization, V.M. and Y.P.O.; Supervision, Y.P.O.; Validation, V.M.; Visualization, V.M.; Writing–original draft, V.M. and Y.P.O.; Writing–review & editing, V.M. and Y.P.O. All authors have read and agreed to the published version of the manuscript.

Funding: This research received no external funding.

Institutional Review Board Statement: Not applicable.

Informed Consent Statement: Not applicable.

Data Availability Statement: Not applicable.

Conflicts of Interest: The authors declare no conflict of interest.

References

1. Zhang, F.; Wang, L.; Coskun, S.; Pang, H.; Cui, Y.; Xi, J. Energy management strategies for hybrid electric vehicles: Review, classification, comparison, and outlook. *Energies* **2020**, *13*, 3352. [CrossRef]
2. Duhr, P.; Christodoulou, G.; Balerna, C.; Salazar, M.; Cerofolini, A.; Onder, C.H. Time-optimal gearshift and energy management strategies for a hybrid electric race car. *Appl. Energy* **2021**, *282*, 115980. [CrossRef]
3. Guo, N.; Zhang, X.; Zou, Y.; Guo, L.; Du, G. Real-time predictive energy management of plug-in hybrid electric vehicles for coordination of fuel economy and battery degradation. *Energy* **2021**, *214*, 119070. [CrossRef]
4. Li, Q.; Chen, W.; Liu, S.; You, Z.; Tao, S.; Li, Y. Power management strategy based on adaptive neuro-fuzzy inference system for fuel cell-battery hybrid vehicle. *J. Renew. Sustain. Energy* **2012**, *4*, 013106. [CrossRef]
5. Allahvirdizadeh, Y.; Mohamadian, M.; HaghiFam, M.R.; Hamidi, A. Optimization of a fuzzy-based energy management strategy for a PV/WT/FC hybrid renewable system. *Int. J. Renew. Energy Res.* **2017**, *7*, 1686–1699.
6. Yavasoglu, H.A.; Tetik, Y.E.; Ozcan, H.G. Neural network-based energy management of multi-source (battery/UC/FC) powered electric vehicle. *Int. J. Energy Res.* **2020**, *44*, 12416–12429. [CrossRef]
7. Montazeri-Gh, M.; Pourbafarani, Z. Near-optimal SOC trajectory for traffic-based adaptive PHEV control strategy. *IEEE Trans. Veh. Technol.* **2017**, *66*, 9753–9760. [CrossRef]
8. Singh, K.V.; Bansal, H.O.; Singh, D. Development of an adaptive neuro—Fuzzy inference system–based equivalent consumption minimization strategy to improve fuel economy in hybrid electric vehicles. *IET Electr. Syst. Transp.* **2021**, *11*, 171–185. [CrossRef]
9. Suhail, M.; Akhtar, I.; Kirmani, S.; Jameel, M. Development of progressive fuzzy logic and ANFIS control for energy management of plug-in hybrid electric vehicle. *IEEE Access* **2021**, *9*, 62219–62231. [CrossRef]
10. Kamel, A.A.; Rezk, H.; Abdelkareem, M.A. Enhancing the operation of fuel cell-photovoltaic-battery-supercapacitor renewable system through a hybrid energy management strategy. *Int. J. Hydrogen Energy* **2021**, *46*, 6061–6075. [CrossRef]
11. Song, Z.; Hofmann, H.; Li, J.; Hou, J.; Han, X.; Ouyang, M. Energy management strategies comparison for electric vehicles with a hybrid energy storage system. *Appl. Energy* **2014**, *134*, 321–331. [CrossRef]
12. Gaber, M.; El-Banna, S.; El-Dabah, M.; Hamad, O. Designing and implementation of an intelligent energy management system for electric ship power system based on adaptive neuro-fuzzy inference system (ANFIS). *Adv. Sci. Technol. Eng. Syst. J.* **2021**, *6*, 195–203. [CrossRef]
13. Tian, X.; He, R.; Xu, Y. Design of an energy management strategy for a parallel hybrid electric bus based on an IDP-ANFIS scheme. *IEEE Access* **2018**, *6*, 23806–23819. [CrossRef]
14. Ding, N.; Prasad, K.; Lie, T.T. Design of a hybrid energy management system using designed rule-based control strategy and genetic algorithm for the series-parallel plug-in hybrid electric vehicle. *Int. J. Energy Res.* **2021**, *45*, 1627–1644. [CrossRef]
15. Colvin, R. *Advances in Automotive Technologies*; Springer: Berlin/Heidelberg, Germany, 2019; Volume 84, ISBN 9789811559464.
16. Zhang, X.; Guo, L.; Guo, N.; Zou, Y.; Du, G. Bi-level energy management of plug-in hybrid electric vehicles for fuel economy and battery lifetime with intelligent state-of-charge reference. *J. Power Sources* **2021**, *481*, 228798. [CrossRef]
17. Cai, C.H.; Du, D.; Liu, Z.Y. Battery state-of-charge (SOC) estimation using adaptive neuro-fuzzy inference system (ANFIS). *IEEE Int. Conf. Fuzzy Syst.* **2003**, *2*, 1068–1073. [CrossRef]
18. Shaik, R.B.; Kannappan, E.V. Application of adaptive neuro-fuzzy inference rule-based controller in hybrid electric vehicles. *J. Electr. Eng. Technol.* **2020**, *15*, 1937–1945. [CrossRef]
19. Li, P.; Jiao, X.; Li, Y. Adaptive real-time energy management control strategy based on fuzzy inference system for plug-in hybrid electric vehicles. *Control Eng. Pract.* **2021**, *107*, 104703. [CrossRef]
20. Karaboga, D.; Kaya, E. Adaptive network-based fuzzy inference system (ANFIS) training approaches: A comprehensive survey. *Artif. Intell. Rev.* **2019**, *52*, 2263–2293. [CrossRef]
21. Zhang, F.; Hu, X.; Langari, R.; Wang, L.; Cui, Y.; Pang, H. Adaptive energy management in automated hybrid electric vehicles with flexible torque request. *Energy* **2021**, *214*, 118873. [CrossRef]
22. Zhang, L.; Ye, X.; Xia, X.; Barzegar, F. A real-time energy management and speed controller for an electric vehicle powered by a hybrid energy storage system. *IEEE Trans. Ind. Inform.* **2020**, *16*, 6272–6280. [CrossRef]
23. Zhang, Q.; Li, G. A predictive energy management system for hybrid energy storage systems in electric vehicles. *Electr. Eng.* **2019**, *101*, 759–770. [CrossRef]
24. Zhang, Q. Applied sciences strategy for hybrid electric vehicles based on driving cycle recognition. *Appl. Sci.* **2020**, *10*, 696.
25. Wieczorek, M.; Lewandowski, M. A mathematical representation of an energy management strategy for hybrid energy storage system in electric vehicle and real-time optimization using a genetic algorithm. *Appl. Energy* **2017**, *192*, 222–233. [CrossRef]

26. Sarkar, J.; Bhattacharyya, S. Application of graphene and graphene-based materials in clean energy-related devices Minghui. *Int. J. Energy Res.* **2012**, *33*, 23–40. [CrossRef]
27. Gomes, G.F.; da Cunha, S.S.; Ancelotti, A.C. A sunflower optimization (SFO) algorithm applied to damage identification on laminated composite plates. *Eng. Comput.* **2019**, *35*, 619–626. [CrossRef]
28. Mirjalili, S.; Gandomi, A.H.; Mirjalili, S.Z.; Saremi, S.; Faris, H.; Mirjalili, S.M. Salp swarm algorithm: A bio-inspired optimizer for engineering design problems. *Adv. Eng. Softw.* **2017**, *114*, 163–191. [CrossRef]
29. Mirjalili, S.; Mirjalili, S.M.; Hatamlou, A. Multi-verse optimizer: A nature-inspired algorithm for global optimization. *Neural Comput. Appl.* **2016**, *27*, 495–513. [CrossRef]
30. Saremi, S.; Mirjalili, S.; Lewis, A. Grasshopper optimisation algorithm: Theory and application. *Adv. Eng. Softw.* **2017**, *105*, 30–47. [CrossRef]
31. Mirjalili, S.; Mirjalili, S.M.; Lewis, A. Grey wolf optimizer. *Adv. Eng. Softw.* **2014**, *69*, 46–61. [CrossRef]
32. Rezk, H.; Al-Oran, M.; Gomaa, M.R.; Tolba, M.A.; Fathy, A.; Abdelkareem, M.A.; Olabi, A.G.; El-Sayed, A.H.M. A novel statistical performance evaluation of most modern optimization-based global MPPT techniques for a partially shaded PV system. *Renew. Sustain. Energy Rev.* **2019**, *115*, 109372. [CrossRef]
33. Abdalla, O.; Rezk, H.; Ahmed, E.M. Wind-driven optimization algorithm based global MPPT for PV system under non-uniform solar irradiance. *Sol. Energy* **2019**, *180*, 429–444. [CrossRef]
34. Tolba, M.; Rezk, H.; Diab, A.A.Z.; Al-Dhaifallah, M. A novel robust methodology based salp swarm algorithm for allocation and capacity of renewable distributed generators on distribution grids. *Energies* **2018**, *11*, 2556. [CrossRef]
35. Yadav, N.; Yadav, A.; Bansal, J.C.; Deep, K.; Kim, J.H. *Harmony Search and Nature Inspired Optimization Algorithms: Theory and Applications, ICHSA 2018*; Springer: Berlin/Heidelberg, Germany, 2019; Volume 741, ISBN 9789811307607.
36. Mirjalili, S. Particle swarm optimization. *Stud. Comput. Intell.* **2019**, *780*, 15–31. [CrossRef]

energies

MDPI

Article

Real Time Hardware-in-Loop Implementation of LLC Resonant Converter at Worst Operating Point Based on Time Domain Analysis

Kiran Kumar Geddam [1] and Elangovan Devaraj [2,*]

[1] School of Electrical Engineering, Vellore Institute of Technology, Vellore 632014, India; gkiran.kumar2018@vitstudent.ac.in
[2] TIFAC-CORE, School of Electrical Engineering, Vellore Institute of Technology, Vellore 632014, India
* Correspondence: elangovan.devaraj@vit.ac.in

Abstract: The inductor inductor capacitor (LLC) resonant topology has become more popular for deployment in high power density and high-efficiency power converter applications due to its ability to maintain zero voltage switching (ZVS) over a wider input voltage range. Due to their ease of operation and acceptable accuracy, frequency domain-related analytical methods using fundamental harmonic approximation (FHA) have been frequently utilized for resonant converters. However, when the switching frequency is far from the resonant frequency, the circuit currents contain a large number of harmonics, which cannot be ignored. Therefore, the FHA is incapable of guiding the design when the LLC converter is used to operate in a wide input voltage range applications due to its inaccuracy. As a result, a precise LLC converter model is needed. Time domain analysis is a precise analytical approach for obtaining converter attributes, which supports in the optimal sizing of LLC converters. This work strives to give a precise and an approximation-free time domain analysis for the exact modeling of high-frequency resonant converters. A complete mathematical analysis for an LLC resonant converter operating in discontinuous conduction mode (DCM)—i.e., the boost mode of operation below resonance—is presented in this paper. The proposed technique can confirm that the converter operates in PO mode throughout its working range; in addition, for primary MOSFET switches, it guarantees the ZVS and zero current switching (ZCS) for the secondary rectifier. As a function of frequency, load, and other circuit parameters, closed-form solutions are developed for the converter's tank root mean square (RMS) current, peak stress, tank capacitor voltage, voltage gain, and zero voltage switching angle. Finally, an 8 KW LLC resonant converter is built in the hardware-in-loop (HIL) testing method on RT-LAB OP-5700 to endorse the theoretical study.

Keywords: HIL; LLC resonant converter (LLC-RC); soft switching; time domain analysis; ZVS; ZCS

Citation: Geddam, K.K.; Devaraj, E. Real Time Hardware-in-Loop Implementation of LLC Resonant Converter at Worst Operating Point Based on Time Domain Analysis. *Energies* **2022**, *15*, 3634. https://doi.org/10.3390/en15103634

Academic Editor: Anna Richelli

Received: 6 April 2022
Accepted: 3 May 2022
Published: 16 May 2022

Publisher's Note: MDPI stays neutral with regard to jurisdictional claims in published maps and institutional affiliations.

Copyright: © 2022 by the authors. Licensee MDPI, Basel, Switzerland. This article is an open access article distributed under the terms and conditions of the Creative Commons Attribution (CC BY) license (https://creativecommons.org/licenses/by/4.0/).

1. Introduction

The LLC-RC has received a great deal of attention due to its high power density, soft switching, and high-efficiency operation. It has been used in many industrial applications, such as on-board battery chargers, panel TVs, adapters for electronic equipment, server power supplies, light-emitting diode drivers, and so on [1–5]. This converter has the benefit of accomplishing ZVS for a wider input voltage and load range, allowing it to run at high frequencies without sacrificing efficiency due to switching losses, resulting in smaller component sizes and higher power density. By placing an additional inductor in parallel with the series resonant converter (SRC), an LLC-RC is formed as shown in Figure 1. Light load regulation concerns in SRC can be overcome by adding this third resonant element. Therefore, it permits the converter to be operated in boost mode (i.e., voltage gain > 1) and increases the efficiency. Furthermore, at no additional cost, the added inductor may be combined with the transformer as the magnetizing inductance. Nonetheless, this topology

is challenging to evaluate due to its various resonant components and different operation modes [6].

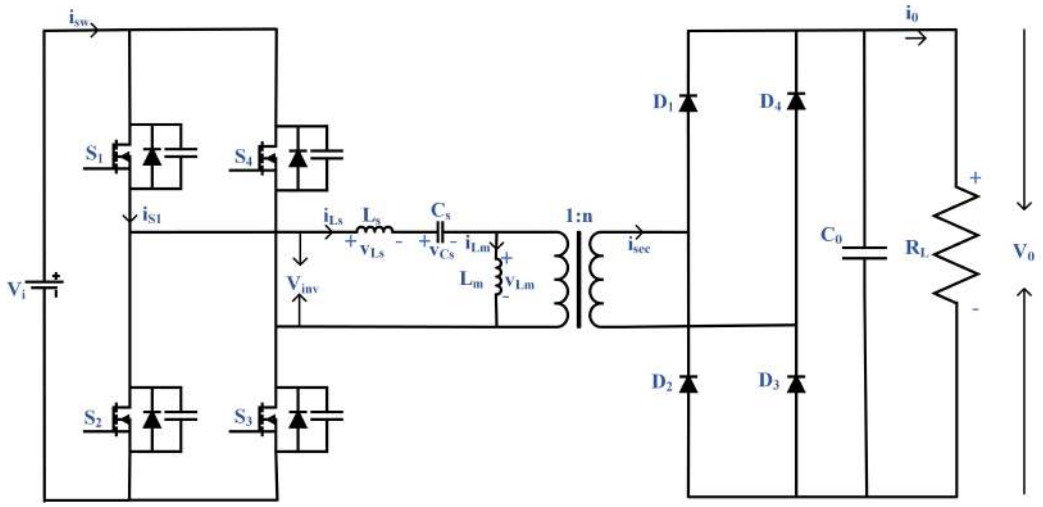

Figure 1. Full-bridge LLC resonant converter.

The LLC-RC operates in three subintervals, namely P, O, and N. When the magnetizing inductor voltage is a positive output voltage, then that subinterval is called the P-subinterval. Similarly, when the magnetizing inductor voltage is a negative output voltage, then that subinterval is called the N-subinterval. In both the above subintervals, the current runs in the secondary rectifier, while in the O-subinterval, the output voltage will not appear across the magnetizing inductor. Therefore, in the O-subinterval, no current flows through the secondary rectifier. These three subintervals form the basis of LLC-RC's 11 major operating modes, which are PO, PN, PON, O, and OPO modes below resonance and O, P, OP, NP, OPO, and NOP modes above resonance [7]. The O and OPO operating modes occur over the whole switching frequency range with no load and low output power, respectively. In the PO operation mode, for example, during half of the switching period, the LLC-RC initially operates in the P-subinterval and then in the O-subinterval. Similarly, for the PON operation mode, the LLC-RC initially operates in the P-subinterval, followed by O, and finally operates in the N-subinterval [8].

Analysis techniques have a significant impact on the precision and efficiency of the parameter design in LLC-RC design. There are four major analytical techniques for the LLC-RC based on the current literature, a list of which is provided below:

- Frequency-domain analysis (FDA) [4];
- Frequency domain with time-domain partial correction [9];
- Frequency domain with time-domain complete correction [10]; and
- Time-domain analysis (TDA) [11–16].

FHA is a popular frequency-domain resonant converter analysis approach that considers voltage and current waveforms as purely sinusoidal at the fundamental frequency and ignores additional high-order harmonics [17,18]. Although FHA offers a simple approach to calculating the DC gain, the precision diminishes when the switching frequency moves away from the resonant frequency as the voltage and current waveforms become non-sinusoidal. In practice, however, FHA can be enhanced by taking account of high-order distortions [19,20] or integrating parasites into the analysis [21]. Furthermore, harmonic analysis approaches fail to uncover the LLC converter's different operating modes.

Numerous design techniques based on FDA have been recommended because of the ease of FDA. For instance, in [22], the magnetizing inductor value L_m is governed by comparing the loads. The magnetizing inductance must satisfy $R_{eq} = 2\pi \times f_s \times L_m$ for the operating point to be at its most efficient, where f_s is the switching frequency. A

voltage gain and power factor requirement must be taken into account when selecting an inductor's inductance.

The LLC resonant tank characteristics can be calculated by iteratively setting the operational switching frequency upper and lower bounds. Using the ZVS operation constraints of the primary switches, the magnetizing inductor is calculated in [23]. After that, the resonant tank parameters can be calculated using the quality factor "Q" and inductor ratio "K" established using the voltage gain curve. The following are some of the drawbacks of frequency-domain analysis-based design techniques.

- FDA-based design techniques are primarily reliant on engineering practice, such as how to choose the Q and K values, which is not universal, and the outcomes differ from one situation to the next;
- Only the most basic soft switching and voltage gain needs are taken into account in the design.

An analytical approach combining the partial time-domain corrections and frequency domain is proposed in [9]. In this technique, the equivalent load in DCM is altered by using TDA. This method's accurateness is considerably enhanced over FHA, but it still makes a large number of assumptions, which reduces its accuracy. For the LLC-RC, in [10], the authors developed an approach in which both the resonant factor and the equivalent load are adjusted, although the method of derivation is difficult and the accuracy increment is not apparent. The above-mentioned issues still remain despite efforts to increase accuracy through the methods of approaches based on FDA with partial and complete corrections in the time domain.

State space investigation is an additional option to be employed, which can describe the current and voltage waveforms accurately [24,25]. However, the interpretation and usage are convoluted and challenging. The literature available in [26,27] is based on operational modes and is mainly concentrated on analyzing the resonant voltage and current behavior according to different modes rather than calculating the DC gain. More valuable in directing the design is an exact DC gain characteristic rather than precisely stated current and voltage characteristics.

The LLC-RC has not been subjected to any additional assumptions in the TDA. There is a strong correlation between theoretical and actual results. The fundamental drawback of time-domain analysis is that it is difficult to solve nonlinear equations because of its complexity. Design techniques established on TDA have been developed to make maximum use of the LLC resonant tank. An automated computer-aided design technique based on the LLC converter power loss model is presented in [15], where the optimum design result may be reached by setting the parameters for the design variables to their limits. System voltage gain operating points are designed as the peak gain operating points of the LLC-RC in [8,14] depending on whether they are operating in PN or PON modes. The LLC resonant tank may be used to its full potential with this design technique; however, the ZVS operation for the primary switches may be compromised at the operating point of maximum gain. Additionally, the text fails to explicitly identify the optimization goal, which is mostly up to the designer. Because of the high processing requirements of these design methods, they are difficult to implement. It is necessary to solve all of the LLC-RC operation modes and boundary conditions in [15], which makes the design process more difficult. We need to find out about the PN and PON operating modes, as well as the boundary conditions that exist between them. Furthermore, because there is no set beginning point, there are a plethora of design options.

In this paper, a simplified analysis of the LLC resonant tanks' DCMs has been thoroughly investigated in PO mode under the worst case instead of PN or PON modes. Due to the possibility of several resonant frequencies, DCM modeling for three or more resonant element converters based on FHA and prolonged descriptive function is highly approximate in nature. Numerous studies have attempted to solve analytical problems for multi-element resonant converters such as LLC, LCC, and LCLC using a state-space time domain method. Few authors have investigated the TDA operating above the resonant

point of the LLC-RC. The majority of these publications make certain assumptions, such as a linear increasing magnetizing current, sinusoidal output current, and complete output diode conduction. The majority of these studies have focused solely on estimating the maximum voltage gain at or around the resonance point. In the current literature, there has not been much consideration devoted to the examination and derivation of closed-form solutions for ZVS angle, component stress, active power, RMS current, switch turn-off current, and other circuit design parameters in DCM mode. As a result, the circuit parameters are incorrectly selected.

This paper strives, by offering a precise model, to bridge this gap. LLC-RCs have demonstrated the exact derivation of the tank RMS current, tank capacitor voltage, converter voltage gain, peak stress, and ZVS. This research provides researchers with user-friendly technologies that allow them to quickly specify parameters, examine trade-offs, prototype the final product design quickly, and perform precise magnetic examination. As an action of the frequency, load, and other circuit parameters, closed-form solutions are developed for converter peak stress, tank capacitor voltage, voltage gain, ZVS angle, and tank RMS current. The rest of this article is structured in the following manner: the time-domain analysis introduction is presented in Section 2. Section 3 discusses the steady state time domain analysis. A complete step-by-step design procedure for LLC-RC is presented in Section 4. Then, the simulation and experimental results are presented in Section 5. Finally, the conclusions are provided in Section 6.

2. Time-Domain Analysis Introduction

The LLC-RC's typical circuit is shown in Figure 1. During the first half of the switching cycle, there are three subintervals. As long as the voltage across the magnetizing inductor is held at $(+V_o)/\mathrm{n}$, the subinterval is defined as "P". The subinterval is "N" when the voltage is held down at $(-V_o)/\mathrm{n}$, and the "O" subinterval occurs when no current runs through the secondary side of the transformer [8]. The LLC-RC operates primarily in the following six modes of operation: PO, PON, PN, NP, NOP, and OPO, which are determined by the sequences of these three subintervals. An LLC-RC running in PO mode first operates in the P-subinterval, followed by the O-subinterval, for half of the switching time.

Figure 2 depicts the significant waveforms produced when the LLC-RC is working in the PO mode. The switch current i_{S1} is negative before the driving signal S_1 is supplied; thus, its anti-parallel diode will turn on and perform the ZVS process on S_1. In the same way, the remaining switches (S_2–S_4) are capable of the ZVS process. The secondary diodes (D_1–D_4) can accomplish ZCS functioning based on the waveform of the transformer secondary current i_{sec}. The PO and OPO modes of the LLC-RC are extremely efficient because the primary switches and secondary diodes operate in ZVS and ZCS modes, respectively [28]. Other operating modes, such as PON or PN modes, do not ensure ZVS functioning for the primary switches, resulting in worse overall system efficiency. The switching frequency in NOP or NP mode is higher than the resonance frequency, and the secondary diodes cannot perform ZCS. Design considerations include making sure it can function in OPO or PO modes across the complete working range. The other three analytical techniques had significant errors; therefore, the resonant tank components were designed using time-domain analysis. The analysis for PO mode is identical to that for the OPO mode, which follows in the next section.

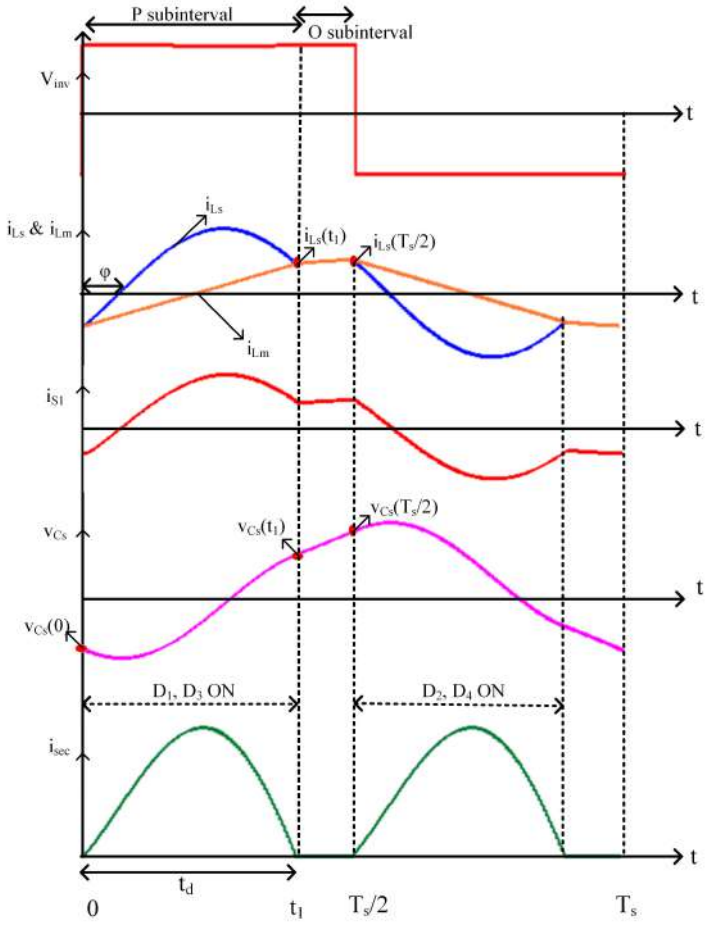

Figure 2. LLC converter steady state waveforms in PO mode.

3. Steady State Time-Domain Analysis

The variable-frequency controlled LLC-RC's steady state time-domain analysis is presented in this section. In order to keep the bridge stable, two complementary gating signals are used, each having a duty cycle of 0.5%. Figure 1 depicts the overall configuration of the LLC-RC in PO mode, as well as the corresponding equivalent circuit that results. Figure 3A,B illustrates the analogous circuits for an LLC resonant converter working in the P and O stages, respectively. In order to analyze the converter's steady state performance, the following assumptions are made.

- The rectifier diodes, MOSFET switches and transformer are ideal;
- The filter capacitor is sufficiently big to maintain a stable voltage at the output;
- The capacitance of a MOSFET is quite small;
- The dead time between switches is not taken into account.

The reasons for choosing the PO operating mode are summarized as follows.

- The most typical mode of operation for an LLC-RC is the PO mode. Generally, the LLC-RC is intended to operate in this mode in order to attain ZVS for the primary switches and ZCS for the secondary diodes;
- The resonant tank control capabilities of an LLC converter can be increased by constructing it in the operation modes of PN or PON even when the peak gain operating point occurs in these modes [8,14]. The peak gain for the primary switch is also the barrier between ZVS and ZCS operation. When constructing an LLC-RC in PON or PN modes, the ZVS action may fail, reducing the efficiency of the converter;
- Furthermore, to obtain the ZVS operation in the PON or PN operating mode, a large dead-time is required. Excessive dead-time will have a negative impact on the

converter's efficiency. As a result, in terms of soft switching, the PO mode is favored above the PN or PON modes;

- In terms of performance, the PO mode is almost identical to the maximum gain mode. As a result, the voltage gain lost by using the worst-case PO operating mode design is negligible, and the PO mode may be utilized to estimate the peak gain as well;
- For closed-loop designs, this guarantees control stability by using negative gain–frequency curve slopes in the PO mode. Because of this, the PO mode of operation is recommended for LLC converters. A control instability problem can arise when the operating point of the gain–frequency curve varies in PN or PON mode, which is when the gain–frequency curve is operated at its boundary.

Figure 2 depicts the LLC converter operational waveforms in boost mode. The resonant tank is driven by a square wave input generated by the full bridge's variable switching frequency control. The ZVS angle is indicated by ϕ, which is a measurement of the exact ZVS and t_d. Differential equations utilizing KCL/KVL have been developed for each mode. For the sake of analysis, the subsequent quantities have been defined:

$$Z_0 = \sqrt{\frac{L_s}{C_s}} \tag{1}$$

$$Z_1 = \sqrt{\frac{L_s + L_m}{C_s}} \tag{2}$$

$$\omega_r = \frac{1}{\sqrt{L_s C_s}} \tag{3}$$

$$\omega_{r1} = \frac{1}{\sqrt{(L_s + L_m) C_s}} \tag{4}$$

$$\omega = \frac{\omega_{sw}}{\omega_r} \tag{5}$$

$$K = \frac{L_m}{L_s} \tag{6}$$

where Z_0 = characteristic impedance, L_m = magnetizing inductance, L_s = resonant inductance, C_s = resonant capacitor, ω_r = series resonant angular frequency, ω_{r1} = parallel resonant angular frequency, ω = angular normalized frequency, and ω_{sw} = angular switching frequency.

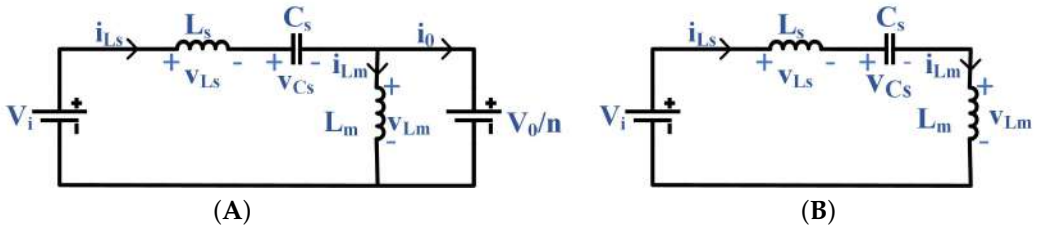

Figure 3. Equivalent circuits in PO mode, (**A**) energy transfer period in P mode, (**B**) freewheeling period in O mode.

3.1. Energy Transfer Period ($0 - T_1$)

The starting values of the magnetizing current, i_{Lm}, and resonant tank current, i_{Ls}, are identical. The currents have distinct wave patterns and deviate because the series resonant capacitor, C_s, and inductor, L_s, are in resonance, and the magnetizing inductor is restrained to the output voltage. The magnetizing current, i_{Lm}, increases linearly when the clamped output voltage $(+V_o)/n$ is applied. i_{Ls} starts out with a negative value, crosses the zero line, and then equals i_{Lm} at time t_1. According to KCL, the output rectifier is responsible for

supplying any leftover current to the load. This period lasts until $t_1 = t_d\ T_{sw}/2$, where t_d is the diode to switch conduction ratio. The differential equations that represent this mode are as follows:

$$V_i - \frac{V_0}{n} = L_s \frac{di_{Ls}(t)}{dt} + v_{Cs}(t) \tag{7}$$

$$i_{Ls}(t) = C_s \frac{dv_{\mathrm{Cs}}(t)}{dt} \tag{8}$$

$$i_{Lm}(t) = \frac{1}{L_m} \int_0^t \frac{V_0}{n} dt + i_{Lm}(0) \tag{9}$$

Solving (7)–(9),

$$i_{Ls}(t) = i_{Ls}(0)\cos(\omega_r t) + \left[\frac{V_i - \frac{V_0}{n} - v_{Cs}(0)}{Z_0}\right]\sin(\omega_r t) \tag{10}$$

$$i_{Lm}(t) = \frac{\frac{V_0}{n}}{L_m} t + i_{Lm}(0) \tag{11}$$

$$v_{Cs}(t) = Z_0 i_{Ls}(0)\sin(\omega_r t) + v_{Cs}(0)\cos(\omega_r t) + \left[V_i - \frac{V_0}{n}\right][1 - \cos(\omega_r t)] \tag{12}$$

$$i_0(t) = i_{Ls}(t) - i_{Lm}(t) \tag{13}$$

3.2. Freewheeling Period ($t_1 - T_{sw}/2$)

The diodes are turned off naturally when i_{Lm} and i_{Ls} are equal at the completion of the first interval, and thus the secondary side no longer receives the primary side energy. Now, L_m is not fixed to the output voltage; it begins to resonate with the series L_s and C_s, enabling the series resonant current to pass through it. Therefore, there is a shifting of resonant frequency from ω_r to ω_{r1}. This mode's differential equations are as follows:

$$V_i = L_s \frac{di_{Ls}(t)}{dt} + v_{Cs}(t) + v_{Lm}(t) \tag{14}$$

$$i_{Ls}(t) = C_s \frac{dv_{Cs}(t)}{dt} \tag{15}$$

$$v_{Lm}(t) = L_m \frac{di_{Lm}(t)}{dt} \tag{16}$$

Solving the above equations, we get

$$i_{Ls}(t) = i_{Ls}(t_1)\cos[\omega_{r1}(t - t_1)] - \frac{v_{Cs}(t_1)}{Z_1}\sin[\omega_{r1}(t - t_1)] + \frac{V_i}{Z_1}\sin[\omega_{r1}(t - t_1)] \tag{17}$$

$$v_{Cs}(t) = Z_1 i_{Ls}(t_1)\sin[\omega_{r1}(t - t_1)] + v_{Cs}(t_1)\cos[\omega_{r1}(t - t_1)] + V_i[1 - \cos(\omega_{r1}(t - t_1))] \tag{18}$$

$$i_{Ls}(t) = i_{Lm}(t) \tag{19}$$

The transfer of energy only occurs between 0 and t_1, where t_1 alters on t_d. As a result, t_d cannot be considered as a fixed value when computing the starting current, or the voltage values and the voltage gain, for LLC-RC since it changes depending on the load circumstances. Closed-form expressions would not apply to all loading scenarios. Therefore, for an exact TDA, starting values of capacitor voltage, resonant current, and voltage gain are proven to be implicit functions of t_d and ω. Thus, the average output current may be expressed as follows:

$$I_0 = \frac{2}{T_{sw}} \int_0^{t_1} (i_{Ls}(t) - i_{Lm}(t))dt \tag{20}$$

$$I_0 = \frac{2}{T_{sw}\omega_r} \left[i_{Ls}(0)\sin(\omega_r t_1) + \left[\frac{V_i - \frac{v_0}{n} - v_{cs}(0)}{z_0} \right] (1 - \cos(\omega_r t_1)) - \frac{V_0 \omega_r^2}{n\omega_r L_m} \frac{t_1^2}{2} - i_{L_m}(0)\omega_r t_1 \right] \tag{21}$$

The steady-state waveforms exhibit anti-half-wave symmetry. Therefore, the evaluation may be conducted for half a switching cycle using the resulting circumstances:

$$i_{Ls}(0) = i_{Lm}(0) = -i_{Ls}\left(\frac{T_{sW}}{2}\right) \tag{22}$$

$$v_{Cs}(0) = -v_{Cs}\left(\frac{T_{sW}}{2}\right) \tag{23}$$

$$i_{Ls}(t_1) = i_{Lm}(t_1) \tag{24}$$

Equations to evaluate the resonant capacitor voltage, $v_{Cs}(0)$, initial series resonant current, $i_{Ls}(0)$, and voltage gain are obtained by a reduction of the resultant set of equations. As a consequence, the resultant equations can be written in the following form:

$$i_{Ls}(0) = -V_i\alpha_1 + nGV_i\beta_1 \tag{25}$$

$$v_{Cs}(0) = -V_i\alpha_2 + nGV_i\beta_2 \tag{26}$$

where

$$\alpha_1 = \frac{2(Z_1\sin(x)\cos(y) + Z_0\cos(x)\sin(y)}{L} \tag{27}$$

$$\beta_1 = \frac{Z_1\sin(x)\cos(y) + Z_0\cos(x)\sin(y) + Z_1\sin(x) - Z_0\sin(y)}{L} \tag{28}$$

$$\alpha_2 = \frac{\sin(x)\sin(y)\left(Z_1^2 - Z_0^2\right)}{L} \tag{29}$$

$$\beta_2 = \frac{Z_1^2\sin(x)\sin(y) - Z_1Z_0(1 - \cos(x) - \cos(y))}{L} \tag{30}$$

$$L = 2Z_1Z_0 + 2Z_1Z_0\cos(x)\cos(y) - \sin(x)\sin(y)\left(Z_1^2 + Z_0^2\right) \tag{31}$$

$$x = \frac{\omega_r}{\omega_{sw}} t_d\pi \tag{32}$$

$$y = \frac{\omega_{r1}}{\omega_{sw}}(1 - t_d)\pi \tag{33}$$

Therefore, for the DCM boost operating mode, the voltage gain, G, is expressed as follows:

$$G = \frac{V_0}{nV_i} = \frac{[\sin(x) + \alpha_1 Z_0(1 - \cos(x)) + \alpha_2\sin(x)]}{\left[t_d\frac{T_{sw}Z_0}{2\,L_m} + \sin(x) + \beta_2\sin(x) + \beta_1 Z_0(1 - \cos(x))\right]} \tag{34}$$

The negative current of $i_{Ls}(0)$ is the turn-off current because of the anti-half wave symmetry of the steady state waveforms, as illustrated in (22). To simplify the equation, we may replace (32) and (33) in (21) to obtain the following value of the average output current:

$$I_0 = \left[A_1(\sin(x)) + B_1(1-\cos(x)) - \frac{nGV_i x^2}{2\omega_r L_m} - i_{Cs}(0)x \right] \frac{\omega}{\pi} \tag{35}$$

where

$$A_1 = i_{Ls}(0) \tag{36}$$

$$B_1 = \frac{[V_i - nGV_i - v_{Cs}(0)]}{Z_0} \tag{37}$$

The equivalent AC load can be calculated by using the above expression of average output voltage:

$$V_o = I_o R_{load} \tag{38}$$

$$R_{load} = \frac{V_0}{\left[A_1 \sin(x) + B_1(1-\cos(x)) - \frac{G\,V_i x^2}{2\omega_r Lm} - i_{Cs}(0)x \right] \frac{\omega}{\pi}} \tag{39}$$

In DCM, R_{load} is reliant on t_d and ω, which is given in the expression (39). In contrast to the usual equation given by R_{ac}=$\frac{8}{\pi^2}R_{eq}$, this is applicable for the continuous conduction mode of operation, i.e., in the above resonance operation. The equation used to determine the ZVS angle is

$$\phi = \frac{\pi}{\omega} \tan^{-1}\left(\frac{-A_1}{B_1} \right) \tag{40}$$

The resonant tank inductor current's RMS value is given by

$$i_{Ls_RMS} = \sqrt{\frac{\pi}{\omega}\left(I_{RMS_P} + I_{RMS_O}\sqrt{\frac{L_S + L_m}{L_S}} \right)} \tag{41}$$

where

$$I_{RMS_P} = \left(A_1^2 + B_1^2 \right) \left[\frac{x}{2} - \frac{1}{4}\left\{ \sin\left[2\left(x + \tan^{-1}\left(\frac{A_1}{B_1} \right) \right) \right] + \sin\left[2\tan^{-1}\left(\frac{A_1}{B_1} \right) \right] \right\} \right] \tag{42}$$

$$I_{RMS_O} = \left(A_2^2 + B_2^2 \right) \left[\frac{y}{2} - \frac{1}{4}\left\{ \sin\left[2\left(y + \tan^{-1}\left(\frac{A_2}{B_2} \right) \right) \right] + \sin\left[2\tan^{-1}\left(\frac{A_2}{B_2} \right) \right] \right\} \right] \tag{43}$$

I_{RMS_P} and I_{RMS_O} are the RMS currents for the modes P and O, respectively. Mode O variables are defined as follows:

$$A_2 = i_{Ls}(t_1) \tag{44}$$

$$B_2 = \frac{V_i - v_{Cs}(t_1)}{Z_1} \tag{45}$$

4. Complete Step-by-Step Design of an LLC-RC

In this section, the design of an LLC-RC is explained in detail. The following are the primary design steps:

- Determine the ratio of transformer turns;
- Determine the amount of DC gain required;
- Select Q and K in such a way that the output voltage gain matches the desired G_{max} when the converter is working in PO mode;

- Determine the resonant components.

Table 1 summarizes the system requirements for a typical LLC-RC application.

Table 1. System Specifications.

Parameter	Designator	Value
Input voltage range	V_{in_min}–V_{in_max}	24–32 V
Input nominal voltage	V_{in_nom}	28 V
Output voltage	V_{0_min}–V_{in_max}	48 V
Rated output power	P_o	8000 W
Series resonant frequency	f_r	100 kHz

Step 1: Determine the ratio of transformer turns

The maximum and minimum DC gain requirements for the resonant LLC tank may be derived using the transformer turns ratio.

The n_{sp} (secondary to primary transformer turns ratio) should be calculated as follows:

$$n_{sp} = \frac{V_{0_max} + V_{0_min}}{(2 * V_{in_nom})} = 1.7143 \tag{46}$$

A well-balanced resonant LLC converter's functioning at low circulating current and at frequencies below and above the resonance is ensured by this method of calculating n_{sp}. In addition, the resonant tank's buck and boost areas are both covered by unity gain at the resonant frequency.

Step 2: Determine the amount of DC gain required

The required minimum and maximum values of DC gain are calculated as shown below:

$$G_{dc_min} = \frac{V_{0_min}}{V_{in_max} * n_{sp}} = 0.874 \tag{47}$$

$$G_{dc_max} = \frac{V_{0_max}}{V_{in_min} * n_{sp}} = 1.666 \tag{48}$$

The DC gain range of 0.87 to 1.7 is chosen for overloading and other realistic parasitics.

Step 3: Select Q and K

From the gain vs quality factor curves and normalized frequency vs gain curves as shown in Figures 4 and 5, Q and K are selected as 0.3 and 5, respectively.

Step 4: Determine the resonant components

$$L_S = \frac{\left(Q * R_{0_ratedpri}\right)}{(2 * \pi * f_r)} = 0.0468\,\mu\text{H} \tag{49}$$

$$C_s = \frac{1}{\left(2 * \pi * f_r * Q * R_{0_ratedpri}\right)} = 54.134\,\mu\text{F} \tag{50}$$

$$L_m = K * L_s = 0.23396\,\mu\text{H} \tag{51}$$

where

$$R_{0_ratedpri} = \frac{R_{0_rated}}{n_{sp}} \tag{52}$$

Table 2 shows the different values of minimum and maximum gains, normalized frequencies, switching frequencies, resonant frequency, RMS, and peak currents of switch, average, and peak currents of the diode, as well as stress on the capacitor at different set of K values with the same quality factor. From the table below, it is observed that values of Q = 0.3 and K = 5 contribute to a narrow range of frequency deviation, low turn-off current, and low circulating currents compared to other conditions. Low-voltage stress on

the resonant capacitance and higher power density owing to the smaller size of resonant capacitance and overall magnetics are also ensured by this combination of components.

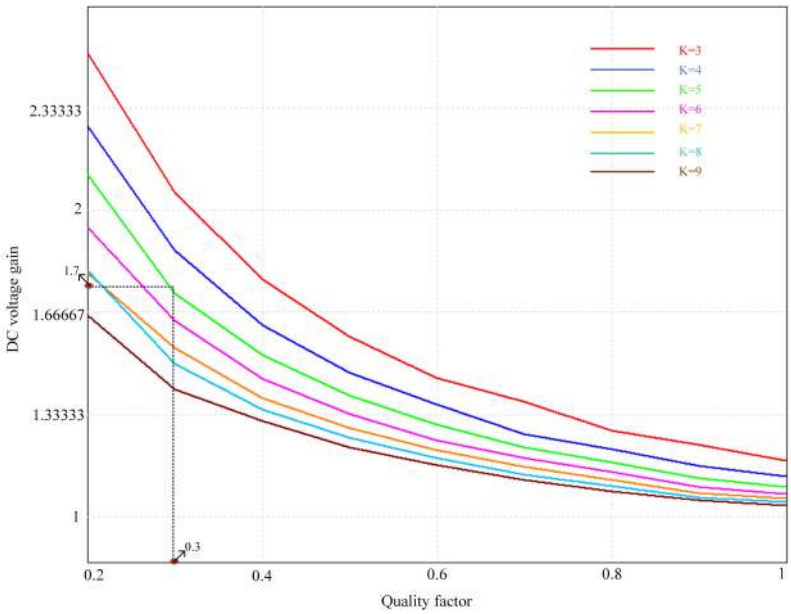

Figure 4. Plots of quality factor and DC voltage gain with different values of K.

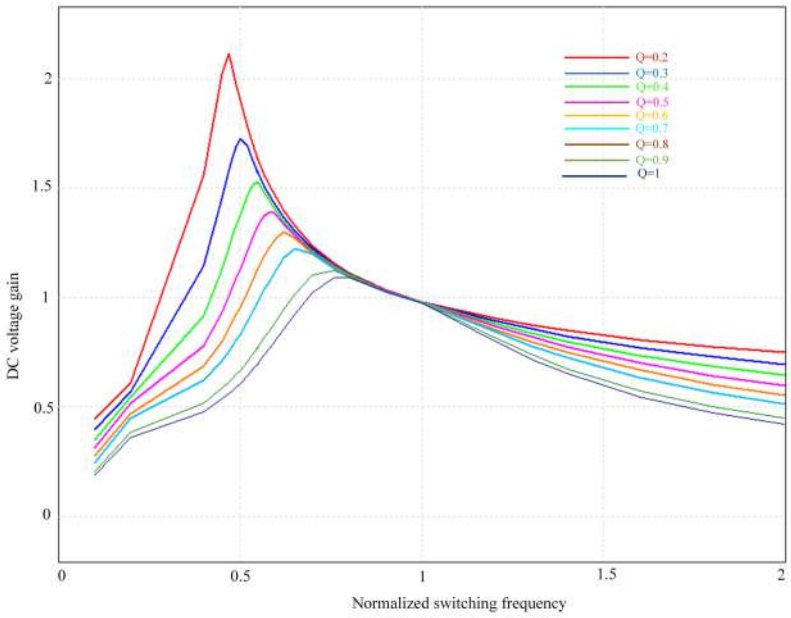

Figure 5. Plots of normalized switching frequency and DC voltage gain with different values of Q.

Table 2. Design candidates.

Q	K	G_{dcmin}-G_{dcmax}	Normalized Frequency	f_{sw} (KHz)	f_r (KHz)	i_{sw_RMS} (A)	i_{sw_peak} (A)	v_{sw_peak} (V)	$i_{d_average}$ (A)	i_{d_peak} (A)	i_{Lm_peak} (A)	i_{Cs_RMS} (A)	v_{Cs_peak} (V)	L_s (µH)	C_s (µF)	L_m (µH)
0.3	3	0.87	1.18	118	100	170.83	499.75	32	62.83	206.80	318.64	341.66	11.80	0.0468	54.134	0.14
0.3	3	1.67	0.85	85	100	254.83	718.98	32	83.96	323.76	541.90	509.66	55.86	0.0468	54.134	0.14
0.3	4	0.87	1.23	123	100	151.110	438.460	32	62.75	198.84	228.96	302.220	9.975	0.0468	54.134	0.187
0.3	4	1.67	0.81	81	100	224.47	653.42	32	83.94	330.063	411.17	448.95	51.03	0.0468	54.134	0.187
0.3	5	0.87	1.27	127	100	141.24	406.28	32	62.71	194.390	177.290	282.49	9.015	0.0468	54.134	0.234
0.3	5	1.66	0.78	78	100	208.490	626.14	32	83.39	336.37	329.79	416.98	22.38	0.0468	54.134	0.234
0.3	6	0.87	1.3	130	100	135.69	387.15	32	62.73	191.74	144.39	271.39	8.46	0.0468	54.134	0.281
0.3	6	1.67	0.74	74	100	204.63	636.74	32	83.94	354.88	276.15	409.27	45.480	0.0468	54.134	0.281
0.3	7	0.87	1.33	133	100	131.89	374.22	32	62.62	189.66	120.75	263.78	8.043	0.0468	54.134	0.328
0.3	7	1.67	0.71	71	100	202.39	648.97	32	83.89	368.91	236.090	404.78	43.63	0.0468	54.134	0.328
0.3	8	0.87	1.35	135	100	129.52	365.46	32	62.64	188.450	104.12	259.049	7.79	0.0468	54.134	0.374
0.3	8	1.66	0.69	69	100	199.90	655.56	32	83.34	376.83	205.27	399.80	42.10	0.0468	54.134	0.374
0.3	9	0.87	1.37	137	100	127.68	358.87	32	62.58	187.42	91.11	255.37	7.57	0.0468	54.134	0.421
0.3	9	1.67	0.66	66	100	202.79	683.98	32	83.62	395.59	181.28	405.58	40.85	0.0468	54.134	0.421
0.3	10	0.87	1.38	138	100	126.58	354.1	32	62.68	186.92	81.53	253.16	7.47	0.0468	54.134	0.468
0.3	10	1.66	0.64	64	100	203.75	701.41	32	83.38	407.05	161.79	407.50	39.77	0.0468	54.134	0.468

Loss Examination of LLC-RC

By turning on the primary power MOSFETs with ZVS and turning off the secondary rectifier diodes with ZCS, the LLC-RC reduces the overall switching loss. The losses for MOSFET are conduction, turn-off, and driving losses. The losses for the diode are conduction losses. Core and copper losses are transformer losses. Table 3 summarizes the different component losses and their associated calculations [29,30].

Table 3. Loss analysis for LLC-RC.

Name of the Device	Loss Calculation
MOSFET	Gate-Driving loss = $4 * \left(\frac{1}{2} * C_{gs} * V_{gs}^2\right) * f_s$
	Turn-off loss = $4 * \frac{f_s * v_i * i_i\left(t_r + t_f\right)}{2}$
	Conduction loss in MOSFET = loss in MOSFET+ loss in antiparallel diode = $4 * i^2_{\text{mos_RMS}} * R_{ds} + 4\left(V_d * i_{\text{anti_avg}} + i^2_{\text{anti_RMS}} * R_{body}\right)$
Transformer	Core loss = $2 * K_h * f_s^m * B_{ac}^n * M_{core}$
	Copper loss = $2 * \left(i^2_{\text{pri_RMS}} * R_{\text{ac_pri}} + i^2_{\text{sec_RMS}} * R_{\text{ac_sec}}\right)$
Diode	Conduction loss of diodes = $4 * \left(\frac{1}{2} * \frac{P_0}{V_0} * V_F + i^2_{\text{diode_RMS}} * R_d\right)$

5. Simulation and Experimental Results

5.1. Simulation Results

Figure 6 shows the simulation results for the LLC-RC at minimum input voltage with the optimum design values. V_{S_1} and i_{S_1} indicate that the voltage across the switch and current through the switch at rated power when the input voltage equals 24 V. i_{sec} is the secondary current flowing through the rectifier diodes. With the optimum designed values, the output voltage V_0 of the converter is regulated at 48 V. It is clearly observed that the converter is functioning in PO mode. The currents i_{Lm} and i_{Ls} share the same starting currents at the beginning of the stage P. After that, they separate in various wave shapes. As L_m is confined to $+V_o/\text{n}$, i_{Lm} expands linearly, whereas i_{Ls} changes sinusoidally, since L_s and C_s are in resonance. Both the secondary rectifier diodes are switched off when i_{Lm} and i_{Ls} intersects at the end of stage P, and then the LLC-RC advances to stage O. In addition to that, i_{S_1} lags behind V_{S_1}, which indicates that the input impedance is inductive and the ZVS operation for primary switches is achieved. Furthermore, i_{sec} drops to zero well before the relevant rectifier turn-off signal arrives, ensuring that the rectifier diodes does not suffer from reverse recovery issues and is able to operate in ZCS mode.

Figure 7 shows the simulation waveforms of the gate driver signal (V_{gs}) and drain-source voltage (V_{ds}) of the switch S_1. The worst situation for the ZVS operation of the converter is when the input voltage hits the minimum value and the output power reaches the maximum value. It is observed that the V_{ds} is completely zero before the V_{gs} is turned on. Therefore, for the whole operating range, ZVS operation is achieved.

5.2. Experimental Results

The proposed model of LLC-RC is verified using HIL simulator OP5700, RT-LAB, programmable control board (PCB-E06-0560), MSOx3014T, and probes. The PCB is used to communicate between both the simulation and real controller using analog outputs and digital inputs. The configuration of the real-time implementation setup is depicted in Figure 8. HIL systems are frequently utilized for real-time simulations of engineering systems before implementing the prototyping tests. Stacks are capable of rapidly creating and synchronizing prototypes. The plant and controller are placed in OPAL-RT to enable the system to operate at real-time clock speeds. This process can be considered as a real-time system simulation due to high-speed nanosecond to microsecond OPAL-RT sampling rate. The user's PC is used to execute the RT-digital LAB's simulator commands. RT-LAB is used to edit, build, load, and execute the prototype. The requirements and specifications of the HIL stack are given in Table 4. The circuit parameters pertaining to various components are shown in Table 5.

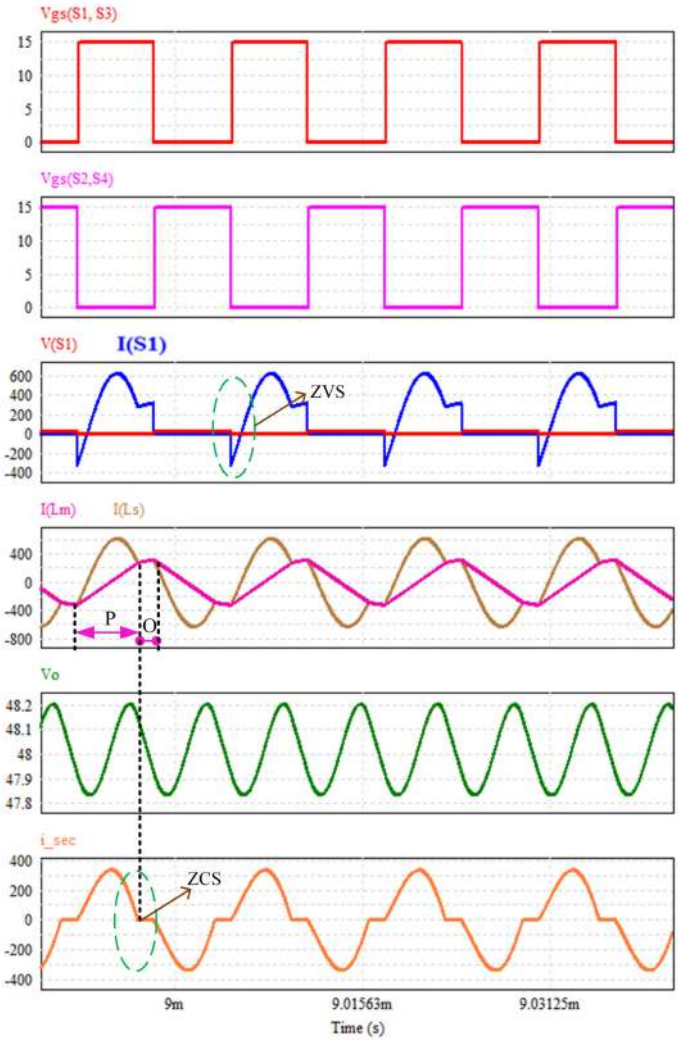

Figure 6. Simulations waveforms at minimum input voltage.

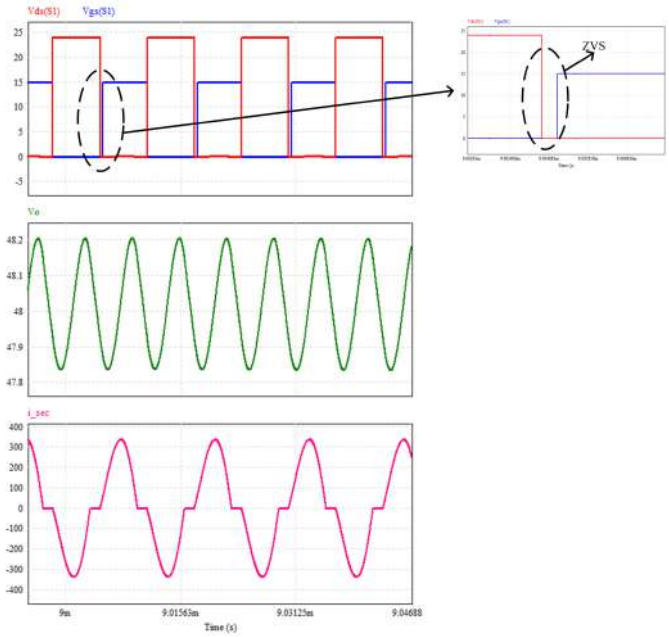

Figure 7. Simulation waveforms of the gate driver signal (V_{gs}) and drain-source voltage (V_{ds}).

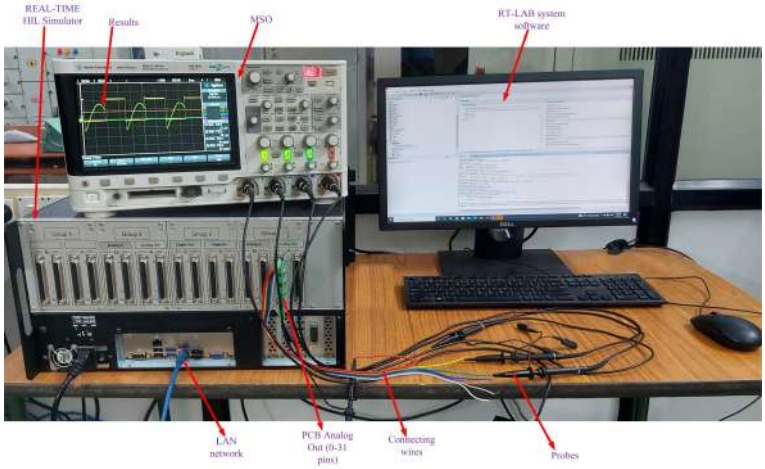

Figure 8. HIL experimental setup for the LLC-RC.

Table 4. Hardware-in-loop (HIL) system specifications.

Name of the Device	OP5700 Simulator
FPGA	Xilinx® Virtex® 7 FPGA on VC707 board Processing speed: 200 ns–20 µs
I/O Lines	256 lines, routed to eight analog or digital, 16 or 32 channels
High-speed communication ports	16SFP sockets, up to 5 GBps
I/O connectors	Four panels of four DB37 connectors
Monitoring connectors	Four panels of RJ45 connectors
PC interface	Standard PC connectors
Power rating	Input: 100–240 VAC, 50–60 Hz, 10/5 A, Power: 600 W

Table 5. Parameters pertaining to various circuit components.

Name of the Component	Parameter
Primary MOSFET (S_1–S_4)	VISHAY SQJQ140E
Rectifier diodes (D_1–D_4)	VISHAY VS-403CNQ100PbF
Turns ratio (n_{sp})	1:1.72
Resonant capacitor (C_s)	54.134 µF
Resonant inductor (L_s)	0.04679 µH
Magnetizing inductor (L_m)	0.23395 µH

Figure 9 shows the implementation method of HIL testing. It consists of an OPAL-RT real-time HIL simulator, ethernet switch, ethernet cable, and desktop computer for the graphical user interface (GUI). The RT-LAB software for OPAL-RT is used in HIL testing. The ethernet cable is connected between the ethernet switch of OPAL-RT and desktop computer for the GUI.

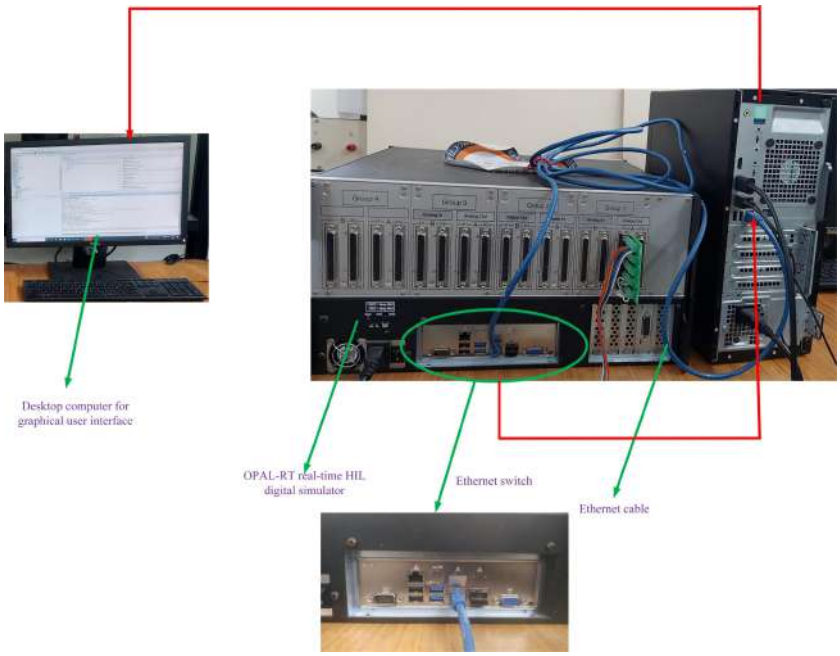

Figure 9. The HIL testing setup.

Figure 10 shows the experimental results of the LLC-RC at the worst operating point; i.e., at minimum input voltage with rated power. From the results, it is observed that the converter is operating in PO mode with a switching frequency of 77 KHz—a small deviation from theoretical 78 KHz because of parasitics of the converter. In addition, i_{S_1} lags behind the V_{S_1} in the entire operating range, which indicates that the input impedance is inductive and the ZVS action for primary switches is realized. The secondary current i_{sec} operates in discontinuous conduction mode; therefore, the secondary rectifier diodes achieve ZCS operation.

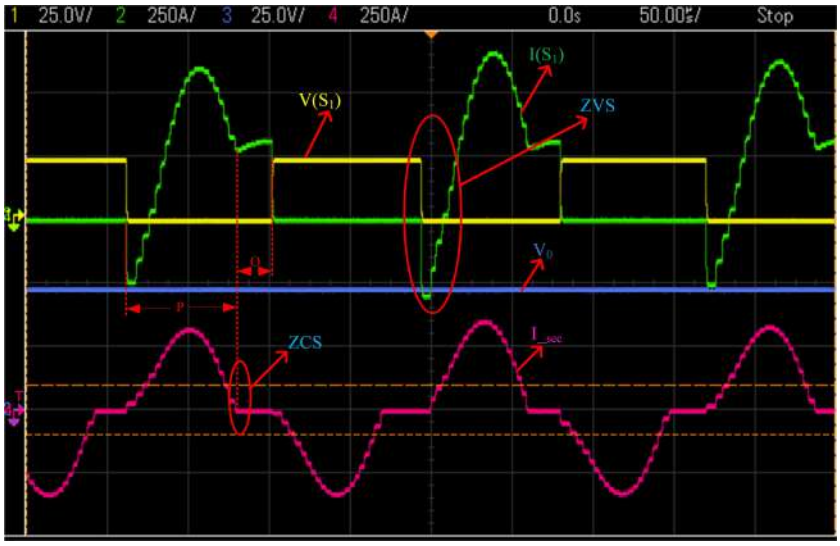

Figure 10. Experimental waveforms of V_{S_1} and I_{S_1}, V_0 and I_{sec} at minimum input voltage with rated power.

To verify the primary switches' ZVS functionality, an experimental waveform of the V_{gs} and V_{ds} of switch S_1 is shown in Figure 11. It is observed that the V_{ds} is completely zero before the V_{gs} is turned on. Therefore, for the whole operating range, ZVS operation is achieved.

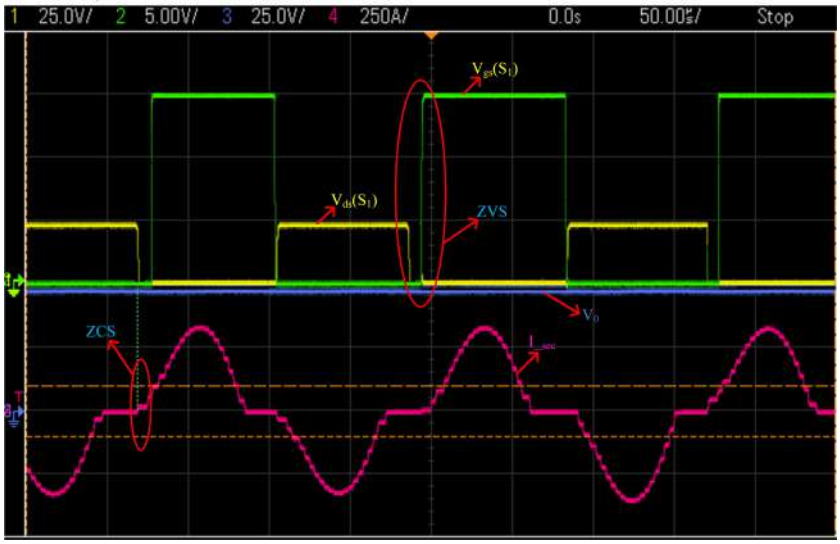

Figure 11. Experimental waveforms of the V_{gs} and V_{ds} showing ZVS operation under the worst condition.

Figure 12 shows the efficiency curve of the LLC-RC at minimum input voltage with various output power levels. At the output power of 5000 W, the measured maximum efficiency is about 93.4%, and at rated power, a measured maximum efficiency of 90.1% is achieved.

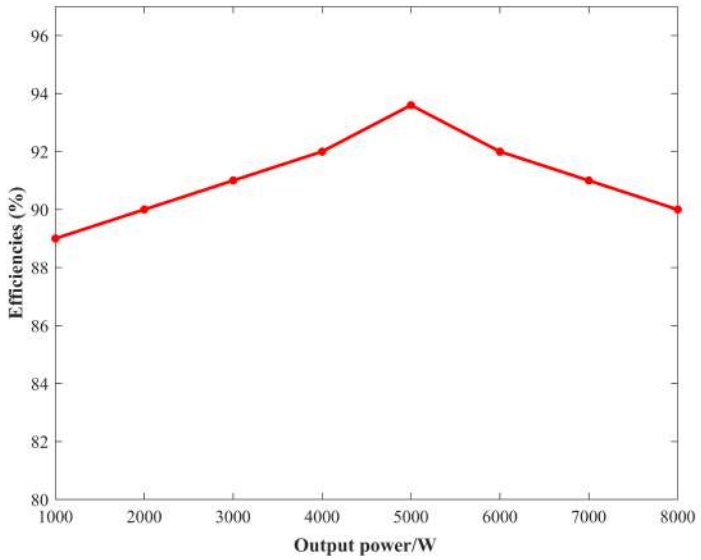

Figure 12. Efficiency of the converter at various output powers.

Table 6 shows the comparison of simulation and experimental values of the designed converter. Due to the internal parasitics of the converter, there is a slight variation from simulation to experiment.

Table 6. Comparison of simulation and experiment parameters.

Design Parameter	Simulation Value	Experimental Value
Q	0.3	0.3
K	5	5
f_{sw} (KHz)	78	77
f_r (KHz)	100	98.61
i_{sw-RMS} (A)	208.49	206.2
$i_{sw-peak}$ (A)	626.14	619.3
$V_{sw-peak}$ (V)	32	24
$i_{d-average}$ (A)	83.39	80.5
i_{d-peak} (A)	336.37	331
$i_{Lm-peak}$ (A)	329.79	325.1
i_{Cs-RMS} (A)	416.98	409.5
$v_{Cs-peak}$ (V)	22.38	22
L_s (µH)	0.0468	0.0468
C_s (µF)	54.134	54.134
L_m (µH)	0.23396	0.23396

6. Conclusions

This article proposed a complete step-by-step precise TDA for LLC-RC working in DCM boost mode with secondary current. The converter operates in PO mode throughout its working range, and for primary MOSFET switches, it guarantees the ZVS and ZCS for the secondary rectifier. The generated closed-form analytical formulas for ZVS angle, voltage gain, and RMS current are applicable at any operating point, below or above the resonant frequency. The worst-case scenario is taken into account while designing the converter, including the converter operating mode, ZVS for primary switches, RMS current of the resonant inductor, and voltage stress for the resonant capacitor. Then, all the potential design candidates are listed in Table 2, with different values of K that provide a narrow frequency variation, low turn-off current, and lower circulating currents. Measured maximum efficiencies of 93.4% and 90.1% are achieved at the output power of 5000 W and at the rated output power, respectively. Table 6 shows the comparison of simulation and experimental values of the designed converter. Finally, both the simulation and experimental results were provided in order to validate the theoretical analysis.

Author Contributions: Conceptualization, K.K.G. and E.D.; Data curation, K.K.G.; Formal analysis, K.K.G.; Investigation, K.K.G. and E.D.; Methodology, K.K.G. and E.D.; Software, K.K.G. and E.D.; Supervision, E.D.; Validation, E.D.; Visualization, E.D.; Writing—original draft, K.K.G. and E.D.; Writing—review & editing, E.D. All authors have read and agreed to the published version of the manuscript.

Funding: This research received no external funding.

Institutional Review Board Statement: Not applicable.

Informed Consent Statement: Not applicable.

Data Availability Statement: Not applicable.

Conflicts of Interest: The authors declare no conflict of interest.The funders had no role in the design of the study; in the collection, analyses, or interpretation of data; in the writing of the manuscript, or in the decision to publish the results.

References

1. Zhou, Q.; Liu, Y.; Li, Z.; He, Z. A Coupled-Inductor Interleaved LLC Resonant Converter for Wide Operation Range. *Energies* **2022**, *15*, 315. [CrossRef]
2. Manuel, D.; Kutschak, M.; Pulsinelli, F.; Rodriguez, N.; Morales, D.P. On the Practical Evaluation of the Switching Loss in the Secondary Side Rectifiers of LLC Converters. *Energies* **2021**, *14*, 5915.
3. Tran, Y.K.; Freijedo, F.D.; Dujic, D. Open-loop power sharing characteristic of a three-port resonant LLC converter. *CPSS Trans. Power Electron. Appl.* **2019**, *4*, 171–179. [CrossRef]
4. Wei, Y.; Altin, N.; Luo, Q.; Nasiri, A. A high efficiency, decoupled on-board battery charger with magnetic control. In Proceedings of the 2018 7th International Conference on Renewable Energy Research and Applications (ICRERA), Paris, France, 14–17 October 2018; pp. 920–925.

5. Wei, Y.; Luo, Q.; Alonso, J.M.; Mantooth, A. A magnetically controlled single-stage AC–DC converter. *IEEE Trans. Power Electron.* **2020**, *35*, 8872–8877. [CrossRef]
6. Yang, B.; Chen, R.; Lee, F.C. Integrated magnetic for LLC resonant converter. In Proceedings of the APEC. Seventeenth Annual IEEE Applied Power Electronics Conference and Exposition (Cat. No. 02CH37335), Dallas, TX, USA, 10–14 March 2002; pp. 346–351.
7. Wei, Y.; Wang, Z.; Luo, Q.; Mantooth, H.A. MATLAB GUI Based Steady State Open-Loop and Closed-Loop Simulation Tools for Different LLC Converters With all Operation Modes. *IEEE Open J. Ind. Appl.* **2021**, *2*, 320–336. [CrossRef]
8. Fang, X.; Hu, H.; Shen, Z.J.; Batarseh, I. Operation mode analysis and peak gain approximation of the LLC resonant converter. *IEEE Trans. Power Electron.* **2011**, *27*, 1985–1995. [CrossRef]
9. Ivensky, G.; Bronshtein, S.; Abramovitz, A. Approximate analysis of resonant LLC DC-DC converter. *IEEE Trans. Power Electron.* **2011**, *26*, 3274–3284. [CrossRef]
10. Liu, J.; Zhang, J.; Zheng, T.Q.; Yang, J. A modified gain model and the corresponding design method for an LLC resonant converter. *IEEE Trans. Power Electron.* **2016**, *32*, 6716–6727. [CrossRef]
11. Deng, J.; Li, S.; Hu, S.; Mi, C.C.; Ma, R. Design methodology of LLC resonant converters for electric vehicle battery chargers. *IEEE Trans. Veh. Technol.* **2013**, *63*, 1581–1592. [CrossRef]
12. Deng, J.; Mi, C.C.; Ma, R.; Li, S. Design of LLC resonant converters based on operation-mode analysis for level two PHEV battery chargers. *IEEE/ASME Trans. Mechatron.* **2014**, *20*, 1595–1606. [CrossRef]
13. Hu, Z.; Wang, L.; Qiu, Y.; Liu, Y.F.; Sen, P.C. An accurate design algorithm for LLC resonant converters—Part I. *IEEE Trans. Power Electron.* **2015**, *31*, 5435–5447. [CrossRef]
14. Hu, Z.; Wang, L.; Qiu, Y.; Liu, Y.F.; Sen, P.C. An accurate design algorithm for LLC resonant converters—Part II. *IEEE Trans. Power Electron.* **2015**, *31*, 5448–5460. [CrossRef]
15. Yu, R.; Ho, G.K.Y.; Pong, B.M.H.; Ling, B.W.K.; Lam, J. Computer-aided design and optimization of high-efficiency LLC series resonant converter. *IEEE Trans. Power Electron.* **2011**, *27*, 3243–3256. [CrossRef]
16. Xu, H.; Yin, Z.; Zhao, Y.; Huang, Y. Accurate design of high-efficiency LLC resonant converter with wide output voltage. *IEEE Acess* **2017**, *5*, 26653–26665. [CrossRef]
17. Bhat, A.S. Analysis and design of LCL-type series resonant converter. *IEEE Trans. Ind. Electron.* **1994**, *41*, 118–124. [CrossRef]
18. Steigerwald, R.L. A comparison of half-bridge resonant converter topologies. *IEEE Trans. Power Electron.* **1988**, *3*, 174–182. [CrossRef]
19. Bhat, A.S. A generalized steady-state analysis of resonant converters using two-port model and Fourier-series approach. *IEEE Trans. Power Electron.* **1998**, *13*, 142–151. [CrossRef]
20. Forsyth, A.J.; Ward, G.A.; Mollov, S.V. Extended fundamental frequency analysis of the LCC resonant converter. *IEEE Trans. Power Electron.* **2003**, *18*, 1286–1292. [CrossRef]
21. Lee, B.H.; Kim, M.Y.; Kim, C.E.; Park, K.B.; Moon, G.W. Analysis of LLC resonant converter considering effects of parasitic components. In Proceedings of the INTELEC 2009-31st International Telecommunications Energy Conference, Incheon, Korea, 18–22 October 2009; pp. 1–6.
22. Lin, R.L.; Lin, C.W. Design criteria for resonant tank of LLC DC-DC resonant converter. In Proceedings of the IECON 2010-36th Annual Conference on IEEE Industrial Electronics Society Conference, Glendale, CA, USA, 7–10 November 2010; pp. 427–432.
23. Jung, J.H.; Kwon, J.G. Theoretical analysis and optimal design of LLC resonant converter. In Proceedings of the 2007 European Conference on Power Electronics and Applications, Aalborg, Denmark, 2–5 September 2007; pp. 1–10.
24. Batarseh, I.; Liu, R.; Ortiz-Conde, A.; Yacoub, A.; Siri, K. Steady state analysis and performance characteristics of the LLC-type parallel resonant converter. In Proceedings of the 1994 Power Electronics Specialist Conference-PESC'94, Taipei, Taiwan, 20–25 June 1994; pp. 597–606.
25. Vukšić, M.; Beroxsx, S.M.; Mihoković, L. The multiresonant converter steady-state analysis based on dominant resonant process. *IEEE Trans. Power Electron.* **2010**, *26*, 1452–1468. [CrossRef]
26. Lazar, J.F.; Martinelli, R. Steady-state analysis of the LLC series resonant converter. In Proceedings of the APEC 2001 Sixteenth Annual IEEE Applied Power Electronics Conference and Exposition (Cat. No. 01CH37181), Anaheim, CA, USA, 4–8 March 2001; pp. 728–735.
27. Oeder, C.; Bucher, A.; Stahl, J.; Duerbaum, T. A comparison of different design methods for the multiresonant LLC converter with capacitive output filter. In Proceedings of the 2010 IEEE 12th Workshop on Control and Modeling for Power Electronics (COMPEL), Boulder, CO, USA, 28–30 June 2010; pp. 1–7.
28. Costa, V.S.; Perdigao, M.S.; Mendes, A.S.; Alonso, J.M. Evaluation of a variable-inductor-controlled LLC resonant converter for battery charging applications. In Proceedings of the IECON 2016-42nd Annual Conference of the IEEE Industrial Electronics Society, Piazza Adua, Firenze, Italy, 24–27 October 2016; pp. 5633–5638.
29. Fang, Z.; Cai, T.; Duan, S.; Chen, C. Optimal design methodology for LLC resonant converter in battery charging applications based on time-weighted average efficiency. *IEEE Trans. Power Electron.* **2014**, *30*, 5469–5483. [CrossRef]
30. Yang, C.H.; Liang, T.J.; Chen, K.H.; Li, J.S.; Lee, J.S. Loss analysis of half-bridge LLC resonant converter. In Proceedings of the 2013 1st International Future Energy Electronics Conference (IFEEC), Tainan, Taiwan, 3–6 November 2013; pp. 155–160.

energies

MDPI

Article

Steady State Modeling and Performance Analysis of a Wind Turbine-Based Doubly Fed Induction Generator System with Rotor Control

Belqasem Aljafari [1], Jasmin Pamela Stephenraj [2], Indragandhi Vairavasundaram [2,*] and Raja Singh Rassiah [3]

[1] Department of Electrical Engineering, College of Engineering, Najran University, Najran 11001, Saudi Arabia; bhaljafari@nu.edu.sa
[2] School of Electrical Engineering, Vellore Institute of Technology, Vellore 632014, India; jasmin.pamela2020@vitstudent.ac.in
[3] Department of Energy and Power Electronics, Vellore Institute of Technology, Vellore 632014, India; rrajasingh@vit.ac.in
* Correspondence: indragandhi.v@vit.ac.in

Abstract: The utilization of renewable energy sources aids in the economic development of a country. Among the various renewable energy sources, wind energy is more effective for electricity production. The doubly fed induction generator is an extensively known wind turbine generator for its partially rated power converters and dynamic performance. The doubly fed induction generator assists the wind turbine to function with a wide speed range. Hence, the steady-state performance analysis of a doubly fed induction generator helps enable it to operate efficiently at a specific wind turbine speed. In this paper, a 2 MW variable speed pitch regulated doubly fed induction generator with a speed range of 900–2000 rpm was opted for steady-state analysis. This was followed by the design and modelling of a doubly fed induction generator in Matlab/Simulink environment, and the analyses were performed using mathematical equations computed via Matlab coding. The steady-state magnitudes were calculated with rotor magnetization $i_{dr} = 0$. The closed-loop stator flux-oriented vector control is applied to the rotor side converter for controlling the designed doubly fed induction generator model. The simulation results were compared with computational values to establish a workable model with less than 10% error. The simulation model can be used for predicting the performance of the machine, fault analysis, and validation of existing DFIG at a steady state.

Keywords: doubly fed induction generator; wind turbine; renewable energy; rotor control; steady state model

Citation: Aljafari, B.; Pamela Stephenraj, J.; Vairavasundaram, I.; Singh Rassiah, R. Steady State Modeling and Performance Analysis of a Wind Turbine-Based Doubly Fed Induction Generator System with Rotor Control. *Energies* **2022**, *15*, 3327. https://doi.org/10.3390/en15093327

Academic Editor: Davide Astolfi

Received: 31 March 2022
Accepted: 30 April 2022
Published: 3 May 2022

Publisher's Note: MDPI stays neutral with regard to jurisdictional claims in published maps and institutional affiliations.

Copyright: © 2022 by the authors. Licensee MDPI, Basel, Switzerland. This article is an open access article distributed under the terms and conditions of the Creative Commons Attribution (CC BY) license (https://creativecommons.org/licenses/by/4.0/).

1. Introduction

Energy plays a vital role in the day-to-day existence of human life. A major part of energy generation comes from burning fossil fuels, such as coal and natural gas. With increasing concern over the emission of greenhouse gases and the reducing capacities of non-renewable resources, increased attention is being paid to the consumption of renewable energy sources. Renewable energy sources have a positive impact on the improvement in the economy of a country. Amid the different types of renewable energies, wind power has been extensively used for its low impact on the environment, reduced cost, and other benefits [1–3]. In general, the wind system tends to have fixed speed or variable speed wind turbine (WT) generators. The variable speed WT is the most popular among them for extracting the maximum energy from the wind [4]. Customary variable speed WT generators do not allow frequency regulation resulting in changes in grid frequency, and this highlights the necessity for frequency regulation technologies in WTs [4–6].

The doubly fed induction generator (DFIG) stands out to be one of the most sought-after systems as WT generators. In DFIG, the stator windings are directly coupled to the grid, while the rotor windings are connected through slip-rings and back-to-back

voltage source converters [7]. The converter at the grid side is termed grid side converter (GSC) and at the rotor side as rotor side converter (RSC). These are coupled by DC-link, which assists to retain the voltage deviations within an acceptable range. Such a structure offers several advantages such as fixed frequency power generation under variable wind speeds, decoupled control of active and reactive power, and different operating modes. In addition, the DFIG has the choice of small converter ratings, and consequently fewer losses with better efficiency and reduced cost. At present, the DFIG structure contributes to approximately 50% of the wind power market [8]. The RSC control embraced robust stator flux-oriented vector control (FoC) as it is the most comprehensive and proven one. The purpose of the vector control is to make the AC machine behave like a DC machine, which includes carrying out a decoupling between the flux and torque components. In DFIG, the FoC allows to decouple the active and reactive powers effectively, and hence it is employed for analyzing the DFIG under a steady state (SS). Similarly, the main function of GSC control is to keep the DC-link voltage almost constant and to provide reactive power when required as per the grid codes. The control technique adopted for it is the grid voltage-oriented vector control. It also maintains the output frequency fixed on the other hand the output voltage will be adjusted in order to facilitate the active and reactive power exchange.

1.1. Literature on DFIG Steady-State Analysis (SSA)

Many attempts have been made to carry out the SSA of DFIG due to its ever-increasing popularity. However, a comprehensive SSA along with a computer simulation model and performance analysis would provide a detailed understanding of the DFIG wind turbine's operational characteristics. With this viewpoint, the present work was carried out and the relevant literature is presented. In 2018, a SS mathematical model of DFIG was derived using the spatial vector technique under different operation zones of the wind turbine [9]. This method allows determining the operating points of any wind turbine by knowing the data and parameters of the wind turbine. In the same year, the stator flux-oriented vector control of DFIG-based wind turbines using space vector pulse width modulation was carried out and their performances were studied in [10] and found to be more effective. Later, in 2019, a computer simulation of DFIG and a vector control implementation for GSC and RSC were carried out to provide active power to the grid [11]. Subsequently, the stator field-oriented control (SFOC) of DFIM was discussed in [12], which is based on the sliding mode flux observer algorithm and the strategy is found to be effective under parameter variations. In 2020, the SSA of DFIG is presented with different magnetizing strategies for specific operating wind turbine modes [13]. This work discusses the mathematical modelling of DFIG in SS using stator flux-oriented vector control which is found too effective. In 2021, simplified SS modelling of DFIG with its operational features in a stand-alone wind energy conversion system with rotor control is discussed in [14]. Later, an SS solution to synchronous DFIG (sDFIG) orientated by references of the rotor flux for RSC and stator voltage for GSC is suggested. The analysis is summarized, and it is concluded that the sDFIG performs well when wind speed is lower than its critical value [15]. Another recent article on DFIM rotor flux orientation vector control with machine modelling for a wide speed range application is discussed in [16]. In 2022, the computation of SS values of DFIG using an accurate method for calculation is proposed in [17]. The simulation time domain results summarize that the SS values are matching with initialization values. As stated above, a comprehensive work of SS performance analysis with a working computer simulation model could be a promising work.

1.2. Significance of the Paper

The SSA of DFIG can be implemented in a global optimization environment to design the DFIG converters associated with the wind turbine. The analytical technique is a useful tool for minimizing the non-linear optimization process, which may be time-consuming and inefficient for handling digital issues. A single solution for the rotor control variables V_r and

ψ exists for each SS operating point. This helps to derive the SS characteristics from a given torque-speed array emulating a three-blade wind turbine. Proper SS conditions prevent the system from numerical instability. A computer simulation study of the DFIG generation system makes it possible to create an adequate model description. The design purpose is an interpretation of the physical nature of work processes as well as the developer systems' competency needs. The developed computer simulation shall be used to investigate the DFIG in a wide speed range of 900 to 1800 rpm. The SSA under certain operating modes provides information about the syst-em's behavior including stator and rotor active power, power losses, current variations, and voltage variations. The overall paper structure is as follows: initially, a literature review on the present work is briefly presented with the paper's significance in Section 1. Section 2 describes the SS mathematical modelling, MATLAB simulation and the control of a doubly fed induction generator is presented. In Section 3, the steps for implementing and analyzing the DFIG's SS performance are presented along with the results. In Section 4, the validation of the system design with SS plots is carried out with relevant results and a comparative analysis is presented. Finally, the findings are concluded in Section 5.

2. Modelling, Simulation, and Control of DFIG

In the wind power sector, the DFIG based wind turbine with a variable speed variable-pitch control scheme is the most prevalent wind power generator. This machine may be used as a grid-connected or stand-alone unit. To optimally extract the power from the wind and precisely predict its performance, a complete insight of the modelling, control, and SSA of this machine in both operation modes is required. In this paper, the author design and examine three-phase PWM voltage source converter models defined in the ABC and DQO synchronous reference frames, as well as their control strategies. Furthermore, utilizing Matlab/Simulink software, a DFIG-based wind turbine model coupled to a constant voltage and frequency grid is designed, as well as its associated generator control framework. This control mechanism, as well as the SS behavior of the wind plant, are clearly outlined. Figure 1 shows the DFIG models as well as the three-phase two-level PWM voltage source converter models. The control schemes are also necessary to achieve optimum output power from the wind turbine. The RSC control and the GSC control are two of these control techniques. The GSC controller is used to keep the voltage across the capacitor constant and ensure that the grid operates at a unity power factor. The torque, active power, and reactive power are all controlled by the rotor-side converter controller. As the most complete and established RSC control, it is coupled with powerful stator flux-oriented vector control. The vector control's goal is to make the AC machine act like an independently stimulated DC machine, which involves decoupling the flux and torque components.

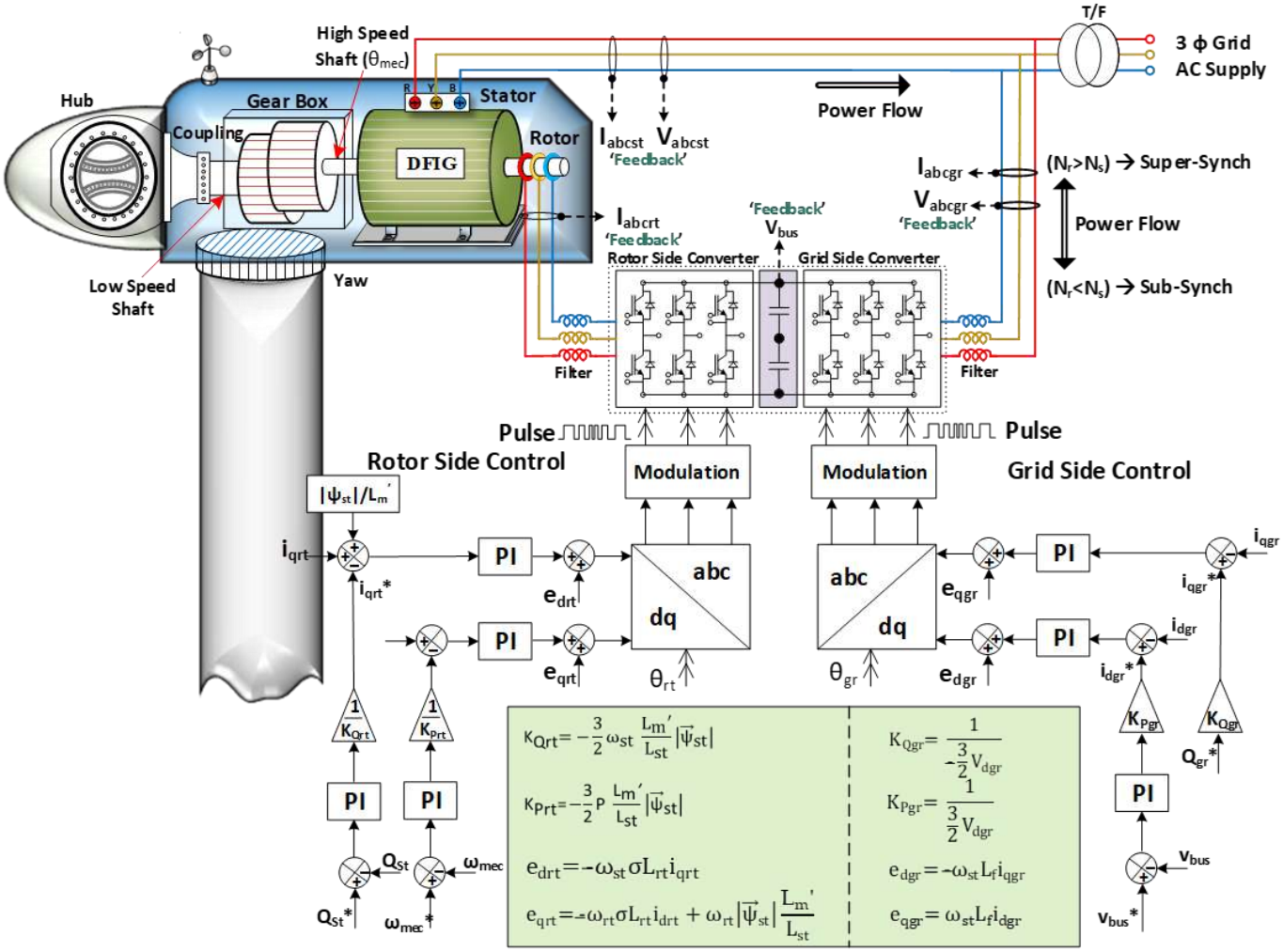

Figure 1. Configuration of DFIG wind turbine with RSC and GSC control.

2.1. SS Model of DFIG

The model comprises a DFIG specifically a wound rotor induction generator which has a power converter connected to the sliprings of the rotor. The stator is directly coupled to the grid. The various parameters of the machine are defined in Table A1. For deriving the SS magnitudes of DFIG by magnetizing the machine through a rotor with i_{dr} = 0, the step-by-step procedure is as follows [13]. By assuming SS and the alignment of the stator flux with the d-axis, it is possible to obtain the following sets of the equation:

$$i_{dst} = \frac{\left|\vec{\psi}_{st}\right|}{L_{st}} \tag{1}$$

$$i_{qst} = -\frac{L_m\prime}{L_{st}}\, i_{qrt} \tag{2}$$

$$v_{dst} = R_{st}\, i_{dst} \tag{3}$$

$$v_{qst} = R_{st} i_{qst} + \omega_{st}\left|\vec{\psi}_{st}\right| \tag{4}$$

$$\left|\vec{v}_{st}\right|^2 = v^2_{dst} + v^2_{qst} \tag{5}$$

$$T_{em1} = -\frac{3}{2} p\, \frac{L_m\prime}{L_{st}}\left|\vec{\psi}_{st}\right| i_{qrt} \tag{6}$$

First, it is necessary to calculate the stator flux amplitude of the machine. From these six sets of equations, it is easy to compute the stator flux using Equations (7)–(10). For the calculation of stator flux, we only need the parameters of the machine, stator voltages, stator currents, and torque.

$$\left|\vec{\psi}_{st}\right| = \sqrt{\frac{-B\prime \pm \sqrt{B\prime^2 - 4A\prime C\prime}}{2A'}} \tag{7}$$

$$A\prime = \left(\frac{R_{st}}{L_{st}}\right)^2 + \omega_{st}^2 \tag{8}$$

$$B\prime = \frac{4}{3}\,\frac{R_{st} T_{em1} \omega_{st}}{p} - |v_{st}|^2 \tag{9}$$

$$C\prime = \left(\frac{2}{3}\frac{R_{st} T_{em1}}{p L_m\prime}\right)^2 \tag{10}$$

Once the flux is obtained, the remaining SS magnitudes can be calculated using the below equations in a step-by-step manner. The rotor current is derived using the following three equations.

$$i_{drt} = 0 \tag{11}$$

$$i_{qrt} = \frac{T_{em1}}{-\frac{3}{2} p \frac{L_m\prime}{L_{st}} \left|\vec{\psi}_{st}\right|} \tag{12}$$

$$\left|\vec{i}_{rt}\right|^2 = i_{drt}^2 + i_{qrt}^2 \tag{13}$$

The magnitude of the stator currents,

$$\left|\vec{i}_{st}\right|^2 = i_{dst}^2 + i_{qst}^2 \tag{14}$$

The rotor speed and slip using the following two equations

$$\omega_{rt} = \omega_{st} - \omega_{mec} \tag{15}$$

$$s = \frac{\omega_{rt}}{\omega_{st}} \tag{16}$$

The rotor voltages from the following three equations.

$$v_{drt} = R_{rt} i_{drt} - \omega_{rt} \sigma L_{rt} i_{qrt} \tag{17}$$

$$v_{qrt} = R_{rt} i_{qrt} + \omega_{rt} \sigma L_{rt} i_{qr} + \omega_{rt} \frac{L_m\prime}{L_{st}} \left|\vec{\psi}_{st}\right| \tag{18}$$

$$\left|\vec{v}_{rt}\right|^2 = v_{drt}^2 + v_{qrt}^2 \tag{19}$$

The rotor fluxes using,

$$\psi_{drt} = L_m\prime i_{dst} + L_{rt} i_{drt} \tag{20}$$

$$\psi_{qrt} = L_m\prime i_{qst} + L_{rt} i_{qrt} \tag{21}$$

$$\left|\vec{\psi}_{rt}\right|^2 = \psi_{drt}^2 + \psi_{qrt}^2 \tag{22}$$

The active powers of the machine, stator, and rotor by

$$P_{mec} = T_{em1}\frac{\omega_{mec}}{p} \tag{23}$$

$$P_{st} = \frac{3}{2}(v_{dst}i_{dst} + v_{qst}i_{dst}) \tag{24}$$

$$P_{rt} = \frac{3}{2}(v_{drt}i_{drt} + v_{qrt}i_{drt}) \tag{25}$$

The reactive powers of the stator and rotor

$$Q_{st} = \frac{3}{2}(v_{qst}i_{dst} + v_{dst}i_{qst}) \tag{26}$$

$$Q_{rt} = \frac{3}{2}(v_{qrt}i_{drt} + v_{drt}i_{qrt}) \tag{27}$$

The efficiency for motoring mode using Equation (28) and generator mode using Equation (29).

$$\eta_{DFIM} = \frac{P_{mec}}{P_{st} + P_{rt}} \Big| If,\ P_{mec} > 0 \tag{28}$$

$$\eta_{DFIM} = \frac{P_{st} + P_{rt}}{P_{mec}} \Big| If,\ P_{mec} < 0 \tag{29}$$

where, i_{dst}, i_{qst}, v_{dst}, v_{qst}, i_{drt}, i_{qrt}, v_{drt}, v_{qrt}, Ψ_{drt}, and Ψ_{qrt} are the current, voltages, and flux alignment in the d-axis and q-axis. $\left|\vec{\psi}_{st}\right|$, $\left|\vec{\psi}_{rt}\right|$, $\left|\vec{v}_{st}\right|$, $\left|\vec{v}_{rt}\right|$, $\left|\vec{i}_{st}\right|$, and $\left|\vec{i}_{rt}\right|$ are the magnitudes of flux, current, and voltage. T_{em1}, ω_{st}, ω_{rt}, ω_{mec}, s, P_{mec}, P_{st}, P_{rt}, Q_{st}, and Q_{rt} is the torque, speed, slip, active, and reactive powers of the machine. η_{DFIM} is the efficiency of the machine. $L_m\prime$, L_{st}, L_{rt}, R_{st}, and R_{rt} are the self, mutual inductances, resistances of the stator, and rotor windings. The subscript notation st and rt is used to indicate the stator and rotor.

2.2. Simulation of DFIG

The overall simulation model of the electrical system, which comprises the DFIG, is shown in Figure 2. An asynchronous machine was used to represent the DFIG model with its rotor parameters referred to as the stator side. The stator was connected to a three-phase programmable voltage source. The rotor was connected to a power electronic converter RSC implemented by a universal bridge with three arms and ideal switches. We used a two-level PWM generator to control the RSC. The control signal for the PWM generator (V_{abc_ref}) came from the RSC control block. Instead of a GSC, a DC voltage source was used to simplify the system. Zero-order hold was used at the input for the control block for I_r, V_s, θ, and ω_m to make the system work as close to reality as possible. All the elements presented a constant sample time $1/f_{sw}$. The DC voltage source had the same value as bus voltage. In the RSC control block, a field-oriented control for current loops was considered for controlling the RSC. It is discussed in the next subsection.

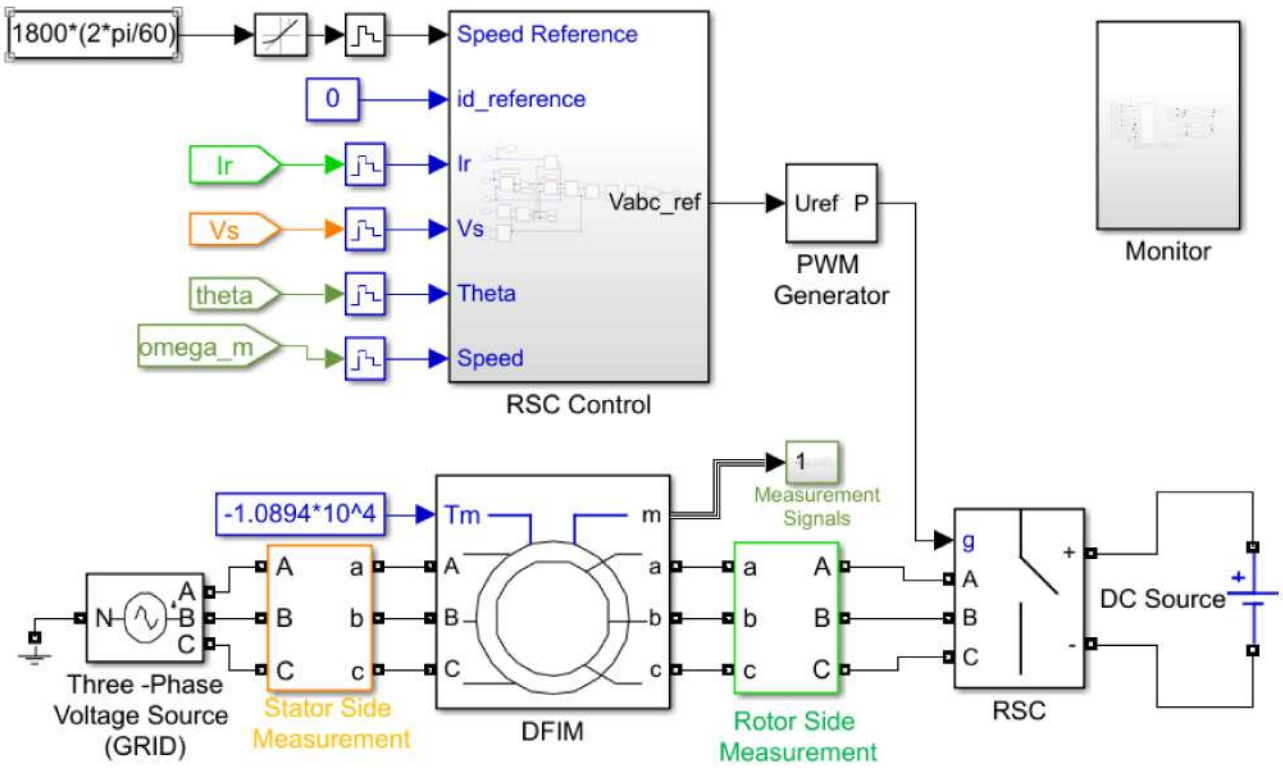

Figure 2. Simulation model of a 2 MW DFIG with RSC Control.

2.3. Implementation of RSC Control

The control block implemented the DFIG vector control in the synchronous reference frame as shown in Figure 3. The id reference and speed reference were initially set to zero. I_r and vs. were obtained from the three-phase measurements block and ω_m were obtained from the measurement signals output of the DFIG model.

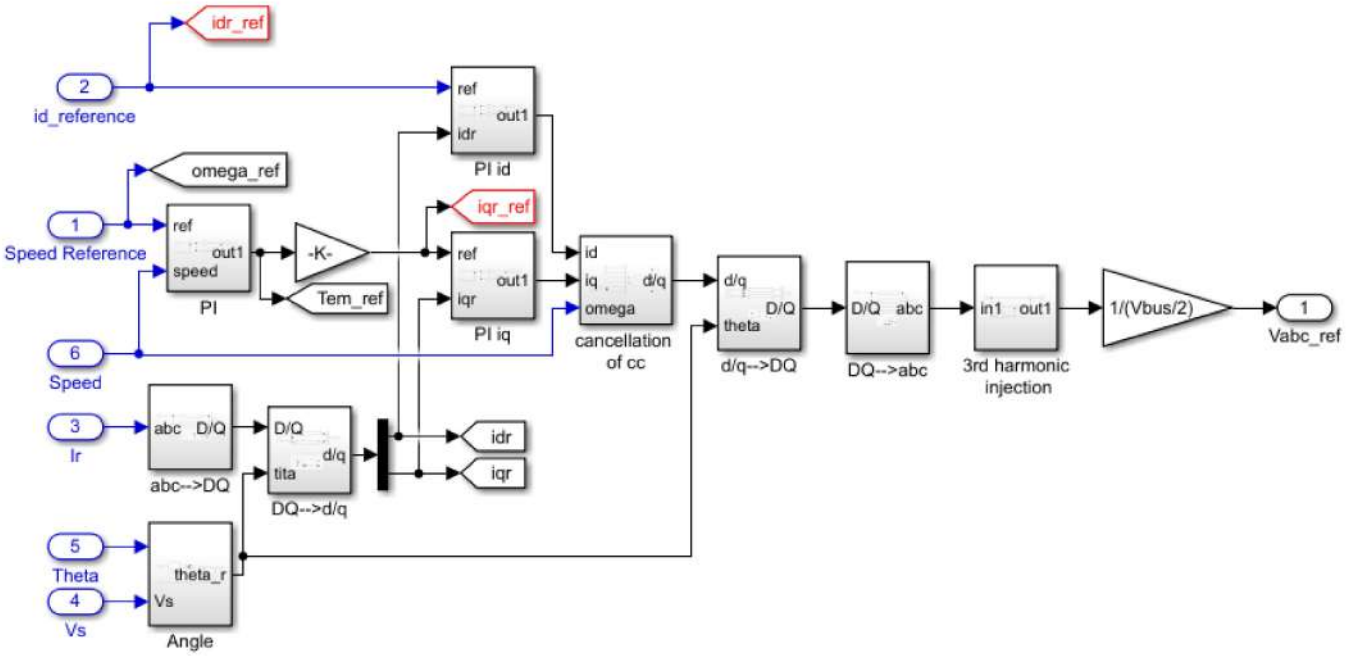

Figure 3. Stator flux-oriented Vector Control of RSC of DFIG.

The two inner current control loops use the transformation blocks dq to DQ, DQ to abc, abc to DQ, and DQ to dq. The PWM generator used a normalized triangular wave (−1 to 1), so the control block output was also normalized using the gain block with value $1/(V_{bus}/2)$. A third harmonic injection at the control output was used to extract more voltage for a given dc–dc bus voltage. It allowed the output voltage to be improved by 15%. The transformation angle θ_r was obtained from the stator voltages angle thetas and rotor angle θ_m. It was given as inputs to the transformation blocks. In the outer loop, a speed PI regulator was implemented to control the speed of the machine. The upper and lower limits were defined by T_{em}. In the inner loop, two PI regulators were required to control the id and i_q currents according to the reference values. The k_p and k_i values were found using the transfer function of the designed system. The upper and lower limits were defined by V_{bus}/sqrt (3). The cross-coupling terms were cancelled using the cancellation of cc block. The i_{dr} and i_{qr} were obtained from the output of transformation blocks of the rotor current Ir. The output of the speed PI regulator was multiplied by the gain to give the i_{qr_ref}. Thus, the stator flux-oriented vector control was implemented.

3. SS Performance Analysis of DFIG

The DFIG's working characteristics are influenced by both the applied stator voltage and the injected rotor voltage. The direct and quadratic components of the injected rotor voltage are defined as proportional to the stator voltage for simulation purposes and are varied to observe the effect of changes in the active and reactive powers, copper losses, electromagnetic torque, power factor, and fluxes characteristics. In this article, the different operational points are used to depict DFIG's behavior. For analyzing the performance of DFIG under SS operating conditions, the following steps are involved in the programming:

Step 1: Start executing the program.
Step 2: Initialize the DFIM parameters (Table A1) and read the torque-speed array for emulating a 3-blade wind turbine.
Step 3: Check for condition, if the slip is equal to the maximum slip.
Step 4: If true, go to step 10; Otherwise, go to step 5.
Step 5: Calculate the stator and rotor parameters along with the mechanical parameters under each operating point extracted from the torque-speed array.
Step 6: Determine the operating mode with mechanical torque value; go to step 7, if torque is positive; go to step 8, if torque is negative.
Step 7: Calculate the efficiency for doubly fed induction motor; then go to step 3.
Step 8: Calculate the efficiency for doubly fed induction generator; then go to step 3.
Step 9: Plot the results; stator and rotor current (I_s and I_r), stator and rotor power (P_r and P_s | Q_s and Q_r), electromagnetic torque (T_{em}) and speed (n), and efficiency.
Step 10: Program executed.

The SSA is mainly about the representative magnitudes of the DFIG model. The torque-speed data array as an input that emulates a 3-blade WT obtained from a 2 MW "Mitsubishi-MWT 92" wind turbine datasheet. The obtained parameters are provided in Table A1. During the execution, the SS magnitudes from a minimum speed of 900 rpm to a maximum speed of 1800 rpm are calculated. Further, through the MATLAB program, the parameters are calculated for different rotor speeds and plotted as per the Equations (1)–(29). Figure 4 shows the rotor generation strategy, that makes the d-axis rotor current zero (I_{dr} = 0).

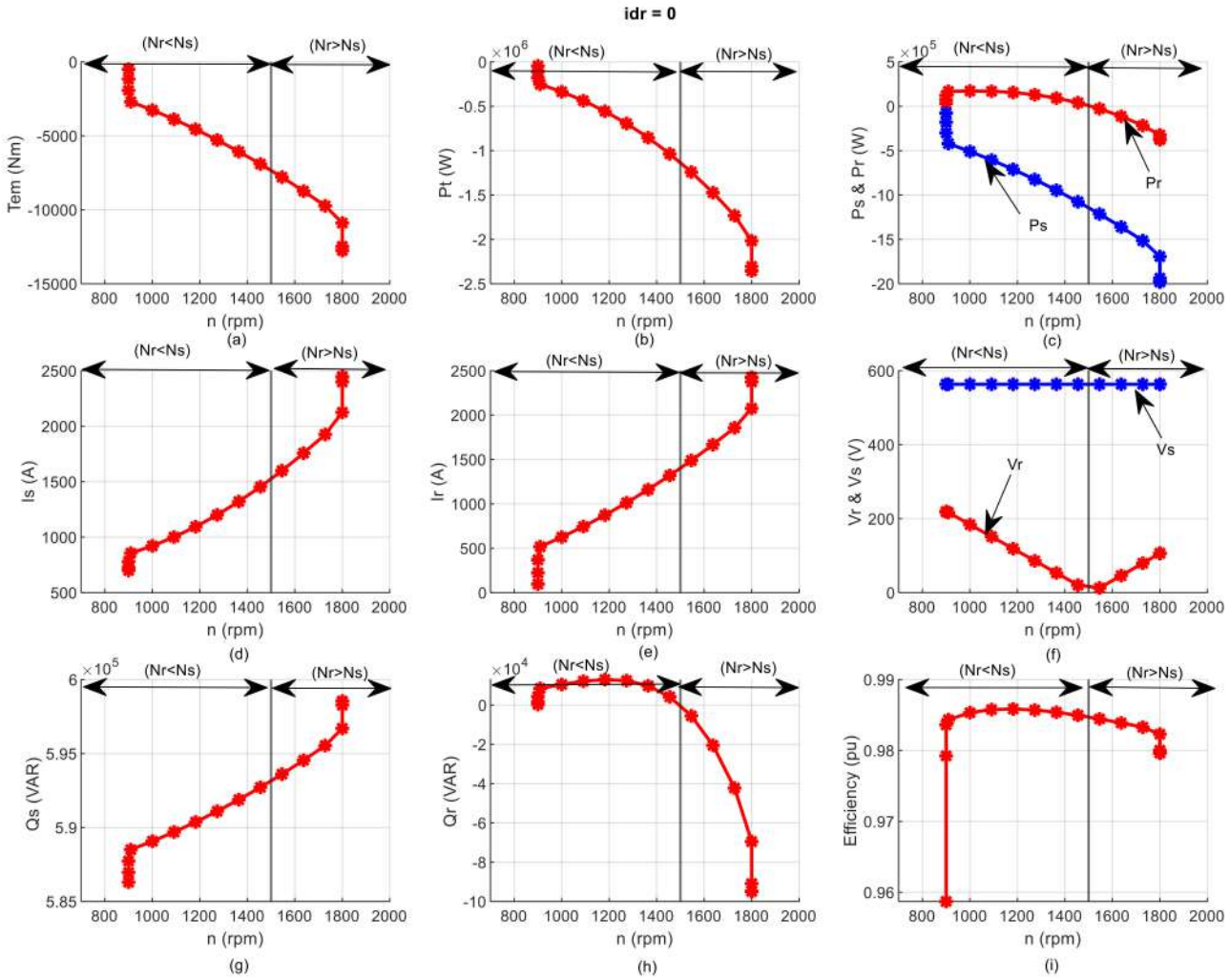

Figure 4. SS Characteristics of 2 MW DFIG Idr = 0; (**a**) Torque, (**b**) Total Power, (**c**) Stator and Rotor Power, (**d**) Stator Current, (**e**)Rotor Current, (**f**) Stator and Rotor Voltage, (**g**) Stator Reactive Power, (**h**) Rotor Reactive Power, (**i**) Efficiency.

Here in Figure 4a, the torque (Tem) is negative so the machine in this case operates as a generator. In Figure 4b, we have the mechanical power (Pt), which is nothing but the product of torque and speed. Then in Figure 4c, we have the active power of the rotor and stator (Pr and Ps). The maximum active power is around 2 MW. Max rotor power is around 400 kW. The active power of the rotor is negative and positive depending on the rotational speed. In Figure 4d,e, we have the stator (Is) and rotor currents (Ir). The rotor current is bigger than the stator current. Accordingly, in Figure 4g,h, we have the stator reactive power (Qs) and rotor reactive power (Qr). We can see that Qs increase with the rise in rotor speed whereas Qr decreases with a rise in rotor speed. Then, in Figure 4f we have the stator (Vs) and rotor voltages (Vr). We can see that the stator is directly connected to the grid, so the stator voltage amplitude is always constant. Whereas the rotor voltage magnitudes depend on the speed. At synchronous speed, it is minimum. At the two extremes, we have high voltages. We are working with a rotor referred to as the stator, so these magnitudes are not real magnitudes. If we convert to the rotor side and work, we will have the voltages very near to stator voltages. Finally, in Figure 4i we have the efficiency of the DFIG at a SS.

Here, we have the mechanical power (P_m), which is nothing but the product of torque and speed. Then we have the active power of the rotor and stator (P_r and P_s). The stator active power is much bigger than the rotor active power. The maximum active power is around 2 MW. Max rotor power is around 400 kW. The active power of the rotor is negative

and positive depending on the rotational speed: the stator currents, red $Q_r = 0$ and blue for $I_{dr} = 0$. When we make $Q_r = 0$, the I_s is lower than when $I_{dr} = 0$. On the contrary, for the rotor current, we see that with $I_{dr} = 0$, the rotor current is lower. Then we have the stator and rotor voltages. We can see that the stator is directly connected to the grid, so the stator voltage amplitude is always constant. Whereas the rotor voltage magnitudes depend on the speed. At synchronous speed, it is minimum. At the two extremes, we have high voltages. We are working with a rotor referred to as the stator, so these magnitudes are not real magnitudes. If we convert to the rotor side and work, we will have the voltages very near to stator voltages. Then we have the reactive power. With $I_{dr} = 0$, we have high reactive power, and with the other generation strategy, which has 0 reactive power. Finally, rotor reactive power behavior in both cases, and finally, we have the efficiency.

The steps followed for the analysis using SS equations are discussed as a flowchart in Figure 5. The left branch discusses the computational method using mathematical equations. The right branch discusses the performance analysis of DFIG using the MATLAB/Simulink model. In the end, the results are compared to validate the simulation.

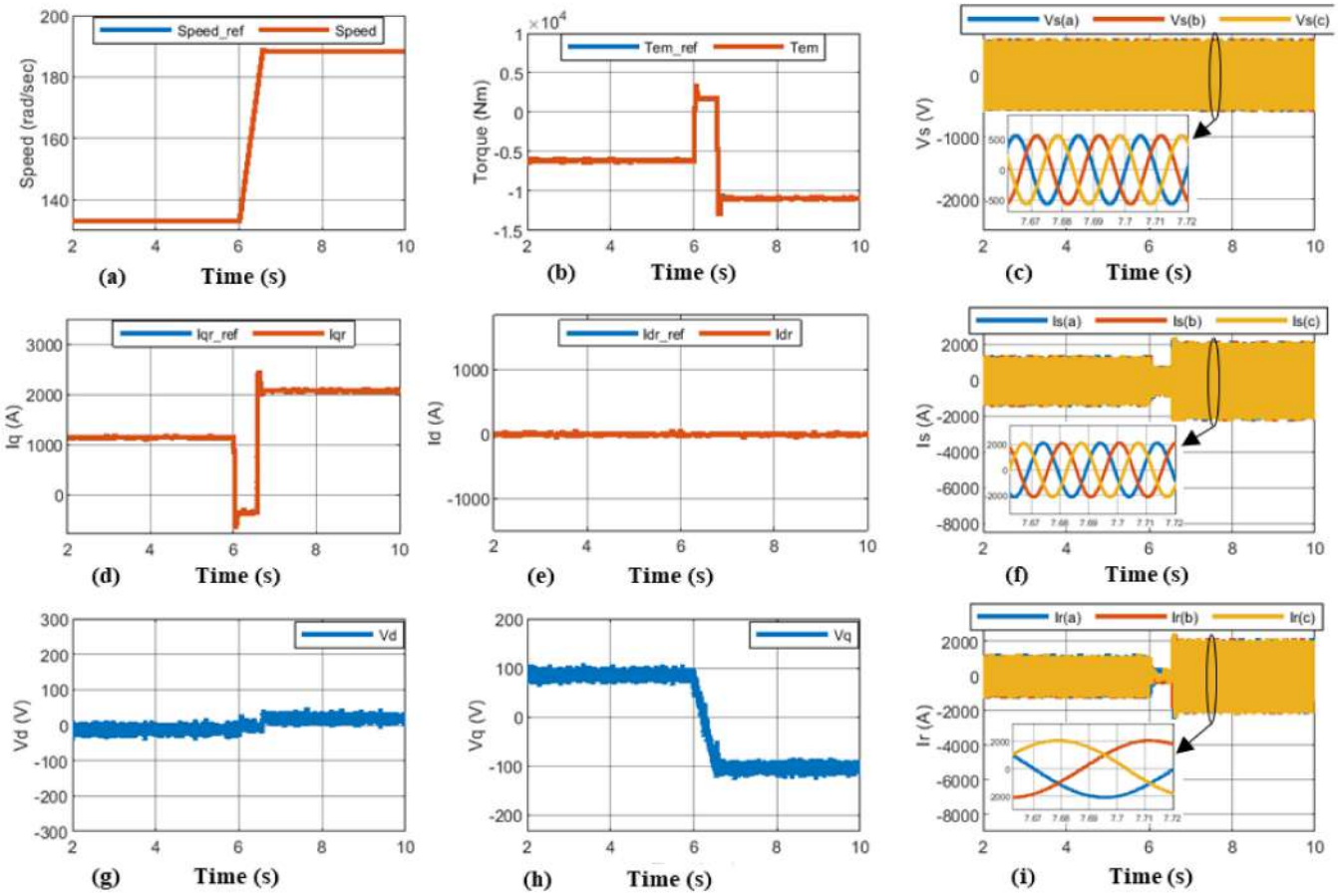

Figure 5. SS response of the simulated system with a rotor speed of 188.5 rad/sec; (**a**) Speed, (**b**) Torque, (**c**) Stator Voltage, (**d**) q-axis Current, (**e**) d-axis Current, (**f**) Stator Current, (**g**) d-axis voltage, (**h**) q-axis Voltage, (**i**) Rotor Current.

4. Results and Discussion

The developed model is simulated in the following procedure for obtaining the results,

Step 1: From the SS graph, the values are selected corresponding to the speed, of 1800 rpm. Thus, the speed reference is given as 1800*(2*pi/60).
Step 2: The rate limiter for speed variation is set with the slew rate of 100 radians per second (100/1).
Step 3: Set the load torque of simulation to −10,894 Nm corresponding to the speed of 1800 rpm. The negative torque signifies generator mode.
Step 4: The time constant of the speed PI regulator is reduced to 1/4th of its value to make the speed regulator work four times faster.
Step 5: Strong perturbation is caused because the machine is directly connected to the grid, which is not done in practical situations. The startup transient is ignored as the focus of this work to analyze the machine under SS.
Step 6: Run the simulation.

4.1. Simulation Results

The simulation results of SSA at two different operating points of 1800 rpm with load torque of −10,894 and 1273.21 rpm with a torque of −5285, can be seen in Figure 6a,b. The change in operating point is initiated at a time instant of 6 s through a step signal. For a smooth transition, a rate limiter has been used with a rate of 100/seconds. The model is run with a reference speed of 1273.21 rpm and torque of −5285 Nm and at 6 s, the rotor reference speed is changed to 188.4 rad/s ((1364 rev/min × 2π rad/rev)/(60s/min) = 188.4 rad/s) corresponding to 1800 rpm. The operating point shifts from subsynchronous mode to super-synchronous mode. The synchronous speed of the machine is 1500 rpm. The new SS is reached at 6.5 s. The speed controller tracks the reference value for both subsynchronous and super-synchronous modes. The machine operates in subsynchronous mode and later switches to super-synchronous speed as per the reference. The rotor and stator currents have the value corresponding to the specific operating point in Figure 5 corresponding to a rotational speed of 1273.2 rpm and 1800 rpm with rotor magnetizing technique (idr = 0). The rotor voltages (sqrt(Vdr^2 + Vqr^2)) also follow the same. The absolute active power and reactive powers of the system will be obtained with correct voltages and currents.

The I_{dref} (Figure 5e) is maintained at 0, as we maintain reactive power at zero during a SS. The I_q current (Figure 5d) varies from 1176 A to 2103 A, to reach the new operating point corresponding to a speed-torque (1800 rpm & −10,602 Nm). I_q is responsible for controlling the torque. The current controllers work properly as the d and q component currents follow the reference. The rotor voltages V_d and V_q (Figure 5g,h) vary in such a way that along with the rotor current, the generator generates the required real power of approximately 130 kw and 323 kw. The stator voltage in Figure 5c is constant with a peak amplitude of 563 V as no variation is made at the stator. The stator current in Figure 5f changes from 1362 A to 2079 A as the stator of the generator nearing synchronous speed draws less power. The rotor current in Figure 5i changes from 1174.5 A corresponding to a SS of 133 rad/sec and during synchronous speed, the frequency of rotor current becomes zero (DC). After crossing synchronous speed, the generator operates at super synchronous speed with a rotor current of 2019 peak amplitude. The machine operates as a conventional 3 phase synchronous generator.

4.2. Comparative Analysis

The steps followed for the analysis using SS equations are discussed in the flowchart, depicted in Figure 6. The left branch discusses the computational method using mathematical equations. The right branch discusses the performance analysis of DFIG using the MATLAB/Simulink model. In the end, the results are compared to validate the simulation.

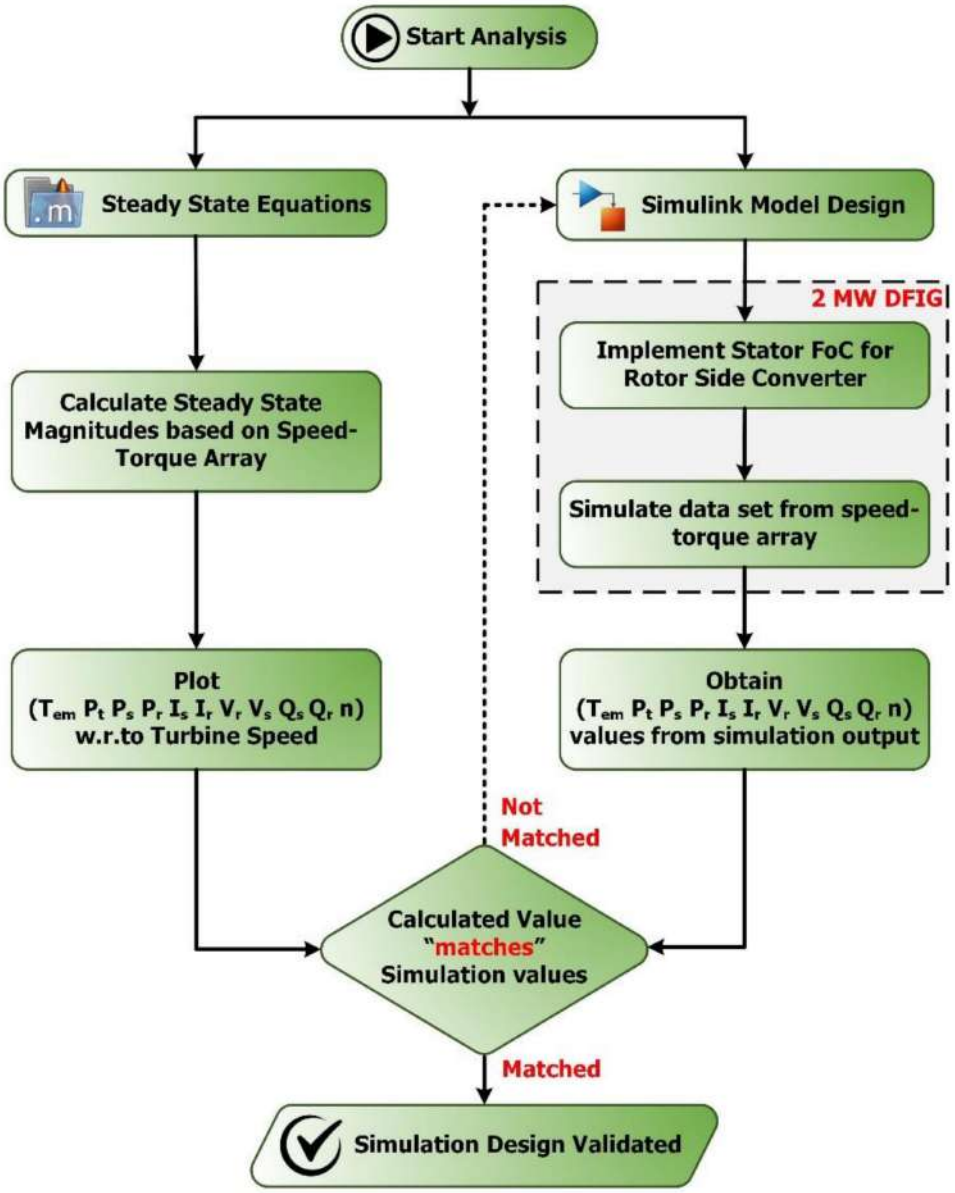

Figure 6. Process of DFIG's SS performance analysis.

The most representative SS magnitudes of DFIG and they are compared to the calculated SS values available in Figure 5 corresponding to Idr = 0 for a rotational speed of 1800 rpm and 1273.21 rpm. It is observed that the SS magnitudes both computed and simulated are similar in Figures 7–14. The results are tabulated for further analysis. The SS magnitudes obtained through programming for two different operating points corresponding to a speed of 1800 rpm and 1273.21 rpm are shown in Figures 7a, 8a, 9a, 10a, 11a, 12a, 13a and 14a. The simulation model is run for these two operating points from 0 s to 6 s for a speed of 1273.21 rpm and from 6 s to 10 s for a speed of 1800 rpm. The most significant magnitudes are shown in Figures 7b, 8b, 9b, 10b, 11b, 12b, 13b and 14b. The values of stator current are calculated to be 1200.52 A, which is similar to the simulated SS value of 1362.82 A for a speed of 1273.21 rpm. Again, for a speed of 1800 rpm, the calculated value of stator current is 2124.85 A and the SS value of 2079.7 A is within comparable limits. Figure 7a,b show the values for comparison.

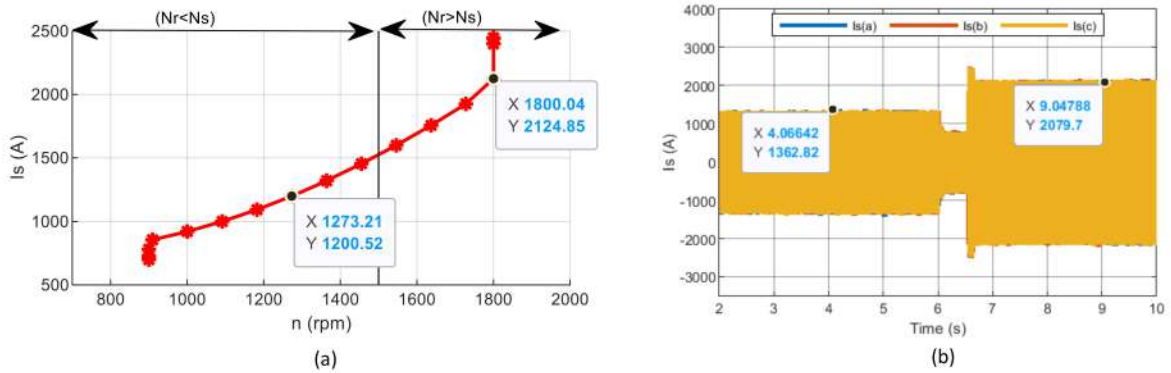

Figure 7. (**a**) Calculated stator current; (**b**) Stator current of the designed system.

The values of rotor current are calculated to be 1011.98 A, which is similar to the simulated SS value of 1214.42 A for a speed of 1273.21 rpm. Again, for a speed of 1800 rpm, the calculated value of stator current is 2076.2 A and the SS value of 2114.37 A is within comparable limits. Figure 8a,b show the values for comparison.

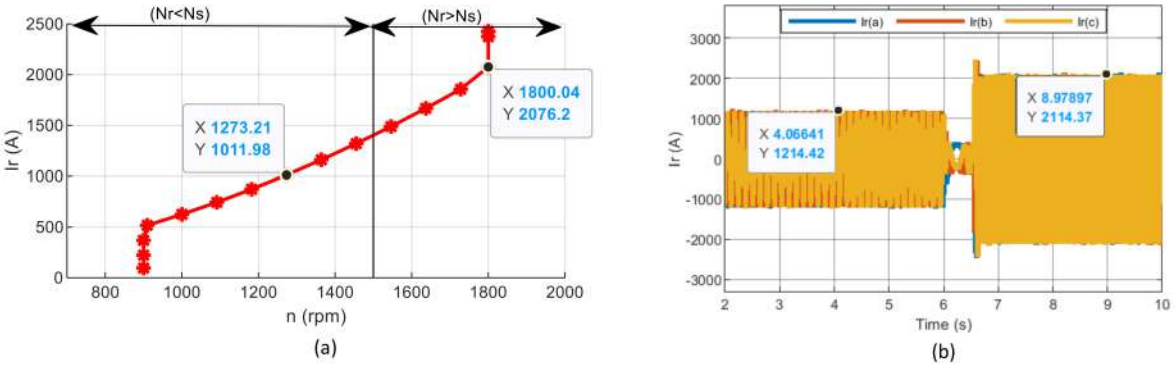

Figure 8. (**a**) Calculated rotor current; (**b**) Rotor current of the designed system.

The values of stator voltage are calculated to be 563.383 V, which is similar to the simulated SS value of 563.382 V for all operating points as the stator voltage remains constant. Figure 9a,b show the values for comparison.

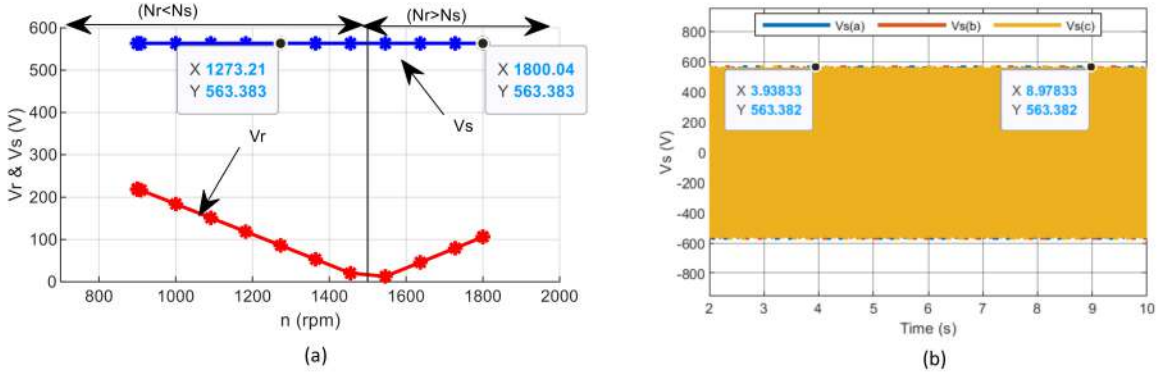

Figure 9. (**a**) Calculated stator voltage; (**b**) Stator voltage of the designed system.

The values of rotor voltages are calculated to be 86.0158 V, which is similar to the simulated SS value of 87.1958 V for a speed of 1273.21 rpm. Again, for a speed of 1800 rpm, the calculated value of stator current is 106.294 V and the SS value of 104.47 V is within comparable limits. Figure 10a,b show the values for comparison.

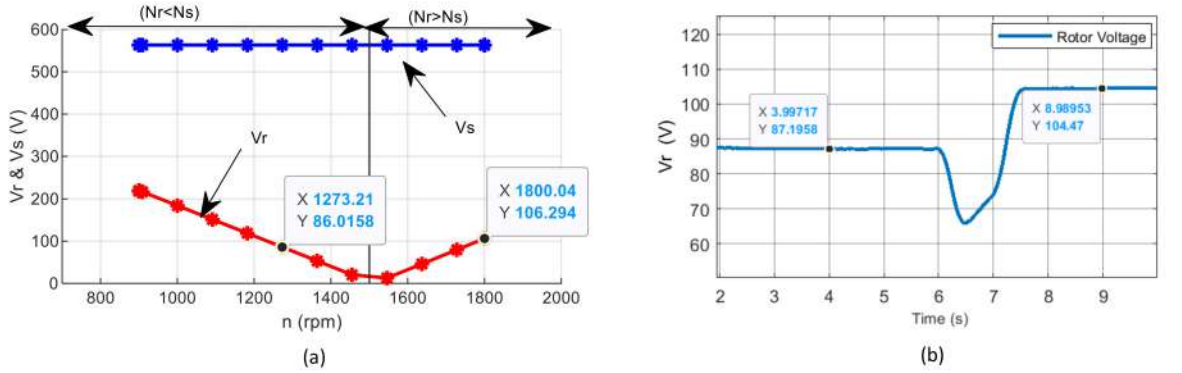

Figure 10. (**a**) Calculated rotor voltage; (**b**) Rotor voltage of the designed system.

The stator real power in Figure 11b, varies from 824.698 kW to 1693.45 kW corresponding to a speed of 133.33 rad/sec (1273.21 rpm) to 188.5 rad/sec (1800 rpm) and is comparable with the calculated value of −824.545 kW and −1693.620 kW as shown in Figure 11a. The stator real power in Figure 12b, varies from 824.698 kW to 1693.45 kW corresponding to a speed of 133.33 rad/sec (1273.21 rpm) to 188.5 rad/sec (1800 rpm). With a transition peak of 261.395 kW. The stator reactive power in Figure 13b, remains constant at 589.357 kVAR. The rotor real power in Figure 11b varies from 130.217 kW to 319.068 kW corresponding to a speed of 133.33 rad/sec (1273.21 rpm) to 188.5 rad/sec(1800 rpm). The rotor reactive power in Figure 13b changes from 14.067 kVAR to −64.57 kVAR to meet the reactive power demands during subsynchronous and super-synchronous conditions.

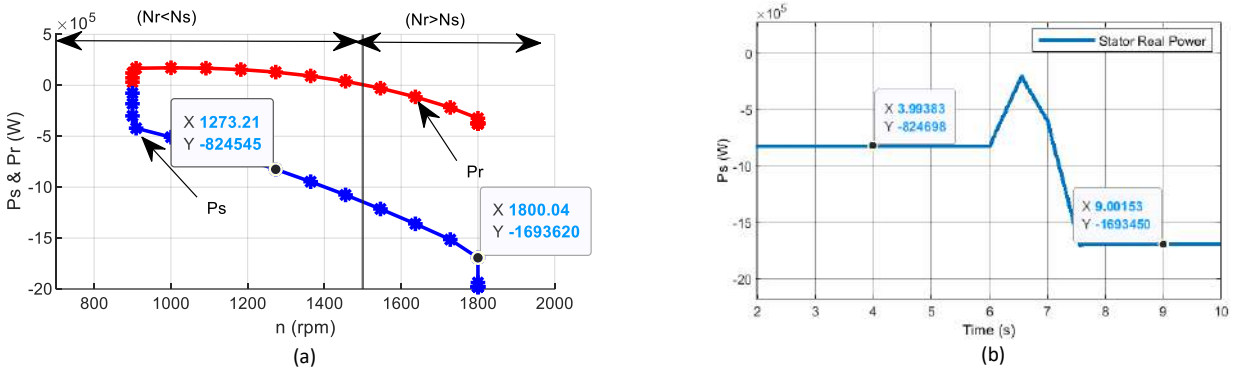

Figure 11. (**a**) Calculated stator real power; (**b**) Stator real power of the designed system.

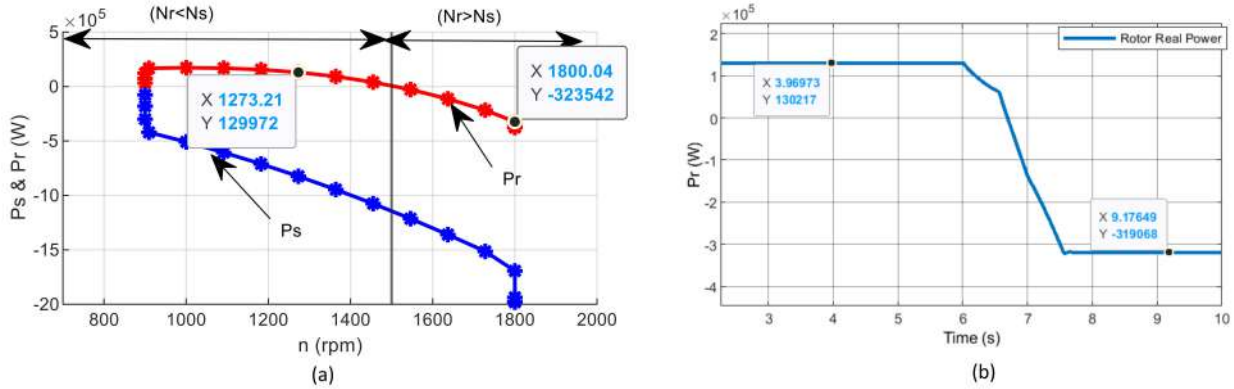

Figure 12. (**a**) Calculated rotor real power; (**b**) Rotor real power of the designed system.

The stator reactive power in Figure 13b, varies from 589.357 kVAR to 590.238 kVAR for change in speed from 1273.21 rpm to 1800 rpm. This is similar to the calculated values of 591.097 kVAR and 596.696 kVAR in Figure 13a.

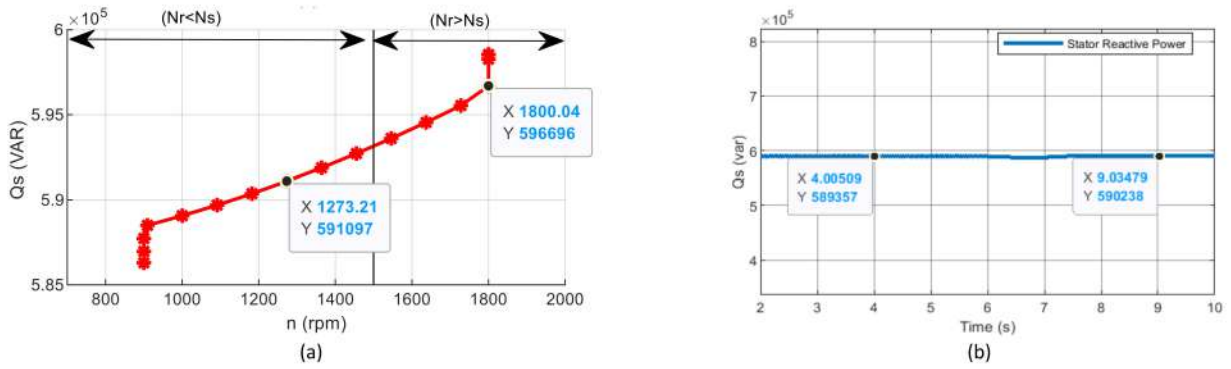

Figure 13. (**a**) Calculated stator reactive power; (**b**) Stator reactive power of the designed system.

The rotor reactive power in Figure 14b changes from 14.067 kVAR to −64.57 kVAR to meet the reactive power demands during subsynchronous and super-synchronous conditions. The values are comparable to the calculated values of 12.4827 kVAR and −69.5111 kVAR in Figure 14a.

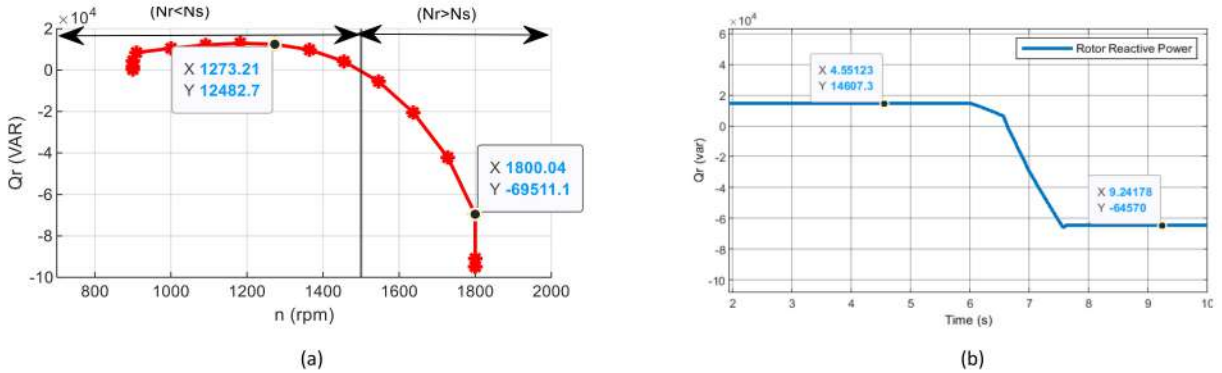

Figure 14. (**a**) Calculated rotor reactive power; (**b**) Rotor reactive power of the designed system.

The values of I_s, I_r, V_s, V_r, P_s, P_r, Q_s, and Q_r obtained through computation and simulation for the specific operating point are tabulated in Table 1. The error between the computed and simulated values are calculated and it is found that an overall error of less than 10% is observed for a speed of 1800 rpm and an error of less than 20% is observed for an operating speed of 1273.21 rpm. Hence, it is established from the acquired results that the designed system is working properly and can be used for future analysis.

Table 1. Comparison of SS magnitudes.

SS Magnitudes	Nr = 1273.21 rpm/T = −5285 Nm			Nr = 1800 rpm/T = −10,894 Nm		
	Computed Values	**Simulated Values**	**Error (%)**	**Computed Values**	**Simulated Values**	**Error (%)**
Stator Current (I_s) (A)	1200.52	1362.82	13.51 ↑↑	2124.85	2079.7	2.12 ↓↓
Rotor Current (I_r) (A)	1011.98	1194.6	18.04 ↓↓	2076.2	2114.37	1.83 ↑↑

Table 1. *Cont.*

SS Magnitudes	Nr = 1273.21 rpm/T = −5285 Nm			Nr = 1800 rpm/T = −10,894 Nm		
	Computed Values	**Simulated Values**	**Error (%)**	**Computed Values**	**Simulated Values**	**Error (%)**
Stator Voltage (V_s) (V)	563.383	563.382	–	563.383	563.382	–
Rotor Voltage (V_r) (V)	86.0158	87.1958	1.37 ↑↑	106.294	104.47	1.71 ↓↓
Stator Real Power (P_s) (W)	−824,545	−824,698	–	−1,693,620	−1,693,450	–
Rotor Real Power (P_r) (W)	129,972	130,217	0.18 ↑↑	−323,542	−319,068	1.38 ↓↓
Stator Reactive Power (Q_s) (VAR)	591,097	589,357	0.29 ↓↓	596,696	590,238	1.08 ↓↓
Rotor Reactive Power (Q_r) (VAR)	12,482.7	14,607.3	17.02 ↑↑	−69,511.1	−64,570	7.10 ↓↓

↑↑ indicates percentage increased from computed value; ↓↓ percentage decreased from the computed value.

5. Conclusions

In this paper, the SS performance analysis of the DFIG based WT with rotor magnetizing strategy I_{dr} = 0 and the DFIG system design in MATLAB/Simulink is presented. For the analysis, a 2 MW DFIG WT was chosen with torque-speed datasets of an MWT 92 Mitsubishi WT design. The SS magnitudes of the DFIG were computed based on SS equations and the values were plotted. These SS values were further used for the validation of the designed system for a specific operating mode corresponding to a rotor speed of 1800 rpm. The simulation results were, in turn, compared with the calculated value and the overall error in SS magnitudes was found to be less than 10% which shows the acceptable performance of the designed system. The designed system can be used by the scientific community for a detailed study of the wind turbine based DFIG such as WT behavior under fault, performance under various test conditions, and for further research on the topic.

Author Contributions: All authors contributed equality in each task towards the paper. More specifically: B.A. and J.P.S.: Page: 16 conceptualization; I.V.: methodology; J.P.S.: software; R.S.R.: validation; J.P.S.: formal analysis; R.S.R.: investigation; B.A.: resources; J.P.S.: data curation; J.P.S. and I.V.: writing—original draft preparation; R.S.R.: writing—review and editing; J.P.S.: visualization; I.V.: supervision; I.V.: project administration; B.A.: funding acquisition; All authors have read and agreed to the published version of the manuscript.

Funding: This research was funded by the Deanship of Scientific Research at Najran University Research Funding Program under the General Research Funding program, grant code (NU/-/SERC/10/649).

Institutional Review Board Statement: Not applicable.

Informed Consent Statement: Not applicable.

Data Availability Statement: Not applicable.

Acknowledgments: The authors are thankful to the Deanship of Scientific Research at Najran University for funding this work under the General Research Funding program grant code (NU/-/SERC/10/649).

Conflicts of Interest: The authors declare that they have no conflict of interest to report regarding the present study.

Nomenclature

i_{dst}	d-axis stator side current (A)
i_{qst}	q-axis stator side current (A)
v_{dst}	d-axis stator side voltage (V)
v_{qst}	q-axis stator side voltage (V)
i_{drt}	d-axis rotor side current (A)
i_{qrt}	q-axis rotor side current (A)
v_{drt}	d-axis rotor side voltage (V)
v_{qrt}	q-axis rotor side voltage (V)
Ψ_{drt}	d-axis rotor flux (Wb)
Ψ_{qrt}	q-axis rotor flux (Wb)
$\left\lvert\vec{\psi}_{st}\right\rvert$	Magnitude of stator flux (Wb)
$\left\lvert\vec{\psi}_{rt}\right\rvert$	Magnitude of rotor flux (Wb)
$\left\lvert\vec{v}_{st}\right\rvert$	Magnitude of stator voltage (V)
$\left\lvert\vec{v}_{rt}\right\rvert$	Magnitude of rotor voltage (V)
$\left\lvert\vec{i}_{st}\right\rvert$	Magnitude of stator current (A)
$\left\lvert\vec{i}_{rt}\right\rvert$	Magnitude of rotor currents (A)
A′,B′,C′	Constants used for calculations
I_{abcst}	Stator Currents (A)
I_{abcgr}	Grid Currents (A)
V_{bus}	DC link voltage (V)
I_{qrt}^{*}	q-axis grid current reference (A)
ω_{mec}^{*}	Rotor electrical speed reference (rad/sec)
K_{Qrt}, K_{Prt}	Constants used to derive the rotor current ref.
p	Number of pole pairs
i_{dgr}	d-axis grid side current (A)
V_{dgr}	d-axis grid side voltage (V)
$L_m\prime$	Mutual Inductance (H)
L_{st}	Stator Inductance (H)
L_{rt}	Stator Inductance (H)
R_{st}	Stator Resistance (Ω)
R_{rt}	Rotor Resistance (Ω)
T_{em1}	Electromagnetic Torque of machine (Nm)
ω_{st}	Frequency of stator voltages and currents (rad/s)
ω_{rt}	Frequency of rotor voltages and currents (rad/s)
ω_{mec}	Rotor electrical speed (rad/s)
s	Slip of the machine
P_{mec}	Mechanical Power at turbine shaft (W)
P_{st}	Active power of the stator (W)
P_{rt}	Active power of the rotor (W)
Q_{st}	Reactive power of the stator (VAR)
Q_{rt}	Reactive power of the rotor (VAR)
η_{DFIM}	Efficiency of the machine
V_{abcst}	Stator voltages (V)
V_{abcgr}	Grid Voltages (V)
I_{abcrt}	Rotor Currents (A)
V_{bus}^{*}	DC link voltage reference (V)
Q_{st}^{*}	Stator reactive power reference (VAR)
K_{Qgr}, K_{Pgr}	Constants used to derive the grid current ref.
e_{drt}, e_{qrt}	Cancellation of cross coupling terms in rotor currents
e_{dgr}, e_{qgr}	Cancellation of cross coupling terms in grid currents
i_{qgr}	q-axis grid side current (A)
V_{qgr}	q-axis grid side voltage (V)

Appendix A

Table A1. Parameters of the proposed DFIG.

Parameters	Ratings
Machine stator frequency in Hz	$*f_{sm} = 50$
Machine stator power in watts	$*P_{sm} = 2 \times 10^6$
Machine rated speed in rpm	$*N_m = 1500$
Machine stator voltage in volts	$*V_{sm} = 690$
Machine stator current in amps	$*I_{sm} = 1760$
Machine torque in Nm	$*T_{em} = 12{,}732$
Poles	$p = 4$
turns ratio (stator to rotor)	$u = 1/3$
Machine rotor voltage in volts	$*V_{rm} = 2070$
Slip (max)	$S_{max} = 1/3$
Machine rotor voltage referred to stator	$V_{rm_stator} = (V_{rm}*s_{max})*u$
Stator resistance in ohms	$R_{st} = 2.6 \times 10^{-3}$
Leakage inductance (stator/rotor) in Henry	$L_{lsr} = 0.087 \times 10^{-3}$
Magnetizing inductance in Henry	$L_m' = 2.5 \times 10^{-3}$
Rotor resistance referred to stator in ohm	$R_{rt} = 2.9 \times 10^{-3}$
Stator inductance in Henry	$L_{st} = L_m' + L_{lsr}$
Rotor inductance in Henry	$L_{rt} = L_m' + L_{lsr}$
DC bus voltage referred to stator in volts	$V_{bus} = V_{rm_stator} \times \sqrt{2}$

* *rated value of the machine*

References

1. Ntanos, S.; Skordoulis, M.; Kyriakopoulos, G.; Arabatzis, G.; Chalikias, M.; Galatsidas, S.; Batzios, A.; Katsarou, A. Renewable Energy and Economic Growth: Evidence from European Countries. *Sustainability* **2018**, *10*, 2626. [CrossRef]
2. Sawant, M.; Thakare, S.; Rao, A.P.; Feijóo-Lorenzo, A.E.; Bokde, N.D. A Review on State-of-the-Art Reviews in Wind-Turbine- and Wind-Farm-Related Topics. *Energies* **2021**, *14*, 2041. [CrossRef]
3. Javadi, M.A.; Ghomashi, H.; Taherinezhad, M.; Nazarahari, M.; Ghasemiasl, R. Comparison of Monte Carlo Simulation and Genetic Algorithm in Optimal Wind Farm Layout Design in Manjil Site Based on Jensen Model. In Proceedings of the 2021 7th Iran Wind Energy Conference (IWEC2021), Shahrood, Iran, 17–18 May 2021.
4. Artigao, E.; Martín-Martínez, S.; Honrubia-Escribano, A.; Gómez-Lázaro, E. Wind turbine reliability: A comprehensive review towards effective condition monitoring development. *Appl. Energy* **2018**, *228*, 1569–1583. [CrossRef]
5. Li, Q.; Cherian, J.; Shabbir, M.S.; Sial, M.S.; Li, J.; Mester, I.; Badulescu, A. Exploring the Relationship between Renewable Energy Sources and Economic Growth. The Case of SAARC Countries. *Energies* **2021**, *14*, 520. [CrossRef]
6. Dao, C.; Kazemtabrizi, B.; Crabtree, C. Wind turbine reliability data review and impacts on levelised cost of energy. *Wind. Energy* **2019**, *22*, 1848–1871. [CrossRef]
7. Justo, J.J.; Mwasilu, F.; Jung, J.W. Doubly-fed induction generator-based wind turbines: A comprehensive review of fault ride-through strategies. *Renew. Sustain. Energy Rev.* **2015**, *45*, 447–467. [CrossRef]
8. Hossain, M.E. A new approach for transient stability improvement of a grid-connected doubly fed induction genera-tor–based wind generator. *Wind Eng.* **2017**, *41*, 245–259. [CrossRef]
9. Quispe, M.I.C.; Cárdenas, F.V.C.; Quispe, E.C. A Method for Steady State Analysis of Doubly Fed Induction Generator. In Proceedings of the 2018 IEEE ANDESCON, Santiago de Cali, Colombia, 22–24 August 2018.
10. Nora, Z.; Nadia, B.; Nadia, B.S.A. Contribution to PI Control Speed of a Doubly Fed Induction Motor. In Proceedings of the 2018 6th International Conference on Control Engineering & Information Technology (CEIT), Istanbul, Turkey, 25–27 October 2018.
11. Nam, N.H. Modeling, Algorithm Control And Simulation Of Variable-Speed Doubly-Fed Induction Generator In Grid Connected Operation. In Proceedings of the 2019 26th International Workshop on Electric Drives: Improvement in Efficiency of Electric Drives (IWED), Moscow, Russia, 30 January–2 February 2019.
12. Zerzeri, M.; Jallali, F.; Khedher, A. Robust FOC Analysis of a DFIM using an SMFO: Application to Electric Vehicles. In Proceedings of the 2019 International Conference on Signal, Control and Communication (SCC), Hammamet, Tunisia, 16–18 December 2019.
13. Naveed, I.; Zhao, G.; Yamin, Z.; Gul, W. Steady State Performance Analysis of DFIG with Different Magnetizing Strategies in a Pitch-Regulated Variable Speed Wind Turbine. In Proceedings of the 2020 4th International Conference on Power and Energy Engineering (ICPEE), Xiamen, China, 19–21 November 2020.
14. Sharawy, M.; Shaltout, A.A.; Abdel-Rahim, N.; Youssef, O.E.M.; Al-Ahmar, M.A. Simplified Steady State Analysis of Stand-Alone Doubly Fed Induction Generator. In Proceedings of the 2021 22nd International Middle East Power Systems Conference (MEPCON), Assiut, Egypt, 14–16 December 2021.

15. Li, S.; Li, L. Steady-state Solution and Evaluation Indices of DFIG Operating at Synchronous Speed (sDFIG). In Proceedings of the 2021 IEEE Sustainable Power and Energy Conference (iSPEC), Nanjing, China, 23–25 December 2021.
16. Arjun, G.T.; Jyothi, N.S.; Neethu, V.S. Vector Control of Doubly fed Induction Machine for an Electric Vehicle Application. In Proceedings of the 2021 International Conference on Recent Trends on Electronics, Information, Communication & Technology (RTEICT), Bangalore, India, 27–28 August 2021.
17. Karthik, D.R.; Kotian, S.M.; Manjarekar, N.S. An Accurate Method for Steady State Initialization of Doubly Fed Induction Generator. In Proceedings of the 2022 IEEE International Conference on Power Electronics, Smart Grid, and Renewable Energy (PESGRE), Trivandrum, India, 2–5 January 2022.

MDPI
St. Alban-Anlage 66
4052 Basel
Switzerland
Tel. +41 61 683 77 34
Fax +41 61 302 89 18
www.mdpi.com

Energies Editorial Office
E-mail: energies@mdpi.com
www.mdpi.com/journal/energies

MDPI
St. Alban-Anlage 66
4052 Basel
Switzerland

Tel: +41 61 683 77 34

www.mdpi.com

ISBN 978-3-0365-6718-1